

# Structural Health Monitoring

8th Asia Pacific Workshop on  
Structural Health Monitoring (8APWSHM),  
Queensland, Australia

Edited by

N. Rajic, M. Veidt, A. Mita,  
N. Takeda, W.K. Chiu

M|R|F

# Structural Health Monitoring

## 8APWSHM

8th Asia Pacific Workshop on Structural Health Monitoring (8APWSHM), proceedings only, Queensland, Australia

Editors

**N. Rajic<sup>1</sup>, M. Veidt<sup>2</sup>, A. Mita<sup>3</sup>, N. Takeda<sup>4</sup>, W.K. Chiu<sup>5</sup>**

<sup>1</sup>Defence Science & Technology Group, Fishermans Bend, Victoria, Australia

<sup>2</sup>School of Mechanical & Mining Engineering, University of Queensland, Queensland, Australia

<sup>3</sup>Department of System Design Engineering, Keio University, Yagami Campus, Yokohama, Japan

<sup>4</sup>Department of Advanced Energy, Graduate School of Frontier Sciences, Division of Transdisciplinary Sciences, The University of Tokyo, Kashiwa, Chiba, Japan

<sup>5</sup>Department of Mechanical & Aerospace Engineering, Monash University, Victoria, Australia

### Peer review statement

All papers published in this volume of “Materials Research Proceedings” have been peer reviewed. The process of peer review was initiated and overseen by the above proceedings editors. All reviews were conducted by expert referees in accordance to Materials Research Forum LLC high standards.

Copyright © 2021 by authors

 Content from this work may be used under the terms of the Creative Commons Attribution 3.0 license. Any further distribution of this work must maintain attribution to the author(s) and the title of the work, journal citation and DOI.

Published under License by **Materials Research Forum LLC**  
Millersville, PA 17551, USA

Published as part of the proceedings series  
**Materials Research Proceedings**  
Volume 18 (2021)

ISSN 2474-3941 (Print)  
ISSN 2474-395X (Online)

ISBN 978-1-64490-130-4 (Print)  
ISBN 978-1-64490-131-1 (eBook)

This book contains information obtained from authentic and highly regarded sources. Reasonable efforts have been made to publish reliable data and information, but the author and publisher cannot assume responsibility for the validity of all materials or the consequences of their use. The authors and publishers have attempted to trace the copyright holders of all material reproduced in this publication and apologize to copyright holders if permission to publish in this form has not been obtained. If any copyright material has not been acknowledged please write and let us know so we may rectify in any future reprint.

Distributed worldwide by

**Materials Research Forum LLC**  
105 Springdale Lane  
Millersville, PA 17551  
USA  
<http://www.mrforum.com>

Manufactured in the United States of America  
10 9 8 7 6 5 4 3 2 1

# Table of Contents

*Preface*

*Committees*

## **Magnetic Pre-Loading for a Tonpilz-Type Acoustic Projector**

Scott D. Moss, Ethan J. G. Ellul, Mason Paxevanos, George Jung, David Munk, Joel Smithard.. 1

## **Topology Optimisation for High Frequency Vibration Energy Harvesting**

David J. Munk, Ethan J. G. Ellul, Scott D. Moss..... 10

## **Comparative Assessment of Distributed Strain Measurement Technologies**

Kieran Pryor, Matthew Stevens, Michael Forsey, Suzana Turk ..... 21

## **Comparative Evaluation of a High Operating Temperature Midwave Infrared Detector for Automated Non-Destructive Inspection of Composite Damage**

Jaslyn Gray, Michael Woodrow, Cédric Rosalie, Nik Rajic..... 29

## **Residual Stress Measurement of Additively Repaired Ti-6Al-4V Using Fibre Optic Sensing**

Matthew Stevens, Kieran Pryor, Suzana Turk ..... 37

## **Trans-Jacket Fibre Bragg Gratings for In-Situ Health Monitoring of Defence Platforms in Harsh Environments**

Naizhong Zhang, Claire Davis, Chiu Wing Kong, Suzana Turk ..... 45

## **Low-Energy Sonic Thermographic Inspection of Impact Damage in Aerospace Composites**

Kelly A. Tsoi, Chris Brooks, Nik Rajic, Cedric Antolis..... 53

## **A Machine Learning Approach for Anaerobic Reactor Performance Prediction Using Long Short-Term Memory Recurrent Neural Network**

Benjamin Steven Vien, Leslie Wong, Thomas Kuen, L. R. Francis Rose, Wing Kong Chiu ..... 61

## **Development of Scum Geometrical Monitoring Beneath Floating Covers Aided by UAV Photogrammetry**

Leslie Wong, Benjamin Steven Vien, Yue Ma, Thomas Kuen, Frank Courtney, Jayantha Kodikara, Francis Rose, Wing Kong Chiu..... 71

## **Quasi-Active Thermography for Structural Health Assessment of Large Geomembranes**

Yue Ma, Leslie Wong, Benjamin Steven Vien, Thomas Kuen, Nik Rajic, L.R. Francis Rose, Jayantha Kodikara, Wing Kong Chiu..... 79

## **Quantitative Monitoring of Osseointegrated Implant Stability Using Vibration Analysis**

Shouxun Lu, Benjamin Steven Vien, Matthias Russ, Mark Fitzgerald, Wing Kong Chiu ..... 87

## **Acoustic Emission of Metallic Specimen with Surface Defect During Fatigue Crack Growth**

X. Yao, B.S. Vien, N. Rajic, L.R.F. Rose, C.H.J. Davies, W.K. Chiu ..... 95

## **Computational Study of Scattering Elastic Waves Due to a Tereido Marine Borer-Like Cylindrical Defect Embedded in an Isotropic Solid Cylinder**

Ahmed Murgab Mohammed Mahil, Wing Kong Chiu, Benjamin Vien..... 105

<b>Estimation of Maximum Drift of MDOF Shear Structures Using Only One Accelerometer</b> Kangqian Xu, Akira Mita.....	113
<b>Life-Cycle Monitoring of CFRP using Piezoelectric Sensors Network</b> Xiao Liu, Yishou Wang, Xinlin Qing .....	121
<b>Assessment of the Structural Integrity of Timber Utility Poles Using Ultrasonic Waves</b> Jad El Najjar, Samir Mustapha.....	131
<b>Monitoring of the Operational Conditions in Steel Pipes Using Fiber Optic Sensors</b> Michel Saade, Samir Mustapha.....	146
<b>Gaussian Mixture Model Based Damage Evaluation for Aircraft Structures</b> Qihui Xu, Shenfang Yuan, Yuanqiang Ren .....	154
<b>In-Situ Strain Monitoring in Deltoid of Composite T-joints using Optical Fiber</b> Shinsaku Hisada, Shu Minakuchi, Nobuo Takeda .....	161
<b>A Nonlinear Cable Bracing Inerter System for Vibration Control</b> Xinlei Ban, Songtao Xue, Jianfei Kang, Kohju Ikago, Liyu Xie .....	170
<b>Estimation Method of Maximum Inter-Story Drift Angle of Wood-Frame House using Two Accelerometers</b> Ryusei Fukuzawa, Akira Mita, Tomonori Murakami .....	179
<b>Acoustic Emission-Based Diagnosis Using AlexNet: How Wave Propagation Effects Classification Performance</b> Sebastian Felix Wirtz, Sevki Onur Doruk, Dirk Söffker.....	186
<b>Improving the Drive-by Bridge Inspection Performance by Vehicle Parameter Optimization</b> Yifu Lan .....	195
<b>Reinforcement Learning for Structural Health Monitoring based on Inspection Data</b> Simon Pflingstl, Yann Niklas Schoebel, Markus Zimmermann .....	203
<b>Optimal Waiting Position of a Home Robot for Risk Communication Considering Behavior Patterns of an Occupant</b> Akira Mita, Keita Watanabe, Ami Ogawa .....	211
<b>Preventing Deterioration of Active Vibration Control Effect Due to Aging Deterioration and Damage based on Deep Learning</b> Miao Cao, Songtao Xue .....	217
<b>Evaluation of Measurement Accuracy of the MEMS Accelerometer for Long Period and Large Amplitude Vibration</b> Kenta Hirai, Hiroaki Harada, Hirotaka Imaeda, Akira Mita, Takeshi Suzuki, Hironobu Yao, Shinji Kitagawa, Minoru Kakinuma, Yoshiyuki Komiya.....	225
<b>Vibration-Based Detection of Loosened Bolts on Pipes Attached to Bridges</b> Kobayashi Daiki, Ikeguchi Yuta, Nakagawa Masafumi, Aratake Atsushi .....	233
<b>Extraction of Parameters for 90-degree Turn Prediction Using the IMU-based Motion Capture System</b> Ami Ogawa, Kanako Takeda, Akira Mita.....	241

<b>Analysis of CFRP Laminates Properties under Different Layup Structure using Finite Element Analysis</b>	
Xinye Liu, Jinhui Cai, Jiusun Zeng, Fang Ye, Wing Chiu.....	249
<b>Seismic Fragility Analysis of Mid-Story Isolation Buildings</b>	
Xiao Song, Songtao Xue .....	255
<b>Optimal Design of Tuned Mass Damper Inerter for Base-Isolated Buildings</b>	
Dawei Li, Kohju Ikago, Songtao Xue .....	263
<b>A 3D Printed, Constriction-Resistive Sensor for the Detection of Ultrasonic Waves</b>	
Saeb Mousavi, Philippe Blanloeuil, Thailammai Vinoth, David Howard, Chun H. Wang .....	272
<b>Damage Identification of High-speed Maglev Guideway Girder Based on Modal Identification</b>	
XiangYun Kong, JingYu Huang, XiaoNong Wang, ShuoWei Wang, Liang Zhao, ZhiHong Fang.....	278
<b>Changes in Center of Mass during Preliminary Motion for Prediction of Direction Change</b>	
Nene Sugimoto, Ami Ogawa, Akira Mita.....	287
<b>Innovation and Practice of Cable-Pylon Anchorage Zone Using Group Aggregated Anchor System</b>	
Yonggao Yin, Qian Li, Jiangguo Lv, Zhu Yu.....	294
<b>Experimental Research on the Bearing Capacity of the Widening Segment of Precast Small Box Girder</b>	
Liqiao Xia, Qian Li, Han Ding, Zengshun Tian.....	302
<b>Experimental Research on the Effectiveness of Speed Reduction Markings based on Drivers' Operating Performance: A Driving Simulation Study</b>	
Han Ding, Li Cui, Xiaohua Zhao, Wanheng Li .....	311
<b>Numerical Simulation on Micro-damage Detection In CFRP Composites Based on Nonlinear Ultrasonic Guided Waves</b>	
Chang Jiang, Weibin Li, Mingxi Deng, Ching-Tai Ng .....	325
<b>Novel Outside-Facility Renovation Technology to Improve Cost-Effectiveness by Long-Term Safe Use</b>	
Masaki Waki, Soichi Ishikawa, Gen Kobayashi, Ryouichi Kaneko, Hiroaki Tanioka.....	331
<b>Technique for Analyzing Relationship Between Unbalanced Load and Structural Deterioration in Outside Facilities</b>	
Soichi Ishikawa, Gen Kobayashi, Masaki Waki, Ryouichi Kaneko, Hiroaki Tanioka.....	337
<b>Structural Health Monitoring (SHM) of Space Structures</b>	
Aswin Haridas, Holger Speckmann .....	343
<b>Research on Fatigue Life of Lifting Equipment Based on Nonlinear Cumulative Damage Theory</b>	
Li Chen, Keqin Ding .....	352

*Keyword Index*  
*About the Editor*

## Preface

The year 2020 will long be remembered for the COVID19 pandemic. The 8th Asia-Pacific Workshop on Structural Health Monitoring (8APWSHM) was scheduled to take place from the 9<sup>th</sup> to 11<sup>th</sup> of December 2020 in Cairns, Queensland, Australia. However, extensive travel restrictions and border closures forced by the pandemic left the committee with a choice between cancelling the workshop and continuing with a “proceedings-only” event. The committee chose the latter, mindful that the work of the SHM community can and must continue in spite of lock-downs, social-distancing and border closures. We are very grateful to the workshop participants for submitting their work and to the reviewers for their time and dedication in assessing submissions. The papers in this collection reflect work which has been assessed as technically original and significant.

Structural health monitoring is multi-disciplinary. For it to be successfully developed and implemented in a practical timeframe requires constructive engagement amongst a diverse spectrum of academics, researchers, original equipment manufacturers (OEMs) and end-users, civilian and military alike. Basic and applied research is necessary to develop and demonstrate SHM concepts and systems that are capable of satisfying stringent sensitivity, reliability and confidence requirements.

The OEMs and end-users have a critical role in helping define the problems, establish the requirements and the practical limitations, and to assist the development of business cases for technology insertion. These interactions foster the ‘technology pull’ required to facilitate rapid implementation of technology.

We wish to thank the following sponsors for their contribution to the success of this event:

- The Defence Science and Technology Group
- Department of Mechanical and Aerospace Engineering, Monash University
- US Navy Office of Naval Research – Global (ONR-Global)

We wish also to express our gratitude to the reviewers, contributors and participants, without whom the 8APWSHM proceedings would not have been possible. Finally, a special thanks to the Secretariat, Ms Gillian Chin for her tireless effort in keeping things on track which was crucial to managing the submissions and producing these proceedings.

**Dr Nik Rajic**

Aerospace Division  
Defence Science and Technology Group  
Fishermans Bend, Victoria, Australia

**Prof Martin Veidt**

Department of Mechanical & Mining Engineering  
Queensland University  
St. Lucia, Queensland  
Australia

**Prof Wingkong Chiu**

Department of Mechanical & Aerospace Engineering  
Monash University  
Clayton, Victoria  
Australia

**Prof Akira Mita**

Department of System Design Engineering  
Keio University  
Yokohama, Japan

**Prof Nobuo Takeda**

Department of Advanced Energy  
Graduate School of Frontier Sciences  
The University of Tokyo  
Japan

# 8APWSHM 2020 COMMITTEE

## Organising Committee Workshop Chairpersons

**N. Rajic**  
Defence Science  
and Technology  
Group, Australia

**M. Veidt**  
Queensland  
University,  
Australia

**W.K. Chiu**  
Monash  
University,  
Australia

**A. Mita**  
Keio University,  
Japan

**N. Takeda**  
University of  
Tokyo, Japan

## Local Organising Committee

T. Chan (QUT, Australia)

J. Kodikara (Monash University, Australia)

S. Moss (DSTG, Australia)

C. Davis (DSTG, Australia)

Y. Lu (Monash University, Australia)

C. Rosalie (DSTG, Australia)

## Conference Secretariat

G. Chin (Monash University, Australia)

## International Organising Committee

D. Adams (Vanderbilt University, USA)

S. Alampalli (New York State Department of  
Transportation, USA)

C. Boller (Universität des Saarlandes, Germany)

M. Buderath (Airbus, Germany)

F.K. Chang (Stanford University, USA)

M. Derriso (USAF, AFRL, USA)

K.Q. Ding (China Special Equipment Inspection  
and Research Institute, China)

S.S. Ding (CRRC

Qingdao Sifang Co Ltd, China)

V. Giurgiutiu (University of  
South Carolina, USA)

M. Gresil (University of Manchester, UK)

A. Guemes (Universidad Politecnica  
de Madrid, Spain)

P. Huthwaite (Imperial College, UK)

H. Li (Harbin Institute of Technology, China)

C. Lissenden (Penn State University, USA)

Y.C. Koay (VicRoads, Australia)

C.G. Koh (National University of Singapore,  
Singapore)

D. Le (Texas Technical University, USA)

V. Le Cam (IFSTTAR, Nantes, France)

Y. Lei (Xiamen University, China)

K. Loh (University of California,  
San Diego, USA)

J.Lynch (University of Michigan, USA)

A. Mal (University of California,  
Los Angeles, USA)

H. Muruyama (The University of Tokyo, Japan)

T. Nagayama (The University of Tokyo, Japan)

W. Ostachowicz (Polish Academy  
of Sciences, Poland)

B. Prosser (NASA Langley Research  
Center, USA)

L. Richards (NASA Armstrong Flight Research  
Center, USA)

N. Salowitz (University of Wisconsin, USA)

L. Salvino (US Office of Naval Research, USA)

H. Sohn (KAIST, Korea)

H. Speckmann (Airbus Operations GmbH,  
Germany)

D. Stargel (USAF, AFOSR, USA)

Z. Su (Hong Kong Polytechnic University,  
Hong Kong)

M. Todd (University of California,  
San Diego, USA)

H. Widyastuti (Sepuluh Nopember Institute of  
Technology, Indonesia)

S.T. Xue, (Tohoku Institute of Technology,  
Sendai, Japan)

F.G. Yuan (North Carolina State  
University, USA)

S.F. Yuan (Nanjing University of Aeronautics  
and Astronautics, China)

## Sponsors

The Organising Committee would like to express our sincere appreciation to the following sponsors:



**Australian Government**

**Department of Defence**  
Science and Technology



# Magnetic Pre-Loading for a Tonpiliz-Type Acoustic Projector

Scott D. Moss<sup>a\*</sup>, Ethan J. G. Ellul<sup>b</sup>, Mason Paxevanos<sup>c</sup>, George Jung<sup>d</sup>,  
David Munk<sup>e</sup>, and Joel Smithard<sup>f</sup>

Defence Science and Technology Group, Aerospace Division, 506 Lorimer Street, Fishermans  
Bend, Victoria, Australia, 3207

<sup>a</sup>scott.moss@dst.defence.gov.au, <sup>b</sup>ethan.ellul@dst.defence.gov.au, <sup>c</sup>mason.pax@gmail.com,  
<sup>d</sup>george.jung@dst.defence.gov.au, <sup>e</sup>david.munk@dst.defence.gov.au,  
<sup>f</sup>joel.smithard@dst.defence.gov.au

\* Corresponding author. Tel.: +61-3-9626-7958; fax: +61-3-9626-7089.

© 2020 Commonwealth of Australia

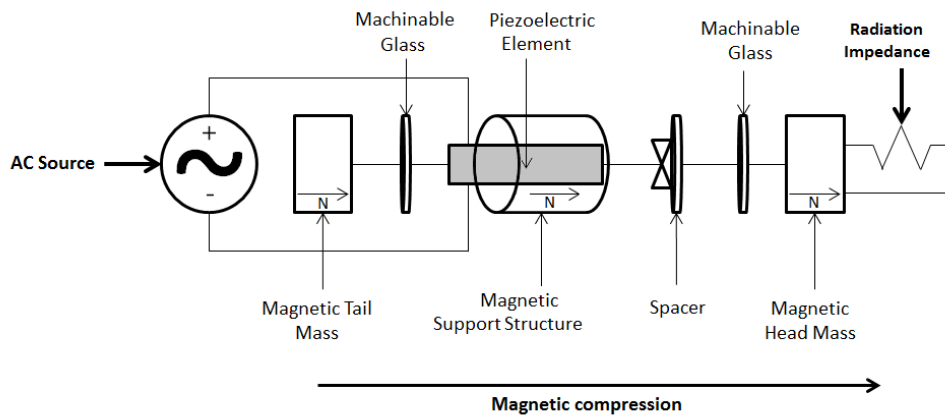
**Keywords:** Magnetic Force, Tonpiliz, Acoustic Projector, Relaxor Ferroelectric Single Crystal

**Abstract.** This paper describes a new magnet-based method for applying a compressive pre-load to the piezoceramic elements of a Tonpiliz-type acoustic projector, with the advantage of lower damping due to mechanical friction and a greater range of unhampered resonant motion since no plate spring is required. The Tonpiliz-type acoustic projector can be applied to structural health monitoring studies involving air coupled ultrasound. Acoustic model predictions and the measured behaviour of a relaxor ferroelectric single crystal (RFSC) based prototype device, operating in air, are presented and show good correlation. With a 5 V drive, at 9420 Hz resonance, the prototype device generates a sound pressure level of 113 dB measured at an axial distance of 5 mm. The maximum peak tip displacement of the device's head mass is predicted to be 0.7  $\mu\text{m}$  at resonance. This is well within the 2  $\mu\text{m}$  displacement produced by the 90 N magnetic pre-load, thus protecting the RFSC ceramic element from damaging tensile stress.

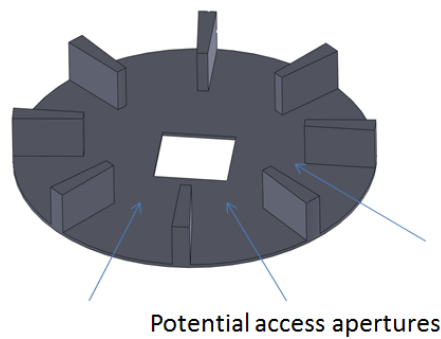
## Introduction

Tonpiliz acoustic projector designs typically use an axial bolt/nut, known as a tie-rod, to provide a static compressive pre-load to their constituent piezoceramic drive elements [1-3]. This compression prevents the elements from being driven into tension where they will likely fail. The resonant behaviour of Tonpiliz designs is accommodated via a plate spring positioned mechanically in series with the piezoelectric drive elements [1]. The greater the pre-load, the greater the potential amplitude of operation. Tonpiliz projectors are often associated with undersea operation [4,5], however they can also operate in air as an acoustic source for structural inspection techniques [6-8]. Recently, relaxor ferroelectric single crystals (RFSC) have been explored for use in electroacoustic applications including Tonpiliz projectors, with their giant piezoelectric properties and high coupling coefficients proving beneficial [9-11]. The magnetic pre-loading approach described in this paper, and reported in reference [12], offers an alternate method for mechanically compressing the piezoceramic elements in an acoustic projector, permitting a simple, compact design with less frictional loss. The principles of operation will be discussed next, followed by a discussion of a multiphysics model developed for the prototype device.

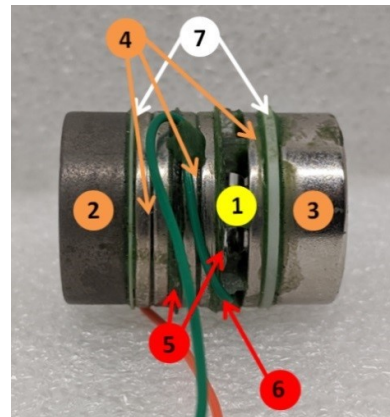
The principle design features for the magnetic pre-loading approach are shown in Fig. 1. The magnetic support structure depicted schematically in Fig. 1a is a series of ring magnets around a rectangular piezoelectric plate-element. The head magnet is attracted to the magnetic support structure, applying a compression to both the piezoceramic (RFSC hereafter) element and the spacer. The tail magnet completes the magnetic circuit. An example spacer is shown in Fig. 1b, with vertical ligaments that are designed to have a mechanical stiffness approximately ten times less than the crystal transducer. The ligament arrangement also protects the RFSC element from bending stress if the device is mounted horizontally. The centre of the spacer contains a square hole which aids crystal positioning during device manufacture. Fig. 1c shows a photograph of a prototype device, the tail and head magnets (labelled ‘2’ and ‘3’ respectively) having 20 mm diameter, the hidden RFSC element (labelled ‘1’), and the thin disks of machinable glass (MACOR™ [13], labelled ‘7’) that protect the element from damage during mechanical loading.



(a)



(b)



(c)

Figure 1. (a) Schematic of the magnetically pre-loaded Tonpilz-type acoustic projector. (b) Schematic of the polycarbonate spacer. (c) Photograph of a prototype device showing: 1) Relaxor ferroelectric single crystal located inside the device, i.e. not visible, 2) SmCo base mass, 3) NdFeB head mass, 4) high temperature NdFeB rings, 5) polycarbonate spacers, 6) aperture in polycarbonate support allowing wire access, 7) machinable glass disks.

*Table 1. Physical properties of a free RFSC element.*

Physical Property	Value for (011) Mn-PMN-PZ-PT
Relative Permittivity, $\Sigma_{33}^T$	2500
Phase-Transition / Curie Temperatures, $T_{R-T}/T_C$ (°C)	145/200
Coercive Field, $E_c$ (kV/cm)	6
Piezo Constant, $d_{32}$ (pC/N)	-900
Coupling Factor, $k_{32}$	0.86
Compliance, $s_{22}^E$ ( $10^{-12}$ m <sup>2</sup> /N)	69
Mechanical Quality, $Q_m$	1000

**Modelling**

This section will discuss the multiphysics model developed to predict the behaviour of the acoustic projector shown in Fig. 1. The frequency-domain model developed for the prototype device couples (i) solid-mechanics, (ii) piezoelectrics, and (iii) pressure-acoustics in the air domain, and follows the approach described in reference [14]. Material properties for the RFSC element were taken from reference [15], with the more important material properties reproduced in Table 1. The model mesh used is shown in Fig. 2a, and has 75k elements. The mesh density of the hemispherical air domain was determined via a rule that there should be at least 6 nodes per wavelength for the highest modelled frequency,  $f_{MAX} = 12$  kHz. The radius of the air domain was set to  $r_{AIR} = \{2(c_{AIR}/f_{MAX})\}$  where  $c_{AIR} = 330$  m/s. Figure 2b shows a close-up of the modelled prototype. Only the dynamic parts of the device were included in the model: the head magnet shown in pink, the RFSC element  $12 \times 4 \times 4$  mm<sup>3</sup>, and four  $1 \times 1 \times 1$  mm<sup>3</sup> polymer cubes approximating the effect of the eight vertical polycarbonate ligaments shown in Fig. 1b. The modelled peak drive voltage was assumed to be 5 V. Total mechanical damping for the prototype device was approximated by applying an isotropic structural loss factor (inverse of quality factor) to the RFSC element. The yellow coloured boundaries shown in Fig. 2b were set as fixed constraints. The modelled frequency range was 8-12 kHz, and using 0.025 kHz steps with 147k degrees-of-freedom the model took approximately 16 minutes to solve on a modern desktop PC.

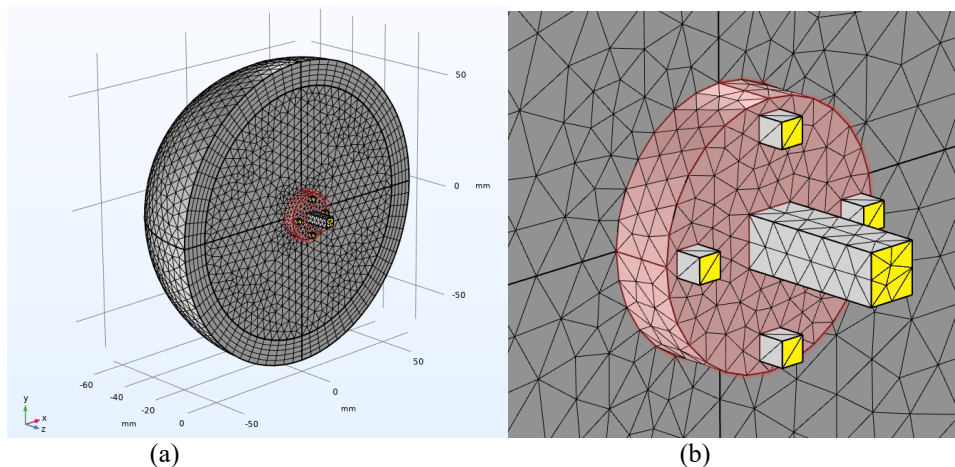


*Figure 2. (a) Mesh used for multi-physics modelling of the acoustic projector, and (b) close-up showing the modelled prototype.*

## Experimental

This section will present a brief overview of the device construction, and discuss the experimental arrangement used to characterise the acoustic behaviour of the prototype device.

As mentioned earlier, the prototype device shown in Fig. 1c uses an RFSC element being (011) poled Mn-PMN-PZ-PT having dimensions  $12 \times 4 \times 4 \text{ mm}^3$ . An impedance sweep for a free RFSC element is provided in Fig. 3 and shows an impedance of  $756 \text{ k}\Omega$  at  $1000 \text{ Hz}$ , equivalent to a free capacitance of  $214 \text{ pF}$ . The prototype device was assembled using a structural adhesive (Click Bond CB359) with the RFSC element, magnets, and machinable glass disks bonded into place. Wires were connected to the RFSC element using silver epoxy (Chemtronics CW2400). After assembly, one week was allowed for the adhesives to cure at room temperature, after which the measured capacitance reduced to  $\sim 152 \text{ pF}$ . The magnetic arrangement for the prototype device uses a samarium cobalt (SmCo) base mass, a neodymium boron iron (NdFeB) head mass, and high temperature NdFeB rings. The compressive force produced by the magnetic arrangement is estimated at  $90 \text{ N}$ , producing an estimated  $2 \text{ }\mu\text{m}$  of compressive displacement on the RFSC element.

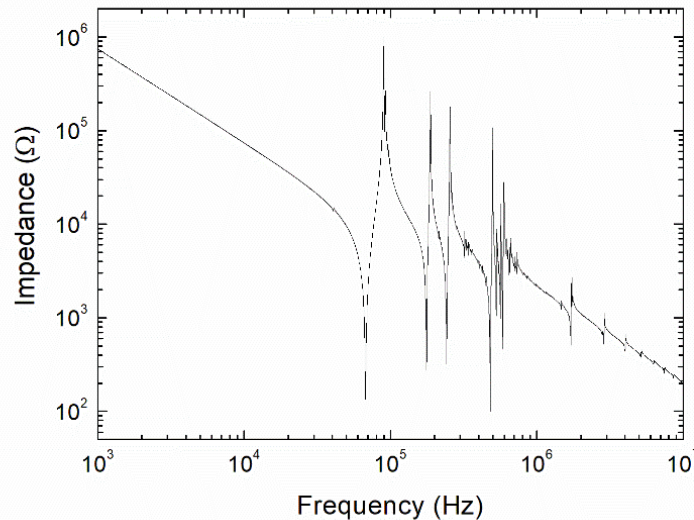
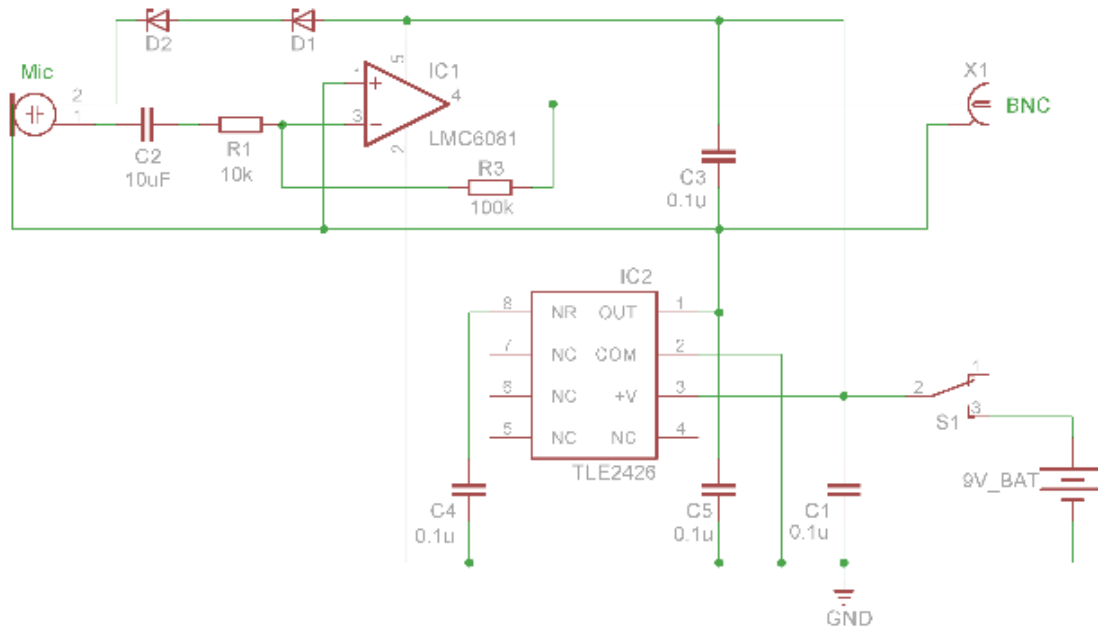


Figure 3. Measured impedance of a  $12 \times 4 \times 4 \text{ mm}^3$  Mn-PMN-PZ-PT element.

A miniature high-performance microphone (Knowles Zero-Height SiSonic, SPU0410LR5H-QB) was used to measure acoustic pressure in air. The microphone has a reasonably flat sensitivity curve  $\pm 2 \text{ dB}$  between  $0.1\text{-}10 \text{ kHz}$ , and can also be used to measure ultrasonic frequencies up to  $80 \text{ kHz}$ . Figure 4a shows a schematic of the  $10 \times$  gain preamplifier circuit built to power and interrogate the microphone. The circuit was designed to run off a  $9 \text{ V}$  battery and uses a voltage splitter to produce a symmetrical  $\pm 4.5 \text{ V}$  supply for the amplifier. Power to the microphone is supplied via two forward biased Zener diodes, limiting the voltage to less than  $3.6 \text{ V}$ . The direct current (DC) blocking capacitor was chosen so that its effective impedance is insignificant at the frequencies of interest. A photograph of the sound measurement arrangement is shown in Fig. 4b, with a prototype device mounted on a large steel backing plate, and the gap between the prototype device and the microphone measured with an error of  $\pm 0.25 \text{ mm}$ . The drive signal for the prototype device was continuous wave with  $5 \text{ V}$  peak. The reference level for acoustic sound pressure measurement in air is  $20 \text{ }\mu\text{Pa}$ ; the sound pressure level (SPL) of  $1 \text{ Pa}$  can hence be found via the calculation  $20 \times \log(1 \text{ [Pa]}/0.00002 \text{ [Pa]}) = 94 \text{ dB SPL}$ . The voltage

reference level for dBV is 1 V, dividing by 20 and taking the inverse log we find -38 dBV = 0.0126 V. Therefore, at 1 Pa, the sensitivity is 0.0126 V/Pa.



(a)



(b)

Figure 4. (a) Microphone circuit, and (b) sound measurement arrangement.

## Results and discussion

The measured acoustic response of the prototype device is discussed including the measured quality factor, which is important for accurate modelling. A comparison with the model predicted acoustic pressure and sound pressure levels is undertaken, and the predicted acoustic power and head mass displacements are discussed.

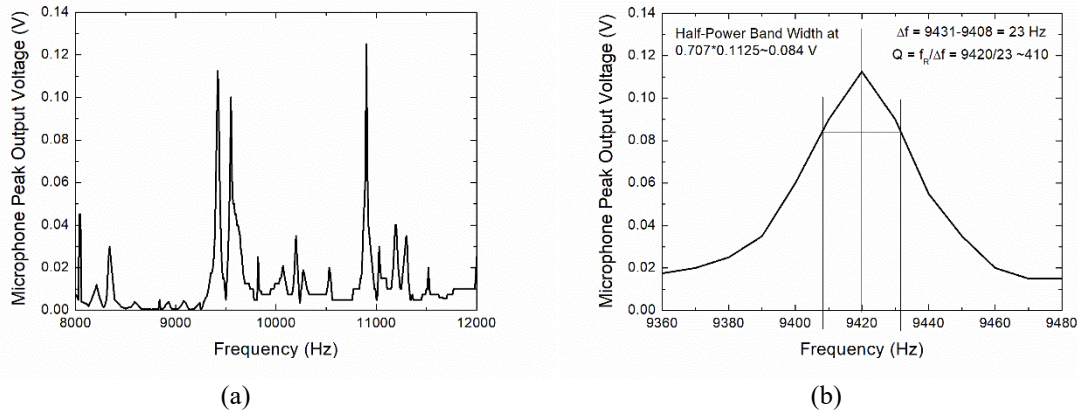


Figure 5. (a) Measured voltage equivalent for sound pressure level, and (b) half-power-bandwidth for 9420 Hz resonance.

Figure 5(a) shows the measured peak output voltage, across the range 8-12 kHz, with a distance of 5 mm between the top surface of the prototype device and the microphone. The measured resonance found at 9420 Hz is assumed to be the peak of interest. Using a 5 V peak drive signal at a frequency of 9420 Hz, the measured output from the microphone circuit (Fig. 4a) was 2.25 V peak-peak. Dividing this output by the 10x gain factor of the preamplifier circuit and also by 2x (and thus converting to peak values) yields the 0.1125 V maximum peak voltages shown in Fig. 5a and 5b. The 0.1125 V peak microphone output is equivalent to  $0.1125 \text{ [V]} / 0.0126 \text{ [V/Pa]} \sim 8.93 \text{ Pa}$ . Based on this pressure, the measured sound pressure level is  $20 \cdot \log(8.93 \text{ [Pa]} / 0.00002 \text{ [Pa]}) = \sim 113 \text{ dB SPL}$ . Figure 5b shows a close-up of the peak at 9420 Hz, from which the measured quality factor  $Q = 410$  was calculated using the half-power bandwidth at the voltage multiple of 0.707. As expected, the measured quality factor is smaller than that of the RFSC crystal dielectric loss (i.e. Table 1, material  $Q_M=1000$ ), with additional damping due to adhesive bond-lines, parasitic reactive elements, and friction. Inverting the measured quality factor yields the isotropic structural loss factor value of 0.0024, which was implemented in the multiphysics model, yielding the model predictions shown in Fig. 6 a-d for a drive of 5 V peak at the model predicted resonance frequency 8750 Hz.

The modelled acoustic pressure shown in Fig. 6a and 6b indicates a 38 mm wavelength, which is expected. A second-order exponential fit was made to envelope the modelled acoustic pressure, approximated by the red curves in Fig. 6b. The exponential fit details for the upper envelope is inset into Fig. 6b; this envelope equation is used to calculate the maximum peak acoustic pressure of  $\sim 9.03 \text{ Pa}$  at the location  $z = -5 \text{ mm}$ , i.e. 5 mm away from the end of the magnetic head mass. The 9.03 Pa acoustic pressure prediction is a good match to the 8.93 Pa measured at the same location (as discussed in the paragraph above). The model predicted SPL distribution is shown in Fig. 6c, with a maximum predicted 116 dB SPL right at the end surface of the head mass. Both the predicted and measured sound pressure levels are 113 dB SPL at a distance 5 mm from the head mass. With a 5 V drive at the resonant frequency 8750 Hz, the model predicts a peak displacement of  $0.7 \mu\text{m}$  for the head mass, and a total radiated acoustic

power of  $\sim 1.3$  mW (Fig. 6d), both of which have yet to be experimentally validated. The  $0.7 \mu\text{m}$  peak displacement produced at resonance is well within the  $2 \mu\text{m}$  compressive displacement produced by the magnetic arrangement, so theoretically the RFSC element should be protected from damage due to tensile loading. It is expected that the magnetic pre-load arrangement will continue to protect the RFSC element from tensile stress as higher acoustic powers and frequencies, including ultrasonic and beyond, are explored in future work.

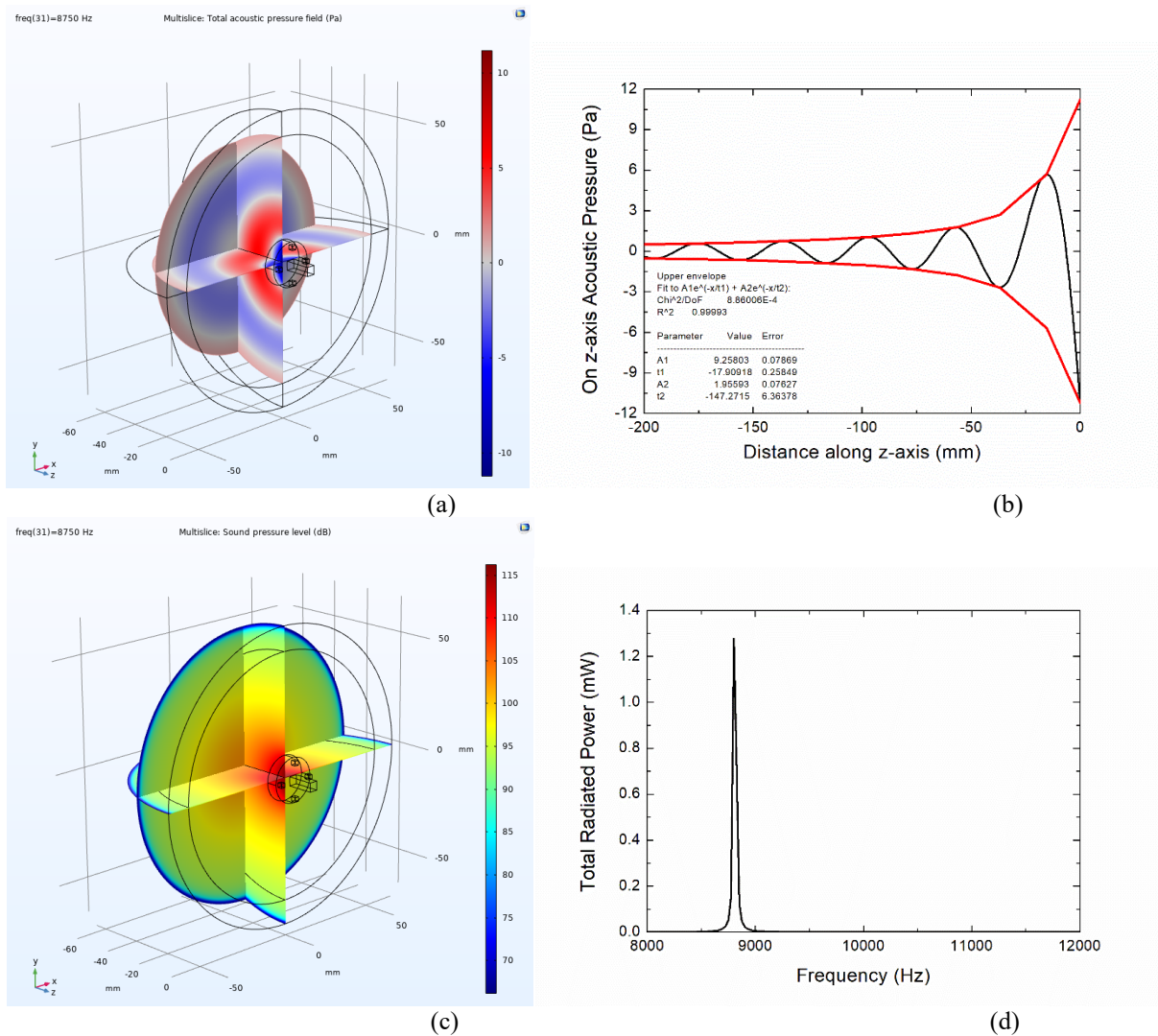


Figure 6. Model predictions of (a) acoustic pressure, (b) pressure distribution in axial (z-axis) direction with red envelope functions, (c) sound pressure level, and (d) total radiated power.

## Conclusion

This paper reports on a new magnet-based method for applying a compressive pre-load to the piezoceramic drive element of a Tonpitz-type device. This method of compression does not require a plate spring, which means there is less mechanical friction and therefore lower damping. To demonstrate the magnetic pre-loading approach, a relaxor ferroelectric single crystal based Tonpitz-type device has been developed. The device will be used as an acoustic source for structural health monitoring studies, such as air coupled ultrasound. Acoustic model

predictions and the measured behaviour of a prototype device, operating in air, are presented and show good correlation. With a 5 V, 9420 Hz drive, the prototype device generates acoustic pressures of 9 dB at a 5 mm axial distance from the device, equivalent to a sound pressure level of 113 dB. Model predictions of the acoustic pressures and sound pressure levels correlate well with measured values. The tip displacement of the magnetic head mass at resonance is predicted to be 0.7  $\mu\text{m}$  peak, well within the 2  $\mu\text{m}$  displacement produced by the 90 N of compressive force generated by the magnetic arrangement, thus protecting the ceramic transducer element from damaging tensile loading.

## References

- [1] P. Kurt, M. Şansal, İ. Tatar, C. Duran, S. Orhan, Vibro-acoustic design, manufacturing and characterization of a tonpilz-type transducer, *Applied Acoustics*. 150 (2019) 27-35.  
<https://doi.org/10.1016/j.apacoust.2019.02.003>
- [2] T. Inoue, T. Sasaki, K. Sugiuchi, A. Hattori, A Design Method for Tonpilz Piezoelectric Underwater Transducer, *Jpn. J. Appl. Phys.* 29 (1990) 56-58.  
<https://doi.org/10.7567/JJAPS.29S1.56>
- [3] S. C. Thompson, R. J. Meyer, D. C. Markley, Performance of tonpilz transducers with segmented piezoelectric stacks using materials with high electromechanical coupling coefficient, *The Journal of the Acoustical Society of America*. 135 (2014) 155.  
<https://doi.org/10.1121/1.4837217>
- [4] J.-N. Decarpigny, B. Hamonic, O.B. Wilson, The design of low frequency underwater acoustic projectors: present status and future trends, *IEEE Journal of Oceanic Engineering*. 16 (1991) 107 – 122. <https://doi.org/10.1109/48.64890>
- [5] A. Amin, E. McLaughlin, H. Robinson, L. Ewart, Mechanical and Thermal Transitions in Morphotropic PZN-PT and PMN-PT Single Crystals and Their Implications for Sound Projectors, *IEEE Trans. Ultrasonics, Ferroelectrics, and Freq. Control*. 54 (2007) 1090 - 1095.  
<https://doi.org/10.1109/TUFFC.2007.362>
- [6] K. A. Tsoi, N. Rajic, Non-destructive Evaluation of Aircraft Structural Components and Composite Materials at DSTO Using Sonic Thermography, DSTO-TN-0986, 2011.
- [7] W. Hillger, D. Ilse, L. Bühling, H. Ing. Büro, Lamb-Waves for Air-coupled Ultrasonic Testing with one-sided Access, 8th European Workshop on Structural Health Monitoring (EWSHM 2016), 2016.
- [8] J. Buckley, Air Coupled Ultrasound – A Millennial Review, 15<sup>th</sup> World Conference on Non-Destructive Testing, 2000.
- [9] K. Zhang, Y. Chen, K. Peng, The Study of 32-Mode Single Crystal Longitudinal Transducer, IEEE/OES China Ocean Acoustics Symposium, 2016.  
<https://doi.org/10.1109/COA.2016.7535709>
- [10] S. Zhang, F. Li, X. Jiang, J. Kim, J. Luo, X. Geng, Advantages and challenges of relaxor-PbTiO<sub>3</sub> ferroelectric crystals for electroacoustic transducers – A review, *Progress in Materials Science*, Volume 68, March 2015, Pages 1-66. <https://doi.org/10.1016/j.pmatsci.2014.10.002>

- [11] C. Okawara, H. Robinson, J. Stace, A. Amin, "Electromechanical properties of high-coupling  $(1-\xi)\text{Pb}(\text{Zn}_{1/3}\text{Nb}_{2/3})\text{O}_3-(\xi)\text{PbTiO}_3$  single crystals for sound projectors", IEEE Transactions on Ultrasonics, Ferroelectrics, and Frequency Control. 57 (2010) 1497 - 1504. <https://doi.org/10.1109/TUFFC.2010.1580>
- [12] Australian Provisional Patent 20200900680, Vibration Energy Transduction Devices and systems, 5<sup>th</sup> March 2020.
- [13] <https://www.corning.com/au/en/products/advanced-optics/product-materials/specialty-glass-and-glass-ceramics/glass-ceramics/macor.html>
- [14] <https://www.comsol.com/model/piezoelectric-tonpiliz-transducer-11478>
- [15] B. S. Vien, S. D. Moss, W. K. Chiu, J. Thornton, C. Rosalie, N. Rajic, T. F. Doughney, and H. J. Kissick, Measured Lamb wave radiation patterns from  $\langle 011 \rangle$  Mn-PMN-PZT relaxor ferroelectric disks on an isotropic plate, Appl. Phys. Lett. 113 (2018) 122902. <https://doi.org/10.1063/1.5044671>

# Topology Optimisation for High Frequency Vibration Energy Harvesting

David J. Munk<sup>a</sup>, Ethan J. G. Ellul<sup>b</sup> and Scott D. Moss<sup>c\*</sup>

Defence Science and Technology Group, Aerospace Division, 506 Lorimer Street, Fishermans Bend, Victoria, Australia, 3207

<sup>a</sup>david.munk@dst.defence.gov.au, <sup>b</sup>ethan.ellul@dst.defence.gov.au,  
<sup>c</sup>scott.moss@dst.defence.gov.au

\* Corresponding author. Tel.: +61-3-9626-7958; fax: +61-3-9626-7089.

© 2020 Commonwealth of Australia

**Keywords:** Vibration Energy Harvesting, Topology Optimisation, Helicopter Gearbox

**Abstract.** Topology optimisation has been used to design a piezoelectric energy harvester capable of harvesting the vibration present on a helicopter gearbox. The gearbox vibrations, with frequencies in the kilo-hertz range and having amplitudes of 10-100g (where  $g = 9.81 \text{ m/s}^2$ ), are generated by gear-meshing within the transmission. These accelerations, large in amplitude and high in frequency, are ideal sources for vibration energy harvesting, with the harvested power potentially used to power autonomous condition-based-maintenance systems. This paper will discuss the first and simplest of the harvesters that were designed and manufactured, i.e. a 0.51 mm thick spring steel cantilever that uses a Pz27 piezoceramic transducer, which is sensitive to 1900 Hz gearbox vibrations and can produce 300  $\mu\text{W}$  from a 2g host acceleration.

## Introduction

Downtime for routine maintenance and checks, in both commercial and military environments, can leave equipment out of operation for extended periods. While this maximises operational safety, it also comes with a potentially costly reduction in availability. Structural Health Monitoring systems (SHMs) can minimise this downtime by providing an ongoing assessment of structural condition, permitting the detection and monitoring of safety-critical degradation [1,2].

Powering SHMs can be problematic, with these systems often being placed in difficult to access positions and unable to be powered locally. A potential solution is the pairing of low-power SHMs with energy harvesters, siphoning ambient vibrational energy in the environment and converting it into usable electrical energy. One well-studied method of capturing waste mechanical energy is via piezoelectric-based vibrational energy harvesting (PEH) [3]. PEH devices based on traditional piezoceramics  $\text{Pb}[\text{Zr}_x\text{Ti}_{1-x}]\text{O}_3$  (PZT) [4] have been thoroughly explored over the past two decades, with recent reviews indicating that power densities of 10-100  $\text{mW/cm}^3$  are achievable [5,6]. This paper will discuss a high-frequency PEH prototype device designed using a recently developed topology optimisation algorithm, known as Bi-directional Evolutionary Structural Optimisation (BESO), to tune the device to the principal gear-meshing frequency of a Bell 206B-1 Kiowa helicopter main rotor transmission at 1900 Hz [6].

Topology optimisation has been identified as the most challenging and economically rewarding task in structural design [7]. Generally speaking, topology optimisation seeks to find the best location to place structure in a given design domain subjected to predefined objectives, constraints, loads and boundary conditions. The main advantage of topology optimisation over



other structural optimisation techniques is that no specified initial structural topology needs to be presumed *a priori*. Over the last few decades, since the introduction of material distribution methods [8], topology optimisation has been rapidly developed into a design tool used by the engineering industry [9][10][11].

The optimal design of structures subjected to vibration was first considered in the 1970s in the form of shape optimisation with respect to the fundamental and higher-order eigenfrequencies of transversely vibrating beams [12]. Many studies have considered dynamic stability as the objectives [13] where it is advantageous to keep the natural frequencies of the structure away from any driving frequencies. Ultimately, the goal of this work is to develop an in-situ energy harvesting device that can utilise these frequencies to power a low-power condition based SHM system to monitor a helicopter during flight. This paper discusses the modelling, optimisation, and testing of such a device under laboratory conditions, being exposed to accelerations of up to 2.0g. These results are then compared to initial models, and the feasibility for use on the helicopter transmission is discussed.

### Principles of Operation

As mentioned in the introduction, the principal gear-meshing frequency of a Bell 206B-1 Kiowa helicopter main rotor transmission is 1900 Hz with other significant vibration at 2250 Hz and 2500 Hz [6]. The aim of the device reported in this paper is to harvest vibrational energy at the dominant 1900 Hz frequency - the cantilevered topology was optimised to be sensitive to this frequency. This is the first step in designing a PEH that is sensitive to all three of the main meshing-frequencies, work that will be reported elsewhere. The harvester discussed in this paper, shown schematically in Fig. 1, is a topology optimised cantilever with a piezoceramic disk transducer, the combination of which is tuned to 1900 Hz. The topology optimised design was waterjet-cut from spring steel and secured between two steel plates to form the root. Finite element modelling was used to find the region of highest in-plane stress, upon which the PZT disk was mounted using silver epoxy.

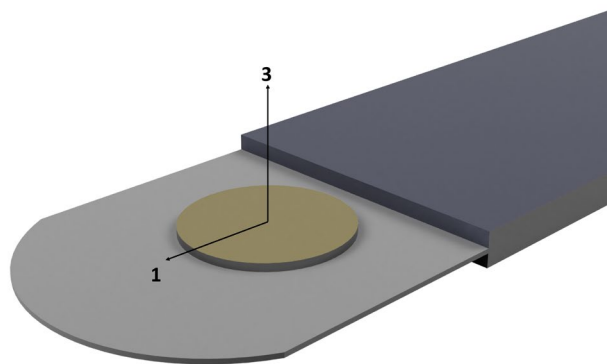


*Figure 1. Schematic of the piezoelectric energy harvester showing the thin topology optimised cantilever manufactured from spring steel, with the thicker root section, and the PZT disk transducer with crystalline orientation.*

### Theory

The aim of this study is to design a cantilever energy harvesting device that leverages the available vibration energy in a helicopter gearbox. Accelerometer data has indicated that the

largest  $g$ -load on the gearbox being considered, that of a Bell 206B-1 Kiowa helicopter, is  $12g$  and occurs at a frequency of  $1900$  Hz [6]. Investigations to date have shown that the resonance frequency of the harvesting device plays a key role in the device's power output [14]. Furthermore, the mass of the energy harvesting device is proportional to the stored mechanical energy. This study implements a topology optimisation algorithm to tune the resonance frequency of a cantilever energy harvesting device to the vibration frequency of the maximum  $g$ -load from a Bell 206B-1 Kiowa helicopter gearbox while keeping the volume of the structure as high as possible. Therefore, the design problem can be mathematically defined as follows:

$$\begin{aligned} & \text{maximise: } V \\ & \text{subject to: } \omega_1 = 1900 \end{aligned}$$

where  $V$  and  $\omega_1$  are the volume and fundamental frequency of the energy harvesting device, respectively. Therefore, the optimisation algorithm finds the structural topology that has the largest volume with a fundamental frequency of  $1900$  Hz. In this study, a recently developed Bi-directional Evolutionary Structural Optimisation (BESO) algorithm is used to solve the design problem [15]. The BESO algorithm developed in [15] replaces the traditional heuristic optimality criteria method with an integer-linear program (ILP) and, thus, enables the handling of multiple constraints. Nevertheless, the method is evolutionary in the sense that only gradual design changes are permitted in each iteration. Therefore, a neighbourhood constraint must be employed to ensure that only small design changes in each iteration are made. The BESO algorithm uses the finite element formulation to solve the physics of the problem. Hence, the design problem can be formulated as an optimisation problem as follows:

$$\begin{aligned} & \text{maximise: } V(\mathbf{x}) \\ & \text{subject to: } ([K] - \omega_n^2[M])\phi_n = 0 \\ & \omega_1 = 1900 \\ & \sum_{i \in x=0} \Delta x_i \leq \eta_a \cdot N \\ & \sum_{i \in x=1} \Delta x_i \geq -\eta_r \cdot N \\ & x_i \in \{0, 1\} \quad \forall i \in [1, N] \end{aligned}$$

where  $\mathbf{x}$  is the design variable vector and  $x_i$  is the  $i^{th}$  design variable,  $[K]$  and  $[M]$  are the global stiffness and mass matrices of the structure,  $\omega_n$  and  $\phi_n$  are the natural mode frequency and shape of the structure,  $\eta_a$  and  $\eta_r$  determine the maximum number of elements added and removed in each iteration and  $N$  is the number of design variables. The binary design variable  $x_i$  physically represents the density of the  $i^{th}$  element; where, in this study, a hard-kill BESO method [16] is employed. The BESO method solves the discrete problem, resulting in clear structural boundaries. Therefore, the resulting topologies can be manufactured by traditional methods or additively if complex topologies result.

In order to guarantee that a solution to the optimisation problem exists, some restrictions on the resulting design must be introduced [17]. Experience has shown that filtering of the sensitivity function is a highly efficient way to ensure mesh in-dependency [18]. Furthermore, it has been shown to give results that are stable under mesh refinement and maintains a minimum

length scale. In this study, a filter scheme is used to smooth the element sensitivity numbers across the entire domain [17].

As mentioned, the optimisation algorithm translates the physical equations into the finite element formulation to solve the physics of the problem. Therefore, to determine the natural frequencies and mode shapes of the structure, the undamped and unloaded equations of motion must be solved. The equations of motion are defined as follows:

$$[M]\ddot{\mathbf{x}} + [K]\mathbf{x} = 0$$

where  $\mathbf{x}$  is the displacement vector of the structure. To solve the above equation a harmonic solution, i.e.  $\mathbf{x} = \phi_n \cdot \sin(\omega_n \cdot t)$ , is assumed. By implementing the harmonic solution in the equations of motion the following eigenvalue problem results:

$$([K] - \omega_n^2[M])\phi_n = 0$$

which can be solved for both the natural frequencies,  $\omega_n$ , and modes shapes,  $\phi_n$ , respectively. The finite element model and the first mode shape for the optimised cantilever, having a fundamental frequency of 1900 Hz, is illustrated in Fig. 2.

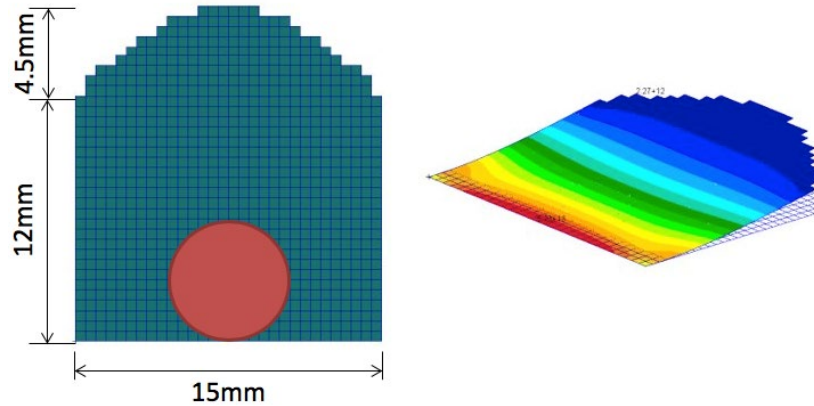


Figure 2. Finite element model and first mode shape of optimised cantilever for 1900 Hz

To determine the performance of the energy harvesting device, the open circuit voltage can be used as a measure of the potential output power. The total electric charge ( $Q$ ) is mathematically defined as follows:

$$Q = CV$$

where  $C$  is the equivalent capacitance and  $V$  is the electric potential. Therefore, the open circuit voltage across the piezoelectric material can be found from:

$$V_{oc} = \frac{1}{C} \int \int [d]\boldsymbol{\sigma} \cdot d\mathbf{A}$$

where  $[d]$  is the piezoelectric strain tensor,  $\boldsymbol{\sigma}$  is the mechanical stress vector and  $\mathbf{A}$  is the area vector in the three planes (Fig. 1). In this work the finite element method (FEM) is used to solve the physical equations.

## Experimental

This section describes the fabrication process for the prototype harvester, including the waterjet cutting of the spring steel cantilever and the bonding of the PZT transducers. Also detailed are the experimental characterisations of the prototype harvester that have been undertaken, including impedance analysis of the PZT transducer, and voltage and power measurements as a function of drive acceleration and frequency, and load resistance.

### *Energy Harvester Assembly*

As mentioned in section 2, the cantilevered section of the topology optimised energy harvester (Fig. 1) was fabricated using 0.51 mm thick carbon spring steel (AISI 1095, elastic modulus 190-210 GPa, Poisson's ratio 0.27-0.3, density 7860 kg/m<sup>3</sup>). The beams were cut using a CNC driven waterjet cutter (Techni). The waterjet pressure was 50 kPSI, and the diameter of the water beam was 0.5-0.8 mm with cutting grit (GMA garnet, composed of >97% almandite garnet) located on the perimeter of the waterjet. The cantilevered section was secured between two spring steel root-plates that were each 0.89 mm thick. The root-plates were bonded to the cantilevered section using 0.2 mm thick polypropylene scrimcloth and a structural adhesive (Click Bond CB359).

Figure 1 shows the PZT disk transducer type chosen for the topology optimised harvester. The PZT disk has a 6.35 mm diameter and is 0.5 mm thick, and is a soft-relaxor (Pz27, Navy II PZT-5A analogue, Ferroperm, Meggit A/S) with a piezoelectric charge constant,  $d_{31} \sim 150$  pC/N and with an electromechanical coupling factor,  $k_{31} \sim 0.3$ . The PZT disks were characterised using an impedance analyser (Solartron SI 1260) before and after bonding to the cantilevered section. A silver loaded epoxy (Chemtronics CW2400) was used to bond the PZT disks at high stress locations identified by FEA. During bonding a light pressure was applied in a circular motion to minimise the thickness of the epoxy layer beneath the disk with the goal of reducing damping on the piezoelectric disk [19] but increasing the presence of a spew fillet [20]. Thin copper wires were then bonded to the centre of each disk with the silver epoxy, and wire was additionally bonded on the exposed cantilever layer on the upper right side of the root to form a ground path.

### *Harvester Characterisation*

The prototype harvester was mounted onto a host mass and a sinusoidal host acceleration was applied in the vertical '3' direction (Fig. 1) by an electro-dynamic shaker. Impedance frequency sweeps were conducted on the mounted harvester, yielding an estimate of the device's resonant frequency. Frequency sweeps were conducted during which the harvester's peak open circuit output voltage was recorded. The sweeps were repeated under a range of applied resistive loads with the associated voltage and power outputs determined. For vibrational testing, topologies were individually secured to the host mass, mounted on an electro-dynamic shaker (TIRA Vib Modal-Vibration Test System) using neodymium rare-earth magnets (N42, 50 mm x 5 mm x 3.4 mm, partially visible in Fig. 3). The shaker arrangement is limited to drive levels equivalent to a maximum host acceleration of 2g (where  $g = 9.81$  m/s<sup>2</sup>).

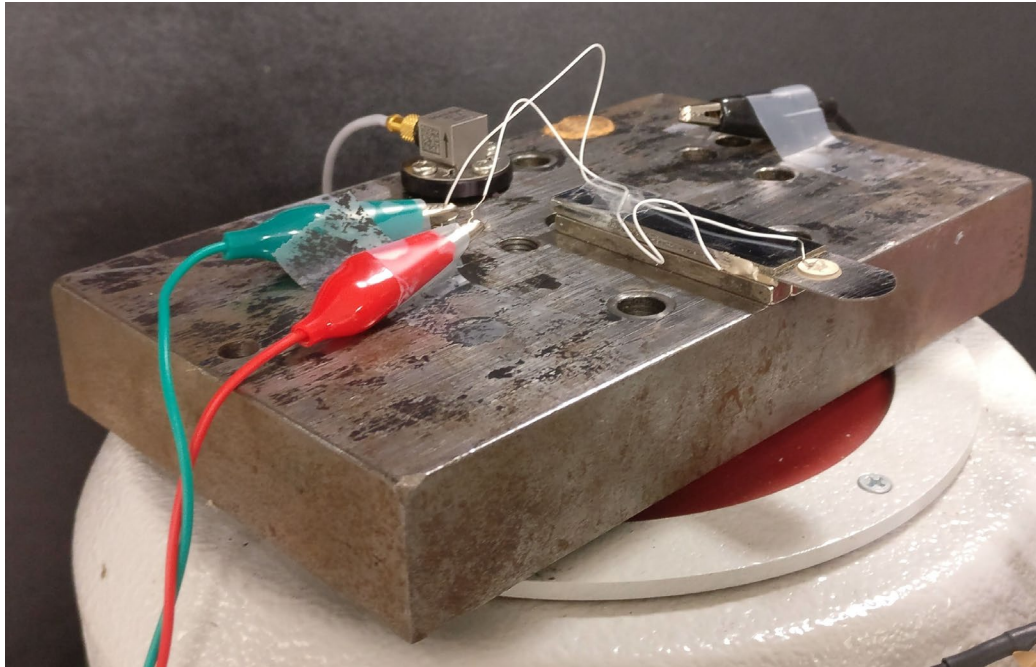


*Figure 3. Photograph of the experimental arrangement showing the harvester mounted to the shaker/host mass with 'rails' magnet arrangement, and nearby accelerometer (cube geometry).*

A loop controller (Brüel and Kjær 7541) was used to generate 0.2g host vibrations over the frequency range of 1000 Hz to 3000 Hz with a sweep rate of 20 Hz/s. For higher drive levels, open loop experiments were performed using a signal generator, fed into an amplifier, to sweep the 1000-3000 Hz range at a sweep rate of 200 Hz/s. These open loop tests were performed at host accelerations of 1g and 2g with the drive levels set at the harvester's resonant frequency; however, the host acceleration could not be kept constant across all frequencies due to equipment limitations. The harvester's optimum load was determined using 0.2g frequency sweeps and varying the load resistance in the range 10 k $\Omega$  to 150 k $\Omega$  (resistor decade box Tenma 72-7270). The same optimum load resistor was then used for sweeps at 1g and 2g to find the maximum output power.

### **Results and Discussion**

This section will examine the frequency response of the harvester's impedance, compare model predictions and measured response of the harvesters open circuit output voltage as a function of frequency and host acceleration, and finally present measured resistor sweeps and measurements of output power versus frequency.

Figure 4 illustrates the measured impedance of a Pz27 disk bonded to the harvester cantilever arrangement shown in Fig. 3. The clamped capacitance of the bonded disk was  $\sim 910$  pF, with clamped relative permittivity 1620. The 100 mV drive voltage of the impedance analyser excited an electromechanical resonance near 1873 Hz with an amplitude of 80 k $\Omega$ . This resistor value was used to set the approximate midpoint of the resistor range examined to find the optimum load (I.e. range 10 k $\Omega$  to 150 k $\Omega$ ).

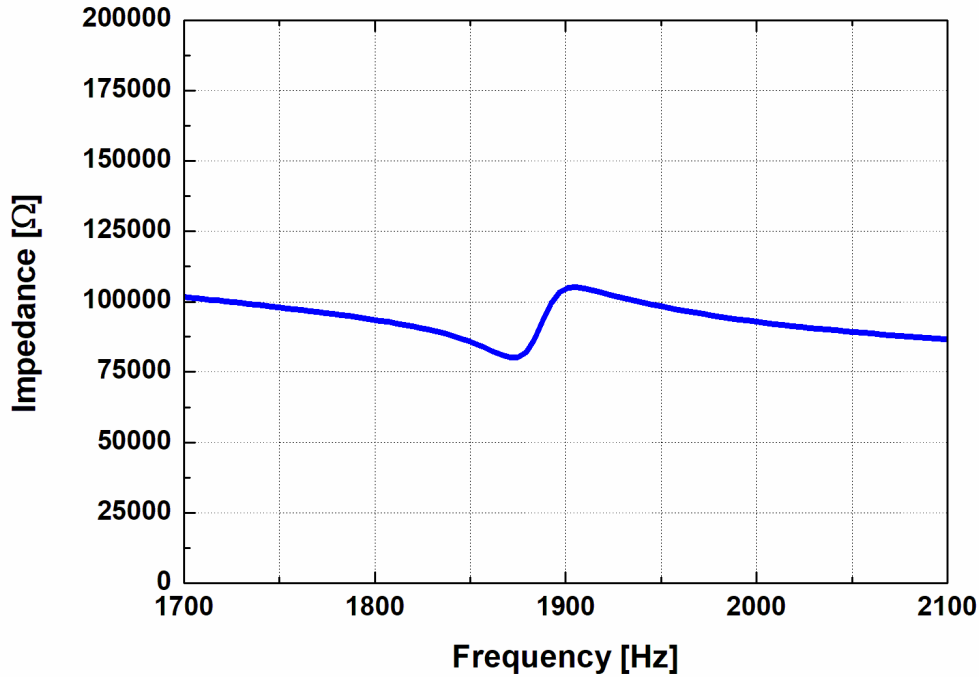


Figure 4. Measured impedance curve from a PZT disk mounted on a prototype harvester.

Figures 5a and 5b show the predicted and measured open circuit harvester output voltage as a function of host frequency and acceleration, respectively. Both the predicted and measured results show the output voltage increasing linearly with host acceleration. Under all drive accelerations the resonant peaks occur just below the 1900 Hz design goal, with the peak voltage of 9 V predicted and observed for a 2g host acceleration. There is a strong correlation between the predicted and measured harvester responses, indicating that the model contains sufficient physics to describe the device's open circuit behaviour, and that second order effects due to bondline thickness and spew fillet size are not significantly affecting the device behaviour.

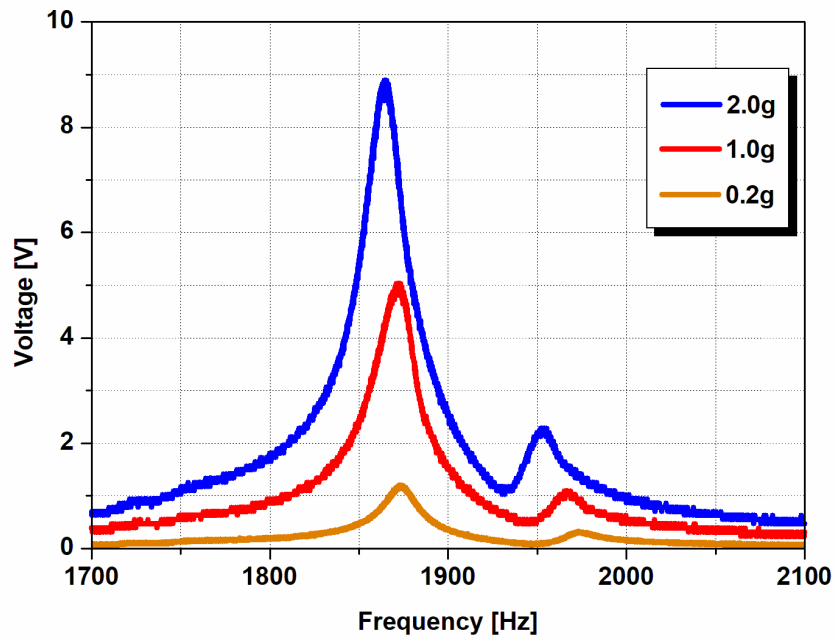
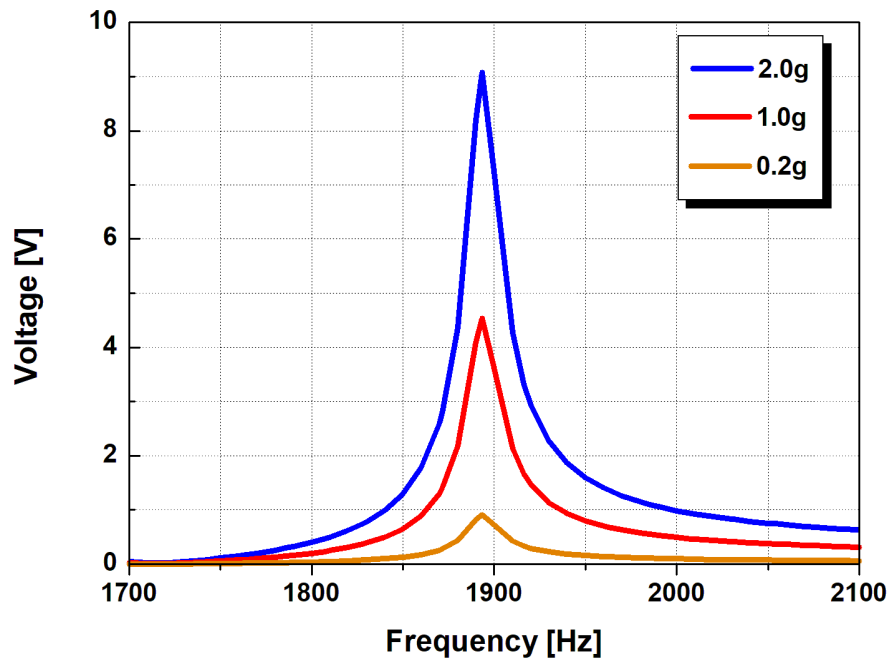


Figure 5. (a) Modelled open circuit voltage versus frequency, and (b) measured open circuit voltage versus frequency.

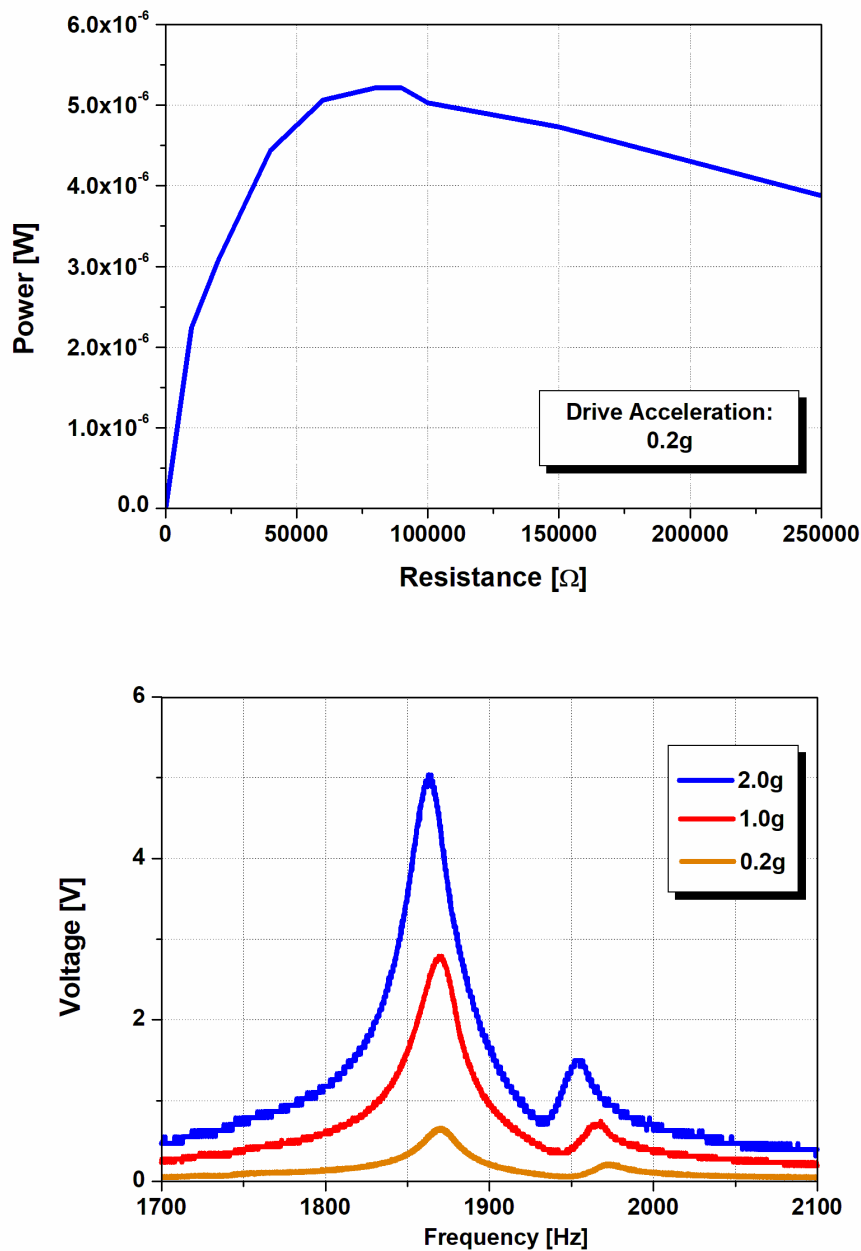


Figure 6. (a) Measured peak voltage and power versus resistive load. (b) Measured output voltage at optimum resistive load 85 kΩ and host excitations of 0.2g, 1g and 2g.

Figure 6a shows the measured output power from the harvester as a function of resistive load, collected using 0.2g closed-loop frequency sweeps. The maximum output power is ~5.1 μW under a host excitation of 0.2g at 1870 Hz, and occurs with a load of 85 kΩ, which is close to the 80 kΩ impedance measured in Fig. 4. This suggests that an impedance sweep can provide a good estimate of optimum load, at least for devices based on traditional piezoceramics. There is a smaller resonance near 1950-1980 Hz that appears to be an artefact of the experimental

arrangement and likely due to minor irregularities at the cantilever root-line of the three-layer structure of the device. Figure 6b shows the measured output voltage from the harvester under an 85 k $\Omega$  resistive load, and as a function of frequency and drive acceleration. As might be expected the output voltages under electrical load are just over half of that measured under open circuit [21], with the resonant frequencies shifted 2-3 Hz lower. The peak output power under a 2g host excitation was  $\sim 300 \mu\text{W}$ , equivalent to a peak power density of  $18.5 \text{ mW/cm}^3$ , at the lower end of the 10-100  $\text{mW/cm}^3$  range discussed in the introduction. As mentioned earlier, the principal mesh frequency Bell 206B-1 Kiowa helicopter main rotor transmission occurs at 1900 Hz and is 12g. Under a 12g excitation the harvester's output voltage might be expected to increase by a factor of 6 compared with the 2g results presented here, up to around 30 V. The electric field produced across the disk by this voltage is well below the coercive field of PZT-5A analogues,  $\sim 1.2 \text{ kV/mm}$  [22], hence is insufficient to induce depolarisation of the transducer element. Assuming a factor of 6 increase in output voltage, then the power might be expected to increase by a factor of 36 to around 11 mW, which would be useful for powering many sensor types.

### Conclusion

A topology optimised vibration energy harvester has been reported. The harvester is based on an optimised 0.51 mm thick spring-steel cantilever with a piezoceramic Pz27 disk transducer 6.35 mm diameter. The harvester is optimised to harvest from the principal gear-meshing frequency of a Bell 206B-1 Kiowa helicopter main rotor transmission which occurs at 1900 Hz and has an amplitude of 12g. Impedance frequency analysis of a prototype harvester indicated that the fundamental vibration mode of the device was located at 1870 Hz and at 80 k $\Omega$ . Subsequent testing of the device using an electro-dynamic vibration shaker, under a host excitation of 0.2g showed a resonance at 1870 Hz with an optimum load at 85 k $\Omega$ , similar to that measured using impedance analysis. In the laboratory under a host excitation of 2g and 1870 Hz the harvester produced  $\sim 300 \mu\text{W}$  with a power density of  $18.5 \text{ mW/cm}^3$ , suggesting that the device may generate up to 11 mW if mounted on a Bell 206B-1 Kiowa helicopter main rotor transmission.

### References

- [1] N. Rajic, S. Galea, Thermoelastic Stress Analysis and Structural Health Monitoring: An Emerging Nexus, *Structural Health Monitoring*. 14 (2015) 57-72. <https://doi.org/10.1177/1475921714548936>
- [2] A. Baker, N. Rajic, C. Davis, Towards a practical structural health monitoring technology for patched cracks in aircraft structure, *Composites Part A: Applied Science and Manufacturing*. 40 (2009) 1340-1352. <https://doi.org/10.1016/j.compositesa.2008.09.015>
- [3] A. Erturk, D. J. Inman, *Piezoelectric energy harvesting*, Wiley, United Kingdom, 2011. <https://doi.org/10.1002/9781119991151>
- [4] T. Ikeda, *Fundamentals of Piezoelectricity*, Oxford University Press, New York, 1996.
- [5] Z. Yang, S Zhou, J Zu, D. Inman, High-Performance Piezoelectric Energy Harvesters and Their Applications, *Joule*. 2 (2018) 642-697. <https://doi.org/10.1016/j.joule.2018.03.011>
- [6] T. F. Doughney, S. D. Moss, D. Blunt, W. Wang, H. J. Kissick, Relaxor ferroelectric transduction for high frequency vibration energy harvesting, *Smart Mater. Struct.* 28 (2019) 065011. <https://doi.org/10.1088/1361-665X/ab15a5>
- [7] D. J. Munk, G. A. Vio, G. P. Steven, Topology and shape optimization methods using evolutionary algorithms: a review, *Struct. Multidisc. Optim.* 52 (2015) 613-631. <https://doi.org/10.1007/s00158-015-1261-9>

- [8] M. P. Bendsoe, N. Kikuchi, Generating optimal topologies in structural design using homogenization, *Comput. Methods Appl. Mech. Eng.* 71 (1988) 197–224. [https://doi.org/10.1016/0045-7825\(88\)90086-2](https://doi.org/10.1016/0045-7825(88)90086-2)
- [9] J. D. Deaton, R. V. Grandhi, A survey of structural and multidisciplinary continuum topology optimization: post 2000, *Struct. Multidisc. Optim.* 49 (2014) 1–38. <https://doi.org/10.1007/s00158-013-0956-z>
- [10] O. Sigmund, K. Maute, Topology optimization approaches, *Struct. Multidisc. Optim.* 48 (2013) 1031–1055. <https://doi.org/10.1007/s00158-013-0978-6>
- [11] G. I. N. Rozvany, A critical review of established methods of structural topology optimization, *Struct. Multidisc. Optim.* 37 (2009) 217–237. <https://doi.org/10.1007/s00158-007-0217-0>
- [12] N. Olhoff, Optimization of vibrating beams with respect to higher order natural frequencies, *Journal of Structural Mechanics* 4 (1976) 87–122. <https://doi.org/10.1080/03601217608907283>
- [13] D. J. Munk, G. A. Vio, G. P. Steven, Novel moving isosurface threshold technique for optimisation of structures under dynamic loading, *AIAA Journal*, 55 (2017) 638-651. <https://doi.org/10.2514/1.J054692>
- [14] F. Goldschmidtboeing, P. Woias, Characterization of different beam shapes for piezoelectric energy harvesting, *Journal of Micromechanics and Microengineering*, 18 (2008). <https://doi.org/10.1088/0960-1317/18/10/104013>
- [15] D. J. Munk, A bidirectional evolutionary structural optimization algorithm for mass minimization with multiple structural constraints, *International Journal for Numerical Methods in Engineering*, 118 (2019) 93 – 120. <https://doi.org/10.1002/nme.6005>
- [16] X. Huang, Y. M. Xie, Bi-directional evolutionary topology optimization of continuum structures with one or multiple materials, *Computational Mechanics*, 43 (2009) 393 – 401. <https://doi.org/10.1007/s00466-008-0312-0>
- [17] O. Sigmund, J. Petersson, Numerical instabilities in topology optimization: a survey on procedures dealing with checkerboards, mesh-dependencies and local minima, *Structural Optimization*, 16 (1998) 291 – 299. <https://doi.org/10.1007/BF01214002>
- [18] M. P. Bendsoe, O. Sigmund, *Topology Optimization: Theory, Methods and Applications*, 1st Edition (2003) Springer Berlin. [https://doi.org/10.1007/978-3-662-05086-6\\_2](https://doi.org/10.1007/978-3-662-05086-6_2)
- [19] T. J. Johnson, D. Charnegie, W. W. Clark, Energy harvesting from mechanical vibrations using piezoelectric cantilever beams, *Proc. of SPIE*. 6169 (2006) 61690D. <https://doi.org/10.1117/12.659466>
- [20] S. D. Moss, S. C. Galea, I. G. Powlesland, M. Konak, A. A. Baker, In-situ health monitoring of a bonded composite patch using the strain ratio technique, *Proc. SPIE*, 4235 (2001) 363-374. <https://doi.org/10.1117/12.420878>
- [21] S. Roundy, P. K. Wright, J. M. Rabaey, *Energy Scavenging for Wireless Sensor Networks with Special Focus on Vibrations*, Springer, Boston, 2004. <https://doi.org/10.1007/978-1-4615-0485-6>
- [22] M. W. Hooker, *Properties of PZT-Based Piezoelectric Ceramics Between –150 and 250C*, NASA/CR-1998-208708, Langley Research Center, 1998.

# Comparative Assessment of Distributed Strain Measurement Technologies

Kieran Pryor<sup>a</sup>, Matthew Stevens<sup>b</sup>, Michael Forsey<sup>c</sup> and Suzana Turk<sup>d</sup>

Defence Science and Technology Group, 506 Lorimer Street, Fishermans Bend, VIC, 3207, Australia

<sup>a</sup>kieran.pryor@dst.defence.gov.au, <sup>b</sup>matthew.stevens@dst.defence.gov.au,  
<sup>c</sup>michael.forsey2@dst.defence.gov.au, <sup>d</sup>suzana.turk@dst.defence.gov.au

© 2020 Commonwealth of Australia

**Keywords:** Fibre Optics, Continuous Fibre Gratings, Distributed Strain Measurement, Digital Image Correlation, Finite Element Analysis

**Abstract.** Fibre optic (FO) distributed strain sensing technology has introduced a significant new capability for structural health monitoring (SHM). FO sensing (FOS) offers a simpler installation process with improved resistance to corrosion and electromagnetic interference compared to traditional electrical resistance foil strain gauges (FSGs) which unlike FOS is limited to single point measurements. Previous FO distributed strain measurement studies at the Defence Science and Technology Group showed good correlation between strain measurements derived from a proprietary continuous fibre grating system and FSGs. This paper compares a commercially available, non-proprietary FO sensing system and digital image correlation (DIC) against industry standard FSGs and finite element analysis (FEA) predictions.

## Introduction

A hair-like optical fibre spanning 13 m can provide the equivalent sensing capability of 2,000 individual foil strain gauges [1] but without the cumbersome and weight prohibitive electrical wiring. FO distributed strain sensing technology aims to modernise structural monitoring and assessment from FSGs and single point fibre optic sensors that provide discrete strain measurement at a structural feature of interest. Distributed sensing provides broad strain measurement coverage at relatively low cost without the weight and ongoing maintenance burden of large FSG installations, and can resolve strain gradients across the length of a feature or structure.

Distributed sensing is achieved using a low reflectivity grating, which is a small periodic change in refractive index of the glass fibre core, written over the entire fibre length as it is being fabricated in a draw tower. This configuration is known as a continuous fibre grating [1]. These sensing systems rely on spatially interrogating the backscattered light from the gratings via optical frequency domain reflectometry (OFDR), which measures the spectral shift of the backscattered light in time (via a fast Fourier transform) and then scales by the known number of gratings to correlate the change in observed length to a change in strain [2]. The change in the central reflected wavelength (Bragg wavelength) can be quantified by Equation 1 [3]:

$$\lambda_b = 2n_{eff}\Lambda \quad (\text{Eq. 1})$$

Where  $\lambda_b$  is the Bragg wavelength,  $n_{eff}$  is the effective refractive index of the optical fibre and  $\Lambda$  is the inter-grating spacing.

DIC is an optical measurement technique for measuring displacements. This measurement is achieved by using a pair of cameras in stereo to track a stochastic pattern of dots applied to the surface of the object of interest. Computer software is then used to track the changes in grey value patterns in small neighbourhoods called subsets in the captured images and compare their displacement relative to a reference image taken at the start of testing. Using these changes in subset location allows changes in displacement and associated strain values to be determined.

FEA offers the ability to predict the theoretical strain distribution in a test article, which can be used to verify the suitability and optimise the installation location of sensors for a range of structural loading conditions. FEA is used in the present work to predict the strain distribution in a plate coupon with a centre hole. This centre-hole coupon is advantageous for evaluating and testing the capability limitations of fibre optic and other sensing technologies because the hole produces a region of relatively high strain gradient under loading. This paper reports on a comparative study of a commercially available FO sensing system and DIC against FSGs and FEA predictions for future application in SHM of airframe test articles undergoing full-scale fatigue testing.

### **Experimental Method**

An aluminium alloy 2024-T3 coupon of dimensions  $400 \times 100 \times 3$  mm with a 20 mm diameter centre hole was instrumented and tested under two loading conditions. A quasi-static tensile load, increased from 1 to 22 kN in increments of 1 kN, was applied to compare measured distributed strain data at different load levels and strain gradients. A small notch was then introduced at the edge of the centre-hole adjacent to the bonded FO sensor and constant amplitude cyclic loading applied to initiate and grow a fatigue crack along a path intersecting the FO sensor. Strain measurements were recorded to assess the performance of the FO sensors in the strain field ahead of the crack tip and in the crack wake.

The coupon was instrumented with a 3 m sensing length of commercially supplied all-grating fibre (FBGS) which was interrogated using an OFDR based measurement system (Sensuron Summit). This sensing system combination offers a minimum spatial resolution of 1.6 mm and a notional  $\pm 1 \mu\epsilon$  accuracy. Norland optical adhesive was used to adhere six parallel sensing lines to the aluminium alloy substrate, along the loading axis, and with unbonded serpentine loops between lines. Strain data was analysed and presented using MATLAB.

For DIC, a pair of Basler Ace acA4112-30um 12MP/30FPS cameras with Tokina Macro 100 mm lens set to F11 with an exposure time of 1.5 ms was mounted to a common rail. The relative angle and distance between the cameras was optimised to focus on the centre of the hole, with sufficient illumination provided by a pair of Nila Varsa LED lights. A white base-coat of Rust-oleum Flat Ultra Cover 2X paint was applied over a  $150 \text{ mm} \times 100 \text{ mm}$  area. A stochastic pattern stencil of 0.1 mm dots was applied using airbrushing with an enamel based flat-black paint. The stencil was subsequently removed. Cameras were controlled using Correlated Solution's VICSnap software to capture synchronised calibration images as well as images during testing, either manually or with a digital trigger signal sent from the test frame controller. Subsequent image processing was completed in the VIC3D application, with exported data being provided as image stills, movies, and CSV files. The accuracy of strain data from this DIC system is notionally  $\pm 50 \mu\text{m}$  with 0.15 mm spatial resolution.

Three Kyowa copper plated 120-ohm (KFGS-1-120-D9-23 N10C2) foil strip strain gauges (FSGs) were instrumented to measure strain in the direction of loading. Each strip gauge comprised 5 sensing points adhered to the aluminium alloy substrate using M-Bond adhesive

according to standard procedure. These FSGs offer 2 mm spatial resolution and a notional  $\pm 1 \mu\epsilon$  accuracy. Data from the FSGs was similarly analysed within MATLAB.

Quarter symmetry of the coupon was used in the FEA and the measured data was presented in a consistent form.

### Results and Discussion

The instrumentation layout with far-field and hole-edge strain measurement positions are shown alongside DIC displacement and strain maps in Figure 1. A 0.13 degree out of plane twist was observed due to grip misalignment. This twist contributed a torsional strain to the coupon, estimated to be in the range 220-470  $\mu\epsilon$ , as shown in Figure 1 (right); it is also surmised to be responsible for the irregular strain signal features in Figure 1 (right) which are most significant at the hole-edge, illustrated by the relatively large difference in longitudinal strain between the left and right sides of the hole. This grip misalignment was not rectified due to time constraints and was not accounted for in the FEA. As a consequence, it was accepted that FOS and DIC determined strain values would likely vary from FEA predictions. All strain measurement approaches were zeroed so that zero measured strain coincided with zero FEA predicted strain under grip pressure and no applied axial load.

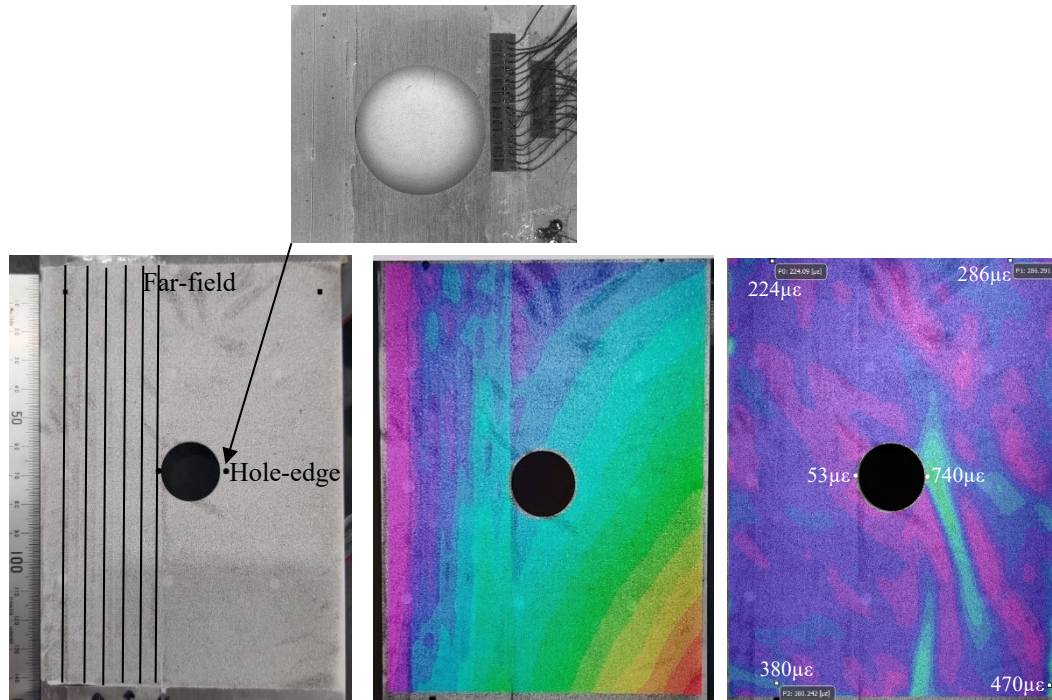


Figure 1. Instrumented test area photo (left) showing far-field and hole-edge strain measurement positions with FO region on the left side (shown as vertical lines), DIC dot paint covering the entire test area and FSG position on back side of coupon (arrowed); DIC z-displacement map (z-direction is normal to the page) under grip pressure and zero load (centre) showing 0.13 degree out of plane twist as indicated by red-coloured corner; and, DIC strain map under grip pressure and zero load (right) showing asymmetric strain due to twist.

A comparison of FEA, FSG, FOS and DIC determined strain values at static loads ranging from 1 to 22 kN at the far field and hole-edge strain measurement positions are shown in Figure

2. The far-field measurement position was located far enough away from the hole such that there was no significant strain gradient. As no FSGs were applied in this region, no FSG measurements were available for comparison. Figure 2 (left) show FO and DIC strain values in relatively good agreement. As expected, the FO and DIC strain values were higher (by ~16%) than the FEA predictions due to the additional strain induced by the twist. Comparison of the strain measurements adjacent to the hole edge showed reasonable agreement between the FOS, FSG and DIC values, Figure 2 (right). Again, the measured strains were higher (by ~17%) than the FEA predictions because of the twist in the coupon not accounted for in FEA.

It is surmised that the predicted and measured strain values would better align in the absence of the twist. Discrepancies may also have resulted from small errors in the location of the different sensors adjacent to the hole edge where strain gradients are relatively high, Figure 3. FEA of the coupon test section confirmed a steep strain gradient adjacent to the hole edge, as shown in Figure 3.

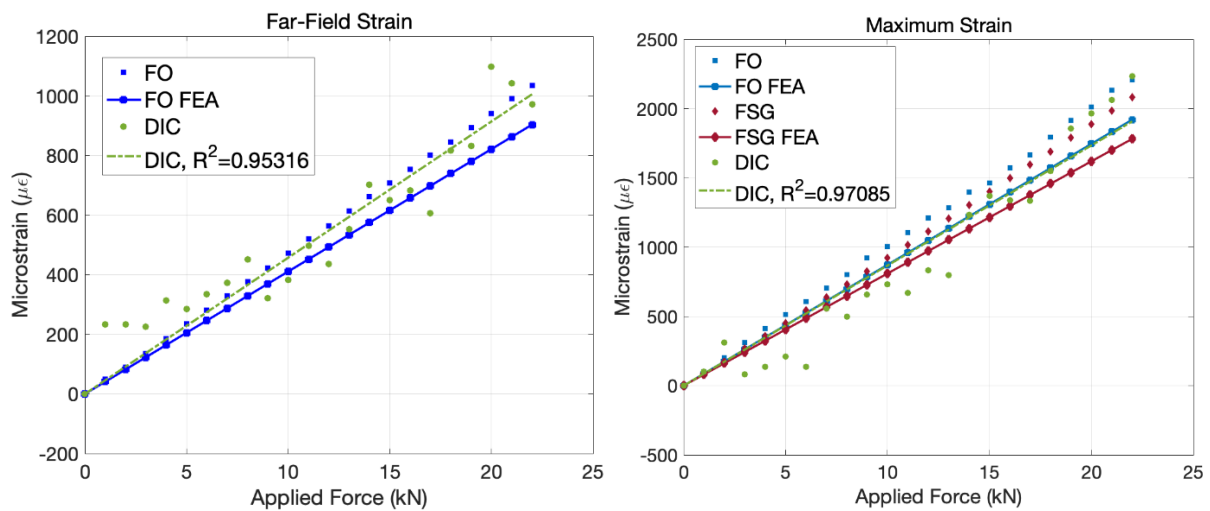


Figure 2. Comparison of measured and FEA predicted strain at static loads ranging from 1 to 22 kN at far-field (left) and hole-edge (right) strain positions of the test area (refer to Figure 1, left).

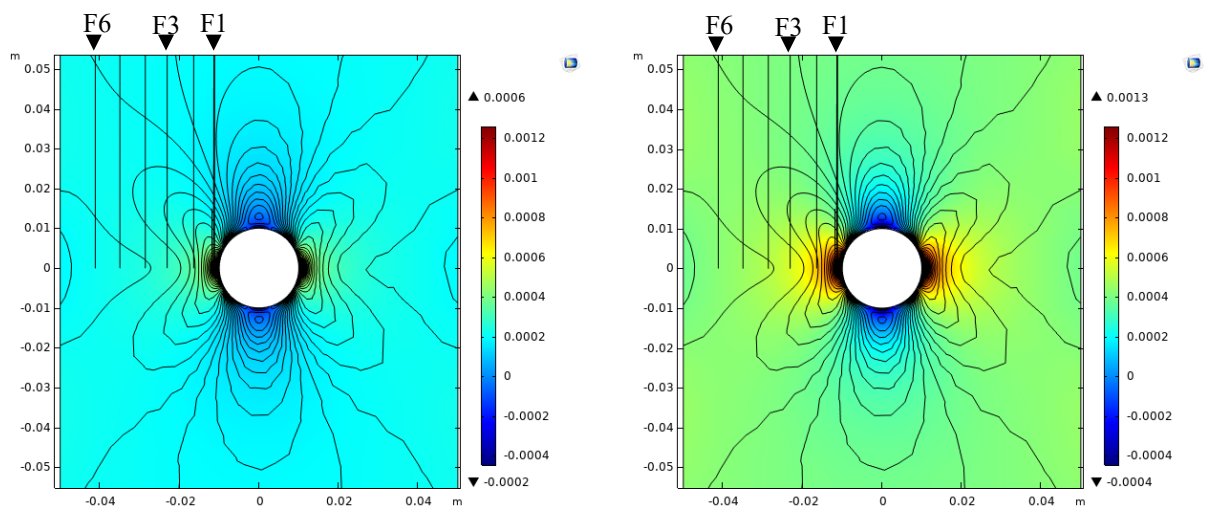


Figure 3. FEA of coupon test area at 10 kN (left) and 20 kN (right) showing complex strain distribution around the hole and steep strain gradients at the hole edge. The vertical lines indicate FO line positions (labelled F1 to F6) with F1 being closest to the hole edge.

Previous work using two different FO sensors under the same loading conditions showed data loss at high strain gradients [4]. In that study, data loss occurred at strain gradients greater than  $48 \mu\epsilon/\text{mm}$ , and as strain gradients increased further, the OFDR returned erroneous data. No data losses were observed in Figure 2 during quasi-static tensile loading in the current study, up to a strain gradient of  $146 \mu\epsilon/\text{mm}$  [4].

The scatter in strain estimates obtained from DIC was partly due to manually selecting strain locations from the raw pixel grid data for each image's processed data file. This is not as accurate between each file as selecting a point location on the image. Defining a point of interest in the image processing software and having the software track and save that point's relative location change and the corresponding strain information between each image data file would possibly provide more consistent data. For future testing it is recommended that points of interest be defined in the software prior to exporting of image data as this is a more streamlined process and avoids any possible error from the data analyst manually tracing a single data point through each data file.

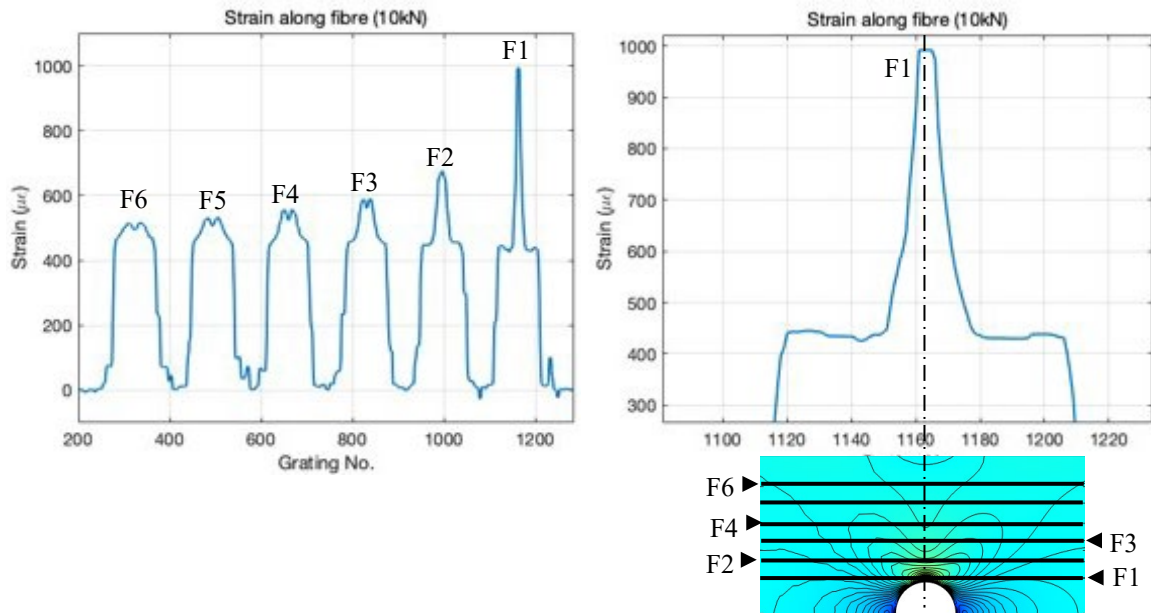


Figure 4. Strain profile measured along the entire length of FO at 10 kN (left). The six adhered lines of FO (labelled F1 to F6) span the length of the test area and are parallel to the loading direction. The FO line closest to the hole edge (labelled F1, right) shows peak strain at the hole centre-line.

The strain profile measured parallel to the loading direction along the entire length of FO sensor at a 10 kN static load is shown in Figure 4. The six peaks (Figure 4, left) represent six 150 mm lines of adhered FO sensor snaking the length of the test area (Figure 4, bottom) with the line closest to the hole edge (labelled F1) showing a peak strain at the hole centre-line (Figure 4, right). The magnitude of strain diminishes for each subsequent FO line away from the hole edge. Also, the strain profile changes from single (F1 and F2) to double peak (F3 to F6), in agreement with the FEA contour lines (Figure 4, bottom). Regions in the graph showing zero strain correspond to unbonded fibre (i.e. the looped fibre at the end of each adhered line). There is slight asymmetry to the peak shoulders which possibly corresponds to an effect from the twist. Figures 5 to 7 should be considered in the same orientation shown in Figure 4, where distance from the hole represents a distance parallel to the loading direction. As mentioned previously,

quarter symmetry of the coupon was used for FEA and the measured data presented here likewise takes advantage of the quarter symmetry.

A comparison of strain profiles obtained from FEA, FSG, FOS and DIC at 10 kN and 20 kN static loads along FOS line F1 (Figure 4), are shown in quarter symmetry in Figures 5 and 6. The FO strain profile mirrors that of the FEA prediction at both loads (Figure 5) with the FOS values being higher for the reason suggested previously. FO signal saturation, i.e. flattening of the strain profile, was observed at the hole edge due to a strain gradient sensing limit in the FOS system. The limit of the present system is an improvement over previously studied Rayleigh and continuous fibre Bragg grating sensor systems applied in a similar circumstance [4]. The strain profiles derived from FSGs (Figure 6) broadly agree with the FOS and FEA obtained strain profiles shown in Figure 5. Differences in measured strain values possibly correspond to small relative differences in the position of each sensor technology with respect to the hole edge, where strain gradients are relatively high. It is noted in Figure 6 that DIC determined strains vary significantly compared to other techniques and from 10 kN to 20 kN DIC values do not double with doubling of the load. Again, this is surmised to be due in part to manually selecting strain locations from the raw pixel grid data for each image's processed data file which introduces additional error relative to selecting a point location on the image.

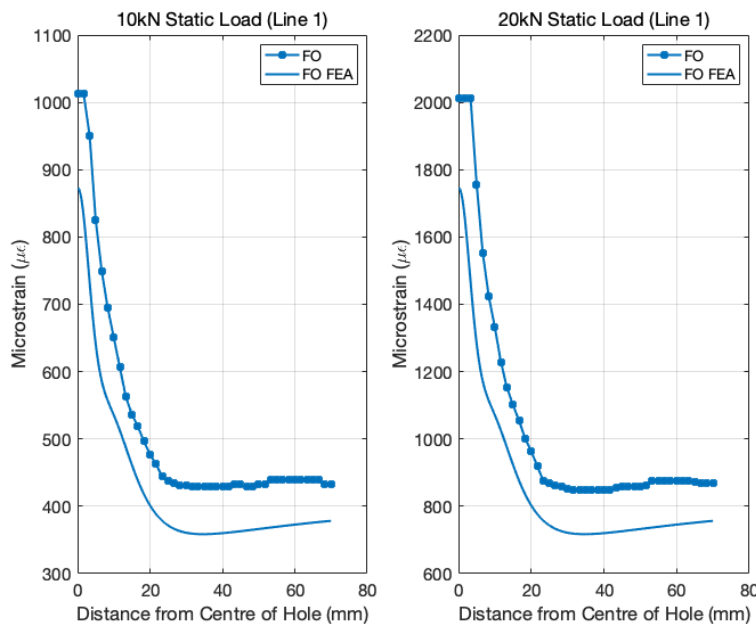


Figure 5. Strain profile obtained from FEA and FO line F1 (Figure 4) for 10 kN (left) and 20 kN (right) static loads.

FOS strain measurements were monitored during cyclic loading of the coupon at a 15 kN amplitude and representative data for FO lines F2 to F6 are presented in Figure 7. The three graphs (Figure 7 left to right) correspond to the fatigue crack tip approaching, passing under and having passed FO line F2, respectively. As expected, the strain at F2 increased as the crack tip approached and passed under F2 then decreased significantly in the crack wake. F2 continues to show limited strain profile response in the crack wake as the fibre in this section bridges the open crack. The strain values and profile along FO line F3 also respond to these events.

FO signal saturation was evident for the F2 peak in the three graphs presented in Figure 7. The strain gradient at F2 at the point of saturation was approximately 410  $\mu\epsilon/\text{mm}$ . In previous

testing of another system, erroneous data appeared at a comparatively much lower gradient of  $48 \mu\epsilon/\text{mm}$  [4].

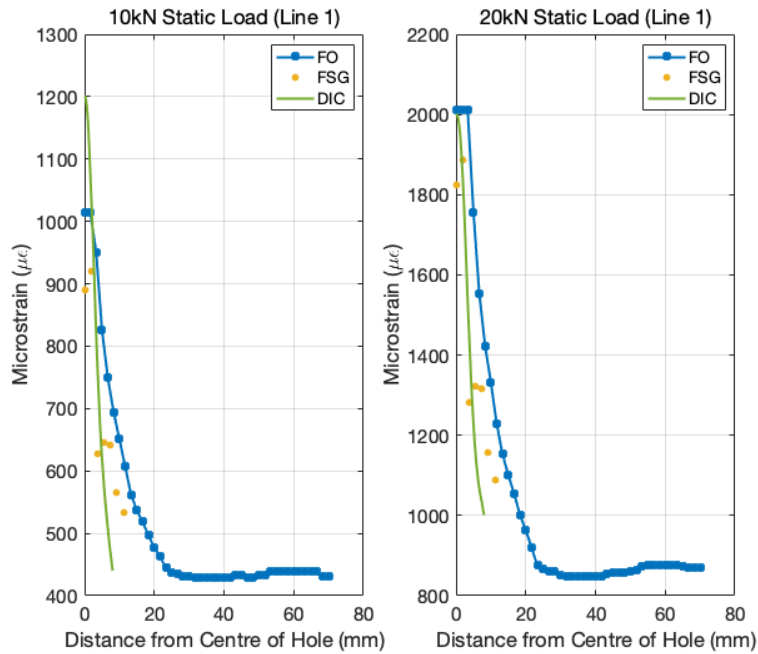


Figure 6. Strain profile corresponding to FO line F1, compared to FSG and DIC obtained values at 10 kN (left) and 20 kN (right) static loads.

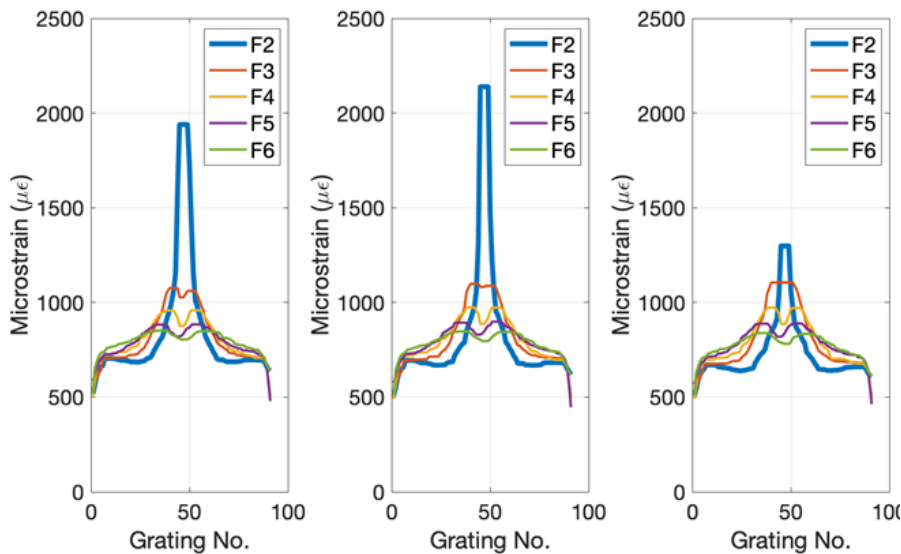


Figure 7. Strain measured at FO line F2 (Figure 4) as the crack tip approaches F2 (left); as the crack tip passes under F2 (centre); and, after crack tip passing F2 (right).

### Conclusions

This paper presented the results from an experimental assessment of a commercially available, non-proprietary distributed strain sensor based on all-grating fibre technology. The performance of the FO sensing system was compared to experimental strain measurements provided by DIC and FSGs. Strain measurements from all three methods were also compared to FEA predictions.

Comparison of the measured strain profiles and values showed reasonable agreement between the FOS, FSG and DIC values and with FEA predictions. It is surmised that the predicted and measured strain values would better align in the absence of an unintended twisting load caused by grip misalignment. FOS signal saturation, i.e. flattening of the strain profile at the peak tip, was observed at the hole-edge due to a strain gradient limit in the interrogation system. This minor data loss at the strain profile peak tip was observed for strain gradients greater than  $146 \mu\epsilon/\text{mm}$  in the current study. FOS systems studied previously showed a corresponding strain gradient limit of  $\sim 48 \mu\epsilon/\text{mm}$ . In this respect, the FOS system evaluated in the current study is a significant improvement. The distributed strain mapping capability together with the small size, light weight and fatigue resistance of FOS offers significant advantages over foil strain gauges for long-term monitoring purposes.

For future work, streamlining the integration and implementation of the measurement techniques by defining feature points of interest in the DIC software prior to exporting image data is recommended. Trialling FO distributed strain sensing and DIC technologies on full-scale fatigue test articles for further evaluation is also recommended.

### **Acknowledgements**

The authors gratefully acknowledge the contributions of Mr Daniel Bitton for his technical assistance in coupon instrumentation and the DST Group Fatigue and Fracture Laboratory for facilitating the mechanical test. They also acknowledge Mr Cedric Rosalie and Ms Maria Salagaras for their assistance with FEA modelling.

### **References**

- [1] All Grating Fibres (AGF), 2020, FBGS, viewed 9th October 2020.
- [2] Zhou, DP, Chen L & Bao X, Distributed dynamic strain measurement using optical-frequency domain reflectometry, *Applied Optics*, 55:24 (2016) 6735-6739.  
<https://doi.org/10.1364/AO.55.006735>
- [3] Alemohammad, H 2018, 'Opto-Mechanical Fiber Optic Sensors', Elsevier, United Kingdom.
- [4] Peter Ziros, Claire Davis, Nik Rajic. Distributed Strain Measurements using Continuous Fibre Bragg Gratings. DST-Group-TR-3473, April 2018.

# Comparative Evaluation of a High Operating Temperature Midwave Infrared Detector for Automated Non-Destructive Inspection of Composite Damage

Jaslyn Gray<sup>a\*</sup>, Michael Woodrow<sup>b</sup>, Cédric Rosalie<sup>c</sup>, Nik Rajic<sup>d</sup>

Defence Science and Technology Group, 506 Lorimer Street, Fishermans Bend, VIC, 3207, Australia

<sup>a</sup>jaslyn.gray@dst.defence.gov.au, <sup>b</sup>michael.woodrow@dst.defence.gov.au, <sup>c</sup>cedric.rosalie@dst.defence.gov.au, <sup>d</sup>nik.rajic@dst.defence.gov.au

© 2020 Commonwealth of Australia

**Keywords:** Line Scan Thermography, Composites, Dynamic Pulse Phase Thermography, Non-destructive Testing, Barely Visible Impact Damage, Robotic Inspection

**Abstract.** A new high operating temperature (HOT) midwave infrared (MWIR) imaging core is experimentally evaluated for use in automated inspection of composite impact damage by line scan thermography (LST). This evaluation is undertaken as part of a broader effort to develop an autonomous inspection capability for aerospace composite structures, deployable by ground and aerial robotic systems. The performance of the HOT MWIR core is assessed against a high-performance cooled photon-detector camera, an uncooled microbolometer core and an uncooled microbolometer camera, on two carbon epoxy laminate test specimens: one containing flat-bottom-hole synthetic defects and the other barely visible impact damage (BVID) introduced by controlled low-velocity impact. These test panels are scanned using a 3-axis robotic LST apparatus, at speeds of 25 and 100 mm/s. The HOT MWIR core is shown to match the detection performance of the cooled camera, and to significantly outperform both microbolometers. The high performance of this core combined with its relatively low mass, size and power consumption offers an encouraging basis for the development of a drone-deployable LST inspection capability.

## Introduction

The use of carbon fibre reinforced polymer (CFRP) components in aircraft construction has increased steadily over time. For example, a typical airframe manufactured in the 1970s contained approximately 5% by weight in CFRP, whilst a modern A350 contains over 50% [1]. This trend is continuing. CFRPs have many practical advantages over metals for aircraft construction, including a higher strength and stiffness to weight ratio and better corrosion and fatigue resistance. However, they are more prone to damage by impact. Barely visible impact damage (BVID) [2] is of particular concern as this type of damage is difficult to detect by visual inspection and if left undetected can result in component failure. This has driven interest in more rapid and reliable methods of BVID detection, sizing and analysis. Automated and autonomous inspection by aerial and ground robotic systems [3,4] is an emerging area of interest with the potential to significantly reduce inspection time and cost relative to current practice.

Several different non-destructive testing (NDT) methods have been applied to BVID inspection [5]. These can be broadly categorised into contact or non-contact methods; contact methods, e.g. ultrasonic, eddy current and liquid penetrant, are generally considered to be more

accurate but time consuming, whereas non-contact methods are generally faster and more versatile [6]. Active infrared thermography (AIT) [7] is a key non-contact method. AIT uses an external energy source, most commonly a high intensity lamp, to heat a subject and the resulting surface temperature distribution is observed with an infrared camera. The delaminations associated with BVID impede through-thickness heat flow resulting in a locally lower rate of cooling, thus producing a surface temperature contrast.

Line Scan Thermography (LST) is a variant of AIT wherein a line source of heat moves at constant speed over the test area which is observed by an infrared camera moving in unison with the source [8]. LST has the capacity to inspect large areas of structure at relatively high speed and the potential to be deployed by either an unmanned aerial vehicle (UAV) or unmanned ground vehicle (UGV) [9]. Preliminary work toward realising such a capability was undertaken using a 3DOF Cartesian robot and was reported in [10]. In this previous work, experimental testing on laminate samples containing BVID produced generally encouraging results, but it also demonstrated that a relatively high-performance infrared imaging capability is necessary to achieve satisfactory detection results; specifically, a cooled photon imager was shown to significantly outperform a microbolometer. However, cooled detectors are relatively large and expensive and for these reasons impractical for the drone-based inspection application under consideration.

The recent emergence of high operating temperature (HOT) medium wave infrared (MWIR) imaging core technology offers a potential solution. These HOT MWIR cores employ a type II strained layer superlattice (T2SL) sensor material which suppresses dark current noise at significantly higher detector operating temperatures ( $\sim 120$  K) than are required for traditional cooled photon detectors ( $\sim 77$  K) [11]. This reduced cooling requirement results in a device which is comparatively much smaller, lighter, and power efficient, whilst achieving similar imaging performance.

The principal aim of the present work is to experimentally evaluate the LST inspection performance of this new class of infrared imaging device against a conventional high-performance cooled photon camera and two uncooled microbolometers. Complementary multiphysics-based simulations of the LST process are also undertaken to verify a new image processing approach called dynamic pulse phase thermography (DPPT) which is used to extract defect signatures from raw data obtained from the different imaging devices.

## Experimental Testing

LST experiments were undertaken using a 3-axis Cartesian robotic facility illustrated in Fig. 1(a).

Translation along the three axes is achieved using brushless DC motors which are driven through a programmable logic controller (PLC). The LST sensing apparatus comprises an infrared imager and luminaire installed at the base of the z-axis robot arm. The luminaire (Fig. 1(b)) contains a polished metal parabolic reflector which focuses light from a 118 mm long 150 W quartz-halogen lamp positioned at the reflectors focal point, to a line width of  $\sim 20$  mm at a distance 500 mm from the lamp. Previous work has shown that this line width is sufficient to produce reliable indications of the composite damage targeted in the present investigation [10].

Table 1 lists the four IR imaging devices considered in this study along with relevant specifications. The last three rows of this table illustrate the profound difference in size, mass and power consumption of uncooled HOT MWIR detectors compared to a typical cooled camera. Henceforth, these imagers will be referred to by the designation given in Table 1.

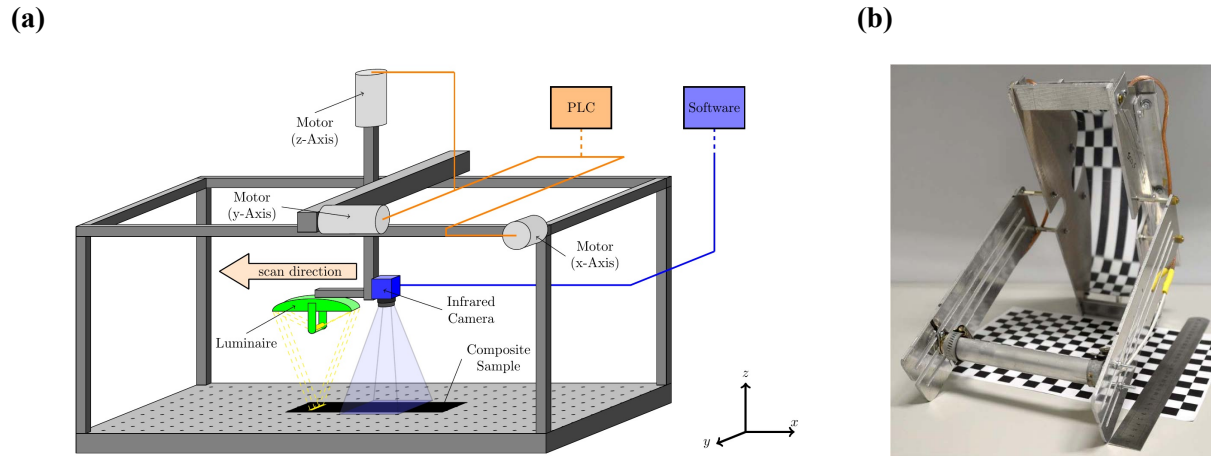


**Fig. 1:** (a) Schematic of 3-axis Cartesian robot showing key LST system components. (b) Luminaire comprising a lamp and parabolic reflector, with 300 mm ruler shown for scale.

**Table 1:** Infrared imager specifications.

Type	Microbolometer	Microbolometer	Cooled Photon detector	HOT Photon detector
Manufacturer and model	FLIR Boson A640	Xenics Gobi 640	FLIR SC6000	FLIR Neutrino LC
Designation	$\mu$ B-VOx	$\mu$ B-aSi	PD-cooled	PD-HOT
Detector	Vanadium Oxide	Amorphous Silicon	Indium Antimonide	HOT MWIR
Spectral range [ $\mu$ m]	7.5–13.5	8.0–14.0	3.0–5.0	3.4–5.0
Published NETD [mK]	50	55	18	30
Array size	640×512	640×480	640×512	640×512
Frame rate [Hz]	60	50	100	60
Dimensions ((L×W×H)) [mm]	21×21×11	79×49×49	320×141×159	79×45.5×61
Mass [g]	7.5 (without lens)	263	4500	380
Power [W]	+0.5	4.5	50	4.5

### Composite test samples

Two composite panels were examined in this study (see Fig. 2). The first panel is a rectangular laminate 330 x 240 x 2.5 mm in size and consisting of 9 plies of M18/1/43% G939 carbon-epoxy biaxial pre-preg in the layup [45/0/0/-45/0/-45/0/0/45]<sub>1</sub>. This panel contains six flat bottom holes (FBH) of 5, 10, and 20 mm diameters at two different depths corresponding to a residual panel thickness of 1 and 1.5 mm, as illustrated in Fig. 2(a). The second panel is also a rectangular, 470 x 100 x 4 mm in size and consists of 30 plies of IM7/977-3 carbon-epoxy pre-preg in the lay-up [45/0/0/-45/90]<sub>s3</sub>. This second laminate contains a single BVID feature introduced by a 10 J controlled low-velocity impact. The presence of BVID in this panel was previously verified by flash thermography and pulse-echo ultrasonic testing, with indications produced by these methods shown in Fig. 2(b). The inspection surfaces of both samples were given a thin coating of high-emissivity matt black paint in preparation for LST testing.

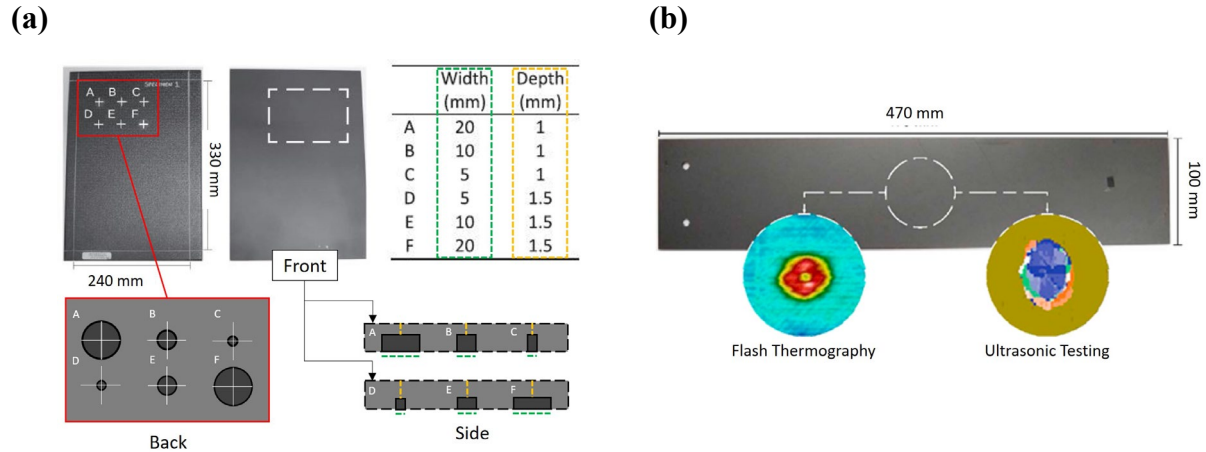


**Fig. 2:** (a) Composite panel containing six FBH defects. Back face showing FBH and front face with high emissivity paint coating. White dotted rectangle indicates area where defects are located. (b) BVID panel with damage confirmed by flash thermography and ultrasonic testing.

### Test and Processing Methodology

LST inspections of the FBH and BVID test panels were undertaken using the four previously described imagers. A single scan consisted of one sweep of the sensor head in the x-direction at a constant speed of 25 mm/s and 100 mm/s. Data acquired from each scan was post-processed using DPPT to produce a set of phase maps that were used as the basis for the performance comparison between detectors. The DPPT approach was detailed previously in [10]. For the purposes of the present article the salient feature of DPPT is that it maps thermal contrasts produced by sub-surface defects into dipole-like phase signatures, as will become clear in the following sections.

### Numerical Simulations

Numerical simulations of the heat diffusion physics associated with an LST inspection were undertaken for two reasons: (i) to produce synthetic data for verification that the DPPT algorithm is functioning correctly and (ii) to foster insight into the LST process and in particular the effect of scan speed on the defect signature. The simulations were conducted using the COMSOL 5.3 software package. Only the FBH sample was considered and was modelled as a three-dimensional transversely isotropic plate, with Table 2 listing the relevant material properties used for the simulation. The heat source was modelled as a Gaussian pulse (see Fig. 3) with a full-width at half-maximum dimension of 20 mm. The laminate was meshed using tetrahedral elements and the solution was advanced in time steps of 0.01 s.

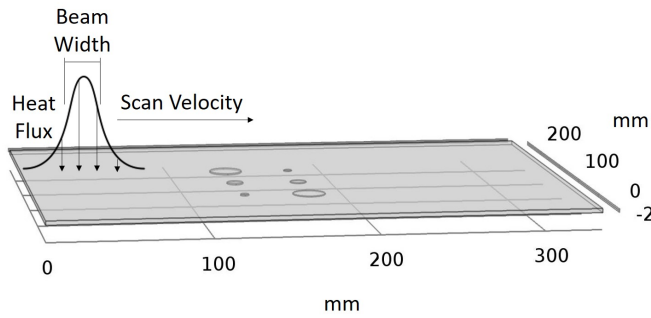


**Fig. 3:** Modelled plate geometry with key parameters.

**Table 2:** Material properties and simulation parameters.

Material properties and parameters	
Density ( $\rho$ ) [kg/m <sup>3</sup> ]	1530
Heat capacity ( $C_p$ ) [J/(kg K)]	950
Lateral thermal conductivity ( $K_x, K_y$ ) [W/mK]	3.19
Thickness thermal conductivity ( $K_z$ ) [W/mK]	0.57
Scan velocity [mm/s]	25,100
Beam width [mm]	20
Defect diameter [mm]	20, 10, 5

Two scan velocities were considered in the simulation: 25 mm/s and 100 mm/s, which correspond to the velocities also considered in the experimental work. Fig. 4(a) shows a representative surface temperature distribution from a simulation conducted at a 25 mm/s scan speed, at a time ~ 8 seconds after the source has passed over the centre of the FBH region, which corresponds to peak contrast for the FBH signatures. A 1.35 s time window corresponding to when the defects are in the field of view of the IR imager during an experimental scan (between 14.65-16 s on the scale shown in Fig. 4(a)) was processed using DPPT to produce the phase map in Fig. 4(b).

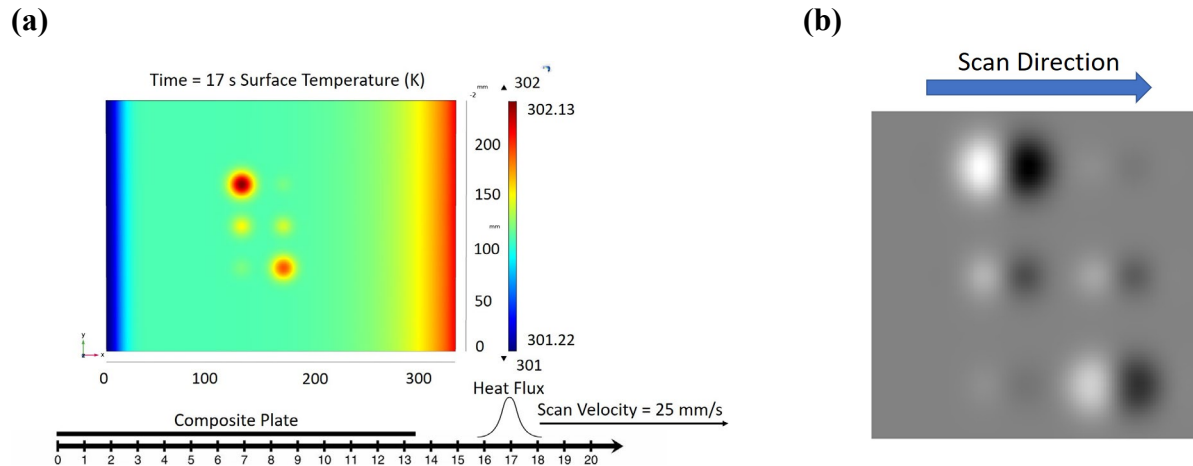


**Fig. 4:** (a) Surface temperature distribution obtained from simulation of a 25 mm/s scan of FBH panel; timeline indicates heat flux position relative to panel.  
 (b) Corresponding DPPT phase map at 945 mHz, 120 mm square region of interest.

The circular dipole signatures in Fig. 4(b) closely resemble experimentally obtained signatures reported in [10] and thus confirm proper functioning of the DPPT algorithm. Additionally, this result provides validation of the modelling capability, which is important for future development of this approach in allowing different inspection parameters and scenarios to be investigated in a simulated environment with confidence.

## Results and Discussion

Experimentally obtained FBH panel scan results corresponding to the four different IR imagers are compared in Fig. 5. These scans were undertaken at 25 and 100 mm/s, and the results correspond to the phase at 945 mHz, obtained from DPPT applied to a 1.35 s data window.

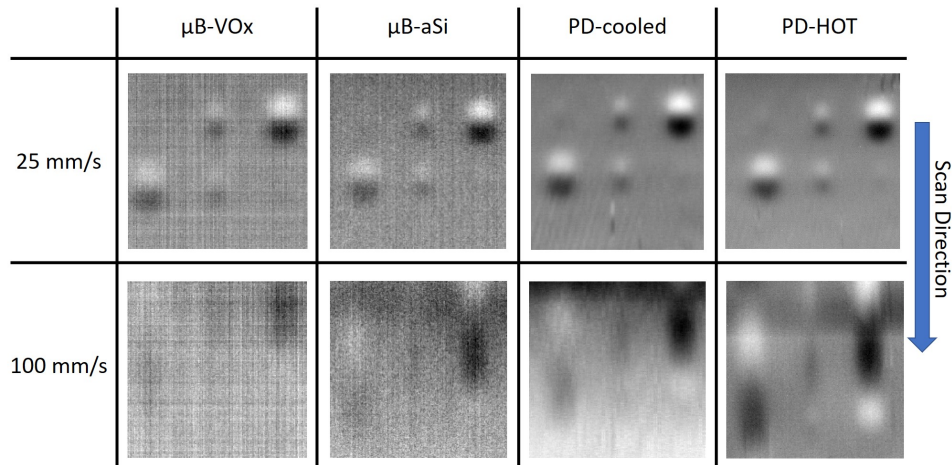


**Fig. 5:** Phase maps corresponding to FBH panel scanned at 25 mm/s and 100 mm/s for each IR imager. The region of interest is square with side dimension of 120 mm.

These results show that the 20 mm and 10 mm diameter FBH defects are well resolved at the slowest scan speed for all imagers. However, for the 5 mm diameter defects, signatures are discernible, albeit faintly, only for the PD-cooled and PD-HOT imager results. The performance gap between these devices and the two microbolometers is more significant in the high scan-speed results (bottom row). Here, even the larger diameter defects are barely visible in the  $\mu\text{B-VOx}$  results, and only marginally more visible in the  $\mu\text{B-aSi}$  results. The PD-HOT imager yields noticeably better results than the PD-cooled camera, which is interesting given the relative noise equivalent temperature difference (NETD) specifications of these devices (see Table 1). It is to be noted that the failure to resolve between the two rows of defects at the 100 mm/s scan speed is due to a trade-off between scan speed and spatial resolution in LST, an issue that will be considered more thoroughly in a separate study.

The experimental results obtained from the PD-HOT core and PD-cooled camera for the FBH panel were also compared to corresponding predictions from the previously described numerical model, as shown in Fig. 6. This comparison illustrates remarkably good correlation, which provides further confidence in the developed model.

Fig. 7 shows results obtained for the BVID panel using the PD-HOT and PD-cooled imagers, at scan speeds of 25 and 100 mm/s. Signatures corresponding to the BVID are discernible in all four cases, but are strongest at the faster scan speed, presumably because of the shorter time available for heat diffusion. This result is encouraging from the viewpoint of developing a rapid inspection capability deployable by drone, for which HOT-MWIR imaging core technology appears well suited.

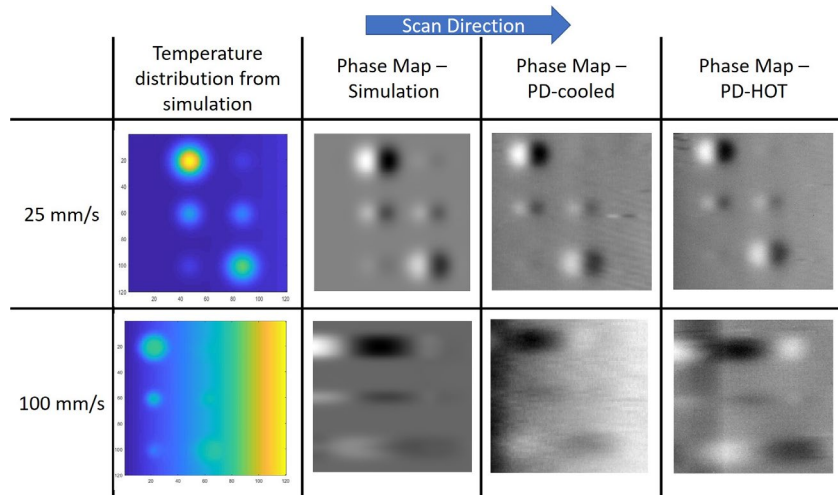


**Fig. 6:** Comparison of phase maps obtained from simulation and experimentally for the PD-cooled and PD-HOT imagers at scan speeds of 25 mm/s and 100 mm/s. The region of interest and time window is unchanged from the previously described case.

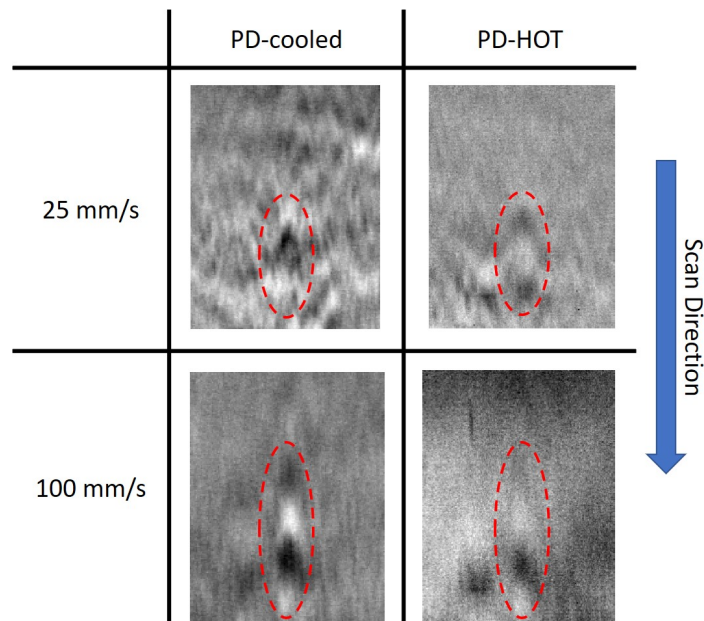


**Fig. 7:** Phase maps corresponding to BVID panel scanned at scan speeds of 25 mm/s and 100 mm/s using the PD-cooled and PD-HOT imagers. Dashed ellipse outlines defect signature ellipse. The region of interest is 85 mm x 110 mm and observation time was 1.35 seconds.

**Conclusion**

A new high operating temperature mid-wave infrared imaging core has been experimentally evaluated for use in rapid automated inspection of composite damage by line scan thermography. The performance of this device was tested against an amorphous silicon microbolometer, a vanadium oxide microbolometer and a mid-wave cryogenically-cooled photon detector camera on composite laminates with flat-bottom-hole synthetic defects and barely visible impact damage. On both laminates the imaging core significantly outperformed the microbolometers and yielded comparable performance to the cooled camera. Given this core is a fraction of the

mass and size of a typical cooled camera and consumes considerably less power, these results are encouraging for the development of a drone-deployable composite inspection capability using line scan thermography.

### Acknowledgment

The authors acknowledge Mr. Chris Brooks, Mr. Daniel Bitton and Mr. Stephen van der Velden for their assistance in the experimental work.

### References

- [1] Mouritz, Adrian P, Introduction to aerospace materials, Elsevier, 2012.  
<https://doi.org/10.1533/9780857095152>
- [2] Morton J, Godwin EW, Impact response of tough carbon fibre composites, Composite Structures, 1989 Jan 1;13(1):1-9. [https://doi.org/10.1016/0263-8223\(89\)90069-X](https://doi.org/10.1016/0263-8223(89)90069-X)
- [3] Mavromatidis, L.E. & Dauvergne, J.-L & Lunazzi, Renato & Batsale, Jean-Christophe, First experiments for the diagnosis and thermophysical sampling using pulsed IR thermography from unmanned aerial vehicle (UAV), Quantitative InfraRed Thermography, 2014.  
<https://doi.org/10.21611/qirt.2014.213>
- [4] V. Kostopoulos, S. Psarras, T. Loutas, G. Sotiriadis, I. Gray, M.J. Padiyar, I. Petrunin, J. Raposo, L. Zanolli, Fragonara, V. Tzitzilonis, K. Dassios, D. Exarchos, G. Andrikopoulos, G. Nikolakopoulos, Autonomous Inspection and Repair of Aircraft Composite Structures, IFAC-PapersOnLine, Volume 51, Issue 30, 2018, Pages 554-557, ISSN 2405-8963.  
<https://doi.org/10.1016/j.ifacol.2018.11.267>
- [5] Hossein TOWSYFYAN, Ander BIGURI, Richard BOARDMAN, Thomas BLUMENSATH. Successes and challenges in non-destructive testing of aircraft composite structures. Chinese Journal of Aeronautics, Volume 33, Issue 3, 2020, Pages 771-791.  
<https://doi.org/10.1016/j.cja.2019.09.017>
- [6] S. Gholizadeh. A review of non-destructive testing methods of composite materials, Procedia Structural Integrity, 2016, vol. 1, pp. 50-57. <https://doi.org/10.1016/j.prostr.2016.02.008>
- [7] Prakash, R.V., John, M., Post-impact Fatigue Damage Analysis of Quasi Isotropic CFRP Laminates through Infrared Thermography, Frattura ed Integrita Strutturale, 2019.  
<https://doi.org/10.3221/IGF-ESIS.49.50>
- [8] Lison, M., Hendrick, P., Servais, P., Dufour, Y., Evaluation of NDT by robotic line scan thermography on composite air-craft parts, Structural Health Monitoring 2017: Real-Time Material State Awareness and Data-Driven Safety Assurance - Proceedings of the 11th International Workshop on Structural Health Monitoring, IWSHM 2017, 1, pp. 86-93.  
<https://doi.org/10.12783/shm2017/13853>
- [9] Shakeb Deane, Nicolas P. Avdelidis, Clemente Ibarra-Castanedo, Hai Zhang, Hamed Yazdani Nezhad, Alex A. Williamson, Tim Mackley, Maxwell J. Davis, Xavier Maldague, Antonios Tsourdos, Application of NDT thermographic imaging of aerospace structures, Infrared Physics & Technology, Volume 97, 2019, Pages 456-466.  
<https://doi.org/10.1016/j.infrared.2019.02.002>
- [10] James Moran, Nik Rajic. Remote line scan thermography for the rapid inspection of composite impact damage, Composite Structures, Volume 208, 2019, Pages 442-453.  
<https://doi.org/10.1016/j.compstruct.2018.10.038>
- [11] FLIR Systems, Inc., “Why HOT MWIR Might Be a Better Fit than Uncooled LWIR”, FLIR Systems, Inc., [Online]. Available: <https://www.flir.com>. [Accessed: Nov. 06, 2020].

# Residual Stress Measurement of Additively Repaired Ti-6Al-4V Using Fibre Optic Sensing

Matthew Stevens<sup>1,a\*</sup>, Kieran Pryor<sup>2,b</sup> and Suzana Turk<sup>3,c</sup>

<sup>1</sup>Defence Science and Technology Group, 506 Lorimer Street, Fishermans Bend, VIC, 3207, Australia

<sup>a</sup>[matthew.stevens@dst.defence.gov.au](mailto:matthew.stevens@dst.defence.gov.au), <sup>b</sup>[kieran.pryor@dst.defence.gov.au](mailto:kieran.pryor@dst.defence.gov.au),  
<sup>c</sup>[suzana.turk@dst.defence.gov.au](mailto:suzana.turk@dst.defence.gov.au)

© 2020 Commonwealth of Australia

**Keywords:** Fibre Optics, Distributed Strain Sensing, Continuous Fibre Gratings, Residual Stress, Laser Metal Deposition

**Abstract.** Laser metal deposition (LMD) is a laser-based additive manufacturing (AM) technology that offers significant advantages in the production and repair of bespoke and valuable parts targeting applications in the aerospace, tooling and medical industries. A significant problem with AM is the development of high residual stresses, deformation and cracking. Advanced sensing technologies can be a useful tool for characterising residual stress (RS) and the structural response of AM aerospace components under fatigue loading conditions. This paper reports on a feasibility study assessing the performance of fibre optic (FO) distributed strain measurement technology to measure surface RS in comparison to traditional electrical resistance strain gauges and the contour method. The results from this study will be used to justify further experimental work.

## Introduction

LMD applications have been targeted for repairing intricate geometries and structural restoration of specialised high value components such as sintered tools and aerospace components [1,2]. Metallic powder is blown through a deposition nozzle and heated with a laser to produce a metallic bead that is deposited, layer by layer and track by track, to build-up a part or to add layers of material to an existing part. The nozzle system shrouds the work area with shield gas thereby eliminating the requirement for enclosures with controlled environments and thus providing exciting opportunities for Defence applications.

LMD delivers high density deposited material with a strong metallurgical bond to the substrate. However, the repeated and highly localised heating and cooling lead to non-uniform thermal expansion and contraction which results in a complicated distribution of RS in the heat affected zone (HAZ) and distortion of the part [3,4]. Similar to the HAZ in welding, RSs are detrimental to the structural integrity of the part, with warping and stress concentrations promoting fatigue cracking and inducing unpredictable buckling in service.

The nature and magnitude of RS in the deposited material and substrate affect the integrity of the component. In a previous study RS was reported to be lower transverse to the deposition track and for shorter track lengths, due to higher remnant heat leading to smaller temperature gradients which in turn leads to lower RS [5]. The HAZ and molten pool had an elongated shape in the deposition direction and the temperature gradient was pronounced due to the relatively low thermal conductivity of Ti6Al4V [6]. This could induce an uneven RS profile with peak RS coinciding with the final track deposit and laser stop position [7].



Methods for measuring RS include the contour method, a destructive and time-intensive test that determines RS by creating a free surface and measuring the resulting deformation due to RS redistribution. It delivers a 2D through-thickness RS contour map. Neutron diffraction delivers a non-destructive through-thickness line measurement but is sample-size restrictive and time-intensive. In the present study, a non-destructive alternative is proposed using FO sensing (FOS), a rapidly evolving technology which has been considered for structural health monitoring of airframes, bridges and pipelines.

Developments in FOS using continuous fibre gratings allow this technology to offer a densely distributed strain measurement capability. Distributed sensing is achieved using a low reflectivity grating, which is a small periodic change in refractive index of the glass fibre core, written over the entire fibre length as it is being fabricated in the draw tower. This configuration is known as a continuous fibre grating [8]. These sensing systems rely on spatially interrogating the backscattered light from the gratings via optical frequency domain reflectometry (OFDR), which measures the spectral shift of the backscattered light in time (via a fast Fourier transform) and then scales this shift by the known number of gratings to correlate changes in length to corresponding changes in strain [9].

It was proposed that FOS could potentially deliver surface RS measurements comparable to the well-established contour method in a shorter timeframe. Therefore, this paper reports on a feasibility study assessing the performance of FO distributed strain measurement technology to measure surface RS in comparison to industry standard electrical resistance foil strain gauges (FSGs) and the contour method reported in [4]. The results from this feasibility study will be used to justify further experimental work.

### Experimental Method

**Material.** Rectangular section fatigue coupons, measuring  $200 \times 19 \times 6.35$  mm, were manufactured from Ti-6Al-4V plate, Figure 1(a). A section measuring  $19 \times 12.7 \times 0.8$  mm was machined out of the centre gauge length (Figure 1, BL-GO) and repaired with one layer of laser deposited Ti-6Al-4V powder. The RS distributions of two deposition strategies were studied: LMD-1 is a continuous raster scan with deposition tracks parallel to the coupon length and loading direction, Figure 1(b); and LMD-2 which is a continuous raster scan with deposition tracks perpendicular to the coupon length and loading direction, Figure 1(c). Five coupons were tested in total, two LMD-1 and three LMD-2 type coupons. The baseline and baseline grind-out coupons are shown in Figure 1(a) for reference only. Thermal cycling and RS from the repair process resulted in coupon bowing, Figure 2.

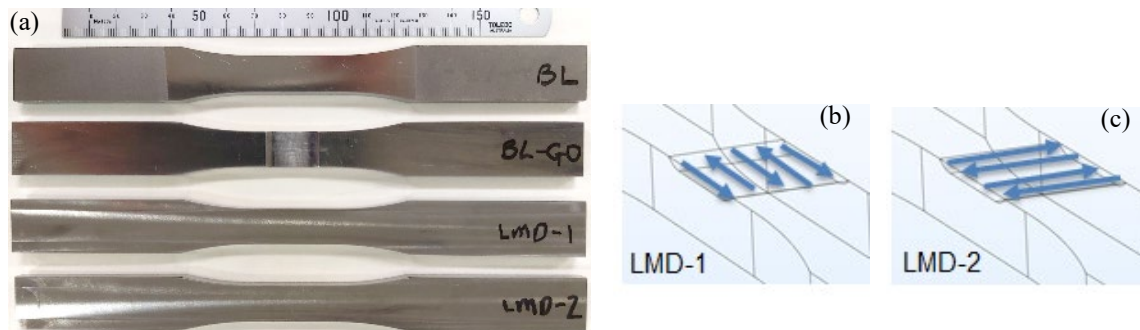


Figure 1. Fatigue coupons: (a) baseline (BL) with no repair; baseline grind-out (BL-GO) with no repair but indicates repair area; laser metal deposition (LMD-1) repair tracks parallel to coupon gauge length and loading direction, refer to (b); and (LMD-2) repair tracks perpendicular to coupon gauge length and loading direction, refer to (c).



Figure 2. Side view of fatigue coupons pinned down on left hand side, showing BL (bottom), BL-GO (centre) and bowing of LMD-1 and LMD-2 repaired coupons (top, labelled LMD-1 and LMD-2).

**Instrumentation.** The coupons were instrumented with a 3 m sensing length of commercially supplied all grating fibre (FBGS) that was interrogated using an OFDR based measurement system (Sensuron Summit). This sensing system combination offers a minimum spatial resolution of 1.6 mm and a notional  $\pm 1 \mu\epsilon$  accuracy.

Loctite EA9309.3NA epoxy was used to adhere the sensing fibres to the titanium alloy substrate in parallel lines along the gauge and loading axis in a looping format with unbonded loops, Figure 3(a). Twelve sensing lines were adhered with four parallel lines on the repair face and back face and two parallel lines on the side gauges, Figure 3(b).

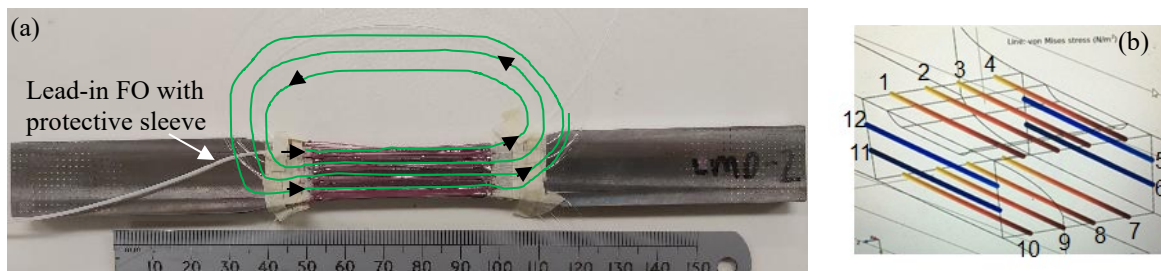


Figure 3. FO instrumentation layout: (a) lead-in FO begins at top left with four parallel lines adhered on the repair face showing unbonded loops, and (b) adhering and looping format continued wrapping around the coupon in a clockwise direction.

An example LMD-2 coupon was instrumented with FOS and FSGs for direct strain data comparison and validation with an industry standard technique. Two Kyowa copper plated 120-ohm KFG-1-120-D9-11N10C2 FSGs were adhered in line along one half of the coupon gauge length and repair area to measure strain in the direction of loading, Figure 4. An optical fibre was adhered in line with the FSGs on the other half of the coupon, with another two FO lines adhered directly adjacent to the FSGs and spanning the gauge length. The strain gauges were adhered to the titanium alloy substrate using M-Bond adhesive. These FSGs provide 2 mm spatial resolution and a notional  $\pm 1 \mu\epsilon$  accuracy. A National Instruments Data Acquisition (NI DAQ) chassis and NI-9235 8-channel C series strain/bridge input module were used to capture FSG data. For comparison to published data, FOS and FSG strain data were converted to stress using Equation 1, where  $\sigma$  is stress,  $E$  is elastic modulus (121 GPa) and  $\epsilon$  is the measured strain.

$$\sigma = E \times \epsilon \tag{1}$$

**Load Application.** Coupon loads were applied using a 100 kN servo-hydraulic mechanical testing machine in a National Association of Testing Authorities (NATA) certified laboratory. The upper coupon grip was secured with hydraulic wedge-grip jaw faces. While the lower coupon grip was unclamped, instrumentation was calibrated and zeroed. Residual stress was recorded when the lower coupon grip was secured with grip pressure and zero applied load,

forcing the bowed coupon to straighten. Therefore, the RS distributions reported in this paper were equal in magnitude but opposite in sign to those accumulated during the repair, that is, RS was measured in reverse. FSG and FO strain data was recorded during a 0-40 kN ramp load excursion to enable comparison between the two sets of measurements.



Figure 4. Two FSGs (labelled) were instrumented in line along one half of the coupon gauge length and repair area to measure strain in the direction of loading. An FO sensor was adhered in line with the FSGs on the other half of the coupon (labelled FO L3) with a second (labelled FO L2) and third FO line (labelled FO L3) adhered directly adjacent to the FSGs and spanning the gauge length.

### Results and Discussion

Strain profiles along the gauge length measured with the FOS and FSGs at zero uniaxial load and at 40 kN are compared in Figure 5, with the data arranged as instrumented in Figure 4. It is to be noted that when the coupon is clamped under grip pressure a straightening moment results, which explains the non-zero RS profile at zero applied load. The strain profiles are in general agreement, with evidence of an uneven RS profile both along and across the gauge length. This observation is consistent with other reported studies [4,6]. The highest RS was recorded in FO L2, with a peak value of 153 MPa, while the peak stress value at maximum applied load occurred in FO L1. Although not shown here, coupon fatigue initiation and fracture occurred between FO L1 and FO L2 approximately -6 mm from the repair centre where the FO line graphs overlap at maximum applied load, Figure 5(b). The peak RS for the five coupons tested are summarised in Table 1 and ranged between 107-179 MPa, with these values correlating well with the severity of bowing. This range is consistent with near-surface RS values measured by the contour method reported in [4]. RS values are expected to vary between coupons due to thermal cycling of multiple clad coupons on a build plate which leads to different bowing profiles. These results show that FOS can provide a reasonable estimate for the RS distribution and of the peak stress at high load, for this application.

Table 1. Summary of measured coupon bowing and residual stress obtained from FO sensors.

Repair Strategy	Bowing [mm]	Peak Residual Strain [ $\mu\epsilon$ ]	Peak Residual Stress [MPa]
LMD-1	5.06	1478	179
LMD-1	3.74	1047	127
LMD-2	3.05	882	107
LMD-2	4.21	1220	148
LMD-2	4.77	1265	153

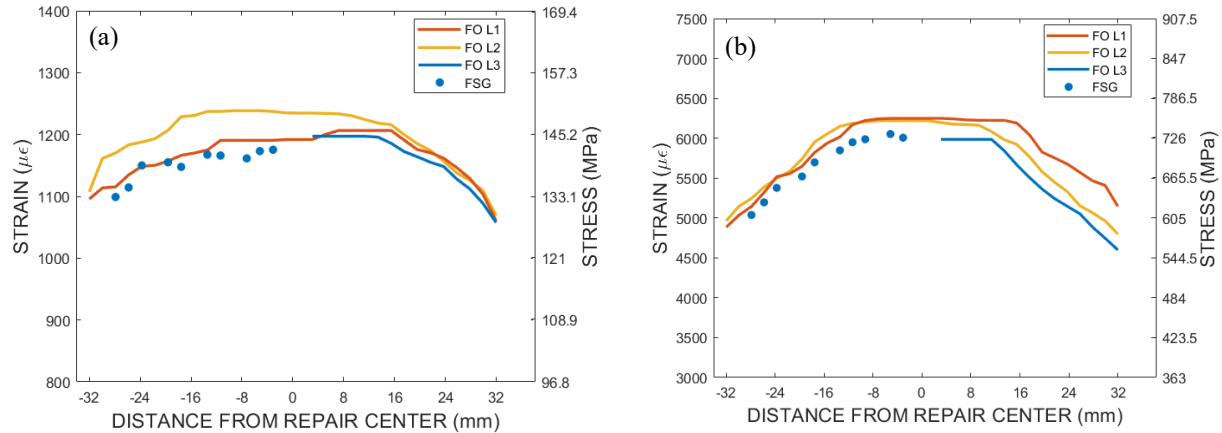


Figure 5. Example LMD-2 strain profiles along the gauge length from FO sensors and FSGs are presented at two load conditions: zero applied load, corresponding to residual stress distribution (a), and at 40 kN, corresponding to an applied stress of 500 MPa (b).

Results from the coupon fatigue testing, including FOS determined RS values and profiles, are presented in the following format through Figures 6-9: the residual stress distribution along the entire fibre length for all four coupon sides (refer to Figure 3), a magnified view of the peak RS which is shown in the same orientation as the coupon photos, i.e. left to right along the gauge length, and coupon photos showing the instrumented gauge, the machined section indicating repair area and the fatigue fracture location.

**LMD-1 Results.** The RS distribution for an example LMD-1 coupon is shown in Figure 6(a). As mentioned previously, RS values reported in this paper are equal in magnitude but opposite in sign to those accumulated during the repair. Under grip pressure and zero axial load, the repair face was in tension while the back face was in compression. Regions in the graphs showing zero strain correspond to un-bonded fibre, i.e. the looped fibre at the end of each adhered line, Figure 6(a) and 6(b). The RS profile both along and across the gauge length was uneven, indicated respectively by the different peak values and asymmetric profiles labelled F1 to F4 in Figure 6(a) (the corresponding FOS lines are labelled in Figure 6(c)). These profiles indicate increasing RS along the gauge length from left to right and across the gauge from F4 to F1. The maximum RS, corresponding to profile F1 (shown magnified in Figure 6b), was 179 MPa and occurred at the repair and HAZ interface. This maximum coincided with the coupon fracture and fatigue initiation location (arrowed in Figure 6c).

The RS distribution for another example LMD-1 coupon is shown in Figure 7(a). The RS profile both along and across the gauge length was uneven, with profiles labelled F1 to F4 showing increasing RS along the gauge length from left to right and across the gauge from F1 to F4. The maximum RS corresponding to profile F4 was 127 MPa and coincided with the coupon fracture and fatigue initiation location (arrowed in Figure 7c).

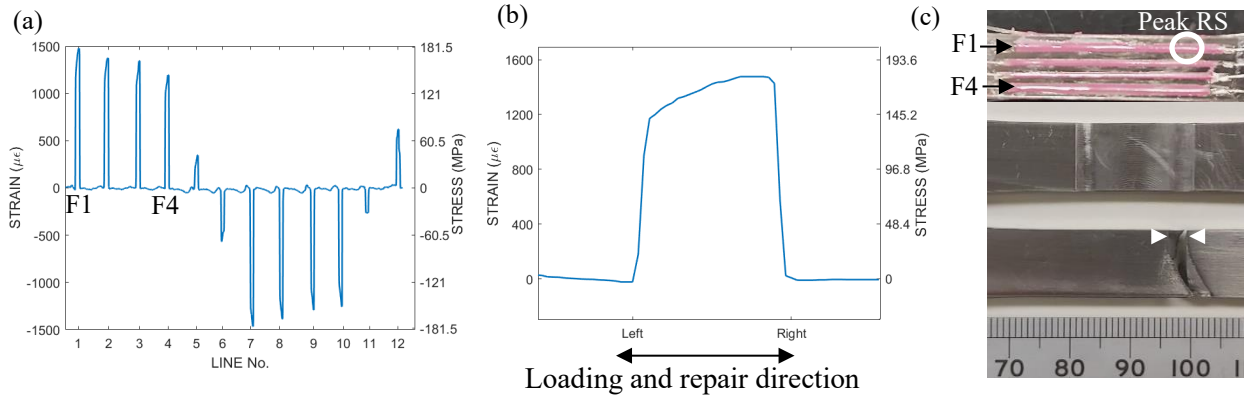


Figure 6. The RS profile labelled F1, shown magnified in (b) and labelled in (c), indicates the peak RS location. Peak RS aligned with the fatigue crack initiation and fracture location arrowed in (c).

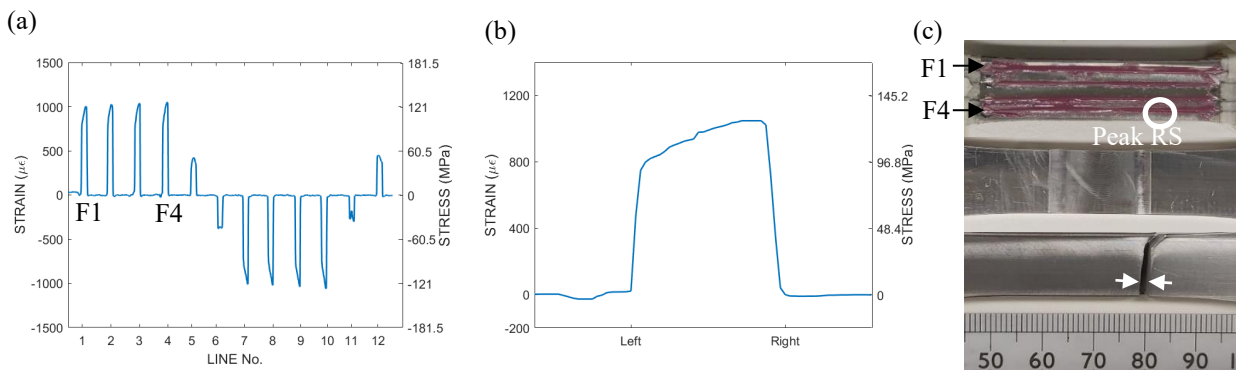


Figure 7. As in Figure 6, the RS distribution for another representative LMD-1 coupon. Peak RS aligned with the fatigue crack initiation and fracture location arrowed in (c).

LMD-2 Results. The RS distribution for an example LMD-2 coupon is shown in Figure 8(a), noting FOS instrumentation began on the back of the coupon in this case. The RS profile both along and across the gauge length was more evenly distributed than for the LMD-1 coupons, referring to profiles labelled F7 to F10 in Figure 8(a) and 8(c). The peak RS occurred in F10 (shown magnified in Figure 8b and labelled in Figure 8c) and was ~148 MPa. This peak RS coincided with the coupon fracture and fatigue initiation location (arrowed in Figure 8c).

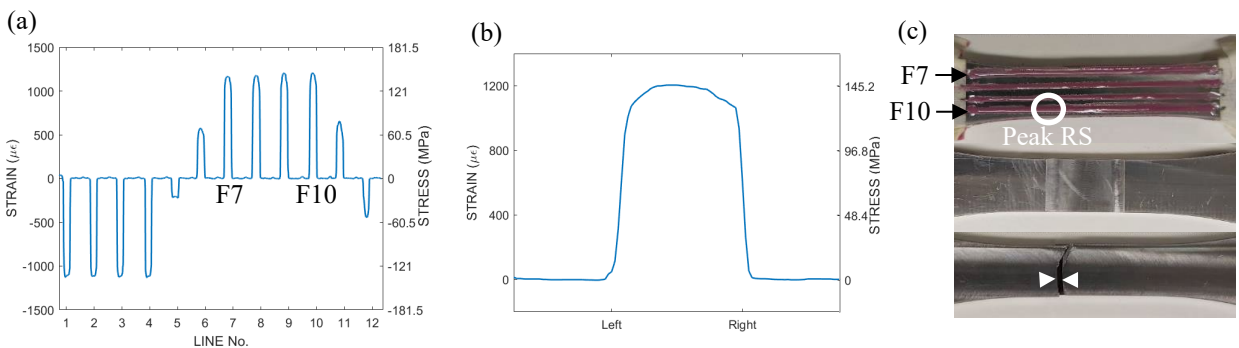


Figure 8. The RS distribution for a representative LMD-2 coupon. Peak RS aligned with the fatigue crack initiation and fracture location arrowed in (c).

The RS distribution for another example LMD-2 coupon is shown in Figure 9(a). The RS profile along the gauge length was uneven, referring to the four asymmetric profiles labelled F1 to F4. These profiles showed increasing RS along the gauge length from left to right. The maximum RS corresponding to profile F3 was 107 MPa and did not coincide with coupon fracture and fatigue initiation location (arrowed in Figure 9c). In this case, fatigue cracking initiated and propagated from the coupon side and although significant RS was noted on both coupon sides it did not align with the fracture and initiation location. A significant surface-breaking feature was observed at the fatigue crack origin outside of the repair area in the substrate material. The stress concentration associated with the feature likely had a greater impact on fatigue crack initiation than RS.

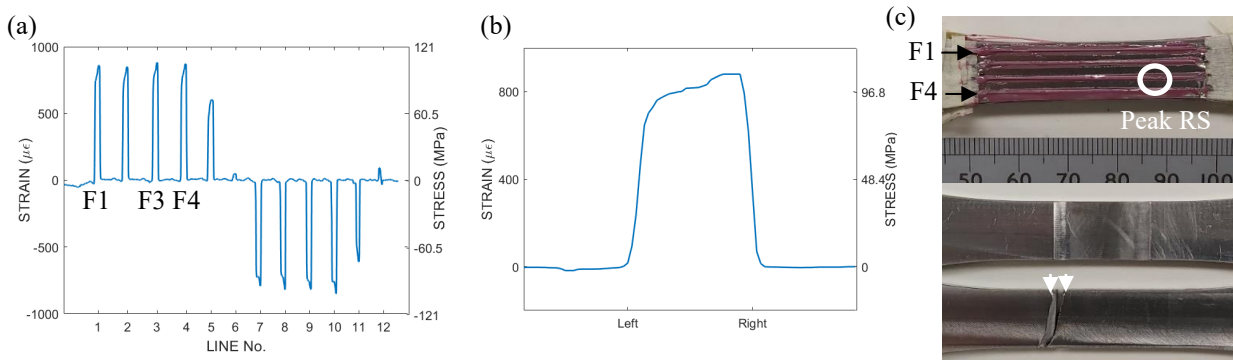


Figure 9. RS distribution for another LMD-2 coupon is shown in (a). Peak RS did not align with the fatigue crack initiation and fracture location, arrowed in (c).

Overall, the LMD-1 strategy produced a significantly uneven RS profile both across and along the gauge length in the deposition direction compared to LMD-2. This was consistent with the HAZ and molten pool having an elongated shape in the deposition direction and it is likely that the peak RS coincided with the final track deposit and laser stop position [6,7]. LMD-2 produced a more evenly distributed RS profile with a slight trend towards the laser stop position. This is likely due to the shorter deposition tracks having higher remnant heat which leads to smaller temperature gradients and lower RS.

## Conclusions

RS values derived from FOS and FSGs were generally consistent, with the peak RS for the five coupons tested ranging between 107-179 MPa. This range was also consistent with near-surface RS values determined by the contour method. RS values and profiles are expected to vary between coupons due to thermal cycling of multiple clad coupons on a build plate. The results showed FOS strain measurements to reflect with relatively good accuracy the surface RS distribution and peak stress values under load, thereby validating the suitability of FOS for the investigation of surface RS in laser repaired coupons of the type considered. Additionally, the study showed FOS can identify surface RS hotspots and therefore potential failure locations. Due to the limited number of tests in the present study, further testing is required to confirm this correlation and understand the effect of applied stress on fatigue initiation and fracture location, as well as fatigue life.

The FOS RS estimates reported in this paper were obtained by forcing bowed coupons to straighten, which limits the application of this approach to relatively thin structures. Although, the contour method provides a through-thickness RS map, it is destructive and cannot be economically applied for every LMD sequence. However, with FOS used as a complimentary

technique, it was possible to characterise surface RS for every coupon in the test matrix which identified correlations between peak RS values and the failure location.

Future work will investigate the RS distribution and structural response of LMD repairs during cyclic loading. The test matrix will incorporate two stress levels and repair strategies to establish a correlation between repair direction, fatigue life and stress with fatigue fracture initiation and location. The aim is to understand whether RS mapping can assist prediction of failure location of repaired coupons. These findings will be validated with post-test fractography.

### Acknowledgements

The authors gratefully acknowledge Ms Yi Rye Choi for providing her coupons as a platform to demonstrate the fibre optic sensing capability. They also acknowledge the facilities and technical assistance of the Fatigue and Fracture Laboratory, Mr Daniel Bitton and Material State Awareness Laboratory at DST Group.

### References

- [1] Q. Liu, M. Janardhana, B. Hinton, M. Brandt & K. Sharp, Laser cladding as a potential repair technology for damaged aircraft components. *International Journal of Structural Integrity* (2011) 2:314-31. <https://doi.org/10.1108/17579861111162914>
- [2] M. Leino, J. Pekkarinen & R. Soukka, The role of laser additive manufacturing methods of metals in repair, refurbishment and remanufacturing – enabling circular economy. *Physics Proceedings* (2016) 83:752-60. <https://doi.org/10.1016/j.phpro.2016.08.077>
- [3] H. Liu & F. Liou, Residual stress modeling and deformation measurement in laser metal deposition process. *New Challenges in Residual Stress Measurements and Evaluation*, 18/12/2019. <https://doi.org/10.5772/intechopen.90539>
- [4] Y.R. Choi, S.D. Sun, Q. Liu, M. Bradt & M. Qian, Influence of deposition strategy on the microstructure and fatigue properties of laser metal deposited Ti-6Al-4V powder on Ti-6Al-4V substrate. *International Journal of Fatigue* 130 (2020) 105236. <https://doi.org/10.1016/j.ijfatigue.2019.105236>
- [5] H. Ali, H. Ghadbeigi & K. Mumtaz, Effect of scanning strategies on residual stress and mechanical properties of selective laser melted Ti6Al4V, *Materials Science & Engineering A*, 712 (2018) 175-187. <https://doi.org/10.1016/j.msea.2017.11.103>
- [6] I. Yadroitsev & I. Yadroitsava, Evaluation of residual stress in stainless steel 316L and Ti6Al4V samples produced by selective laser melting. *Virtual and Physical Prototyping*, 10:2 (2015) 67-76. <https://doi.org/10.1080/17452759.2015.1026045>
- [7] M. Turski & L. Edwards, Residual stress measurement of a 316L stainless steel bead-on-plate specimen utilising the contour method. *International Journal of Pressure Vessels and Piping*, 86:1 (2009) 126-131. <https://doi.org/10.1016/j.ijpvp.2008.11.020>
- [8] All Grating Fibres (AGF), 2020, FBGS, viewed 9<sup>th</sup> October 2020
- [9] Zhou, DP, Chen L & Bao X, Distributed dynamic strain measurement using optical-frequency domain reflectometry, *Applied Optics*, 55:24 (2016) 6735-6739. <https://doi.org/10.1364/AO.55.006735>

# Trans-Jacket Fibre Bragg Gratings for In-Situ Health Monitoring of Defence Platforms in Harsh Environments

Naizhong Zhang<sup>1,a\*</sup>, Claire Davis<sup>2,b</sup>, Chiu Wing Kong<sup>1,c</sup>, Suzana Turk<sup>2,d</sup>

<sup>1</sup>Department of Mechanical and Aerospace Engineering, Monash University, Wellington Rd, Clayton VIC. 3800, Australia

<sup>2</sup>Defence Science and Technology Group, 506 Lorimer Street, Fishermans Bend, VIC 3207, Australia

<sup>a</sup>Naizhong.Zhang1@monash.edu, <sup>b</sup>Claire.Davis@dst.defence.gov.au,  
<sup>c</sup>Wing.Kong.Chiu@monash.edu, <sup>d</sup>Suzana.Turk@dst.defence.gov.au

**Keywords:** Optical Fibre Sensors, Fibre Bragg Gratings, Grating Inscription, Trans-Jacket Gratings, Sensor Fatigue

**Abstract.** Packaged optical fibre sensors offer excellent strength and resistance to environmental degradation, but the reported reliability and durability of fibres containing fibre Bragg gratings (FBGs) varies greatly. This is partly due to the fabrication methodologies used to create the sensors. The trans-jacket grating inscription technique uses an infrared laser to write gratings into the fibre core through the polymer coating. This method eliminates the need for harsh coating removal processes and exposure of the glass fibre core and thus dramatically reduces fibre damage during grating fabrication. In addition, the automated trans-jacket inscription process introduces greater flexibility to control the writing parameters, facilitating a consistent process for producing robust, fatigue resistant distributed FBG sensing arrays with reliable and repeatable performance that could revolutionise their application in structural health monitoring (SHM). This paper reports on the durability and reliability of Bragg gratings with different fibre geometries, dopants, and photo-sensitising approaches to compare the overall fatigue performance of trans-jacket FBG sensors. Both type I gratings which are inscribed using a laser power intensity below the damage threshold of the glass core, and type II gratings which are inscribed exceeding this threshold, are considered. The fatigue performance of these FBG sensors was assessed using a custom designed electro-dynamically actuated loading assembly. It is concluded that type I trans-jacket gratings have a significantly higher fatigue life compared to type II gratings for the same fatigue loading regime. Despite the lower fatigue life, type II trans-jacket gratings are found to perform significantly better than conventional electrical foil gauges. Therefore, trans-jacket gratings have significant potential for application as dense sensing arrays in harsh operational environments in defence and aerospace industries.

## Introduction

FBGs are periodic variations in the refractive index of the fibre core. They are inscribed by photo-sensitising the glass and then exposing the fibre core side to laser light with a spatially modulated intensity pattern [1,2]. The grating is designed to act as a narrow-band reflector, reflecting light of a specific wavelength known as the Bragg wavelength and transmitting light at all other wavelengths. FBG sensors have been widely used as sensing elements for strain, temperature, and pressure measurement over the last decade [3-5].

FBG sensors are small, flexible, relatively simple to fabricate, corrosion resistant, and immune to electromagnetic interference (EMI), making them well suited to embedded strain and

temperature monitoring applications [6-8]. However, the reported performance variability of FBG sensors impedes their wider acceptance and application. This is partly due to the various commercial fabrication methodologies used to create the sensors [9]. For example, the conventional stripped and recoated FBG writing method involves manual handling that introduces surface damage in the unprotected region of the glass, which affects the fibre's long-term reliability and durability [10,11]. Ang et al [12] reported a fatigue failure strain of 5000  $\mu\epsilon$  when a stripped and re-coated FBG embedded in composite material was tested, which is only 10% of the tensile strain limit for pristine fibres.

Trans-jacket inscription of FBGs relies on femtosecond laser pulses to direct focused energy into the fibre core through the fibre coating. This technique relies on maintaining the laser focus in the core of the fibre to avoid damage to surrounding fibre and coating materials. This is a relatively new technique which has emerged following recent improvements in beam stability and pulse energy for ultrafast lasers. The resulting gratings maintain the mechanical robustness of the pristine fibre, which is paramount for fatigue resistance [13]. A novel aspect to the inscription methodology employed by these researchers was an active feedback mechanism to keep the beam focused in the core of the fibre during inscription, which may be a factor in the superior fatigue performance of these gratings. This methodology was employed to manufacture both type I and type II FBGs in the current study, providing a set of sensors for systematic fatigue testing.

FBGs written using continuous wave (CW) lasers at low energy intensities are referred to as type I gratings, also known as standard gratings [2]. In the present work, the type I trans-jacket FBGs were manufactured according to the experimental procedure and parameters detailed in [13,14]. Type II gratings, also called damage induced gratings, are written by multi-photon excitation with higher intensity laser energies that exceed the damage threshold of the glass core [2]. Type II gratings can tolerate much higher temperatures compared with type I gratings, and are often adopted in high temperature sensing environments. The fatigue performance of type II gratings has not been extensively studied but, given that the glass is essentially damaged in the region of the grating [15,16], it is expected that there will be some deterioration in the fatigue performance compared to type I gratings.

The fatigue performance characteristics of foil strain gauges (FSG) are not ideal for long-term full-scale fatigue testing (FSFT) of aerospace platforms [17]. In a previous fatigue study FSGs tested at a load amplitude of 1000  $\mu\epsilon$  were found to last in the order of 100 million cycles; at 5200  $\mu\epsilon$  the fatigue life was significantly less, ~1000 cycles, and at 7000  $\mu\epsilon$  the fatigue life was further reduced to ~100 cycles [18]. It was considered unusual for a typical FSG to survive more than 200,000 cycles at  $4000 \pm 2000 \mu\epsilon$  [19]. Thus, the prospect of a durable and fatigue-resistant optical fibre strain sensor offers significant benefits for this and similar applications. The wiring and soldered connections associated with a large number of foil strain gauges can lead to reliability issues and excessive weight on the structure can influence test results. In addition, the ability to multiplex large numbers of sensors along a single fibre enables significant scale and complexity reduction relative to a wired sensor system, using a medium which is immune to electromagnetic interference. To validate that trans-jacket FBGs have potential to replace FSGs in the field for long-term structural health monitoring of aerospace platforms, this paper evaluates the fatigue performance of type I and type II trans-jacket FBG sensors fabricated with different fibre geometries, dopants, and photo-sensitising approaches.

## Experimental Methods

A novel electro-dynamically actuated fibre loading rig was designed and constructed which can operate at relatively high frequency (see Fig. 1). The dynamic range of this rig was designed to induce tensile strains in an optical fibre of up to 36,000  $\mu\epsilon$  at a fixed 100 Hz cyclic loading frequency [20].

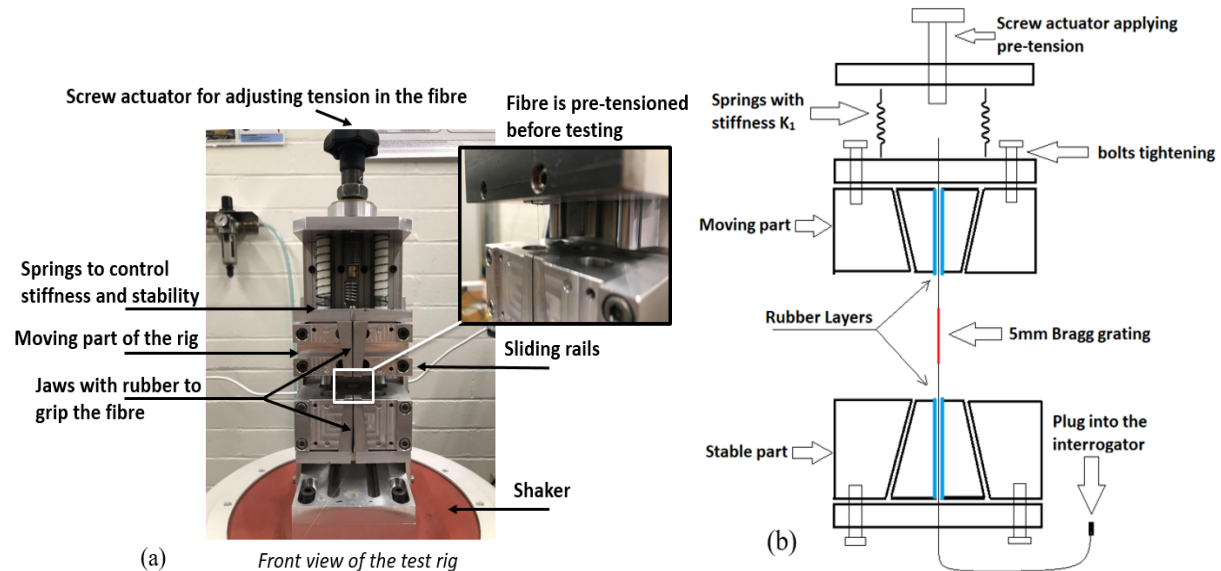


Figure 1. (a) Picture of optical fibre test rig bolted to an electrodynamic shaker. (b) Schematic illustrating working principle of the test rig [20], with the FBG mounted between the moving part and the stable part (labelled).

The reflection and transmission spectra are mainly determined by the grating length, index contrast, and grating pitch of the FBG sensor [21]. Pre- and post-fatigue test FBG reflection and transmission spectra were characterised by a high-resolution tunable laser (Yenista TS100) combined with a component tester (Yenista, CT400). The key features of the FBGs, such as centre Bragg wavelength, side lobes, and reflectivity were studied to determine whether fatigue loading had any impact on the spectral profile and, in the case of the fractured fibres, whether the fracture occurred within the region of the grating, which is indicated by a drop in reflectivity.

Constant amplitude sinusoidal loading was delivered by a high capacity electrodynamic shaker (TIRA S50350) controlled by a Vibration Research Corporation 8500 vibration controller. The amplitude of this loading was adjusted manually to achieve the desired level of cyclic strain in the fibre using the fibre signal as feedback, see Fig. 2 (a). Fig. 2 (b) shows a signal from a trans-jacket FBG sensor corresponding to a strain excursion from 0 to 25,000  $\mu\epsilon$  at 100 Hz.

The strain induced in the FBG sensor was measured continuously using an industrial grade optical sensing interrogator (Micron Optics Si255). The Bragg wavelength for an unstrained FBG sensor tested in the loading rig was 1560 nm. The available dynamic strain range of the interrogator is approximately 130,000  $\mu\epsilon$  across a wavelength of 1460 nm to 1620 nm. Therefore, the interrogator provides sufficient wavelength range for the strains considered in the present work.

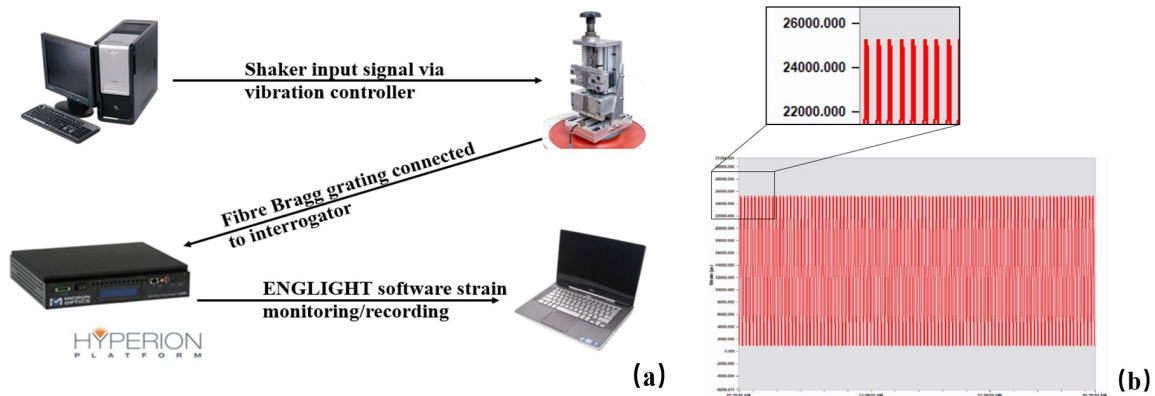


Figure 2. (a) Complete fatigue testing experimental setup. (b) An example time history of the strain response to directly monitor strain in fibre.

A total of 160 trans-jacket FBG sensors were fatigue tested. The optical fibres were supplied by OFS and FibreCore to span a range of different fibre sizes and dopant levels, as shown in Table 1. The silica fibre core was doped with germanium to increase refractive index compared to the fibre cladding and to increase photo-sensitivity.

Table 1. Optical fibre specifications.

Optical fibre	Operating Wavelength (nm)	Mode field diameter, nominal ( $\mu\text{m}$ )	Core diameter ( $\mu\text{m}$ )	Clad diameter ( $\mu\text{m}$ )	Numerical aperture, nominal	Dopant (mol%)
OFS: BF06160-02 ClearLite POLY (4.6/125, 0.21NA)	1310-1550	5.8 @ 1550 nm	4.6	125 $\pm$ 2	0.21	10
OFS: BF04446 ClearLite POLY (8.4/125, 0.11NA)	1310-1550	10.5 @ 1550 nm	8.4	125 $\pm$ 2	0.11	3
Fibercore: SM1500 (4.2\80)P	1520-1650	4.0-4.5 @ 1550 nm	4.2	80	0.29-0.31	20
Fibercore: SM1500 (9\125)P	1550-1650	8.5-9.9 @ 1550 nm	9	125.1	0.13-0.15	3

80 gratings of each type (type I & type II) were tested. The sensors were carefully fabricated under contract via a research agreement with an academic provider. Half of the fibres were deuterium loaded. The introduction of deuterium (D loading) can significantly reduce the energy required to inscribe a fibre grating using an IR laser, and hydrogen or deuterium loading of bulk doped glasses can significantly increase the femtosecond IR-induced index change [22].

Preliminary tests showed that type II gratings fractured at approximately 17,000  $\mu\epsilon$ , while type I gratings could withstand extended cycling at strains up to 36,000  $\mu\epsilon$  (maximum range of the loading apparatus) without failure. These results informed the development of loading

sequences used in the systematic testing of the fibres, which are shown in Tables 2 and 3, corresponding to the type I and type II gratings respectively.

*Table 2. Incremental loading sequence for type I gratings.*

Peak Strain ( $\mu\epsilon$ )	30000	32000	34000	36000
Loading cycles (million)	0.5	0.5	0.5	0.5

*Table 3. Incremental loading sequence for type II gratings.*

Peak Strain ( $\mu\epsilon$ )	12000	14000	16000	18000
Loading cycles (million)	0.5	0.5	0.5	0.5

### Results and Discussion

Table 4 shows fatigue performance results corresponding to the type I gratings. All of the type I gratings survived the full loading sequence listed in Table 2, i.e. a maximum load of 36,000  $\mu\epsilon$  and an aggregate 2 million loading cycles. These results suggest that type I gratings are suitable for applications involving severe mechanical loading, well beyond what would be experienced in a typical aerospace strain monitoring application.

*Table 4. Fatigue test results for type I gratings.*

FBG sensors	Deuterium loaded	Specimens tested	Fatigue results
OFS:BF04446, ClearLite POLY (8.4/125,0.11NA)	Y&N	30	30000-36000 $\mu\epsilon$ , 2 million cycles of loading survived
OFS: BF06160-02, ClearLite POLY (4.6/125, 0.21NA)	Y&N	10	30000-36000 $\mu\epsilon$ , 2 million cycles of loading survived
FibreCore: SM1500(4.2/80) P	Y&N	30	30000-36000 $\mu\epsilon$ , 2 million cycles of loading survived
Fibercore: SM1500 (9/125) P	Y&N	10	30000-36000 $\mu\epsilon$ , 2 million cycles of loading survived

Table 5 shows the fatigue performance results corresponding to the type II gratings. The mean fatigue failure strain for each category of type II grating was approximately 17,000  $\mu\epsilon$ .

Although the failure strains of the type II gratings were significantly lower compared to that of the type I gratings, they far exceed the operational strains in most practical applications. The results were also considered against the reported fatigue performance of FSGs. The type II gratings tested in the present work significantly outperform the specialty fatigue resistant (M-Series) FSGs, which reportedly are capable of withstanding only one million loading cycles at a strain amplitude of 2500  $\mu\epsilon$  [18].

Figure 5 depicts schematically the fatigue failure locations recorded for the type II gratings (marked by a cross). As shown, all of the fractures occurred within or adjacent to the 5 mm sensor grating. A comparison of the pre- and post-fatigue reflection spectra (Fig. 5, top-left) shows a significant change in reflectivity in response to a fracture located within the grating. In contrast, when the fracture occurred outside of the grating there was relatively little change in reflection spectrum (Fig. 5, right), which is expected since the grating remains intact. Similar behaviour was witnessed for the type I gratings, as illustrated in Figure 6.

Table 5. Fatigue results for type II gratings.

Fibre tested	Deuterium loaded	Samples tested	Mean failure strain ( $\mu\epsilon$ )	95% confidence interval
OFS: BF06160-02, ClearLite POLY (4.6/125 0.21NA)	Y	15	17600	$\pm 324$
OFS: BF06160-02, ClearLite POLY (4.6/125 0.21NA)	N	15	17900	$\pm 400$
OFS: BF04446, ClearLite POLY (8.4/125 0.11NA)	Y	5	17600	$\pm 445$
OFS: BF04446, ClearLite POLY (8.4/125 0.11NA)	N	5	16200	$\pm 500$
Fibercore: SM1500 (4.2/80) P	Y	5	17300	$\pm 588$
Fibercore: SM1500 (4.2/80) P	N	5	18100	$\pm 480$
FibreCore: SM1500(9/125) P	Y	15	17100	$\pm 473$
FibreCore: SM1500(9/125) P	N	15	16400	$\pm 643$

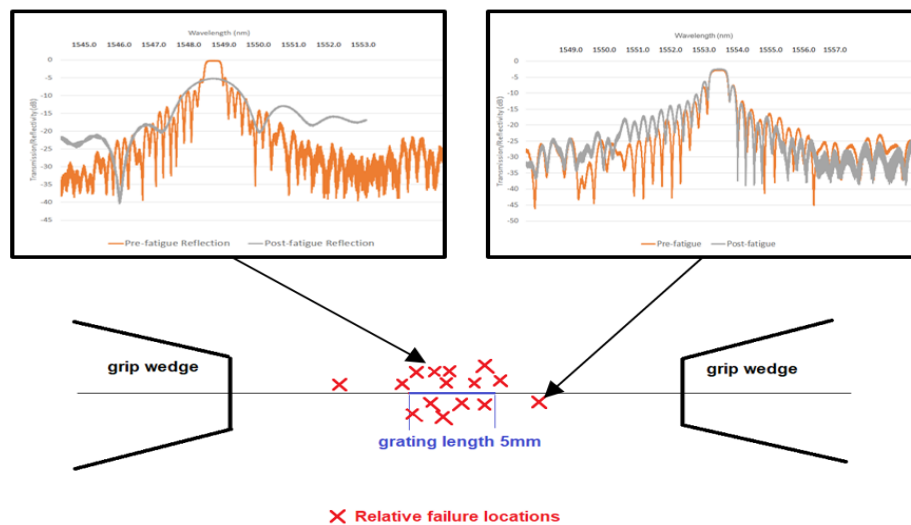


Figure 5. Summary of failure locations schematically represented for one sample set of type II gratings.

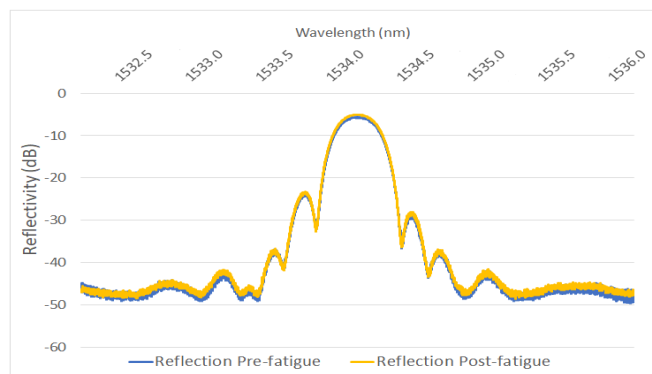


Figure 6. Pre- and post-fatigue reflection spectra of a type I grating.

## Conclusions

This paper has reported on the durability and reliability of Bragg gratings with different fibre geometries, dopants, and photo-sensitising approaches to compare the overall fatigue performance of type I and type II trans-jacket FBG sensors. The fatigue performance of these sensors was assessed using a custom designed electro-dynamically actuated loading assembly. It was concluded that type I trans-jacket gratings have a significantly higher fatigue life compared to type II gratings for the same fatigue loading regime. Despite the lower fatigue life, type II trans-jacket gratings are found to perform significantly better than conventional electrical foil gauges. Therefore, trans-jacket gratings have strong potential for application as dense sensing arrays in harsh operational environments in defence and aerospace industries.

The results also illustrated that photo-sensitising, glass dopant and fibre geometry had no discernable impact on the mechanical performance of trans-jacket FBGs. The next stage of this research will focus on developing and testing reliable broad-area fatigue resistant attachment techniques for this new class of sensor.

## References

- [1] G. Meltz, W. W. Morey, and W. H. Glenn, "Formation of Bragg gratings in optical fibers by a transverse holographic method," *Opt. Lett.*, 1989, doi: 10.1364/ol.14.000823.  
<https://doi.org/10.1364/OL.14.000823>
- [2] R. Kashyap, *Fiber Bragg Gratings*. 2010. <https://doi.org/10.1016/B978-0-12-372579-0.00004-1>
- [3] A. D. Kersey *et al.*, "Fiber grating sensors," *J. Light. Technol.*, vol. 15, no. 8, pp. 1442–1462, 1997. <https://doi.org/10.1109/50.618377>
- [4] Y. J. Rao, "In-fibre Bragg grating sensors," *Meas. Sci. Technol.*, vol. 8, no. 4, pp. 355–375, 1997. <https://doi.org/10.1088/0957-0233/8/4/002>
- [5] M. Majumder, T. K. Gangopadhyay, A. K. Chakraborty, K. Dasgupta, and D. K. Bhattacharya, "Fibre Bragg gratings in structural health monitoring-Present status and applications," *Sensors and Actuators, A: Physical*. 2008.  
<https://doi.org/10.1016/j.sna.2008.04.008>
- [6] R. Di Sante, "Fibre optic sensors for structural health monitoring of aircraft composite structures: Recent advances and applications," *Sensors (Switzerland)*. 2015.  
<https://doi.org/10.3390/s150818666>
- [7] R. Ramly, W. Kuntjoro, and M. K. A. Rahman, "Using embedded fiber bragg grating (FBG) sensors in smart aircraft structure materials," 2012. <https://doi.org/10.1016/j.proeng.2012.07.218>
- [8] K. C. Chuang and C. C. Ma, "Tracking control of a multilayer piezoelectric actuator using a fiber bragg grating displacement sensor system," *IEEE Trans. Ultrason. Ferroelectr. Freq. Control*, 2009. <https://doi.org/10.1109/TUFFC.2009.1287>
- [9] M. W. Rothhardt, C. Chojetzki, and H. R. Mueller, "High-mechanical-strength single-pulse draw tower gratings," 2004. <https://doi.org/10.1117/12.567801>
- [10] K. O. Hill and G. Meltz, "Fiber Bragg grating technology fundamentals and overview," *J. Light. Technol.*, 1997. <https://doi.org/10.1109/50.618320>

- [11] H. J. Yoon and C. G. Kim, “The mechanical strength of fiber Bragg gratings under controlled UV laser conditions,” *Smart Mater. Struct.*, 2007. <https://doi.org/10.1088/0964-1726/16/4/045>
- [12] J. Ang, H. C. H. Li, I. Herszberg, M. K. Bannister, and A. P. Mouritz, “Tensile fatigue properties of fibre Bragg grating optical fibre sensors,” *Int. J. Fatigue*, 2010. <https://doi.org/10.1016/j.ijfatigue.2009.11.002>
- [13] M. Bernier, F. Trépanier, J. Carrier, and R. Vallée, “High mechanical strength fiber Bragg gratings made with infrared femtosecond pulses and a phase mask,” *Opt. Lett.*, vol. 39, no. 12, p. 3646, 2014. <https://doi.org/10.1364/OL.39.003646>
- [14] J. Habel, T. Boilard, J. S. Frenière, F. Trépanier, and M. Bernier, “Femtosecond FBG written through the coating for sensing applications,” *Sensors (Switzerland)*, vol. 17, no. 11, pp. 1–12, 2017. <https://doi.org/10.3390/s17112519>
- [15] C. W. Smelser, S. J. Mihailov, and D. Grobnic, “Formation of Type I-IR and Type II-IR gratings with an ultrafast IR laser and a phase mask,” *Opt. Express*, 2005. <https://doi.org/10.1364/OPEX.13.005377>
- [16] L. Südrrie, M. Franco, B. Prade, and A. Mysyrowicz, “Study of damage in fused silica induced by ultra-short IR laser pulses,” *Opt. Commun.*, 2001. [https://doi.org/10.1016/S0030-4018\(01\)01152-X](https://doi.org/10.1016/S0030-4018(01)01152-X)
- [17] C. Davis, S. Tejedor, I. Grabovac, J. Kopczyk, and T. Nuyens, “High-strain fiber bragg gratings for structural fatigue testing of military aircraft,” *Photonic Sensors*, 2012. <https://doi.org/10.1007/s13320-012-0066-3>
- [18] “The Fatigue Life of Electrical Strain Gauges,” *HBM*, 2020. <https://www.hbm.com/en/8153/new-technote-fatigue-life-of-electrical-strain-gauges/> (accessed Oct. 27, 2020).
- [19] J. C. Middleton, “Strain gauge performance during fatigue testing,” *Strain*, vol. 22, no. 3, pp. 135–140, 1986. <https://doi.org/10.1111/j.1475-1305.1986.tb00608.x>
- [20] N. Zhang, C. Davis, W. K. Chiu, T. Boilard, and M. Bernier, “Fatigue performance of type I fibre bragg grating strain sensors,” *Sensors (Switzerland)*, vol. 19, no. 16. 2019. <https://doi.org/10.3390/s19163524>
- [21] S. R. Abdullina and A. A. Vlasov, “Suppression of side lobes in the fiber Bragg grating reflection spectrum,” *Optoelectron. Instrum. Data Process.*, 2014. <https://doi.org/10.3103/S8756699014010105>
- [22] C. W. Smelser, S. J. Mihailov, and D. Grobnic, “Hydrogen loading for fiber grating writing with a femtosecond laser and a phase mask,” *Opt. Lett.*, vol. 29, no. 18, p. 2127, 2004. <https://doi.org/10.1364/OL.29.002127>

# Low-Energy Sonic Thermographic Inspection of Impact Damage in Aerospace Composites

Kelly A. Tsoi<sup>a\*</sup>, Chris Brooks<sup>b</sup>, Nik Rajic<sup>c</sup> and Cedric Antolis<sup>d</sup>

Defence Science and Technology Group, 506 Lorimer Street, Fishermans Bend 3207, Australia

<sup>a</sup>Kelly.Tsoi@dst.defence.gov.au, <sup>b</sup>Christopher.Brooks@dst.defence.gov.au

<sup>c</sup>Nik.Rajic@dst.defence.gov.au, <sup>d</sup>s3448276@student.rmit.edu.au

© 2020 Commonwealth of Australia

**Keywords:** Sonic Thermography, Non-Destructive Testing, Low Energy, Kissing Bonds

**Abstract.** This paper details an investigation into the use of an alternate sonic thermography inspection process which uses both low-energy acoustic coupling and an inexpensive microbolometer camera to detect barely visible impact damage in composite structures. The impetus is to create a system that is affordable, robust, rugged and easy to use in the field. This paper shows that the new system is capable of detecting barely visible impact damage with a performance comparable to that of conventional sonic thermography.

## Introduction

The transformation of the Australian Defence Force (ADF) aviation fleet has seen a significant investment in next generation aircraft platforms, bringing cutting-edge war fighting capabilities to the ADF. Many of these platforms contain significant quantities of composite materials, e.g. F-35A, MRH90 and Tiger ARH. The many advantages of composite materials over metals for structural applications have to be balanced against some shortcomings, such as increased susceptibility to impact damage, especially barely visible impact damage (BVID), as well as kissing bond delaminations. These damage modes are particularly insidious, as they are difficult to detect with conventional non-destructive inspection (NDI) techniques and can cause significant reductions in the static and fatigue strength of components.

Sonic thermography (ST) is an NDI technique that has proven to be effective on a large variety of composite defects and flaws such as BVID, kissing bonds and delaminations [1]-[2]. ST relies on the use of an acoustic horn, typically operating in the frequency range 20-40 kHz, to transfer acoustic waves to the structure under inspection. These acoustic waves pervade the structure and interact with the faying surfaces of damaged zones, causing frictional heating. When this heat diffuses to the surface it can be detected using an infrared camera (Fig. 1). The technique works well in the laboratory, however transitioning the technology to the field is challenging. Traditionally, cooled infrared (IR) cameras are used for such inspections, due to their relatively high temperature sensitivity. However, IR cameras of this type are expensive, fragile and bulky to use and transport. In addition, the effective transfer of high frequency acoustic waves from an acoustic horn is reliant on the entire contact area of the horn tip sitting flush against the structure under inspection. For structures that are not completely flat, as is common for many aircraft components, insufficient energy may be transferred resulting in reduced frictional heating and therefore reduced ability to detect defects and delaminations.

A technique has been developed, and is described here, that uses only 5% of the acoustic power typically applied in traditional ST. This alternative form of ST, referred to here as Low-Amplitude Synchronous Sonic Thermography (LASST), uses a cross-correlation technique



previously implemented in a thermoelastic stress analysis (TSA) approach described in [3]. TSA is based on the thermoelastic effect wherein an object under elastic deformation produces small reversible changes in temperature. These reversible temperature changes can be detected when the object under investigation is mechanically cycled at a known frequency. Knowledge of this frequency is used to extract the relatively small linearly-correlated signature from thermal imagery obtained from a low-cost microbolometer.

Analogously, LASST uses an acoustic horn which is cycled on and off at a known frequency, with the thermal signature generated by frictional heating at flaw surfaces synchronously averaged with respect to the known modulation frequency. Earlier researchers explored the use of a similar process, which has been variously described as amplitude modulated lock-in vibrothermography [4], ultrasound lock-in thermography [5] and ultrasound burst phase thermography [6], however these implementations all used high power ultrasound (from 300 W up to 1.6 kW) and a cooled focal plane array infrared camera. In LASST, the power levels required from the horn are lower by a factor of 20 compared to standard ST and a lightweight, low-cost microbolometer is used. The present paper describes an experimental comparison of LASST against conventional ST and phased array ultrasonic testing (PAUT) on composite laminates containing BVID.

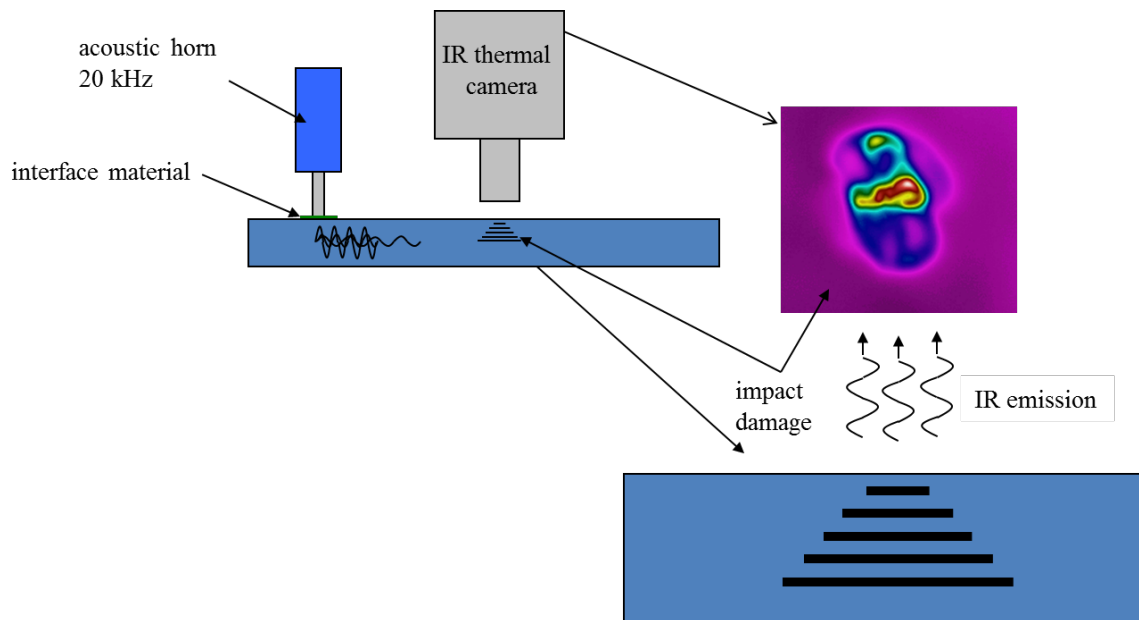


Figure 1. Schematic showing basic operation of ST inspection.

## Experiment

A series of quasi isotropic IM7/977-3 [45,0,0,-45,90]3S laminate plate coupons measuring 300 mm x 100 mm x 4 mm were impacted at three energy levels within the BVID regime; at 5.36 J, 10.72 J and 21.44 J. The size and lateral extent of the damage was determined using PAUT.

In traditional implementations of ST the acoustic horn is typically driven at power levels of 100's of watts over durations in the order of 1 s [1]. An interface material of felt is used to improve energy transfer from the horn into the specimen, and to prevent possible marring of the surface from the horn. As previously remarked, the resulting thermal signature is typically

recorded using a cryogenically-cooled photon detector. Such cameras have a relatively high sensitivity, with noise equivalent temperature difference (NETD) values typically  $< 20$  mK, but also are relatively large, with dimensions of approximately 200 mm x 150 mm x 150 mm and weigh many kilograms. Although the sensitivity of these cameras is relatively high, post processing techniques are still typically applied to the raw thermographic data to improve the probability of detecting a defect; these techniques include pulsed phase thermography (PPT) [7] and principal component thermography (PCT) [8].

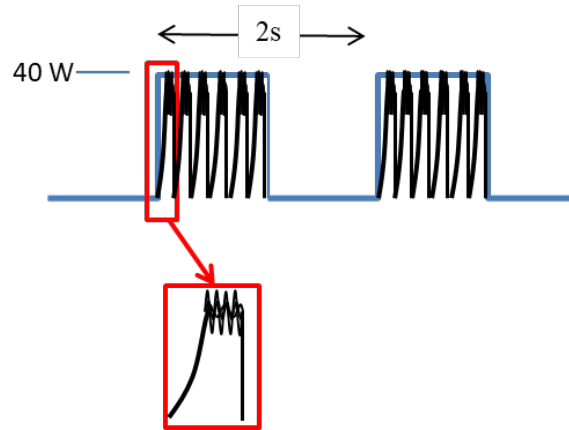


Figure 2. Insonification waveform used in LASST.

In the present implementation of LASST, pulsed insonification is required as the ultrasonic generator is unable to supply a steady output at low power. Sonic insonification pulses were generated at a frequency of 6 Hz, with each insonification ramping up from zero to the chosen energy level within 0.15 s. The acoustic horn power was modulated using a square wave with a base frequency of 0.5 Hz, which gives 1 s of pulsed insonification and 1 s of zero insonification. Each complete 2 s pulse is considered one cycle, and we collect 20 cycles, which is defined as one block, so each block takes 40 s to complete. The thermal signature is synchronously averaged against the base frequency of the square wave. The low magnitude of the base frequency is important to enable enough time for the thermal signature to diffuse from the substructure to the surface where it can be detected.

Two infrared imaging systems were used in the present study; (i) a FLIR SC6000 cooled photon detector operating in the 2-5 micron wavelength band with an NETD of 20 mK, and (ii) a Xenics Gobi 640 amorphous-silicon microbolometer operating in the 8-12 micron wavelength band and with an NETD of 50 mK. The comparatively small size of the microbolometer is illustrated in Fig. 2.

Due to the relatively low intensity and short duration power bursts required by the LASST approach, a thinner interface layer than is customarily applied in ST was able to be used in this work. A thin layer of cardboard, similar to a business card, was found to be sufficient to enable good energy transfer whilst also protecting the surface.

The cross-correlation process applied to the raw video signal in LASST results in two measured signal components: a component in phase with the excitation, which is denoted by the symbol X, and a component in quadrature with the excitation, which is denoted by the symbol Y. Corresponding amplitude ( $r$ ) and phase ( $\Theta$ ) components can be calculated from these measured components. Unfortunately, because of unknown latencies in the data acquisition system the precise phase relationship between the thermal response and the acoustic excitation was not able

to be determined. An empirical phase calibration was instead applied by assigning the relative phase between the X component and the drive signal at the centre of the impact zone to zero. The phase component relates to the time it takes for the heat to diffuse to the surface, which should approach zero at the centre of the impact zone because any surface, or near-surface damage will produce an approximately instantaneous thermal response to the insonification. This phase calibration process ensures that any unknown or variable latencies in the data acquisition system do not produce inconsistencies between different sets of results. **Fig. 4** shows the effect of this calibration process on X and Y components obtained from a typical inspection of BVID. As expected, the amplitude component, r, is unchanged by a shift in phase.



Figure 3. Xenics Gobi microbolometer (left) and FLIR SC6000 photon detector (right).

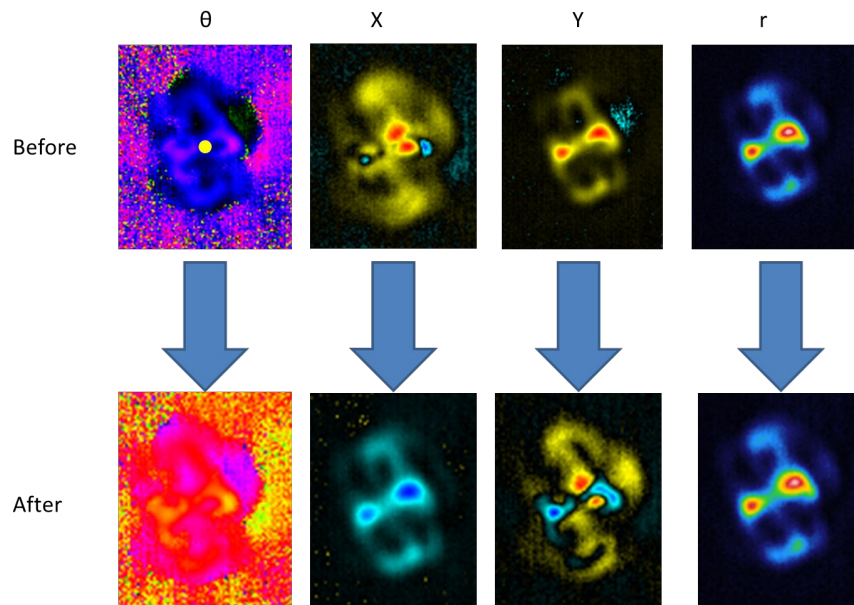


Figure 4. Effect of phase calibration on signal components obtained for 21.44 J impact specimen. The yellow spot at the centre of  $\Theta$  indicates the position where the calibration was performed.

In Fig. 5, the sub-surface damage area at a depth range 0.8-1.2 mm, determined from PAUT, has been outlined in red, and deeper damage, in the depth range 1.2-2.4 mm, in yellow. These

have been overlaid on the LASST X and Y components to illustrate the good correlation between the X component signature and near surface damage, and between the Y component signature and deeper damage. This is to be expected as the Y component is in quadrature with the horn excitation and therefore corresponds to a delayed response such as would occur for a signal transported from sub-surface layers by heat diffusion.

A comparison of signal strength with energy level was also conducted. It was observed that 30 W was the minimum power level required to elicit a detectable signature in the BVID samples considered here. A comparison between the 30 W and 40 W scans is shown in Fig. 6 for a 21.44 J impact specimen, where the 40 W scan exhibits significantly less noise and better signal definition. Based on this result, 40 W was the minimum energy level applied in all subsequent inspections examining this particular type of damage.

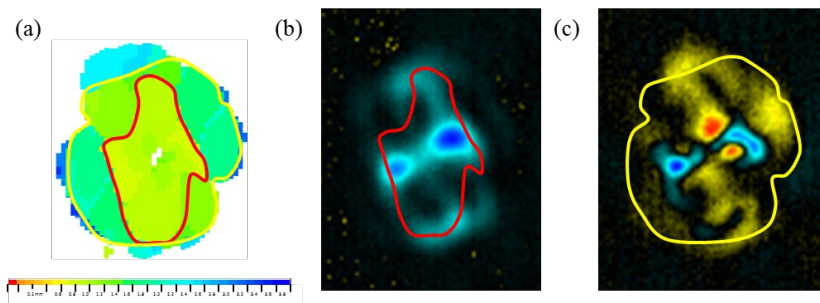


Figure 5. Comparison of (a) PAUT, (b) X component and (c) Y component from LASST for 21.44 J impact specimen, 40 W, 800 s. Depth range 0.8-1.2 mm is outlined in red and 1.2-2.4 mm in yellow.

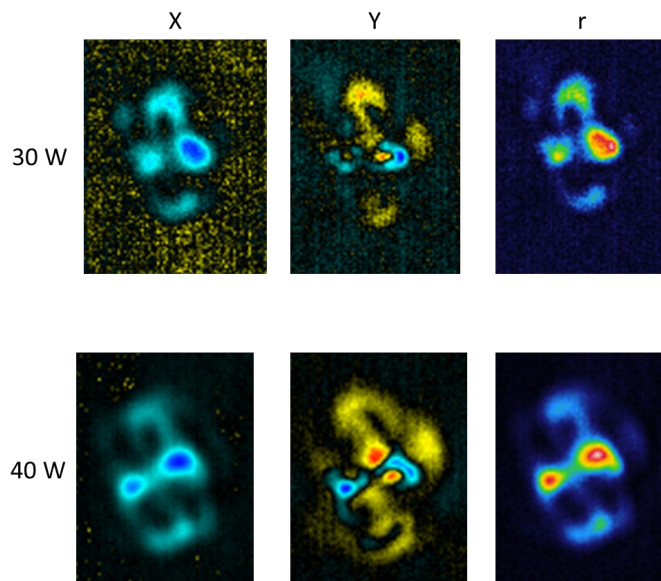


Figure 6 Effect of insonification energy level for 21.44 J impact specimen. Shown are the X, Y and r components for 30 W (above) and 40 W (below).

The duration of the scans was varied from 80 s to 800 s to determine the minimum length of time during which LASST should be performed to optimise the thermal signature, using a 40 W insonification power level. A comparison of the results for increasing scan duration is shown for X and Y components in Fig. 7. An easily distinguished BVID signature is evident in both X and Y components at 80 s, however from 320 s onwards the damage indication becomes more refined and specific areas of damage are more easily delineated, which is an expected result of the cross-correlation process. For the remainder of the experiments a scan duration of 800 s was used to ensure that the most defined thermal response was obtained.

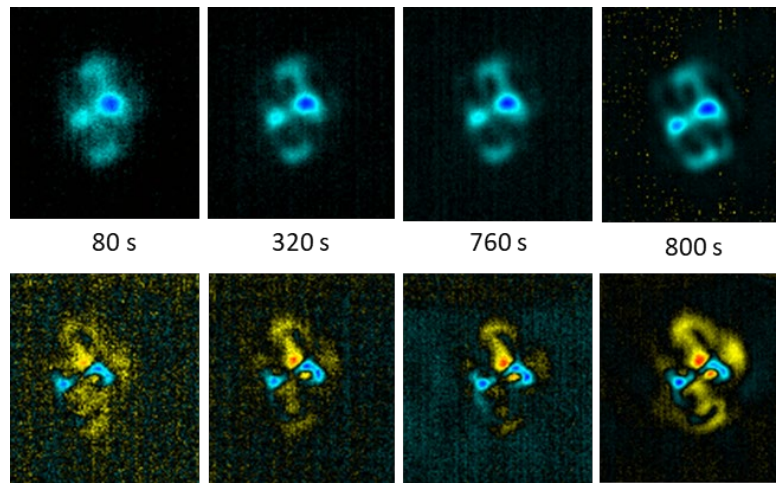


Figure 7. Comparison of component X (above) and Y (below) for LASST thermographs of BVID in 21.44 J impact specimen, over increasing duration of scans at 40 W insonification.

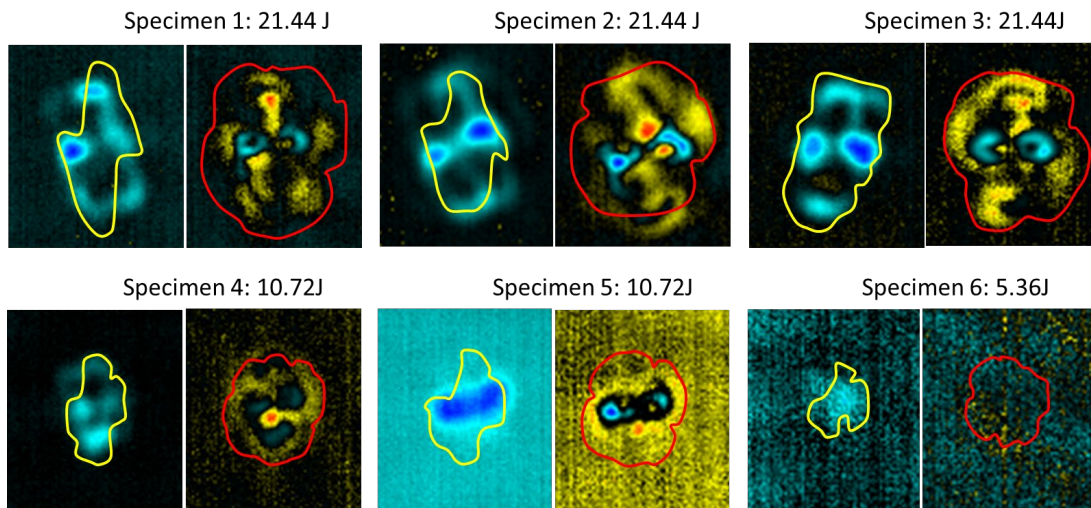


Figure 8. Overlay of damage area obtained from PAUT corresponding to depth ranges of 0.2-1.2 mm (yellow) and 1.2-2.2 mm (red), onto the X and Y components for each specimen; the impact energies are also listed.

Fig. 8 shows the X and Y components for each impact specimen; as before, the yellow outline corresponds to the damage area in the depth range 0.2-1.2 mm and the red outline to the damage area in the depth range 1.2-1.8 mm, both obtained from the PAUT scans. As indicated

previously, the X component should relate most strongly to near-surface damage and the Y component to deeper damage, and to the extent that the Y signature is consistently larger in area than the X signature, they do. An exception is the 5.36 J impact case, for which a Y component signature could not be detected.

Fig. 9 shows a comparison between results obtained from a 21.44 J specimen using the photon detector and the microbolometer. The former provides a more detailed signature of the damage when compared with the microbolometer results, however the main features of the defects are discernible in both. The photon detector result also contains evidence of vibration modes, or standing waves, established in the specimen by the acoustic excitation, which are not present in the microbolometer result, presumably due to the lower sensitivity of that camera. This could be viewed as a practical advantage to using a microbolometer, as these vibrational signatures have the potential to obscure indications of damage.

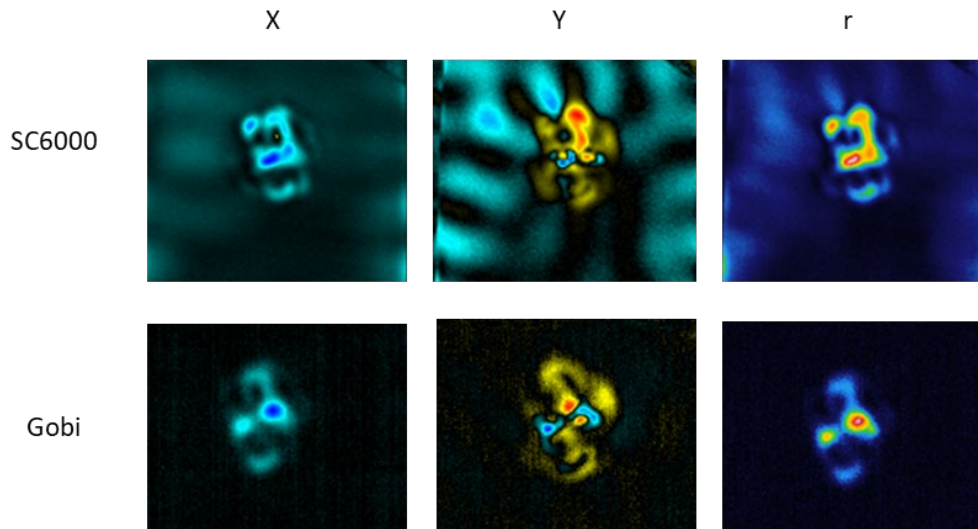


Figure 9. X, Y and r components measured on 21.44 J impact specimen, using a photon detector (top row) and microbolometer (bottom row).

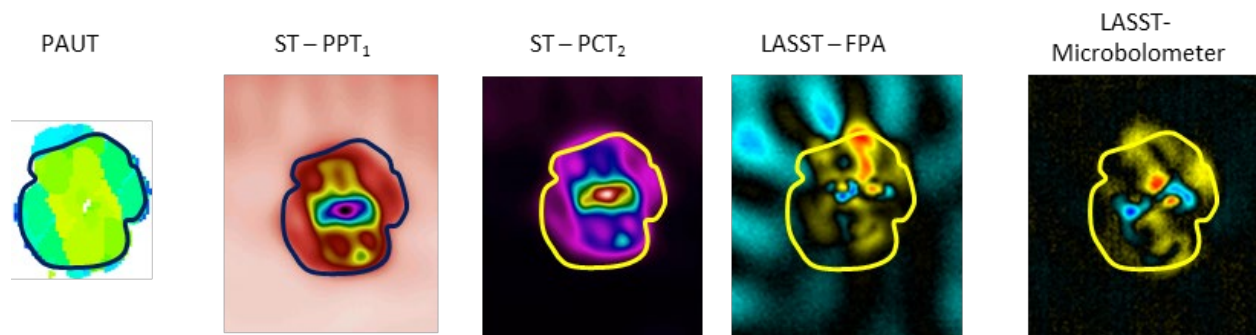


Figure 10. Comparison of PAUT, traditional ST ( $PPT_1$  and  $PCT_3$ ) processed over 2 s and LASST (Y component) from the FPA and microbolometer for 21.44 J impact specimen.

Finally, a comparison between the results obtained from LASST, conventional ST and PAUT are shown in Fig. 10, with the outline being the traced damage area from the PAUT result corresponding to damage up to 1.8 mm in depth. The ST results correspond to an insonification time of 1 s with the response recorded over a 2 s observation time and then post processed using

the PPT and PCT methods described in [7] and [8] respectively. Both show indications matching the area of the PAUT indication, as well as signal features which correlate with the different depths of damage. The LASST signatures are similar in area but have sharper signal features, some of which correlate with features in the PAUT scan. When combined with the corresponding X component results in the first column of Fig. 9, the LASST technique is seen to be effective for the detection and sizing of BVID in these panels. It should be noted that the LASST results required a pulsed insonification and observation time of 800s in total.

### Conclusions

The results from this study have indicated that LASST implemented using a low cost microbolometer is an effective means of identifying BVID and performs comparably to conventional ST implemented using a cooled photon detector. In some cases the extent of damage identified using LASST was smaller than that obtained from PAUT, which may be due to the relatively low excitation power being insufficient to generate frictional heating across the full extent of a defect. While LASST requires a longer observation time than traditional ST, it has two significant comparative advantages: it uses significantly less power so it reduces the risk of marring the surface of the structure under inspection and it enables use of a low-cost microbolometer which makes this technique much more portable, robust and affordable.

### References

- [1] K.A. Tsoi and N. Rajic, "Non-destructive evaluation of aircraft structural components and composite materials at DSTO using sonic thermography", DSTO Technical Note, DSTO-TN-0986 2011.
- [2] K. Tsoi, C. Antolis and N. Rajic, "Penetration Depth Limits of Active Thermography for Detection of Impact Damage in Carbon Fibre Composites", 22nd International Conference on Composite Materials, 2019.
- [3] N. Rajic and D. Rowlands, "Thermoelastic stress analysis with a compact low-cost microbolometer system", Quantitative InfraRed Thermography Journal, 10 (2013) 135-158. <https://doi.org/10.1080/17686733.2013.800688>
- [4] J. Rantala, D. Wu & G. Busse, "Amplitude-Modulated Lock-In Vibrothermography for NDE of Polymers and Composites", Journal of Research in Nondestructive Evaluation, 7:4, (1996) 215-228. <https://doi.org/10.1080/09349849609409580>
- [5] Salerno, A, Dillenz, A. Wu, D. Rantala J. and Busse, G., "Progress in ultrasound lockin thermography", Quantitative Infrared Thermography 4, (1998), 154-160. <https://doi.org/10.21611/qirt.1998.024>
- [6] Zweschper, T, Riegert, G., Dillenz, A. and Busse, G., "Frequency-modulated elastic wave thermography," Proc. SPIE 5073, Thermosense XXV, 2003. <https://doi.org/10.1117/12.488547>
- [7] X. Maldague and S. Marinetti, "Pulse Phase Infrared Thermography", J. Appl. Phys., 79, (1996) pp. 2694-2698, 1996. <https://doi.org/10.1063/1.362662>
- [8] N. Rajic. "Principal Component Thermography". DSTO Technical Report DSTO-TR-1298, 2002.

# A Machine Learning Approach for Anaerobic Reactor Performance Prediction Using Long Short-Term Memory Recurrent Neural Network

Benjamin Steven Vien<sup>1, a\*</sup>, Leslie Wong<sup>1, b</sup>, Thomas Kuen<sup>2, c</sup>, L. R. Francis Rose<sup>3, d</sup>  
and Wing Kong Chiu<sup>1, e</sup>

<sup>1</sup>Department of Mechanical and Aerospace Engineering, Monash University, Wellington Rd, Clayton, VIC 3800, Australia

<sup>2</sup>Melbourne Water Corporation, 990 La Trobe Street, Docklands, VIC 3008, Australia

<sup>3</sup>Defence Science and Technology Group, 506 Lorimer Street, Fishermans Bend, VIC 3207, Australia

<sup>a</sup>ben.vien@monash.edu, <sup>b</sup>Leslie.Wong@monash.edu, <sup>c</sup>Thomas.Kuen@melbournewater.com.au  
<sup>d</sup>Francis.Rose@dst.defence.gov.au, <sup>e</sup>wing.kong.chiu@monash.edu

**Keywords:** Machine Learning, Data Analysis, Anaerobic Reactor, Data Preparation, Long Short-Term Memory, Artificial Neural Network

**Abstract.** Predictive models are important to help manage high-value assets and to ensure optimal and safe operations. Recently, advanced machine learning algorithms have been applied to solve practical and complex problems, and are of significant interest due to their ability to adaptively ‘learn’ in response to changing environments. This paper reports on the data preparation strategies and the development and predictive capability of a Long Short-Term Memory recurrent neural network model for anaerobic reactors employed at Melbourne Water’s Western Treatment Plant for sewage treatment that includes biogas harvesting. The results show rapid training and higher accuracy in predicting biogas production when historical data, which include significant outliers, are preprocessed with z-score standardisation in comparison to those with max-min normalisation. Furthermore, a trained model with a reduced number of input variables via the feature selection technique based on Pearson’s correlation coefficient is found to yield good performance given sufficient dataset training. It is shown that the overall best performance model comprises the reduced input variables and data processed with z-score standardisation. This initial study provides a useful guide for the implementation of machine learning techniques to develop smarter structures and management towards Industry 4.0 concepts.

## Introduction

Melbourne Water’s self-powered Western Treatment Plant (WTP) at Werribee, Victoria, Australia [1], provides essential sewage treatment and under normal operating condition, its biological digestion process produces 65,000m<sup>3</sup> methane-rich biogas per day. This biogas is harvested and used to generate 7MW renewable electrical energy per day which is worth \$8 million (AUD) per year. The anaerobic treatment lagoons are covered by 2-mm thick high-density polyethylene (HDPE) floating sheets, approximately 450m x 170m, to capture odorous and greenhouse gases produced by the bacteria in the sewage under the covers. The untreated raw sewage content, such as fats, oil, floating solids and buoyed sludge or other fibrous material, may be carried to the surface of the lagoon by small bubbles, potentially forming into a solid mass called ‘scum’. The scum in the anaerobic lagoon is a mixture of floating solids, undigested

sludge and trapped gases formed during anaerobic digestions. This scum can accumulate under the covers, amassing into a large iceberg-like body, which is called ‘*scumberg*’. The formulation of *scumbergs* has the potential to adversely impact the structural integrity of the HDPE floating covers and block the pathway of biogas, thereby affecting the WTP performance. Due to the complex nature of the scum accumulation and *scumbergs* formation, it is very difficult to develop analytical or rule-based computing models for forecasting their effects on the performance of the anaerobic reactors and the structural integrity of the HDPE floating covers. Consequently, the only reliable performance data can only be obtained from the actual measurements at the sewage processing plant as the processes cannot reliably be scaled down to a laboratory-sized simulation. Therefore, there is a need for ‘smart’ real-time monitoring and diagnostic-prognostic capability modelling for the operation and management of this high-value asset based on current and/or historical operational data.

In many practical cases, physical systems for which explicit rules are either unknown or too difficult to determine, cannot be accurately modelled using traditional computing methods. In the last few decades, machine learning (ML) techniques have been extensively employed in engineering applications, which include structural engineering [2-4], water reservoir operations [5, 6], and structural health monitoring [7-9]. Artificial neural networks (ANN) are one of the machine learning-based algorithms that mimic the information processing and knowledge acquisition in the human brain. ANN is highly desirable due to its ability to model nonlinearity and predict accurately even in the presence of noisy and incomplete data of the real-world system. Furthermore, it can adaptively update its model in response to changing environments over time [10, 11] which makes ANNs an ideal candidate for solving complex engineering problems. However, ANNs are unable to provide justifications for their solutions and can be unpredictably inaccurate when extrapolating solutions for problems outside the network training domain.

A recurrence neural network (RNN) is a special type of ANN for sequential data modelling which store some past information. However, traditional RNNs have the problem of gradient vanishing/exploding and lack of long-term memory ability [12]. Long Short-Term Memory (LSTM) network was first proposed by Hochreiter and Schmidhube [13] to overcome the limitation of RNNs. LSTM network can effectively learn long-term dependencies between time steps and is superior to most RNN prediction methods [13]. In short, the difference between the traditional RNN and LSTM is the internal operation of the recurrent cell. In a traditional RNN, only one internal state exists and it is recomputed in every time step, whereas an LSTM cell has an additional self-connected memory cell state in which information can be stored; these memory cells are managed by cell gates, allowing learning of long-term dependencies [13]. There is significant interest in using LSTM network architecture for time-series forecasting for various engineering application including wind-power, solar power and electric load [14-17]. This architecture can also be expected to be highly advantageous for producing data-driven and adaptive predictive models based on ANN techniques for optimal biogas harvesting while ensuring the structural integrity of the floating covers.

In this paper, an LSTM network architecture, which comprises one sequence input layer followed by one LSTM layer, a fully-connected layer (consisting of one neuron) and an output layer, is developed and demonstrated to predict the biogas production of WTP anaerobic reactor. The investigation includes a parametric study to design the LSTM network topology, which includes data pre-processing, optimising the number of hidden units in an LSTM layer and training parameters, refer to Figure 1. A historical data sample from WTP is partitioned to train

the LSTM network input and recurrent weights and biases and to evaluate the trained models' performance. In this study, MATLAB R2020a was used to develop the LSTM network. This study reports on the data preparation of the real-life dataset of the anaerobic reactor and environment readings and the development of LSTM network architecture for biogas production prediction.

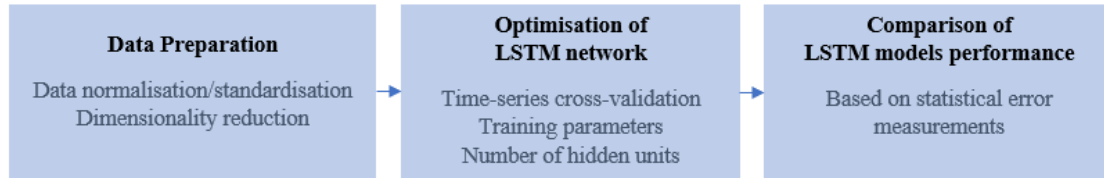


Figure 1: Schematic depiction of the procedure for the development and evaluation of LSTM models.

## Method

### Data Preparation

A real-world historical dataset of the 25W anaerobic reactor at WTP consists of 14 variables with 365 daily readings from November 2018 to October 2019 as collected by Melbourne Water (shown in Table 1), was used to train and develop the LSTM prediction models. The output variable is biogas production, whereas the remaining variables are treated as inputs for the prediction. Data pre-processing is an important stage for designing ML models, which primarily entails transforming raw data into a clean and useable format. Data normalisation/standardisation is a standard pre-processing technique that changes the values in a dataset to a common scale without misrepresenting the difference in the range of variables. For RNN/LSTM models, this is a crucial procedure to ensure stability and improve network training and performance [17]. In this study, two common data scaling techniques are applied and investigated: z-score standardisation (standardised variables), rescales data to have zero mean and standard deviation of 1 and min-max normalisation (normalised variables), linearly transforms data in the range [-1, 1] [18].

Normally, it is advantageous to reduce the number of inputs by removing redundant variables to improve the speed learning algorithm and eliminate overfitting to a degree. A feature selection technique aims to reduce the number of features (inputs) by using a correlation-based method to filter the correlated variables. In this study, Pearson's correlation coefficient is employed to measure the association between the input variables (refer to Figure 2). Based on the correlation matrix, 7 inputs variables, viz. average  $I_{main}$  average and minimum  $I_{s1}$ , average and minimum  $I_{s2}$ , average temperature  $T_A$  and average rainfall  $R$ , are selected for the reduced number of input variables (relative to the original 14 input variables) for the LSTM network model investigation.

Table 1: Historical WTP 25W anaerobic reactor daily data.

MAIN VARIABLES	UNITS	VARIABLES	MEAN	MAX	MIN	STANDARD DEVIATION	QUARTILE 1 (25%)	QUARTILE 2 (50%)	QUARTILE 3 (75%)
Main Inlet $I_{main}$	ML/d	Average	269.1	361.2	151.2	27.9	250.6	266.0	286.3
		<b>MAXIMUM</b>	<b>356.3</b>	<b>422.0</b>	<b>183.0</b>	<b>23.4</b>	<b>347.0</b>	<b>363.0</b>	<b>367.0</b>
		Minimum	120.4	344.0	0.0	47.3	95.0	113.0	139.0
SECONDARY INLET 1 $I_{s1}$	ML/D	<b>AVERAGE</b>	<b>7.6</b>	<b>123.2</b>	<b>0.0</b>	<b>16.3</b>	<b>0.0</b>	<b>1.1</b>	<b>7.2</b>
		Maximum	49.4	353.0	0.0	67.6	0.0	22.0	72.0
		<b>MINIMUM</b>	<b>0.04</b>	<b>15.0</b>	<b>0.0</b>	<b>0.8</b>	<b>0.0</b>	<b>0.0</b>	<b>0.0</b>
Secondary Inlet 2 $I_{s2}$	ML/d	Average	4.3	208.2	0.0	18.2	0.1	1.0	2.7
		<b>MAXIMUM</b>	<b>35.8</b>	<b>591.0</b>	<b>0.0</b>	<b>94.9</b>	<b>1.0</b>	<b>2.0</b>	<b>4.0</b>
		Minimum	0.6	4.0	0.0	1.0	0.0	0.0	1.0
ATMOSPHERIC TEMPERATURE $T_A$	°C	<b>AVERAGE</b>	<b>17.2</b>	<b>33.6</b>	<b>6.6</b>	<b>5.2</b>	<b>12.6</b>	<b>16.4</b>	<b>20.9</b>
		Maximum	25.9	46.0	11.0	6.9	21.0	25.0	31.0
		<b>MINIMUM</b>	<b>11.5</b>	<b>25.0</b>	<b>2.0</b>	<b>4.7</b>	<b>8.0</b>	<b>11.0</b>	<b>15.0</b>
Rainfall $R$	mm	Average	1.4	81.8	0.0	5.2	0.0	0.0	0.6
<b>BIOGAS PRODUCTION <math>g</math></b>	<b>NM<sup>3</sup>/HR</b>	<b>AVERAGE</b>	<b>2868.0</b>	<b>3825.5</b>	<b>35.8</b>	<b>468.8</b>	<b>2548.3</b>	<b>2876.7</b>	<b>3162.7</b>

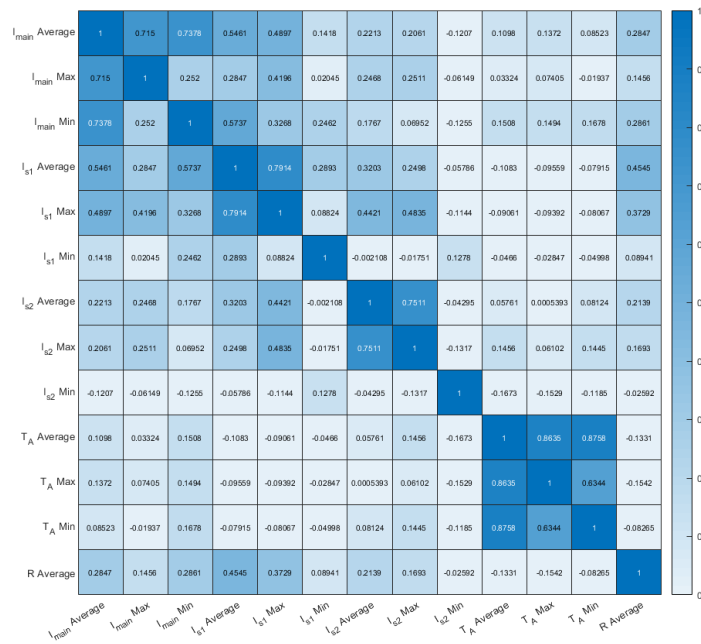


Figure 2: Heatmap of Pearson's correlation matrix on the input variables.

Model Validation

To ensure generalisation from the training data, it is essential that part of the test data set is preserved, unseen by the ML during training. Otherwise, the model is likely to overfit, yielding high accuracy on the training data, but failing to generalise from the training dataset, thereby resulting in poor predictive performance on new data. To evaluate trained ML models, *k*-fold

cross-validation technique is a common resampling procedure that randomly splits the dataset into  $k$  groups then trains the model on all groups except one that is reserved for testing the model [19]. Chronological ordered cross-validation, where training sets consist of observations that occur prior to those that form the testing set, is more suitable for time-series and sequential data modelling [20]. This study employed an expanding window (also known as forward-chaining) cross-validation with datasets partitioned into 6 nearly evenly distributed train-test sets (approximately 60 data points), equating to a 5-split (iteration) procedure, refer to Figure 3. The average error values of the 5 splits were used to evaluate the models' overall performance.

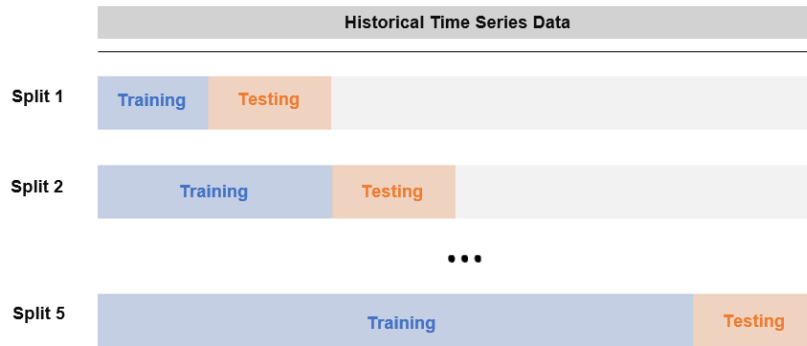


Figure 3: Expanding window 5-split time-series cross-validation.

The performances of LSTM models were compared and assessed based on the statistical error measurements; mean square error (MSE), mean absolute error (MAE) [21] and coefficient of determination ( $R^2$ ). It should be noted that the error measurements are calculated based on the standardised and normalised output variables. The training of the neural network used MSE as the loss function and stochastic gradient descent with momentum as the optimisation algorithm, which introduces learning variables, the learning rates and momentum parameter [22], to overcome problems of slow or non-convergence encountered in traditional gradient descent methods.

In this study, the several LSTM models were developed using standardised data with full and reduced input variables denoted as SFIV and SRIV models, respectively, and normalised data with full and reduced input variables denoted as NFIV and NRIV models, respectively. The study firstly investigated the optimal training parameters and the number of hidden units of a single LSTM layer for each model. Furthermore, the performances based on the error measurements for each best performing model were compared.

## Results and Discussion

Firstly, the optimum number of epoch (the number of times that the whole dataset is passed to the network) was determined by evaluating the average MSE, MAE and  $R^2$  of the 5 splits. In this investigation, a 10-hidden-unit LSTM layer was considered with epoch varying from 10 to 2000. The initial learning rate was 0.01, and the learning rate schedule was set to *piecewise*, where the learning rate was reduced by a factor of 0.2 after half of the number epochs had passed and the gradient threshold/clipping was 1. The optimal epoch for both SFIV and SFIV models are 50, and for NFIV and NRIV models are 100 and 200, respectively, refer to Table 2. Below or beyond these optimal epoch values will likely lead to underfit or overfit the trained models. It should be noted that inspection of learning curves (loss error over epoch/iteration) is necessary to monitor the behaviour of the model and ensure convergence.

Table 2: Optimisation of the number of epochs for SFIV, SRIV, NFIV and NRIV LSTM models.

Number of Epochs	Standardised						Normalised					
	Full Input Variables			Reduced Input Variables			Full Input Variables			Reduced Input Variables		
	MAEave	MSEave	R <sup>2</sup>	MAEave	MSEave	R <sup>2</sup>	MAEave	MSEave	R <sup>2</sup>	MAEave	MSEave	R <sup>2</sup>
10	285.00	1.32E+05	0.10	365.31	2.12E+05	0.10	869.52	9.88E+05	0.09	969.90	1.14E+06	0.08
20	286.40	1.40E+05	0.12	278.83	1.31E+05	0.12	407.43	2.81E+05	0.04	372.13	2.08E+05	0.11
50	<b>234.69</b>	<b>9.07E+04</b>	<b>0.19</b>	<b>243.28</b>	<b>9.86E+04</b>	0.14	312.79	1.66E+05	0.09	286.55	1.37E+05	0.12
100	288.34	1.40E+05	0.15	264.63	1.22E+05	0.18	<b>247.24</b>	<b>1.03E+05</b>	0.15	271.95	1.17E+05	0.16
200	331.70	1.84E+05	0.13	316.57	1.62E+05	<b>0.23</b>	270.04	1.22E+05	0.11	<b>250.78</b>	<b>1.01E+05</b>	0.14
500	387.92	2.59E+05	0.09	299.14	1.53E+05	0.12	285.78	1.33E+05	0.09	253.47	1.11E+05	0.15
1000	357.40	2.18E+05	0.10	404.02	2.66E+05	0.09	274.00	1.24E+05	0.18	265.73	1.16E+05	0.08
2000	413.71	3.11E+05	0.07	451.33	3.35E+05	0.06	343.56	2.09E+05	<b>0.19</b>	337.19	1.89E+05	<b>0.26</b>

Table 3: Error measurements for the different number of hidden units in one LSTM layer for SFIV, SRIV, NFIV and NRIV models. **Underlined** and **bolded** are the best and top three results, respectively, according to the error measurements.

Number of hidden units	Standardised						Normalised					
	Full Input Variables			Reduced Input Variables			Full Input Variables			Reduced Input Variables		
	MAEave	MSEave	R <sup>2</sup>	MAEave	MSEave	R <sup>2</sup>	MAEave	MSEave	R <sup>2</sup>	MAEave	MSEave	R <sup>2</sup>
1	252.08	1.06E+05	0.11	289.21	1.37E+05	0.18	266.65	1.19E+05	<b>0.15</b>	262.72	1.10E+05	<b>0.20</b>
2	236.63	8.47E+04	0.19	301.30	1.46E+05	0.13	251.98	1.04E+05	0.12	249.69	9.84E+04	0.19
3	272.17	1.23E+05	0.12	249.26	1.05E+05	0.15	252.15	9.94E+04	0.13	262.57	1.18E+05	0.14
4	253.41	1.03E+05	<b>0.21</b>	239.56	9.10E+04	0.20	242.12	9.39E+04	0.12	257.48	1.09E+05	0.16
5	264.54	1.16E+05	0.12	269.79	1.22E+05	0.18	255.78	1.06E+05	0.14	262.08	1.15E+05	0.15
6	268.25	1.19E+05	0.12	<b>211.63</b>	<b>7.12E+04</b>	<b>0.23</b>	<b>240.75</b>	<b>9.17E+04</b>	0.14	248.19	1.01E+05	<b>0.24</b>
7	240.02	9.66E+04	0.17	277.97	1.35E+05	0.18	276.55	1.29E+05	0.06	<b>246.79</b>	<b>9.68E+04</b>	0.14
8	243.68	9.36E+04	0.16	256.87	1.12E+05	0.18	245.00	9.93E+04	0.15	<b>246.51</b>	9.82E+04	<b>0.20</b>
9	269.03	1.19E+05	0.16	244.66	1.01E+05	0.17	267.92	1.17E+05	0.09	<b>239.89</b>	<b>9.12E+04</b>	0.17
10	234.69	9.07E+04	0.19	243.28	9.86E+04	0.14	247.24	1.03E+05	<b>0.15</b>	250.78	1.01E+05	0.14
11	<b>220.62</b>	<b>7.86E+04</b>	<b>0.21</b>	254.31	1.07E+05	0.20	246.10	9.74E+04	0.10	254.13	1.09E+05	0.12
12	232.63	9.27E+04	0.12	<b>215.77</b>	<b>7.70E+04</b>	<b>0.22</b>	267.47	1.12E+05	0.13	248.03	9.97E+04	0.16
13	247.47	9.80E+04	0.11	239.92	9.44E+04	0.21	266.36	1.10E+05	0.12	262.21	1.13E+05	0.13
14	<b>226.39</b>	<b>8.46E+04</b>	0.19	273.90	1.20E+05	0.12	<b>241.01</b>	9.70E+04	0.13	249.87	<b>9.68E+04</b>	0.17
15	237.23	8.83E+04	<b>0.22</b>	245.71	9.58E+04	0.16	253.61	9.76E+04	0.08	269.82	1.17E+05	0.16
16	<b>227.06</b>	<b>8.11E+04</b>	0.20	268.90	1.19E+05	0.17	<b>238.66</b>	<b>9.28E+04</b>	<b>0.18</b>	254.71	1.03E+05	0.15
17	249.80	9.94E+04	0.17	<b>219.38</b>	<b>8.10E+04</b>	<b>0.24</b>	251.85	9.88E+04	0.08	249.27	9.79E+04	0.13
18	260.56	1.13E+05	0.15	246.12	1.00E+05	0.15	306.20	1.43E+05	0.06	262.87	1.07E+05	0.12
19	251.33	1.02E+05	0.20	255.63	1.06E+05	0.13	243.84	<b>9.28E+04</b>	0.11	249.16	9.96E+04	0.16
20	281.16	1.26E+05	0.14	235.06	8.63E+04	0.19	258.16	1.11E+05	0.11	258.39	1.03E+05	0.14

Based on the error measurements, the optimal number of hidden units in a one LSTM layer for SFIV and SRIV models are 11 and 6, respectively and for NFIV and NRIV models are 6 and 9, respectively, as indicated in Table 3. The coefficients of determination were compared to evaluate the models with different pre-processed data. It is shown that NFIV and NRIV models performed relatively poorly compared to data pre-processed with z-score standardisation, refer to

Tables 3 and 4, and this is evident in Figures 4 and 5. This is because extreme outliers exist in the historical data and are retained during the learning process. In practice, data standardisation is more robust in handling outliers/extremities or non-uniformly distributed data than min-max normalisation. Furthermore, the models with normalised variables took relatively longer to train.

Table 4: Error measurement of the best performing LSTM models for each split cross-validation.

Best Performing Model	Error	k <sup>th</sup> Split				
		1	2	3	4	5
Standardised Full Input Variables 11-hidden-unit LSTM layer	MAE	245.53	219.31	207.35	221.90	209.04
	MSE	7.58E+04	9.82E+04	6.92E+04	8.46E+04	6.55E+04
	R <sup>2</sup>	0.25	0.31	0.18	0.00	0.30
Standardised Reduced Input Variables 6-hidden-unit LSTM layer	MAE	227.76	228.51	219.14	188.64	194.11
	MSE	6.79E+04	9.99E+04	7.17E+04	6.11E+04	5.55E+04
	R <sup>2</sup>	0.30	0.40	0.06	0.04	0.37
Normalised Full Input Variables 6-hidden-unit LSTM layer	MAE	243.54	265.65	241.49	224.25	228.84
	MSE	7.65E+04	1.26E+05	8.67E+04	9.17E+04	7.75E+04
	R <sup>2</sup>	0.15	0.35	0.04	0.00	0.13
Normalised Reduced Input Variables 9-hidden-unit LSTM layer	MAE	264.45	230.47	227.97	243.22	233.33
	MSE	9.08E+04	1.03E+05	7.89E+04	9.61E+04	8.79E+04
	R <sup>2</sup>	0.11	0.28	0.22	0.17	0.09

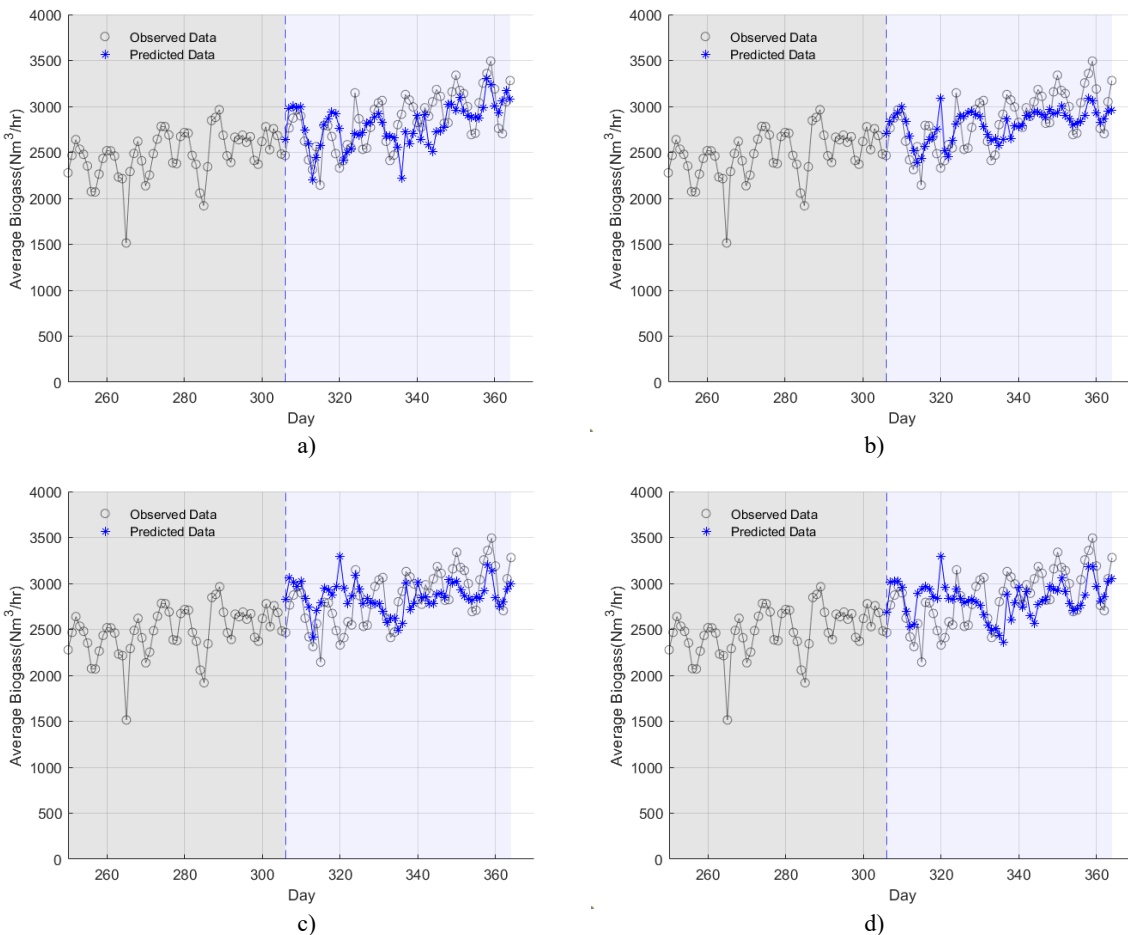


Figure 4: 5<sup>th</sup> split predicted biogas production of the best performing LSTM models: a) SFIV, b) SRIV, c) NFIV and d) NRIV models.

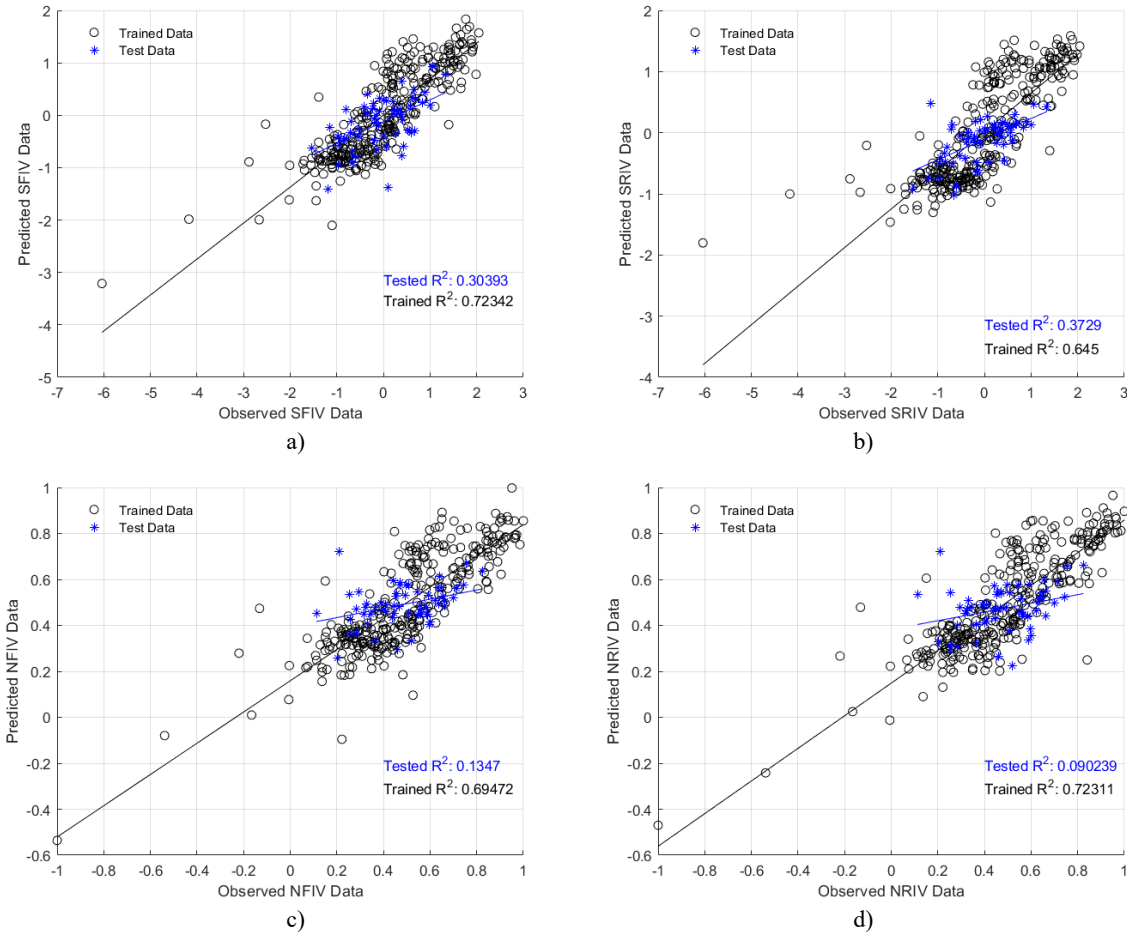


Figure 5: Predicted and observed plots of the best performing LSTM models on the 5<sup>th</sup> split; a) SFIV, b) SRIV, c) NFIV and d) NRIV models.

The best LSTM model is the SRIV model and it is shown that the other best performing models can also generalise and predict with good accuracy after the last split (refer to Table 4). The substantial improvement in the models’ performance on the last split suggests most of the dependencies and key features can be learnt in the first four data partition sets.

**Conclusion**

This study has reported on the development of an ANN architecture for predicting the performance of WTP anaerobic reactor. With the currently available dataset, the findings have shown that an LSTM network can be utilised to predict biogas production. It is shown that the prediction model with data standardisation yields higher accuracy and outperforms the max-min normalisation for the WTP historical dataset, which included significant outliers. The LSTM model trained by using standardised data with reduced input variables yields the best average performance on all splits. It is shown that the LSTM predicting model with a reduced number of input variables via Pearson’s correlation coefficient selection method can achieve good accuracy given sufficient dataset training. Ongoing studies on the data preparation and development of ML algorithms and their architectures for WTP performance forecasting as well as the monitoring of floating cover structural integrity are underway in integrating AI-enable approach for future management and operation of this critical asset.

## Acknowledgments

Financial supports provided by Australia Research Council (Linkage Project Grant) (ARC LP170100108) and Melbourne Water Corporation are gratefully acknowledged. The in-kind contributions from Melbourne Water are also gratefully acknowledged.

## Reference

- [1] Melbourne Water. *Western Treatment Plant Virtual Tour*. 2020 30 September 2020 [cited 2020 30 November]; Available from: <https://www.melbournewater.com.au/water-data-and-education/learning-resources/water-and-sewage-treatment-plants/western-treatment-0>.
- [2] Madhiarasan, M. and S. Deepa, A novel criterion to select hidden neuron numbers in improved back propagation networks for wind speed forecasting. *Applied intelligence*, 2016. 44(4): p. 878-893. <https://doi.org/10.1007/s10489-015-0737-z>
- [3] Moosazadeh, S., E. Namazi, H. Aghababaei, A. Marto, H. Mohamad, and M. Hajihassani, *Prediction of building damage induced by tunnelling through an optimized artificial neural network*. *Engineering with Computers*, 2019. 35(2): p. 579-591. <https://doi.org/10.1007/s00366-018-0615-5>
- [4] Liu, H. and Y. Zhang, Deep learning-based brace damage detection for concentrically braced frame structures under seismic loadings. *Advances in Structural Engineering*, 2019. 22(16): p. 3473-3486. <https://doi.org/10.1177/1369433219859389>
- [5] Ehsani, N., B.M. Fekete, C.J. Vörösmarty, and Z.D. Tessler, *A neural network based general reservoir operation scheme*. *Stochastic environmental research and risk assessment*, 2016. 30(4): p. 1151-1166. <https://doi.org/10.1007/s00477-015-1147-9>
- [6] Maier, H.R., A. Jain, G.C. Dandy, and K.P. Sudheer, Methods used for the development of neural networks for the prediction of water resource variables in river systems: Current status and future directions. *Environmental modelling & software*, 2010. 25(8): p. 891-909. <https://doi.org/10.1016/j.envsoft.2010.02.003>
- [7] Deng, L. and D. Yu, *Deep learning: methods and applications*. *Foundations and trends in signal processing*, 2014. 7(3-4): p. 197-387. <https://doi.org/10.1561/20000000039>
- [8] Liu, H. and Y. Zhang, Deep learning based crack damage detection technique for thin plate structures using guided lamb wave signals. *Smart Materials and Structures*, 2019. 29(1): p. 015032. <https://doi.org/10.1088/1361-665X/ab58d6>
- [9] Agarwal, S. and M. Mitra, Lamb wave based automatic damage detection using matching pursuit and machine learning. *Smart materials and structures*, 2014. 23(8): p. 085012. <https://doi.org/10.1088/0964-1726/23/8/085012>
- [10] Basheer, I.A. and M. Hajmeer, *Artificial neural networks: fundamentals, computing, design, and application*. *Journal of microbiological methods*, 2000. 43(1): p. 3-31. [https://doi.org/10.1016/S0167-7012\(00\)00201-3](https://doi.org/10.1016/S0167-7012(00)00201-3)
- [11] Engelbrecht, A.P., *Computational intelligence: an introduction*. 2007: John Wiley & Sons.

- [12] Bengio, Y., P. Simard, and P. Frasconi, *Learning long-term dependencies with gradient descent is difficult*. IEEE transactions on neural networks, 1994. 5(2): p. 157-166. <https://doi.org/10.1109/72.279181>
- [13] Hochreiter, S. and J. Schmidhuber, *Long short-term memory*. Neural computation, 1997. 9(8): p. 1735-1780. <https://doi.org/10.1162/neco.1997.9.8.1735>
- [14] Gensler, A., J. Henze, B. Sick, and N. Raabe. Deep Learning for solar power forecasting—An approach using AutoEncoder and LSTM Neural Networks. in 2016 IEEE international conference on systems, man, and cybernetics (SMC). 2016. IEEE. <https://doi.org/10.1109/SMC.2016.7844673>
- [15] Bouktif, S., A. Fiaz, A. Ouni, and M.A. Serhani, Optimal deep learning lstm model for electric load forecasting using feature selection and genetic algorithm: Comparison with machine learning approaches. Energies, 2018. 11(7): p. 1636. <https://doi.org/10.3390/en11071636>
- [16] Yu, R., J. Gao, M. Yu, W. Lu, T. Xu, M. Zhao, J. Zhang, R. Zhang, and Z. Zhang, *LSTM-EFG for wind power forecasting based on sequential correlation features*. Future Generation Computer Systems, 2019. 93: p. 33-42. <https://doi.org/10.1016/j.future.2018.09.054>
- [17] Le, X.-H., H.V. Ho, G. Lee, and S. Jung, Application of long short-term memory (LSTM) neural network for flood forecasting. Water, 2019. 11(7): p. 1387. <https://doi.org/10.3390/w11071387>
- [18] Han, J., J. Pei, and M. Kamber, *Data mining: concepts and techniques*. 2011: Elsevier.
- [19] Rodriguez, J.D., A. Perez, and J.A. Lozano, *Sensitivity analysis of k-fold cross validation in prediction error estimation*. IEEE transactions on pattern analysis and machine intelligence, 2009. 32(3): p. 569-575. <https://doi.org/10.1109/TPAMI.2009.187>
- [20] Hyndman, R.J. and G. Athanasopoulos, *Forecasting: principles and practice*. 2018: OTexts.
- [21] Hajihassani, M., D.J. Armaghani, H. Sohaei, E.T. Mohamad, and A. Marto, Prediction of airblast-overpressure induced by blasting using a hybrid artificial neural network and particle swarm optimization. Applied Acoustics, 2014. 80: p. 57-67. <https://doi.org/10.1016/j.apacoust.2014.01.005>
- [22] Ruder, S., An overview of gradient descent optimization algorithms. arXiv preprint arXiv:1609.04747, 2016.

## Development of Scum Geometrical Monitoring Beneath Floating Covers Aided by UAV Photogrammetry

Leslie Wong<sup>1,a\*</sup>, Benjamin Steven Vien<sup>1,b</sup>, Yue Ma<sup>1,c</sup>, Thomas Kuen<sup>2,d</sup>,  
Frank Courtney<sup>2,e</sup>, Jayantha Kodikara<sup>3,f</sup>, Francis Rose<sup>4,g</sup> Wing Kong Chiu<sup>1,h</sup>

<sup>1</sup>Department of Mechanical & Aerospace Engineering, Monash University, Clayton, VIC 3008, Australia

<sup>2</sup>Melbourne Water Corporation, 990 La Trobe Street, Docklands, VIC 3008, Australia

<sup>3</sup>Department of Civil Engineering, Monash University, Clayton, VIC 3008, Australia

<sup>4</sup>Defence Science and Technology Group, 506 Lorimer Street, Fishermans Bend, VIC 3207, Australia

<sup>a</sup>Leslie.Wong@monash.edu, <sup>b</sup>ben.vien@monash.edu, <sup>c</sup>yue.ma@monash.edu,  
<sup>d</sup>Thomas.Kuen@melbournewater.com.au, <sup>e</sup>frank.courtney@melbournewater.com.au,  
<sup>f</sup>Jayantha.kodikara@monash.edu, <sup>g</sup>Francis.Rose@dst.defence.gov.au,  
<sup>h</sup>wing.kong.chiu@monash.edu

**Keywords:** Remote Sensing, Structural Health Monitoring, Non-Contact Inspection, UAV Photogrammetry, HDPE Membrane, Floating Cover, Scums, Sewage Treatment

**Abstract.** Floating covers are used on anaerobic lagoons at waste-water treatment plants for odour control and the harvesting of biogas. Scum is an unwanted by-product of the anaerobic digestion of raw sewage. This matter can form into a large mass of material, and when it floats to the surface and solidifies, it is called a scumberg to differentiate it from the scum which may still be in a semi-solid state. Given the continual inflow of raw sewage into the lagoon, the potential movement of the scum can deform the floating cover. One of the challenges pertaining to the structural health assessment of the floating cover hinges upon the difficulty in monitoring the development and geometrical profile of scum underneath the cover. The current measurement of scum requires the inspector to physically access the scum either from multiple discrete access ports within the floating cover or by using highly-skilled divers in the lagoon. In collaboration with Melbourne Water, a non-contact UAV-aided photogrammetry technique has been deployed to quantify the development of scum underneath the cover. It is shown that the digital elevation model obtained from photogrammetry correlates well with direct laser based measurements of elevation, and that cluster analysis can be used in conjunction with the digital elevation model to estimate the qualitative hardness level of the scum beneath the cover, thereby providing a viable alternative to time-consuming walk the cover type inspections. It is also shown that the total scum depth as predicted from the digital elevation model correlates well with the measurements taken through the access ports. This method could be a more effective alternative to current practice.

### Introduction

Melbourne Water owns and operates a large wastewater treatment facility in Werribee, Victoria, Australia (Western Melbourne), which is known as the Western Treatment Plant (WTP) [1]. Figure 1a shows part of the treatment process at the WTP. WTP treats more than 300 billion litres of Melbourne's sewage annually (more than half of Melbourne's wastewater) via a combination of lagoon systems and activated sludge plants. At the WTP, the raw and untreated

sewage is first directed into anaerobic lagoons to remove the solids. The first treatment lagoon at the WTP is covered with numerous sheets of high-density polyethylene (HDPE) geomembranes for odour control and biogas harvesting. The floating covers are designed to be flexible enough to accommodate the effect of geometric changes in the shape and surface area of cover resulting from the varying the level of the water surface. Figure 1b shows a schematic cross-sectional view of the covered anaerobic lagoon. A suitable anaerobic environment is provided for bacterial to break down the organic material into sludge, thereby releasing methane-rich biogas, which can be harvested and used to generate electricity to run the site and potentially exports surplus electricity to the grid.

The velocity of the sewage decreases as it enters the very large lagoon, and this facilitates the preliminary sedimentation of the suspended solids in the raw sewage. Material in the sewage, such as oils, grits, fats, greases, fibrous substance and floatable solids can be transported to the water surface of the lagoon while still under the cover. Over time, scum can consolidate and accumulate at the water surface to form scumbergs, which can impose forces on the cover which have the potential to result in undesirable displacement. The continual inflow of raw sewage and the resultant movement of the scumbergs can further deform and stress the floating cover to an extent that may approach the intended limits of the covers's design. Therefore, the need to monitor the development and geometrical profile of "scum" underneath the cover of an anaerobic lagoon will provide the crucial information for assessing the structural health of the floating cover.

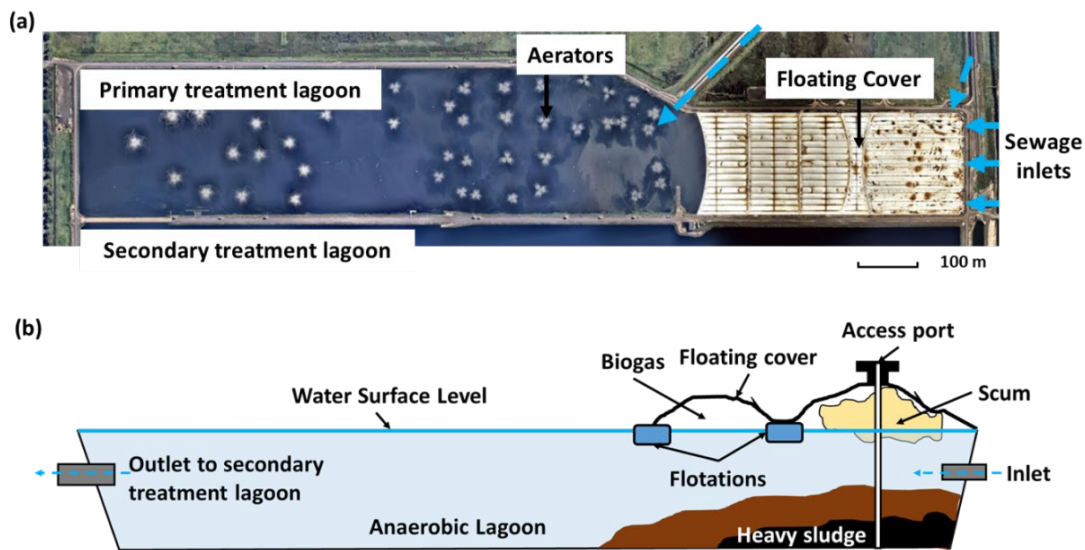


**Figure 1.** (a) Satellite view of part of the wastewater treatment process at Western Treatment Plant (WTP) and (b) schematic of the situation under the cover of an anaerobic lagoon

Currently, inspectors “walk the covers” to qualitatively identify the extend and define the hardness of the scum by “feeling” the different response of the cover when stepping on. It is difficult to objectively determine the edge of the scums in its various stages of formation with this method. A detailed walk-the-cover inspection typically occurs over a few days. Staff at WTP are tasked to perform the measurements of the scum depth and cover elevation profile twice every year via laser survey, cover walks, direct access to the scum through the access ports on the cover or by sending divers into the lagoon.

Melbourne Water is currently considering the deployment of regular UAV flights/surveys over the covers at the WTP. UAV- aided photogrammetry is a safe and time-efficient assessment

technique [2, 3], which can be remotely operated to conduct scanning without coming into contact with the asset and thereby also reducing the need for intrinsically safe inspection equipment. The work presented builds on the previous work as described in [4, 5]. This paper compares the UAV-aided photogrammetry output – digital elevation model (DEM) of the cover with existing walk-the-cover inspection data and physical scum depth measurement taken through the cover’s access ports. The accuracy of the DEM model is also verified using manual measurements recorded by an independent contractor. This work also forms a crucial part of developing the non-contact UAV-based photogrammetry technique to assist with the maintenance and operation of the floating covers especially in mapping the geometrical information of the scum.

### UAV photogrammetry set up

One of the anaerobic lagoon at the WTP is used for this case study, see Figure 2. Only the first part of the lagoon is covered, and the dimension of the cover is measures 450 m × 170 m. Six ground control points (GCPs, and refer to Figure 2) were marked on the concrete area around the anaerobic lagoon and their accurate GPS location determined for calibration purposes. A Hex Rotor UAV - DJI M600 Pro with Zenmuse X5 (15 mm lens) [6], was utilised to conduct the scanning over the floating cover of this lagoon with a single flight path mode set in Pix4DCapture [7]. The configuration is set to have 80% images overlapping at both forward and side direction. The scan was conducted at a height of 50 m above the floating cover and the scan took approximately 30 minutes.

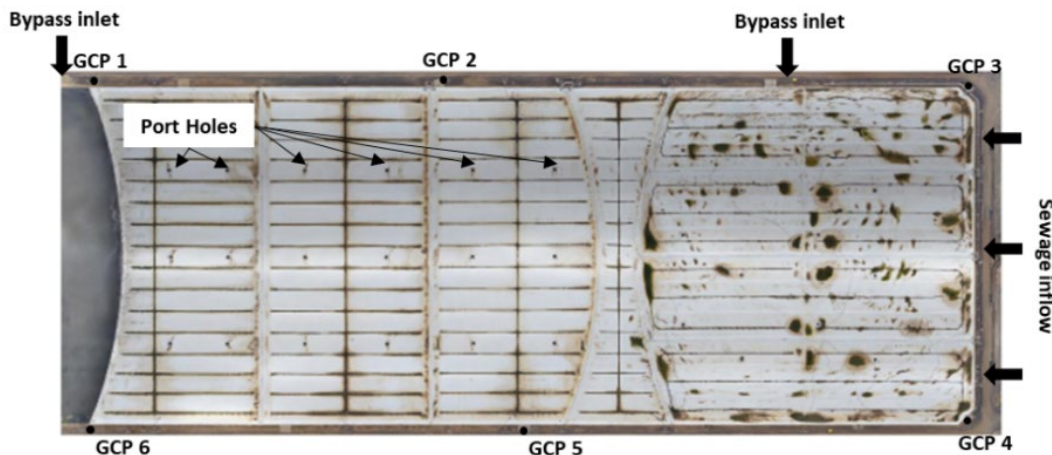


*Figure 2. Orthophoto of the covered anaerobic lagoon at the WTP*

Metashape Professional by Agisoft [8] was then used for post-processing of the images taken from the scan (photogrammetry). Agisoft Metashape adopts computer vision algorithms as described in [9, 10, 11] which allows the user to set the quality of aligning images, building dense clouds, mesh and capable of generating the DEM. All the metadata (e.g. GPS location and camera setting) of the images were first imported to Agisoft Metashape Professional for alignment purposes. All settings (including image alignment and dense cloud configuration) were set to its “High” when post-processing the images acquired from the scan. The GPS (Easting and Northing) of all the GCPs were also loaded to generate a scaled DEM. A total of 893 aerial images were taken and Agisoft Metashape were used to constructed the DEM model with a spatial resolution of 1.14 cm per pixel.

The accuracy of the DEM is first established with an elevation survey conducted by a Melbourne Water independent contractor. The elevation above water level of 39 points on the cover were

measured using IMEX i77R rotating red beam laser with each of the corresponding measurement point presented in Figure 3. The elevation above water surface level obtained from the constructed DEM was then compared with the measurement obtained from the laser survey and plotted in Figure 4. The accuracy of the DEM is evident with a  $R^2$  of 0.9729. The validation of this DEM highlights the reliability and the confidence of using the constructed DEM to assess the floating cover.

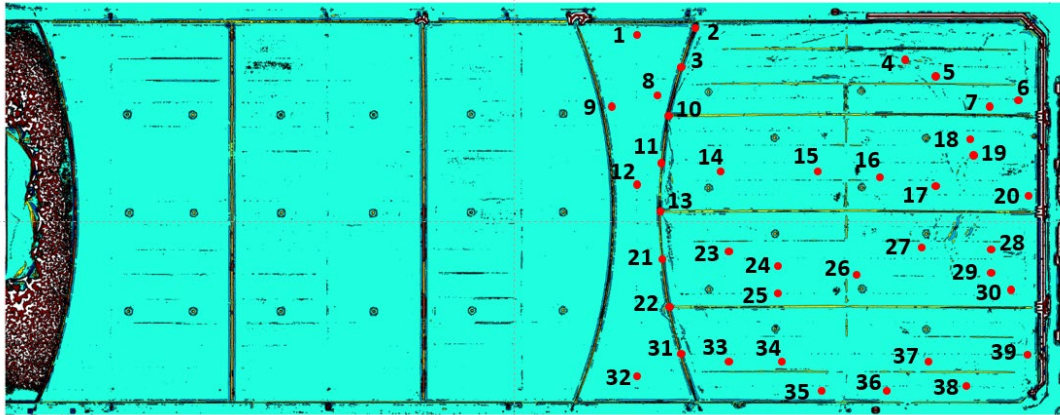


Figure 3. Location of the laser survey readings on the cover of the anaerobic lagoon at WTP

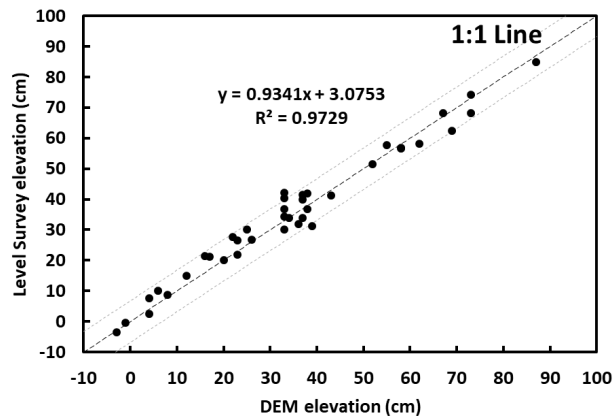
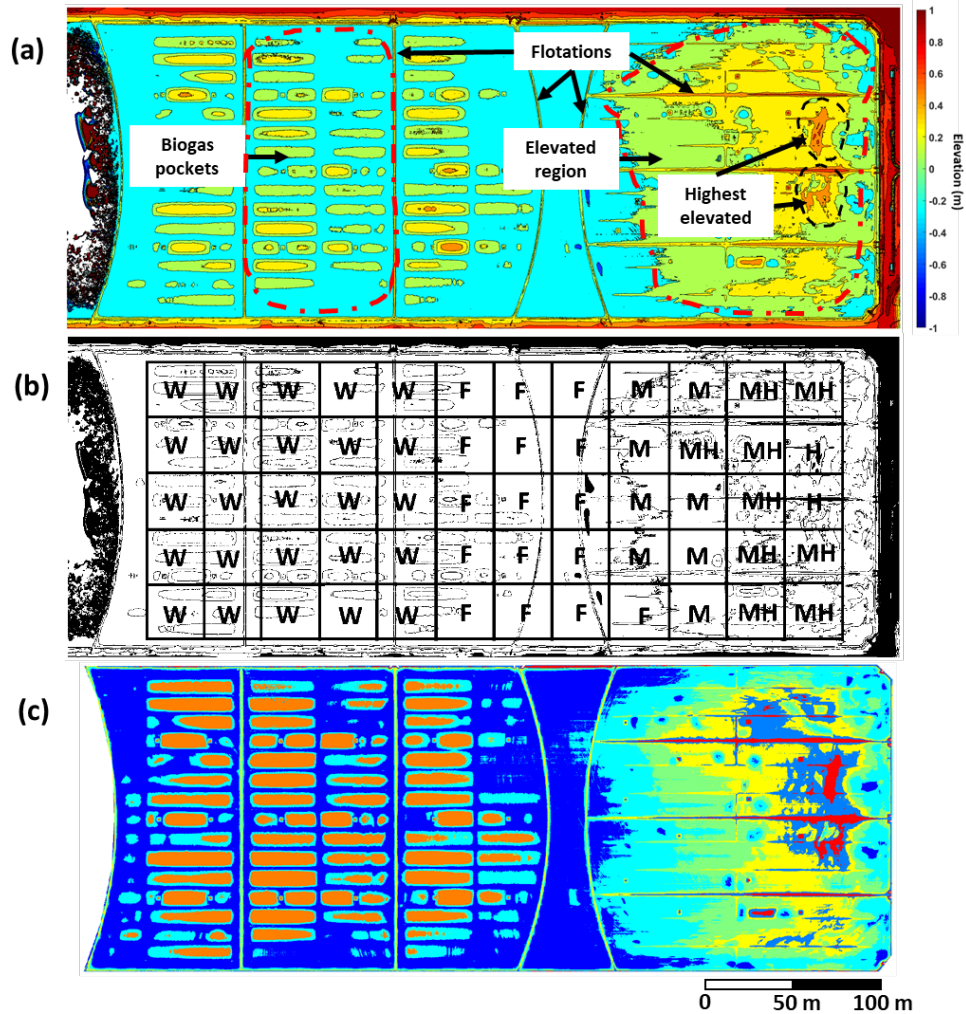


Figure 4. Correlation between both elevation measurement methods (above water level) - level survey and UAV-aided photogrammetry

### Correlation between cover walk inspection and DEM

Figure 5a shows the DEM of the scanned cover at the lagoon and represent the height of the cover above water surface level of the lagoon. The constructed DEM shows that the covers at the regions in the vicinity of the sewage inlet are highly elevated especially along the middle section. These highly elevated regions could potentially be due to the accumulation of hard scums at the water surface level. In addition, multiple pockets of biogas (left-hand side of the DEM) can also be observed. Figure 5b shows a grid indicating the qualitative state of “hardness” of the scum (H – hard, MH – medium hard, M – medium, F – fluffy, or soft, scum and W – watery), as determined by the Monash Team one month after the UAV scan.



**Figure 5.** (a) Digital elevation model (DEM) of the cover, (b) qualitative scum hardness survey (H-Hard, MH-Medium Hard, M-Medium, F-Fluffy and W-Watery) via cover walk inspection and (c) k-means based image segmentation on DEM with 7 clusters

Clustering analysis is one of the common unsupervised machine learning (ML) techniques, which is used to find hidden patterns or grouping from datasets without labelled responses. Image segmentation applies k-mean clustering to partition the data into ‘k’ distinct clusters based on distance to the centroid of a cluster. The built-in MATLAB function, *imsegkmeans* [12] is utilised to segment the DEM into different clusters. A 7 k-means clustering is applied with the aim to cluster the 5 different levels of scum hardness based on elevation of the cover as well as identifying the biogas pocket and flotations (below the cover to provide biogas channel for harvesting as shown in Figure 1b). The result of the clustering is presented in Figure 5c. By using the elevation of cover above water level, the cluster coloured in red correlates well with the ‘H’ region as indicated in Figure 5b. In addition, the cluster for both ‘MH’ and ‘M’ region can also easily be identified, as well as the biogas pockets. Due to only considering the elevation data, the clustering method is having difficulties in identifying the border between the region ‘F’ and ‘W’. The reason can be due to a subtle difference between the elevation at both ‘F’ and ‘W’ regions. Theoretically, this may potentially be improved by applying the quasi-active thermal imaging technique reported in [13] to identify the ‘F’ region and the ‘W’ region. This idea has

been proposed by Melbourne Water and a large-scale experiment is currently under preparation for imminent implementation. Nevertheless, the DEM image segmentation method is adequate to outline the area of the 'M', 'MH' and 'H' regions beneath the cover, which can already significantly reduce the current practice of walk-around inspection.

### **Correlation between physical scum depth measurement and DEM**

The total depth of the scum is measured at the access ports in the cover. The process requires the personnel to walk on the cover to access to the port holes. A long and stiff rod is slowly inserted into the access ports. Once the personnel "feel" a difference in pressure from below (going from hard or semi-hard scum to liquid sewage), the depth is then recorded as the "scum depth" with a tolerance of 0.1m.

This section explores the relationship between the digital elevation model of the cover above water surface level and the physical measurements of the total depth, or thickness, of the scum in the lagoon. Physical measurements were taken at the 30 access ports of the cover approximately one month after the UAV photogrammetry flight. The elevation above water surface level at these port holes can also be obtained from the constructed DEM. The correlation of the DEM at each access port is plotted in Figure 6 with the total scum depth at its corresponding access port. A best-fit line is plotted in Figure 6 with a  $R^2$  of 0.7757. For the scum depth prediction, it is assumed that the elevation of cover above water level bears a linear relationship with the scum depth. The elevation due to the biogas pocket and flotation are first suppressed. A factor of 3.55 is multiplied with the elevation above water surface level across the entire processed DEM to obtain a "predicted" scum depth profile across the entire cover. The contour plot of the predicted scum depth is presented in Figure 7a. A cross-sectional view of the predicted scum depth across the covered lagoon is then compared with the averaged scum depth obtained from physical measurement, see Figure 7b. Figure 7b shows good agreement between the predicted scum depth against the actual scum depth (averaged). However, Figure 7a also shows that it is hard to fully remove or suppress the elevation due to flotations (floating structure to provide path for biogas collection underneath the cover, see Figure 5a) especially around where the hard scum accumulated. Nevertheless, the capability of using DEM to predict the scum depth is demonstrated and the prediction model can potentially be improved by study the entire historical scum depth data.

### **Conclusion**

This paper shows the viability of using an efficient UAV photogrammetry inspection methodology to monitor the geometrical information of scum growth beneath the floating cover at the covered anaerobic lagoon the Western Treatment Plant (WTP). These details are important and when collated periodically (e.g. monthly), will give the operators at the Western Treatment Plant insight into the operation of the lagoon and for the structural health assessment of the floating cover. This paper has also explored the correlation of the digital elevation model (DEM) obtained from UAV photogrammetry with (1) scum hardness and (2) scum depth. The following dot points summarise the findings of the work presented.

- UAV photogrammetry techniques were used to construct the digital elevation model (DEM) of the scanned cover. K-mean image segmentation was applied on the constructed DEM to estimate the hardness of substrate. The substrate hardness clustering correlates well especially the Hard, Medium Hard and Medium regions with the current practice of walk-around inspection.

- The constructed DEM is noted to correlate well with the laser survey (ground truth) measurement with  $R^2$  of 0.9729.
- A linear assumption is made between the scum depth and cover's elevation above water level. At current stage, some features (flotations, ballasts and water puddles) on the cover are suppressed to reduce the error for the prediction. The predicted scum depth has a good correlation with the ground truth (physical scum depth measurement). The linear assumptions will need to be further examined in the future with historical data.
- UAV photogrammetry techniques are considered to be a cost-effective alternative to current scum inspection and measurement practices at WTP.

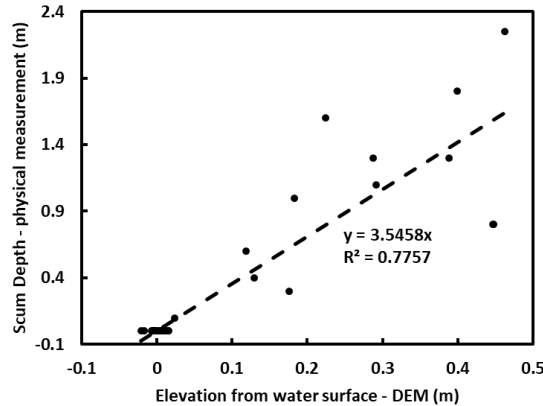


**Figure 6.** Correlation between the total scum depth and elevation above water surface level obtained from DEM

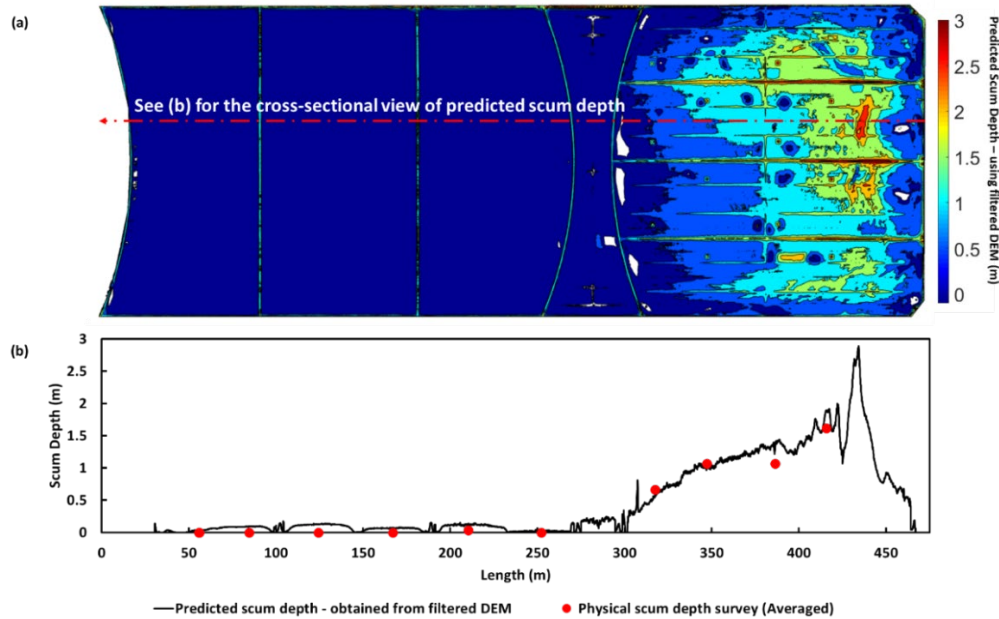


**Figure 7 (a)** Contour plot for the predicted scum depth obtained from filtered DEM and **(b)** cross-sectional view of scum depth along the highlighted line in Figure 7(a)

### Acknowledgement

The financial support provided by Melbourne Water and Australia Research Council Linkage Grant (ARC LP170100108) is gratefully acknowledged.

## Reference

- [1] MelbourneWater, "Sewage Treatment process at Western Treatment Plant," Melbourne Water, 30 October 2019. [Online]. Available: <https://www.melbournewater.com.au/water-data-and-education/learning-resources/water-and-sewage-treatment-plants/western-treatment-0> [Accessed December 2019].
- [2] Ong, W., Chiu, W.K., Kuen, T. and Kodikara, J., "Determination of the state of strain of large floating covers using unmanned aerial vehicle (UAV) aided photogrammetry," *Sensors*, vol. 17, p. 1731, 2017. <https://doi.org/10.3390/s17081731>
- [3] Eisenbeiss, H. and Sauerbier, M., "Investigation of UAV systems and flight modes for photogrammetric applications," *Photogrammetric Record*, vol. 26, pp. 400-421, 2011. <https://doi.org/10.1111/j.1477-9730.2011.00657.x>
- [4] Wong, L., Courtney, F., Vien, B., Kuen, T., Douglas, P., Ma, Y., Kodikara J. and Chiu, W. K., "Structural Assessment of Large Membrane Structures using an Unmanned Aerial Vehicle aided Photogrammetry: Determination of Flight Parameters and Trials at the Western Treatment Plant," *Journal of Nondestructive Evaluation, Diagnostics and Prognostics of Engineering Systems*, vol. 2, no. 040902, pp. 1-8, 2019. <https://doi.org/10.1115/1.4044637>
- [5] Chiu, W. K., Ong, W., Kuen, T., and Courtney, F. "Large structures monitoring using unmanned aerial vehicles," *Procedia Engineering. 6th Asia Pacific Workshop on Structural Health Monitoring (APWSHM)*, vol. 188, pp. 415-423, 2017. <https://doi.org/10.1016/j.proeng.2017.04.503>
- [6] DJI, *Matrice 600 PRO User Manual V1.0*, DJI, 2018.
- [7] Pix4D, "Pix4Dcapture," Pix4D S.A., 2019. [Online]. Available: <https://www.pix4d.com/product/pix4dcapture>. [Accessed December 2019].
- [8] Agisoft, *Agisoft Metashape User Manual: Professional Edition, Version 1.5*, [www.agisoft.com](http://www.agisoft.com), 2019.
- [9] Barazzetti, L., Forlani, G., Remondino, F., Roncella, R., and Scaioni, M., "Experiences and achievements in automated image sequence orientation for close-range photogrammetric projects," in *Proceedings SPIE 8085, Videometrics, Range Imaging and Applications XI, 80850F*, Munich, May 2011. <https://doi.org/10.1117/12.890116>
- [10] Westoby, M., Brasington, J., Glasser, N., Hambrey, M., and Reynolds, J., "Structure-from-motion photogrammetry: a low-cost, effective tool for geoscience applications," *Geomorphology*, vol. 179, pp. 300-314, 2012. <https://doi.org/10.1016/j.geomorph.2012.08.021>
- [11] Triggs, B., Zisserman, A., and Szeliski, R., "Bundle adjustment. A modern synthesis, Vision Algorithms: Theory and Practice.," in *Proceedings of International Workshop on Vision Algorithms, September 1999*, Springer-Verlag, 2000. <https://doi.org/10.1007/3-540-44480-7>
- [12] MathWorks, "K-means clustering based image segmentation (imsegkmeans)," 2018. [Online]. Available: <https://au.mathworks.com/help/images/ref/imsegkmeans.html>. [Accessed 2020].
- [13] Ma, Y., Wong, L., Vien, B., Kuen, T., Kodikara, J., and Chiu, W.K., "Quasi-active thermal imaging of Large Floating covers using ambient solar energy," *Remote Sensing*, vol. 12, p. 3455, 2020. <https://doi.org/10.3390/rs12203455>

## Quasi-Active Thermography for Structural Health Assessment of Large Geomembranes

Yue Ma<sup>1,a,\*</sup>, Leslie Wong<sup>1,b</sup>, Benjamin Steven Vien<sup>1,c</sup>, Thomas Kuen<sup>2,d</sup>,  
Nik Rajic<sup>3,e</sup>, L.R. Francis Rose<sup>3,f</sup>, Jayantha Kodikara<sup>4,g</sup>, and Wing Kong Chiu<sup>1,h</sup>

<sup>1</sup>Department of Mechanical & Aerospace Engineering, Monash University, Clayton, VIC 3008, Australia

<sup>2</sup>Melbourne Water Corporation, 990 La Trobe Street, Docklands, VIC 3008, Australia

<sup>3</sup>Defence Science and Technology Group, 506 Lorimer Street, Fishermans Bend, VIC 3207, Australia

<sup>4</sup>Department of Civil Engineering, Monash University, Clayton, VIC 3008, Australia

<sup>a</sup>yue.ma@monash.edu, <sup>b</sup>Leslie.Wong@monash.edu, <sup>c</sup>ben.vien@monash.edu,

<sup>d</sup>Thomas.Kuen@melbournewater.com.au, <sup>e</sup>Nik.Rajic@dst.defence.gov.au,

<sup>f</sup>Francis.Rose@dst.defence.gov.au, <sup>g</sup>Jayantha.kodikara@monash.edu,

<sup>h</sup>wing.kong.chiu@monash.edu

**Keywords:** Quasi-Active Thermography, Structural Health Monitoring, Geomembrane, Floating Covers, Sewage Treatment Plant

**Abstract.** High density polyethylene (HDPE) geomembranes (approximately 8 hectares each) are employed as floating covers at the wastewater treatment plant of Melbourne Water in Werribee, Australia. The anaerobic lagoons at the plant rely on these HDPE geomembrane floating covers to capture both the biogas and odours. Given the nature of the plant and the harsh environmental conditions, a non-contact inspection method that can cover a vast expanse is the preferred approach for the structural health monitoring and assessment of the cover. This paper presents an exploratory investigation on the use of a quasi-active thermography technique to detect the presence of artificially induced part-through defects on a HDPE geomembrane specimen. The proposed method utilises a naturally occurring heat source (solar radiation) as the thermal stimulus. An infrared thermal camera and a pyranometer were used to record the thermal responses of the HDPE material as a result of solar intensity variation. The viability of using periodic cloud cover transients to drive this inspection technique is reported. In addition, an image processing algorithm is formulated based on the relative summation of the transient events to enhance the identification of the defects. The findings show that the observed thermal transients can be used to define the presence of defects both when the underside of the material is in contact with water or with air, and thereby provides a promising approach for the structural health monitoring of these high-value assets.

### Introduction

Geomembranes have been widely used in both environmental and mining applications, particularly for landfill liners, as well as floating covers in anaerobic and aerobic reactors in wastewater treatment plants. Raw sewage enters the large covered lagoons at the start of the wastewater treatment process, and biogas is a by-product of the anaerobic digestion process that is the first step in breaking down the untreated sewage. The HDPE membrane covers which float on the sewage in these lagoons play a significant role, (1) in harnessing the biogas for the generation of electricity that powers the entire plant and (2) preventing the odourous and

greenhouse gases from being released to the atmosphere. There are several large floating covers located at Melbourne Water's Western Treatment Plant (WTP) at Werribee, Melbourne, Australia. These floating covers are made out of 2 mm thick high-density polyethylene (HDPE) material and cover an area of 470 m × 170 m (refer to Figure 1). Approximately 65,000 m<sup>3</sup> of biogas per day is harvested from these covers, which is used to generate 7 MW of renewable energy per day [1].



*Figure 1. Aerial view of floating cover in western plant treatment*

Since the raw sewage is untreated when entering the lagoon system, fats, oils, solids or other fibrous materials may eventually be transported to the surface of the lagoon under the cover[2]. This material, known as scum, can expand in spread and depth and become harder over time, potentially developing into a large solid mass that is referred to as a “scumberg” as parts of it may rise above the water surface level even when under the cover. The existence of scumbergs results in the local deformation of the cover, and furthermore, hardened scum may scratch the underside of the geomembrane if it moves and generate part-through defects. These floating covers are valuable assets for the utilities and hence developing an effective structural health monitoring method to evaluate the integrity of these large floating covers is necessary for safe, effective, and efficient operation of the plant. The current evaluation method requires an inspector to walk on these covers and conduct a time-consuming visual inspection. Therefore, a non-contact structural health monitoring (SHM) technology can potentially improve the efficiency and safety of the inspection of these large-scale covers.

This paper introduces a quasi-active thermography technique to detect the presence of part-through defects on the HDPE cover material. The results reported were obtained from a series of experiments conducted on a rooftop that is fully exposed to the prevailing weather conditions. The proposed technique utilises variations in the ambient solar radiation to detect and identify these defects. This approach provides a new quasi-active thermal imaging method to evaluate the structural integrity of large-scale floating structures, as the basis for SHM.

### **Quasi-active thermography**

Thermography, or the use of thermograms, is based on the infrared energy emitted by an object and detected with a thermal camera. Thermographic methods can be classified as either active or passive. Active methods require a thermal stimulus from a power source external to the object. The most commonly used source is an optical lamp which thermally stimulates the surface with either a relatively short heat pulse or a periodic fluctuation of heat. Defects are identified by temperature contrasts arising from differential rates of heating and cooling relative to undamaged regions of the object, which are caused by differences in thermal conductivity or thermal mass. These temperature contrasts can be detected as a variation in infrared (IR) emission from the surface [3].

Omar [3] applied active thermography to evaluate the bond strength and adhesion integrity of a HDPE plastic joint, demonstrating that defects within HDPE can be monitored. Flores-Bolarin [4] applied active thermography to determine the depth of defects in HDPE subjects .

In passive thermography, monitored objects have naturally occurring thermal contrasts which are established via ambient or operational stimuli – e.g. boiler operation [5], and therefore do not require a separate heat source. Both methods have been used to monitor a wide range of structures [6-8], and polymer materials [9, 10].

The size of the floating cover poses several challenges to the application of active thermography. One of them is the requirement to heat the entire structure simultaneously and uniformly. In addition, the use of electronic devices in proximity to the covers is restricted because of the potentially flammable environment associated with the methane-rich biogas produced under the covers. The application of conventional active thermography on structures as large as the floating covers at WTP would require a large amount of thermal energy and time to ensure the uniform flow of the heat flux into the structure and is therefore considered impracticable for use in the real-world of the WTP.

In this paper, a quasi-active thermography method is deployed[11] where natural sunlight is proposed as the heat source for conducting an inspection of these large structures. The radiation from sunlight is considered to be relatively uniformly deposited over the expanse of the covers at WTP. The shading from clouds will temporarily block the solar radiation and will generate a thermal transient on the surface of the geomembrane material. This paper investigates whether variations in cloud-cover can provide transients in timescales that enable the detection of defects in the cover material. The aim of this study is to experimentally investigate the application of quasi-active thermography under laboratory conditions on an exposed rooftop.

In this study, a sample of the HDPE geomembrane material in use at WTP, with artificially induced defects, was supported in a test rig on an exposed roof top. The test membrane had a series of part-through thickness reductions simulating defects. Given that the floating cover can be in direct contact with the raw sewage, and can be separated from the raw sewage by the presence of the biogas, the test membrane was supported on the test rig with parts of the underside of the cover material in contact with water, and the remaining parts in contact with an air gap between the surface of the water and the membrane (to simulate the trapped biogas).

### **Identification of transient event due to cloud movement**

The IR emissivity spectrum of HDPE geomembrane was measured using Fourier-Transform Infrared (FTIR) spectroscopy, which indicated that the HDPE geomembrane is suitable for infrared thermography. The HDPE geomembrane specimen (1 m × 1 m x 2 mm thickness) was clamped onto the aluminium test rig, as shown in Figure 2(a). An Apogee SP-110 pyranometer [12] was installed on the specimen to monitor the irradiation of the specimen surface. An A615 FLIR infrared thermal camera [13] which contains an uncooled Vanadium Oxide detector array of size 640 × 480, was placed beside the geomembrane to record the temperature of the surface of the geomembrane. This equipment setup allows continuous monitoring of the power of solar radiation, through which the transient events due to cloud interference (i.e. shading) can be identified and then correlated with the information obtained from infrared imaging over an extended period of time. The infrared imaging during these transient events is studied in detail.

A preliminary test was first conducted by placing the experimental set up outdoors for 1 hour (see Figure 2(b)) in order to identify the transient event and optimise the resolution and time recording parameters. Both solar intensity and thermal imagery was recorded at a sampling rate of 3 Hz over the test period. Figure 3 shows the solar intensity history measured by the

pyranometer, as well as the temperature variation measured at a point from the thermal imagery, over an observation window of 1 hour. The experiment was conducted on a cloudy day. The pyranometer data showed that the sun was unobstructed by clouds on three occasions during the test period (see Figure 3). During each cloud transition event, associated temperature transients in the membrane are evident. The first event which happened between 12:12:30 and 12:23:20 of the experiment is labelled in Figure 3. The transient event started at 12:12:30 when the pyranometer recorded a change in solar intensity. The temperature transient in the membrane is evident after a few seconds into the cloud-cover event, i.e. the geomembrane temperature increased. According to the pyranometer data, the sun reappeared from the cloud at 12:23:20. A corresponding thermal transient end point was recorded after several seconds into this event (geomembrane temperature increased). Figure 3 suggests that a cloud-cover event can result in a temperature change in the membrane of up to 5° C.



**Figure 2.** (a) HDPE geomembrane specimen (b) Experiment set up of quasi-active thermal imaging

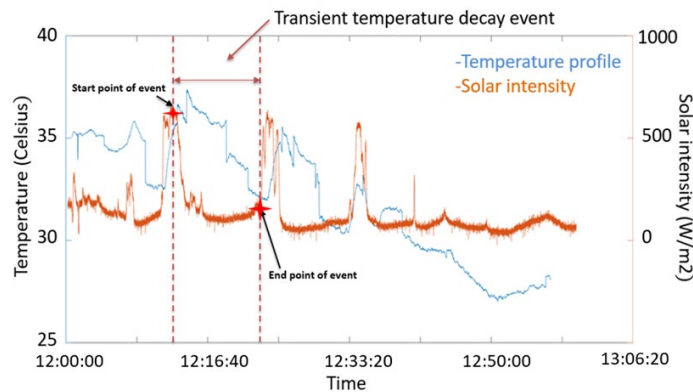


**Figure 3.** Temperature profile on HDPE membrane and solar intensity measured in-situ

### Processing of thermal image

In the above validation investigation, it was shown that the thermal transients of the HDPE geomembrane can be generated by exposure to cloud-cover events. The quality of the raw thermal images in thermography is inevitably degraded due to the background temperature variations at different times in a day, making it difficult to set an appropriate threshold of temperature variation that would indicate the presence of a defect, and the defects are difficult to identify in a single captured thermal image. Therefore, the proposed technique compares the relative temperature changes for a series of thermal images that are recorded at different times during the day. A defect detection algorithm is developed to relate the measured thermal signal (i.e. from the camera) with the radiation signal (i.e. from the pyranometer), and to enhance the

ability to detect the part-through defects on the floating cover. The hypothesis for the algorithm is as follows: clouds will at first provide shade thus reducing solar irradiation of the cover material, thereby initiating a transient event; hence, this will lead to a change in temperature on the surface of the geomembrane. So, to enhance the quality of the thermal image, the following temperature change index  $\Delta T$  is formulated,

$$\Delta T = \sum_{j=1}^m \sum_{i=1}^{n_j} T_{j(i)}(x, y) - T_{j(1)}(x, y) \quad (\text{Eqn. 1})$$

The index  $i$  represents the number of the currently recorded frame in each event, the index  $j$  is the number of cloud shading events in the experiment,  $m$  is the total number of transient events, and  $n_j$  is the total number of frames in the  $j$ th transient event.  $T_{j(i)}(x, y)$  is the temperature in frame  $i$  in event  $j$  at pixel  $(x, y)$  and  $T_{j(1)}(x, y)$  is the temperature in the initial frame in event  $j$  at pixel  $(x, y)$ . It is anticipated and assumed that multiple cloud shading events will occur over the duration of an experiment. This index calculates the sum of temperature changes at every pixel in the infrared image by comparing with the first frame in the corresponding event as defined by the trigger. A threshold signal value in the pyranometer data is used as a trigger to acquire the transients. Transient events are manually selected based on the local maximum solar intensity and local minimum solar intensity. The cooling transient event is set when a cloud shading is detected (corresponding to a decrease in solar intensity).

#### Detection of part-through defects when touching water

At the wastewater treatment plant, it is known that the geomembrane can both be in contact with the liquid sewage underneath and raised from the sewage by pockets of biogas that lift up the cover in other regions. Assuming that defects can be present in regions that are both in contact with liquid sewage or with biogas, this experimental investigation focuses on identifying defects when the underside of the HDPE sample is both on air and on water.

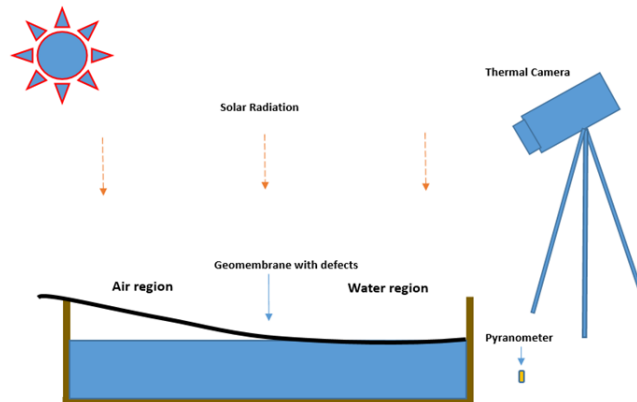


**Figure 4.** Experiment set up of detecting part-through defects on air and on water

As shown in Figure 4, a part of the membrane specimen floats on the water to simulate the liquid sewage region at the treatment plant and the remaining portion has an air gap to simulate the pockets of biogas beneath the floating cover. As shown in Figure 5, a series of part-through defects were created on the underside surface of a  $0.5 \text{ m} \times 1 \text{ m} \times 2 \text{ mm}$  membrane using laser cutting equipment. The dimensions of these defects are shown in Table 1. Defects number 1, 2, 5 and 6 were located in the air region, and defects number 3, 4, 7 and 8 were located in the water region. The experiment was taken outside for 1 hour and exposed to multiple cloud shading

events. Figure 6 shows solar intensity in these regions decreases abruptly and results in thermal transients in the membrane material. As shown in Figure 7 (a), the regions of air and water contact are readily distinguished in the raw thermal image. The higher thermal resistance of air compared with water resulted in a local temperature increase relative to the part of the membrane resting on the water surface. The right section of the test specimen is located over the water region. The heat absorbed in the membrane in this region is transferred efficiently into the water which has a higher specific heat than air, resulting in a lower temperature relative to the left section. Using the raw thermal image only defect number 1 and 2 which have the largest depth and width can be identified, whereas the defects in the water region could not be readily detected.

The temperature variations in thermal imagery corresponding to the transient events were processed using Eqn 1. The results obtained are shown in Figure 7 (b). It can be seen that all the defects can now be clearly identified, and the profiles of defects in the air region are clearer. Defects in the water region can be detected, but due to heat being more easily absorbed by water, the profiles are not as clear as those in the air region. In addition, the profiles of defects 5-8 which have 0.5 mm defect depth are not as clear as the profile of defects 1-4 which have 1 mm defect thickness.

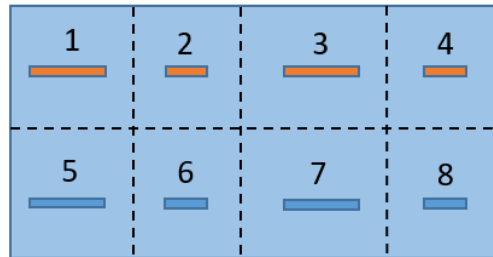


**Figure 5.** HDPE geo-membrane with different dimensions of under surface scratch damage

*Table 1* Details of artificially created damages in each region on the membrane

Defects number	Defect length (cm)	Defect width (cm)	Defect thickness (mm)
1	10	1	1
2	5	1	1
3	10	0.5	1
4	5	0.5	1
5	10	1	0.5
6	5	1	0.5
7	10	0.5	0.5
8	5	0.5	0.5

These results demonstrate that thermography based on naturally occurring transient events can be effectively exploited to capture part-through defects of HDPE materials in contact with air or water. It is also noted that defects on a membrane with an underside in contact with water are harder to detect than those on regions with an underside in contact with air. The results in Figure 7 (b) show that detectability is greatly enhanced by calculating the index presented in Eqn. 1 for defects in contact with air (simulating biogas) or water (simulating liquid sewage).

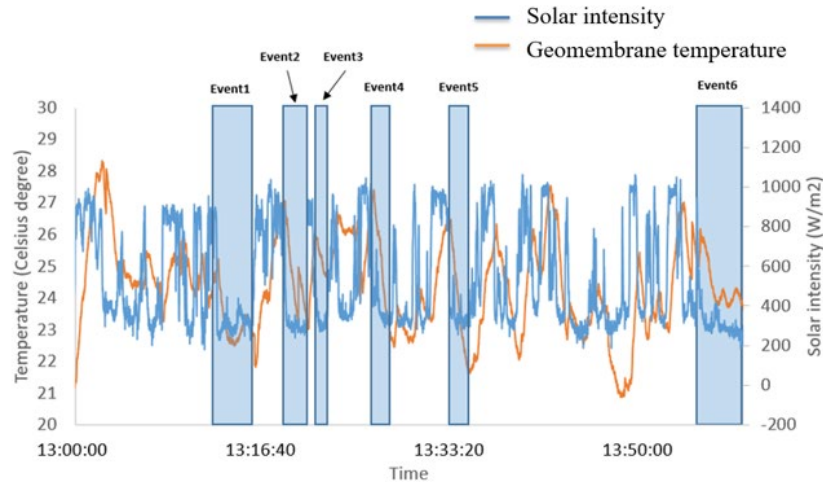


Figure 6. History of temperature evolution and solar intensity with 6 highlighted transient events

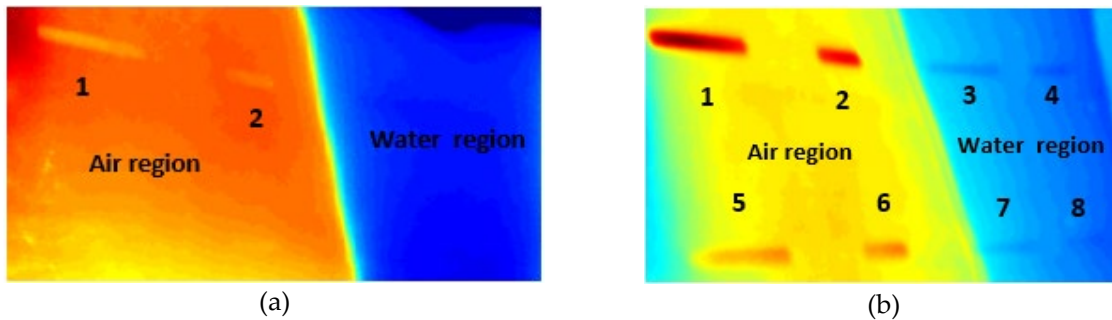


Figure 7. (a) Raw infrared thermal image (b) processed thermal image with Eqn (1)

## Conclusions

This paper reports a quasi-active thermography technique to evaluate the structural health condition of large-scale floating covers in sewage treatment plants. The technique relies on transient temperature decay events caused by variations in solar radiation on the surface of HDPE geomembranes due to variations in cloud cover. Thermal imaging is then possible for defects that induce variations in thermal conductivity or thermal mass of the membrane. An algorithm was devised to aid defect detection using sunlight with transient cloud shading events. From the above experiments, the results and findings indicate that:

- Quasi-active thermography with the aid of naturally occurring solar radiation fluctuations is able to detect part-through defects on the cover. Transient events from cloud cover were suitable for thermal imaging of defects on HDPE geomembranes.
- Thermography can distinguish between membrane regions that are in contact with air relative to water, and part-through defects of different depths in these two regions can be imaged. Defects in air contact regions are easier to detect.

In future work, the quantitative relation between defect thickness and temperature evolution in the material will be investigated, and in-situ verifications carried out. The technologies developed have the potential to provide an economical, real-time and robust method to maintain the structural integrity of large-scale membrane-like structures and extend the service life span of geomembranes in treatment plants, thereby providing a promising approach for SHM of these high-value assets.

## Acknowledgement

The financial support provided by Melbourne Water and Australia Research Council Linkage Grant (ARC LP170100108) is gratefully acknowledged.

## References

- [1] Chiu, W.K., et al., *Large Structures Monitoring Using Unmanned Aerial Vehicles*. 2017. p. 415-423. <https://doi.org/10.1016/j.proeng.2017.04.503>
- [2] Wong, L., et al., Remote Monitoring of Floating Covers Using UAV Photogrammetry. *Remote Sensing*, 2020. 12(7): p. 1118. <https://doi.org/10.3390/rs12071118>
- [3] Omar, M., et al., Infrared thermography for inspecting the adhesion integrity of plastic welded joints. *NDT & E International*, 2006. 39(1): p. 1-7. <https://doi.org/10.1016/j.ndteint.2005.04.008>
- [4] Flores-Bolarin, J. and R. Royo-Pastor. Infrared thermography: A good tool for nondestructive testing of plastic materials. in *Proceedings of the 5th European Thermal-Sciences Conference*, Eindhoven, The Netherlands. 2008.
- [5] Taole, R., R. Falcon, and S. Bada, *The impact of coal quality on the efficiency of a spreader stoker boiler*. *Journal of the Southern African Institute of Mining and Metallurgy*, 2015. 115(12): p. 1159-1165. <https://doi.org/10.17159/2411-9717/2015/V115n12a3>
- [6] Swiderski, W. and D. Szabra. Possibility of defect detection in multi-layered composite materials used for military applications by IR thermography. in *Proc. of the 5th International Workshop on Advances in Signal Processing for Non-Destructive Evaluation of Materials*, Quebec City, Canada. 2005.
- [7] Jorge Aldave, I., et al., *Review of thermal imaging systems in composite defect detection*. *Infrared Physics and Technology*, 2013. 61(C): p. 167-175. <https://doi.org/10.1016/j.infrared.2013.07.009>
- [8] Rajic, N. and S. Galea, Thermoelastic stress analysis and structural health monitoring: an emerging nexus. *Structural Health Monitoring*, 2015. 14(1): p. 57-72. <https://doi.org/10.1177/1475921714548936>
- [9] Steinberger, R., et al., Infrared thermographic techniques for non-destructive damage characterization of carbon fibre reinforced polymers during tensile fatigue testing. *International Journal of Fatigue*, 2006. 28(10): p. 1340-1347. <https://doi.org/10.1016/j.ijfatigue.2006.02.036>
- [10] Kafieh, R., T. Lotfi, and R. Amirfattahi, *Automatic detection of defects on polyethylene pipe welding using thermal infrared imaging*. *Infrared Physics & Technology*, 2011. 54(4): p. 317-325. <https://doi.org/10.1016/j.infrared.2010.12.010>
- [11] Ma, Y., et al., Quasi-Active Thermal Imaging of Large Floating Covers Using Ambient Solar Energy. *Remote Sensing*, 2020. 12(20): p. 19. <https://doi.org/10.3390/rs12203455>
- [12] Apogee, Apogee instruments owner's manual pyranometer models SP-110 and SP-230, Logan, USA, Editor. 2020.
- [13] FLIR, *User's manual FLIR A6xx series*, O. FLIR systems: Wilsonville, United States Editor. 2016.

# Quantitative Monitoring of Osseointegrated Implant Stability Using Vibration Analysis

Shouxun Lu<sup>1,a,\*</sup>, Benjamin Steven Vien<sup>1,b</sup>, Matthias Russ<sup>2,3,c</sup>, Mark Fitzgerald<sup>2,3,d</sup>  
and Wing Kong Chiu<sup>1,e</sup>

<sup>1</sup>Department of Mechanical & Aerospace Engineering, Monash University, Wellington Rd, Clayton Vic 3800, Australia

<sup>2</sup>The Alfred Hospital, 55 Commercial Road, Melbourne Vic 3004, Australia

<sup>3</sup>National Trauma Research Institute, 89 Commercial Road, Melbourne Vic 3004, Australia

<sup>a</sup>shouxun.lu@monash.edu, <sup>b</sup>ben.vien@monash.edu, <sup>c</sup>M.Russ@alfred.org.au,  
<sup>d</sup>M.Fitzgerald@alfred.org.au, <sup>e</sup>wing.kong.chiu@monash.edu

**Keywords:** Osseointegrated Implant, Vibrational Response, Vibration Analysis, Finite Element Modelling

**Abstract.** Reliable and quantitative assessments for the stability of the osseointegrated prostheses are desirable and advantageous in ensuring the success of the installation and long-term performance. However, the common evaluation techniques are qualitative, where their accuracy of which relies on the surgeon's experience. This computational study investigates the potential of using vibrational response to evaluate the stability of the osseointegrated implant using finite element simulation. This paper mainly focuses on the resonance frequency shift and mode shape changes associated with the degree of osseointegration which is simulated by varying bone-implant interface Young's modulus. The resonance frequency of the specific torsional modes increases 211% and 155% for low-frequency (0 to 1800Hz) and high-frequency (1800 to 5000Hz) ranges respectively, as the simulated osseointegration process. Moreover, the torsional mode change from the implant to the femur-implant system is clearly evidenced. The findings highlight the potential application of vibration analysis on the assessment of implant stability.

## Introduction

Osseointegrated implant, of which intramedullary part inserting into the skeletal system directly, provides joint mobility and control of the prosthesis with the sensory feedback from the ground [1-3]. This surgical treatment is developed based on a biological phenomenon, which is known as "osseointegration". Osseointegration is a highly complex and dynamic process, which constructs a direct mechanical connection between bone and biocompatible material gradually [4-6]. This functional structure allows the load transmission through the bone-implant interface. The common material of the osseointegrated implant is a titanium alloy due to its great biocompatibility and high resistance to the repeated load and corrosion [3, 4, 7]. Even though the osseointegrated implant has been described as the preferred surgical treatment for the amputee, the success of the osseointegrated requires relative strict prerequisites such as sufficient primary (mechanical) stability to promote bone regeneration and remodeling [1, 8, 9]. Otherwise, the formation of fibrous tissue at the bone-implant interface will hinder the initial osseointegration [3, 10, 11]. After the accomplishment of primary stability, the osseointegration starts with bone tissue formation at the bone-implant interface. This mechanical structure requires adequate time for rehabilitation to be capable of the full weight of patient [2, 3, 12]. The integrity of this

structure is also known as secondary stability and therefore, the secondary stability is highly related to the state of osseointegration.

The conventional methods used to assess the implant stability such as clinical X-ray, pull-out test and magnetic resonance imaging (MRI) are invasive and subjective where their accuracy is highly dependent on the surgeon's experience [1, 13-16]. Recently, there is a significant research interest in using non-invasive approaches to monitor implant stability. Vibration analysis is a non-destructive structural health monitoring technique, which was firstly used in evaluating bone fracture healing [17-19] and monitoring the total hip arthroplasty loosening [20-23]. The methodology of using the dynamic response of the bone-implant system to assess the stiffness at the bone-implant interface is widely recognized [1, 21, 24]. Recent researches have also shown that the stiffness change at the bone-implant interface was related to the state of osseointegration [20, 24, 25]. Shao. et. al.[1] conducted an experiment on an amputee during his rehabilitation process and their results illustrated a gradually increase in the resonance frequency until the implant is capable of full weight load bearing. Moreover, a previous experimental study on rabbit tibias, implants were installed into different size predrilled cavities to simulate secure-fit and loose-fit connection [26]. Their result demonstrated that the bone-implant system with the loose-fit connection had lower initial resonance frequency compared to those with the secure-fit condition. In addition, the study conducted by Carins et. al.[14, 27] exhibited higher resonance frequencies and that the associated mode shapes are more sensitive to the stiffness change at the bone-implant interface. Similar findings were also reported in [21, 22, 25, 28, 29].

The objective of this paper is to investigate the vibrational response on monitoring the degree of osseointegration at the bone-implant interface via finite element simulation. This vibrational-based approach is based on the detection of the shift in resonance frequency and mode shape change to assess the level of osseointegration.

### Methodology

In the computational analysis, the bone model used in this project was based on an artificial femur model scanned by a structured light 3D scanner. The femur model consists of two parts: the cortical shell and spongy bone (see Fig. 1a). The material of femur-implant model was assumed to be homogeneous and isotropic [30, 31]. The material properties of the femur and implant system [32-34] are described in Table 1. The novel osseointegrated endoprosthesis implant model was developed based on the design concept proposed by Russ et al.[35]. As shown in Figure 1b, the novel implant model consists of two parts: Extramedullary (EM) strut and Intramedullary (IM) stem. The implant model was generated by using the Shell function in the SolidWorks. The contour of the EM strut and IM stem have certain tolerance with the outer surface of the cortical shell and medullary cavity for the application of femur-implant interface layer.

*Table 1: Material properties of the femur and implant system.*

Material	Young's modulus [MPa]	Poisson's Ratio
Cortical shell	17600	0.3
Spongy bone	13000	0.36
Titanium alloy	113800	0.342

A thin layer, which used to simulate the osseointegration, was applied to the femur-implant interface, as illustrated in Fig 2. The layer thickness at EM strut and IM stem surfaces were set to

0.985mm and 0.5mm, respectively. The surfaces of the femur-implant interface layer were bonded with both implant and femur model.

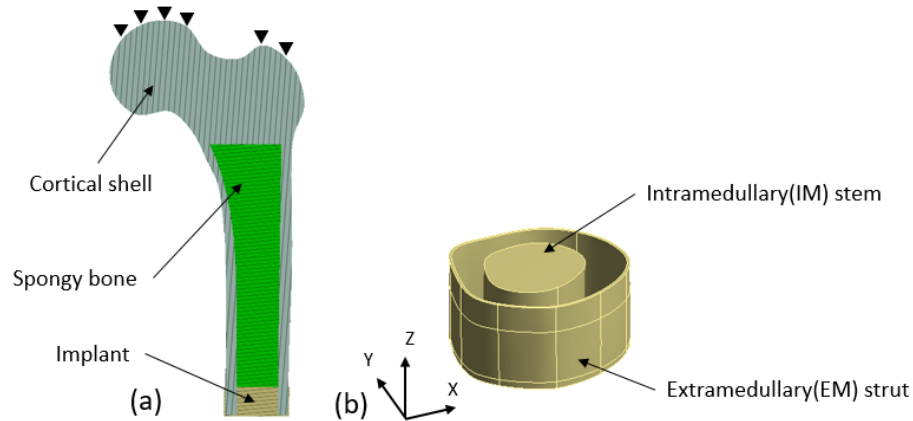


Fig. 1: (a) Cross-section of the computational femur model and (b) Implant.

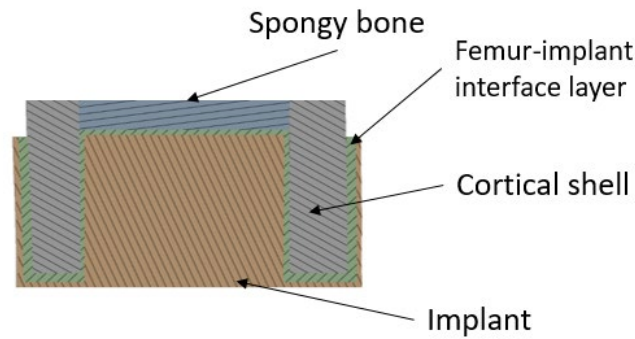


Fig. 2: Cross-section of the femur-implant interface.

ANSYS 19.0 Modal analysis was performed to determine the dynamic response of the femur-implant model. The femur model was fixed at the proximal end to simulate constraints from muscle and pelvis, as illustrated in Fig. 1a. The type of element was set to “Quadratic Tetrahedrons” to avoid stress singularity at sharp corners. The global mesh size was set to 5mm, which was optimized by a mesh convergence test with 5% convergence error for the maximum von Mises stress on the femur. In addition, the mesh around the interface was further refined with a localized body sizing of 1.5mm. The modal analysis mainly focused on the frequency range of 0 to 5000Hz as mentioned in [14, 27].

This computational analysis aims to investigate the resonance frequency shift and mode shape change under various conditions of primary and secondary stability. Hence, as illustrated in Table 2, Young’s modulus ( $E$ ) of femur-implant interface layer was varied from 0.001% to 100% that of the cortical shell ( $E_c$ ) were investigated to simulate the process from 0% osseointegration to fully osseointegrated implant as mentioned in [36]. The method of employing the variation in  $E$ , is similar to the application of adhesive at the femur-implant interface to simulate the process of osseointegration in several experiments mentioned in [17, 37-39].

Table 2: Young's modulus of the layer ( $E$ ) relative to that of cortical shell.

Percentage[% $E_c$ ]	0.001	0.0025	0.005	0.0075	0.01	0.05	0.1	0.5	1	10	100
$E$ [MPa]	0.176	0.44	0.88	1.32	1.76	8.8	17.6	88	176	1760	17600

**Result**

The deformation in y-axis direction along z-axis was shown in Fig. 3. This deformation shows the presence of the torsional mode. The results demonstrated in Fig 3a and 3c, where the implant is not osseointegrated with the femur, shows only the implant responding ( $TI$ ). When the implant is fully osseointegrated, the torsion response of the entire femur-implant system (denoted as  $TS$ ) is recorded (see Fig 3b and 3d).

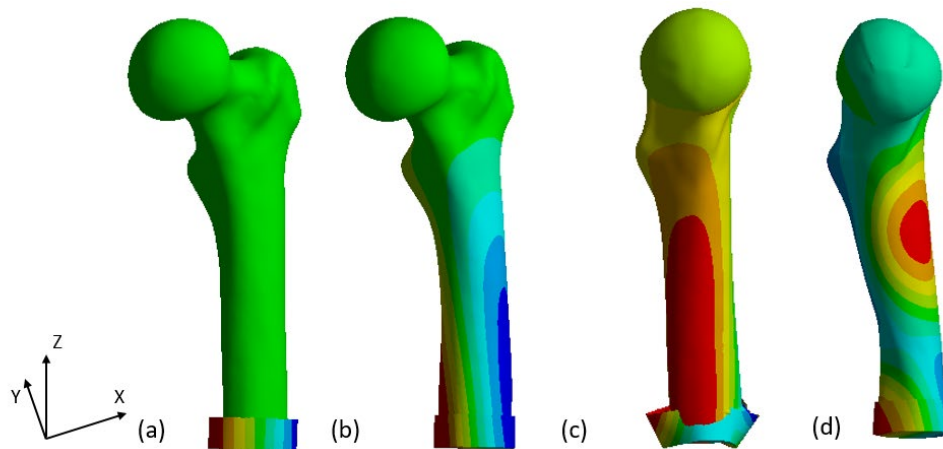


Fig. 3: Low-frequency torsional mode of: (a) implant ( $TI$ ) with 0.001% $E_c$ ; (b) femur-implant system ( $TS$ ) with 100% $E_c$  and high-frequency: (c)  $TI$  with 0.0025% $E_c$ ; (d)  $TS$  with 100% $E_c$ .

Figure 4 demonstrated the variation of the resonance frequency with the simulated osseointegration ( $SO$ ) process in both low-frequency (0 to 1800Hz) and high-frequency (1800 to 5000Hz) ranges. The percentage on the plot indicated that the resonance frequency gradually increased relative to the first torsional frequency, along the  $SO$  process.

In the early stage of  $SO$  process, the change of resonance frequency could be easily identified in both frequency ranges. The resonance frequency of the specific torsional modes increases 211% and 155% for low- and high-frequency ranges respectively, as the  $SO$  process. As illustrated in Fig. 3a, there is a significant increase in the resonance frequency of  $TI$  from 568.45Hz to 1433.2Hz, as  $E$  increased to 0.01%  $E_c$ . Similar smooth variation in resonance frequency was identified in the high-frequency range. This result was in accordance with [1, 22, 28], suggesting that the frequency shift of the system increases along the mode shape complexity increasing. The change of frequency indicated a clear correlation between the  $E$  and resonance frequency in the early stage of  $SO$  and the result agrees with the findings in Cairns et. al. study [14].

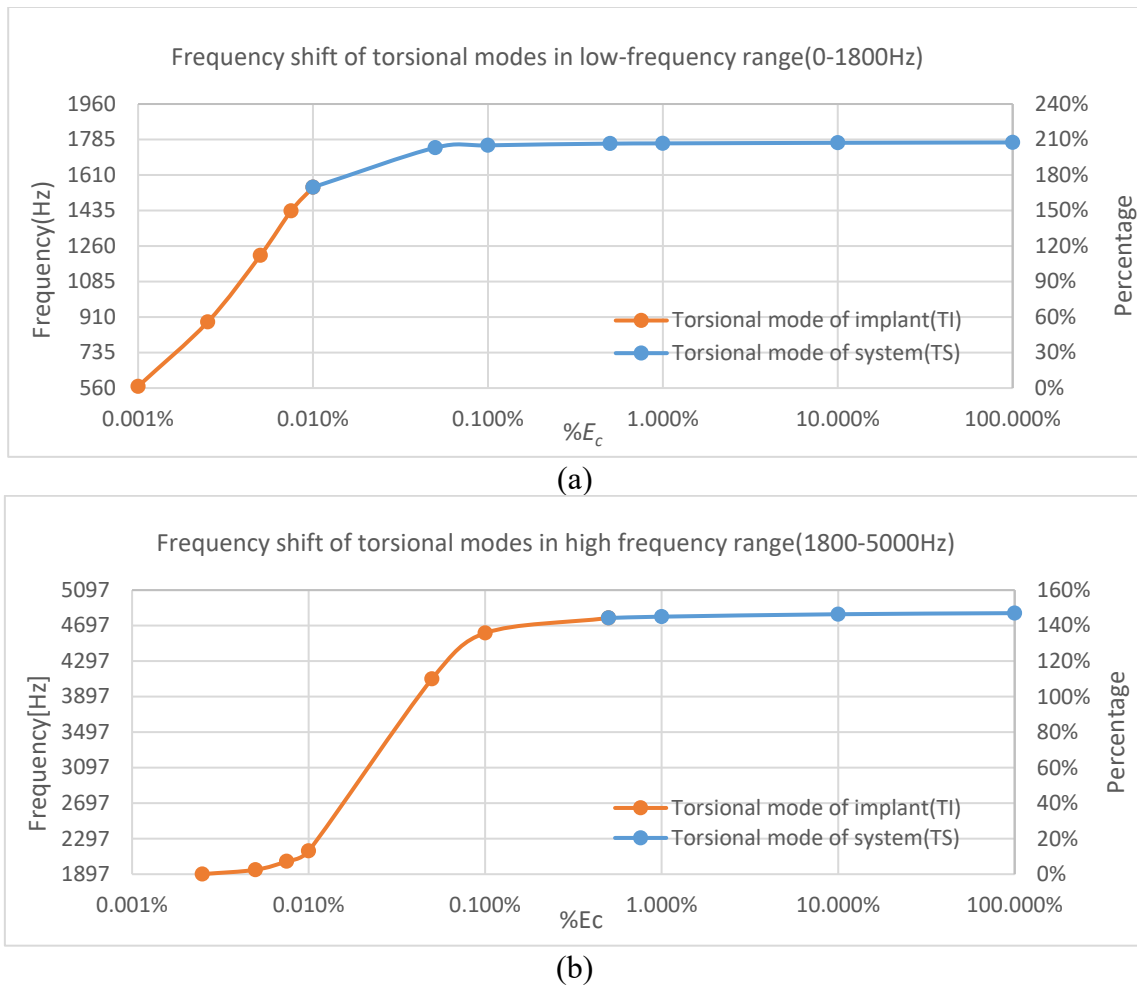


Fig. 4: Frequency shift of torsional modes in frequency range: (a) 0-1800Hz; (b) 1800-5000Hz.

Moreover, the mode located at 568.45Hz was observed to initially vibrate as implant torsional mode *TI* and then migrated to system torsional mode *TS* at 1770.6Hz, with the process of *SO*. The transformation, from the significant vibration at implant to torsional mode of the femur-implant system, was apparent in high-frequency range as well. However, beyond 1%  $E_c$ , the frequency shift caused by the change of  $E$  was negligible for both low- and high-frequency ranges after the mode shape change.

Even though the sensitivity of this method was constrained in the relative small  $E$  value, this variation in frequency and mode shape were significant, suggesting that monitoring the resonance frequency and mode shape change could aid in early detection of insufficient stability, thereby decreases the likelihood of failure in osseointegration.

### Conclusion

This paper reveals the preliminary concept that monitoring the primary and secondary stability of the femur treated with novel implant design could be evaluated with the dynamic response of vibration. The finite element investigation has demonstrated that the resonance frequency increased gradually along the *SO* process. The result has also demonstrated the significant shift in resonance frequency, 211% and 155% for low- and high-frequency ranges respectively, indicating the potential of vibration analysis on the quantitative evaluation of the implant

stability at the early stage of osseointegration. Furthermore, the identification of mode shape change enhanced the evaluation of stimulated osseointegration process. Future work is currently in progress to investigate this vibrational analysis method on various length of residual femur.

### **Funding**

This research is funded by US Navy Office of Naval Research (N00014-18-1-2336). The financial supported provided by the Office of Naval Research is gratefully acknowledged.

### **Conflict of Interest**

The author declares that there is no conflict of interest regarding the publication of this paper.

### **Ethical approval**

This article does not contain any studies with human participants or animals performed by any of the authors.

### **References**

- [1] Shao, F., et al., *Natural frequency analysis of osseointegration for trans-femoral implant*. Ann Biomed Eng, 2007. 35(5): p. 817-24. <https://doi.org/10.1007/s10439-007-9276-z>
- [2] Hagberg, K., et al., Osseoperception and osseointegrated prosthetic limbs, in Psychoprosthetics. 2008, Springer. p. 131-140. [https://doi.org/10.1007/978-1-84628-980-4\\_10](https://doi.org/10.1007/978-1-84628-980-4_10)
- [3] Ward, D. and K. Robinson, *Osseointegration for the skeletal fixation of limb prostheses in amputations at the trans-femoral level*. The osseointegration book: From calvarium to calcaneus. Berlin (Germany): Quintessence, 2005: p. 463-76.
- [4] Isaacson, B.M. and S. Jeyapalina, *Osseointegration: a review of the fundamentals for assuring cementless skeletal fixation*. Orthopedic Research and reviews, 2014. 6: p. 55-65. <https://doi.org/10.2147/ORR.S59274>
- [5] Brånemark, R., et al., *Osseointegration in skeletal reconstruction and rehabilitation: a review*. Journal of rehabilitation research and development, 2001. 38(2): p. 175.
- [6] Morelli, F., et al., Influence of bone marrow on osseointegration in long bones: an experimental study in sheep. Clinical oral implants research, 2015. 26(3): p. 300-306. <https://doi.org/10.1111/clr.12487>
- [7] Agarwal, R. and A.J. García, Biomaterial strategies for engineering implants for enhanced osseointegration and bone repair. Advanced Drug Delivery Reviews, 2015. 94. <https://doi.org/10.1016/j.addr.2015.03.013>
- [8] Lu, S., et al., Non-radiative healing assessment techniques for fractured long bones and osseointegrated implant. Biomedical engineering letters, 2020. 10(1): p. 63-81. <https://doi.org/10.1007/s13534-019-00120-0>
- [9] Vien, B.S., et al., A stress wave-based health monitoring concept on a novel osseointegrated endoprosthesis design. 2018.
- [10] Østbyhaug, P.O., et al., Primary stability of custom and anatomical uncemented femoral stems: A method for three-dimensional in vitro measurement of implant stability. Clinical Biomechanics, 2010. 25(4): p. 318-324. <https://doi.org/10.1016/j.clinbiomech.2009.12.012>
- [11] Lioubavina-Hack, N., N.P. Lang, and T. Karring, *Significance of primary stability for osseointegration of dental implants*. Clinical Oral Implants Research, 2006. 17(3): p. 244-250. <https://doi.org/10.1111/j.1600-0501.2005.01201.x>

- [12] Thesleff, A., B. Håkansson, and M. Ortiz-Catalan, Biomechanical Characterisation of Bone-anchored Implant Systems for Amputation Limb Prostheses: A Systematic Review. *Annals of Biomedical Engineering*, 2018. 46(3): p. 377-391. <https://doi.org/10.1007/s10439-017-1976-4>
- [13] Vayron, R., et al., *Ultrasonic evaluation of dental implant osseointegration*. *Journal of Biomechanics*, 2014. 47(14): p. 3562-3568. <https://doi.org/10.1016/j.jbiomech.2014.07.011>
- [14] Cairns, N.J., et al., *Evaluation of modal analysis techniques using physical models to detect osseointegration of implants in transfemoral amputees*. Conference proceedings: ... Annual International Conference of the IEEE Engineering in Medicine and Biology Society. IEEE Engineering in Medicine and Biology Society. Conference, 2011: p. 1600-1603. <https://doi.org/10.1109/IEMBS.2011.6090463>
- [15] Dhert, W., et al., *A finite element analysis of the push-out test: Influence of test conditions*. *Journal of Biomedical Materials Research Part A*, 1992. 26(1): p. 119-130. <https://doi.org/10.1002/jbm.820260111>
- [16] Johansson, C.B., L. Sennerby, and T. Albrektsson, A removal torque and histomorphometric study of bone tissue reactions to commercially pure titanium and Vitallium implants. *International Journal of Oral & Maxillofacial Implants*, 1991. 6(4).
- [17] Chiu, W.K., et al., *Vibration-based healing assessment of an internally fixated femur*. *Journal of Nondestructive Evaluation, Diagnostics and Prognostics of Engineering Systems*, 2019. 2(2): p. 021003. <https://doi.org/10.1115/1.4043276>
- [18] Chiu, W.K., et al., Towards a Non-Invasive Technique for Healing Assessment of Internally Fixated Femur. *Sensors*, 2019. 19(4): p. 857. <https://doi.org/10.3390/s19040857>
- [19] Chiu, W., et al., *Effects of mass loading on the viability of assessing the state of healing of a fixated fractured long bone*. *Journal of Rehabilitation and Assistive Technologies Engineering*, 2019. 6: p. 2055668319842806. <https://doi.org/10.1177/2055668319842806>
- [20] Li, P., N. Jones, and P. Gregg, *Vibration analysis in the detection of total hip prosthetic loosening*. *Medical engineering & physics*, 1996. 18(7): p. 596-600. [https://doi.org/10.1016/1350-4533\(96\)00004-5](https://doi.org/10.1016/1350-4533(96)00004-5)
- [21] Varini, E., et al., Assessment of implant stability of cementless hip prostheses through the frequency response function of the stem–bone system. *Sensors and Actuators A: Physical*, 2010. 163(2): p. 526-532. <https://doi.org/10.1016/j.sna.2010.08.029>
- [22] Jacques, S.V., C. Pastrav, and G. Van der Perre. Analysis of the fixation quality of total hip replacements using a vibrational technique. in *ASME 7th Biennial Conference on Engineering Systems Design and Analysis*. 2004. American Society of Mechanical Engineers. <https://doi.org/10.1115/ESDA2004-58581>
- [23] Alshuhri, A.A., et al., Development of a non-invasive diagnostic technique for acetabular component loosening in total hip replacements. *Med Eng Phys*, 2015. 37(8): p. 739-45. <https://doi.org/10.1016/j.medengphy.2015.05.012>
- [24] Bediz, B., H.N. Özgüven, and F. Korkusuz, *Vibration measurements predict the mechanical properties of human tibia*. *Clinical biomechanics*, 2010. 25(4): p. 365-371. <https://doi.org/10.1016/j.clinbiomech.2010.01.002>
- [25] Jacques, S., et al., *Vibration analysis of orthopaedic implant stability: exploratory finite element modelling*. *Proceedings of the Belgian Day on Biomedical engineering*, 2002.

- [26] Huang, H.M., et al., *Early detection of implant healing process using resonance frequency analysis*. Clinical oral implants research, 2003. 14(4): p. 437-443. <https://doi.org/10.1034/j.1600-0501.2003.00818.x>
- [27] Cairns, N.J., et al., Ability of modal analysis to detect osseointegration of implants in transfemoral amputees: a physical model study. Med Biol Eng Comput, 2013. 51(1-2): p. 39-47. <https://doi.org/10.1007/s11517-012-0962-0>
- [28] Qi, G., W.P. Mouchon, and T.E. Tan, *How much can a vibrational diagnostic tool reveal in total hip arthroplasty loosening?* Clinical Biomechanics, 2003. 18(5): p. 444-458. [https://doi.org/10.1016/S0268-0033\(03\)00051-2](https://doi.org/10.1016/S0268-0033(03)00051-2)
- [29] Rieger, J.S., et al., Loosening detection of the femoral component of hip prostheses with extracorporeal shockwaves: a pilot study. Med Eng Phys, 2015. 37(2): p. 157-64. <https://doi.org/10.1016/j.medengphy.2014.11.011>
- [30] Dong, Y., et al., Finite Element Analysis of Absorbable Sheath to Prevent Stress Shielding of Tibial Interlocking Intramedullary Nail. IOP Conference Series: Materials Science and Engineering, 2017. 224. <https://doi.org/10.1088/1757-899X/224/1/012052>
- [31] Helgason, B., et al., Risk of failure during gait for direct skeletal attachment of a femoral prosthesis: a finite element study. Medical engineering & physics, 2009. 31(5): p. 595-600. <https://doi.org/10.1016/j.medengphy.2008.11.015>
- [32] Pal, S., Design of artificial human joints & organs. 2014: Springer. <https://doi.org/10.1007/978-1-4614-6255-2>
- [33] Oftadeh, R., et al., *Biomechanics and mechanobiology of trabecular bone: a review*. Journal of biomechanical engineering, 2015. 137(1). <https://doi.org/10.1115/1.4029176>
- [34] Dalstra, M., et al., *Mechanical and textural properties of pelvic trabecular bone*. Journal of biomechanics, 1993. 26(4-5): p. 523-535. [https://doi.org/10.1016/0021-9290\(93\)90014-6](https://doi.org/10.1016/0021-9290(93)90014-6)
- [35] RUSS, M., et al., Development of a Novel Osseointegrated Endoprosthesis, Combing Orthopaedic and Engineering Design Principles, and Structural Health Monitoring Conc. Structural Health Monitoring 2017, 2017(shm). <https://doi.org/10.12783/shm2017/14244>
- [36] Wang, W. and J.P. Lynch, IWSHM 2017: Application of guided wave methods to quantitatively assess healing in osseointegrated prostheses. Structural Health Monitoring, 2018. 17(6): p. 1377-1392. <https://doi.org/10.1177/1475921718782399>
- [37] Vien, B.S., et al., A Quantitative Approach for the Bone-implant Osseointegration Assessment Based on Ultrasonic Elastic Guided Waves. Sensors, 2019. 19(3). <https://doi.org/10.3390/s19030454>
- [38] Chiu, W.K., et al., *Healing assessment of fractured femur treated with an intramedullary nail*. Structural Health Monitoring, 2019: p. 1475921718816781. <https://doi.org/10.1177/1475921718816781>
- [39] Claes, L.E. and J.L. Cunningham, *Monitoring the mechanical properties of healing bone*. Clin Orthop Relat Res, 2009. 467(8): p. 1964-71. <https://doi.org/10.1007/s11999-009-0752-7>

# Acoustic Emission of Metallic Specimen with Surface Defect During Fatigue Crack Growth

X. Yao<sup>1,a\*</sup>, B.S. Vien<sup>1,b</sup>, N. Rajic<sup>2,c</sup>, L.R.F. Rose<sup>2,d</sup>, C.H.J. Davies<sup>1,e</sup>,  
W.K. Chiu<sup>1,f</sup>

<sup>1</sup> Department of Mechanical and Aerospace Engineering, Monash University, Wellington Rd, Clayton, VIC 3800, Australia

<sup>2</sup> Defence Science and Technology Group, 506 Lorimer Street, Fisherman's Bend, VIC 3207, Australia

<sup>a</sup>Xinyue.Yao@monash.edu, <sup>b</sup>ben.vien@monash.edu, <sup>c</sup>Nik.Rajic@dst.defence.gov.au,

<sup>d</sup>Francis.Rose@dst.defence.gov.au, <sup>e</sup>Chris.Davies@monash.edu,

<sup>f</sup>Wing.Kong.Chiu@monash.edu

**Keywords:** Acoustic Emission, Fatigue Crack, Wave Propagation, Lamb Wave

**Abstract.** Acoustic emission is defined as the phenomena whereby transient elastic waves are generated by the rapid release of localized sources within a material. During fatigue crack growth, the formation of new crack surfaces is associated with a sudden release of energy, which constitutes acoustic sources for acoustic emission. This paper investigates the acoustic emission signature arising from fatigue test of a metallic specimen under tensile fatigue test. In this experimental study, dog-bone aluminium alloy specimen with a surface defect was fatigued to failure. It is found that the acoustic emission characteristics are different during the propagation of surface crack, because the source is changing. The results provide a useful guide in identifying source origin based on the characteristics of the acoustic emission waveform.

## Introduction

Aluminium alloys have been used in aerospace since the 1920s. The strength, hardness, and corrosion resistance of aluminium alloys increased dramatically as the aerospace industry developed. Although composite materials have been employed over recent decades, aluminium alloys are still widely used and contribute to over 50% of the total weight of an aircraft [1]. It is known that aluminium alloys are susceptible to fatigue damage and there has been a significant amount of research towards the development of structural health monitoring methodologies to detect and monitor the onset of fatigue damage and the eventual fatigue crack growth [2-5].

The advanced non-destructive testing methods for metal material include near-infrared cameras (NIR), laser ultrasonics, and X-ray computed tomography [6-8]. Although these methods can reveal the defect by image clearly, there is still a need for a non-destructive method which has the potential to reveal the fatigue failure stages. In-situ acoustic emission (AE) testing is a widely used non-destructive testing approach for locating and classifying defects in rock, concrete, composite, and metal [9-14]. It is a real-time monitoring method of efficiency and high-performance and is used in monitoring equipment under active stress or machining processes [15-17]. According to previous research, AE has the potential to predict the stages of crack propagation during operation [4, 5, 18-20]. Thus, the AE method has a real and significant application in real-time structural health monitoring. When using AE to monitor fatigue crack growth, the possible AE sources include the formation of a new fracture surface and the rubbing or clapping of interface crack surface [21, 22].

The transient wave in an AE signal is called hit, and it is usually understood as “an isolated and separated” waveform [23]. Previous studies on AE were focusing on hit-related information during fatigue tests, including the relationship between count rate and material rolling direction [24], and the relationship between count number on fatigue cycle and crack propagation rate [5]. Nevertheless, recent works on AE have focused on waveform pattern analysis and highlighted the importance of studying AE waveform [25, 26], because it could provide more information than only analysing hit-related characteristics. It is found that AE signals of aluminium alloys 7075-T6 have peak frequencies around 100 kHz, 260 kHz and 600 kHz [20]. Other research also found different frequency peaks of low carbon steel [26] or aluminium alloy 2024 T3 [27]. Studies on AE waveforms are often challenging because the amplitude and frequency of AE waveforms can vary significantly. Sause and Hamstad stated that the frequency characteristics could be relatively irrelevant in some cases, because the AE sensors were of variety and could affect collected frequency [28]. For example, some sensors may provide more information on frequency than others [25]. Therefore, it is important to have a more comprehensive rule to cluster AE hits, so wave modes identification becomes very important.

The elastic waves excited by AE signal in a thin plate-like structure are Lamb waves, which have symmetric modes and asymmetric modes. The most frequently discussed modes include zero-order asymmetric mode (A0), zero-order symmetric mode (S0), and first-order asymmetric mode (A1). The group velocities for distinct wave modes vary with frequency due to its dispersive nature and can be used in identifying wave modes. The most frequently used AE sensors are piezoelectric wafer active sensors and typically are threshold-based sensors that only record AE signals which exceed the set threshold level to discard possible background noise [26]. Unlike the active wave sensing approach, where guided waves are excited by a transmitter sensor [29], AE is a passive monitoring approach that listens for waves generated by rapid energy released from the structures themselves. Making use of this phenomenon, by aligning the theoretical dispersion curve with the wavelet transform, certain wave modes can be identified [30]. The influence of the source location in the thickness direction to AE wave modes has been investigated by some researchers for plate-like structure. Hamstad [31] showed that the PLB source location in the thickness direction of plate affects the generated wave modes: the in-plane PLB signal near top of the edge has only A0 mode, and that near mid-plane has both A0 and S0 modes. Yu et al. [32] differentiated the delaminations and transverse cracks of composites by A0/S0 mode amplitude ratio. They also conducted an FEA of a thin plate with monopole input source, and results indicated that as the source location moved closer to the surface from the mid-plane, the ratio of A0 and A1 modes increased, and that of S0 decreased. As a result, wave mode decomposition results have the ability to indicate source locations and source origins.

This paper presents a set of findings in using AE to monitor the fatigue crack development in an aluminium plate-like specimen. In describing the formation of new fatigue crack surface as a source of acoustic emission, the paper reports on the differences in the stress wave generated by propagating radial crack front.

## Methods

*Experimental method.* The samples tested were dog-bone specimens with gauge width 40mm of and thickness of 3mm (Fig. 1a) made from aluminium alloy 6060 (Al6060) and its material properties are shown in Table 1. It has a thin surface defect (2mm length, around 0.5mm width, and 0.5mm depth) in the centre of the specimen (shown in Fig. 1b). The defect was first drilled with a 0.5 mm diameter drill for 0.5 mm depth in the middle, and then a 2 mm length 0.5 mm

depth line crack was engraved over it. The artificial defect was intended to cause stress concentration and initialise the fatigue fracture.

Table 1: Al6060 specimen with through-thickness defect material properties.

<b>Young's Modulus</b>	<b>68 GPa</b>
<b>Poisson's Ratio</b>	<b>0.33</b>
<b>Density</b>	<b>2.7 g/cm<sup>3</sup></b>
<b>Tested yield stress</b>	<b>100 MPa</b>
<b>Tested ultimate stress</b>	<b>150 MPa</b>

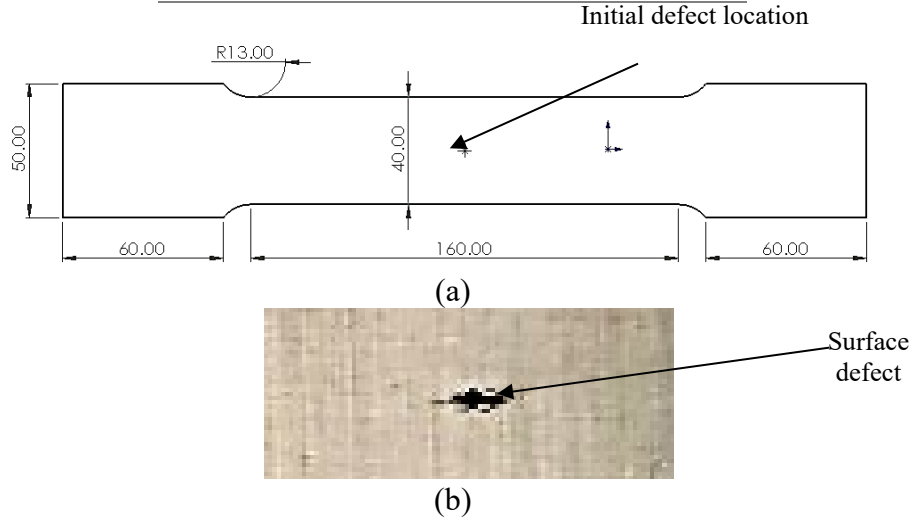


Figure 1. (a) Dimension of samples. (b) Surface defect.

The specimens were fatigue tested using MTS machine Model 647. The specimens were tested cyclically from 43MPa to 74MPa until failure with R ratio 0.58. The fatigue cycling was paused when significant hits were recorded so that the fatigue fracture can be observed, and the AE waveform and the corresponding fatigue cycle were analysed afterwards.

The Physical Acoustic Corporation acoustic emission sensors and recording system were used in the experiments. Two wideband PKWDI sensors detected from 200kHz to 850kHz were used, and they were connected to a two-channel Micro Structural Health Monitoring, with a 26 dB build-in pre-amplifier. The centres of the sensors are both 20 mm away from the defect.

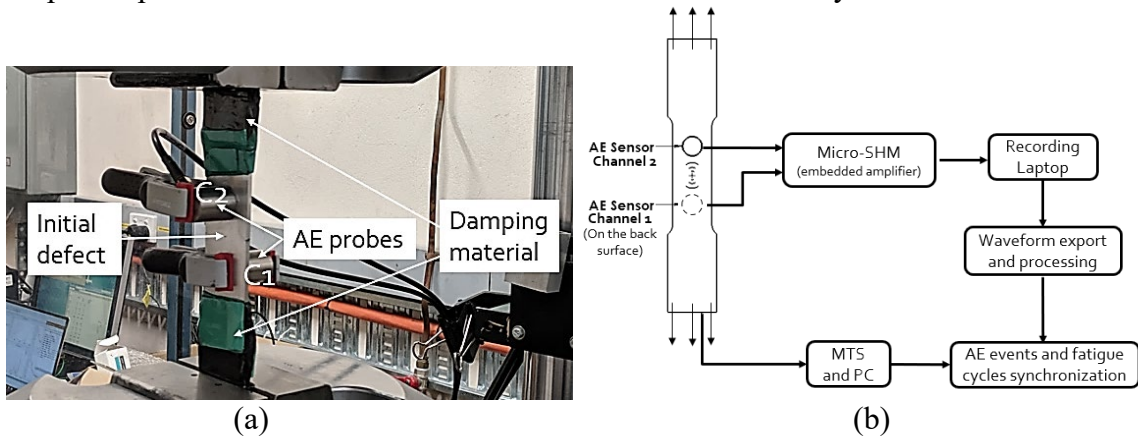


Figure 2. (a) Photo of the experimental set-up. (b) Illustration of equipment set-up.

The threshold setting of the acoustic emission equipment was done using a widely accepted artificial simulating source for acoustic emission, which was Hsu-Nielsen source, or also called pencil lead break (PLB) source [33]. In order to mitigate the test specimen from the noise generated by the MTS machine, the regions of the test specimen in the vicinity of the grips were treated with a damping layer (MegaSorber type DIS8) [34]. The damping sheets were cut into small pieces and carefully attached on both ends of the specimen, and the threshold setting was adjusted accordingly. Because the specimen was not symmetric, Channel 1 (C1) was placed on the non-defect side, and Channel 2 (C2) was placed on the initial surface defect side (see Fig. 2a).

## Results and discussions

*Hit-related Feature Discussion.* The hits were applied a high pass 60 kHz filter first to eliminate the low frequency vibration noise. The valid AE source from the defect should be from the area around the initial crack, which is in the middle of two sensors. Thus, the AE events of two channels were synchronized using the waveform event synchronization function in the AE-win software, where the hits were synchronized according to the time of collection. The event definition time was set as 50  $\mu$ s to allow some error. Thus, the AE hits collected by only one of the sensors was discarded.

The fatigue crack fracture surface of the specimen is shown in Fig. 3. The crack propagated radially from the initial surface defect until the other surface and then progressed to the edge of the specimen.

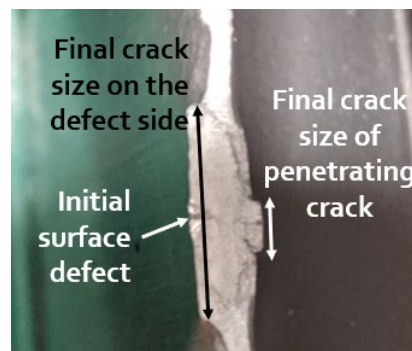


Figure 3. Final crack surface after fatigue test till to failure.

In Fig. 4a, the hit number increases slightly at the beginning of the test when the specimen was still settling, and the number almost keeps identical until a rapid increase in the last 10,000 cycles before failure. The majority of the events happened during the last 10,000 cycles of total 191341 cycles. In Fig. 4b, there are large-amplitude hits at the end of the test due to the specimen broke into two pieces, while the amplitudes of other hits are very consistently between 0 and 0.011 volts. It can be seen that the amplitude between hit 1000 to hit 3000 has a relatively constant amplitude between 0.007 volts and 0.01 volts, while from hit 4000 to hit 5700, the amplitudes are alternating between two values that have a relatively big difference: around 0.003 volts and around 0.007 volts. This will be discussed more in the next section with the time difference between two hits together.

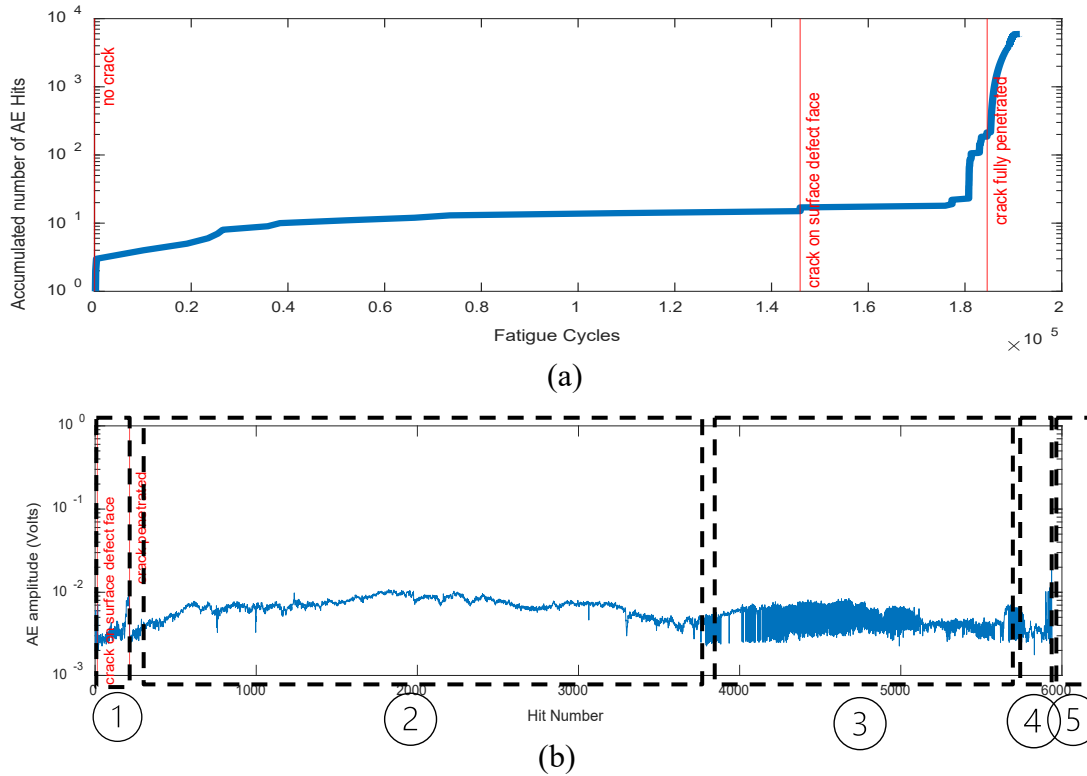


Figure 4. (a) Number of AE hits vs fatigue cycles. (b) Amplitude of each hit during test.

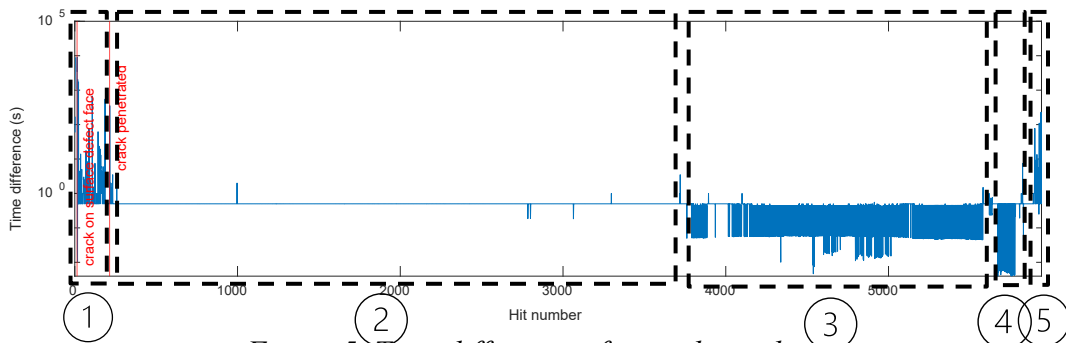


Figure 5. Time difference of two adjunct hits.

*Source and Waveform Discussion.* The hits were divided into 5 periods according to the time difference between the current signal and its adjacent previous hit, shown in Fig. 5. In addition, the Fast Fourier Transformation (FFT) of each hit from both channels are illustrated in Fig. 6. The description details of each period are written in Fig. 7 column 1. In period 1, the time difference shown in Fig. 5 is random. when there was crack seen on only one side of the specimen, the FFT diagram of C1 and C2 shows 260 kHz are dominant. In period 2, the time differences are consistently 0.5s. When the fatigue crack penetrated through the surface to the opposite side of the initial defect, the dominant frequency of 260 kHz and around 600kHz is getting more obvious. In period 3, the time difference in Fig. 5 alternates between 0.05 and 0.44s, and that of period 4 alternates between 0.005 and 0.5s. In period 5, the time difference becomes random again as period 1. In addition, the time takes for another hit to arrive of period 1 and 5 are obviously longer than period 2 to 4. It is also worth noting that from period 2 to 4 when the crack is propagating, the time difference is regular: for period 2, it is one hit per cycle

because the load frequency is 2Hz; for period 3 and 4, there are two hits per loading cycle. Relating to the amplitude diagram, in period 2, when the time difference is consistent, the amplitude is relatively consistent as well. In period 3 and 4, when the time difference is close to 0 seconds, the amplitude is around 0.003 volts; when the time difference is around 0.5 seconds, the amplitude is about 0.007 volts.

In Bhuiyan and Giurgiutiu' study [27], they clustered the AE hits according to the frequency characteristics, and it was found that for some clustered groups, the frequency characteristics of hits collected, amplitudes of hits and the fatigue load level that the hit happens are almost identical for each hit. The results in this paper is similar to their findings about the consistency between hit signatures and fatigue cycles. However, they did not present the hit over the whole fatigue process. In this paper, it is found that this consistency is true during the whole fatigue test after crack arise. In addition, their specimen is a symmetric specimen with a through-hole, while this paper shows that the asymmetric specimen with surface defect also have similar results. Unfortunately, this paper did not synchronise hit with load level as accurate as their work.

The regular hit arising time in Fig. 5 indicates that the possible source origin could be from the opening and closing of the crack, or crack extension itself. In [35], It is found that the hits from crack extensions or inclusion fractures happened when maximum load is applied, and only take up to 10 % of the total AE activity. The load is not synchronised in this paper, so for future work, synchronisation with the fatigue load would be considered to identify hits from crack extensions.

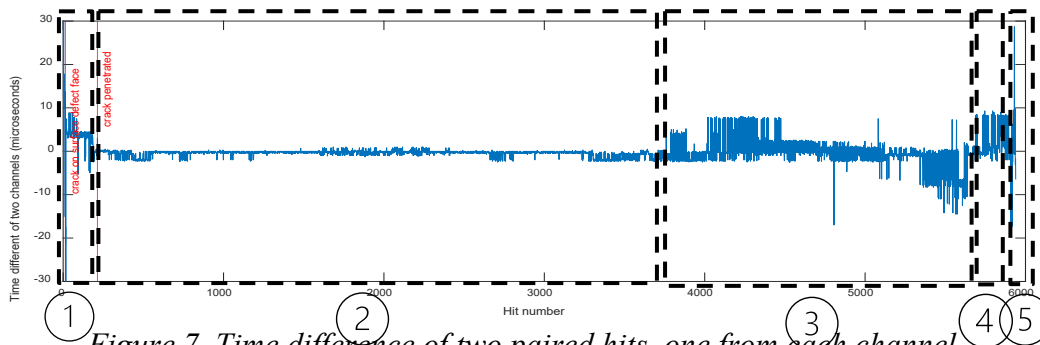


Figure 7. Time difference of two paired hits, one from each channel.

Refer to Fig. 7, most of the values of the time difference between two paired hits are within 8  $\mu$ s, so this means that the source location is within the middle area of two sensors. In period 2, generally, the time arriving difference is very small and relatively consistent. From this phenomenon, it can be speculated that these hits are from one same source in the middle, and because it is happening once per fatigue cycle after crack just penetrated, it is highly likely to be caused by closure/friction of the crack surface. In period 3 and 4, the source in period 2 is still there, but there exists one more source that is happening very close to the previous one ( $\Delta t$  is 0.05s or 0.005s). This new source is highly likely from the separation of stuck crack faces [35]. The reasons why this source did not arise in period 2 is that, in period 2, the defect has just penetrated and has only the crack labelled 1 (see Fig. 8), while in the later fatigue stage, crack labelled 2 arose and it is more likely to cause AE activity when separating because of the saw shape [27].

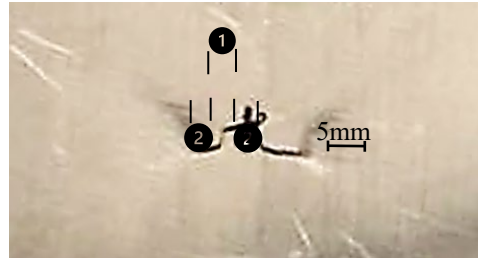
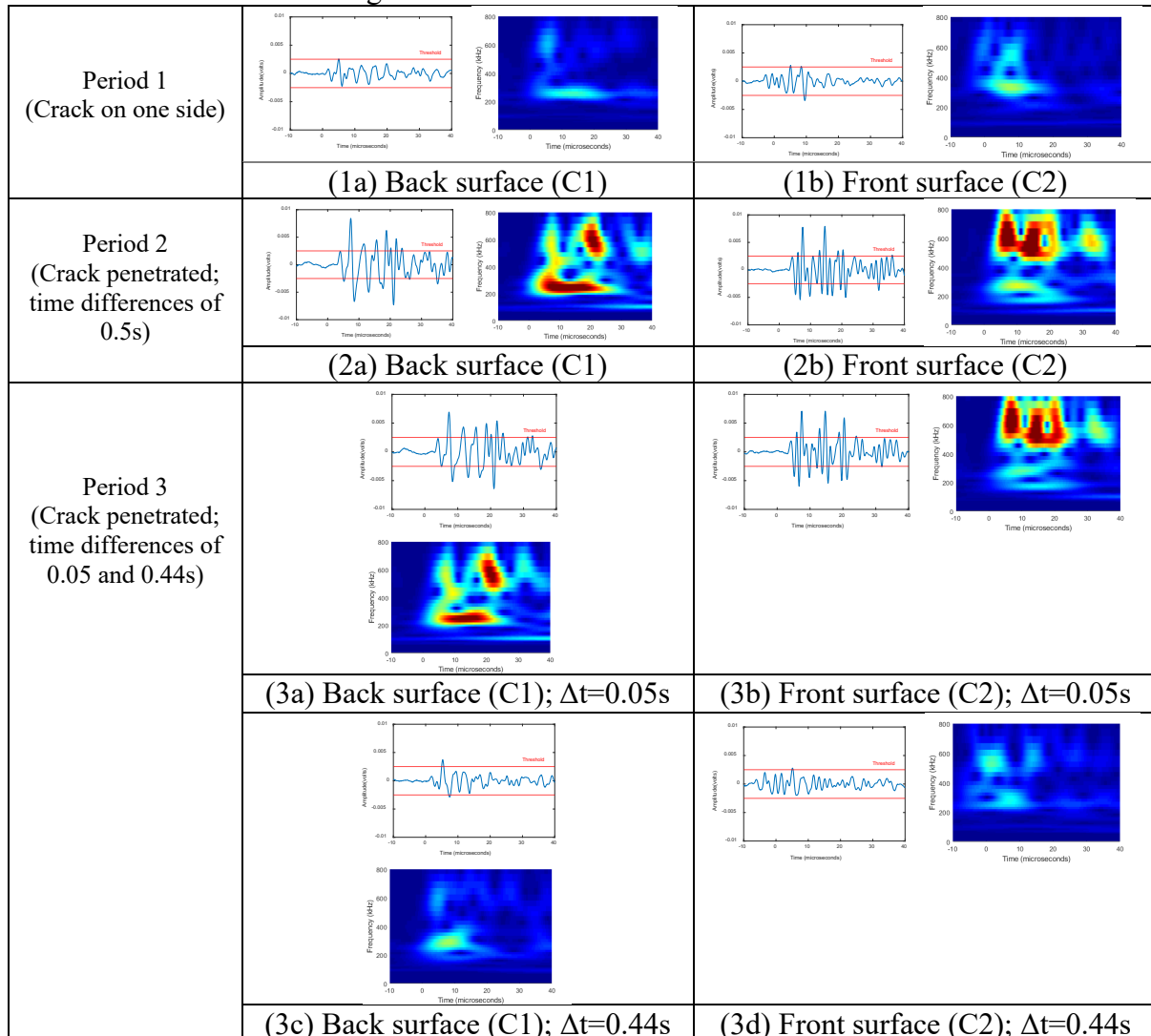


Figure 8. Crack profile on the back surface before failure.

To study the dominant frequency characteristics in detail of each period, seven example waveforms were shown in each stage to illustrate the evolution of dominant frequency for both channels. Fig. 9 shows the wavelet transform of the AE events during the surface crack propagation. The first waveform was collected when there existed crack only on one surface, the amplitude of that is small compared to the later ones. The 270 kHz frequency is more obvious. For waveform from period 2, period 3 when  $\Delta t$  is 0.05s, and period 4 when  $\Delta t$  is 0.005s, a higher frequency around 600 kHz arises for both channels. For period 3 when  $\Delta t$  is 0.44s and period 4 when  $\Delta t$  is 0.5s, the lower frequency still dominates. Possible reasons for this frequency shifting could be of different source origin.



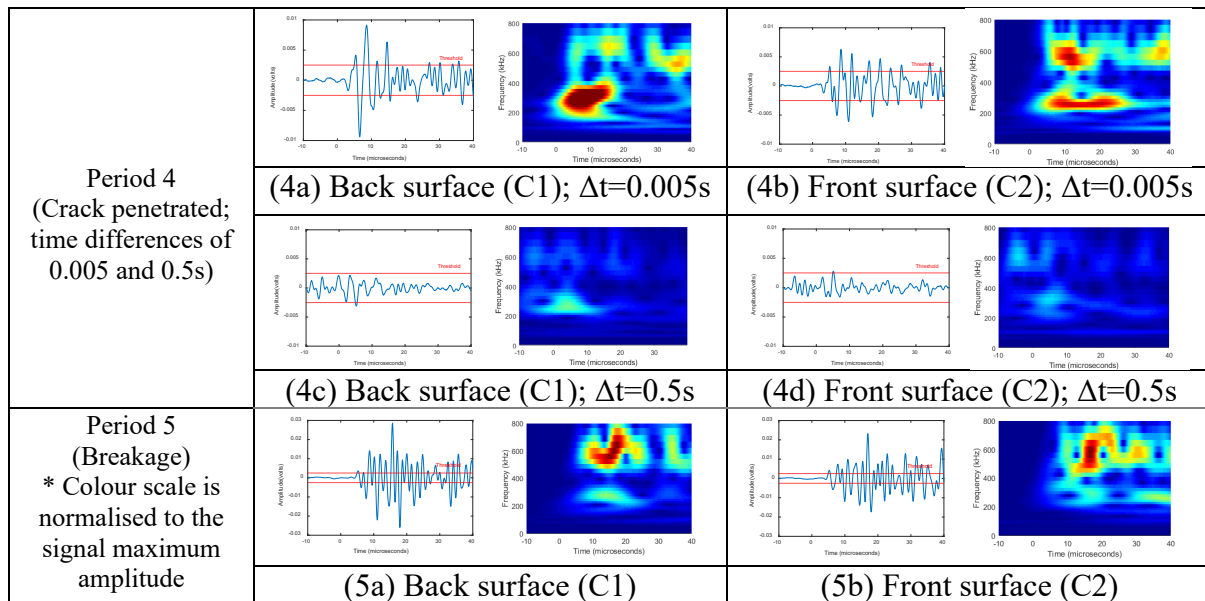


Figure 9. 7 chosen waveforms and corresponding wavelet transform.

Because the actual source arising time is unknown in this situation, and the source is only 20 mm from the sensor, it can be inaccurate to align the wavelet transform with the dispersion curve just by observing. Whilst similar observations can be qualitatively made, a better description of the modal content of the acoustic emission is required in order to delineate the contribution from S<sub>0</sub>, A<sub>0</sub> and A<sub>1</sub> modes during the period of fatigue crack propagation. Knowledge of the measured dispersion curve is necessary to delineate the contributions from these wave modes and to derive quantitative ratios of the guided-wave modes to describe the fatigue crack propagation. This highlights the limitation of the current measurement technique and underscores the potential of using a multi-element sensing arrangement described by Rajic et al [36].

## Conclusion

This paper has reported the acoustic signature of an artificial surface defect on dog-bone shaped Al6060 specimens under tensile fatigue test. It is found that most of AE events were collected in very late fatigue stage. Closure/friction and separation of crack surface contribute to most of the AE activities for the surface defect specimen. In addition, different source origins have a different ratio of dominant frequencies. This phenomenon indicates that, by monitoring AE waveforms, it is possible to predict the source of AE. Future work will account for wave modes decomposition on the fatigue crack propagation process and its associated AE characteristics.

## References

- [1] A. P. Mouritz, *Introduction to aerospace materials*. Elsevier, 2012. <https://doi.org/10.1533/9780857095152>
- [2] W. H. Ong and W. K. Chiu, "Designing for Lamb Wave Based In Situ Structural Health Monitoring," *Key Engineering Materials*, vol. 558, pp. 411-423, 2013. <https://doi.org/10.4028/www.scientific.net/KEM.558.411>
- [3] J. Jones, "Enhancing the Accuracy of Advanced High Temperature Mechanical Testing through Thermography," *Applied Sciences*, vol. 8, no. 380, p. 19, 2018. <https://doi.org/10.3390/app8030380>
- [4] C. K. Lee, P. D. Wilcox, B. W. Drinkwater, J. Scholey, M. Wisnom, and M. Friswell, "Acoustic emission during fatigue crack growth in aluminium plates," *Proceedings of the ECNDT, Berlin, Germany*, pp. 25-29, 2006. <https://doi.org/10.4028/0-87849-420-0.23>

- [5] T. M. Roberts and M. Talebzadeh, "Acoustic emission monitoring of fatigue crack propagation," *Journal of constructional steel research*, vol. 59, pp. 659-712, 2003. [https://doi.org/10.1016/S0143-974X\(02\)00064-0](https://doi.org/10.1016/S0143-974X(02)00064-0)
- [6] H. Helvajian *et al.*, "Evaluation of laser ultrasonic testing for inspection of metal additive manufacturing," presented at the Laser 3D Manufacturing II, 2015.
- [7] M. Mazurek and R. Austin, "Nondestructive Inspection of Additive Manufactured Parts in the Aerospace Industry," vol. 3,
- [8] A. Thompson, I. Maskery, and R. K. Leach, "X-ray computed tomography for additive manufacturing: a review," *Measurement Science and Technology*, vol. 27, no. 7, 2016. <https://doi.org/10.1088/0957-0233/27/7/072001>
- [9] M. J. Eaton, R. Pullin, and K. M. Holford, "Acoustic emission source location in composite materials using Delta T Mapping," *Composites Part A: Applied Science and Manufacturing*, vol. 43, no. 6, pp. 856-863, 2012. <https://doi.org/10.1016/j.compositesa.2012.01.023>
- [10] J. Fortin, S. Stanchits, G. Dresen, and Y. Gueguen, "Acoustic Emissions Monitoring during Inelastic Deformation of Porous Sandstone: Comparison of Three Modes of Deformation," *Pure and Applied Geophysics*, vol. 166, no. 5-7, pp. 823-841, 2009. <https://doi.org/10.1007/s00024-009-0479-0>
- [11] S. K. Al-Jumaili, M. J. Eaton, K. M. Holford, M. R. Pearson, D. Crivelli, and R. Pullin, "Characterisation of fatigue damage in composites using an Acoustic Emission Parameter Correction Technique," *Composites Part B: Engineering*, vol. 151, pp. 237-244, 2018. <https://doi.org/10.1016/j.compositesb.2018.06.020>
- [12] W. Zhou, W.-z. Zhao, Y.-n. Zhang, and Z.-j. Ding, "Cluster analysis of acoustic emission signals and deformation measurement for delaminated glass fiber epoxy composites," *Composite Structures*, vol. 195, pp. 349-358, 2018. <https://doi.org/10.1016/j.compstruct.2018.04.081>
- [13] J. P. McCrory *et al.*, "Damage classification in carbon fibre composites using acoustic emission: A comparison of three techniques," *Composites Part B: Engineering*, vol. 68, pp. 424-430, 2015. <https://doi.org/10.1016/j.compositesb.2014.08.046>
- [14] D. G. Aggelis, E. Z. Kordatos, and T. E. Matikas, "Acoustic emission for fatigue damage characterization in metal plates," *Mechanics Research Communications*, vol. 38, no. 2, pp. 106-110, 2011. <https://doi.org/10.1016/j.mechrescom.2011.01.011>
- [15] J. G. e. E. Govekar, I. Grabec, "Analysis of acoustic emission signals and monitoring of machining process," *Ultrasonics*, vol. 38, pp. 598-603, 2000. [https://doi.org/10.1016/S0041-624X\(99\)00126-2](https://doi.org/10.1016/S0041-624X(99)00126-2)
- [16] I. Inasaki, "Application of acoustic emission sensor," *Ultrasonics*, vol. 36, pp. 273-281, 1998. [https://doi.org/10.1016/S0041-624X\(97\)00052-8](https://doi.org/10.1016/S0041-624X(97)00052-8)
- [17] H. A. Kishawy, H. Hegab, U. Umer, and A. Mohany, "Application of acoustic emissions in machining processes: analysis and critical review," *The International Journal of Advanced Manufacturing Technology*, vol. 98, no. 5-8, pp. 1391-1407, 2018. <https://doi.org/10.1007/s00170-018-2341-y>
- [18] S. M. C. C. M. SCALA, "Acoustic Emission during Fatigue Crack Propagation in the Aluminium Alloys 2024 and 2124," *Materials Science and Engineering*, vol. 61, pp. 211-218, 1983. [https://doi.org/10.1016/0025-5416\(83\)90102-7](https://doi.org/10.1016/0025-5416(83)90102-7)
- [19] T. Lindley, I. Palmer, and C. Richards, "Acoustic emission monitoring of fatigue crack growth," *Materials Science and Engineering*, vol. 32, no. 1, pp. 1-15, 1978. [https://doi.org/10.1016/0025-5416\(78\)90206-9](https://doi.org/10.1016/0025-5416(78)90206-9)
- [20] H. Chang, E. Han, J. Wang, and W. Ke, "Acoustic emission study of corrosion fatigue crack propagation mechanism for LY12CZ and 7075-T6 aluminum alloys," *Journal of materials science*, vol. 40, no. 21, pp. 5669-5674, 2005. <https://doi.org/10.1007/s10853-005-1300-9>

- [21] S. M. Cousland and C. Scala, "Acoustic emission during the plastic deformation of aluminium alloys 2024 and 2124," *Materials Science and Engineering*, vol. 57, no. 1, pp. 23-29, 1983. [https://doi.org/10.1016/0025-5416\(83\)90023-X](https://doi.org/10.1016/0025-5416(83)90023-X)
- [22] R. Joseph, M. Y. Bhuiyan, and V. Giurgiutiu, "Acoustic emission from vibration of cracked sheet-metal samples," *Engineering Fracture Mechanics*, vol. 217, 2019. <https://doi.org/10.1016/j.engfracmech.2019.106544>
- [23] R. Unnorsson, "Hit Detection and Determination in AE Bursts," in *Acoustic Emission - Research and Applications*, 2013, ch. Chapter 1. <https://doi.org/10.5772/54754>
- [24] S. M. K. Cousland and C. Scala, "Acoustic emission from the aluminium alloy 6061-T651," *Journal of materials science letters*, vol. 3, no. 3, pp. 268-270, 1984. <https://doi.org/10.1007/BF00726813>
- [25] M. Y. Bhuiyan, B. Lin, and V. Giurgiutiu, "Acoustic emission sensor effect and waveform evolution during fatigue crack growth in thin metallic plate," *Journal of Intelligent Material Systems and Structures*, vol. 29, no. 7, pp. 1275-1284, 2017. <https://doi.org/10.1177/1045389X17730930>
- [26] H. Bi, Z. Li, D. Hu, I. Toku-Gyamerah, and Y. Cheng, "Cluster analysis of acoustic emission signals in pitting corrosion of low carbon steel," *Materialwissenschaft und Werkstofftechnik*, vol. 46, no. 7, pp. 736-746, 2015. <https://doi.org/10.1002/mawe.201500347>
- [27] M. Y. Bhuiyan and V. Giurgiutiu, "The signatures of acoustic emission waveforms from fatigue crack advancing in thin metallic plates," *Smart Materials and Structures*, vol. 27, no. 1, p. 015019, 2018. <https://doi.org/10.1088/1361-665X/aa9bc2>
- [28] M. Sause and M. Hamstad, "7.14 Acoustic Emission Analysis," in *Comprehensive Composite Materials II*, 2018, pp. 291-326. <https://doi.org/10.1016/B978-0-12-803581-8.10036-0>
- [29] W. J. Staszewski, B. C. Lee, L. Mallet, and F. Scarpa, "Structural health monitoring using scanning laser vibrometry: I. Lamb wave sensing," *Smart Materials and Structures*, vol. 13, no. 2, pp. 251-260, 2004. <https://doi.org/10.1088/0964-1726/13/2/002>
- [30] M. Hamstad, A. O'GALLAGHER, and J. Gary, "A wavelet transform applied to acoustic emission," *J. Acoust. Emiss*, vol. 20, pp. 39-61, 2002.
- [31] M. Hamstad, "Acoustic emission signals generated by monopole (pencil lead break) versus dipole sources: finite element modeling and experiments," *Journal of acoustic emission*, vol. 25, pp. 92-106, 2007.
- [32] F. Yu, Q. Wu, Y. Okabe, S. Kobayashi, and K. Saito, "The identification of damage types in carbon fiber-reinforced plastic cross-ply laminates using a novel fiber-optic acoustic emission sensor," *Structural Health Monitoring: An International Journal*, vol. 15, no. 1, pp. 93-103, 2016. <https://doi.org/10.1177/1475921715624503>
- [33] N. Hsu and B. FR, "Characterization and calibration of acoustic emission sensors," 1981.
- [34] "Vibration Isolation: Megasorber DIS8 Self-Adhesive Vibration Isolation and Damping Sheet," ed: Megasorber Pty Ltd, 2018.
- [35] K. Ono, "Acoustic emission," in *Springer Handbook of Acoustics*: Springer, 2014, pp. 1209-1229. [https://doi.org/10.1007/978-1-4939-0755-7\\_30](https://doi.org/10.1007/978-1-4939-0755-7_30)
- [36] N. Rajic, C. Rosalie, S. van der Velden, L. F. Rose, J. Smithard, and W. K. Chiu, "A novel high density piezoelectric sensing capability for in situ modal decomposition of acoustic emissions," in *Proceedings of the 9th European Workshop on Structural Health Monitoring July*, 2018, pp. 10-13,

# Computational Study of Scattering Elastic Waves Due to a Teredo Marine Borer-Like Cylindrical Defect Embedded in an Isotropic Solid Cylinder

Ahmed Murgab Mohammed Mahil<sup>a,\*</sup>, Wing Kong Chiu<sup>b</sup> and Benjamin Vien<sup>c</sup>

Department of Mechanical and Aerospace Engineering, Monash University, Wellington Rd, Clayton, VIC 3800, Australia

<sup>a</sup>ahmed.mohammedmahil@monash.edu, <sup>b</sup> wing.kong.chiu@monash.edu,  
<sup>c</sup>ben.vien@monash.edu

**Keywords:** Bulk Waves, Scattered Field, Finite Element Analysis, Group Velocity, Cylindrical Defect

**Abstract.** This paper showcases a quantitative investigation of scattering of ultrasonic waves experiences when impinging on a cylindrical defect inside a solid cylinder. Such cylindrical bores reduce the structural capacity of the cylinder, these defects constitute an even greater risk as they cannot be observed from the surface. The focal point investigated herein is to develop a better understanding of the wave's scattering when interacting with defects of cylindrical bore, mimicking the Teredo marine borer, within the solid cylinder. Two-dimensional Finite Element simulations are carried out using ABAQUS software. A 200 kHz 5.5 cycle Hann windowed excitation on an isotropic cylinder is simulated a point source excitation at the circumference of the cylinder is used. The scattering wave fields from a range of defect diameters through the solid cylinder are presented. Using Two-Dimensional Fast Fourier Transform, the wave mode and velocity of the scattered wavefield along various directions was identified in cylindrical coordinates, to decouple the wave modes. Computational results are presented for the scattering pattern as a function of cylindrical bore diameter size relative to wavelength. This study serves as an efficient approach when choosing an input for ultrasonic imaging, with the aim to obtain high fidelity imaging resolution for structural health monitoring applications.

## Introduction

Marine borers especially the oyster family Teredo, also known as shipworm, have been known to cause wooden piles to lose their structural adequacy[1, 2]. The main problem with detecting these borers is that they burrow within the piles without leaving any distinguishable marks on the pile's surface which makes it hard to detect their existence by current methods. The focal point investigated in this paper is to develop a better understanding of the stress wave's scattering when interacting with defects of cylindrical bore shape within the solid cylinder. The defects mimic the Teredo marine borers that burrow in gun-barrel wooden structural piles Fig 1.



Figure 1. Teredo borers inside a gun-barrel wooden pile illustration[3].

Current methods to identify Teredo defects are laborious and ineffective in early detection of the marine borers such as quasi non-destructive testing using resistograph. [4]. Other methods such as X-ray scanner radiographs are hazardous, expensive and qualitative in nature [5, 6] and they are considered complementary methods to other mechanical and acoustic approaches. The most used non-destructive testing (NDT) method currently used is broadband stress waves using a hammer and ultrasonic receivers, this method depends on the time-of-flight (TOF) of the wave to determine the defect existence. In order to roughly learn about the defect location when using broadband impulses, iterative methods such as Algebraic Reconstruction Technique are utilised [7]. The issue with this method is that it does not assist in characterising the geometry of the defects or produce high fidelity images. To be able to deduce such information scattered wave field analysis are incumbent as well as the input signal's type.

In terms of the geometrical fundamentals of the Teredo defect, it can be approximated as a cylinder. Early work such as [8, 9] investigated hollow cylinders embedded in a solid infinite isotropic medium as a scatterer and laid the formulation of plane waves scattering for compressional/longitudinal (P) and shear (S) waves experiencing mode conversion, while Lewis et al [10] generalised the formulations for a solid cylindrical scatterer. Furthermore, in composites [11] studied scattering for single modes by a cylindrical fibre and [12] developed a theoretical framework to study multiferroic composites that consist of randomly distributed fibres. Stress wave propagation in anisotropic wood formulations was investigated by [13]. Yan et al [14] used TOF to assess damage in timber poles using broadband excitation using a hammer. Scattered wave directivity patterns for a range of cylindrical defects were investigated in [15, 16] as a function of the wave number and cylindrical defect diameter. TOF is utilised in most of current literature as a primary method of detecting defects in wood using stress waves. However, TOF does not extract all the wavefield information and is limited to estimating the wavefield velocity. In order to achieve early detection of Teredo size defects inside a gun barrel/cylindrical wave guide it is incumbent to conduct a quantitative scatter analysis of the geometrical range for the Teredo Navalis from 5mm up to 10mm [3, 17].

This paper computationally examines a hollow cylinder inside a solid isotropic cylinder and its interactions with elastic bulk waves, for a range of diameters focusing on the scatterer geometry. Despite wood being anisotropic and orthotropic, in this study the scattered wavefield is simulated in isotropic media. This will work as a reference for specific scatterer geometry behaviour in a well-known material. The wave modes, scattered wave patterns and their corresponding amplitudes are reported.

### **Computational Procedure**

In this paper, numerical simulations using explicit dynamic finite element analysis tool in the ABAQUS software are presented. A cross-section of a solid cylinder of 200 mm in diameter is modelled in 2D plane strain for simulating bulk elastic wave propagating inside it. The material set as an isotropic aluminium (density of  $2.7 \text{ kg/m}^3$ , Poisson's ratio of 0.33 and Young's modulus of 69 MPa). The isotropic material 4-node bilinear plane strain elements (CPE4R) were used to mesh the solid cylinder cross-section. In order to decouple wave modes propagating inside the cylinder's bulk the simulation data was converted from cartesian coordinates to polar coordinates in the 2D plane strain simulations with the centre of the defect is set as the point of origin. A narrow-band tone-burst signal carrying a central frequency is used as standard practice for the interpretation of the output signals [18]. For the simulation, the force excitation signal is a 5.5-cycle Hann windowed with a centre frequency of 200 kHz. This loading configuration excites both P and S wave modes in the plane, however dominantly P-wave impinges the defect.

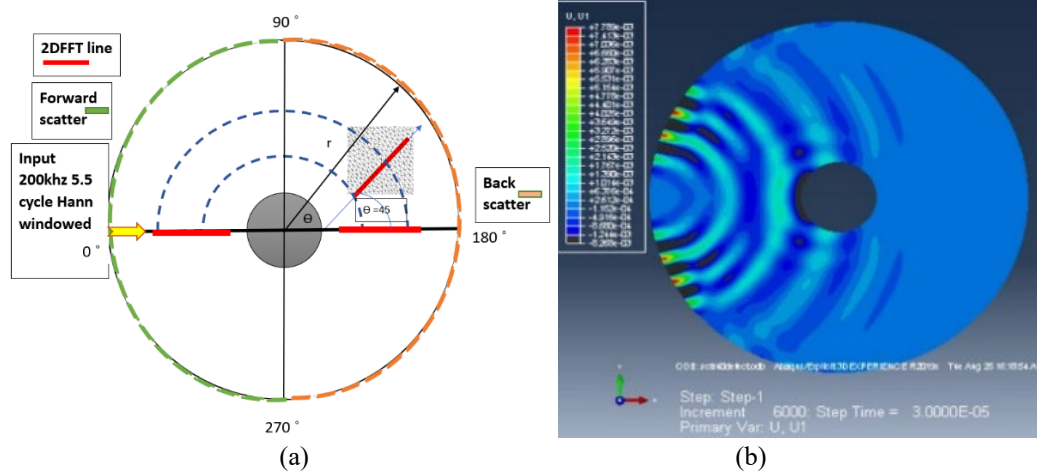


Figure 2. (a) Schematic diagram indicating location of defect and showing the 2D FFT line, excitation point and scattered wave measurements (b). 2D FEA simulations of wave propagation at 30 $\mu$ s

The defect is located in the middle of the cylinder as shown in Fig 2. The cylindrical cross-section is discretised into 0.2mm 4-node bilinear plane strain elements. In Explicit analysis, the element size was set at 0.2mm, which satisfies the spatial requirement to capture ultrasonic wave propagation [19] and the time interval was set at 5ns to ensure the Courant Lewy Condition (CFL) [20] is satisfied, and meets the ABAQUS Explicit Time Integration stability limit of  $0.6L/C$ , where L denotes smallest element length and C the maximum wave velocity [21]. The defect is modelled as an infinite cylindrical defect with a maximum spacing of 0.2mm around the circumference. The dependence of scattered amplitude with respect to defect diameter is investigated by varying the diameter size. The defect diameters (d) considered are of size from 5mm to 10mm diameter with 1mm increment and then from 10mm to 60mm diameter with 10mm increment, in order to investigate the effects when defect diameter is larger than the wavelength  $\lambda \leq d$  and smaller ( $\lambda > d$ ) with respect to an incident P-wave. At a centre frequency of 200kHz, the wavelength for the P wave,  $\lambda_P$ , is 31.6mm and for S wave,  $\lambda_S$ , is 15.8mm. Arrays of sensors were arranged in a straight equidistant line at different angles emerging from the excitation source and at an angle from the defect far side edge. It should be noted that, for  $\lambda \leq d$ , the scattering contribution from the incident S waves are also present.

In order to investigate and verify the behaviour of the bulk waves (P and S waves), the simulations data were processed using two-dimensional fast Fourier transformation (2D FFT); with node sensors at arrays radially away from the source of excitation. 2D FFT is performed on the nodes along lines at 0° and 45° from the defect, as indicated in Fig 2. This is used to identify the dominant bulk wave mode from the 2D FFT, spatial distance is taken at least  $1.5\lambda$  away from the defect edge and over approximately  $2\lambda$  distance with zero padding [22].

The scattered wave field is extracted by subtracting the wave field of the defect simulation from the pristine simulation refer to Eq.1. Furthermore, in order to identify the scatter field modes, 2D FFT is implemented on scattered field data.

$$U_{scatter}(\theta, r, t) = U_{defect}(\theta, r, t) - U_{pristine}(\theta, r, t) \quad (1)$$

The scattered wave displacement is divided into two regions; back and forward scatter fields. They are defined in regions of scatter angle  $270^{\circ}$ - $90^{\circ}$  and  $90^{\circ}$ - $270^{\circ}$  as back and forward respectively. In Fig 6, the way the directivity is obtained is by taking the maximum peak of the envelope of the time signal via the absolute Hilbert transformation, which was performed over the time domain signals measured at points on the circumference away from the defect in the far-field. In this paper time gating is conducted to validate the wave train of the scattered wave modes. Where scattered P wave arrives approximately after  $35\mu\text{s}$  the scattered S wave arrive at  $50\mu\text{s}$ . All the nodes on the circumference were at increments of  $0.5^{\circ}$  from  $0^{\circ}$  to  $360^{\circ}$  and were used to obtain the polar directivity plots. The scattered wave amplitudes were measured at the cylinder circumference. Thus, the backward-scattered amplitudes were measured at  $270^{\circ}$  to  $90^{\circ}$  and the forward-scattered were measured at  $90^{\circ}$  to  $270^{\circ}$ .

**Result**

Simulations were conducted to assess the effect of the defects on the incident wave and to detect mode conversion through 2D FFT results which were superimposed on the analytical wave mode velocities.

**Effect of defect diameter**

The 2D FFT results demonstrate the same pattern of mode conversion regardless of the circular defect sizes, indicating that mode conversion is independent of the defect diameter for the investigated range. From the FE simulations, P and S-waves were observed as depicted in Fig 3. At the  $45^{\circ}$  sensor array, behind the defect as shown in Fig 3. P mode is dominant in radial ( $U_r$ ) direction as for the angular ( $U_{\theta}$ ) direction, we observe a dominant S mode with a very weak P mode. It is clear that the 2D FFT velocity is in good agreement with the theoretical velocities at 200 kHz and 400 rad/m wavenumber which is calculated by the relation  $c = \frac{2\pi}{k}f$  which yields S wave at 3155.185m/s at an agreement with the theoretical velocity 3160m/s as in [23]. The 2D FFT results are slightly skewed when compared to the theoretical lines in Fig 3 due to the angle of the sensor array. In Fig 4, at  $0^{\circ}$  angle sensor’s array before the defect, the P mode is observed in the  $U_r$  direction, while in the  $U_{\theta}$  direction the S mode is present along with a faint P mode. Using polar coordinates helped decouple the wave modes. In Fig 5, at  $0^{\circ}$  angle sensor’s array after the defect we see a dominant P mode in  $U_r$  in  $U_{\theta}$  an S mode with leaking P mode. These results demonstrate the incident wave mode conversion due to interaction with the defect. The observed mode conversion are the same upon varying the defect diameter.

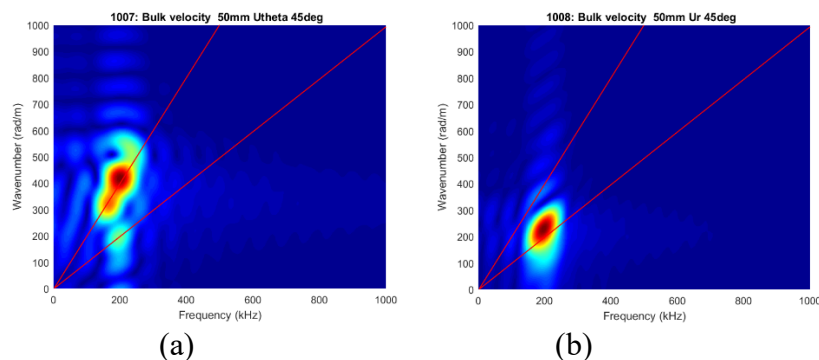


Figure 3. Analytical bulk velocities (P-S) vs 2D FFT for scattered wavefield for the sensor array at  $45^{\circ}$  from defect edge (a) S -wave and weak P-wave  $U_{\theta}$  direction (b) P-wave  $U_r$  direction

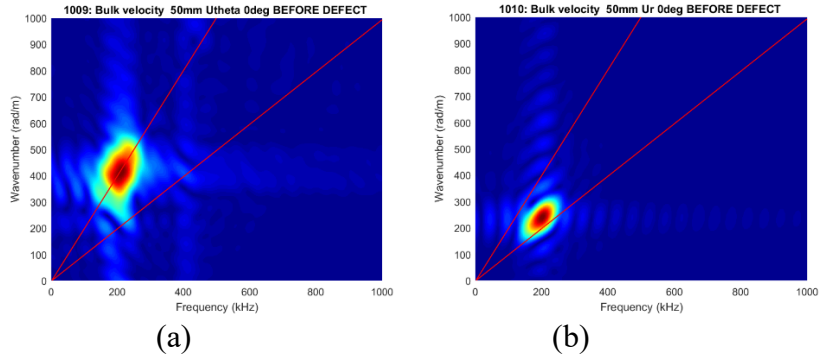


Figure 4. Analytical bulk velocities ( $P$ - $S$ ) vs 2D FFT for scattered wavefield for the sensor array at  $0^\circ$  from defect edge (a)  $S$ -wave  $U_\theta$  direction (b)  $P$ -wave  $U_r$  direction

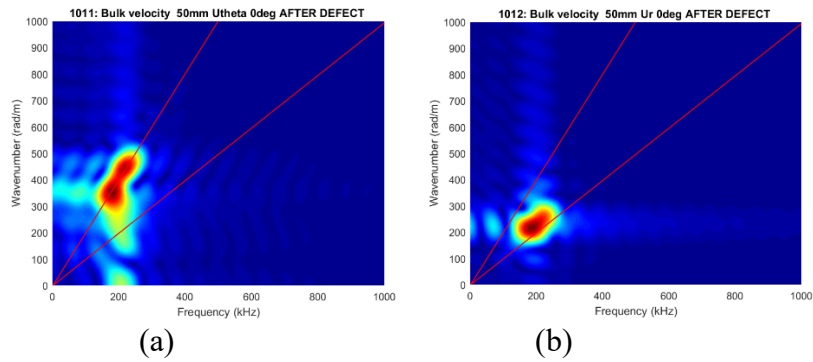


Figure 5. Analytical bulk velocities ( $P$ - $S$ ) vs 2D FFT for scattered wavefield for the sensor array at  $180^\circ$  from defect edge (a)  $S$ -wave and weak  $P$ -wave  $U_\theta$  direction (b)  $P$ -wave  $U_r$  direction

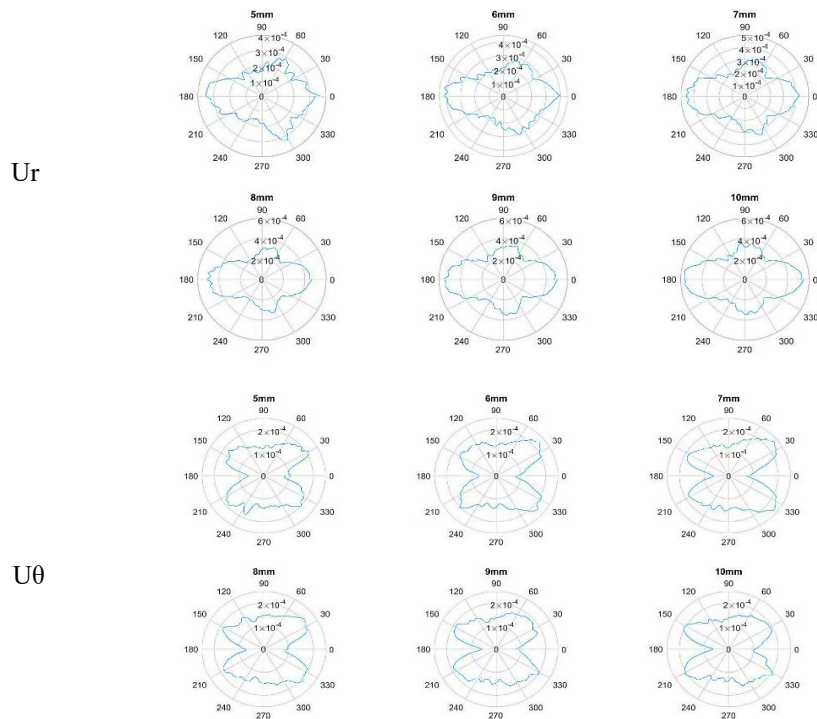


Figure 6. Scattered field amplitude directivity pattern in  $U_r$  direction top and  $U_\theta$  bottom for  $d=$  (5mm to 10mm)

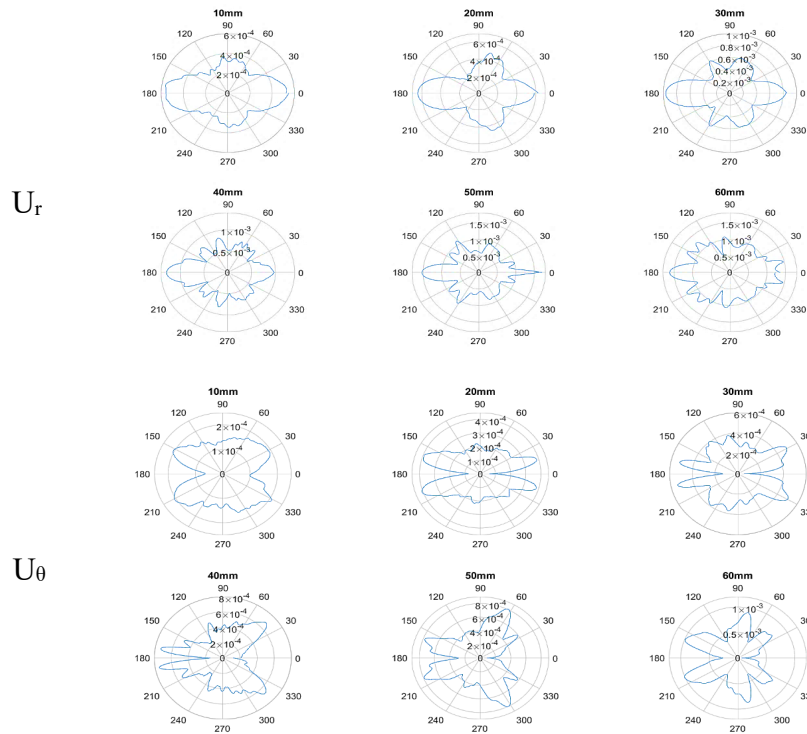


Figure 7. Scattered field amplitude directivity pattern in the  $U_r$  direction top and  $U_\theta$  bottom for  $d = (10\text{mm to } 60\text{mm})$

The scattered wave plot patterns are symmetrical along the horizontal lines in Fig 6 and Fig 7 for both  $U_r$  and  $U_\theta$  direction. Fig 6 demonstrates that the defects from  $d=7\text{mm}$  to  $d=10\text{mm}$  show almost an identical scatter pattern in both  $U_r$  and  $U_\theta$  directions. For the  $U_r$  direction the main lobe is at  $180^\circ$  with a significant but smaller lobe at  $0^\circ$ , along with identical smaller lobes at  $90^\circ$  and  $270^\circ$ . For the  $U_\theta$  direction the main lobes are at  $30^\circ$  and  $330^\circ$ , with significant but smaller identical lobes at  $150^\circ$  and  $210^\circ$ . For  $d=5\text{mm}$  and  $d=6\text{mm}$  a slight difference is observed in the  $U_r$  direction where the main lobe is at  $180^\circ$  with smaller lobes at  $0^\circ$ ,  $60^\circ$  and  $300^\circ$ .

The observations from Fig 7. show that when the defect diameter increases in the  $U_r$  direction the dominant lobe fluctuates between  $0^\circ$  and  $180^\circ$ . At  $d=10\text{mm}$  the main lobe is at  $180^\circ$  with a significant but smaller lobe at  $0^\circ$  along with smaller lobes at  $90^\circ$  and  $270^\circ$ . Similarly, as  $d$  is increased to  $20\text{mm}$  and  $30\text{mm}$  there is a shift in the smaller lobes by  $30^\circ$  and  $60^\circ$  respectively. For  $d=40\text{mm}$  there are smaller lobes at  $130^\circ$ ,  $160^\circ$ ,  $220^\circ$ ,  $250^\circ$  and the lobe at  $0^\circ$  shrinks, these smaller lobes are shifted by  $10^\circ$  upon increasing  $d$  to  $50\text{mm}$  while a sharp main lobe is at  $0^\circ$ . For  $d=60\text{mm}$  the main lobe is at  $180^\circ$  with smaller distinct lobes from  $90^\circ$  to  $270^\circ$ . For the  $U_\theta$  direction the forward scatter energy is focused more along the edge as the defect size increases. For  $d=10\text{mm}$  and  $30\text{mm}$  the main lobes are located at  $30^\circ$  and  $330^\circ$ , while for  $d=20\text{mm}$ ,  $40\text{mm}$  and  $50\text{mm}$  the main lobes are located at  $145^\circ$  and  $205^\circ$ ,  $45^\circ$  and  $315^\circ$ , and  $60^\circ$  and  $300^\circ$  respectively. For  $d=10\text{mm}$  and  $30\text{mm}$  the smaller lobes are located at  $150^\circ$  and  $210^\circ$ , while for  $d=20\text{mm}$ ,  $40\text{mm}$ ,  $50\text{mm}$  and  $60\text{mm}$  the smaller lobes are located at  $25^\circ$  and  $355^\circ$ ,  $150^\circ$  and  $210^\circ$ ,  $145^\circ$  and  $205^\circ$ , and  $150^\circ$  and  $210^\circ$  respectively.

### Discussion

FE results presented in this paper showed that the scattered wave fields directivity patterns are dependent on the defect diameter where the amplitude increase with an order of magnitude. In

the  $U_r$  direction, the Fig 7 plots show that forward and back scattered regions are comparable in size with two similar lobes about the  $\theta=180^\circ$  radial line for  $d=10\text{mm}$  to  $d=40\text{mm}$ . As the defect diameter increase, the forward scatter decreases slightly, and the back scattered increases slightly becoming dominant. The same can be said when  $(\lambda) > d$  for defects from  $d=5\text{mm}$  to  $d=9\text{mm}$ . For  $\lambda \leq d$ , the P incident wave is dominant with along with a weak incident S wave, the scattering wavefield have a contribution from this incident S wave as well. The patterns are only symmetrical on the  $0^\circ$  -axis. This is due to the creeping shear wave [24], coalescing with the leaky Rayleigh wave propagating on the circumference of the defect [25, 26]. This indicates that defect size characterisation can be related to the scattered field amplitude and incident wave mode conversion. Thus, methods of detecting and characterising defects within a solid which rely solely on the reflected wave field do not provide enough information for the characterisation of the defect size.

### Conclusion

The scattered wave field of bulk stress waves in an isotropic solid cylinder with a cylindrical defect using narrow-band tone-burst excitation has been reported. This paper illustrated that the diameter of the cylindrical defect affects the scattered wave pattern and that the scattered pattern can be influenced by incident wave components P and S mode conversion. This study provides a fundamental analysis to address Teredo marine borers defects effects on wave fields. Further, this paper highlights the importance of scattered wave field analysis for defect size characterisation. Future work will address the Teredo defects in a multiple defects' scenario.

### References

- [1] Salmiah, K.R.U., *RESISTANCE OF FIVE TIMBER SPECIES TO MARINE BORER ATTACK*. Journal of Tropical Forest Science, 2015. 27 ((3)): p. 400–412
- [2] Charles, F., et al., *Wood decay at sea*. Journal of Sea Research, 2016. 114: p. 22-25. <https://doi.org/10.1016/j.seares.2016.05.002>
- [3] Kelly, S.W., *UNDERWATER INSPECTION CRITERIA*. 1999, NAVAL FACILITIES ENGINEERING SERVICE CENTER: Port Hueneme, California.
- [4] Nowak, T.P., J. Jasieńko, and K. Hamrol-Bielecka, *In situ assessment of structural timber using the resistance drilling method – Evaluation of usefulness*. Construction and Building Materials, 2016. 102: p. 403-415. <https://doi.org/10.1016/j.conbuildmat.2015.11.004>
- [5] Greenawald, E.C., et al. Underwater x-ray tomography of composite sonar domes via collimated backscatter imaging. in *Nondestructive Evaluation of Materials and Composites II*. 1998. International Society for Optics and Photonics. <https://doi.org/10.1117/12.301510>
- [6] Riis, N., et al., *Limited-data x-ray CT for underwater pipeline inspection*. Inverse Problems, 2018. 34(3): p. 034002. <https://doi.org/10.1088/1361-6420/aaa49c>
- [7] Wang Xiping, F.D., Crystal Pilon, Brian K. Brashaw, Robert J. Ross, and Roy F. Pellerin, *Assessment of decay in standing timber using stress wave timing nondestructive evaluation tools: A guide for use and interpretation*. 2004, United States Department of Agriculture Forest Service Forest Products Laboratory. <https://doi.org/10.2737/FPL-GTR-147>
- [8] Kato, K., *Reflection of sound wave due to a hollow cylinder in an elastic body*. Osaka University, Memoirs of the Institute of Scientific and Industrial Research, 1952. 9: p. 16-20.
- [9] White, R.M., *Elastic Wave Scattering at a Cylindrical Discontinuity in a Solid*. The Journal of the Acoustical Society of America, 1958. 30(8): p. 771-785. <https://doi.org/10.1121/1.1909759>

- [10] Lewis, T.S. and D.W. Kraft, *Mode conversion relation for elastic waves scattered by a cylindrical obstacle in a solid*. The Journal of the Acoustical Society of America, 1974. 56(6): p. 1899-1901. <https://doi.org/10.1121/1.1903529>
- [11] Zhang, J., et al., Study on the Single Scattering of Elastic Waves by a Cylindrical Fiber with a Partially Imperfect Bonding Using the Collocation Point Method. Shock and Vibration, 2018. 2018: p. 1-14. <https://doi.org/10.1155/2018/7516402>
- [12] Kuo, H.-Y., Y.-A. Huang, and C.-H. Sun, Scattering of anti-plane shear waves by arbitrarily distributed circular cylinders in a functionally graded multiferroic fibrous composite. Acta Mechanica, 2017. 229(4): p. 1483-1501. <https://doi.org/10.1007/s00707-017-2079-x>
- [13] Bucur, V., *Acoustics of Wood*. 2nd Edition ed, ed. S.S.i.W. Science. 2006: Springer. <https://doi.org/10.1007/3-540-30594-7>
- [14] Yan, N., Numerical Modelling and Condition Assessment of Timber Utility Poles using Stress Wave Techniques. 2015, University of Technology, Sydney.
- [15] Wang, X. and L. Sudak, Scattering of elastic waves by multiple elastic circular cylinders with imperfect interface. Waves in Random and Complex Media, 2007. 17(2): p. 159-187. <https://doi.org/10.1080/17455030601118376>
- [16] Liu, Y., Wu, R.S. and Ying, C.F., *Scattering of elastic waves by an elastic or viscoelastic cylinder*. Geophysical Journal International, 2000. 142(2): p. 439-460. <https://doi.org/10.1046/j.1365-246x.2000.00173.x>
- [17] Grave, B.H., Natural history of shipworm, *Teredo navalis*, at Woods Hole, Massachusetts. The Biological Bulletin, 1928. 55(4): p. 260-282. <https://doi.org/10.2307/1537080>
- [18] Sikdar, S. and S. Banerjee, Guided wave propagation in a honeycomb composite sandwich structure in presence of a high density core. Ultrasonics, 2016. 71: p. 86-97. <https://doi.org/10.1016/j.ultras.2016.05.025>
- [19] Bingham, J. and M. Hinders, 3D elastodynamic finite integration technique simulation of guided waves in extended built-up structures containing flaws. Journal of Computational Acoustics, 2010. 18(02): p. 165-192. <https://doi.org/10.1142/S0218396X10004097>
- [20] Courant, R., K. Friedrichs, and H. Lewy, *Über die partiellen Differenzgleichungen der mathematischen Physik*. Mathematische annalen, 1928. 100(1): p. 32-74. <https://doi.org/10.1007/BF01448839>
- [21] Leckey, C.A.C., et al., Simulation of guided-wave ultrasound propagation in composite laminates: Benchmark comparisons of numerical codes and experiment. Ultrasonics, 2018. 84: p. 187-200. <https://doi.org/10.1016/j.ultras.2017.11.002>
- [22] Chiu, W.K., L.R.F. Rose, and B.S. Vien, Scattering of the Edge-guided Wave by an Edge Crack at a Circular Hole in an Isotropic Plate. Procedia Engineering, 2017. 188: p. 309-316. <https://doi.org/10.1016/j.proeng.2017.04.489>
- [23] Shull, P.J., *Nondestructive evaluation: theory, techniques, and applications*. 2002: CRC press. <https://doi.org/10.1201/9780203911068>
- [24] Aldrin, J.C., et al., *Scattering of obliquely incident shear waves from a cylindrical cavity*. The Journal of the Acoustical Society of America, 2011. 129(6): p. 3661-3675. <https://doi.org/10.1121/1.3583540>
- [25] Nagy, P.B., M. Blodgett, and M. Golis, *Weep hole inspection by circumferential creeping waves*. NDT & E International, 1994. 27(3): p. 131-142. [https://doi.org/10.1016/0963-8695\(94\)90604-1](https://doi.org/10.1016/0963-8695(94)90604-1)
- [26] Doherty, C. and W.K. Chiu, *Scattering of ultrasonic-guided waves for health monitoring of fuel weep holes*. Structural Health Monitoring, 2012. 11(1): p. 27-42. <https://doi.org/10.1177/1475921710395814>

# Estimation of Maximum Drift of MDOF Shear Structures Using Only One Accelerometer

Kangqian Xu<sup>1,a,\*</sup> and Akira Mita<sup>1,b</sup>

1. Department of System Design Engineering, Keio University, Yokohama, Japan

<sup>a</sup>xukangqian@keio.jp, <sup>b</sup>mita@sd.keio.ac.jp

**Keywords:** Maximum Inter-Story Drift, Shear Structure, Modal Coordinates, State-Space Equation, Kalman Filter

**Abstract.** This paper presents a new method to estimate maximum drifts, relative displacements between adjacent floors, of all stories of multi-degree-of-freedom (MDOF) shear structures using only one floor's absolute acceleration time history response under the ground excitation. The absolute acceleration and relative displacement are formulated in modal coordinates and the state-space expression is derived. Then the numerical simulation for a three-story structure was conducted to verify the performance of the state-space equation. The comparison of the estimated state and input with actual values is made and shows the good agreement. In addition, the relative displacement time histories of all floors were obtained, and the errors of maximum displacements and inter-story drifts were analyzed. The robustness against environmental noise was also investigated by numerical simulations as well. The results of simulations indicate the estimation is satisfactory, and very robust against the environmental disturbance.

## Introduction

The performance of civil infrastructures, such as buildings or bridges, gradually deteriorates under service loads and damage could occur when structures suffer from disasters, such as earthquakes. Here, structural health monitoring (SHM) has been extensively researched over the last few decades as a means of assessing the states of structures [1].

Maximum inter-story drift (drift angle) is an important parameter with which to evaluate the state of a structure. Inter-story drift is relative to the structural deformation capacity, and it is widely used in the design stage to judge whether a building will meet seismic design codes [2] or standards [3, 4]. In the service stage, significant inter-story drift intuitively suggests there may be damage to structural and non-structural members [5]. For seismic isolation structures and supplementally damped buildings, the peak inter-story drift significantly affect the characteristics of bearings and dampers and consequently the dynamic properties of the structures [6-10].

Acceleration responses are easier to detect than displacements in buildings [11], and the accuracy of accelerometers is normally higher than that of displacement sensors. The displacement time history responses relative to the ground can be obtained from the integral of the relative accelerations or a Kalman filter [12, 13], which requires several accelerometers and at least one on the base. These accelerometers need power and data cables, the installation of which entails a significant amount of labor. Moreover, such cables could be damaged, resulting in failure of the sensors during an extreme hazard. To overcome these difficulties, wireless passive sensors [14, 15] based on radiofrequency identification (RFID) or other technologies have been studied. In addition, identification schemes relying on fewer sensors have studied. For example, Yoshimoto et al. [16] used only three accelerometers to detect damage to base-isolated

buildings whose models were simplified by combining linear interpolation or cosine interpolation with the substructure approach. Considering that structures are usually still elastic or slightly non-linear during most earthquakes, we propose a novel way to estimate the maximum relative displacement of all floors in a linear multi-degree-of-freedom (MDOF) structure merely from the acceleration time history response recorded by one sensor installed on a floor.

This paper is organized as follows: Section 2 formulates the structural responses in modal coordinates. Section 3 discusses the results of numerical simulations investigating the applicability and robustness against environmental noise of the proposed approach. Section 4 summarizes this study and points out the potential of this research.

### Formulation of Proposed Method

As shown in Figure 1, the equation of motion of a MDOF structure that is subjected to seismic excitation can be described as:

$$\mathbf{M}\ddot{\mathbf{z}}(t) + \mathbf{C}\dot{\mathbf{z}}(t) + \mathbf{K}\mathbf{z}(t) = -\mathbf{M}\mathbf{r}\ddot{u}_g(t) \tag{1}$$

where  $\mathbf{z}(t)$  denotes the displacement relative to the ground,  $(\cdot)$  means the time derivative,  $\ddot{u}_g(t)$  is the ground acceleration, and  $\mathbf{r}$  represents an  $n \times 1$  unit vector ( $\mathbf{r} = [1 \ \dots \ 1]^T$ );  $\mathbf{M}$ ,  $\mathbf{C}$  and  $\mathbf{K}$  are the structural mass, damping and stiffness matrixes, respectively.

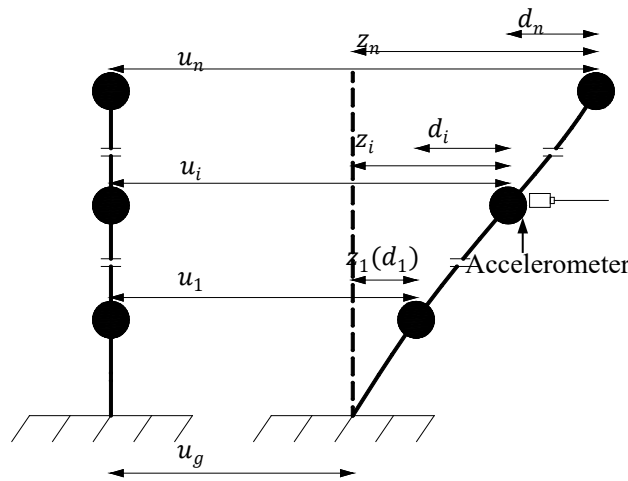


Figure 1. MDOF structure subjected to seismic excitation

By installing one accelerometer on a floor, we can obtain the floor's absolute acceleration time history response  $\ddot{u}_i(t)$ . We will focus on the estimation of the maximum relative displacement  $z_i(t)_{\max}$  or subsequently the inter-story drift  $d_i(t)_{\max}$  of the floor based on the absolute acceleration response.

The relative displacement of the  $i$ th DOF of the MDOF structure can be written in modal coordinates:

$$z_i(t) = \sum_{k=1}^n \phi_{ik} \eta_k(t) \tag{2}$$

where  $\Phi$  represents the mode shapes matrix of the structure,  $\eta(t)$  is the modal coordinate, the subscript  $i$  means the DOF whose response is observed, and the subscript  $k$  denotes the participation mode.

After obtaining the natural frequencies and damping ratios of the structure, we can calculate the modal coordinates by using the Duhamel integral when the structure is excited by a seismic wave  $\ddot{u}_g(t)$ :

$$\eta_k(t) = \frac{\Gamma_k}{\omega_{Dk}} \int_0^t \ddot{u}_g(\tau) \sin \omega_{Dk}(t-\tau) \exp[-\xi_k \omega_k(t-\tau)] d\tau = \Gamma_k v_k(t) \quad (3)$$

where  $\omega$  indicates the natural frequency of the undamped system, the subscript  $D$  denotes the parameter in damped system,  $\xi$  is the damping ratio,  $v_k(t)$  is defined as the modal displacement response caused by a SDOF system whose dynamic parameters are equal to the corresponding parameters in the  $k$ th mode of the MDOF structure under the ground excitation  $\ddot{u}_g(t)$ , and  $\Gamma$  represents the participation factor:

$$\Gamma_k = \phi_k^T \mathbf{M} \mathbf{r} \quad (4)$$

The equation of motion in modal coordinates with mass normalized mode shape gives:

$$\ddot{\eta}_k(t) + 2\xi_k \omega_k \dot{\eta}_k(t) + \omega_k^2 \eta_k(t) = -\phi_k^T \mathbf{M} \mathbf{r} \ddot{u}_g(t), \quad k = 1, 2, \dots, n \quad (5)$$

By substituting Equations (3) and its first time derivative  $\dot{\eta}_k(t)$  into (5), the relative acceleration in modal coordinates  $\ddot{\eta}_k(t)$  can be calculated.

As a result, the absolute acceleration of the  $i$ th floor in physical coordinates can be expressed as:

$$\ddot{u}_i(t) = \sum_{k=1}^n \left( \phi_{ik} \left( \begin{aligned} & \left( 2\xi_k^2 \omega_k - \frac{\omega_k^2}{\omega_{Dk}} \right) \Gamma_k \int_0^t \ddot{u}_g(\tau) \sin \omega_{Dk}(t-\tau) \exp[-\xi_k \omega_k(t-\tau)] d\tau \\ & - 2\xi_k \omega_k \Gamma_k \int_0^t \ddot{u}_g(\tau) \cos \omega_{Dk}(t-\tau) \exp[-\xi_k \omega_k(t-\tau)] d\tau \end{aligned} \right) \right) \quad (6)$$

If we neglect the terms including the damping ratio in the equation [17], the absolute acceleration of the measured DOF can be approximately formulated as:

$$\ddot{u}_i(t) = \sum_{k=1}^n \omega_k^2 \phi_{ik} \eta_k(t) = \sum_{k=1}^n \omega_k^2 \phi_{ik} \Gamma_k v_k(t) \quad (7)$$

We use the modal displacement response  $v_k(t)$  and modal velocity response  $\dot{v}_k(t)$  to constitute the state-space equation. Consequently, the state-space equation in continuous time can be formulated as:

$$\dot{\mathbf{x}}_k = \mathbf{A}_c \mathbf{x}_k + \mathbf{B}_c \mathbf{p}_k + \mathbf{w}_k^x \quad (8)$$

$$\mathbf{y}_k = \mathbf{H}_c \mathbf{x}_k + \mathbf{v}_k \quad (9)$$

$$\mathbf{z}_k = \mathbf{L}_c \mathbf{x}_k \quad (10)$$

where the process noise  $\mathbf{w}_k^x$  and measurement noise  $\mathbf{v}_k$  are assumed to be white, zero-mean, uncorrelated, with known covariance matrixes  $\mathbf{Q}^x$  and  $\mathbf{R}$ , respectively, and the system matrixes are formed by modal parameters.

In the process equation, the input  $\mathbf{p}_k$ , that is the seismic wave  $\ddot{u}_g(t)$ , is unknown because there is no accelerometer on the structural base to record the acceleration. Similar to the reference [13], we use a additional fictitious process combined with a Gaussian random walk model to estimate the input and state simultaneously.

### Numerical Simulation

Numerical simulations were conducted to verify the proposed approach of estimating the relative displacement and inter-story drift from the absolute acceleration of a story. A three-story structure is considered in this section. Figure 2 presents the model together with the structural parameters, including the damped mass and inter-story stiffness. The damping ratios in the first and second modes were assumed as 2% and 3%, respectively, and the damping ratio in the third mode was decided by Rayleigh damping. The structural natural frequencies and damping ratios are listed in Table 1.

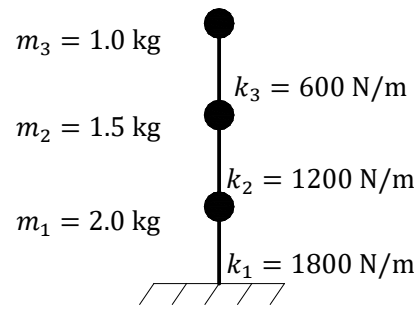
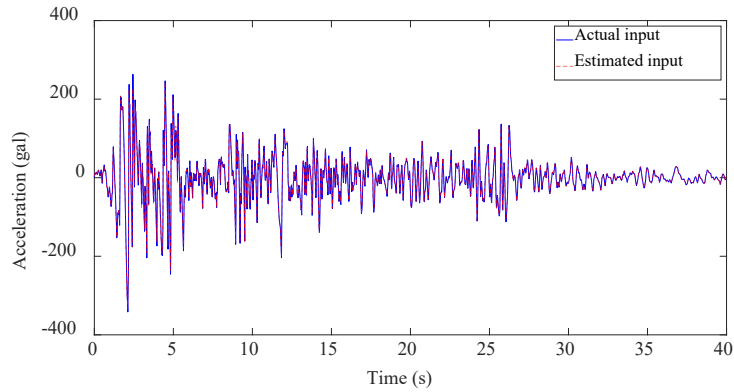


Figure 2. Simulation model of the three-DOF structure

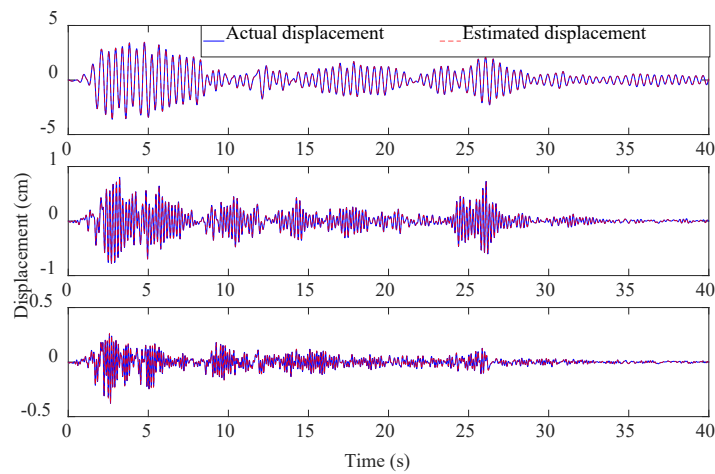
Table 1. Modal information of the three-DOF structure

	Frequency (Hz)	Damping ratio (%)
First	2.31	2.00
Second	4.94	3.00
Third	7.34	4.16

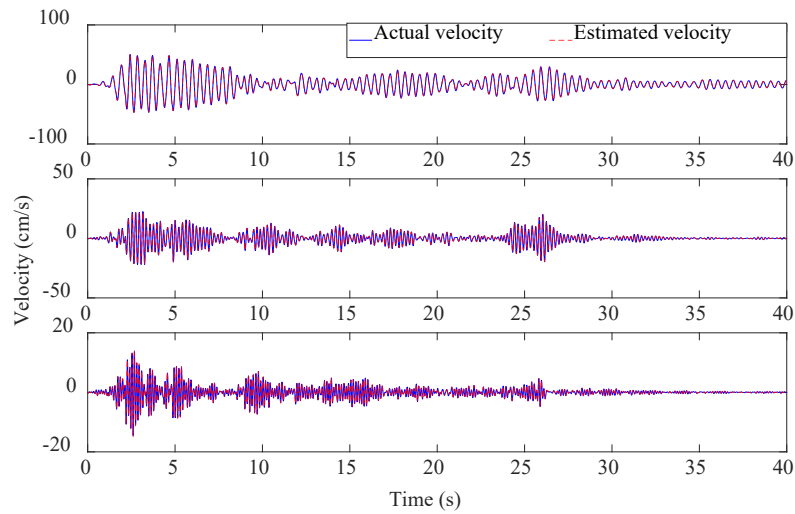
The typical ground acceleration, El Centro earthquake wave (NS component), was taken as an example. The structural time history responses were analyzed by Newmark beta method. We selected the absolute acceleration of the first floor as the observation data. The measurement noise  $\mathbf{R}$ , process noise  $\mathbf{Q}^x$ ,  $\mathbf{Q}^p$  of the state and input were set to  $10^{-2}\mathbf{I}$ ,  $10^{-4}\mathbf{I}$  and  $10^{10}\mathbf{I}$  ( $\mathbf{I}$  is an identify matrix of appropriate dimension), respectively. The input and state including the modal displacement responses  $v_k(\omega_k, \xi_k, \ddot{u}_g, t)$  and modal velocity responses  $\dot{v}_k(\omega_k, \xi_k, \ddot{u}_g, t)$  were evaluated using the Kalman filter. As can be seen in Figure 3, the filter could make a highly accurate estimation of the external force, and the responses in higher modes were recovered as were the lower modal vibrations regardless of their low amplitudes.



(a) Estimated input



(b) Estimated modal displacement responses of first (top), second (middle), and third (bottom) modes



(c) Estimated modal velocity responses of first (top), second (middle), and third (bottom) modes

Figure 3. Input and state estimation using modified Kalman filter

Next, the relative displacements of all floors were calculated using Equation (10). As shown in Figure 4, the estimated time history responses match the actual responses, indicating a good estimation of structural deformation. To consider the effect of environmental noise and investigate the robustness of the proposed approach, the responses were calculated at the 5% and 10% levels of the signal RMS noise. The maximum relative displacement was extracted, and subsequently the maximum inter-story drift was determined. As can be seen in Figure 5, the algorithm performs well at noise level of 5%, and the efficiency will decline as the noise increases. In addition, the estimation of relative displacements of all floors and the inter-story drifts of the bottom floors is robust against the disturbances, and the estimation of inter-story drift of the floor with minor deformation is susceptible to noise.

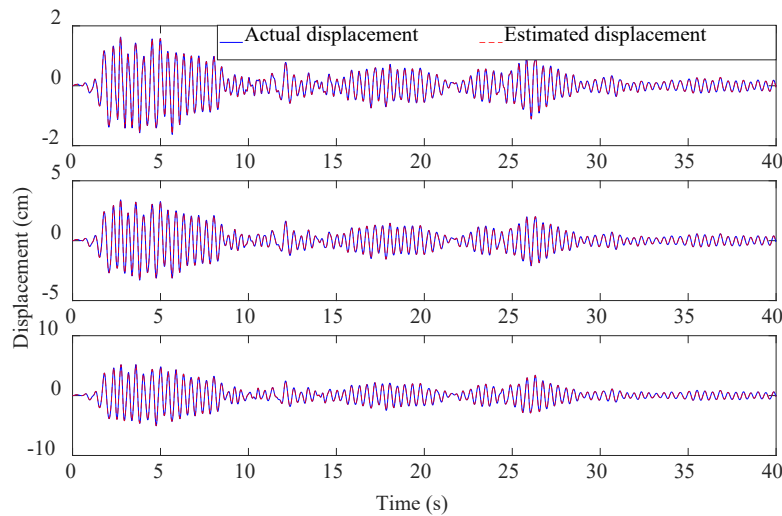
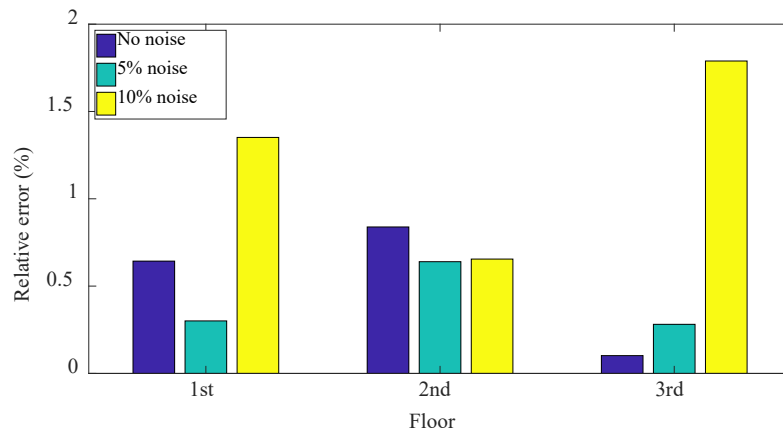
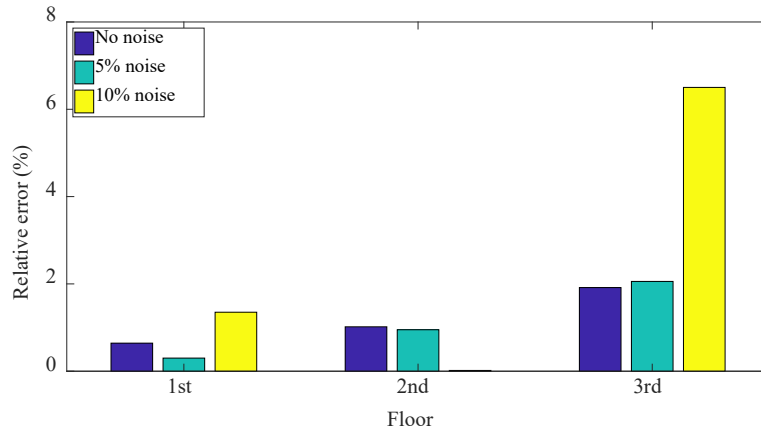


Figure 4. Estimated displacements of first (top), second (middle), and third (bottom) floors



(a) Estimated relative displacement



(b) Estimated inter-story drift

Figure 5. Relative maximum error for different noise levels

### Conclusion

This paper presented a way to estimate the relative displacement time history and maximum inter-story drift of MDOF shear structures merely from the absolute acceleration of a single floor recorded by a sensor. Numerical simulations proved that the system state and undetected input can be simultaneously and accurately estimated based on the state-space system, and the relative displacement time history and maximum inter-story drift can also be obtained with a small error even under strong environmental disturbances, providing reliable evidence for making structural assessments.

On the other hand, in the paper we just investigate a simple scenario in which the modal parameters are known, the structure is linear and mildly damped. In the future, we will focus on the estimation of maximum inter-story drift of the seismic isolation structures and supplementally damped buildings with the unknown modal information.

### Acknowledgements

The study was partially supported by the ‘Design the Future’ Award of Keio University and the KLL (Keio Leading-edge Laboratory) 2019 Ph.D. Program Research Grant.

### References

- [1] Mita A 2003 Structural dynamics for health monitoring Nagoya, Japan: Sankeisha
- [2] 2010 Code for seismic design of building. China: Ministry of Housing and Urban-Rural Development of the People's Republic of China
- [3] 2013 The building standard law. Japan: The Building Center of Japan
- [4] 2010 Minimum design loads for buildings and other structures. USA: American Society of Civil Engineers
- [5] Gomez F, Park J W, Spencer Jr B F 2018 Reference - free structural dynamic displacement estimation method. Structural Control and Health Monitoring, **25** e2209. <https://doi.org/10.1002/stc.2209>

- [6] Kasai K, Mita A, Kitamura H, et al 2013 Performance of seismic protection technologies during the 2011 Tohoku-Oki earthquake. *Earthquake Spectra*, **29** S265-S293. <https://doi.org/10.1193/1.4000131>
- [7] Dan M, Ishizawa Y, Tanaka S, et al 2015 Vibration characteristics change of a base-isolated building with semi-active dampers before, during, and after the 2011 Great East Japan earthquake. *Earthquake and Structures*, **8** 889-913. <https://doi.org/10.12989/eas.2015.8.4.889>
- [8] Siringoringo D M, Fujino Y 2015 Seismic response analyses of an asymmetric base - isolated building during the 2011 Great East Japan (Tohoku) Earthquake. *Structural control and health monitoring*, **22** 71-90. <https://doi.org/10.1002/stc.1661>
- [9] Tong Y, Xie L, Xue S, et al 2017 Performance of a passively-controlled steel building before and after the 2011 great east japan earthquake. *Proceedings of the Eleventh International Workshop on Structural Health Monitoring (California, USA)*. <https://doi.org/10.12783/shm2017/14134>
- [10] Brewick P T, Johnson E A, Sato E, et al 2018 Constructing and evaluating generalized models for a base - isolated structure. *Structural Control and Health Monitoring*, **25** e2243. <https://doi.org/10.1002/stc.2243>
- [11] Feng D, Feng M Q 2016 Vision - based multipoint displacement measurement for structural health monitoring. *Structural Control and Health Monitoring*, **23** 876-890. <https://doi.org/10.1002/stc.1819>
- [12] Gillijns S, De Moor B 2007 Unbiased minimum-variance input and state estimation for linear discrete-time systems with direct feedthrough. *Automatica*, **43** 934-937. <https://doi.org/10.1016/j.automatica.2006.11.016>
- [13] Azam S E, Chatzi E, Papadimitriou C 2015 A dual Kalman filter approach for state estimation via output-only acceleration measurements. *Mechanical Systems and Signal Processing*, **60** 866-886. <https://doi.org/10.1016/j.ymssp.2015.02.001>
- [14] Xue S, Xu K, Liyu X, et al 2019 Crack sensor based on patch antenna fed by capacitive microstrip lines. *Smart Materials and Structures*, **28** 85012. <https://doi.org/10.1088/1361-665X/ab2834>
- [15] Tchafa F M, Huang H 2018 Microstrip patch antenna for simultaneous strain and temperature sensing. *Smart Materials and Structures*, **27** 65019. <https://doi.org/10.1088/1361-665X/aabd47>
- [16] Yoshimoto R, Mita A, Okada K 2005 Damage detection of base - isolated buildings using multi - input multi - output subspace identification. *Earthquake engineering & structural dynamics*, **34** 307-324. <https://doi.org/10.1002/eqe.435>
- [17] Clough R W, Penzien J 2005 *Dynamics of structures USA: Computers & Structures, Inc*

# Life-Cycle Monitoring of CFRP using Piezoelectric Sensors Network

Xiao Liu <sup>a</sup>, Yishou Wang <sup>b</sup> and Xinlin Qing <sup>c\*</sup>

School of Aerospace Engineering, Xiamen University, Xiamen 361005, China

<sup>a</sup>liuxiao@stu.xmu.edu.cn; <sup>b</sup>wangys@xmu.edu.cn; <sup>c</sup>xinlinqing@xmu.edu.cn

**Keywords:** Resin Infusion, Damage Identification, Piezoelectric Sensor Network, Structural Health Monitoring

**Abstract.** Vacuum Assisted Resin Infusion (VARI) process is suitable for manufacturing complex large-scale composite structures and has the potential for low cost and mass production. However, the inappropriate process parameters such as incomplete resin flow and the uneven cure occurred will lead to some defects such as dry spots and delamination. In the present work, the concept of Networked Elements for Resin Visualization and Evaluation (NERVE) with the piezoelectric lead-zirconate-titanate (PZT) sensors as the base unit was used to monitor the internal state of composite structure during its life-time. The capability of PZT sensors in the NERVE to monitor two important parameters during the manufacturing process including the flow front of resin and progress of reaction (POR), was investigated. The Lamb waves generated by PZT, propagating in the mold/composite, was used to measure the parameters. The resin flow front was analyzed using optical detection at the same time. The flow front position over time and the influence of the length of sensing path covered by resin were delivered. The effects of different resin cure state on Lamb signal attenuation and energy leakage were also obtained. The change of amplitude was integrated to get the POR curves, so the resin cure state could be also monitored. After the composite was demoulded, the network was used continuously to identify the artificial damages with the fused probability-based diagnostic imaging (PDI). Experimental results indicate that the NERVE has the ability to realize the full life-cycle health monitoring of composite structures.

## Introduction

Advanced composite materials are being used on almost all modern aircraft due to their advantages of high specific strength, high specific stiffness and tailoring of mechanical properties. However, it is still difficult to precisely manufacture co-cured large-scale carbon fiber reinforced plastics (CFRP) structures and ensure their structural integrity through their life [1]. The life-cycle monitoring of CFRP includes the manufacturing process and the service stage. This paper is about the study demonstrating the sensing method based on the piezoelectric sensors network for continuously monitoring the internal state of composite structures.

As a new type of low-cost molding technology for large-scale composite materials with the advantages of excellent product performance, low porosity and good adaptability [2,3], the VARI has attracted more and more attention in the field of aviation and spaceflight. However, there are still many difficulties in the VARI process, such as the control of the resin flow, the prevention of dry spots and the delamination and residual stress that closely related to the control parameter of the process [4,5]. These flaws seriously jeopardizing the structural health cannot be easily corrected, because the trial-and-error approaches are inefficient and costly to determine suitable process parameters [6-8]. Therefore, it is necessary to carry out in-suit monitoring in the manufacturing process to adjust the process parameters in time to avoid the occurrence of



defects. The VARI process is accompanied by a series of complex reaction processes, such as heat transfer, mass transfer, rheological reaction and polymerization reaction [9]. While the Lamb waves propagating in the homogeneous mold is suitable for the in-line VARI process monitoring, because part of energy of the Lamb wave will leak into the liquid or viscoelastic resin in the filling and curing process. Based on the propagation characteristics of Lamb waves, the signal feature changes of leaky Lamb waves can be used to track different stage of the manufacturing process [10-12]. Different from the previous works, this study embedded several PZT sensors into the composite to obtain Lamb wave signals in a pitch-catch way, which is suitable for the monitoring of large-scale composite.

In the service stage of CFRP, ultrasonic waves are still attractive because of their relatively long distance of propagation and sensitivity to discontinuities along the propagation path [13,14]. The active ultrasonic Lamb waves-based structural health monitoring (SHM) is considered to be one of the promising methods, and PZTs are one kind of preferred actuators and sensors [15]. Among the algorithms for diagnostic imaging, the probability-based diagnostic imaging (PDI) can weaken or even eliminate the direct interpretation of the ultrasonic guided wave signals and the effect of dispersion and anisotropy [16-18].

The Networked Elements for Resin Visualization and Evaluation (NERVE) [19] based on the concept of distributed multifunctional sensor network of SMART (Stanford Multi-Actuator-Receiver Transduction) Layer [20] can monitor the manufacturing parameters (resin flow front and cure state) in the Liquid Composites Molding (LCM) process effectively. This paper firstly carried out the in-suit monitoring of VARI process experiment to validate the influence of the length of sensing path covered by resin and different cure state on Lamb signal attenuation and energy leakage. Then after the composite was demoulded, damage identification experiment was conducted with the fusion PDI approach of multiple frequencies. The experimental results indicated that the NERVE has the ability to realize the full life-cycle health monitoring of composite structures.

## **Manufacturing monitoring**

### ***Experimental setup for VARI process***

Before the experiment, three SMART layers were hollowed out for the resin to flow easily and nine circular PZT sensors ( $\Phi 8 \text{ mm} \times 0.33 \text{ mm}$ ) with the piezoelectric strain constant of about  $d_{33} = 510 \times 10^{-12} \text{ C/N}$  were mounted on the bonding pad of the polyimide film Kapton® substrate, as shown in Fig. 1.

The fiber prefabrication ( $400 \text{ mm} \times 400 \text{ mm} \times 2 \text{ mm}$ ) consisted of eight T300 woven carbon fiber plies was placed in the central area of the surface of a 6061-Aluminum alloy plate mold ( $600 \text{ mm} \times 600 \text{ mm} \times 2 \text{ mm}$ ). Then the layers were inserted into a specific position between the sixth and seventh plies to form a sensor network which were shown in Fig. 5. After that, seal the system and pump the air. Then the ScanGenie II developed by Acellent Technologies, Inc. at Sunnyvale, USA was used for generating and receiving Lamb wave signals as the baselines of different sensing paths. Due to the slight difference in the performance of piezoelectric sensors, the optimal excitation frequencies of different paths are obtained. The sensing paths and different excitation characteristics for manufacturing monitoring in Fig. 1 are listed in Table 1.

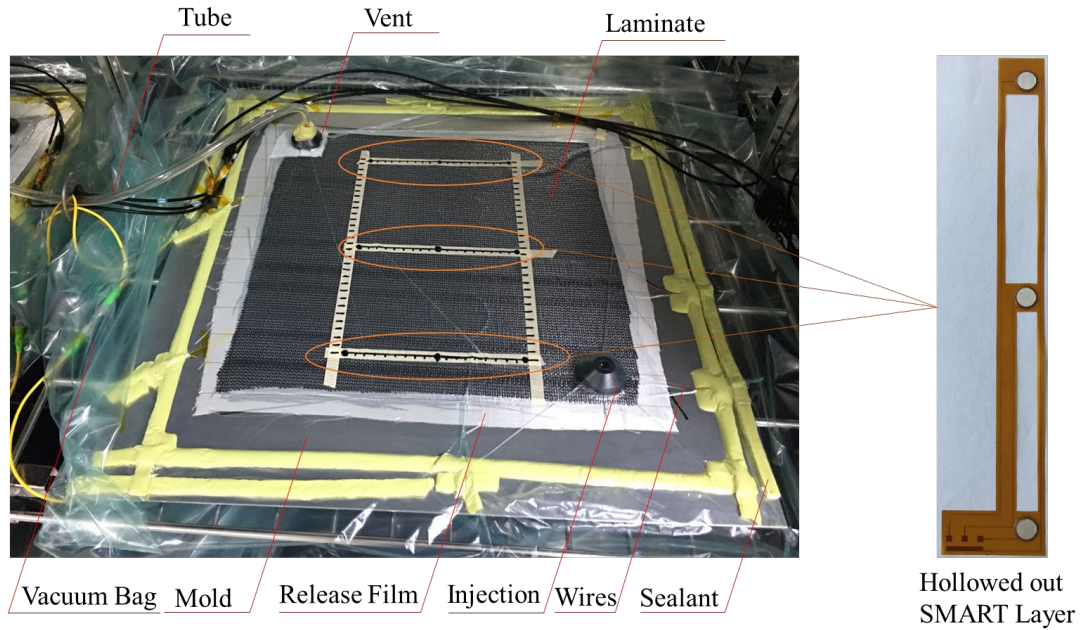


**Fig. 1** The scene picture of the experiment for the VARI process.

**Table 1** Paths and excitation characteristics of piezoelectric sensor network

Path	Amp (V)	f(kHz)	Path	Amp (V)	f(kHz)	Path	Amp(V)	f(kHz)
P4-3	60	190	P4-2	60	180	P8-6	75	170
P5-3	60	180	P5-2	70	190	P9-4	70	180
P6-3	70	220	P6-2	70	180	P9-5	70	180
P7-3	75	170	P7-4	70	190	P9-6	70	190
P8-3	75	160	P7-5	60	180	P7-2	75	180
P9-3	75	180	P7-6	60	190	P8-2	75	160
P4-6	70	170	P8-4	70	160	P9-2	75	160
P7-9	70	190	P8-5	75	160			

Note: P4-3 means the sensing path that Sensor 4 is the actuator and Sensor 3 is the receiver in this paper.

The resin injection was carried out at room temperature. The resin used in this experiment was a mixture of epoxy resin (EC-TDS-IN2-Infusion-Resin) and curing agent (Formulated Amine) with a mixed ratio of 0.3 by weight. The low viscosity of 550 mPa.s at room temperature ensured the infusion of the production. With the injection of resin, the response signals excited by the narrowband five-peak sine waves modulated by Hanning window were collected continuously about every 2 minutes. A camera was placed at the top of the oven to track the resin flow front. After the resin filling process, clamped the resin tube and keep pumping the air. According to the resin cure curves, the whole system was cured at a constant temperature (50 °C) for 6 hours to eliminate the effect of temperature changes on the Lamb waves signal. The response signals were collected every 5 minutes in the resin curing process.

**Experimental results of VARI process**

For each sensing path listed in Table. 1, ninety-five sets of response signals were collected in about 6.5 hours. Among them, the first twenty sets of response signals were collected in the filling process and the others were in the curing process. The complexity of the waveguides and

the influence of experimental environment made it very difficult to determine the modes, so the first wave packet (the fastest mode) was selected to compare the amplitude and attenuation during the whole process.

### Resin filling stage

In the resin filling stage, the normalized amplitude curves versus filling times are shown in Fig. 2. Some interesting issues can be found: the amplitude fluctuated slightly before the corresponding sensing paths were covered by liquid resin. In the optical detection shown in Fig.2, the sequences of the sensors covered by resin were sensor 3,2,6,5. The order of the amplitude curves tended to decline is the same and implied the sequence of the sensing path started to be covered. Then the amplitude continued to decline because partial energy of Lamb waves would leak into the composite through the liquid-solid boundary. When the sensing paths were fully covered, the signals tended to be stable and the amplitude remained zero.

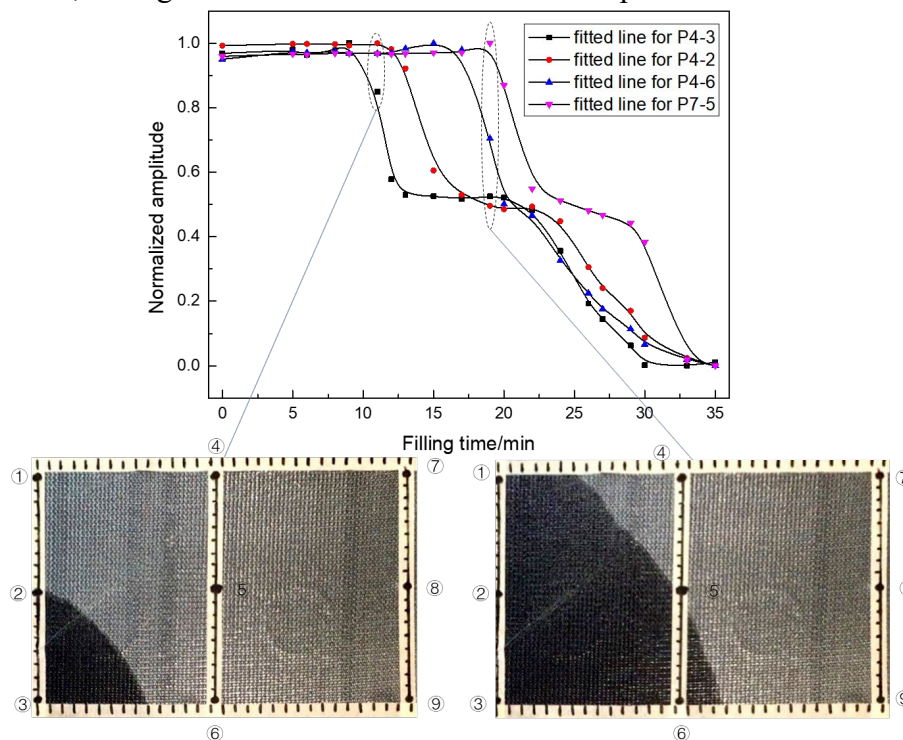


**Fig. 2** The normalized amplitude curves versus filling time and the optical detection results.

In order to reveal the relationship between the resin covering length and the amplitude decrease, four long paths were chosen and the normalized amplitude curves versus length covered by resin were showed in Fig.3. It can be found that the amplitude decreased with the length covered by resin. The signal amplitudes of corresponding paths decrease sharply when the resin flow front reaches near the PZTs (less than 10 cm), no matter the actuator or the receiver. However, when the flow front reached the middle of the path and was more than 10 cm away from the actuator and the receive, the effect of the resin covering length on the signal amplitude is much lower. Thus, the resin flow front in the filling process can be monitored by the Lamb waves effectively.

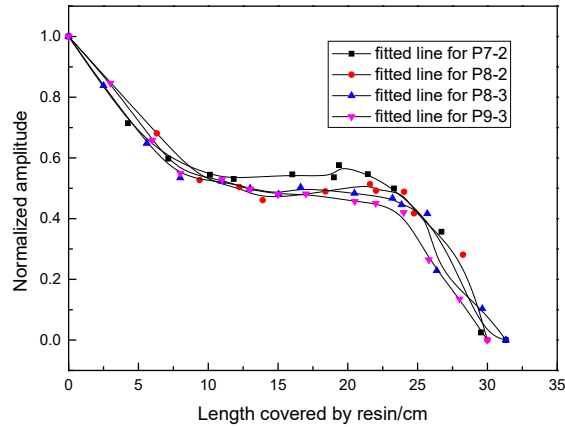


**Fig. 3** The relationship between the resin covering length and the amplitude.

*Resin curing stage*

In the curing stage, the thermoset resin undergoes a molecular crosslinking process during which it changes irreversibly from being viscous liquid to rubbery state and finally to rigid and highly cross-linked polymer solids. The amplitudes rise sharply with the crosslinking reaction and fluctuate slightly until they stabilize.

When the resin is fully cured, it is in the glass state and can be considered as an elastic material. The effect of viscoelasticity on guided waves is negligible. So, the attenuation of the Lamb waves  $\alpha$  at cure time  $t$  was calculated from Eq. (1):

$$\alpha = 20\log(A_0/A_t)/L \tag{1}$$

where  $A_t$  and  $A_0$  are the amplitudes of the first peak in the waveform obtained at cure time  $t$  and the end of the process,  $L$  is the length of the sensing path.

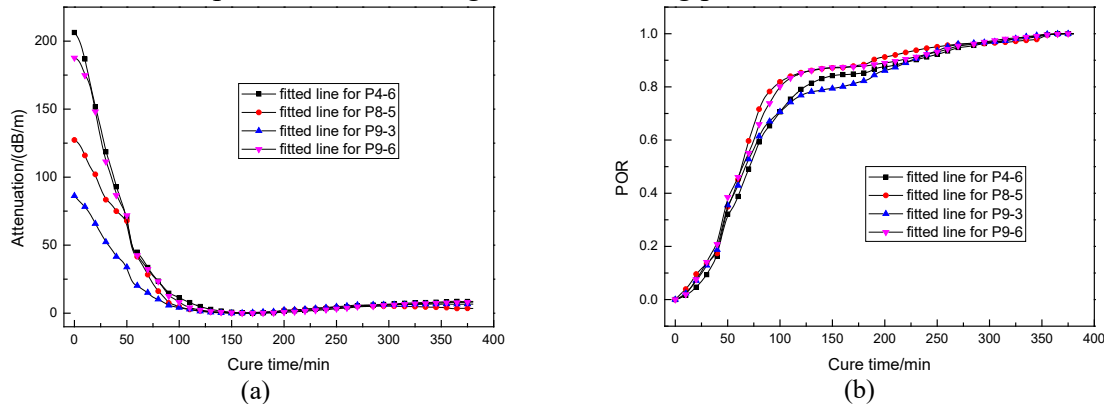


**Fig. 4** (a) The attenuation of the Lamb waves obtained during the cure process; (b) The progress of crosslinking reaction over cure time.

The attenuation curves of the Lamb waves obtained during the cure process are shown in Fig. 4(a). The attenuations reach the maximum at the beginning and decrease with the cure process. At 150 minutes after cure, the attenuations become close to zero and the rate of reaction is very slow until the resin is fully cured.

The normalized amplitude represents the cross-linking process, and the changes of amplitude represent the changes in the rate of reaction. Since the cross-link reaction is irreversible, so the absolute values of changes are integrated using Eq. (2):

$$\int_{t_1}^{t_n} X dt \approx \sum_{i=1}^{n-2} (t_{i+1} - t_i) \frac{1}{2} (|x_{i+2} - x_{i+1}| + |x_{i+1} - x_i|) \quad (2)$$

in which  $x_i$  is the amplitude at time  $t_i$ . Then the data is normalized to get the POR curves of different sensing paths over cure time, which are shown in Fig. 4(b). It can also be concluded that the progress of crosslinking reaction increases with the cure time, and becomes slow after 150 minutes and the resin is fully cured after 300 minutes. So the real-time monitoring of resin cure process can be achieved by the POR curves using the NERVE.

**Service monitoring**

**Experimental setup for damage identification**

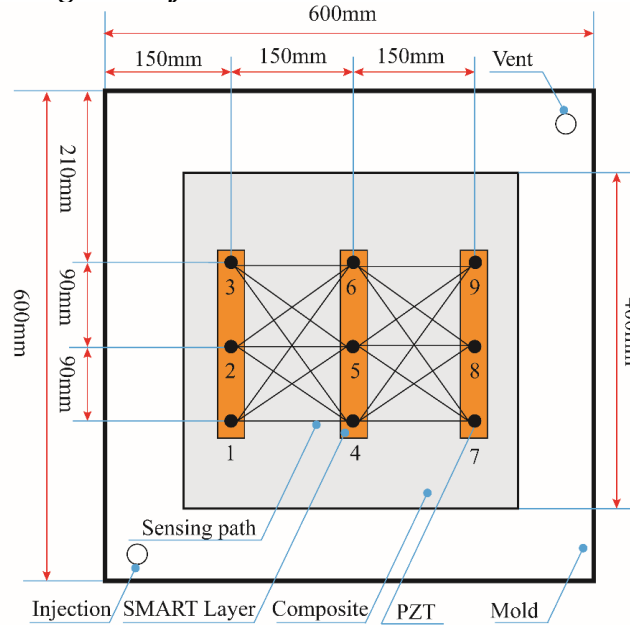


**Fig. 5** The network of sensing paths for damage identification.

After the manufacturing process, the composite was demoulded and the damage identification experiment was carried in the room temperature. The network of sensing paths for damage identification is showed as Fig. 5. To reduce the cost, three cases of six artificial damages with the solid adhesive tape of 20 mm in the diameter and 2 mm in the thickness were bonded on the surface of the panel in this part. Different from the manufacturing process, the frequencies that are more sensitive to the damage in the composite plate needed to be selected. Because the ultrasonic waves decay faster in CFRP than in aluminum, so lower frequencies should be selected. The excitation frequencies are 50 kHz, 60 kHz and 70 kHz for the sensing path in Fig. 5. Three frequencies are fused and the scaling parameter  $\beta$  is set to be 0.3.

**Experimental results for damage identification**

According to the relationship with the sensing paths, six artificial damages can be divided into three cases: the intersection of three paths, the intersection of two paths and only on one path. The different diagnostic images concerning the presence of probability of damages are shown as Fig. 6.

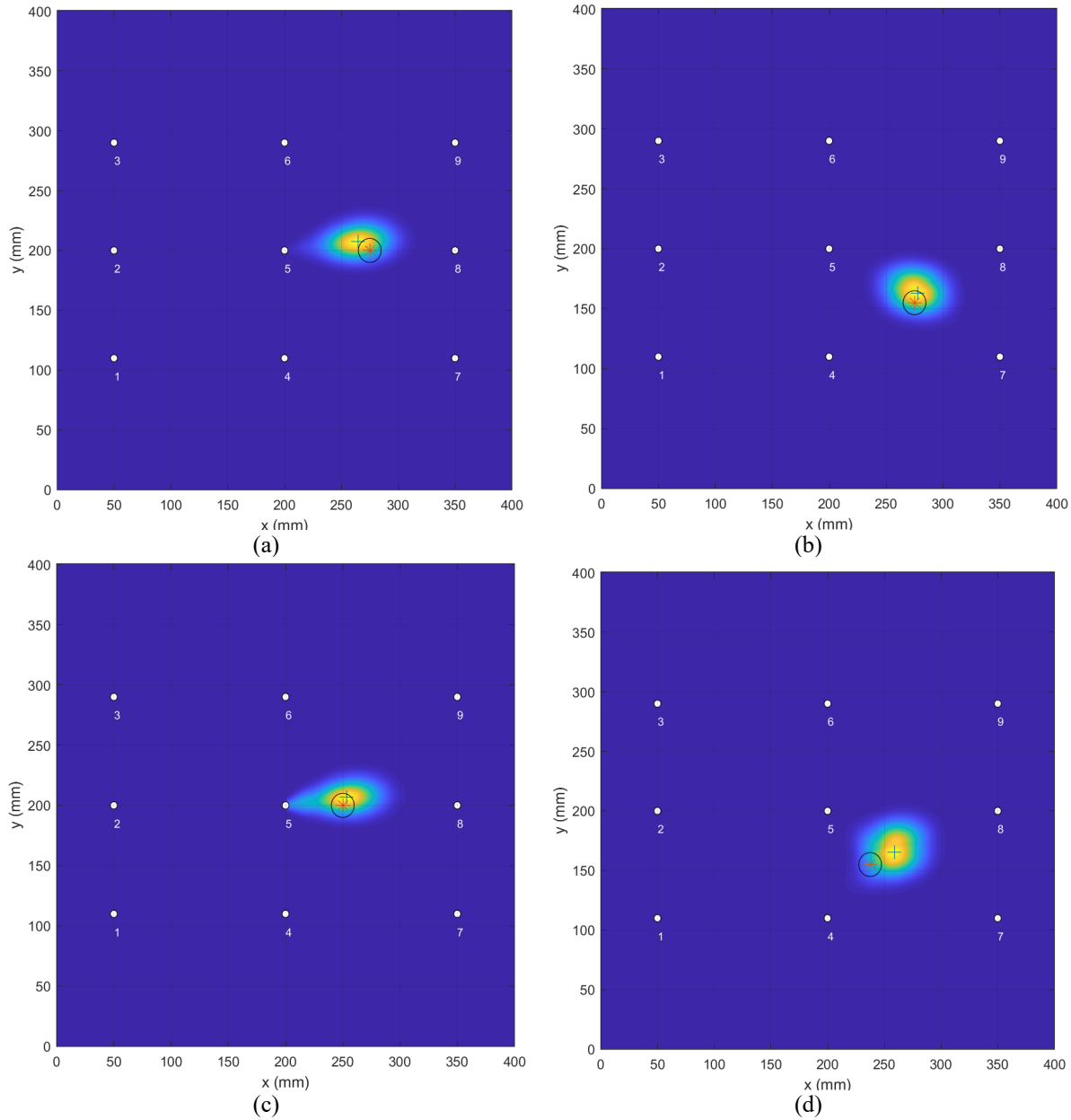


**Fig. 6** The diagnostic images concerning the presence of probability of three cases of damages (the colour coding indicates its relative probability (blue: low to yellow: high), the blue “+” is the damage centers calculated by the fused PDI and the red “\*” is the actual artificial damage center). (a) intersection of three paths, (b) intersection of two paths, (c) and (d) only one path.

The Fig. 6 gives the diagnostic images and the results indicate that the fused PDI algorithm can locate different damages accurately. In order to further quantify the damage detection capability of embedded sensor network, the damage center of actual damage and the results obtained by the PDI are extracted and the relative distances between them are calculated. The relative error which is the ratio of relative distance to the length of the shortest sensing path (150 mm in this paper) is also calculated and showed in Table 2. The maximum localization error is 24.19 mm and the relative error is 16%. The results further indicate that the embedded sensor

network and the fused PDI algorithm are capable of pinpointing damage in the service stage of composite structure.

**Table 2** *The damage identification results of embedded sensor network using fused PDI.*

Number	Actual damage	Fused PDI	Relative distance (mm)	Relative error
1	(275,200)	(265.5,207)	11.80	8%
2	(275,155)	(277.5,162)	7.43	5%
3	(275,245)	(279,243)	4.47	3%
4	(100,200)	(101.5,204.5)	4.74	3%
5	(250,200)	(253.5,207)	7.83	5%
6	(237.5,155)	(258.5,167)	24.19	16%

### Conclusion

The experimental results indicate that the NERVE has the ability to realize the full life-cycle health monitoring of composite structures, including the resin flow front and cure state in manufacturing process and the damage identification in the service stage.

In the resin filling process of the VARI experiment, partial energy of Lamb waves would leak into the composite structure through the liquid-solid boundary. The order of the amplitude curves tends to decline implied the sequence in which the sensing path starts to be covered. When the resin flow front reaches near the PZTs (less than 10 cm), no matter the actuator or the receiver, the signal amplitudes of corresponding paths decrease sharply. But the effect of the resin covering length on the signal amplitude is much lower when the flow front is more than 10 cm away from the sensors. In the resin curing stage, the attenuations reach the maximum at the beginning and decrease with the cure process. At 150 minutes after cure, the attenuations become close to zero and the rate of reaction is very slow until the resin is fully cured, which is the same as the progress of crosslinking reaction by integrating the absolute values of amplitude changes.

After the composite is demoulded, six artificial damages with a kind of solid adhesive tape are bonded on the surface of the panel and the damages are identified using the fused PDI algorithm. The maximum localization error is 24.19 mm and the relative error is 16.13%. The diagnostic images concerning the presence of probability of damages and the damage localization results indicate that the embedded PZT sensor network is capable of pinpointing damage in the service stage of composite structure.

By comparing the propagation characteristic of Lamb waves, the in-line monitoring of the internal state of composite structure during its life time can be achieved by the NERVE under constant temperatures. But the effect of temperature changes on Lamb wave signals should be studied and the corresponding temperature compensation strategy is still a challenging problem needed to be solved in the real manufacturing and service environment.

### Reference

- [1] Minakuchi S, Takeda N, Takeda S I, et al. Life cycle monitoring of large-scale CFRP VARTM structure by fiber-optic-based distributed sensing[J]. *Composites Part A: Applied Science and Manufacturing*, 2011, 42(6):669-676.  
<https://doi.org/10.1016/j.compositesa.2011.02.006>
- [2] Laurenzi S, Casini A, Pocci D. Design and fabrication of a helicopter unitized structure using resin transfer moulding. *Composites Part A: Applied Science and Manufacturing*, 2014, 67:221-232. <https://doi.org/10.1016/j.compositesa.2014.09.007>

- [3] Konstantopoulos S, Hueber C, Antoniadis I, et al. Liquid composite molding reproducibility in real-world production of fiber reinforced polymeric composites: a review of challenges and solutions. *Advanced Manufacturing: Polymer & Composites Science*, 2019,5:3, 85-99. <https://doi.org/10.1080/20550340.2019.1635778>
- [4] Park CH, Woo L. Modeling void formation and unsaturated flow in liquid composite molding processes: a survey and review. *Journal of Reinforced Plastics & Composites* 2011; 30(11):957–977. <https://doi.org/10.1177/0731684411411338>
- [5] Kuentzer N, Simacek P, Advani SG, Walsh S. Correlation of void distribution to VARTM manufacturing techniques. *Composites Part A: Applied Science and Manufacturing*, 2007, 38(3):802–813. <https://doi.org/10.1016/j.compositesa.2006.08.005>
- [6] Khoun L, Palardy G, Hubert P. Relation between volumetric changes of unsaturated polyester resin and surface finish quality of fiberglass/unsaturated polyester composite panels. *Polymer Composites*, 2011, 32(9): 1473-80. <https://doi.org/10.1002/pc.21157>
- [7] Villière, Maxime, Guérout, Sébastien, Sobotka V, et al. Dynamic saturation curve measurement in liquid composite molding by heat transfer analysis. *Composites Part A: Applied Science and Manufacturing*, 2015, 69:255-265. <https://doi.org/10.1016/j.compositesa.2014.11.024>
- [8] Shin DD, Hahn HT. Compaction of thick composites: Simulation and experiment. *Polymer Composites*, 2004, 25(1): 49-59. <https://doi.org/10.1002/pc.20004>
- [9] Wang Y, Li Y, Wu D, et al. Progress on cure monitoring for Liquid Composite Molding. *Aeronautical Manufacturing Technology*, 2017(19):50-59.
- [10] Pavlopoulou S, Soutis C, Staszewski W J. Cure monitoring through time-frequency analysis of guided ultrasonic waves, *Plastics, Rubber and Composites* 41(2012)180-186. <https://doi.org/10.1179/1743289811Y.0000000052>
- [11] Hudson T B, Grimsley B W, Yuan F G. Development of a fully automated guided wave system for in-process cure monitoring of CFRP composite laminates, *Proceeding of 31st American Society for Composites Technical Conference and ASTM Committee*,2016.
- [12] Liu X, Li Y, Zhu J, Wang Y, Qing X. Monitoring of resin flow front and degree of cure in VARI process using multifunctional piezoelectric sensor network. *Polymer Composite*, accepted for publication.
- [13] Predoi M V, Castaings M, Hosten B, et al. Wave propagation along transversely periodic structures[J]. *Journal of the Acoustical Society of America*, 2007, 121(4):1935-0. <https://doi.org/10.1121/1.2534256>
- [14] Castaings M, Lowe M. Finite element model for waves guided along solid systems of arbitrary section coupled to infinite solid media[J]. *Journal of the Acoustical Society of America*, 2008, 123(2):696-0. <https://doi.org/10.1121/1.2821973>
- [15] Qiu L, Liu M, Qing X, et al. A quantitative multidamage monitoring method for large-scale complex composite[J]. *Structural Health Monitoring*, 2013, 12(3):183-196. <https://doi.org/10.1177/1475921713479643>

- [16] Wang D, Ye L, Lu Y, et al. Probability of the presence of damage estimated from an active sensor network in a composite panel of multiple stiffeners[J]. *Composites ence & Technology*, 2009, 69(13):2054-2063. <https://doi.org/10.1016/j.compscitech.2008.11.005>
- [17] Zhanjun Wu, Kehai Liu, Yishou Wang, et al. Validation and evaluation of damage identification using probability-based diagnostic imaging on a stiffened composite panel[J]. *Journal of Intelligent Material Systems & Structures*, 2014.
- [18] Liu K, Ma S, Wu Z, et al. A novel probability-based diagnostic imaging with weight compensation for damage localization using guided waves[J]. *Structural Health Monitoring*, 2016, 15(2):162-173. <https://doi.org/10.1177/1475921715627491>
- [19] Qing X, Liu X, Zhu J, Wang Y. In-situ monitoring of Liquid Composite Molding process using piezoelectric sensor network[J]. *Structural Health Monitoring*, accepted for publication.
- [20] Qing X, Beard S, Kumar K, et al. Advances in the development of built-in diagnostic system for filament wound composite structures. *Composites Science & Technology* 2006; 66(11-12):1694–1702. <https://doi.org/10.1016/j.compscitech.2005.11.007>

# Assessment of the Structural Integrity of Timber Utility Poles Using Ultrasonic Waves

Jad El Najjar<sup>1,a</sup> and Samir Mustapha<sup>2,b,\*</sup>

<sup>1</sup> American University of Beirut, Ashrafieh Beirut, Lebanon

<sup>2</sup> American University of Beirut, Ain El-Mraisse Beirut, Lebanon

<sup>a</sup>jje11@mail.aub.edu, <sup>b\*</sup>sm154@aub.edu.lb

**Keywords:** Structural Health Monitoring, Timber Utility Poles, Guided Waves, Macro Fiber Composites, Damage Detection, Embedded Length Assessment

**Abstract.** In this study, guided stress waves were used to evaluate the conditions of a timber utility pole experimentally and numerically using COMSOL Multiphysics. Macro Fiber Composites (MFCs), due to their flexibility and convenience to install on curved surfaces, were used to actuate and sense guided waves along the tested specimens. Based on the wave propagation characteristics in these types of structures, an MFC actuator ring, which was developed in the previous work, was applied to tune and enhance the propagating wave modes of interest. The designed ring was used to excite longitudinal ultrasonic wave modes, mainly  $L(0,1)$ , for the purpose of determining the embedded length of the pole. For the damage localization a single MFC excitation was used which proved to be more efficient than the actuator ring. Embedding the timber in soil had minimum impact on the wave propagation characteristics, given that the waves were confined in the timber pole with minimal leakage to the surrounding. The embedded length was determined accurately for sound and damage timber, using both experimental and numerical data with an error of less than 3 %. The deterioration in the timber structure, within the embedded region, was also evaluated with high accuracy of 93 %. Based on the obtained results, guided waves have high potential to be used as a non-destructive tool for the assessment and evaluation of timber utility poles.

## Introduction

The use of timber has commenced thousands of years ago and is still being used today in numerous applications. Being easy to manufacture and customize, practices vary from construction work, transportation applications, equipment, and infrastructure. When treated properly, timber can act as a substitute for many renowned materials such as steel and concrete. The cost of transportation and storage is low compared to other materials, in addition to the ability to withstand handling and surface damage due to the lightweight and tough properties [1]. When evaluating the integrity of timber utility poles, two parameters are mainly examined and correspond of the embedded length of the pole and the presence (position) of damage or decay in the embedded section [2]. Currently, surface non-destructive techniques are the most common in timber structures where longitudinal (compressional) and flexural (bending) stress waves are used for the evaluation process. These techniques include sonic echo (SE) and impulse response (IR) tests, where the embedded length and health state of the timber can be evaluated. Condition assessment of timber poles can be performed using guided waves where the presence of decay or damage can be detected. Various studies on this matter have been conducted with the use of machine learning techniques. Dackermann et al. [3] used support vector machines (SVM) on a network of tactile transducers that generate guided waves in timber poles. Different damage



cases were conducted on several timber and concrete pole specimens where the SVM was used to generate classification results for predicting damage conditions. Other signal processing techniques such as fast Fourier transform (FFT) and principal component analysis (PCA) were also used to process data from damaged specimens. In another study, Dackermann et al. [4] presented machine learning methods for pattern recognition to assess the health condition of timber poles. Guided waves were actuated and captured using a multi-sensor array mounted on the pole. Damage detection using a hierarchical data fusion algorithm was applied on timber poles in [5] with the use of guided waves. Multi-sensor arrays were also used in the model where the hierarchical approach lead to an enhanced accuracy when detecting damage in the timber pole.

In this study, guided waves have been used for the assessment of timber poles numerically using COMSOL Multiphysics and experimentally. Important features such as the embedded length and the health state of the timber pole has been evaluated by the means of Macro Fiber Composites (MFCs) (Smart Material corp., 2017). The application of an MFC-ring assisted in the generation of purely longitudinal wave modes, such as mode L(0,1), which were used in the evaluation process. The excitation frequency was selected according to a set of factors such as the number of propagating wave modes, dispersion and the number of MFCs required in the actuator ring. The effect of change in boundary conditions (traction free and soil embedment) on the length estimation and damage assessment was also investigated.

### Numerical FEA Model

Dispersion curves were generated using DISPERSE software [6] for a transversely isotropic timber pole, for the specimen under-study, with properties shown in Table 1. The group velocity can be directly used to characterize the propagating wave modes and can be calculated using the central transit time of each propagating packet. Propagating wave modes in circular structures are dependent on the circumferential order  $n$  [7]. Torsional modes T(n,m) involve the azimuthal component of the displacement vector, and longitudinal modes L(n,m) involve both radial and axial components of the displacement vector with  $n = 0$  where they propagate with axial symmetry along the cylinder [7]. Flexural wave modes are much more complicated and are non-axisymmetric with all three components of the displacement vector. For every circumferential order  $n \geq 1$ , there exists a flexural wave mode of a given family [7]. Group velocity plots for longitudinal and flexural waves of first order are displayed in Fig. 1.

*Table 1 Material properties of transversely isotropic white pine timber [8].*

Property	$E_L$ (GPa)	$E_R$ (GPa)	$E_T$ (GPa)	$G_{LR}$ (GPa)	$G_{LT}$ (GPa)	$G_{RT}$ (GPa)	$\rho$ (kg/m <sup>3</sup> )
Value	11.11	0.866	0.866	0.577	0.577	0.533	380

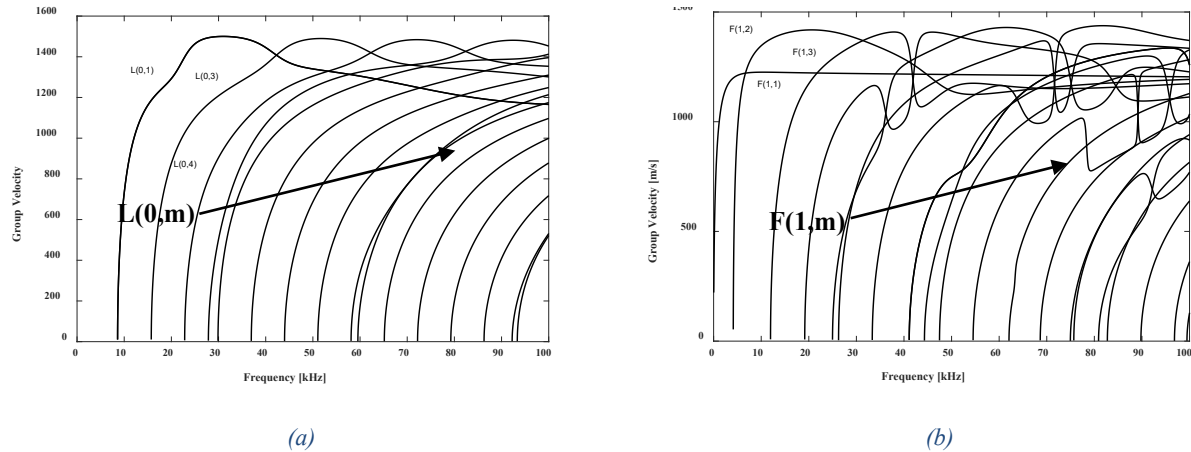


Fig. 1 Dispersion curves: Group velocity versus frequency for (a) longitudinal and (b) flexural wave modes.

Ring Design and Wave Mode Tuning. For the assessment of timber poles, it is important to tune the propagating modes based on the dispersion curves. The high number of waves, from the dispersion curves, was shown to be present even at low frequencies with a significant effect of dispersion. In particular, flexural modes are more complicated than longitudinal ones and are present in high orders (for  $n \geq 1$ ). The generation of non-axisymmetric wave modes (flexural modes) can be restricted by the excitation of a transducer ring of piezoelectric elements, equally spaced around the circumference of the pole [9]. This configuration suppresses flexural modes and enhances the propagation and reflections of longitudinal waves present at the frequency of excitation. In order to suppress flexural modes, the total number of transducers placed around the circumference must be greater than or equal to the highest circumferential order ( $m$ ) of flexural modes propagating at the excitation frequency [9]. From the dispersion curves shown in Fig. 1 (b), there exist  $F(4,m)$  with the highest circumferential order of 4 at 12.5 kHz. This means that a minimum of 4 MFCs must be mounted, equally spaced around the circumference, to suppress the propagating flexural modes at this excitation frequency. At higher frequencies, the maximum circumferential order is  $> 7$  which requires the actuation of  $> 8$  MFCs around the circumference. In our design, the excitation frequency was selected at 12.5 kHz and the MFC ring consisted of 8 elements. This will allow us to experiment three different actuation configurations corresponding of single, four and eight-MFCs. The verification of exciting an MFC ring around the pole's circumference was depicted in our previous study [10]. By actuating multiple MFCs in the ring, unwanted flexural modes were suppressed, and the longitudinal modes propagated with an enhanced amplitude.

Effect of Boundary Conditions and Damage Induction. The evaluation of embedded length and health state of a timber pole was scrutinized numerically using COMSOL Multiphysics [11] by examining the propagation of guided waves in traction free and embedded boundary conditions. For utility poles in specific, the recommended embedment depth is 10% of the total pole's length plus 2 ft (61 cm). The total length of the pole modeled in COMSOL was 5.5 meters, in order to account for a suitable embedment length of 1.45 meters. This selected length was the expected value of an in-service embedded utility pole with an 8-meter length. For the soil – timber interface, a contact node was added to the common surface between both timber and soil where the contact pressure method used was Penalty. Damage was introduced to the timber structure in the embedded section by removing a small section of the timber. The numerical

model for damaged timber was simulated for traction free and embedded models with the application of the MFC ring. Fig. 2 (a) and (b) shows the MFC actuator and sensors placement along with the embedded boundary condition for the damaged model. As for applying mesh to the model, the wavelength found from the dispersion curves were used to calculate the mesh size, where an average of 6-10 elements per wavelength is required [12, 13]. Additional convergence tests were performed on the calculated mesh size and yielded 5.5 mm, with around 16 elements per wavelength.

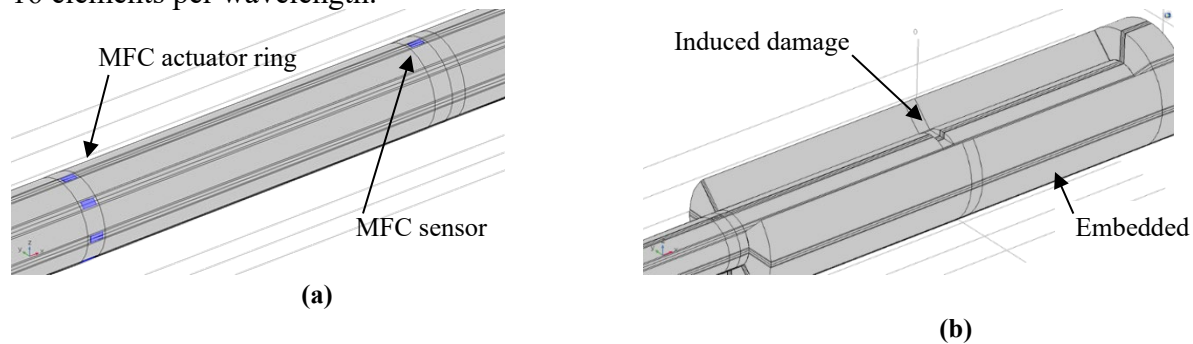


Fig. 2 5.5-meter timber pole in COMSOL: (a) actuator ring and sensor placement and (b) embedded boundary condition for the damaged structure.

### Experimental Setup

One of the most common types of timber in the electric distribution industry (utility poles) is Scots pine (also known as *Pinus Sylvestris* [14] or white pine) which was used in the experimental setup. A validation process was undergone on an 8-meter timber pole where the effect of change in boundary conditions and damage induction was inspected. Multiple MFC actuation configurations (MFC ring) for tuning the propagating waves were tested to determine the embedded length and location of the damage. The embedded length corresponds to the distance between the MFC sensor and bottom edge of the pole, and the damage location corresponds of the distance between the sensor and the damage. MFCs of type M-2814 P1 were coupled to the pole's surface using Loctite's E120 HP epoxy adhesive at different locations along the specimen. In order to create an arrangement where the variable is the embedded condition, a wooden box was inserted at the back end of the pole where soil can be added and removed. Fig. 3 (a) displays the simply supported 8-meter pole where the bottom section was inserted into the box. The testing was only performed on the bottom end of the pole, which was the location of interest, to evaluate the embedded section and acquire less reflections from the top end of the pole. Last, the frequency of excitation was selected at 12.5 kHz and the actuator ring contained 8 MFCs, similar to the numerical model. The actuator ring and sensor placement are shown in Fig. 3 (b).

A damage was induced in the structure where the timber pole was cut in the section located inside the wooden box (embedded section). The experiments were performed for traction free and embedded conditions for sound (pre-damage) and damaged timber to investigate the effect on guided waves and embedment length estimation. The location of the damage was determined from the setups for both boundary conditions. Fig. 3 (c) shows the damage created in the section of the pole, prior to soil embedment. To avoid variations during the experiment, all setups were performed simultaneously. To simulate the embedded condition, soil was added gradually to the wooden box and compressed at each layer to provide as much contact as possible with the surface of the timber pole.



Fig. 3 (a) 8-meter timber utility pole, (b) MFC actuator ring and sensor configuration and (c) Induced damage in the embedded section of the pole.

**Data Acquisition.** The equipment used in the experimental setup were a Keysight 33500B signal generator, EPA-104 Piezo System Inc amplifier, and Keysight InfiniVision DSO-X-3024A oscilloscope. The generated 5-cycle Hanning window input signal to the actuator was passed through the signal amplifier which increased the gain to 300 V peak to peak. Signals from the sensors were then acquired using the oscilloscope at a sampling rate of 2 MHz.

### Results and Analysis

**Effect of Boundary Conditions.** The effect of boundary conditions on determining the embedded length was scrutinized numerically and experimentally on a 5.5-meter and 8-meter timber pole respectively. Multiple MFC configurations were actuated separately which correspond to single, 4-ring and 8-ring actuation at the selected frequency of excitation. Wave mode characterization and the effect of soil are analyzed in this section, for sound timber prior to damage induction. The numerical results acquired were decomposed using the improved complete ensemble empirical mode decomposition with adaptive noise (CEEMDAN) signal processing technique, providing a better understanding of the difference between the two boundary conditions. This method decomposes the input signal into modes that are composed of multiple frequency and amplitude modulated functions. The sum of these modes, or intrinsic mode functions (IMFs), form the complete initial input signal [15]. The IMFs generated can help identify mode reflections and compare two signals more accurately.

Analyzing the acquired numerical signals for sound timber (single MFC atuation) shown in Fig. 4, the reflections from the propagating wave modes appear to have slightly higher amplitudes in the embedded boundary condition than the traction free one. This indicates that not only the wave is contained inside the pole in the embedded condition, but also there is less leakage in soil than in air. Packets arriving at times  $4E-3$ ,  $4.65E-3$  and  $5.2E-3$  seconds have a higher amplitude in the embedded condition. From Fig. 4, the bulk wave propagates at 5000 m/s and arrives at the beginning of the signal, with its reflections from both ends of the pole present at around  $1E-3$  seconds and  $2E-3$  seconds. This bulk wave appears to be non-dispersive where the 5-peak packet maintains its shape as shown in the first and second arrival of the wave, with no change in the frequency components. Flexural modes propagate at 2540 m/s and 1429 m/s indicating F(1,1) and F(1,2). Their reflections arrive at  $2E-3$  and  $3E-3$  from the bottom of the

pole. F(1,1) second reflection from the top end arrives right before 4E-3 seconds. Also, flexural mode F(4,1) of order 4 propagates at 625 m/s. The rest of the high order flexural modes are not indicated in the figure for simplification purposes. Nevertheless, longitudinal modes L(0,1), L(0,2) and L(0,3) propagate at 980 m/s, 780 m/s and 508 m/s respectively. Their reflections are also indicated in the figure, where L(0,1) and L(0,2) arrive at 4E-4 and 4.5E-3 seconds. The 5.5-meter pole provides enough distance for the waves to converge, which results in the propagation of various modes with different orders. As for the effect of soil embedment, no significant effect on flexural mode's first reflections is shown. However, for the second reflection of F(1,1) and the first reflection of L(0,1) and L(0,2), there is a notable increase in the packet's amplitude in the embedded condition.

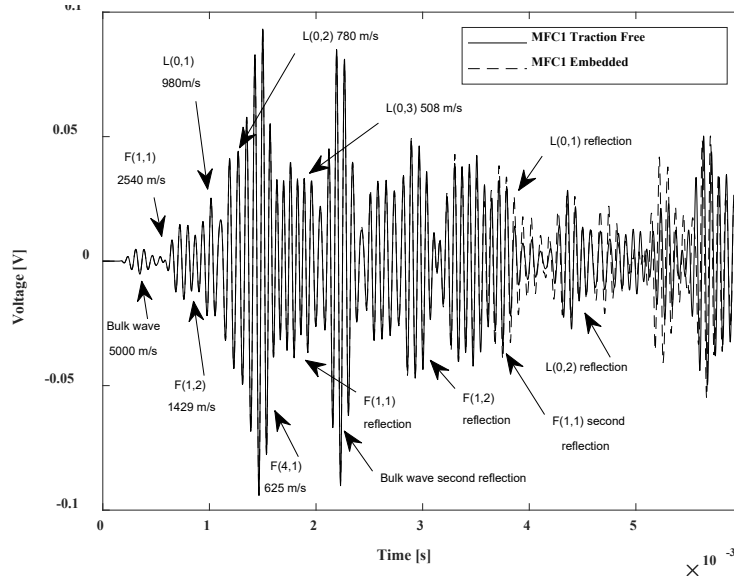


Fig. 4 Numerical results: Propagating wave modes and their reflections for traction free/embedded signals using single MFC actuation at 12.5 kHz.

Similarly, the acquired signals from the experimental single MFC actuation, traction free and embedded boundary conditions (sound wood) were placed above each other and decomposed to examine the difference. Embedding the section of the pole did not have significant effect on the reflecting packets, but rather the waves were confined within the medium with minimal leakage. It can be shown in Fig. 5 that all propagating modes are the same in traction free and embedded signals. Flexural modes F(1,1) and F(1,2) propagate at 2797 m/s and 1768 m/s and arrive early in the acquired signal. The longitudinal modes L(0,1) and L(0,2) arrive right after and propagate at 1140 m/s and 845 m/s respectively along with their reflections arriving at 4E-3 and 5.2E-3 seconds from the bottom edge. Furthermore, F(1,2) and L(0,2) reflect from a knot present at 1.2 meters to the left of the actuator, which appear in the packets at 2.6E-3 and 3.65E-3 seconds. The reflected packets from the knot travel a total distance of 3.2 meters. The effect of soil embedment appears only on the reflection of mode F(1,1) where the packet has a lower amplitude in the embedded condition. However, the rest of the modes reflected are not affected by the addition of soil, which indicates that they are confined in the timber medium with no attenuation and leakage to the outer soil medium.

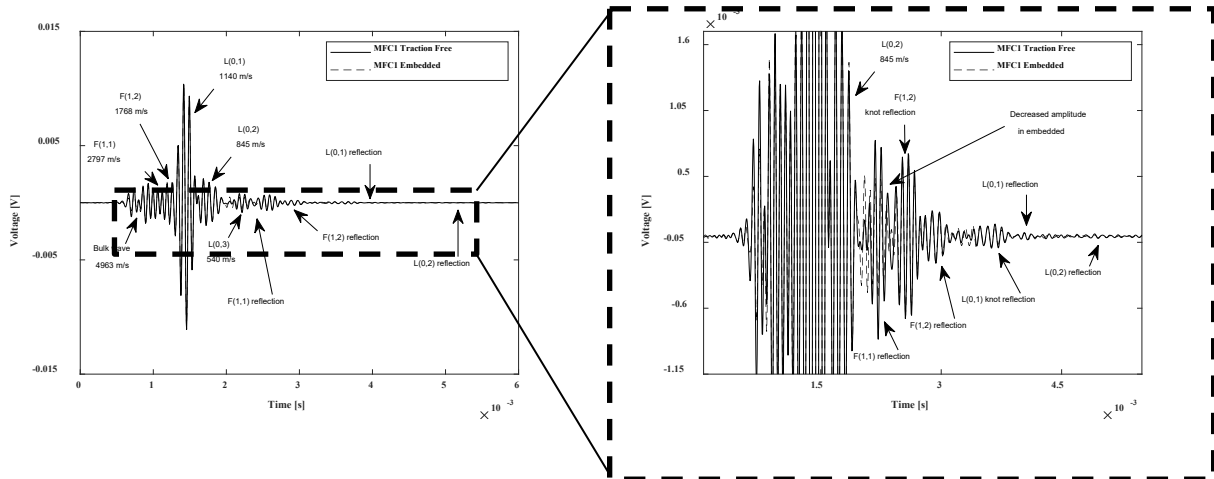


Fig. 5 Experimental results: Propagating wave modes and their reflections– traction free/embedded signals, using single MFC actuation at 12.5 kHz.

Determining the embedded length of the pole can be done by capturing the first and reflected arrival of a certain wave mode. Several modes propagate at 12.5 kHz frequency as shown in the numerical and experimental results, where each identified reflected packet can be used for the length estimation. However, some modes are more sensitive than others with respect to the boundary conditions present, knots and cracks in the structure and the configuration of MFC actuation. Since flexural modes are unwanted due to their complexity and the presence of high order modes, the MFC ring actuation can cancel them out and simultaneously enhance the longitudinal modes and their reflections [16], which can be used for the length estimation.

Signals acquired from actuating 4 and 8 MFCs around the pole’s circumference are shown below for traction free/embedded boundary conditions. Results from the numerical model shown in Fig. 6 confirm that the actuation of multiple MFCs enhances the acquired packets in general, whether they were flexural (unsuppressed) or longitudinal wave modes. For instance, the amplitude of the direct transmission of the bulk wave, L(0,1), L(0,2) and L(0,3) is higher than the ones in single MFC actuation. L(0,1) amplitude (direct transmission) increases by around 60% in the 4 and 8 MFC actuation. The reflection’s amplitude of mode L(0,1) is also enhanced in the 4 ring by 58 %, and 63 % in the 8 ring actuation. Additionally, flexural modes F(1,1) and F(1,2) do not appear to propagate in both MFC ring actuations, meaning they were completely suppressed. However, from Fig. 6 (a) mode F(4,1) still propagates at 630 m/s in the 4 ring actuation where it was not suppressed due to its higher circumferential order. The results from actuating 8 MFCs shown in Fig. 6 (b) confirm the suppression of all flexural modes, including mode F(4,1). Comparing the traction free and embedded signals, no significant difference can be identified as observed in the case of the single MFC actuation. When actuating 4 and 8 MFCs around the circumference, the effect of soil/air on the longitudinal modes’ reflections decreases. However, mode L(0,2) was the most affected by the soil embedment where it had a slightly higher amplitude than the traction free condition. Reflection of longitudinal mode L(0,1) had the same amplitude in the two boundary conditions.

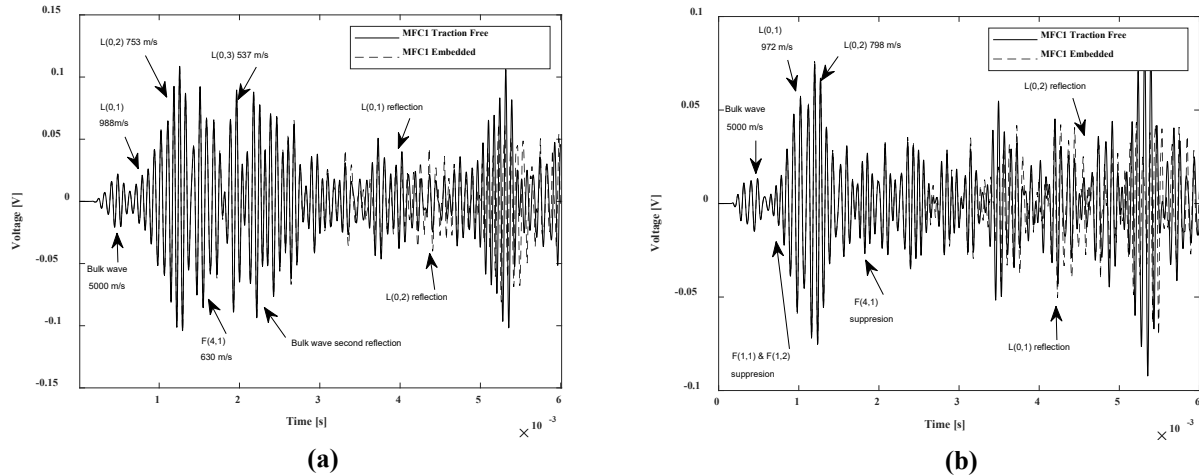


Fig. 6 Numerical results: Propagating wave modes and their reflections for traction free/embedded signals using (a) 4-Ring and (b) 8-Ring MFC actuation at 12.5 kHz.

In the experimental testing, the MFC ring actuation also yields similar results as the numerical. Fig. 7 shows the acquired signal for traction free and embedded conditions using 4 ring (a) and 8 ring (b) MFC actuation. The bulk wave, L(0,1), and L(0,2) attained higher amplitudes than the single MFC actuation. The direct transmission enhancement of the longitudinal modes is around 30 % in both ring actuations, whereas the reflection enhancement is 80% and 93 % in the 4 and 8 ring actuations. Regarding the suppression of flexural modes, the 4 ring actuation was not enough to suppress F(1,1) which arrives at 1E-3 seconds as shown in Fig. 7 (a). However, in the 8 ring actuation shown in Fig. 7 (b), all flexural modes including F(1,1) were suppressed. The rest of the propagating wave modes and their reflections are indicated on the figures. The acquired signals are almost entirely similar for traction free and embedded conditions in both MFC ring actuations, where the effect of soil embedment seems negligible.

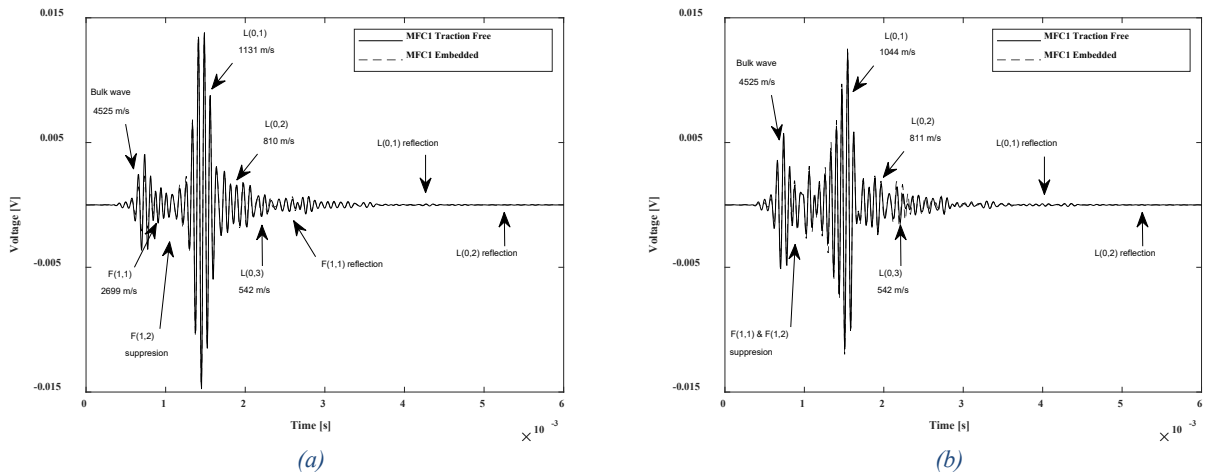


Fig. 7 Experimental results: Propagating wave modes and their reflections for traction free/embedded signals using (a) 4-Ring and (b) 8-Ring MFC actuation at 12.5 kHz.

**Effect of Damage Induction.** The behavior of guided waves in timber has been examined with the change in boundary conditions (traction free and embedded models) for sound wood. In this section, results from inducing damage in the timber structure (embedded section) are shown. The same boundary conditions and MFC actuation configurations were used, at 12.5 kHz frequency. Numerical results from single MFC actuation, embedded boundary condition are displayed in

Fig. 8 (a) for sound (solid line) and damaged timber (dashed line). From the original signal, some difference can be identified after time  $3E-3$  seconds. No solid identification of the damage reflection can be identified, which requires the usage of CEEMDAN to better identify the packets resulting from the damage. The first decomposed mode (IMF 1) is displayed in Fig. 8 (b) where the reflected packets from the edge of the pole and damage are indicated. Flexural and longitudinal modes' direct and reflected transmissions are indicated on the figure. The decomposed signal shows the arrival of F(1,2) from the damage at  $1.8E-3$  seconds, which coincides with the arrival of F(1,1) edge reflection. Longitudinal mode L(0,1) reflects from the damage and arrives solely at  $2.6E-3$  seconds. The packet at  $3.4E-3$  seconds appears to have a higher amplitude in the damaged signal (dashed line) due to the arrival of L(0,2) damage reflection, which coincides with the second reflection of F(1,1) from the top edge of the pole. Last, longitudinal mode L(0,3) propagating at around 508 m/s reflects from the damage and arrives solely at  $4.35E-3$  seconds. Longitudinal modes provide more accurate information about the damage, especially due to the non-concatenated packets such as L(0,1) and L(0,3) reflections from the damage. Due to their higher speed, flexural modes' reflections seem to arrive early in the signal which results in the concatenation with other modes of lower speeds. Therefore, longitudinal modes can be solely used for the damage localization process. The numerical acquired signal from the traction free boundary condition showed similar results as the embedded, with minor differences in the amplitude of the reflected wave modes.

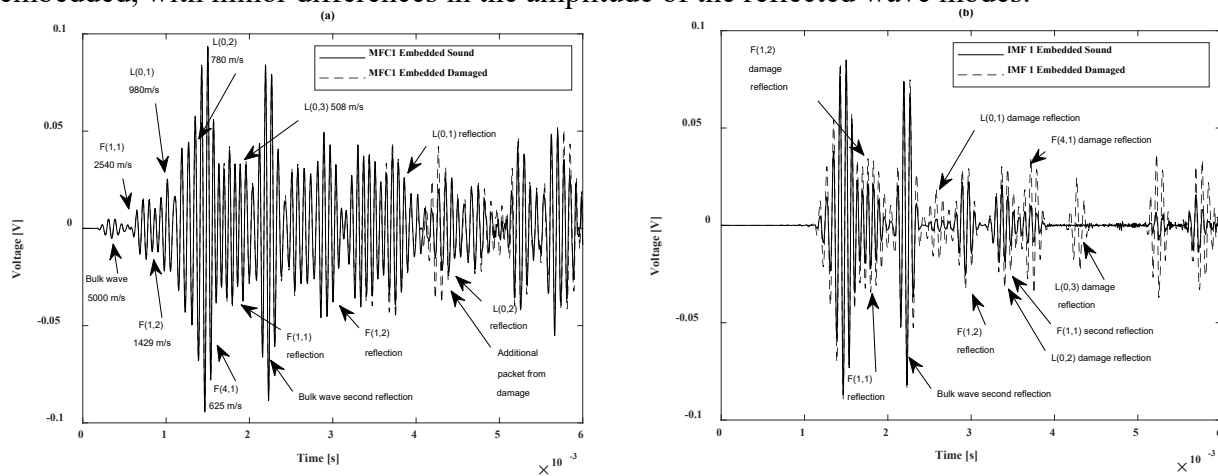
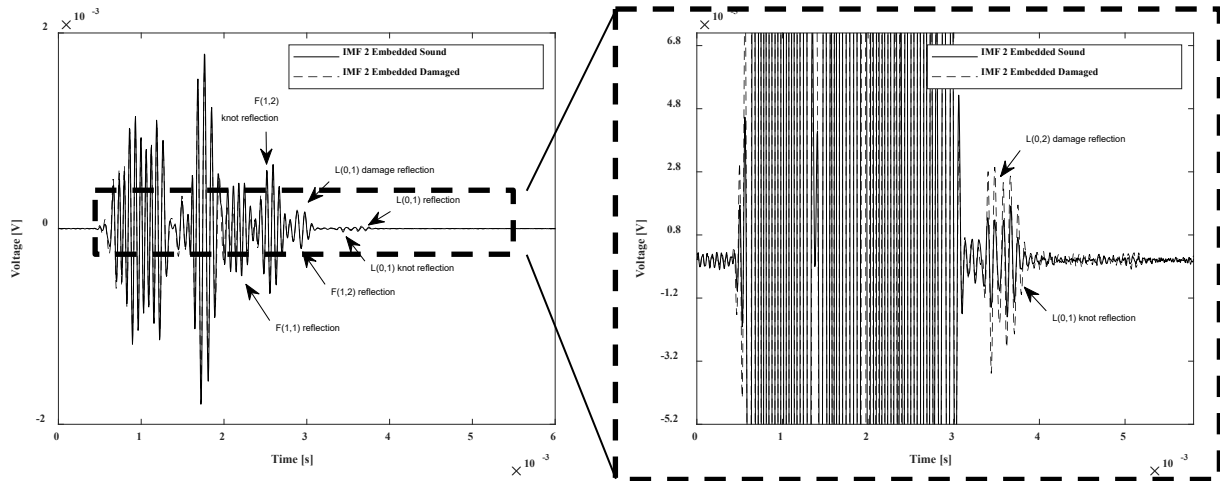


Fig. 8 Numerical results: Embedded sound (solid line) and damaged (dashed line) using single MFC actuation at 12.5 kHz (a) original signal and (b) decomposed signal after CEEMD (IMF 1).

In the experimental validation, the induced damage in the timber structure resulted in much more complicated results than the numerical. Several knots and cracks in the experimental timber specimen cause reflections which complicates the acquired signals. Therefore, the propagating wave mode arrivals could be overlapping in most cases which makes it hard to determine the damage location for more than one mode. The decomposed signal from the embedded condition for single MFC actuation at 12.5 kHz is shown in Fig. 9. The propagating modes are indicated on the figure with their reflections. Flexural modes F(1,1) and F(1,2) arrive at the beginning of the signal and reflect from the bottom edge at  $2E-3$  and  $3E-3$  seconds. Longitudinal modes L(0,1) and L(0,2) propagate at 1140 m/s and 845 m/s respectively and reflect from the bottom edge of the pole. L(0,1) bottom edge reflection acquires a significantly low amplitude in the damaged signal due to the location of the damage between the MFC sensor and the pole's edge. Each of

the two longitudinal modes reflect from the damage and arrive at around  $3E-3$  and  $3.65E-3$  second. The arrival of  $L(0,1)$  damage reflection coincides with the reflection of  $F(1,2)$  from the pole's edge, where the amplitude of the packet in the damaged signal is slightly higher. The damage can still be localized accurately using mode  $L(0,1)$ . Also, the arrival of  $L(0,2)$ 's damage reflection can be indicated which coincides with the arrival of knot reflection of  $L(0,1)$  present at 1.2 meters from the actuator and can be used for the localization process. The acquired signals from the traction free boundary condition showed similar results as the embedded. The amplitude of reflecting packet from the damage is higher for mode  $L(0,1)$  in the traction free condition, which might be due to the timber – soil interface at the damage location.



*Fig. 9 Experimental results: decomposed signal after CEEMD (IMF 2) for embedded sound/damaged using single MFC actuation at 12.5 kHz.*

The single MFC actuation could provide enough information regarding the presence of decay or damage inside the timber specimen. The reflected packets from the damage were identified successfully in both traction free and embedded boundary conditions. However, multiple MFC actuation might not be suitable for damage identification, especially if the damage is located axially along a certain face of the timber pole. For instance, the induced damage in the tested pole lied axially on the same straight line as the MFCs in the single actuation configuration. Therefore, actuating the 4 or 8-ring could prevent the damage reflection to be properly acquired from the sensor. This was depicted numerically and experimentally where the MFC ring was actuated in the damaged condition and compared to the results of the sound specimen.

The results of the damaged timber pole show that the ring actuation has negative effects on damage localization. Fig. 10 show the decomposed (IMF1) numerical signals in the embedded model using 4 and 8 MFC ring actuation. The acquired results show that there is a negligible difference between the sound and damaged timber specimens. Reflection of longitudinal modes  $L(0,1)$  and  $L(0,2)$  from the damage are not captured as the single actuation shown earlier, where the expected time of arrival does not show any packet. This is depicted in the decomposed signals after CEEMD (IMF 1) shown in Fig. 10 (a-b). In the traction free model, actuating 4 and 8 MFCs lead to similar results as the embedded boundary conditions. No reflections from the damage were acquired where they do not appear in the signal, even after applying CEEMD. However, the reflections of  $L(0,1)$  and  $L(0,2)$  from the bottom edge of the pole were successfully captured and are identified on the figures in both MFC ring actuations.

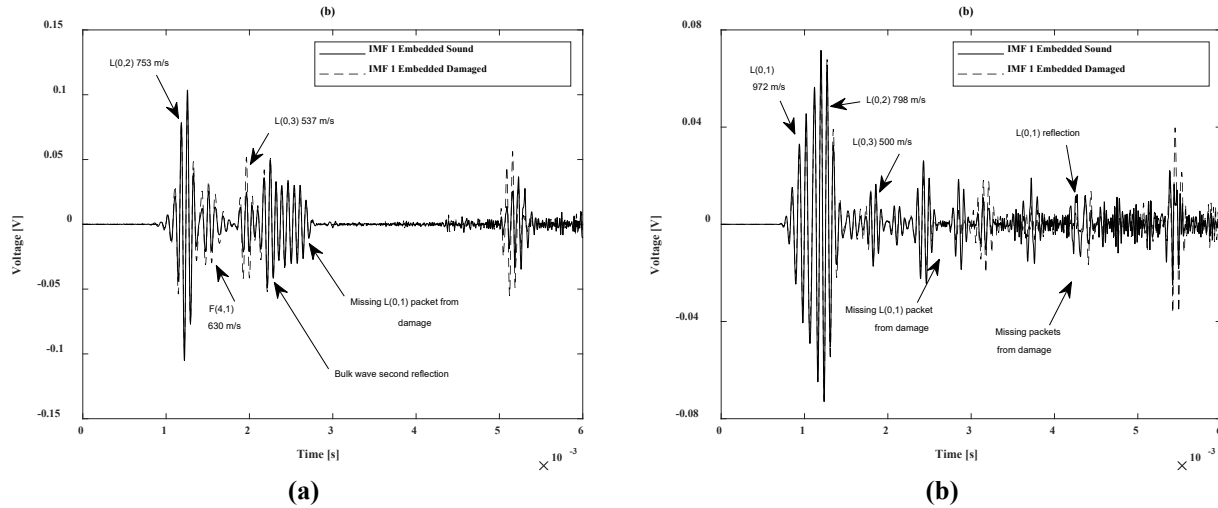


Fig. 10 Numerical results (decomposed signals after CEEMD (IMF 1)): Embedded sound (solid line) and damaged (dashed line) using (a) 4 ring MFC actuation at 12.5 kHz and (a) 8 ring MFC actuation at 12.5 kHz.

In the experimental results, the MFC ring actuation also caused the reflections from the damage to be less exposed. No major difference was determined between the sound and damage timber specimens, even after performing CEEMD.

### Length Estimation and Damage Localization

The estimation of embedment length and damage location can be performed using the resulting reflected packets of a selected wave mode. From the propagation velocity and arrival time of the reflections, the total propagation distance can be calculated. Fig. 11 shows a top view sketch of the pole used in the numerical and experimental validation. The reflecting packets from the bottom edge of the pole can provide an estimation of the distance between the edge and the MFC sensor. As for locating the damage, the reflections resulted can be used to estimate the distance between the damage and the MFC sensor. The actual distance between the MFC sensor and bottom edge of the pole is 1.5 meters, and between the sensor and center of the damage is 79 cm. These values are a reference used for calculating the distance estimation error.

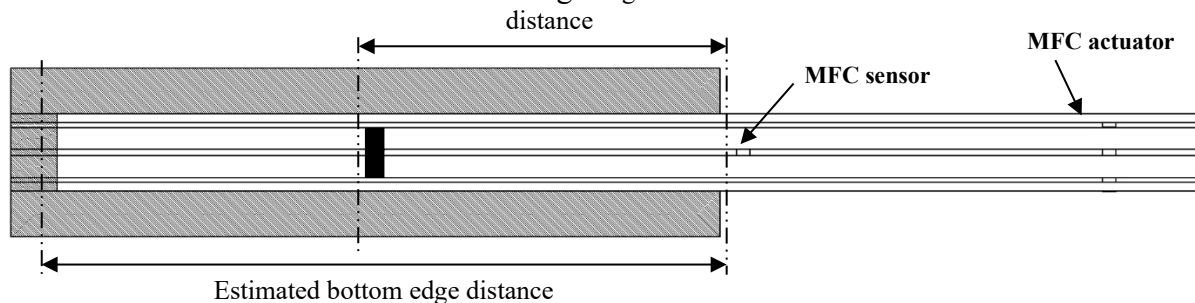


Fig. 11 Top view sketch of the pole specimen displaying the embedded and damage distances to be estimated.

The below equation (Eq. 1) is used to estimate the distance between the MFC sensor and the bottom edge, and the center of the damage.  $V$  is the propagation velocity of the wave mode selected.  $\Delta t$  is the time difference between the first arrival of the selected mode, and the second arrival resulting from the reflection. This reflection could be either from the damage or the

bottom edge of the pole. The total distance (in meters) indicates the propagation distance covered by the wave and must be divided by 2.

$$d = \frac{v \times \Delta t}{2} \tag{1}$$

Several wave modes can be selected to estimate the distances required, which were shown in the results section at 12.5 kHz frequency. However, not all modes can be used due to their complexity and dispersive nature. Longitudinal wave modes can be found in almost all cases, whether in sound/damaged timber or in multiple MFC (ring) actuation where they acquire an enhanced amplitude. Therefore, they can be used for distance estimation.

The distance between the MFC sensor and bottom edge of the pole, which corresponds to the embedment length of the pole, was determined using data from longitudinal mode L(0,1). This mode was selected due to its consistency in all experiments and least dispersive nature, in addition to the amplitude it acquires, which is higher than any other mode in the signal. Table 2 displays the bottom edge distance estimation using the numerical results for 8-ring MFC actuation at 12.5 kHz excitation frequency. The presence of damage in all actuation configurations causes the reflection amplitude from the bottom edge to be lower than the sound timber pole.

*Table 2 Numerical results: Bottom edge distance estimation using mode L(0,1) for 8-ring MFC actuation.*

<i>Actuation</i>	<b>Boundary condition</b>	<b>1<sup>st</sup>arrival time (s)</b>	<b>2<sup>nd</sup>arrival time (s)</b>	<b>Reflection amplitude (mV)</b>	<b>Velocity (m/s)</b>	<b>Estimated distance (m)</b>	<b>Error (%)</b>
<b>8-Ring</b>	<b>Traction Free Sound</b>	0.001023	0.004198	45.3	972	1.543	2.79
	<b>Embedded Sound</b>	0.001023	0.004193	40.2	972	1.541	2.64
	<b>Traction Free Damaged</b>	0.001023	0.004198	35.6	972	1.543	2.79
	<b>Embedded Damaged</b>	0.001023	0.004195	37.3	972	1.542	2.7

Table 3 displays the bottom edge distance estimation using the experimental results for 8-ring MFC actuation. The application of MFC ring actuation causes the reflection amplitude of L(0,1) to increase compared to the single MFC actuation. Also, in the traction free damaged timber pole, the single actuation was not enough for the edge reflection to appear which resulted in a missing packet around 4E-3 seconds. In the embedded damaged pole, single actuation, the reflection from the bottom edge of the pole was captured but at a lower amplitude than the sound timber specimen. The missing packet in the damaged condition does not appear in the 4 and 8-ring MFC actuation, where the distance is estimated normally.

*Table 3 Experimental results: Bottom edge distance estimation using mode L(0,1) for single, 4-ring and 8-ring MFC actuation.*

<i>Actuation</i>	<b>Boundary condition</b>	<b>1<sup>st</sup>arrival time (s)</b>	<b>2<sup>nd</sup>arrival time (s)</b>	<b>Reflection amplitude (mV)</b>	<b>Velocity (m/s)</b>	<b>Estimated distance (m)</b>	<b>Error (%)</b>
<i>8-Ring</i>	<b>Traction Free Sound</b>	0.00151	0.004326	0.1253	1044	1.47	2
	<b>Embedded Sound</b>	0.00151	0.004332	0.121	1044	1.473	1.79
	<b>Traction Free Damaged</b>	0.00151	0.004316	0.064	1044	1.465	2.35
	<b>Embedded Damaged</b>	0.00151	0.004352	0.11	1044	1.4835	1.1

Determining the location of the damage was performed using longitudinal mode L(0,1) for the single MFC actuation. Table 4 shows the damage location estimation using the numerical results acquired.

*Table 4 Numerical results: Damage localization using mode L(0,1) for single MFC actuation.*

<i>Actuation</i>	<b>Boundary condition</b>	<b>1<sup>st</sup>arrival time (s)</b>	<b>2<sup>nd</sup>arrival time (s)</b>	<b>Reflection amplitude (mV)</b>	<b>Velocity (m/s)</b>	<b>Estimated distance (m)</b>	<b>Error (%)</b>
<i>Single</i>	<b>Traction Free Damaged</b>	0.001018	0.00266	3.107	979	0.804	1.71
	<b>Embedded Damaged</b>	0.001018	0.002673	2.83	979	0.81	2.48

Estimating the damage location using the experimental results is shown in Table 5 for the single MFC actuation. In the 4-ring actuation – traction free condition, the reflecting packet from the damage was identified but with a higher error of 7.8 %. It does not appear in the 4-ring – embedded boundary condition, nor in any of the 8-ring MFC actuations.

*Table 5 Experimental results: Damage localization using mode L(0,1) for single MFC actuation.*

<i>Actuation</i>	<b>Boundary condition</b>	<b>1<sup>st</sup>arrival time (s)</b>	<b>2<sup>nd</sup>arrival time (s)</b>	<b>Reflection amplitude (mV)</b>	<b>Velocity (m/s)</b>	<b>Estimated distance (m)</b>	<b>Error (%)</b>
<i>Single</i>	<b>Traction Free Damaged</b>	0.001446	0.002928	0.42	1140	0.845	6.48
	<b>Embedded Damaged</b>	0.001446	0.002928	0.22	1140	0.8245	6.48

It was mentioned in the Effect of Damage Induction section that reflections from other modes were captured and might predict accurately the location of the damage. For instance, in some cases, longitudinal mode L(0,2) appears to reflect from the damage. In the experimental single MFC actuation – embedded condition, reflection of L(0,2) from the damage arrives at 3.7E-3 seconds providing a damage location estimation with 0.886 % error. This mode does not appear

in the 4 and 8-ring MFC actuation experimental results. However, in the numerical results, the damage reflections of mode L(0,2) were acquired in the 8-ring MFC actuation. The damage location was estimated in the traction free and embedded boundary conditions with a 2.75 % error. In addition, damage reflections of flexural modes F(1,1) and F(1,2) were also captured in the single MFC actuation from the numerical results in both boundary conditions simulated. The location of the damage estimated using F(1,1) and F(1,1) resulted in an error of 8.8 % and 5 % respectively. This indicates how the flexural modes are much more complicated than longitudinal modes, due to their highly dispersive nature, which results in inaccuracy when estimating the location of the damage. Assessing the presence of decay/damage in the timber structure proved to be more adequate using the single MFC actuation. Therefore, it is proposed to actuate each MFC in the ring solely at a time, while acquiring the signals on the same plane of actuation. This requires the installment of a sensor ring with the same number of MFCs as the actuator ring.

### Conclusions

In this study, the embedded length of timber utility pole and the presence of damage/decay in the embedded section were scrutinized numerically and experimentally by the use of guided waves (GWs). Macro Fiber Composites (MFCs) proved to be a convenient tool for generating/sensing GWs in timber structures, especially due to their reliability and flexibility to be coupled on curved and rough surfaces. Evaluating the structure's health state was performed with the variation of external boundary conditions, such as soil embedment, and the application of an MFC ring coupled around the pole's circumference. The ring ensured the actuation of the wave modes of interest, such as longitudinal mode L(0,1), with an enhanced amplitude and was recommended for estimating the embedded depth of the pole. The estimation yielded an accuracy of 97 % in both numerical and experimental results, even with the presence of damage in the timber structure. Determining the location of the damage in the embedded section was performed using the single MFC actuation and data from mode L(0,1) with an error of less than 7 %.

### Acknowledgments

We acknowledge the financial support of the University Research Board at the American University of Beirut for their Award #103780.

### References

- [1] EP DeGarmo, JT Black, RA Kohser and BE Klamecki, "Materials and process in manufacturing, 9th ed." Prentice Hall, Upper Saddle River, pp, 1997.
- [2] M Subhani, "A Study on the Behaviour of Guided Wave Propagation in Utility Timber Poles", University of Technology Sydney, 2014.
- [3] U Dackermann, Y Yu, E Niederleithinger, J Li and H Wiggenhauser, "Condition assessment of foundation piles and utility poles based on guided wave propagation using a network of tactile transducers and support vector machines", *Sensors* 17(12), pp 2938, 2017. <https://doi.org/10.3390/s17122938>
- [4] U Dackermann, B Skinner and J Li, "Guided wave-based condition assessment of in situ timber utility poles using machine learning algorithms", *Structural Health Monitoring* 13(4), pp 374-388, 2014. <https://doi.org/10.1177/1475921714521269>

- [5] Y Yu, U Dackermann, J Li and N Yan, "Guided-wave-based damage detection of timber poles using a hierarchical data fusion algorithm", Proc. of Australasian Conference on the Mechanics of Structures and Materials, Lismore, pp 1203-1208, 2014.
- [6] B Pavlakovic and M Lowe, "Disperse Software Manual Version 2.0. 1 6B", Imperial College, London, UK, pp, 2003.
- [7] F Seco and AR Jiménez, "Modelling the generation and propagation of ultrasonic signals in cylindrical waveguides, Ultrasonic waves, 1", InTechOpen, pp 1-28, 2012.  
<https://doi.org/10.5772/29804>
- [8] DE Kretschmann, "Mechanical properties of wood, Wood handbook: wood as an engineering material, 5", Forest Products Laboratory, pp 5.1-5.46, 2010.
- [9] AB Thien, "Pipeline structural health monitoring using macro-fiber composite active sensors", Dissertation, University of Cincinnati, United States, 2006.  
<https://doi.org/10.2172/883462>
- [10] J El Najjar and S Mustapha, "Understanding the guided waves propagation behavior in timber utility poles", Construction and Building Materials, pp 1-21, 2020.
- [11] COMSOL Multiphysics, "Introduction to COMSOL Multiphysics®", COMSOL Multiphysics, Burlington, MA, accessed Feb 9, pp 2018, 1998.
- [12] S Marburg, "Six boundary elements per wavelength: Is that enough?", Journal of Computational Acoustics 10(01), pp 25-51, 2002. <https://doi.org/10.1142/S0218396X02001401>
- [13] S Mustapha and L Ye, "Leaky and non-leaky behaviours of guided waves in CF/EP sandwich structures", Wave Motion 51(6), pp 905-918, 2014.  
<https://doi.org/10.1016/j.wavemoti.2014.03.004>
- [14] D Bieker and S Rust, "Non-destructive estimation of sapwood and heartwood width in Scots pine (*Pinus sylvestris* L.)", Silva Fennica 44(2), pp 267-273, 2010.  
<https://doi.org/10.14214/sf.153>
- [15] MA Fakhri, S Mustapha, J Tarraf, G Ayoub and R Hamade, "Detection and assessment of flaws in friction stir welded joints using ultrasonic guided waves: experimental and finite element analysis", Mechanical Systems and Signal Processing 101, pp 516-534, 2018.  
<https://doi.org/10.1016/j.ymssp.2017.09.003>
- [16] J El Najjar and S Mustapha, "Understanding the Wave Propagation Behavior in Timber Structures towards Application in the Assessment of Utility Timber Poles", Civil Structural Health Monitoring, pp, 2020. <https://doi.org/10.1007/s13349-020-00417-0>

# Monitoring of the Operational Conditions in Steel Pipes Using Fiber Optic Sensors

Michel Saade<sup>1,a</sup> and Samir Mustapha<sup>2,b,\*</sup>

<sup>1</sup>American University of Beirut, Ashrafieh Beirut, Lebanon

<sup>2</sup>American University of Beirut, Ain El-Mraisse Beirut, Lebanon

<sup>a</sup>michelsaade6@gmail.com, <sup>b,\*</sup>sm154@aub.edu.lb

**Keywords:** Pipes Condition Monitoring, Structural Health Monitoring, Fiber Optic Sensing

**Abstract.** Oil and water transport pipeline systems are susceptible to damage due to harsh environmental conditions and operational factors, hence ongoing maintenance and inspection are required. The development of a continuous and reliable monitoring technique will ensure the safety usage of these structures and assist in the extension of their life span. In this study, the monitoring and assessment of pipelines are performed using a network of Fiber Bragg Grating (FBG) sensors mounted along the longitudinal and circumferential directions. The sensitivity of the measurements to assess pressure and flow variation in the pipe, in addition to leakage detection and localization were evaluated. Water at a controlled pressure and flowrate was pumped into the designed six-meter pipe testbed designed for this purpose. Leakage was simulated by opening one of the four designated valves installed on the pipe. The variation in the pressure inside the pipe highly impacted the amplitude of the measured strain increasing it significantly reaching 20%. An increase in flowrate had an inverse effect, it resulted in a 5% decrease in the amplitude of the measured strain drop. The change of hole leakage size greatly influenced the measured signal, resulting in a 55% change in amplitude between a 2 cm<sup>2</sup> and a 5 cm<sup>2</sup> hole leakage. For the location of leakage, only the temporal aspects of the signal were affected resulting in a slight shift in the response time of sensors relative to each other. The results were promising to monitor the structural conditions related to leakage detection and localization, based on the patterns observed.

## Introduction

Pipeline systems are remarkable for their practicality, efficiency, and cost-effectiveness in transporting big quantities of dangerous substances <sup>[1]</sup>, in particular, crude oil and petroleum products <sup>[2]</sup>, when compared with other modes of transport. These pipeline systems can be used for short distances (within refineries or between neighboring installations), and over long distances. Oil and gas products from hundreds of thousands of wells, from which, many are located in remote and hostile areas, are transported through pipelines <sup>[3]</sup>.

The large scale and deployment location of pipeline networks make this transportation method susceptible to various types of failures. These failures may not only cause product loss, but also environmental damages and hazards and potential threats to life <sup>[4, 5]</sup>. Pipeline failures, depending on their location and the nature of the transported substance, can have many negative effects on the economy, the environment, and health. Given the immense scale of the pipeline networks and the severity of possible leakage repercussions, the structural health monitoring (SHM) of pipelines is a challenging yet necessary task. The methods developed over the years



are strictly non-destructive as they must be applied to installed and running pipelines. Several methods have been developed for this purpose <sup>[6]</sup>.

The monitoring of pipeline networks can be performed through externally mounted sensors to detect pipe leakages. These methods are called sensor-based methods. They include the negative pressure wave methods, ultrasonic methods, eddy current, electromagnetic flux, and others <sup>[7]</sup>. Their main advantages are the quantification of the problem as well as their application without the interruption of the normal pipeline operation. <sup>[8-10]</sup>.

Methods based on intelligent pigging have also been developed for the inspection of pipeline systems <sup>[11]</sup>. These methods are particularly useful at detecting and localizing change in wall thickness. However, pipeline operation may need to be disturbed to perform the tests, further the monitoring process is not continuous <sup>[12]</sup>.

Other less common pipeline inspection methods are also available. The single measurement analysis method for instance is used for the monitoring of small-scale pipelines (factory-scale). These methods work by monitoring flow conditions at a single point in the pipeline network <sup>[13]</sup>. Another inspection method is the uncompensated volume balance method in which the sum of flows entering the pipeline and the sum of flows exiting it are compared. If a noticeably large difference is observed, it can indicate a leak in the network <sup>[14]</sup>. Finally, model-based leakage detection methods <sup>[15, 16]</sup> in which a model of the pipeline under-study is simulated can be used for inspecting the pipeline. Flow properties at certain locations in the network are then compared to the flow properties in the same locations of the simulated network. This method needs highly accurate inputs and a computer capable of delivering good results in a reasonable amount of time.

Among the above-listed methods, the most effective leakage localization methods in a pipe during normal operation are the ones with externally mounted sensors. Two of these methods are particularly effective, the negative pressure wave method (NPW) and the temperature-based methods.

NPW methods are concerned with the negative pressure wave that is generated when a pipe starts leaking fluid (change in pressure). This negative pressure wave travels through the fluid in the pipe to neighboring pressure sensors that pick up this change in the operational condition <sup>[10]</sup>. The leakage is then localized using the time difference for the negative pressure wave to reach the two sensors upstream and downstream of the leak location. On the other hand, the temperature-based methods are based on monitoring the temperature of the medium surrounding the pipe. Even though these methods can generally give better outcomes and higher precision than NPW methods, they are subject to noise and errors caused by weather abnormalities or third-party intrusions <sup>[17]</sup>.

In this paper, the operational and structural condition assessment of steel pipes using a sensor network of fiber optic Fiber Bragg Grating (FBG) sensors has been investigated. fiber optic sensors (FOS) was chosen for this application due to its superb capability to provide measurements over long distances. The main aims are to investigate the efficacy of using FBG strain sensors in the structural health and operational condition monitoring of pipelines and develop a good understanding of the effect of flow conditions and leakage on the surface strain in pipelines.

## Methodology

This section describes the developed methodology used in this study. The design of the testbed, and the tested scenarios.

### Experimental approach

Experiments were conducted by recording the strain data of the FBG sensors mounted on the surface of the pipe in multiple scenarios with different pressures, flow rates, leakage locations, and hole leakage sizes. The main concern was to replicate possible leakage scenarios in actual transportation pipelines. All collected data was gathered from the interrogation of the FBG sensors. By attaching the fibers directly to the pipe's surface, the measured fiber strain and its variation were expected to reflect the properties of the flow inside the pipe. Performing tests under different flow and leakage conditions help determine the effects that these parameters have on the output signals. By comparing the signals obtained in various scenarios (by changing one parameter at a time), it was possible to observe the effects that a specific parameter had on the readings.

### Experimental Set-Up

A testbed was specifically designed to demonstrate the feasibility of the application of FBG sensors in monitoring the operational and structural conditions of the pipelines. The testbed consists of a 5.95-m-long, black steel pipe with a nominal diameter of 10" (250 mm) and a thickness of 5 mm. The full experimental set-up is shown in Figure 1. Six holes with different purposes were drilled into the pipe in the radial direction on the pipe. Two holes served as the inlet and exhaust of fluid through the pipe, while the others were used to simulate leakage. All necessary connections were established using 1-inch (25 mm) nominal diameter pipes, elbows, and T connections.

As for the instrumentation, two different types of sensors were used in the set-up; these were supplied by Micron Optics. The sensors placed in the longitudinal direction were temperature-compensated FBG strain sensors (os3155) that were spot welded on the pipe. The sensors mounted in the circumferential direction were optical strain gages (os3100) that were epoxied to the pipe. The six mounted sensors were named S1 through S6, starting from the sensor closest to the pipe's inlet. Sensors S1, S3, S4, and S6 were mounted in the longitudinal direction, whereas sensors S2 and S5 were mounted in the circumferential direction.

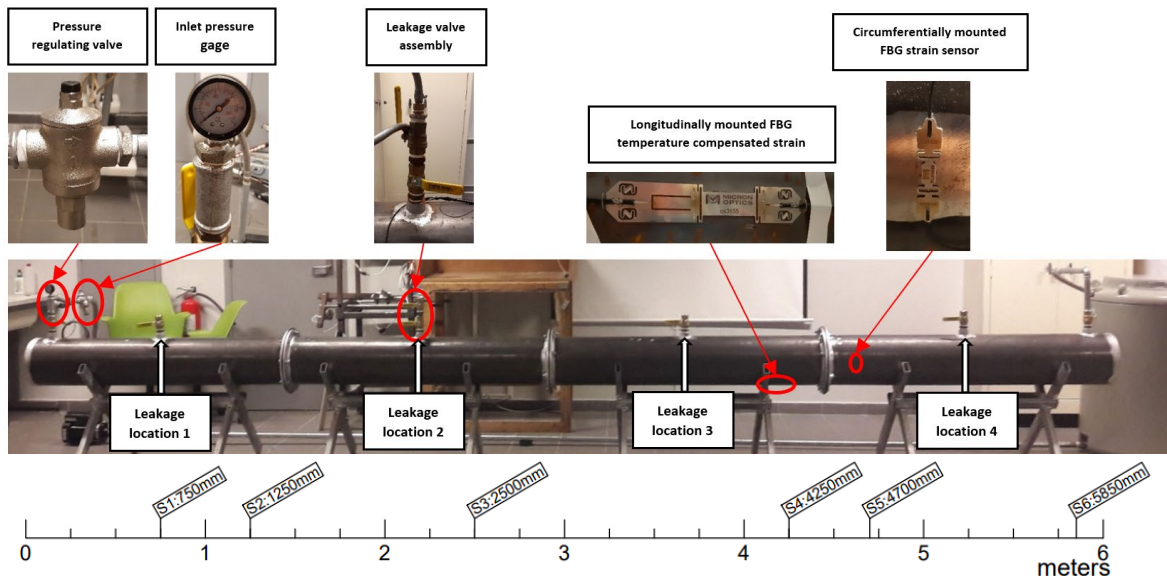


Figure 1: Detailed layout of the testbed and sensor positions.

Experiments were performed using 3 different pressures (60, 80, and 100 kPa), 3 different flow rates (10, 15, and 20 GPM), 4 leakage locations, and 2 leakage hole sizes. A single data point contains 60-second readings of all 6 sensors with a single leakage valve opened at the 30-second mark. Initially collected data contained high noise (signal to noise ratio (SNR) ranged between 1.85 and 10.23) which required filtering. The data was processed and underwent a lowpass filtering with a factor of  $10^{-5}$  and a moving mean filter with a 400 ms range. The signals were then zeroed and trimmed down to 15 seconds to eliminate the redundancy.

### Results and Analysis

Signals generated under different flow and leakage conditions can contain traits or patterns that reflect those conditions. To show these patterns, each flow or leakage parameter can be isolated and analyzed separately. This can be done by fixing three parameters, varying the fourth remaining one, and observing changes in the signals. Due to the trimming of the data, leakage in subsequent figures is simulated at  $t=5$  seconds. In this section, data from sensors S1 and S2 are presented. The choice was made to include the sensor with the highest gain for each mounting direction (S1 is mounted in the longitudinal direction and S2 is mounted in the circumferential direction). However, any sensor combination will yield the same results. Figure 2 and Figure 3 show a plot of the strain variations of S1 and S2 in  $\mu\epsilon$  against time in seconds.

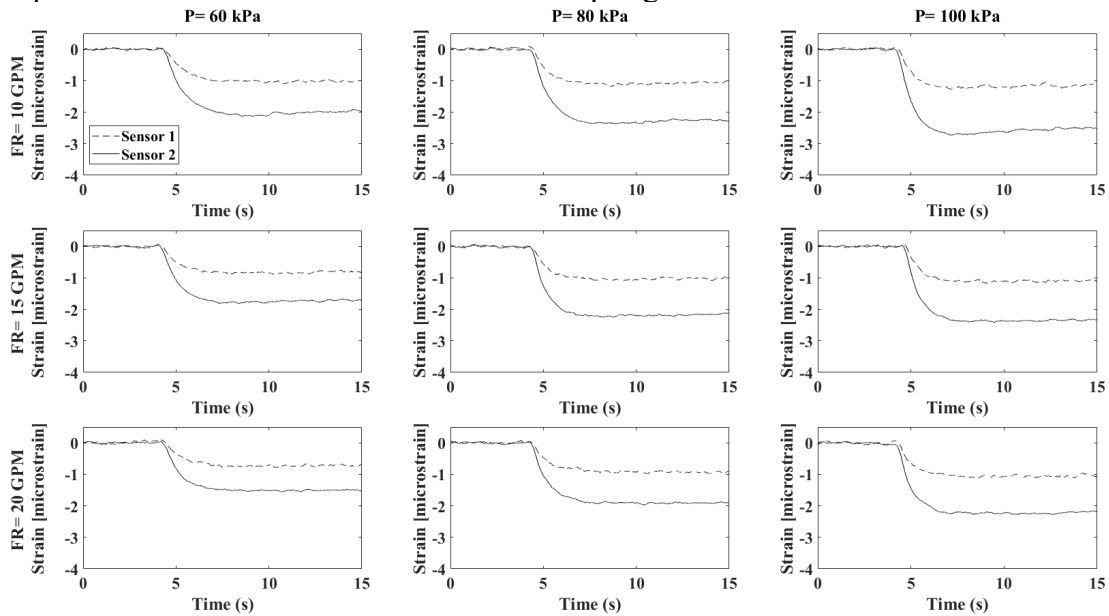
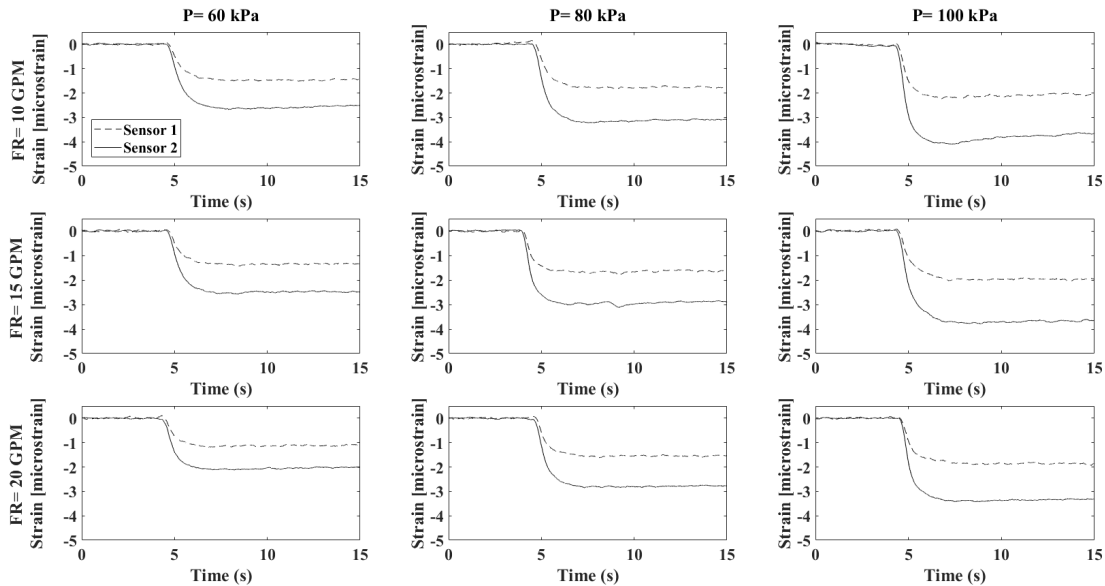


Figure 2: Strain curves with a variation of pressure and flow rate for a small leakage size with leakage simulated at location L1.

Figure 2 shows the surface strain variation measured by sensors S1 and S2 for varying pressures and flow rates. The location of the leakage (L1) and the size of the leakage (small) remain unchanged. Looking at three consecutive plots from top to bottom reveals that increasing the flow rate results in a smaller strain drop at any given pressure. A change in flowrate from 10 to 15 GPM (50% increase) causes on average a 4% decrease in strain drop and a change from 15 to 20 GPM (33% increase) causes a 10% decrease in strain drop. Both circumferential and longitudinal sensors experience the same changes in this scenario. Looking at three consecutive plots from left to right reveals the effect of changing the initial pipe pressure on the signals. An increase in pressure from 60 to 80 kPa (33% increase) causes the amplitude of the strain drop to increase by 31 % for the longitudinally placed sensor and 18% for the circumferentially placed

sensor. Changing the initial pressure from 80 to 100 kPa (25% increase) results in a less pronounced change in strain drop amplitude of 13.5% for both sensors.



*Figure 3: Strain curves with a variation of pressure and flow rate for a large leakage size with leakage simulated at location L1.*

When looking at the same variations with a large leakage hole, strain drop amplitude changes vary slightly (Figure 3). A jump in flowrate from 10 to 15 GPM yields a 7% decrease in strain drop for both sensors and a jump from 15 to 20 GPM yields a 7% decrease in strain drop. Changes in pressure, in this case, are also more noticeable with a 28% increase in strain drop between a 60 and an 80 kPa pressure, and an 18% drop amplitude increase between 80 and 100 kPa. A larger leakage creates a larger strain drop in all observed cases. A 50% increase in strain drop on average is observed between data recorded with a small leakage and data recorded with a large leakage. This increase is consistent with an initial flow rate or pressure.

These observed patterns can be used to determine the flow properties and leakage size at the time of leakage which can help determine possible causes of leakage approximate the extent of damages. However, some signal patterns overlap (i.e. the effects that having a high pressure or a low flowrate have on the signals are similar). Circumferentially placed sensors have a higher gain which reduces the amount of information in the data lost to denoising. But longitudinally placed sensors show a higher sensitivity to changes in flow conditions.

The variation in the location of the leakage did not have any effect on the amplitude of the strain drop. However, it does influence the temporal aspect of the strain curve of the sensors. The time it took each sensor to reach the final steady strain state was slightly increased the farther that sensor was located from the leakage location. This delay is visible in the gap between the time it takes S1 and S2 to reach S1's steady-state strain value. This gap is highlighted in Figure 4.

The time difference between the two intercepts appears to increase the more distant the leakage location is relative to the sensor's position. With few exceptions, this pattern holds for different flow rates, pressures, and leakage sizes. The time differences for different flow and leakage scenarios are shown in Table 1.

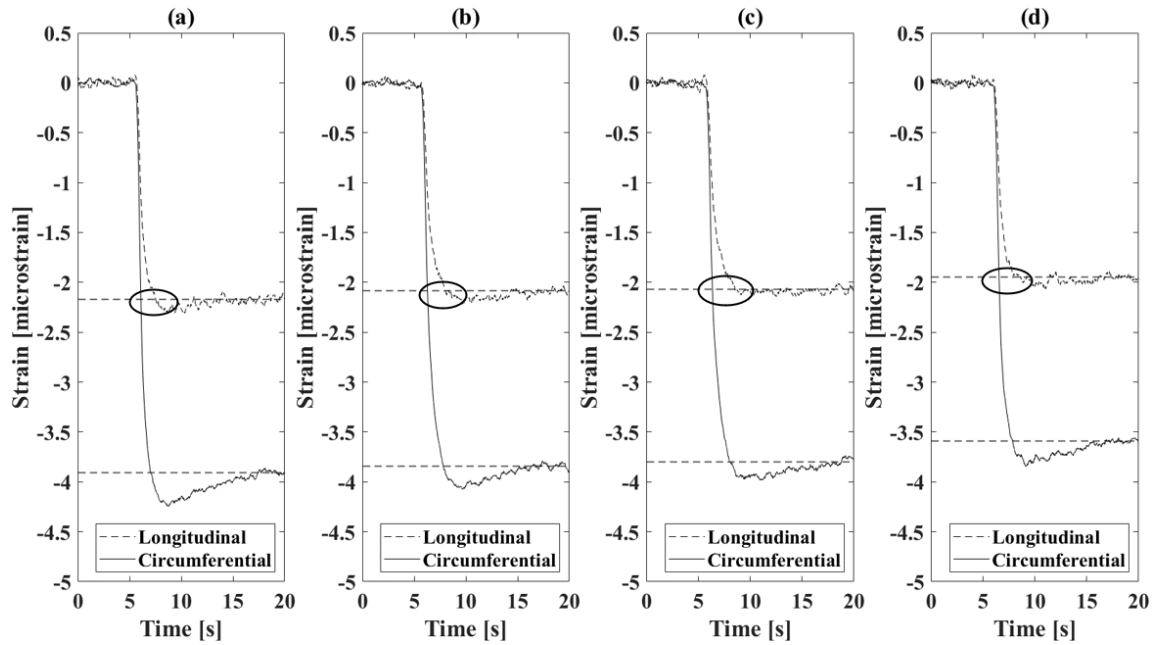


Figure 4: Time gap between the intercepts of S1 and S2 at leakage locations a) L1, b) L2, c) L3, and d) L4 at a pressure of 100 kPa and a flow rate of 10 GPM.

Table 1: Intercept times and time differences for sensors 1 and 2 recorded for different leakage scenarios.

Time intercepts for pressure variations at 15 GPM at leakage location L1 with a small leakage size			
	The intercept of sensor 1 (s)	The intercept of sensor 2 (s)	Time difference (s)
L1	7.525	6.104	1.421
L2	8.029	6.296	1.733
L3	8.552	6.374	2.178
L4	8.544	6.564	1.980
Time intercepts for pressure variations at 15 GPM at leakage location L4 with a small leakage size			
	The intercept of sensor 1 (s)	The intercept of sensor 2 (s)	Time difference (s)
L1	7.626	6.381	1.245
L2	7.547	6.212	1.335
L3	7.939	6.468	1.471
L4	8.152	6.552	1.600
Time intercepts for pressure variations at 15 GPM at leakage location L1 with a large leakage size			
	The intercept of sensor 1 (s)	The intercept of sensor 2 (s)	Time difference (s)
L1	8.147	6.775	1.372
L2	9.133	7.118	2.015
L3	9.118	6.775	2.343
L4	9.327	6.992	2.335
Time intercepts for pressure variations at 15 GPM at leakage location L4 with a large leakage size			
	The intercept of sensor 1 (s)	The intercept of sensor 2 (s)	Time difference (s)
L1	8.091	6.520	1.571
L2	9.284	6.675	2.609
L3	9.843	6.690	3.153
L4	9.081	6.497	2.584

The changes in surface strain measured in this study can be compared to the results reported in previous studies. For instance, tests performed at a pressure of 120 kPa (120 kPa) yielded a change of 5 to 6  $\mu\epsilon$  on the surface of the pipe [18]. Other tests performed at a much higher pressure of 1.2 MPa inflicted 90–120  $\mu\epsilon$  on the surface of the pipe [19]. These tests were both performed on sections of pipe similar to the one used in this work. Oil transportation pipelines typically operate at much higher pressures than those used in the testbed in this study [20], and hence, at much higher hoop stress. Therefore, in the presence of leakage, these high pressures will increase the observed strain drops due to the higher-pressure amplitude of the NPW, guaranteeing a higher SNR and more easily observable and clear strain drop/ patterns.

### Conclusions

In this work, it is clear that pipeline leakages that occur under different operational conditions generate different amounts and variations in the strain patterns on the surface of the pipe. In all the tested scenarios, leakage always resulted in a drop of the strain measured on the surface of the pipe. The amplitude of that drop increased with an increase in pressure, a decrease in flow rate, and an increase in leakage size. The location of the leakage, however, had no effect on the amplitude of that drop but rather on the shape of the signals measured.

### Acknowledgments

We acknowledge the financial support of the University Research Board at the American University of Beirut (Award #103604).

### References

- [1] GA Papadakis, "Assessment of requirements on safety management systems in EU regulations for the control of major hazard pipelines", *Journal of hazardous materials* 78(1-3), pp 63-89, 2000. [https://doi.org/10.1016/S0304-3894\(00\)00217-X](https://doi.org/10.1016/S0304-3894(00)00217-X)
- [2] D Lyons, "Western European cross-country oil pipelines 30-year performance statistics", CONCAWE, 2002.
- [3] JL Kennedy, "Oil and gas pipeline fundamentals, Illustrated ed." Pennwell books, pp, 1993.
- [4] C Sandberg, J Holmes, K McCoy and H Koppitsch, "The application of a continuous leak detection system to pipelines and associated equipment", *IEEE Transactions on Industry applications* 25(5), pp 906-909, 1989. <https://doi.org/10.1109/28.41257>
- [5] HA Kishawy and HA Gabbar, "Review of pipeline integrity management practices", *International Journal of Pressure Vessels and Piping* 87(7), pp 373-380, 2010. <https://doi.org/10.1016/j.ijpvp.2010.04.003>
- [6] P Black, "A review of pipeline leak detection technology, Pipeline Systems, Springer, pp 287-298, 1992. [https://doi.org/10.1007/978-94-017-2677-1\\_23](https://doi.org/10.1007/978-94-017-2677-1_23)
- [7] JP Lynch, CR Farrar and JE Michaels, "Structural health monitoring: technological advances to practical implementations [scanning the issue]", *Proceedings of the IEEE* 104(8), pp 1508-1512, 2016. <https://doi.org/10.1109/JPROC.2016.2588818>
- [8] H Jin, L Zhang, W Liang and Q Ding, "Integrated leakage detection and localization model for gas pipelines based on the acoustic wave method", *Journal of Loss Prevention in the Process Industries* 27, pp 74-88, 2014. <https://doi.org/10.1016/j.jlp.2013.11.006>

- [9] J Zhu, L Ren, S-C Ho, Z Jia and G Song, "Gas pipeline leakage detection based on PZT sensors", *Smart Materials and Structures* 26(2), pp 025022, 2017. <https://doi.org/10.1088/1361-665X/26/2/025022>
- [10] RA Silva, CM Buiatti, SL Cruz and JAFR Pereira, "Pressure wave behaviour and leak detection in pipelines", *Computers & Chemical Engineering* 20, pp S491-S496, 1996. [https://doi.org/10.1016/0098-1354\(96\)00091-9](https://doi.org/10.1016/0098-1354(96)00091-9)
- [11] H Jansen and M Festen, "Intelligent pigging developments for metal loss and crack detection", *INSIGHT-WIGSTON THEN NORTHAMPTON*- 37, pp 421-421, 1995.
- [12] FBI Alnaimi, AA Mazraeh, K Sahari, K Weria and Y Moslem, "Design of a multi-diameter in-line cleaning and fault detection pipe pigging device", *Proc. of 2015 IEEE International Symposium on Robotics and Intelligent Sensors (IRIS)*, pp 258-265, 2015.
- [13] AbM Akib, Nb Saad and V Asirvadam, "Pressure point analysis for early detection system", *2011 IEEE 7th International Colloquium on Signal Processing and its Applications*, Penang, Malaysia, pp, 2011.
- [14] JC Martins and P Selegim, "Assessment of the performance of acoustic and mass balance methods for leak detection in pipelines for transporting liquids", *Journal of Fluids Engineering* 132(1), pp, 2010. <https://doi.org/10.1115/1.4000736>
- [15] C Ponce, M V, G Castañón, L Cayuela and V Puig, "Model-based leak detection and location in water distribution networks considering an extended-horizon analysis of pressure sensitivities", *Journal of Hydroinformatics* 16(3), pp 649-670, 2014. <https://doi.org/10.2166/hydro.2013.019>
- [16] E Hauge, OM Aamo and J-M Godhavn, "Model based pipeline monitoring with leak detection", *Proc. of Seventh IFAC Symposium on Nonlinear Control Systems*, pp, 2007. <https://doi.org/10.3182/20070822-3-ZA-2920.00053>
- [17] A Mishra and A Soni, "Leakage detection using fibre optics distributed temperature sensing", *Proc. of 6th Pipeline Technology Conference*, pp, 2011.
- [18] T Jiang, L Ren, Z Jia, D Li and H Li, "Application of FBG based sensor in pipeline safety monitoring", *Applied Sciences* 7(6), pp 540, 2017. <https://doi.org/10.3390/app7060540>
- [19] Z Jia, L Ren, H Li and W Sun, "Pipeline leak localization based on FBG hoop strain sensors combined with BP neural network", *Applied Sciences* 8(2), pp 146, 2018. <https://doi.org/10.3390/app8020146>
- [20] "Natural Resources Canada", 4-MAY, Access, <<https://www.nrcan.gc.ca/home>>.

# Gaussian Mixture Model Based Damage Evaluation for Aircraft Structures

Qihui Xu, Shenfang Yuan\*, Yuanqiang Ren

Research Center of Structural Health Monitoring and Prognosis, State Key Lab of Mechanics and Control of Mechanical Structures, Nanjing University of Aeronautics and Astronautics, Nanjing, 210016, P. R. China

qh@nuaa.edu.cn, ysf@nuaa.edu.cn, renyuanqiang@nuaa.edu.cn,

**Keywords:** Structural Health Monitoring, Guided Wave Features, Aircraft Fatigue Test, Multi-Dimensional Gaussian Mixture Model, Migration Index

**Abstract.** The Guided Wave (GW) based Structural Health Monitoring (SHM) method is of significant research interest because of its wide monitoring range and high sensitivity. However, there are still many challenges in real engineering applications due to complex time-varying conditions, such as changes in temperature and humidity, random dynamic loads, and structural boundary conditions. In this paper, a Gaussian Mixture Model (GMM) is adopted to deal with these problems. Multi-dimensional GMM (MDGMM) is proposed to model the probability distribution of GW features under time-varying conditions. Furthermore, to measure the migration degree of MDGMM to reveal the crack propagation, research on migration indexes of the probability model is carried out. Finally, the validation in an aircraft fatigue test shows a good performance of the MDGMM.

## Introduction

Structural Health Monitoring (SHM) technology has been gradually developed from basic theoretical research in the laboratory to practical aircraft engineering validations and applications [1,2]. The Guided Wave (GW) based SHM method has been widely studied due to its wide monitoring range and being sensitive to various types of small damage [3]. However, the real in-service conditions of aircraft structure are very complex, with many time-varying factors such as environmental temperature and humidity, random dynamic load and vibration, changing structural boundary condition, noise, and possibly others. The problem of reliable damage evaluation under time-varying conditions has become one of the main obstacles for applying SHM technology to real aircraft structures. These time-varying factors introduce uncertainty effects on GW signal features, leading to lower reliability and stability of SHM techniques in engineering applications.

In recent years, SHM methods based on probability and statistics are gradually studied to deal with the time-varying problem [4]. As an effective probability and statistics tool for characterizing uncertainties of GW signals, the Gaussian mixture model (GMM) has been gradually adopted for damage diagnosis of aerospace structure. Tschöpe and Wolff [5] studied the basic GMM for damage degree classification on simple plate-like structures. However, they did not consider time-varying conditions. Banerjee et al. [6] adopted GMM to classify the crack length of a plate-like repaired composite specimen. The sudden change of the environmental temperature was considered as a time-varying factor in the validation of this method but it is a simple situation. Yuan and Qiu et al. [7] proposed an enhanced dynamic GMM-based damage monitoring method considering the ordinary expectation-maximization algorithm can easily lead to a local optimal solution and a singular solution. The method was validated using the case of hole-edge crack

monitoring of an aluminum plate and a real aircraft wing spar. All the research mentioned above has proved the potential to apply the GMM to solve the time-varying problem. However, deep research is still needed to be performed concerning the GMM for damage evaluation of real aircraft structures under time-varying conditions.

In this article, a Multi-Dimensional GMM(MDGMM) based damage monitoring method is proposed to deal with the uncertainties caused by time-varying conditions under the complex real in-service environment of an aircraft structure. MDGMM is proposed to model the probability distribution of the GW features under time-varying conditions. Furthermore, to measure the migration degree of MDGMM to reveal the damage propagation, the research on migration indexes (MI) of the probability mixture model is also carried out. Finally, validations in an aircraft fatigue test are presented which show a good performance of the MDGMM.

### Aircraft fatigue test and GW signals

#### Setup of the aircraft fatigue test

The monitoring hotspot is located on the inner surface of the aircraft tail. Through visual inspection, the crack continues to grow during the whole aircraft fatigue test. During the different experimental days, the temperature range is 6.8°C to 14.7°C.

A five-cycle sine burst modulated by the Hanning window with the central frequency of 150 kHz is used as the GW excitation signal. The fatigue test lasts 21 days and GW signals are collected during application of the dynamic load. Typical GW signals are shown in Fig. 1. Considering that the crack propagation path is near the direct propagation path of the GW, the direct wave is the main signal segment for crack propagation monitoring. Thus, the length of the signal segment which is adopted to monitor the crack propagation is from  $0.75 \times 10^{-4}$ s to  $1.0 \times 10^{-4}$ s.

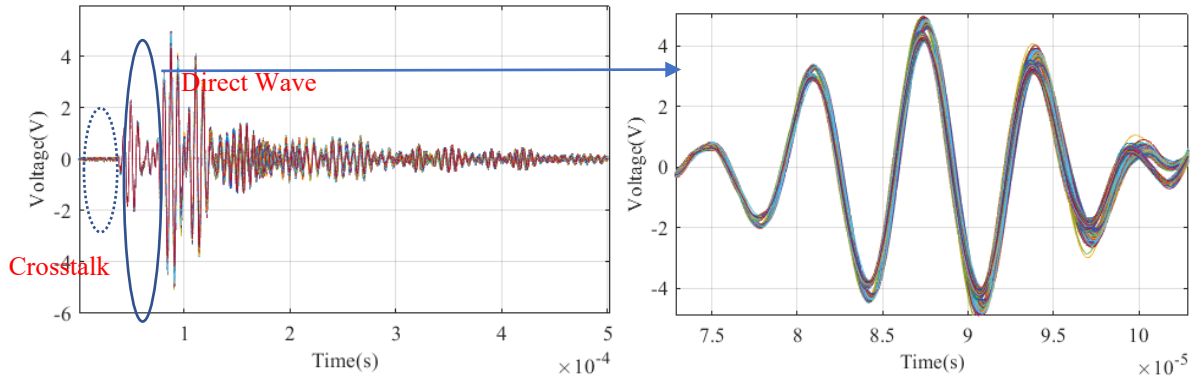


Figure 1. GW signals acquired under time-varying condition

#### GW feature extraction

For crack propagation monitoring by only one GW pitch-catch channel, a damage index (DI) can be used. This DI is used to measure the difference between the monitoring GW signal and the baseline GW signal. In this paper, multi-dimensional  $DI$ s are selected to represent the damage information of the structure.  $DI_1$  is the time-domain cross-correlation.  $DI_2$  is the spectrum magnitude difference and  $DI_3$  is the normalized correlation moment<sup>[8]</sup>.

The  $DI$ s during the fatigue test are shown in Fig.2. In conventional  $DI$  based SHM methods, a  $DI$  threshold is often predefined. When the value of the  $DI$  exceeds the threshold, a damage is assumed to have occurred. However, the variation of GW features introduced by time-varying conditions is random and complex. The evaluation of crack propagation is also difficult to be realized based on the results shown in Fig.2.

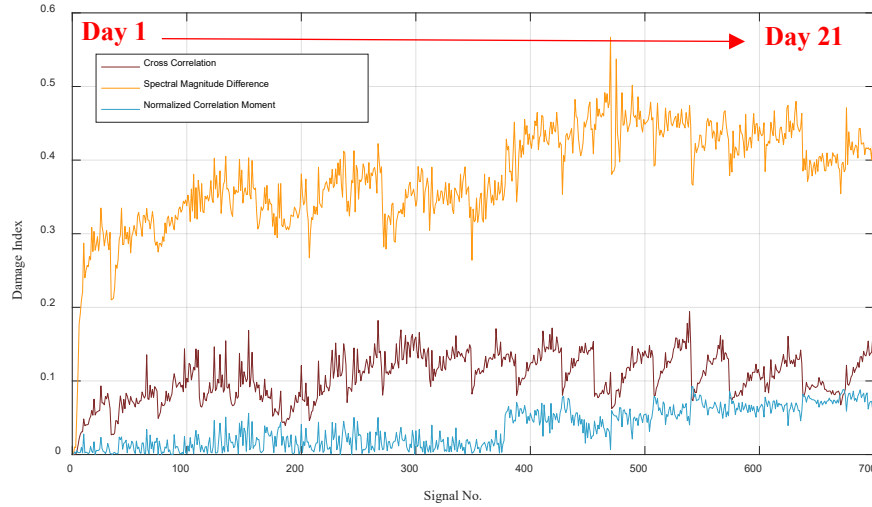


Figure 2. DIs under the dynamic load

### GW-MDGMM based damage evaluation method

#### Damage monitoring principle of the MDGMM

The GW signals acquired under time-varying conditions can be considered as a mixture of uncertain changes. Consequently, the GW feature can be considered as a random variable. Let  $\mathbf{X} = [\mathbf{X}_1, \mathbf{X}_2, \dots, \mathbf{X}_k, \dots, \mathbf{X}_K]$  be a GW feature sample set composed by  $K$  features that are obtained from  $K$  GW signals.  $\mathbf{X}_k$  denotes a  $d$ -dimensional GW feature in the sample set, where  $\mathbf{X}_k = [DI_1, DI_2, \dots, DI_d]^T$  and  $k=1, 2, \dots, K$ . When a monitored structure is in the healthy state, the GW feature sample set only contains the uncertain influence introduced by time-varying conditions. Under this situation, the feature sample set can be regarded as a GW baseline feature sample set.

Assuming that  $\mathbf{X}$  follows a finite mixed distribution, the mixture probability distribution  $\xi(\mathbf{X})$  can be approximately modeled by a Gaussian mixture model (GMM). The GMM is expressed as Eq. 1.

$$\xi(\mathbf{X}|\boldsymbol{\mu}, \boldsymbol{\Sigma}) = \sum_{i=1}^C w_i \xi_i(\mathbf{X}_k|\boldsymbol{\mu}_i, \boldsymbol{\Sigma}_i) \quad (1)$$

Where  $C$  is the number of Gaussian components,  $i=1,2,\dots,C$ . An important step is to determine the number of Gaussian components before modeling.  $w_i$  is the mixture weight of the  $i$ th Gaussian component.  $\boldsymbol{\mu}_i$  and  $\boldsymbol{\Sigma}_i$  are the mean and the covariance matrix of the  $i$ th Gaussian component. The probability density function of each Gaussian component is a multi-dimensional ( $d$ -dimensional) Gaussian function which is expressed as Eq. 2.

$$\xi_i(\mathbf{X}_k|\boldsymbol{\mu}_i, \boldsymbol{\Sigma}_i) = \frac{1}{(2\pi)^{\frac{d}{2}} \sqrt{|\boldsymbol{\Sigma}_i|}} e^{-\frac{1}{2}(\mathbf{X}_k - \boldsymbol{\mu}_i)^T \boldsymbol{\Sigma}_i^{-1} (\mathbf{X}_k - \boldsymbol{\mu}_i)} \quad (2)$$

The expectation-maximization ( $E$ - $M$ ) algorithm is often used to construct the MDGMM [7]. First, the initial value of  $\boldsymbol{\mu}_i$ ,  $\boldsymbol{\Sigma}_i$ , and  $w_i$  can be obtained by the  $k$ -means clustering algorithm. Second, the  $E$ -step and the  $M$ -step are performed iteratively to obtain the optimized  $\boldsymbol{\mu}_i$ ,  $\boldsymbol{\Sigma}_i$ , and  $w_i$ .

*On-line migration measuring of the MDGMM*

The migration measuring result between the on-line monitoring MDGMM and the baseline MDGMM is defined as migration index (MI). Accompanying the damage propagation, two GMMs will be separated gradually. In this paper, Euclidean distance<sup>[9]</sup> (E-distance), Mahalanobis distance<sup>[10]</sup> (M-distance), Bhattacharyya distance<sup>[11]</sup> (B-distance), and KL divergence<sup>[12]</sup> are studied.

The Euclidean distance based model migration index can be calculated by Eq. 3.

$$d(\xi_i(0) \parallel \xi_j(n)) = (\mu_i(0) - \mu_j(n))^T (\mu_i(0) - \mu_j(n)) \tag{3}$$

The Mahalanobis distance based model migration index can be calculated by Eq. 4.

$$d(\xi_i(0) \parallel \xi_j(n)) = (\mu_i(0) - \mu_j(n))^T \left( \frac{\Sigma_i(0) + \Sigma_j(n)}{2} \right)^{-1} (\mu_i(0) - \mu_j(n)) \tag{4}$$

The Bhattacharyya distance based model migration index can be calculated by Eq. 5.

$$d(\xi_i(0) \parallel \xi_j(n)) = \frac{1}{8} (\mu_i(0) - \mu_j(n))^T \left( \frac{\Sigma_i(0) + \Sigma_j(n)}{2} \right)^{-1} (\mu_i(0) - \mu_j(n)) + \frac{1}{2} \ln \frac{|\Sigma_i(0) + \Sigma_j(n)| / 2}{|\Sigma_i(0)|^{1/2} |\Sigma_j(n)|^{1/2}} \tag{5}$$

The K-L divergence based model migration index can be calculated by Eq. 6.

$$d(\xi_i(0) \parallel \xi_j(n)) = \frac{1}{2} \text{tr} \left[ \Sigma_j(n)^{-1} \Sigma_i(0) + [\mu_j(n) - \mu_i(0)]^T \Sigma_j(n)^{-1} [\mu_j(n) - \mu_i(0)] - d - \ln \left( \frac{|\Sigma_j(n)|}{|\Sigma_i(0)|} \right) \right] \tag{6}$$

Where  $\mu_i(0)$ ,  $\Sigma_i(0)$ , and  $w_i(0)$  are the mean, the covariance matrix, and the mixture weight of the  $i$ -th Gaussian component of  $\xi(0)$ , respectively.  $\mu_j(n)$ ,  $\Sigma_j(n)$ , and  $w_j(n)$  are the mean, the covariance matrix, and the mixture weight of the  $j$ -th Gaussian component of  $\xi(n)$ , respectively.  $\text{tr}[\cdot]$  is the matrix trace.

Also, Eq. 7 is the result of considering the difference of the mixture weight between two Gaussian components.

$$D(\xi_i(0) \parallel \xi_j(n)) = \sum_{i=1}^K w_i^0 \min_{j=1}^K \left( d(\xi_i(0) \parallel \xi_j(n)) + \ln \frac{w_i(0)}{w_j(n)} \right) \tag{7}$$

*The MDGMM based damage evaluation process*

When a new GW feature is obtained during an on-line damage monitoring process, a migration method can be adopted to rebuild the MDGMM. Once the on-line migrated MDGMM is obtained, the measuring methods are adopted to determine the crack occurrence.

*Crack propagation monitoring based on the GW-MDGMM*

The first 50 GW features that are obtained from 50 GW signals are used as a GW baseline sample set to construct a baseline MDGMM in the first part shown in Fig.3(a). All GW features are input one by one to calculate the MI. The number of Gaussian components is set to be 3 to cover the GW feature sample set. The baseline MDGMM is shown in Fig.3 (a). Based on the

migration method, some typical on-line migrated MDGMMs accompanying the crack propagation are shown in Fig.3 (b)–(d) respectively.

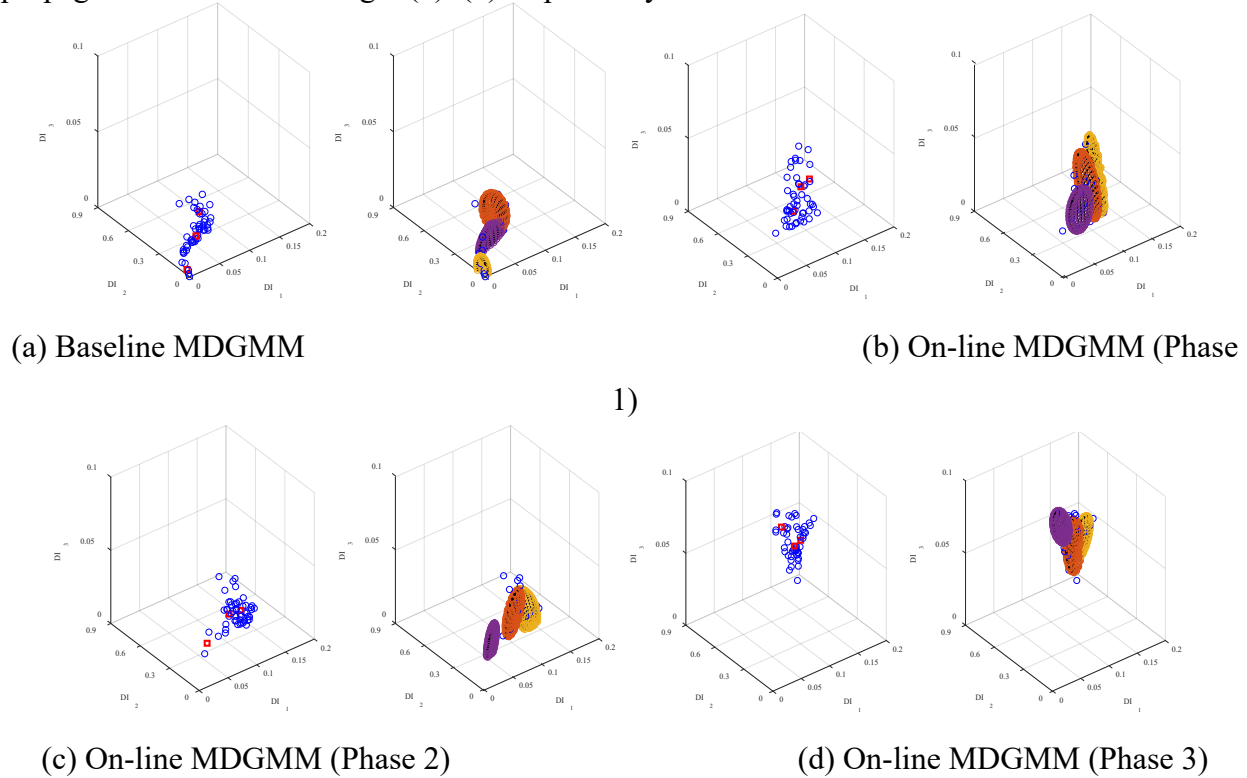


Figure 3. MDGMM migration process

The MIs calculated by Eq. 3-6 are displayed in Fig.4. Compared to the *DI*s shown in Fig.2, the four MIs increase gradually and present a cumulative progressive trend that accompanies the crack growth under fatigue dynamic load. Therefore, a threshold can be easily defined to determine the crack occurrence, and the initial crack propagation can be reliably evaluated depending on the cumulative variation trend of the MIs.

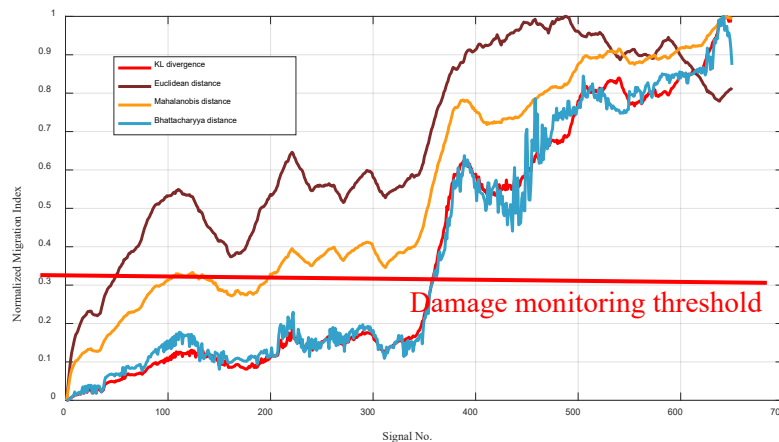


Figure 4. Crack propagation monitoring results

The overall trend of the four MIs is consistent, which indicates that these four distance methods can be used to measure the migration of MDGMM to a certain extent. As shown in Fig.4, the fluctuation of E-distance is large. After 400 monitoring times, E-distance drops

sharply, showing that the reliability and accuracy of E-distance are the lowest. This may be because the E-distance only considers the mean difference but ignores the correlation between samples. The results show that KL divergence and B-distance are similar in measuring MDGMM migration distance. However, the volatility of B-distance is large and its stability is not good. In the early stage of damage monitoring, M-distance shows a larger value, which indicates that the sensitivity of M-distance is relatively high. In summary, M-distance and KL divergence show better performance in migration measuring of MDGMM.

### Conclusion

An MDGMM based damage monitoring method is proposed in this article to improve crack propagation monitoring reliability under time-vary conditions. The monitoring results in an aircraft fatigue test show a good performance of the MDGMM. The whole method is a data-driven based probability and statistics method, with no mechanical models of damage and structure needed.

However, there are several further studies to be performed in the near future. As mentioned before, an important step of the GMM is to determine the number of Gaussian components. Further research is needed to better determine the number of Gaussian components required. For the quantification of damage size, the calculation method of MI must be further improved. The environmental influence such as humidity is low in the fatigue test. More aircraft fatigue tests will be performed shortly under a more complex time-varying condition.

### Acknowledgment

This work is sponsored by National Natural Science Foundation of China (Grant No.51921003, Grant No. 51635008), Jiangsu Provincial Key Research and Development Program of China (Grant No. BE2018123), Priority Academic Program Development of Jiangsu Higher Education Institutions of China.

### References

- [1] Boller C, Chang FK and Fujino Y. Encyclopedia of structural health monitoring. New York: John Wiley & Sons, 2009. <https://doi.org/10.1002/9780470061626>
- [2] Yuan S F, Ren Y Q, Qiu L, Mei H F. A multi-response-based wireless impact monitoring network for aircraft composite structures. *IEEE Transactions on Industrial Electronics*, 2016, 63(12): 7712-7722. <https://doi.org/10.1109/TIE.2016.2598529>
- [3] Su Z, Ye L. Identification of Damage Using Lamb Waves. Springer London, 2009. <https://doi.org/10.1007/978-1-84882-784-4>
- [4] Yuan S F, Zhang J J, Chen J, et al. A uniform initialization Gaussian mixture model-based guided wave-hidden Markov model with stable damage evaluation performance. *Structural Health Monitoring*, 2019, 18(3):853-868. <https://doi.org/10.1177/1475921718783652>
- [5] Tschope C, Wolff M. Statistical Classifiers for Structural Health Monitoring. *Sensors Journal*, IEEE, 2009, 9(11):1567-1576. <https://doi.org/10.1109/JSEN.2009.2019330>
- [6] Banerjee S, Qing X P, Beard S, et al. Prediction of Progressive Damage State at the Hot Spots using Statistical Estimation. *Journal of intelligent material systems and structures*, 2010, 21(6):595-605. <https://doi.org/10.1177/1045389X10361632>
- [7] Qiu L, Fang F, Yuan S F, et al. An enhanced dynamic Gaussian mixture model-based damage monitoring method of aircraft structures under environmental and operational conditions.

Structural Health Monitoring, 2018:147592171875934.

<https://doi.org/10.12783/shm2017/13905>

- [8] Torkamani S, Roy S, Barkey M E, et al. A novel damage index for damage identification using guided waves with application in laminated composites. *Smart Materials & Structures*, 2014, 23(9):095015. <https://doi.org/10.1088/0964-1726/23/9/095015>
- [9] Liberti L, Lavor C, Maculan N, Mucherino A. Euclidean Distance Geometry and Applications. *SIAM Review*. 2014; 56:3-69. <https://doi.org/10.1137/120875909>
- [10] De Maesschalck R, Jouan-Rimbaud D, Massart DL. The Mahalanobis distance. *Chemometrics and Intelligent Laboratory Systems*. 2000; 50:1-18. [https://doi.org/10.1016/S0169-7439\(99\)00047-7](https://doi.org/10.1016/S0169-7439(99)00047-7)
- [11] You C H, Lee K A, Li H. GMM-SVM Kernel with a Bhattacharyya-Based Distance for Speaker Recognition. *Audio Speech & Language Processing IEEE Transactions on*, 2010, 18(6):1300-1312. <https://doi.org/10.1109/TASL.2009.2032950>
- [12] Goldberger J, Gordon S, Greenspan H. An efficient image similarity measure based on approximations of KL-divergence between two Gaussian mixtures// *Proceedings Ninth IEEE International Conference on Computer Vision*. IEEE, 2003. <https://doi.org/10.1109/ICCV.2003.1238387>

# In-Situ Strain Monitoring in Deltoid of Composite T-joints using Optical Fiber

Shinsaku Hisada<sup>1,a</sup>, Shu Minakuchi<sup>1,b</sup> and Nobuo Takeda<sup>1,c,\*</sup>

<sup>1</sup>Department of Advanced Energy, Graduate School of Frontier Sciences, The University of Tokyo, 5-1-5 Kashiwanoha, Kashiwa-shi, Chiba 277-8561, Japan

<sup>a</sup>hisada@smart.k.u-tokyo.ac.jp, <sup>b</sup>minakuchi@smart.k.u-tokyo.ac.jp,  
<sup>c</sup>takeda@smart.k.u-tokyo.ac.jp

**Keywords:** Optical Fiber, T-joint, Deltoid, Process Monitoring

**Abstract.** Composite T-joints have a critical problem that cracks occur in the deltoid during curing because of the cure stress and thermal stress. There are few studies on the behavior of T-joints during curing, and what is actually occurring in the deltoid is not well understood. In the present study, optical fiber was embedded in the deltoid using a new technique to clarify the internal state of the deltoid during curing. The embedded optical fiber successfully measured the process-induced strain distribution in the deltoid. Based on the experimental results and finite element analysis, a failure index for a process-induced failure of deltoid was discussed. An energy-based failure index could precisely predict the process-induced failure.

## Introduction

One of the difficulties in composite structural application is joining components. A T-joint is a typical joining component of aircraft structures and composed of two L-shaped parts, a skin laminate, and a deltoid, which is filling a gap between other components (Fig. 1). In T-joints, it is reported that cracks occur in the deltoid during curing because of the cure stress and thermal stress [1]. This is a critical problem because such cracking significantly reduces the mechanical performance of T-joints. Although many studies on the behavior of T-joints under mechanical loadings have been conducted, studies on the behavior of these joints during curing are very limited, and it is not well understood what is actually occurring inside the deltoid. This is because, to date, there was no technology to evaluate the stress-strain state of the deltoid surrounded by other components during curing. In the present study, strain distribution inside the deltoid is measured using a new technique to embed an optical fiber into the deltoid, and the stress-strain state of the deltoid during curing is analyzed. Based on the experimental results, finite element analysis is conducted and a failure index for a process-induced failure of deltoid is discussed.

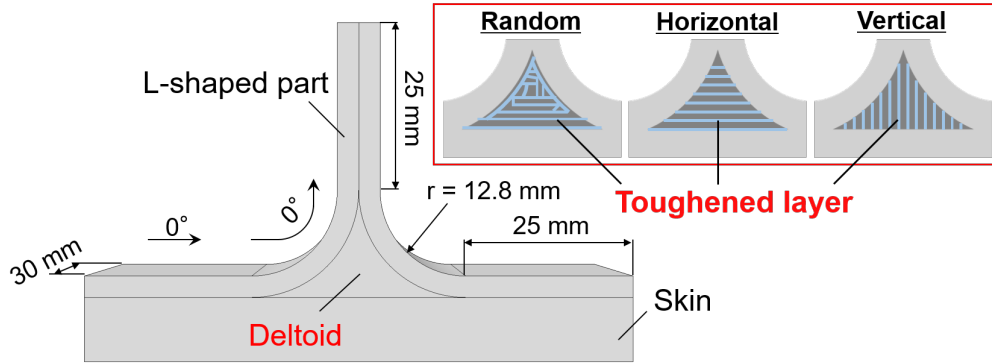


Fig. 1 Schematic of T-joint specimen used for in-situ strain measurement.

### In-Situ Strain Measurement of the Deltoid during Curing

**Distributed-Strain Measurement using an Optical Fiber.** Optical fibers are widely used for strain measurement of composite materials because of various advantages, such as their small diameter and light weight [2]. In this study, strain distribution inside the deltoid was measured using an optical distributed sensor interrogator (ODiSI, LUNA Innovations, Inc.). The ODiSI uses swept-wavelength coherent interferometry [3]. The measurement principle is shown in Fig. 2. One of the split light paths is directly incident on the detector, whereas the other light paths is incident on the optical fiber and causing Rayleigh scattering. The location of the Rayleigh scattering can be determined from the time difference of the two lights. The frequency  $\nu$  of the Rayleigh-scattered light shifts linearly with temperature change ( $\Delta T$ ) and axial strain change ( $\Delta \epsilon$ ); this can be expressed as

$$\frac{-\Delta \nu}{\nu} = K_T \Delta T + K_\epsilon \Delta \epsilon \quad (1)$$

where  $K_T$  and  $K_\epsilon$  are the coefficients. Therefore, the strain can be calculated from the Rayleigh-scattered light frequency by compensating the temperature effect.

### Materials and Methods

A schematic of the specimen is shown in Fig. 1. A unidirectional carbon/epoxy prepreg sheet (T800S/3900-2B; Toray Industries, Inc.) was used in this study. This prepreg has been implemented in primary composite structures of Boeing 787, and has an interlaminar toughened layer to improve the interlaminar fracture toughness and impact resistance. This layer is composed of thermoplastic particles that are dispersed across the prepreg surface. The stacking sequence was  $[0_2/90_2]_{2S}$  (thickness: 3.2 mm) in the L-shaped parts, and  $[0_2/90_2]_{2S3}$  (thickness: 9.6 mm) in the skin laminate. The carbon fibers were oriented in the  $90^\circ$  direction. Since it has been reported that materials with interlaminar toughened layers possess different transverse properties in the parallel direction and in the orthogonal direction to the toughened layer [4], three types of deltoid structures with differently oriented interlaminar toughened layers were prepared to investigate the effect of the toughened layer on the process-induced failure as shown in Fig. 1. An optical fiber (coating diameter  $\phi = 150 \mu\text{m}$ ) was embedded along the centerline of the deltoid in a minimally invasive manner through tiny holes that were machined in the aluminum tool, deltoid, and skin. The holes in the deltoid and skin were made by pressing a thin needle ( $\phi = 0.5 \text{ mm}$ ) into the stacked prepreg sheets using an ultrasonic horn and a jig to adjust the pressing

angle. By using this method, the strain in a closed structure surrounded by tools can be measured (Fig. 3). A K-type thermocouple was also embedded to compensate the effect of the temperature change. The specimens were cured in the autoclave at 180°C under 0.6 MPa pressurization. The Rayleigh-scattered light frequency was measured at 2 mm intervals in the random deltoid and horizontally-aligned deltoid specimens, and at 4 mm intervals in the vertically aligned deltoid specimen.

**Results.** Figure 4 shows the local strain development during curing at the bottom of the random deltoid specimen. After gelation, the chemical cure shrinkage was measured as the cure reaction

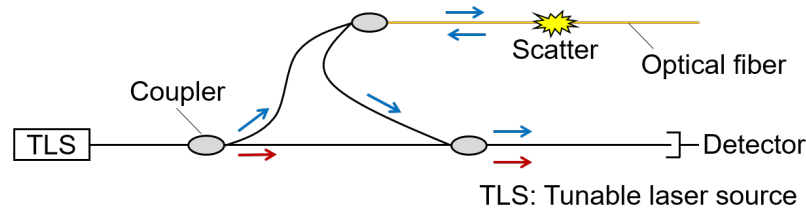


Fig. 2 Distributed-strain measurement principle using an ODiSi.

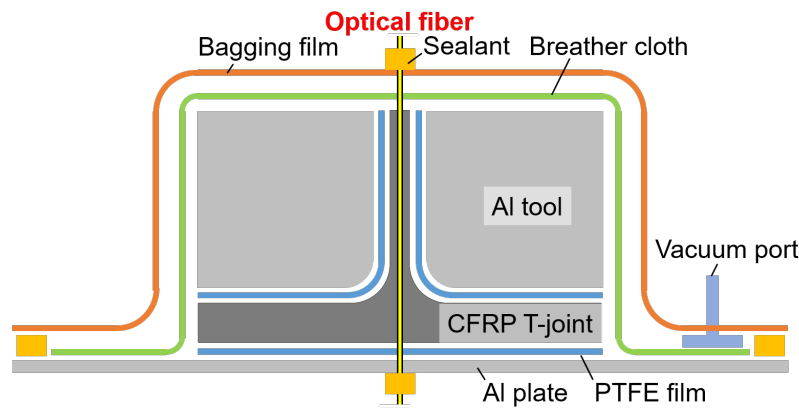


Fig. 3 Assembly and bagging of specimen with optical fiber.

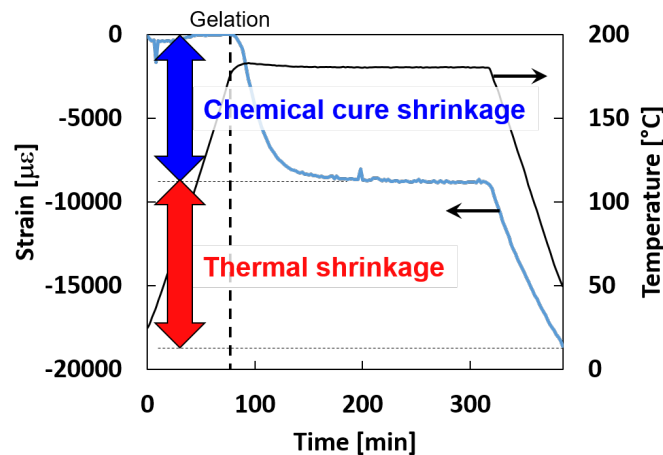


Fig. 4 Local strain development during curing at the bottom of the random deltoid specimen.

proceeded. In addition, the thermal shrinkage was measured during cooling process. Therefore, it was clearly demonstrated that the strain development inside the deltoid can be measured by using the proposed technique. The comparison of the strain distribution in the deltoid at the room temperature for each specimen is shown in Fig. 5. The horizontal and vertical axes represent the amount of strain and the position along the optical fiber path, respectively, with 0 mm corresponding the top of the deltoid, and 16 mm corresponding to the bottom of the deltoid. In all specimens, small strain was measured in the upper region of the deltoid because this region was strongly constrained by the fiber layers of L-shaped parts. The strain increased toward the lower part of the deltoid as the constraint in the axial direction of the optical fiber weakened. Although similar trends of the strain distribution were measured in all specimens, the strain amount was the largest in the horizontally aligned deltoid specimen, and the smallest in the vertically aligned deltoid specimen. This is because larger strain occurs in the direction orthogonal to the toughened layers than in the direction that is parallel to the toughened layer direction as has been demonstrated in previous research [4].

Because failure did not occur in the specimens that were cured under the test conditions of this study, the specimens were cooled at approximately 6°C/min using liquid nitrogen. Deltoid failure occurred at -115 °C for the random deltoid specimen, -40 °C for the horizontally aligned specimen, and -25 °C for the vertically aligned deltoid specimen. A lateral crack forming in the upper region of the deltoid was observed in the random deltoid specimen and the horizontally aligned deltoid

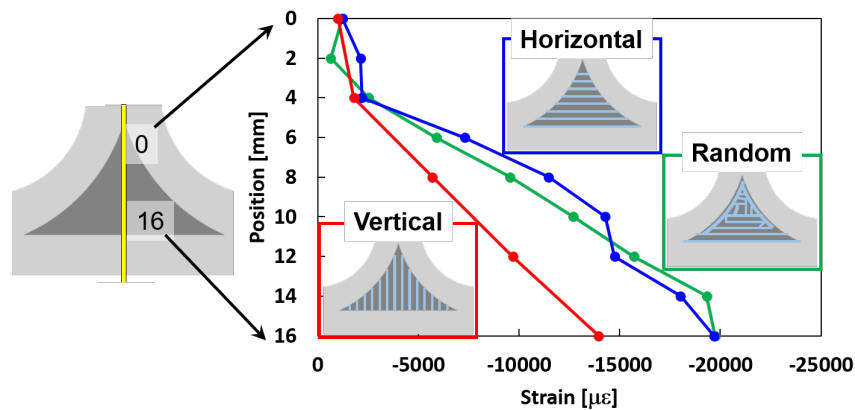


Fig. 5 Comparison of process-induced strain distribution in the deltoid for the three types of specimens.

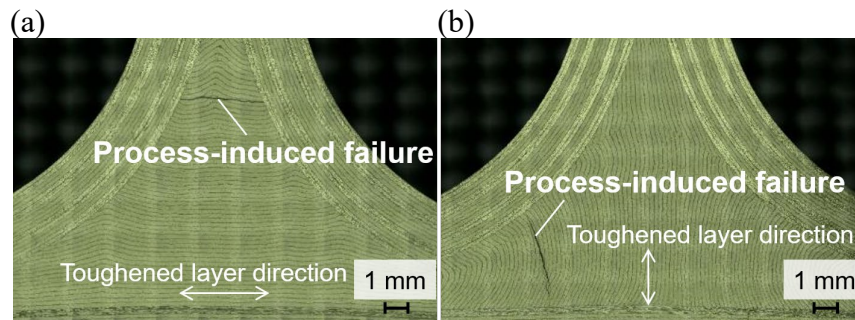


Fig. 6 Micrograph of failure surface.  
 (a) Horizontally aligned deltoid specimen. (b) Vertically aligned deltoid specimen.

specimen, and a vertical crack forming in the lower region of the deltoid was observed in the vertically aligned deltoid specimen (Fig. 6).

### Discussion on the Process-Induced Failure Index using Finite Element Analysis Supported by Strain Measurement

**FEA Methods.** FEA was performed using commercial software Abaqus 2017 (Dassault Systems, Inc.). Considering the symmetry of the T-joint, only a quarter of the T-joint was modeled, and symmetric boundary conditions were set for each plane. The horizontally aligned deltoid specimen was modeled, and the chemical cure shrinkage strain and thermal shrinkage strain associated with temperatures ranging from the curing temperature (180 °C) to the failure temperature (-40 °C) were implemented. In the analysis of the curing stress, an incrementally linear elastic (ILE) model [5] was used to account for a modulus development during curing. In the ILE model, the process of chemical cure shrinkage was divided into several steps, and the corresponding shrinkage strain was implemented as the resin modulus changed after each step. The values of the shrinkage strain and the resin modulus at each step were estimated in the previous study of our research group [4] using two optical fibers. This technique is described in detail in [6]. The material properties of the fiber/resin layer were derived from the estimated resin modulus and carbon fiber properties using the self-consistent field micromechanics model [5]. Furthermore, the material properties of the entire material, including the interlaminar toughened layers, were calculated based on the rule of mixture. Material properties used in the analysis are described in Tables 1-2 [4, 7, 8]. The total curing stress was calculated by adding the stress generated in each step. A user subroutine UMAT of Abaqus was used for the material properties calculations and ILE model calculations.

*Table 1. Resin modulus development and corresponding strain values associated with chemical cure shrinkage [4].*

Step	1	2	3	4	5	6	7	8
$E_m$ [MPa]	8.10	23.5	41.6	60.0	83.0	117	158	167
$\Delta\varepsilon$ [ $\mu\varepsilon$ ]	-960	-920	-690	-520	-380	-270	-270	-290

*Table 2. Properties of materials used in this study [7, 8].*

		Carbon fiber	Interlaminar toughened layer	Optical fiber (Cladding, core)	Optical fiber (Coating)
Elastic moduli [GPa]	$E_{11}$	294	4.6	73.1	1.5
	$E_{22}$	19.5			
	$G_{12}$	27.0			
	$G_{23}$	27.0			
Poisson's ratio	$\nu_{12}$	0.17	0.44	0.16	0.25
	$\nu_{23}$	0.46			

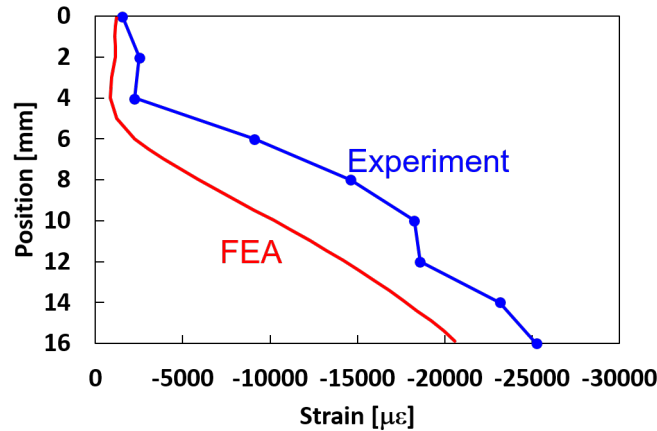


Fig. 7 Comparison of experimental and simulated strain distribution in the horizontally aligned deltoid specimen.

**Results.** Figure 7 shows a comparison of the experimental and simulated strain distribution in the deltoid of the horizontally aligned deltoid specimen. The shapes of the strain distribution curves were similar, and the amount of strain measured in the experiment was slightly larger than the simulated amount of strain. This is likely because actual deltoids are less constrained than their modeled counterparts because of imperfections such as misalignment of the fiber orientation. This result confirmed the validity of the simulated result, and the importance of acquiring in-situ strain using an optical fiber. Figure 8 shows the comparison of the normal stress state in the direction to the upper corner of the deltoid and the actual failure location. Although the maximum stress was generated near the corner of the deltoid, process-induced failure occurred at a location that was slightly distanced from the corner.

**Discussion on the Process-Induced Failure Index.** The FEA result implies that the stress-based failure index cannot be used to predict the location of the process-induced failure of deltoids. Therefore, the use of an energy-based failure index [9, 10] was investigated as a more precise index. The energy release rate can be expressed as the amount of work divided by the crack area.

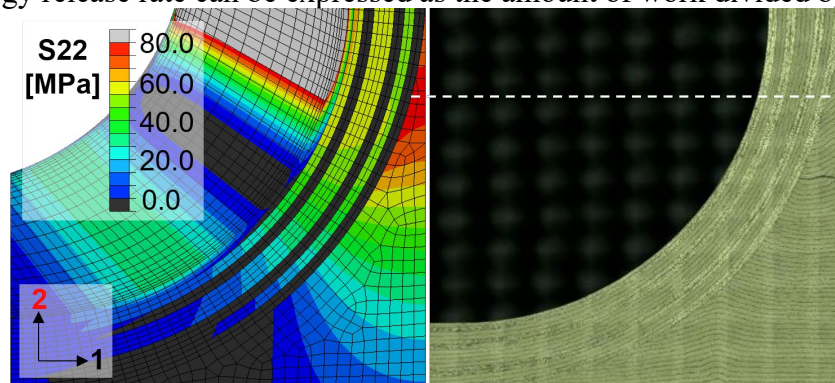


Fig. 8 Comparison of the simulated maximum stress location and actual failure location in the horizontally aligned deltoid specimen.

Therefore, when a crack with a unit length occurs in the 90° layer of the cross-ply laminate under the constant-stress condition, the energy release rate is expressed as follows:

$$G = G_c = \frac{\delta W_0}{t}, \tag{2}$$

where  $G_c$  is the fracture toughness of the material,  $\delta W_0$  is the amount of work required for crack initiation (Fig. 9), and  $t$  is the thickness of the specimen. When the laminate is divided into similar  $n \times n$  laminates, the stiffness values before and after crack initiation are the same as that for the original laminate. Then, the energy release rate can be expressed as follows:

$$G = G_c = \frac{\delta W}{(\frac{1}{n} \times n^2)t} = \frac{\delta W}{nt}, \tag{3}$$

where  $\delta W$  is the amount of work associated with the generation of all cracks. Because the fracture toughness of the material is constant,

$$\delta W = n\delta W_0. \tag{4}$$

According to the similarity law of a triangle,  $\sqrt{n}$  times stress is required to obtain  $n$  times the work (Fig. 9). More specifically, when the width of the  $90^\circ$  layer is  $m$  times,  $1/\sqrt{m}$  times stress is required for crack initiation. At the deltoid, the  $x$  axis and width of the deltoid  $a(x)$  are acquired as shown in Fig. 10, and the normal stress required for crack initiation at the width of  $a(x)$  is  $\sigma(x)$ . If the normal stress required for crack initiation at the unit width is  $\sigma_0$ , then

$$\sigma(x) = \frac{1}{\sqrt{a(x)}} \sigma_0, \tag{5}$$

where

$$\sqrt{a(x)}\sigma(x) = \sigma_0 = const. \tag{6}$$

Because the  $\sqrt{a(x)}\sigma(x)$  value required for crack initiation at a certain location in the deltoid is constant, a crack occurs at the maximum point of this value.

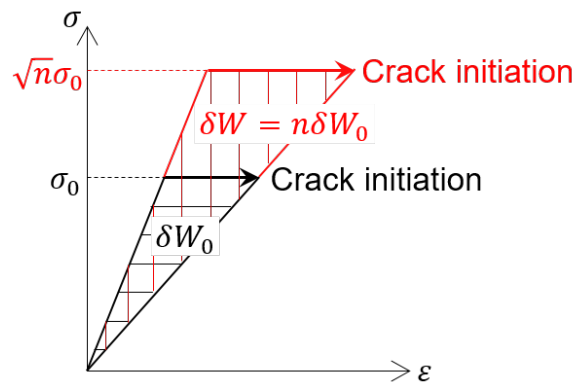


Fig. 9 Amount of work and applied stress required for crack generation.

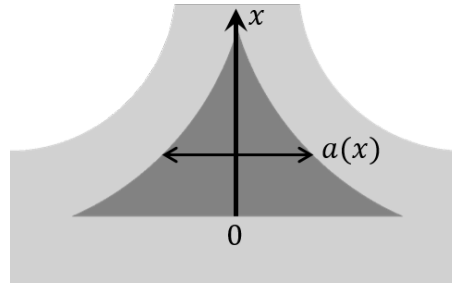


Fig. 10 X axis and width of 90° layer in the deltoid

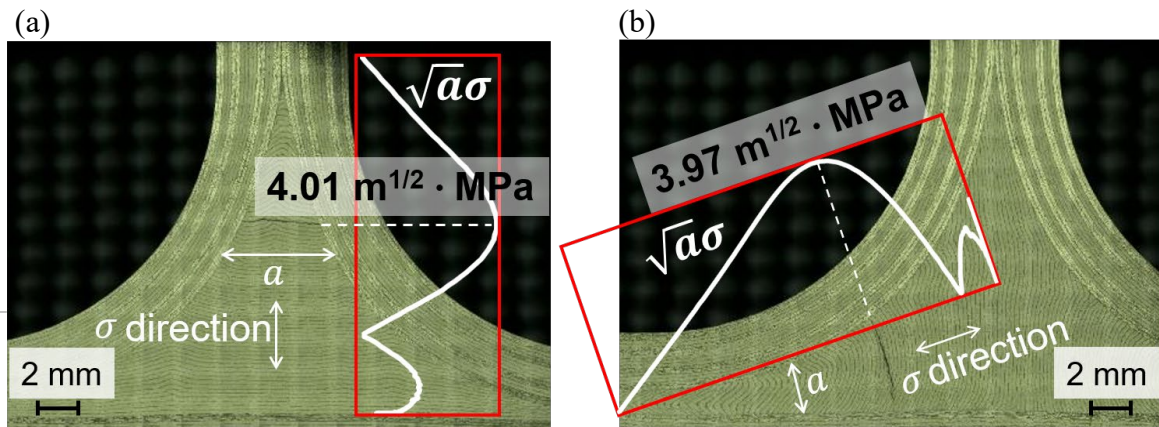


Fig. 11 Comparison of energy-based failure index results and actual failure location.  
 (a) Horizontally aligned deltoid specimen. (b) Vertically aligned deltoid specimen.

Figure 11(a) shows the comparison of the  $\sqrt{a(x)}\sigma(x)$  values derived from the FEA result and the actual failure location in the horizontally aligned deltoid specimen. The location associated with the maximum index value matched well with the failure location in the experiment. The same evaluation was conducted for the vertically aligned deltoid specimen and the result was shown in Fig. 11(b). In the vertically aligned deltoid specimen, the  $x$  axis is taken in the normal direction to the lower left corner because the process-induced failure occurred perpendicular to this axis. As with the horizontally aligned deltoid specimen, the location associated with the maximum index value matched well with the failure location. In addition, the maximum value of  $\sqrt{a(x)}\sigma(x)$  was nearly the same for these two specimens, i.e.,  $4.01 \text{ m}^{1/2}\cdot\text{MPa}$  for the horizontally aligned deltoid specimen, and  $3.97 \text{ m}^{1/2}\cdot\text{MPa}$  for the vertically aligned deltoid specimen. These results confirm that process-induced failure of the deltoid of a composite T-joint occurs when the energy-based requirement is met, and that the effects of the width of the 90° layer should be considered for failure prediction.

### Conclusions

In this study, in-situ strain measurements of the deltoid during curing were conducted using optical fibers. The chemical cure shrinkage strain and thermal shrinkage strain within the deltoid were successfully measured using proposed optical fiber embedment method. From the experiments and FEA supported by the strain measurements with optical fibers, it was confirmed that the process-induced failure of the deltoid of a composite T-joint occurs when the energy-based requirement is met. Based on these results obtained from process monitoring with optical

fiber, it will be possible to devise a method to suppress a process-induced failure of a composite T-joint.

## References

- [1] J. Chen, D. Fox, Numerical investigation into multi-delamination failure of composite T-piece specimens under mixed mode loading using a modified cohesive model, *Compos. Struct.* 94 (2012) 2010-2016. <https://doi.org/10.1016/j.compstruct.2011.12.030>
- [2] B. Lee, Review of the present status of optical fiber sensors, *Opt. Fiber Technol.* 9 (2003) 57-79. [https://doi.org/10.1016/S1068-5200\(02\)00527-8](https://doi.org/10.1016/S1068-5200(02)00527-8)
- [3] S.T. Kreger, D.K. Gifford, M.E. Froggatt, B.J. Soller, M.S. Wolfe, High resolution distributed strain or temperature measurements in single- and multi-mode fiber using swept-wavelength interferometry, In: *Optical Fiber Sensors*, Optical Society of America Technical Digest. (2006) Paper ThE42. <https://doi.org/10.1364/OFS.2006.ThE42>
- [4] S. Niwa, K. Takagaki, S. Minakuchi, N. Takeda, Cure shrinkage monitoring and process analysis of CFRP laminates with interlaminar-resin layers, *J. Jpn. Soc. Compos. Mater.* (in Japanese) 41 (2015) 168-175. <https://doi.org/10.6089/jscm.41.168>
- [5] T.A. Bogetti, J.W. Gillespie, Process-induced stress and deformation in thick-section thermoset composite laminates, *J. Compos. Mater.* 26 (1992) 626-660. <https://doi.org/10.1177/002199839202600502>
- [6] S. Minakuchi, S. Niwa, K. Takagaki, N. Takeda, Composite cure simulation scheme fully integrating internal strain measurement, *Composites Part A* 84 (2016) 53-63. <https://doi.org/10.1016/j.compositesa.2016.01.001>
- [7] R. Higuchi, T. Yokozeki, T. Nagashima, T. Aoki, Evaluation of mechanical properties of noncircular carbon fiber reinforced plastics by using XFEM-based computational micromechanics, *Composites Part A* 126 (2019) 105556. <https://doi.org/10.1016/j.compositesa.2019.105556>
- [8] S. Seki et al., Evaluation of fatigue life of thick CFRP laminates with toughened interlaminar layers in out-of-plane and in-plane transverse directions, *Transactions of the JSME (in Japanese)* 83 (2017) 16-00571-16-00571. <https://doi.org/10.1299/transjsme.16-00571>
- [9] A. Parvizi, K.W. Garrett, J.E. Bailey, Constrained cracking in glass fibre-reinforced epoxy cross-ply laminates, *J. Mater. Sci.* 13 (1978) 195-201. <https://doi.org/10.1007/BF00739291>
- [10] P.P. Camanho, C.G. Davila, S.T. Pinho, L. Iannucci, P. Robinson, Prediction of in situ strengths and matrix cracking in composites under transverse tension and in-plane shear, *Composites Part A* 37 (2006) 165-176. <https://doi.org/10.1016/j.compositesa.2005.04.023>

## A Nonlinear Cable Bracing Inerter System for Vibration Control

Xinlei Ban<sup>1,3,a</sup>, Songtao Xue<sup>1,2,b</sup>, Jianfei Kang<sup>1,c</sup>, Kohju Ikago<sup>3,d</sup> and Liyu Xie<sup>1,e,\*</sup>

<sup>1</sup>Department of Disaster Mitigation for Structures, Tongji University, Shanghai, China

<sup>2</sup>Department of Architecture, Tohoku Institute of Technology, Sendai, Japan

<sup>3</sup>International Research Institute of Disaster Science, Tohoku University, Sendai, Japan

<sup>a</sup>1610229@tongji.edu.cn, <sup>b</sup>xue@tongji.edu.cn, <sup>c</sup>kangjianfei@tongji.edu.cn,  
<sup>d</sup>ikago@irides.tohoku.ac.jp, <sup>e</sup>liyuxie@tongji.edu.cn

**Keywords:** Nonlinear Cable Bracing, Inerter System, Bending-Shear Model, Vibration Mitigation, Optimization Design

**Abstract.** This study proposes a nonlinear cable model for the cable-bracing inerter system (CBIS). In a CBIS, cables are introduced to connect inerter systems and the structure for translation-to-rotation conversion. This CBIS employs an inerter element, a nonlinear cable bracing element and an additional damping element to utilize their synergy benefits. This paper aims to investigate the control effect of the nonlinear CBIS for high-rise buildings that are represented as bending-shear type models. First, a nonlinear inerter system is incorporated into a single-degree-of-freedom (SDOF) system and the mechanical model is proposed. An optimum design method is then developed for a high-rise building system equipped with a CBIS and the time-history analyses are conducted to validate the control effect of the CBIS. It is concluded that the employment of a CBIS can substantially improve the structural performance. A genetic algorithm can be used to obtain optimal parameters of a CBIS, thereby more effectively reducing the dynamic response of high-rise buildings.

### Introduction

The inerter, a recently introduced mechanical element for structural control, has attracted an increasing amount of attention. It has been found to be effective because of their adjustable frequency, mass enhancement effect and damping enhancement principles [1,2]. Inerter is a two-terminal mechanical element [3] which generates a resisting force proportional to the relative acceleration between its two terminals. An apparent mass significantly larger than its physical one is obtained when the translational motion is converted into rotational one [4,5]. In the 1970s, Kawamata [6] developed a type of a fluid inerter designated liquid mass pump, which was a pioneering work applying an inerter in the field of civil engineering. In 1999, Arakaki et al. [7] used the ball screw mechanism to amplify the efficient output force of a viscous damper for suppressing structural vibrations, although the inertance yielded by the device was not used intentionally. Inerter systems have been demonstrated to be highly effective in mitigating both inter-story drifts and floor accelerations for low-rise and medium-rise buildings. Actually, this system is attracting especially for high-rise buildings.

Bracing systems are usually used in the implementation of the inerter system to convert translational movement into rotational one between the structure and the inerter system. In civil engineering field, researchers have developed various types bracing configurations [8] among which steel braces are the most used but few of them involve cables. However, the advantages of cable braces are numerous and incontestable [9]. As the cables are being used only in tension, they are much thinner and lighter than most steel braces. Thus, they have negligible inertia and

they are particularly suitable for the systems in which great accelerations are applied. Furthermore, cables are less expensive than most conventional mechanical components when it is long enough and can be an alternative method for connecting inerters with the main structure.

However, cables involve two important characteristics to be considered seriously when they are applied to the high-rise buildings. One is the undesirable buckling in load-carrying elements [10]. Another is the unilaterality of actuation imposed by using cables. This unilaterality requires an unrestricted space in length. These two characteristics are attributed to the inability of cables to bear compression. Combined with compression-resistant materials [11], the effects of buckling and limitations of the stroke length can be reduced.

The previous study [12] has already proposed the mechanical model of the CBIS and the optimization design method to minimize the magnitudes of structural displacement responses [13]. In this paper, this nonlinear cable model is incorporated into a bending-shear model. First, the motion equations of the nonlinear inerter system are derived. Second, the optimal design problem to minimize the magnitudes of structural displacement responses is formulated to obtain a set of optimal designs for a nonlinear CBIS. Finally, the dynamic time-history analyses are conducted to validate the effectiveness of the CBIS.

**A nonlinear cable bracing inerter system**

*Nonlinear model of the cable braces*

A CBIS uses cable braces to connect inerter systems and main structures for translation-to-rotation conversion. The mechanical system of a CBIS consists of an additional damping element, an inerter element and an equivalent cable bracing element. Fig. 1 shows the layout of the CBIS and the nonlinear cable hysteresis in which the compressive stiffness of the buckling restrainer is several times as large as the tension stiffness.

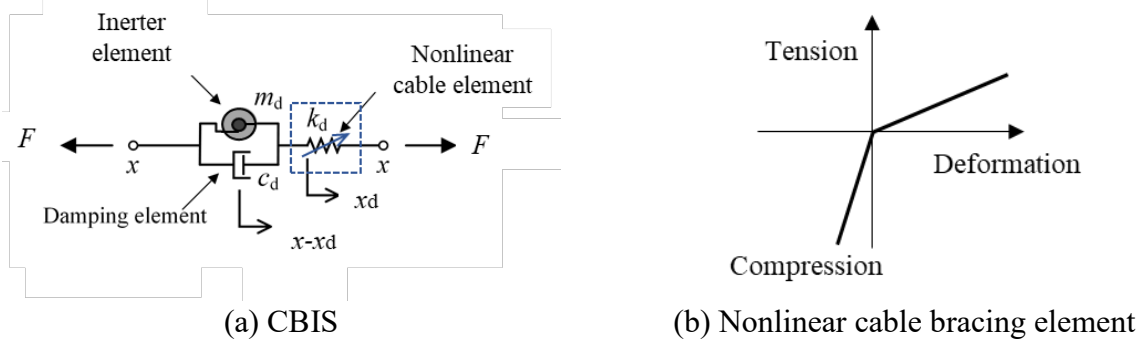


Fig. 1 Mechanical model of the nonlinear CBIS

In Fig.1a,  $m_d$  and  $c_d$  are the inertance and the damping coefficient of the CBIS.  $k_d$  is the equivalent stiffness of the nonlinear cables which is given by Eq. 1:

$$\begin{cases} k_d = k_T, x_d > 0 \\ k_d = k_C, x_d < 0 \end{cases} \quad (1)$$

where  $k_T$  and  $k_C$  are the tension and compressive stiffnesses of the cable bracing element, respectively. The output force  $F$  generated by the CBIS contains two main parts and can be calculated by the following equation:

$$F = k_d x_d(t) = m_d(\ddot{x}_d(t) - \ddot{x}(t)) + c_d(\dot{x}_d(t) - \dot{x}(t)) \quad (2)$$

where  $\mathbf{x}(t)$  and  $\mathbf{x}_d(t)$  donate the displacement of the primary structure relative to the ground and displacement of the cable brace, respectively. Superimposed dots indicate derivatives with respect to the time.

*An SDOF structure equipped with a nonlinear CBIS*

Fig. 2 shows the analysis model of a CBIS-equipped SDOF structure. According to the force equilibrium conditions and the layout of the system, the equation of motion for the controlled structure can be represented as:

$$m\ddot{x}(t) + c\dot{x}(t) + kx(t) + F = -m\ddot{x}_g(t) \tag{3}$$

where  $m$ ,  $c$  and  $k$  denote the mass, damping coefficient and stiffness of the primary structure, respectively;  $\ddot{x}_g(t)$  is the acceleration of ground motion.

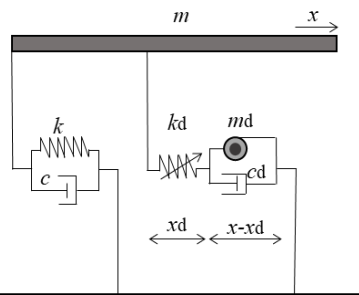


Fig. 2 Analytical model of a CBIS-equipped SDOF structure

**Optimization design of a CBIS controlled multi-degree-of-freedom (MDOF) structure**

*Building model*

We reproduced an analytical model of the Osaka Prefectural Government Building at Sakishima, Osaka [14] from the published data. This 53-storey building has a height of 256 m. The total mass of the building is 78,008 tons, and the characteristics for the analytical model are shown in Table 1. The first three natural angular frequencies are 1.257, 3.734 and 6.367 rad/s, respectively.

In high-rise buildings, the bending deformation cannot be ignored and usually the bending deformation of the higher layer accounts for the a large proportion (as shown in Fig.3). In the 1<sup>st</sup> mode of this structure, the components of shear deformation and bending deformation are similar when the floors are lower than the 43<sup>rd</sup> floor. The proportion of bending deformation gradually increases when the floors are higher than the 43<sup>rd</sup> floor. In the 2<sup>nd</sup> and 3<sup>rd</sup> modes, the bending deformation dominates in the floors above the 43<sup>rd</sup> floor. In Fig.4, bending deformation is the same as shear deformation on the top floor. Therefore, the inerter systems are suggested to be installed vertically on the top of the building to make full use of the vertical component of the bending deformation so that the efficiency of the CBIS can be maximized (as shown in Fig.6).

Table 1 Fundamental periods of the analytical model

Mode	1 <sup>st</sup>	2 <sup>nd</sup>	3 <sup>rd</sup>
Period [s]	5.00	1.68	0.99
Angular frequency	1.257	3.734	6.367

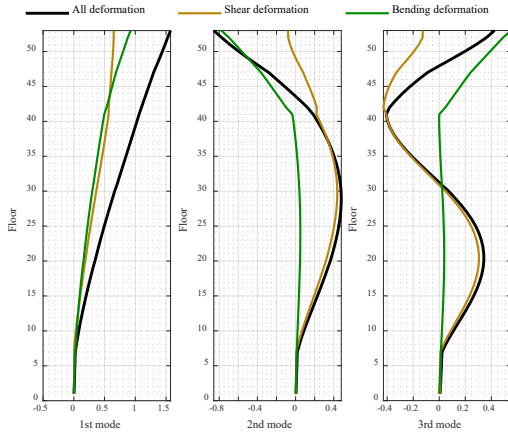


Fig.3 Participation mode vectors of the uncontrolled structure

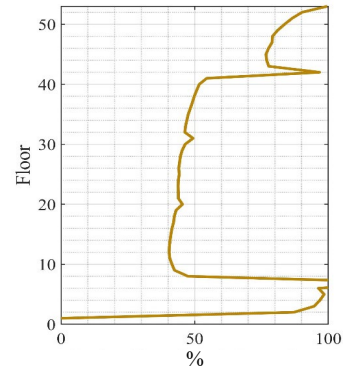


Fig.4 Ratios of bending deformation and shear deformation

*Uncontrolled building*

Considering this 53-storey bending-shear model shown in Fig.5, every storey of this model consists of a rotational and shear springs. These two springs are connected in series. Let  $k_{sj}$  and  $k_{bj}$  denote the shear stiffness and bending stiffness, respectively. Similarly, let  $c_{sj}$  and  $c_{bj}$  denote the damping coefficient of the dashpots arranged in shear and rotational directions, respectively. These two dashpots are also connected in series. The floor mass and its rotational mass moment of inertia are denoted by  $m_j$  and  $J_j$ , respectively.

In this model, every storey has one translational and one rotational degree of freedom. Therefore, the total number of DOF should be 106 (53 in translation and 53 in rotation). We assume that the damping matrix  $C_s$  for the primary structure is proportional to the stiffness matrix and the inherent damping of the 1<sup>st</sup> mode of the structure equals 0.02,  $C_s$  can be obtained as follows:

$$C_s = \frac{2 * 0.02}{\omega_p} K_s \tag{4}$$

where  $\omega_p$  is the first natural angular frequency of the primary structure. The equation of motion for the uncontrolled structure can be written as :

$$M_s \ddot{X}_s + C_s \dot{X}_s + K_s X_s = -M_s \Gamma_s \ddot{x}_g \tag{5}$$

where  $M_s$ ,  $C_s$  and  $K_s$  are the structural mass, damping and stiffness matrixs of the primary structure, respectively.  $X_s$  is the structural deformation vector.  $\Gamma_s$  is a vector with entries equal to unity for translation DOFs and zero for the others.  $X_s$  consists of displacements and rotational angles defined as:

$$X_s = [x_1 \ x_2 \ \dots \ x_N \ \theta_1 \ \theta_2 \ \dots \ \theta_N ]^T \tag{6}$$

where  $x_j$  and  $\theta_j$  are the displacement and rotational angles relative to the ground, respectively. The mass matrix  $M_s$  is defined as :

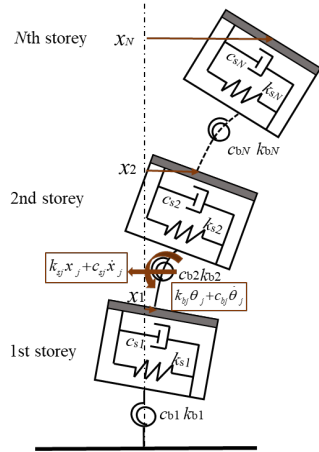


Fig.5 A bending-shear model

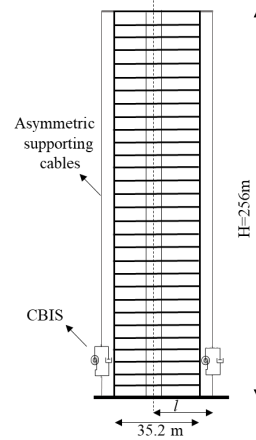


Fig.6 Installation location

$$\mathbf{M}_s = \text{diag}[m_1 \ m_2 \dots m_N \ J_1, J_2 \dots J_N] \quad (7)$$

The influence coefficient vector  $\Gamma_s$  is given by

$$\Gamma_s = [1 \ 1 \ \dots \ 1 \ 0 \ 0 \ \dots \ 0]^T \quad (8)$$

### Building with nonlinear CBIS

Based on the bending-shear model, the equation of motion for the building model with two CBISs under ground motion excitations as illustrated in Fig.6 is derived as Eq.9.

$$\mathbf{M}\ddot{\mathbf{X}} + \mathbf{C}\dot{\mathbf{X}} + \mathbf{K}\mathbf{X} = -\mathbf{M}\Gamma\ddot{x}_g \quad (9)$$

where

$$\mathbf{M} = \begin{bmatrix} \mathbf{M}_s + \mathbf{T}\mathbf{M}_d\mathbf{T}^T & \mathbf{T}\mathbf{M}_d \\ \mathbf{M}_d\mathbf{T}^T & \mathbf{M}_d \end{bmatrix}, \mathbf{C} = \begin{bmatrix} \mathbf{C}_s + \mathbf{T}\mathbf{C}_d\mathbf{T}^T & \mathbf{T}\mathbf{C}_d \\ \mathbf{C}_d\mathbf{T}^T & \mathbf{C}_d \end{bmatrix}, \mathbf{K} = \begin{bmatrix} \mathbf{K}_s & \mathbf{0}_{2N \times 2} \\ \mathbf{0}_{2 \times 2N} & \mathbf{K}_d \end{bmatrix}, \quad (10)$$

$$\mathbf{X} = [\mathbf{X}_s, y_{d1} \ y_{d2}]^T, \Gamma = [\Gamma_s, \mathbf{0} \ 0]^T$$

$$\mathbf{M}_d = \begin{bmatrix} m_d & 0 \\ 0 & m_d \end{bmatrix}, \mathbf{C}_d = \begin{bmatrix} c_d & 0 \\ 0 & c_d \end{bmatrix}, \mathbf{K}_d = \begin{bmatrix} k_d & 0 \\ 0 & k_d \end{bmatrix}, \mathbf{T} = \begin{bmatrix} 0 & 0 \\ 0 & 0 \\ 0 & 0 \\ \dots & \dots \\ \frac{l}{2} & -\frac{l}{2} \end{bmatrix}_{2N \times 2} \quad (11)$$

$\mathbf{T}$  is an installation matrix, denoting the installation location of the CBIS. Let  $l$  be the distance from the center of the core to the tips of cables.  $\mathbf{T}$  transforms the relative displacement vector into the inter-story drift vector.

*Optimization design problem*

A numerical optimization method, genetic algorithm (GA), is used to design the inerter system. Because the inerter systems are installed vertically and only the bending deformation of the structure can be used, the mode with the largest bending deformation should be considered. As shown in Figs.3 and 4, the optimization design target is the 1<sup>st</sup> mode.

Herein, the effective inertance-mass ratio  $\mu$ , supporting spring stiffness ratio  $\kappa$ , and damping ratio of an inerter system  $\zeta$  are defined as:

$$\mu = \frac{M_d}{M_s} = \frac{\phi^T \mathbf{T}^T \mathbf{M}_d \mathbf{T} \phi}{\phi^T \mathbf{M}_s \phi}, \kappa = \frac{K_d}{K_s} = \frac{{}_1\phi^T \mathbf{T}^T \mathbf{K}_d \mathbf{T} {}_1\phi}{{}_1\phi^T \mathbf{K}_s {}_1\phi}, \zeta = \frac{C_d}{2M_s \omega_r} = \frac{{}_1\phi^T \mathbf{T}^T \mathbf{C}_d \mathbf{T} {}_1\phi}{2 {}_1\phi^T \mathbf{M}_s {}_1\phi \omega_r} \quad (12)$$

The inertance-mass ratio  $\mu$  is set to 0.1. The optimization design problem can be expressed mathematically to pursue the optimal solutions:

$$\begin{aligned} &\text{find} && \mathbf{y} = \{\zeta, \kappa, \gamma\} \\ &\text{to minimize} && \sum_{i=1}^{106} x_i^{\max}(\mathbf{y}) \\ &\text{subject to} && \kappa = \frac{(1 - \sqrt{1 - 4\mu})^2}{2(1 + \gamma)\mu} \end{aligned} \quad (13)$$

where the subscript  $i$  denotes the  $i$ -th storey.  $\mathbf{y}$  is the variable vector containing  $\zeta$ ,  $\kappa$  and compression-tension stiffness ratio  $\gamma$ . The sum of the maximum displacement response of the top floor is to be minimized. The average of the compressive and tension stiffnesses of cable braces is equal to the supporting spring stiffness  $k_d$ , and the stiffness ratio  $\kappa$  is constrained to the optimum stiffness obtained from the fixed point method [17]. Using genetic algorithm, we employed an artificial earthquake BCJ-L2 as the input ground motion and obtained a set of optimal parameters listed in Table 2.

Table 2 Optimal design

$\mu=0.1$			
	$\kappa$	$\zeta$	$\gamma$
Constrained range	[0.01,1]	[0.01,1]	[1,20]
Optimal parameters	0.231	0.035	1.118

To verify the optimal parameters of the nonlinear CBIS, dynamic time-history analyses are conducted in the time domain based on the Newmark’s  $\beta$  method ( $\beta=1/4$ ) as shown in Fig.7 and the vibration reduction effects are listed in Table 3. Note that these results are based on the reproduced analytical model and thus they may not accurately represent the performance of the building we referred to.

Table 3 Comparison of structural responses

	Primary structure		Controlled structure		Reduction effects [%]	
	Peak	RMS	Peak	RMS	Peak	RMS
Inter-story drift angle	1/62	1/165	1/133	1/468	53.38	64.74
Absolut acceleration [m/s <sup>2</sup> ]	6.87	1.91	5.67	1.27	17.48	33.51
Displacement [m]	2.12	0.96	0.90	0.33	57.55	65.63

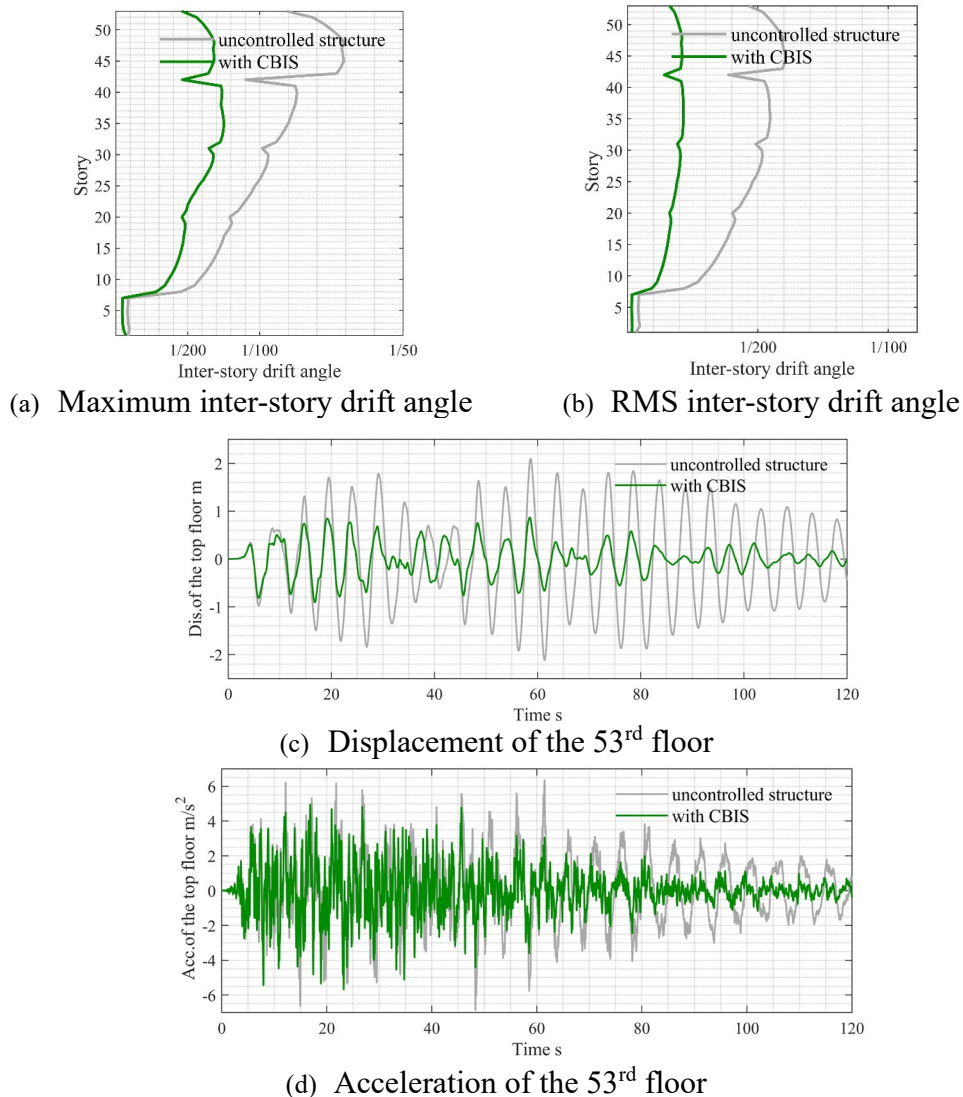


Fig.7 Time history of the 53-storey structure under BCJ-L2

With the optimal parameters, the displacement responses, the acceleration responses and the inter-story drift angles of the primary structure are all well mitigated by the CBIS with asymmetric supporting spring stiffness. This means that when the inerter systems are installed vertically, we can obtain the effect of suppressing overall bending deformation and shear deformation of high-rise buildings.

### Conclusions

This study proposes a nonlinear cable bracing element which can avoid buckling in tension-only cables and thus exploit the damping forces in compression. Dynamic characteristics of a high-rise building incorporated with a novel asymmetric inerter system are examined. A genetic algorithm (GA) was used to determine the parameters of CBISs so as to minimize structural displacement responses. Then, the vibration mitigation effect of the CBIS is evaluated under a synthetic ground motion BCJ-L2 provided by the Building Center of Japan. The most important findings are summarized as follows:

- (1) Genetic algorithm was applied to seismic response analysis of the CBIS-equipped bending-shear building model. With this method, optimum designs of the CBIS can be obtained to minimize the maximum displacement response of the top floor.
- (2) Based on the optimal parameters, the CBIS not only reduces the displacement response and the acceleration response but also significantly mitigates the maximum inter-story drift by 53.38%.
- (3) It is noteworthy to point out that in terms of reducing seismic acceleration responses, the control effect is not as good as the displacement responses. One possible reason is that the position where the CBISs are placed maybe ineffective for controlling the seismic acceleration responses. To pursue better performance, the position optimal design under earthquake and multi-modal control should be the next step of research.

### Acknowledgements

This study was supported by the National Natural Science Foundation of China (Grant No.51778490 and 51978525), Open Research Fund Program of Guangdong Key Laboratory of Earthquake Engineering and Application Technology (Grant No. 2017B030314068), the Natural Science Foundation of Shanghai (Grant No. 20ZR1461800). The first author also would like to gratefully acknowledges the support of the China Scholarship Council by the joint PhD program.

### References

- [1] K. Ikago, K. Saito, N. Inoue, Seismic control of single-degree-of-freedom structure using tuned viscous mass damper, *Earthq. Eng. Struct. Dyn.* 41 (2012) 453-474. <https://doi.org/10.1002/eqe.1138>
- [2] R.F. Zhang, Z.P. Zhao, C. Pan, K. Ikago, S.T. Xue, Damping enhancement principle of inerter system, *Struct. Control Health Monit.* (2020). <https://doi.org/10.1002/stc.2523>
- [3] M.Z.Q. Chen, Y. Hu, L. Huang, G. Chen, Influence of inerter on natural frequencies of vibration systems, *J. Sound. Vib.* 333 (2014) 1874-1887. <https://doi.org/10.1016/j.jsv.2013.11.025>
- [4] Z.P. Zhao, R. F. Zhang, Z. Lu, A particle inerter system for structural seismic response mitigation, *J. Frankl. Inst.* 356 (2019) 7669-7688. <https://doi.org/10.1016/j.jfranklin.2019.02.001>
- [5] Q.J. Chen, Z.P. Zhao, R.F. Zhang, C. Pan, Impact of soil–structure interaction on structures with inerter system, *J. Sound. Vib.* 433 (2018) 1-15. <https://doi.org/10.1016/j.jsv.2018.07.008>
- [6] S. Kawamata, Development of a vibration control system of structures by means of mass pumps. Institute of Industrial Science, University of Tokyo, Tokyo, Japan, 1973.
- [7] T. Arakaki, H. Kuroda, F. Arima, Y. Inoue, K. Baba, Development of seismic devices applied to ball screw: Part 1 basic performance test of rd-series, *J. Archit. Build. Sci.* 5 (1999) 239-244. [https://doi.org/10.3130/aijt.5.239\\_1](https://doi.org/10.3130/aijt.5.239_1)
- [8] J.S. Hwang, J. Kim, Y.M. Kim, Rotational inertia dampers with toggle bracing for vibration control of a building structure, *Eng. Struct.* 29 (2007) 1201-1208. <https://doi.org/10.1016/j.engstruct.2006.08.005>

- [9] S.E. Landsberger, A minimal, minimal linkage: the tension-compression parallel link manipulator, *Robotics Mechatron Manufact. Syst.* 2 (1993) 81-88. <https://doi.org/10.1016/B978-0-444-89700-8.50017-8>
- [10] M. Kurata, R.T. Leon, R. DesRoches, Rapid seismic rehabilitation strategy: concept and testing of cable bracing with couples resisting damper, *J. Struct. Eng.* 138 (2012) 354-362. [https://doi.org/10.1061/\(ASCE\)ST.1943-541X.0000401](https://doi.org/10.1061/(ASCE)ST.1943-541X.0000401)
- [11] H. Kida, K. Kakemoto, N. Hori, K. Ikago, N. Inoue, Control of bending behavior of high rise buildings by tuned viscous mass dampers installed in the vertical direction by support members with nonlinear stiffness properties. Part 3. Study on 3D frame model, *AIJ Annual Convention* (2020).
- [12] L.Y. Xie, X.L. Ban, S.T. Xue, K. Ikago, J.F. Kang, H.S. Tang, Theoretical study on a cable-bracing inerter system for seismic mitigation, *Appl. Sci.* 9 (2019) 4096. <https://doi.org/10.3390/app9194096>
- [13] X.L. Ban S.T. Xue, K. Ikago, Optimal design of a cable-bracing inerter system containing asymmetric supporting spring stiffness, *AIJ Annual Convention* (2020).
- [14] T. Itou, Feasibility study on a tuned hydraulic inerter-damper with large apparent mass incorporated into super high-rise structure, *Tohoku University* (2019).

# Estimation Method of Maximum Inter-Story Drift Angle of Wood-Frame House using Two Accelerometers

Ryusei Fukuzawa<sup>1,a,\*</sup>, Akira Mita<sup>1,b</sup>, Tomonori Murakami<sup>2,c</sup>

<sup>1</sup>Department of System Design Engineering, Keio University, Tokyo, Japan

<sup>2</sup>Mitsui Home Co., Ltd. Technology Research & Development Institute, Tokyo, Japan

<sup>a</sup> ryu.fukufuku99@keio.jp, <sup>b</sup> mita@sd.keio.ac.jp, <sup>c</sup> t-murakami@mitsuihome.co.jp

**Keywords:** Structural Health Monitoring, Maximum Inter-Story Drift Angle, Wood-Frame Construction

**Abstract.** In April 2016, Kumamoto earthquake occurred in Japan and many wooden houses collapsed and many lives were lost because of the second and larger main shock. As a result, the need for Structural Health Monitoring (SHM) for wooden houses is receiving increased attention. In the SHM system, maximum inter-story drift angle is considered as the damage index. We assume that the first story of a wooden house will be damaged so that we need only to focus on the response of this first story. Hence, we install accelerometers on the ground floor and the second floor. In order to estimate the inter-story drift angle, we need to integrate the acceleration records twice. The simple double integration will result in erroneous results. Thus, in this paper, we propose the most appropriate integration method to estimate the maximum story drift angle with high accuracy using two accelerometers.

## Introduction

### *Structural Health Monitoring*

In April 2016, Kumamoto earthquake occurred in Japan and many wooden houses collapsed and many lives were lost. The significant feature of this earthquake was that there were two main shocks and the latter was larger. Thus several houses which survived during the first main shock collapsed during the second main shock resulting in a few casualties as they came back home. This incident reaffirmed the importance and the usefulness of Structural Health Monitoring (SHM) for wooden houses. In the SHM system, maximum inter-story drift angle is considered as the damage index. We assume that the first story of a wooden house will collapse so that we will only focus on the response of this first story. Hence, we install accelerometers on the ground floor and the ceiling of the ground floor. In order to estimate the inter-story drift angle from the sensors, we have to integrate the acceleration records twice. The simple second-order integration without a careful numerical consideration will result in erroneous results. Thus, in this paper, we tried several approaches to propose the most appropriate integration method to estimate the maximum story drift angle with high accuracy using two accelerometers.

### *Previous researches and their problems*

There is very limited research on SHM for wooden houses. The previous research<sup>[1][2]</sup> has focused on simple vibration models and steel-frame buildings. In order to implement SHM systems into wooden houses, it is useful to perform seismic analysis for wooden houses. In addition, it is important to analyze the response characteristics of buildings by vibrating with



various types of seismic waves because the response of the buildings vary greatly depending on the type of seismic waves.

### *The purpose of this research*

In general, it is difficult to obtain accurate displacement time histories from acceleration data due to several sources of noise. This paper aims to establish a method for estimating the maximum inter-story drift angle by analyzing the acceleration data measured in full-scale shaking table tests of a wood-frame house. In the test, we used low-cost MEMS type acceleration sensors along with high-precision sensors to seek the possibility to reduce the system cost.

### **Proposed method**

In this study, we estimate the maximum inter-story drift angle from acceleration data acquired by two types of acceleration sensors using the following three methods. In SHM system, displacement data are often calculated from acceleration sensors installed at the base or inside of the building. We can obtain the relative response displacement by integrating the acceleration data of the base and each floor. However, the measured acceleration data contain small errors due to noise and baseline misalignment of the acceleration sensors. Although these errors are small, these errors are dramatically amplified thorough second-order integration and the displacement tends to diverge. There are two methods for calculating displacement from acceleration: time domain integration and frequency domain integration.

#### *(Method1) Iwan's method*

Iwan's method<sup>[2][3]</sup> is a method to compensate for the acceleration baseline misalignment in the time domain. In this method, the errors in integration are assumed to be derived from the nonlinearity of the accelerometer and acceleration records are classified into three regions as shown in Fig.1.

#### I. Region1

Region1 is defined as a region where the maximum acceleration does not exceed 50 gal from the first point in the acceleration record. The initial baseline misalignment is assumed to be the average of the acceleration records in region1.

$$a_{BL} = \frac{1}{N} \sum_{i=1}^N a_i \quad (1)$$

Where,  $a_{BL}$  is initial baseline misalignment,  $N$  is the number of acceleration data in the region1 and  $a_i$  is acceleration record in the region1.

#### II. Region2

Region2 is defined as a region between region1 and region3. In this region, we calculate the baseline misalignment by finding a value such that the velocity is connected to region3.

#### III. Region3

Region3 is defined as a region where the maximum acceleration does not exceed 50 gal from the last point in the acceleration record. As in region1, the baseline misalignment is

assumed to be constant. In this case, it is calculated by first approximation in the region3 after integrating the acceleration records and obtaining the velocity records.

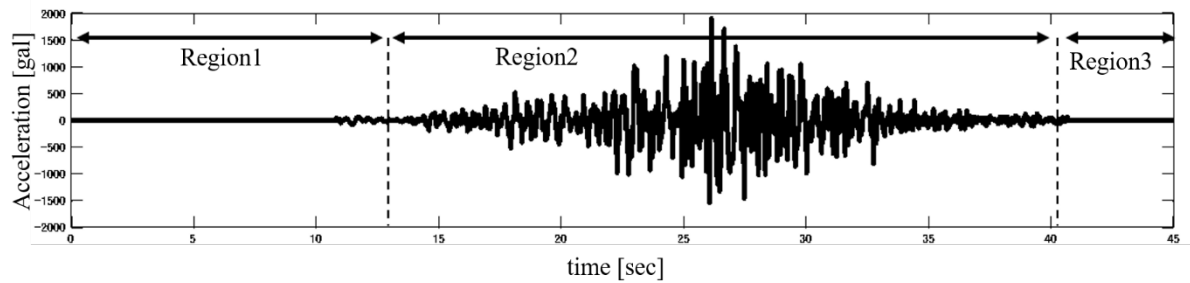


Fig.1 Classification of acceleration record

*(Method2) Method of applying a window function to acceleration record*

In this study, a window function was applied to the acceleration records and the stepwise errors in the acceleration records were corrected by cutting out the main motion. The window function is often used in Fourier analysis and audio compression because it is a function that sets the signals outside the finite interval to zero so that only the signals within the finite interval are cut out. The accuracy of estimating the maximum inter-story drift angle is verified by applying the Hamming window as follows.

$$w_r(n) = \begin{cases} 0.54 - 0.46 \cos\left(\frac{2\pi n}{N-1}\right) & (0 \leq n < N-1) \\ 0 & (n \geq N) \end{cases} \quad (2)$$

*(Method3) Method for calculating the displacement using only the real part of the displacement Fourier spectrum*

We focused on the possibility that high-pass filtering on acceleration records may distort significant data and the maximum story drift angle was estimated using only the real part of the displacement Fourier spectrum. Even when residual displacement occurs in a building, the displacement can be calculated from the real component of the displacement Fourier spectrum.

$$D(\omega) = \int_{-\infty}^{\infty} d(t) \cdot e^{-j\omega t} dt \quad (3)$$

Where,  $d(t)$  is displacement with residual displacement  $d_{\infty}$  and  $D(\omega)$  is frequency function of  $d(t)$ . Moreover, assuming that the time function  $d(t)$  is a casual function, the real part  $D_e(\omega)$  and the imaginary part  $D_o(\omega)$  of the frequency function  $D(\omega) (= D_e(\omega) + jD_o(\omega))$  are in a Hilbert transform relationship as follows.

$$D_o(\omega) = -\frac{1}{\pi} \int_{-\infty}^{\infty} \frac{D_e(s)}{\omega - s} ds \quad (4)$$

$$D_e(\omega) = \frac{1}{\pi} \int_{-\infty}^{\infty} \frac{D_o(s)}{\omega - s} ds \quad (5)$$

The sign function  $\text{sgn}(t)$  is defined as Eq.(6) and (7).

$$\text{sgn}(t) = -1 (t < 0), 0(t = 0), 1(t > 0) \quad (6)$$

$$\text{sgn}(t) \rightarrow \frac{2}{j\omega} \quad (7)$$

Using the sign function  $\text{sgn}(t)$ , the unit step function  $U(t)$  is written as Eq.(8).

$$U(t) = \frac{1 + \text{sgn}(t)}{2} \quad (8)$$

Using the unit step function  $U(t)$ , the time function  $d(t)$  is written as Eq.(9).

$$d(t) = 2U(t) \cdot d_e(t) = 2U(t) \cdot d_o(t) \quad (9)$$

Eq.(9) shows that the time function  $d(t)$  of the displacement can be calculated from only the real part  $D_e(\omega)$  or the imaginary part  $D_o(\omega)$  of the frequency function  $D(\omega)$ . On the other hand, if the time function  $d(t)$  has a residual displacement  $d_\infty (= \lim_{t \rightarrow \infty} d(t) \neq 0)$ , it can be separated into a time limiting function  $d_{TL}(t)$  and a unit step function  $U(t)$  satisfying Eq.(4) and (5).

$$d(t) = d_{TL}(t) + d_\infty \cdot U(t) \quad (10)$$

Eq.(11) can be obtained by Fourier transforming Eq.(10) and the second term is a generalized function with a singularity at  $\omega = 0$ .

$$D(\omega) = D_{TL}(\omega) + d_\infty \cdot \left( \pi\delta(\omega) + \frac{1}{j\omega} \right) \quad (11)$$

As well as the time limiting function  $D_{TL}(\omega)$ , the time function of the displacement  $d(t)$  can be calculated from only the real or imaginary part of the frequency function in the case of residual displacement.

## Estimation results

### *A full-scale shaking table test*

The test house was three-story wooden house with two-by-four method designed by Mitsui Home Corp. The following figures show the south and north elevation. Strain gauge type (AS-10GB) and low-cost MEMS type (LIS3DSH) of accelerometers were used to verify the accuracy of estimating the maximum inter-story drift angle of the first floor by each accelerometer.



Fig.2 Elevation of the building

In this shaking table test, several types of earthquake waves were used for excitation. First, Kumamoto wave was used for 120 times and after that, other waves were used once. Table 1 shows the list of earthquake waves.

Table. 1 Seismic waves

Earthquake	Input scale	Number of times
Kumamoto	100%	120
JMA Kobe	100%	1
Shiogama	100%	1
Tottori	100%	1
Nankai Trough	100%	1

*Estimation accuracy of the maximum inter-story drift angle*

Table3 shows the error of the maximum inter-story drift angle calculated by directly integrating the acceleration record(Before correction) and using the above 3 methods. The error in Table3 represents the error for the true value of the maximum inter-story drift angle calculated from displacement measurement in the shaking table test as shown in Table2.

Table.2 True Value of the maximum inter-story drift angle

Earthquake	Maximum inter-story drift angle [rad]
Kumamoto	1/108
JMA Kobe	1/91
Shiogama	1/59
Tottori	1/40
Nankai Trough	1/23

Table.3 The error for each method

Earthquake	Before correction	Method1	Method2	Method3
Kumamoto	4.2%	42.4%	2.1%	4.2%
JMA Kobe	26.5%	4.4%	8.2%	11.8%
Shiogama	12.4%	5.9%	5.9%	5.9%
Tottori	6.2%	4.9%	4.0%	2.0%
Nankai Trough	6.4%	1.6%	2.3%	2.3%

In method1, the error is worse in Kumamoto indicating that the correction accuracy is sensitive depending on the type of seismic wave. On the other hand, method2 and method3 improved the estimation accuracy of the maximum inter-story drift angle for all seismic waves. The error of both methods is within 12%, which enables us to estimate the maximum inter-story drift angle stably regardless of the type of earthquake. A possible error factor is the difference in the characteristics of each seismic waves. As shown in Fig.3, acceleration response spectrum of Kumamoto and JMA Kobe which has a relatively large error shows that response acceleration around  $T=0.2[s]$  which is the natural period of the building is small. In other words, the error becomes larger for seismic waves with a small S/N ratio around the first natural frequency of the building.

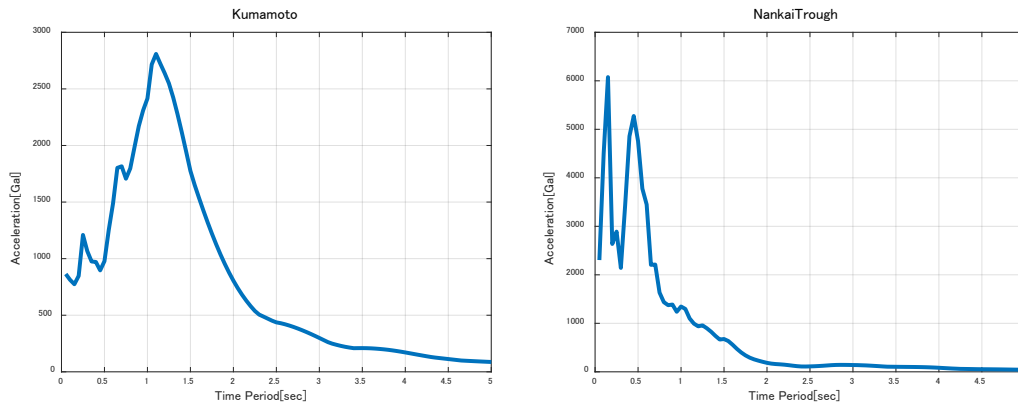


Fig.3 Acceleration response spectrum

*Consideration of accelerometers*

As mentioned above, two types of acceleration sensors were used to measure the acceleration data in this shaking table test. The error of the maximum inter-story drift angle estimated by each accelerometer was compared considering the instrumental characteristics of each accelerometer. The error in Table4 represents the error for the true value of the maximum inter-story drift angle calculated from displacement measurement in the shaking table test as shown in Table2.

*Table.4 The error for each accelerometer*

Earthquake	Method2		Method3	
	Strain-gauge	MEMS	Strain-gauge	MEMS
Kumamoto	2.1%	6.3%	4.2%	6.2%
JMA Kobe	8.2%	4.7%	11.8%	14.5%
Shiogama	5.9%	11.8%	5.9%	9.4%
Tottori	4.0%	8.0%	2.0%	4.0
Nankai Trough	2.3%	2.3%	2.3%	4.5%

Both acceleration sensors were able to estimate the maximum inter-story drift angle for all types of seismic waves within 15%. In other words, this study suggests the possibility of low-cost MEMS type accelerometer for SHM system.

### Conclusion

In this paper, we proposed and compared 3 methods to estimate the maximum inter-story drift angle using accelerometers installed on the first and second floors of a wood frame house. While the estimation accuracy of Iwan's method was not stable, the method of applying a window function to acceleration record and the method for calculating the displacement using only the real part of the displacement Fourier spectrum were able to estimate the maximum inter-story drift angle for all types of seismic data within an error rate of 15%. In addition, the latter method can also be used to evaluate the residual displacement that occurred in a building after an earthquake. It was also suggested that low-cost MEMS type accelerometers can be used for SHM as well as strain gauge type of accelerometers.

### References

- [1] Y Suzuki, A Mita : Output only estimation of inter-story drift angle for buildings using small number of accelerometers, J. Struct. Constr. Eng., AIJ, Vol.81, No.725, 1061-1070, Jul.,2016. <https://doi.org/10.3130/aijs.81.1061>
- [2] Iwan, Wilfred D. and Moser, Michael A. and Peng, Chia-Yen: Some observations on strong-motion earthquake measurement using a digital Accelerograph, Bulletin of the Seismological Society of America (1985) 75 (5): 1225-1246
- [3] G.V. Berg, G.W. Housner : Integral velocity and displacement of strong earthquake ground motion, Bulletin of the Seismological Society of America (1961) 51 (2): 175-189

# Acoustic Emission-Based Diagnosis Using AlexNet: How Wave Propagation Effects Classification Performance

WIRTZ Sebastian Felix<sup>1,a,\*</sup>, DORUK Sevki Onur<sup>2,b</sup> and SÖFFKER Dirk<sup>1,c</sup>

<sup>1</sup> Chair of Dynamics and Control, University of Duisburg-Essen, 47057 Duisburg, Germany

<sup>2</sup>Dokuz Eylul University, Graduate School of Natural and Applied Sciences, Turkey

<sup>a</sup>sebastian.wirtz@uni-due.de , <sup>b</sup>doruk.sevkionur@ogr.deu.edu.tr, <sup>c</sup>soeffker@uni-due.de

**Keywords:** Acoustic Emission, Convolutional Neural Network, Classification, Diagnosis, Reliability, Composite Materials

**Abstract.** Composite materials are frequently used due to light weight and high stiffness. However, the use of composite materials is limited due to several micro-mechanical damage mechanisms, which are currently not well understood. Therefore, Acoustic Emission (AE) is frequently suggested for in-situ diagnosis of composite materials in Structural Health Monitoring. Elastic stress waves in the ultrasound regime are recorded using highly sensitive measurement equipment. Based on suitable analysis and interpretation of the waveform data, different micro-mechanical damage mechanisms such as delamination or fiber breakage can be distinguished. Frequently, data-driven approaches are suggested for classification of AE data. In literature, attenuation of AE due to wave propagation is currently the main limiting factor in AE-based diagnosis. In particular, AE is strongly attenuated in composite materials due to dispersion as dominant attenuation mechanism. Furthermore, depending on the source location, which is usually not known a-priori, different propagation paths are obtained in practice. Therefore, the effect of wave propagation on AE is important and can not be neglected to achieve reliable classification. However, the effect of different propagation paths on the classification performance is often not considered explicitly. Due to dependence of wave propagation behavior on waveform characteristics (e.g. frequency), it can be expected that the impact of wave propagation on AE classification performance depends also on the related source mechanism. Therefore, it is worth to study how classification performance of different source mechanisms is effected by wave propagation. In this paper, the dependence of the classification performance on different propagation distances is experimentally investigated in detail. To achieve highly reproducible AE measurements, different artificial AE sources are induced using surface mounted piezo elements. The corresponding waveforms are measured at two different locations. For classification, a convolutional neural network-based classification scheme is established. The pre-trained AlexNet architecture is fine-tuned using measurements obtained using different excitation signals. The classification performance is evaluated with particular focus on the impact of wave propagation. The variations in propagation distance have a strong impact on the classification performance. As main conclusion for AE-based SHM it can be stated that variations in the propagation path should be considered. Furthermore, the underlying source mechanisms should be taken into consideration for reliable performance estimation.

## Introduction

Acoustic Emission (AE) refers to ultrasound stress waves, which are released from localized sources in a loaded material. Using suitable measurement equipment, AE waveforms can be recorded in-situ and used for diagnosis [1]. Regarding Structural Health Monitoring (SHM) of

composites, the use of Acoustic Emission (AE) is frequently suggested to distinguish between different micro-mechanical damage mechanisms such as delamination, matrix crack, debonding, and fiber breakage [1]. Typically, thin structures such as coupon specimens and plates are used as specimen geometry. Due to the geometry, ultrasound stress waves propagate in two fundamental modes. Using advanced signal processing and interpretation, different damage mechanisms can be distinguished. For instance, digital filtering was suggested for mode separation in [2] and [3]. According to Martinez-Jequier et al. [3] delamination could be identified using modal analysis of AE, whereas additional consideration of the frequency spectrum was necessary to distinguish between the remaining damage mechanisms.

Due to the complexity of AE interpretation, data-driven approaches are frequently suggested for AE-based diagnosis of composite materials. These include e.g. different clustering techniques [4], Support Vector Machine [1], and neural networks [5]. A comparison of modal AE analysis and neural networks is presented by McCrory et al. [5]. In principle, the results of both methods are in good agreement. However, it was stated as an advantage of data-driven approaches that AE data can be classified into more than two classes [5]. Furthermore, the use of frequency and time-frequency domain transformations is of particular importance for classification of AE. It is well known that – compared to classical AE parameters, which are extracted in time domain – peak frequencies are less sensitive to different experimental conditions. For instance, Beheshtizadeh et al. [6] concluded that wavelet transform is superior for the analysis of AE signals because highly detailed representation is obtained especially regarding weak signal components.

In literature, attenuation of AE due to wave propagation was identified as main limitation of AE-based SHM. Different approaches were suggested to compensate the effect of wave propagation, e.g. correction of AE parameters by calibration experiments [7]. However, according to Maillet et al. [8], high frequency components are attenuated stronger and lower values of the frequency centroid are obtained at increasing propagation distance. Furthermore, Asamene et al. [9] pointed out that mode- and frequency-dependent attenuation may have an effect on AE signatures. Moreover, Kharrat et al. [10] reported additional distortion of AE waveforms due to damage accumulation within the material. Also, an effect of external load on the attenuation of AE in a composite plate could be demonstrated in [11]. However, while data-driven approaches are frequently suggested in context of AE, the impact of changes in the propagation path is often not considered explicitly.

In this paper, the dependence of the classification performance on propagation distance is investigated in detail. Particular focus is given to the difference between symmetric and asymmetric wave modes. To achieve highly reproducible AE measurements, different artificial AE sources are induced using surface mounted piezo elements. The remainder of this paper is structured as follows. In Section 2, the experimental setup and the classification scheme using AlexNet architecture are explained in detail. In section 3, experimental results are presented. This includes detailed discussion of the induced AE and the effect of wave propagation on the classification performance for each of the wave modes. Finally, the main conclusions are summarized.

## Methods and materials

The experimental setup is illustrated schematically in Fig. 1. As specimen geometry, a thin plate is chosen, which is a typical specimen geometry for testing of composite materials. The specimen is manufactured from CFRP material and has dimensions of 800 x 800 x 1 mm<sup>3</sup>. In principle, two fundamental modes propagate in this geometry, which are the symmetric (S0) and

asymmetric (A0) mode. Wide specimen dimensions are chosen to reduce the effect of edge reflections. As AE transducers, Piezoelectric Wafer Active Sensors (PWAS) are bonded to the top and bottom surface of the plate. To obtain reproducible waveforms with defined modal content at the sensors, AE transducers are sometimes used in active mode [10]. Here, AE is induced using two active PWAS, as suggested by Su and Ye [12]. The active PWAS T1 and T1b, which are oriented face-to-face through the material, are driven by a frequency generator. Here, windowed sine bursts with 6 cycles at a frequency of 100 kHz are used. By choosing in-phase or out-of-phase excitation of the active PWAS, the dominant mode of propagation can be controlled precisely.

As sensors, PWAS T2 and T3 which are located in a distance of 100 mm and 200 mm from the excitation, are used. Additionally, two PWAS T2b and T3b are bonded face-to-face at the opposite surface of the plate to verify the modal content of measured waveforms. A similar sensor arrangement was used for instance by Martinez-Jequier et al. in [3] to assess the modal content of AE waveforms. The AE waveforms are recorded continuously at a sample rate of 4 MHz. Each excitation burst is triggered by an external signal, which is also recorded for post-processing.

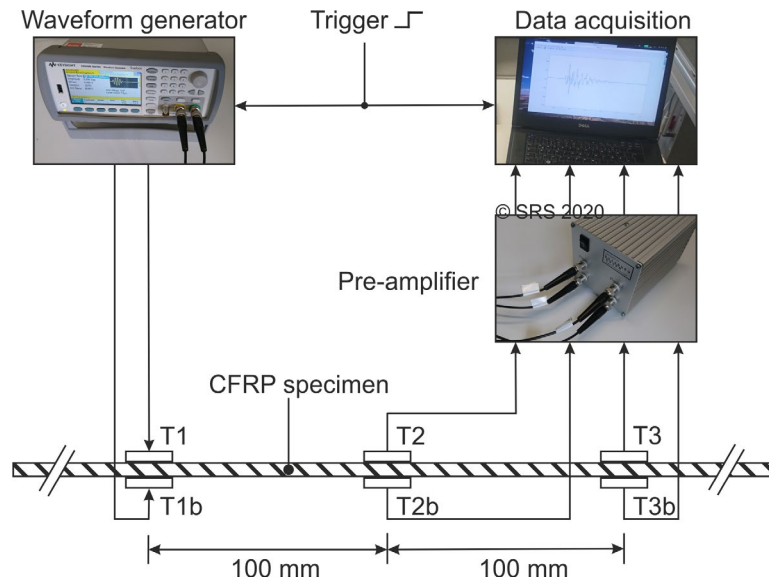


**Fig. 1.** Illustration of the experimental setup (Chair of Dynamics and Control, U DuE, Germany).

Recently, deep learning, which emerged from the field of image classification and computer vision, received significant attention in SHM literature [13]. High classification performance can be achieved with sophisticated neural networks. However, due to the large number of parameters in deep neural networks, training is computationally intensive and a large amount of data is necessary. Therefore, transfer learning is frequently suggested if the amount of training data is limited. One approach to transfer learning is fine-tuning of pre-trained networks [13]. While most of the parameters of trained neural networks – or parts of trained neural networks – are used as initial values, only specific parts of the network are modified. Here, fine-tuning refers to additional training of the modified network with a new dataset. The advantages of using pre-trained networks are that fine-tuning is usually faster, requires less data, and can be realized using a regular desktop computer.

The AlexNet is a Convolutional Neural Network architecture, which was proposed by Krizhevsky et al. [14]. Today, AlexNet is frequently used for transfer learning. For instance, Dorafshan et al. [15] compared the performance of edge detectors, which is an image processing-based approach, and AlexNet for image-based crack detection in concrete. According to the results, improved performance can be achieved using AlexNet architecture. Furthermore, best performance was achieved using fine-tuning as compared to full training of the network. Furthermore, Hemmer et al. [16] suggested a transfer learning approach for classification of faults in rolling element bearings based on vibration and acoustic emission measurements and concluded that fine-tuning of AlexNet scales well to multiclass problems.

The original AlexNet architecture comprises five convolutional layers (conv1 - conv5) and three fully connected layers (fc6 - fc8). For transfer learning, the architecture is usually modified so that it is suitable for the new classification problem. Hemmer et al. [16] replaced the final classification layer to fit the desired number of classes. Lu et al. [17] replaced the last three layers. Additionally, the learning rate can be adapted to focus parameter updates mainly on the modified layers during training, as suggested in [16]. In this paper, the final layer of the architecture is adapted for classification into 4 classes. The modified architecture of the AlexNet is illustrated in Fig. 2. Furthermore, the learning rate of the fully connected layer is increased by a factor of 20 to reduce the impact of training on the parameters of the convolutional layers. During fine-tuning, stochastic gradient descent with momentum algorithm was used with the following settings: initial learning rate:  $1e-4$ , mini batch size: 10, validation frequency: 20.

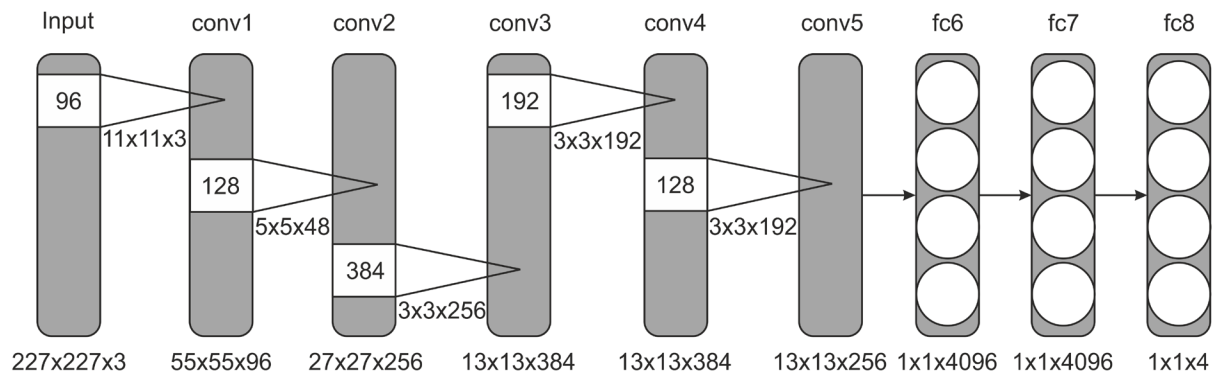


**Fig. 2.** Simplified illustration of modified AlexNet architecture.

### Experimental results

In this section, different classes of artificially induced AE signals are presented. Each AE waveform is measured at two different locations. Furthermore, preprocessing of the waveform data is explained. Finally, classification performance is evaluated in detail. Particular focus is placed on how the classification performance is effected by changes in the propagation path.

To verify the procedure, which was used to induce AE in the plate specimen with defined dominant mode, the modal content of resulting AE measured by the sensors is assessed. To this end, measurements of the two sensors T2 and T2b, which are located face-to-face at the top and bottom surfaces of the plate, are used. Symmetric and asymmetric modes can be separated by adding and subtracting the responses of the sensors at the top and bottom surfaces of the plate, respectively, as suggested in e.g. [3]. From the responses presented in Fig. 3, dominant S0 and A0 mode are observed depending on (a) symmetric (in-phase) and (b) asymmetric excitation (out-of-phase). To investigate the effect of wave propagation on the classification performance, a dataset was recorded comprising AE waveforms with dominant S0 and A0 modes of different

intensity. By choosing different excitation signals, AE waveforms with different modal content were induced. For classification, the waveform data were transformed into frequency domain using continuous wavelet transform. As input to the classifier, images of 227x227x3 are used. Examples of each class are presented in Fig. 4.

Subsequently, AlexNet is used for classification of different AE waveforms. To demonstrate that in principle it is possible to distinguish between waveforms, which are related to different excitations, training and test data are chosen from the same sensor. In each case, a total of 400 samples are used during training and 200 samples during test.

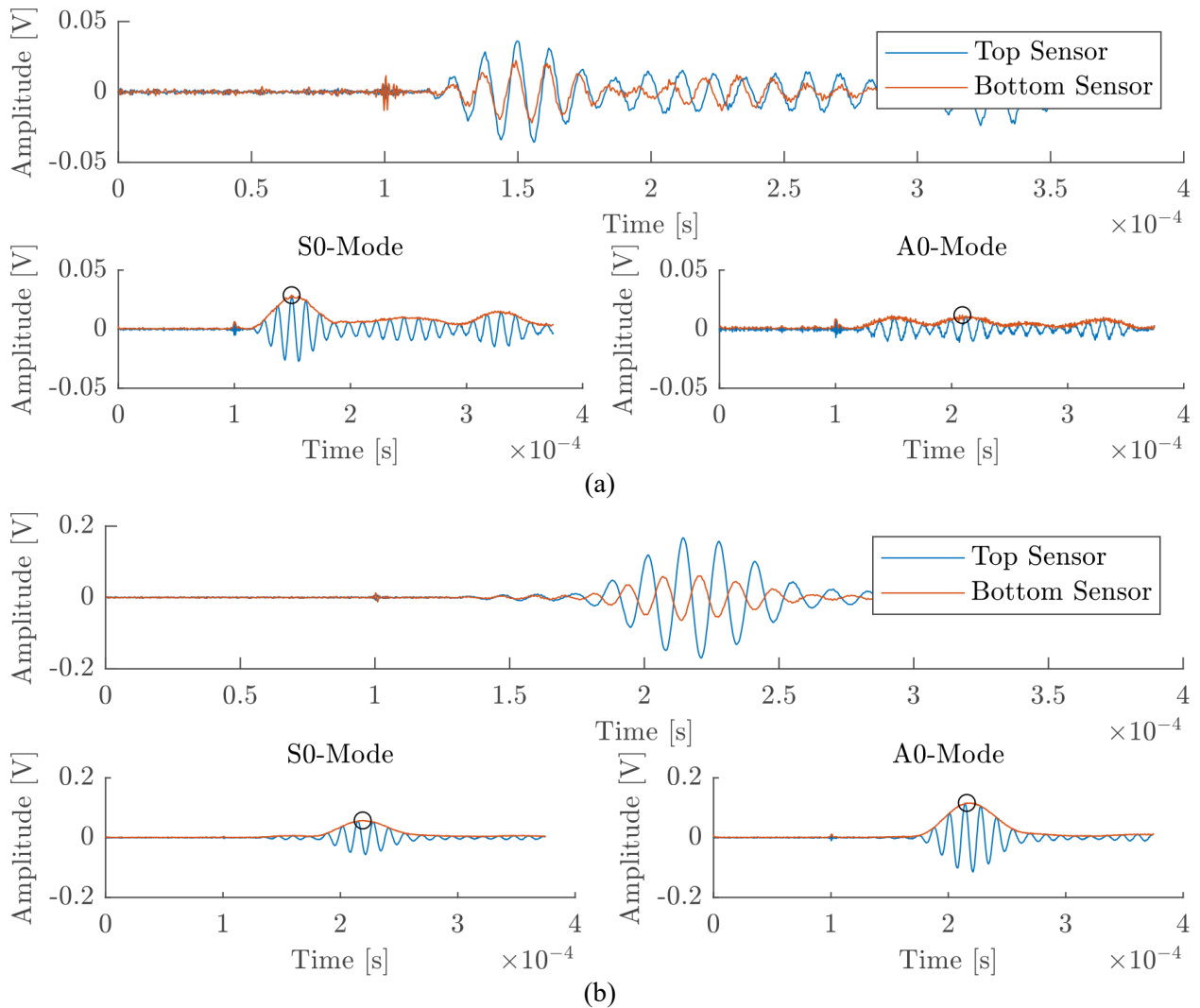


**Fig. 3.** Artificially induced AE with dominant symmetric (a) and asymmetric (b) mode.

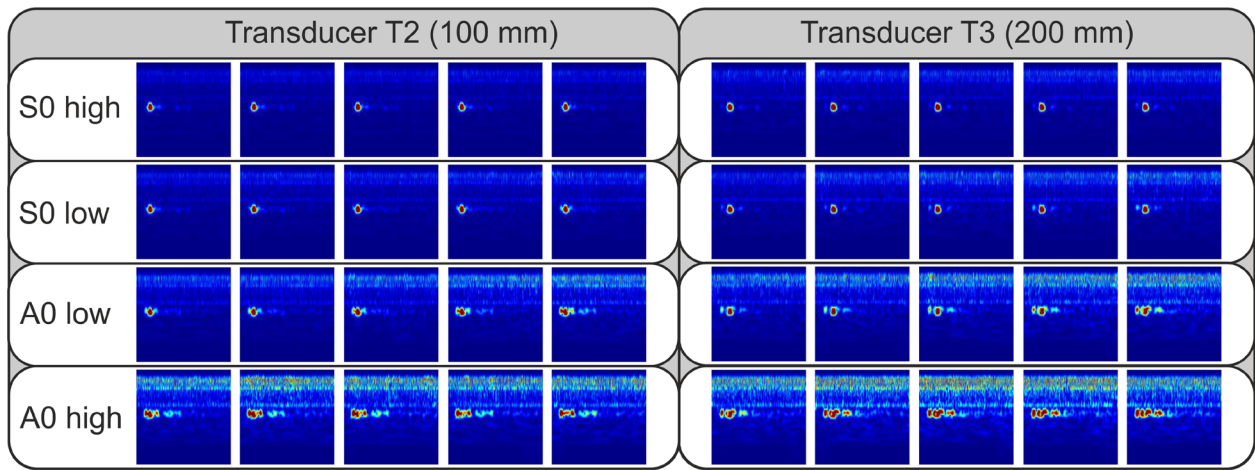


**Fig. 4.** Scalograms of AE waveforms at sensor T2 (left) and sensor T3 (right).

In Fig. 5, the confusion matrices showing test results for the data from the sensors T2 and T3 are presented. In general, good performance of the classifier is achieved and different AE, which are related to symmetrical and asymmetrical excitation, can be distinguished reliably.

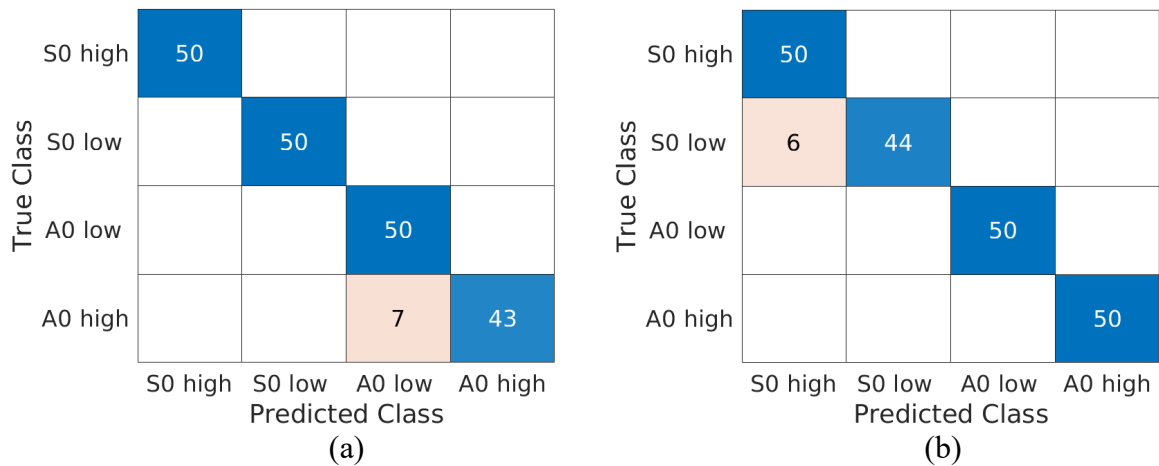


**Fig. 5.** Confusion matrices for (a) sensor T2 and (b) sensor T3.

Finally, the effect of changes in the propagation distance on the performance of the classifier is investigated. To this end, two different cases are considered: (i) the initial propagation distance is increased after training and (ii) the initial propagation distance is decreased after training. Here, data from different sensors were used during training and test. In each case, a total of 400 samples are used for training of the AlexNet. For test, 200 samples are chosen from the other sensor. The corresponding confusion matrices are shown in Fig. 6. It is obvious that the classification performance degrades due to the change in the propagation distance between training and test. However, it is notable that symmetric and asymmetric wave modes are effected differently. In Fig. 6 (a), most of the classification errors are related to asymmetric excitation whereas classification of AE related to symmetric excitations is more difficult in Fig. 6 (b).

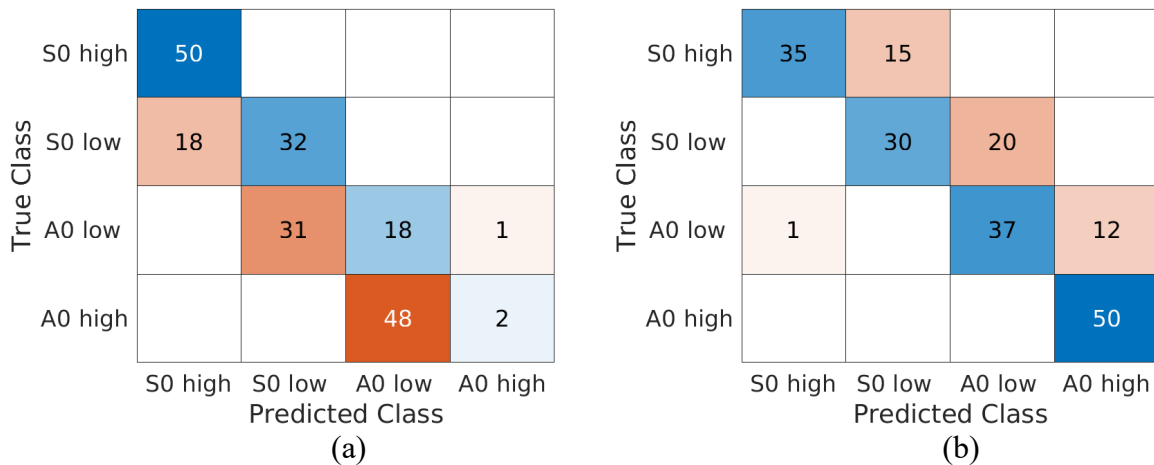


**Fig. 6.** Confusion matrices for (a) Training: T2, Test: T3 and (b) Training: T2, Test: T3.

Similarly, the effect of changes in the propagation distances on the classification performance for both excitations can be observed using cross validation. In Fig. 7, results of 5-fold cross validation are presented. Here, recall is reported to assess the performance for each class. In accordance with the previous results, better performance can be achieved for asymmetric excitations if the propagation distance is increased between training and test. If the propagation distance is reduced between training and test, the performance of the classifier is better for symmetric excitations. Therefore, it can be concluded that the effect of different propagation distances on the classification performance depends also on the underlying source mechanism.

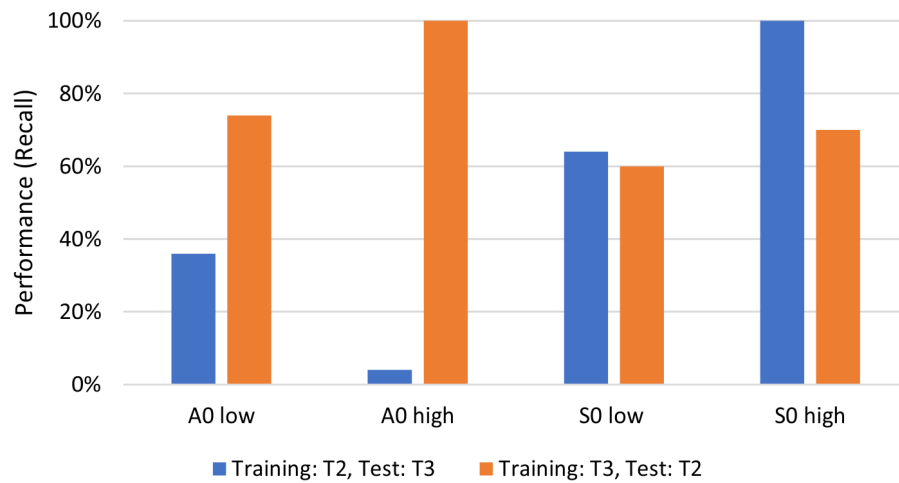


**Fig. 7.** Cross validation results.

In this example, AE signals with dominant symmetric and asymmetric wave mode were chosen, which are in practice related to e.g. fiber breakage and delamination, respectively [2]. It could be shown that in principle, the classification performance at different propagation distances depends on the corresponding wave mode. However, the effect of wave propagation on the classification performance may be different depending on frequency of AE signatures and dispersion characteristics of the material.

## Summary and conclusion

In this paper, a detailed investigation regarding the impact of variations in the propagation distance of AE in composite material on the classification performance is presented. A thin plate is chosen, which is a typical specimen geometry. Artificial AE sources are induced using PWAS transducers, which allows to precisely control the modal content of the AE signals. For classification, a transfer learning approach – i.e. fine-tuning of pre-trained AlexNet architecture – is used. Particular focus is given to the performance of the classifier for AE waveforms with different dominant modes.

The variations in propagation distance have a strong impact on the classification performance. In particular, two different cases in which the propagation distance is i) increased and ii) reduced between training and test. Here, the effect on the classification performance also depends on the dominant wave mode of AE. Therefore, as main conclusion for AE-based SHM it can be stated that variations in the propagation path can not be neglected, also if frequency domain features are used. The robustness of a classifier to variations of the propagation path depends on the dominant mode of the AE waveforms. The underlying source mechanisms should be taken into consideration for reliable performance estimation.

## References

- [1] D. Baccar and D. Söffker, Identification and classification of failure modes in laminated composites by using a multivariate statistical analysis of wavelet coefficients. *Mech Syst Signal Pr* 96 (2017) 77-87. <https://doi.org/10.1016/j.ymsp.2017.03.047>
- [2] F. Dahmene, S. Yaacoubi, M. El Mountassir, N. Bendaoud, C. Langlois and O. Bardoux, On the modal acoustic emission testing of composite structure. *Compos Struct*, 140 (2016) 446-452. <https://doi.org/10.1016/j.compstruct.2016.01.003>
- [3] J. Martínez-Jequier, A. Gallego, E. Suárez, F. J. Juanes and Á. Valea, Real-time damage mechanisms assessment in CFRP samples via acoustic emission Lamb wave modal analysis. *Compos Part B-Eng* 68 (2015) 317-326. <https://doi.org/10.1016/j.compositesb.2014.09.002>
- [4] S. K. Chelliah, P. Parameswaran, S. Ramasamy, A. Vellayaraj and S. Subramanian, Optimization of acoustic emission parameters to discriminate failure modes in glass–epoxy composite laminates using pattern recognition. *Struct Health Monit* 18 (2019) 1253-1267. <https://doi.org/10.1177/1475921718791321>
- [5] J. P. McCrory, S. K. Al-Jumaili, D. Crivelli, M. R. Pearson, M. J. Eaton, C. A. Featherston, M. Guagliano, K. M. Holford and R. Pullin, Damage classification in carbon fibre composites using acoustic emission: A comparison of three techniques. *Compos Part B-Eng* 68 (2015) 424-430. <https://doi.org/10.1016/j.compositesb.2014.08.046>
- [6] N. Beheshtizadeh and A. Mostafapour, Processing of acoustic signals via wavelet & Choi-Williams analysis in three-point bending load of carbon/epoxy and glass/epoxy composites. *Ultrasonics* 79 (2017) 1-8. <https://doi.org/10.1016/j.ultras.2017.04.001>
- [7] S. K. Al-Jumaili, K. M. Holford, M. J. Eaton and R. Pullin, Parameter Correction Technique (PCT): A novel method for acoustic emission characterisation in large-scale composites. *Compos Part B-Eng* 75 (2015) 336-344. <https://doi.org/10.1016/j.compositesb.2015.01.044>

- [8] E. Maillet, C. Baker, G. N. Morscher, V. V. Pujar and J. R. Lemanski, Feasibility and limitations of damage identification in composite materials using acoustic emission. *Compos Part A-Appl S* 75 (2015) 77-83. <https://doi.org/10.1016/j.compositesa.2015.05.003>
- [9] K. Asamene, L. Hudson and M. Sundaresan, Influence of attenuation on acoustic emission signals in carbon fiber reinforced polymer panels. *Ultrasonics* 59 (2015) 86-93.
- [10] M. Kharrat, V. Placet, E. Ramasso and M. L. Boubakar, Influence of damage accumulation under fatigue loading on the AE-based health assessment of composite materials: Wave distortion and AE-features evolution as a function of damage level. *Compos Part A-Appl S* 109 (2018) 615-627. <https://doi.org/10.1016/j.compositesa.2016.03.020>
- [11] S. F. Wirtz, S. Bach and D. Söffker, Experimental results of acoustic emission attenuation due to wave propagation in composites. Annual Conference of the PHM Society, Scottsdale, AZ, USA, September 21-26, 2019.
- [12] Z. Su and L. Ye, Selective generation of Lamb wave modes and their propagation characteristics in defective composite laminates. *P I Mech Eng L-J Mat* 218 (2004) 95-110. <https://doi.org/10.1177/146442070421800204>
- [13] M. Azimi, A. D. Eslamlou and G. Pekcan, Data-Driven Structural Health Monitoring and Damage Detection through Deep Learning: State-of-the-Art Review. *Sensors* 20 (2020) 2778. <https://doi.org/10.3390/s20102778>
- [14] A. Krizhevsky, I. Sutskever and G. E. Hinton, ImageNet Classification with Deep Convolutional Neural Networks. *Adv Neur In* 25 (2012) 1097-1105.
- [15] S. Dorafshan, R. J. Thomas and M. Maguire, Comparison of deep convolutional neural networks and edge detectors for image-based crack detection in concrete, *Constr Build Mater* 186 (2018) 1031-1045. <https://doi.org/10.1016/j.conbuildmat.2018.08.011>
- [16] M. Hemmer, H. Van Khang, K. Robbersmyr, T. Waag and T. Meyer, Fault Classification of Axial and Radial Roller Bearings Using Transfer Learning through a Pretrained Convolutional Neural Network. *Designs* 2 (2018) 56. <https://doi.org/10.3390/designs2040056>
- [17] S. Lu, Z. Lu and Y. D. Zhang, Pathological brain detection based on AlexNet and transfer learning. *J Comput Sci-Neth* 30 (2019) 41-47. <https://doi.org/10.1016/j.jocs.2018.11.008>

# Improving the Drive-by Bridge Inspection Performance by Vehicle Parameter Optimization

Yifu Lan \*

School of Civil and Environmental Engineering, University of New South Wales, Sydney NSW 2052, Australia

**Keywords:** Drive-by Bridge Inspection, Vehicle Bridge Interaction, Vertical Vehicle Displacement, Vehicle Configuration, Parameter Optimization

**Abstract.** Recently, there has been an increasing emphasis in the Indirect bridge health monitoring method employing passing vehicles, which is regarded as one of the most effective approaches in bridge damage screening. However, few researches have been conducted on the Drive-by bridge inspection method using vehicle displacement profile as damage indicator due to the challenges in displacement measurement and result accuracy. This paper proposes an optimization approach of designing the optimum vehicle parameters to improve the performance of vehicle displacement-based Drive-by bridge damage inspection. A generalized Vehicle-Bridge Interaction (VBI) system is built in MATLAB, where the bridge is modelled as a simply supported beam with 10 elements and the passing vehicle is represented as a simplified quarter car. Employing the Monte Carlo methods, the optimum parameters are determined by numerous simulations processed under diverse damage scenarios. Results show that by employing the optimal vehicle parameters, the bridge damages can be detected effectively and accurately for general damage scenarios based on the vehicle displacement profile. The proposed optimization method can contribute to the wide application of vehicle displacement-based Drive-by bridge damage inspection, providing merits in simplicity and visualization.

## Introduction

It is acknowledged that more than 11% of bridges are structurally deficient in the United States, and in Europe most bridges were constructed from 1945 to 1965 (Malekjafarian et al. 2015). Issues faced by bridges these days involve not just increases in traffic loads but also the gradual deterioration due to the environmental impacts over time. The conventional SHM is known as the “sensor-base monitoring”, which requires numerous sensors placed on the bridge, and its performance is highly dependent on the location and sensitivity of sensors (Sohn et al. 2003). For many years, the sensor installation has been regarded as a costly and challenging part of conventional SHM, especially for a bridge under ongoing traffic. In addition to the sensor performance, influences of the environment and ongoing traffic are non-negligible, as sensitive sensors will also be sensitive to environmental noises (Sohn et al. 2003).

To achieve a better performance in feasibility and cost efficiency, an Indirect-SHM method of employing the passing vehicle is proposed by Yang et al. (2004), regarded as one of the most effective approaches in bridge damage detection. Compared with the conventional SHM methods, advantages of the Drive-by inspection method are generally in economy, simplicity, mobility and feasibility (Malekjafarian et al. 2015). Instead of employing numerous instrumentations attached to the bridge, the Drive-by method uses a vehicle as the “moving sensor” to obtain dynamic properties of the bridge via the Vehicle-Bridge Interaction (VBI). The

---

\* Corresponding author at: School of Civil and Environmental Engineering, University of New South Wales, Sydney NSW 2052, Australia  
E-mail address: [elvislannnnn@gmail.com](mailto:elvislannnnn@gmail.com) (Y. Lan)

vehicle employed is regarded as both exciter and receiver with the instrumentation placed on the cart suspension system, which aims at eliminating the noise from the vehicle engine (Lin and Yang 2005). It has been experimental verified that the fundamental frequency of bridge can be successfully extracted by acceleration signals collected from the cart sensor with a travelling speed lower than 40 km/h. Structural damages will lead to changes in bridge dynamic properties, and it is feasible to extract the frequency changes due to bridge damage by tracking the vehicle responses.

Based on diverse damage indicators, there are generally three approaches of bridge damage inspection employing passing vehicles. The first is based on the bridge damping ratio, in which the structural damage is represented as the increase in bridge damping ratio. It is found that the damping ratio increases will lead to changes in the acceleration spectra, and by tracking these changes the damages can be detected and localized (McGetrick et al. 2009). The second is known as the mode shape-based damage inspection method, regarding the mode shape discontinuities as damage representor. Zhang et al. (2012) find that the point impedance can be obtained using the vehicle response when a specialized theoretical vehicle is employed to control the applied force on the bridge, and the amplitude of the point impedance spectra is proportional to the square of the mode shapes. Moreover, an algorithm introduced by Yang et al. (2014) shows that the instantaneous amplitude for the extracted bridge component response of specific mode is equal to the mode shape, which provides high-resolution results. In addition to the approaches introduced above, there is a trend of using displacement profile to detect the structural damages. Traditionally, the bridge deflection shape is always considered as damage representor, where the peak occurred in the displacement profile difference between healthy and damaged bridges could indicate the existence of damage.

However, there are few studies focusing on the vehicle displacement-based methods of damage inspection. Traditionally the measurement of relative vertical vehicle displacement is challenging employing the conventional measuring approaches, especially when the damage is less significant (Yin and Tang 2011). Additionally, the vehicle dynamics could mask the damage characteristics even the highly sensitive sensors are available. The relative displacement maximization and the noise reduction therefore play a key role in the damage detection using vehicle displacement profile as indicator. One of the strategies is to optimize the vehicle configuration parameters. McGetrick and Kim (2013) point out that the vehicle response will be considerably affected by its configuration parameters involving vehicle stiffness, mass and damping. Accordingly, by investigating the parametric impacts and optimizing the vehicle parameters before the bridge health monitoring can contribute to better detection performance.

This paper proposes a new method of Drive-by inspection with parameter optimization, which employs the vehicle displacement profile as damage indicator. The parameter optimization will be firstly processed to determine the vehicle parameters that provide the preferable performance. Secondly, the effectiveness of Drive-by inspection based on vehicle displacement profile difference will be examined in the presence of diverse damage positions and levels.

### **VBI Modelling**

The bridge is established in MATLAB as a simply supported beam with 10 elements while the vehicle is modelled as a quarter car consisting of the main vehicle parameters of  $m_v$  (vehicle mass),  $k_v$  (vehicle stiffness),  $c_v$  (vehicle damping) and  $v$  (vehicle speed). Each element of the bridge has the equal physical properties such as rectangular cross section and density as shown in the Table. 1. The damage in this study is identified as the loss of stiffness caused by structural

defects like cracks. The damage severity is defined as x% reduction in the element, while the damage location is described as the specific element in which the damage occurs.

Table. 1 Bridge Properties

Span Length, L (mm)	Intact Element Stiffness, EI (N*m <sup>2</sup> )	Natural Frequency, Wb (Rad/s)	Mass per unit length, ρ (kg/m)	Road profile severity
25000	3.30E+09	2	4800	Class A

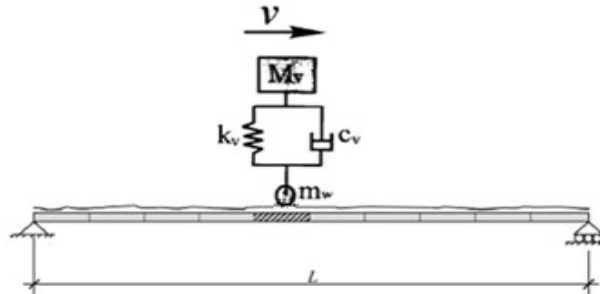


Fig. 1 VBI Model

The VBI process is simulated in MATLAB and the vehicle response can be obtained applying the contact force concept. The equations of motion of the VBI system can be given by equating the contact forces between vehicle and bridge at each moment, and for the time step i are:

$$[m_v] \{\ddot{y}_v\}_i + [c_v] \{\dot{y}_v\}_i + [k_v] \{y_v\}_i = \{f_v\}_i \quad (1)$$

$$[m_b] \{\ddot{y}_b\}_i + [c_b] \{\dot{y}_b\}_i + [k_b] \{y_b\}_i = \{f_b\}_i \quad (2)$$

Where the [m<sub>v</sub>], [c<sub>v</sub>] and [k<sub>v</sub>] represent mass, damping and stiffness matrices of the vehicle respectively. While {y<sub>v</sub>}, {y<sub>v</sub>} and {y<sub>v</sub>} are the acceleration, velocity and displacement of vehicle respectively. Similarly, the [m<sub>b</sub>], [c<sub>b</sub>] and [k<sub>b</sub>] are mass, damping and stiffness for bridge respectively, and {y<sub>b</sub>}, {y<sub>b</sub>} and {y<sub>b</sub>} are bridge acceleration, velocity and displacement respectively. Accordingly, the non-zero components of the vector, {f<sub>v</sub>}<sub>i</sub> represent the dynamic interaction forces:

$$f_{vci} = (w_{bi} + r_i) k_s \quad (3)$$

Where k<sub>s</sub> is the suspension stiffness and w<sub>bi</sub> is the deflection of bridge, while in the equation, r<sub>i</sub> represents the road profile height. and {f<sub>b</sub>}<sub>i</sub> is the applied force vector on the bridge, which is given as:

$$\{f_b\}_i = (w - [m_v] \{\ddot{y}_v\}_i) * \{N_b\}_i \quad (4)$$

Where w is the vehicle gravity weight and {N<sub>b</sub>}<sub>i</sub> is the location function that assigns the interaction force to the element degrees of freedom at the i th step.

By solving the iterative process, the bridge displacement under the vehicle can be calculated until the increase in the bridge displacement is less than the specified percentage. Firstly, it is assumed that there is no deflection occurred on the bridge and the vehicle interactive force is calculated for the whole simulation using Eq. 3. Secondly, the vehicle response is obtained by solving the Eq. 1 using Newmark-beta integration scheme. Thirdly, the vehicle accelerations obtained are used in Eq. 4 to calculate the applied force on the bridge, after which the bridge

deflection vector is calculated by Newmark-beta integration scheme. Lastly, the bridge displacement is computed as below:

$$w_{bi} = \{y_b\}_i^T \{N_b\}_i \quad (5)$$

The vector  $\{y_v\}$  is obtained by repeating the same process for all  $i$  steps, which is the vehicle displacement corresponding to each time step. The process will be proceeded repeatedly using the new  $w_{bi}$  until less than 1% is witnessed in the ratio between the max bridge displacements in the old and new profiles. Fig. 2 below illustrates the VBI algorithm.

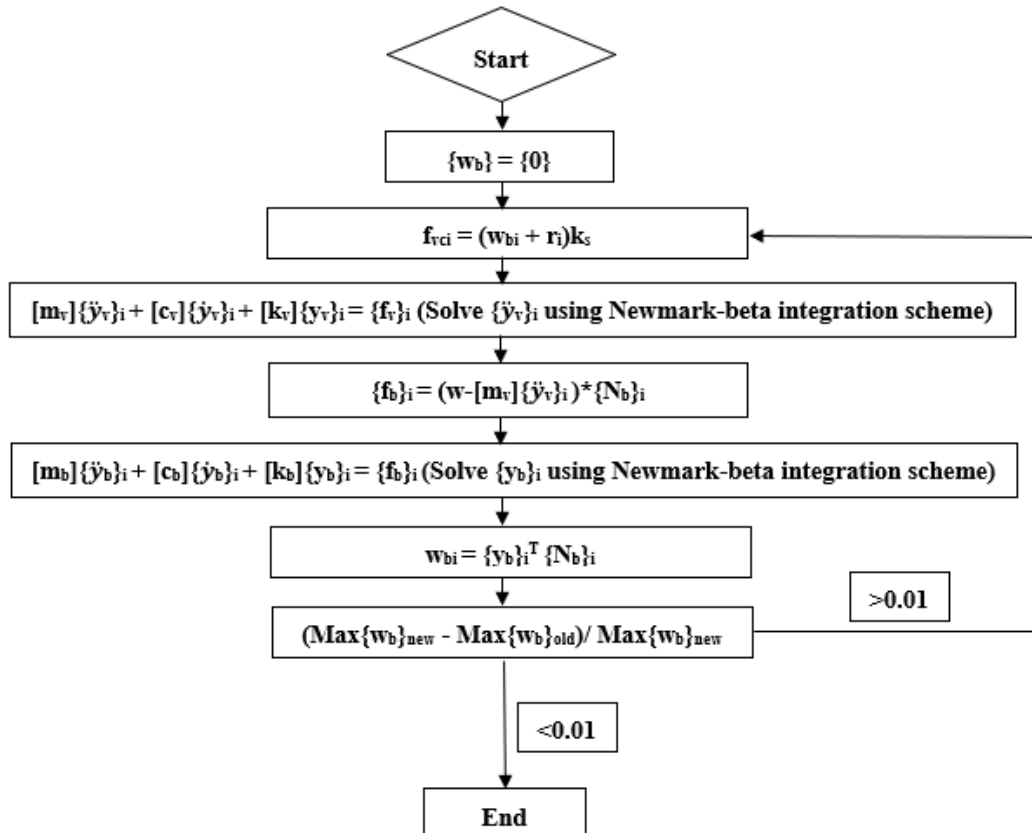


Fig. 2 Flow chart of VBI algorithm

### Optimization of the vehicle parameters

The parameters being assessed involve  $m_v$  (vehicle mass),  $k_v$  (vehicle stiffness),  $c_v$  (vehicle damping) and  $v$  (vehicle speed), which accordingly would have considerable impacts on vehicle responses (McGetrick and Kim 2013). A feasible strategy is by employing the Monte Carlo Method, which aims to solve deterministic problems utilizing repeated samplings, to investigate the parameter effects. Each vehicle parameter of interest in this study is independent (would not affect or be affected by other parameters) and it is reasonable to study these parameters separately.

The value of interest parameter will be changed many times within the range while other 3 vehicle parameters remaining constant to obtain the vehicle responses. The corresponding displacement difference profile of vehicle between healthy and damaged beams will be acquired as the vehicle parameter varies. After that, a diagram of the max displacement differences corresponding to the parameter changes can be generated after many times of repetition, where the optimum vehicle parameters can be designed. Initializing that  $v=15\text{m/s}$ ,  $m_v=10000\text{kg}$ ,

$k_v=250000$  N/m and  $\zeta=0.05$ , the changes in the max displacement differences corresponding to vehicle damping ratio ( $\zeta$ ), vehicle stiffness ( $k_v$ ), vehicle mass ( $m_v$ ) and speed ( $v$ ) respectively for Damaged Element 2 and 5 with 20% severity are given as shown in Fig. 3 – 4.

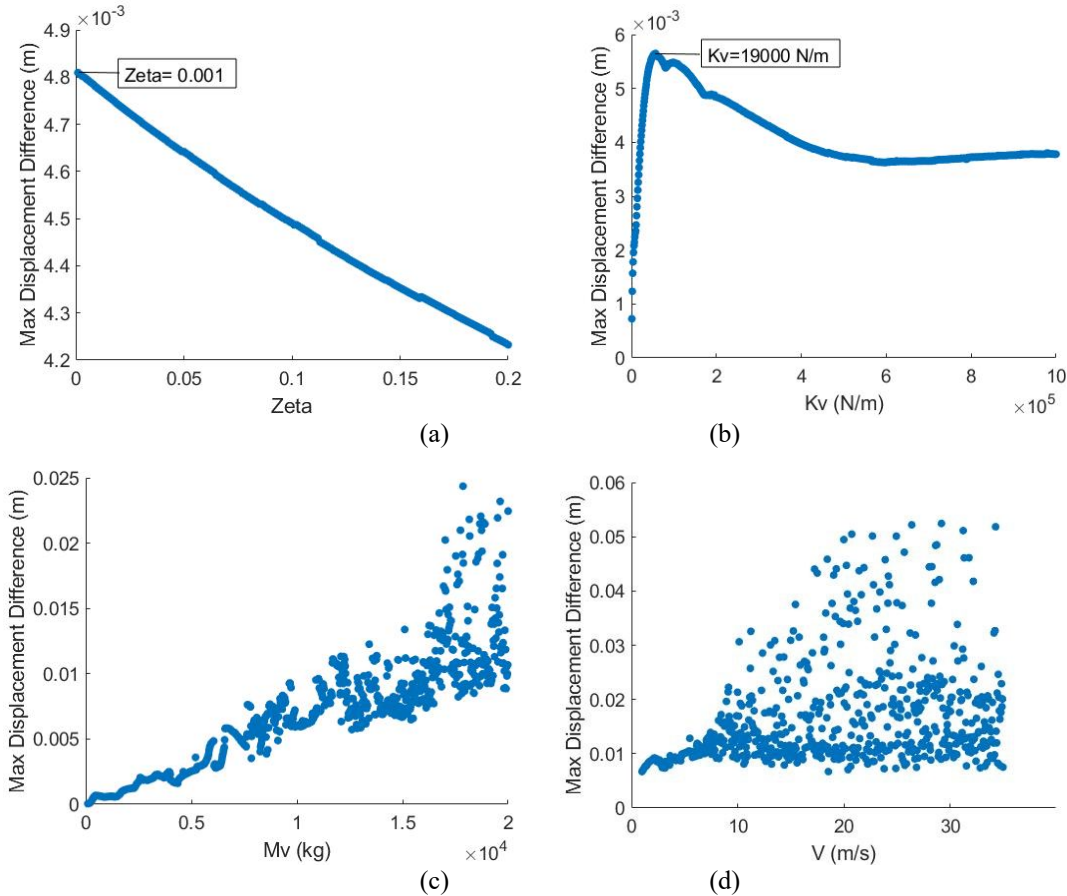


Fig. 3 The max displacement differences corresponding to diverse vehicle parameters for Damaged Element 2: (a) Vehicle damping ratio,  $\zeta$  (b) Vehicle stiffness,  $k_v$  (c) Vehicle mass,  $m_v$  (d) Vehicle speed,  $v$

Summarily, the max displacement difference rises with vehicle mass ignoring some fluctuations and declines as vehicle damping ratio increases. As shown in the relation between  $k_v$  and the max displacement difference, it rises sharply to the peak and then drops dramatically to a lower point. As the  $k_v$  continues to increase, it presents a stable trend of the connection between vehicle stiffness and the max displacement difference. The correlations between vehicle speed and the max displacement difference are blurry when the speed reaches high. As the cart might be “over-excited” with the high travel speed, and this would mask the responses corresponding to bridge damages. Additionally, higher resolution results can be provided by the lower speed of vehicle. Results for damage locations in Element 6 & 8 present similar trends, and the optimal parameters can therefore be acquired as shown in Table 2 below, which provide preferable performances for diverse Damage Situations.

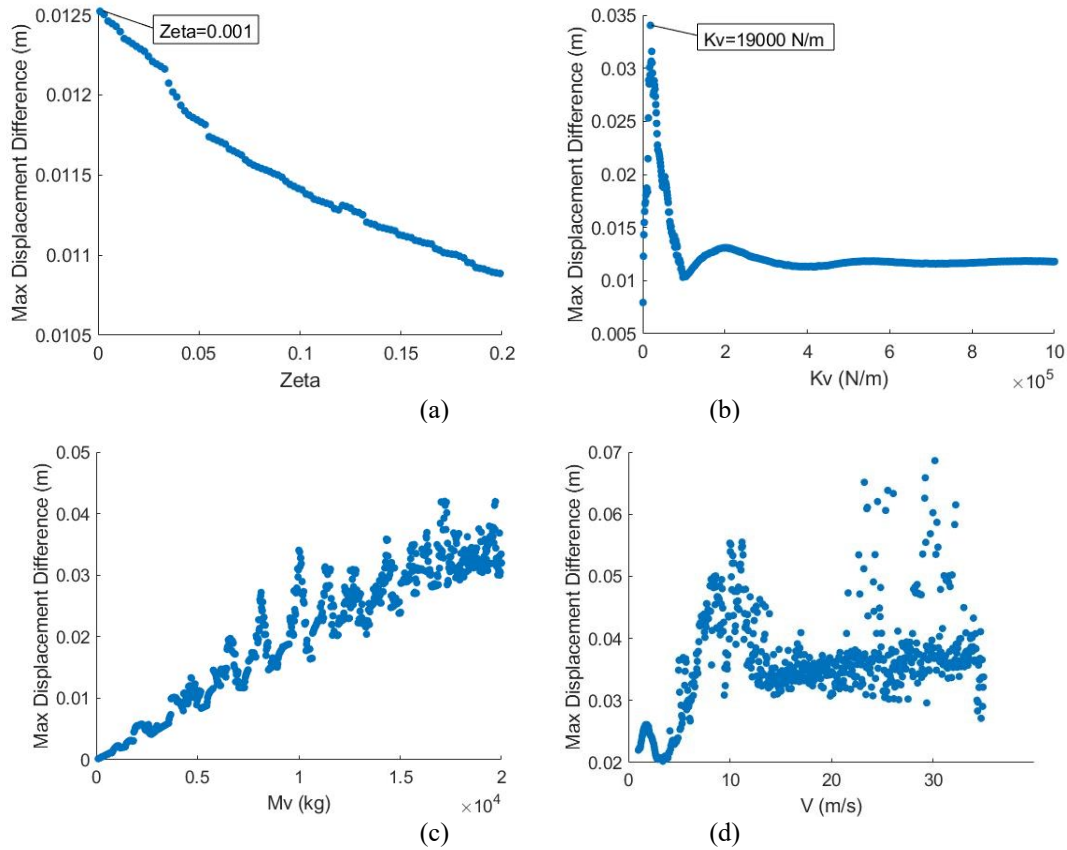


Fig. 4 The max displacement differences corresponding to diverse vehicle parameters for Damaged Element 5: (a) Vehicle damping ratio, zeta (b) Vehicle stiffness,  $k_v$  (c) Vehicle mass,  $m_v$  (d) Vehicle speed,  $v$

Table. 2 The optimum vehicle parameters for diverse damage scenarios

	Damaged Element 2	Damaged Element 5	Damaged Element 6	Damaged Element 8
Zeta	0.001	0.001	0.001	0.001
$K_v$	19000 N/m	19000 N/m	18000 N/m	12000 N/m
$M_v$	20000 kg	20000 kg	20000 kg	20000 kg
V	1 m/s	1 m/s	1 m/s	1 m/s

### Results of damage inspection using the optimum parameters

Damages are presented in Element 2, 5, 6 & 8 with damage level increasing from 10% to 80% gradually, defined as the loss of element stiffness. To detect the damage, the vehicle with optimum parameters obtained above is simulated travelling through the beam. The vehicle displacement difference profiles are then obtained based on the differences between vehicle time histories of damaged beams and the baseline, where the baseline is acquired using the vehicle deflection profile of healthy beam. Ideally, the peaks occurred will accurately indicate the location of damage and the damage levels will be illustrated as the increasement in displacement

difference, which are known as the damage characteristics (Yin and Tang 2011). In damage scenario 1, where the stiffness reduction starts at element 2 (20% L), the peak occurs at around 5 s in Displacement difference profile, 20% of the total time period. When the structural damage occurs in element 5 (50% L), it can be found that the peak is witnessed at about 12.5 s in Displacement difference profile, which is nearly 50% of the total time period. Similarly, in Displacement difference profiles of damage scenario 3 & 4, where bridge damages are presented in element 6 & 8, the peaks occur just before 15 s and 20 s respectively, which are 60% and 80% of the total time period respectively. Generally, as shown in Fig. 5, the displacement difference between baseline (healthy) and that of damaged beam increases gradually as the damage level goes up. The results indicate that this approach presents high accuracy and sensitivity in damage inspection.

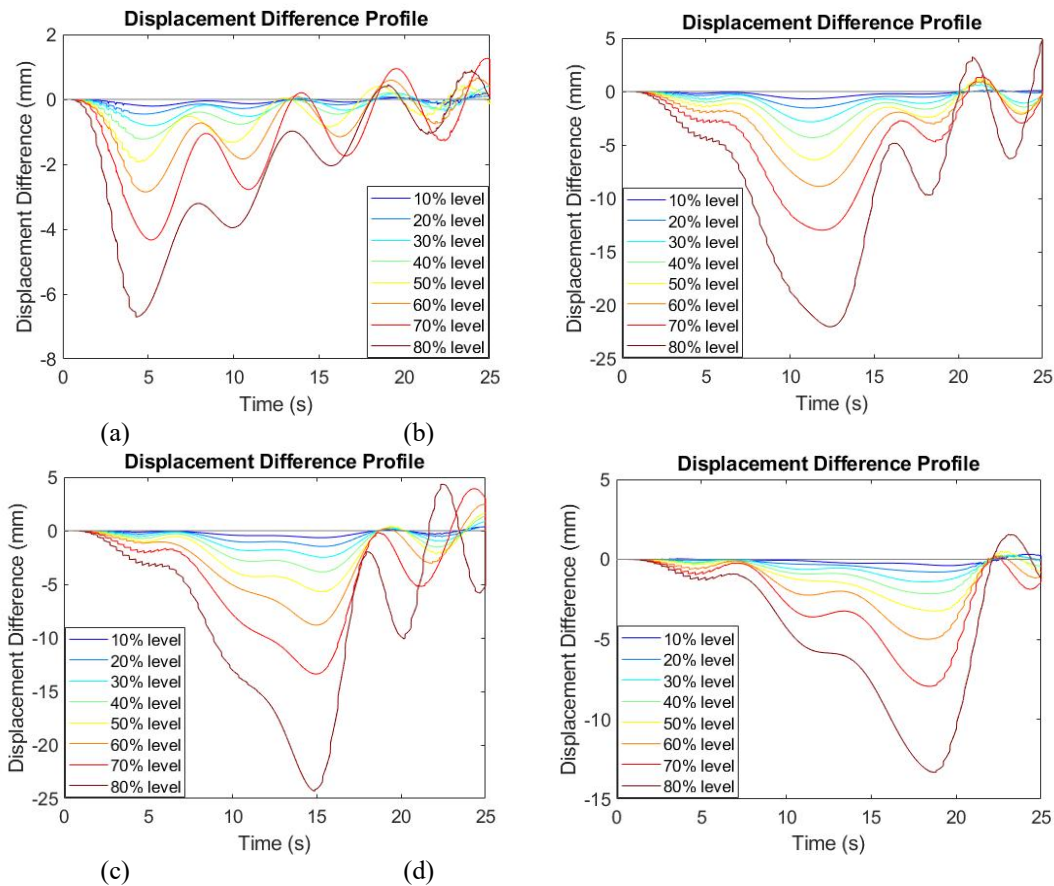


Fig. 5 Displacement Difference Profile for diverse damage locations: (a) Damaged element 2, 20% L (b) Damaged element 5, 50% L (c) Damaged element 6, 60% L (d) Damaged element 8, 80% L

### Conclusion

This paper proposes a new method of Drive-by inspection with parameter optimization employing vehicle displacement as damage indicator. The vehicle time history is adopted employing a simplified VBI system simulated in MATLAB. Then the displacement difference profile of vehicle can be obtained by subtracting the vehicle time histories between baseline and that of damaged bridge, where the baseline is acquired by the first-time run passing through the bridge with healthy condition. In many times of simulations, it is found that the occurrence of

damages can be successfully identified, which is presented as the peak in displacement difference profile, while the damage level is regarded as the increase in displacement difference. To achieve higher accuracy and sensitivity of detection results, this paper proposes a strategy of parameter optimization aiming at maximizing the vehicle displacement profile difference and reducing the noises from vehicle dynamics. The results indicate that the optimum parameters of vehicle can effectively improve the inspection performance for all damage scenarios. With the technique of deflectometer developing rapidly, it is predictable that the role of Vehicle response-based Drive-by inspection will become increasingly emphasized. The effectiveness of this approach can contribute to its wide application to the general health monitoring. To further study its feasibility and applicability in real project, field tests including the environmental effects are required.

## References

- [1] Malekjafarian, A., McGetrick, P. & O'Brien, E. 2015, 'A Review of Indirect Bridge Monitoring Using Passing Vehicles', *Shock and Vibration*, vol.2015, pp.1-16. <https://doi.org/10.1155/2015/286139>
- [2] Sohn, H., Farrar, C.R., Hemez, F.M., Shunk, D.D., Stinemates, D.W., Nadler, B.R. & Czarnecki, J.J. 2003, 'A review of structural health monitoring literature: 1996–2001', *Los Alamos National Laboratory*, USA.
- [3] Yang, Y., Lin, C. & Yau, J. 2004, 'Extracting bridge frequencies from the dynamic response of a passing vehicle', *Journal of Sound and Vibration*, vol. 272, no. 3-5, pp. 471–493. [https://doi.org/10.1016/S0022-460X\(03\)00378-X](https://doi.org/10.1016/S0022-460X(03)00378-X)
- [4] Yang, Y. & Lin, C. 2005, 'Vehicle-bridge interaction dynamics and potential applications', *Journal of Sound and Vibration*, vol. 284, no. 1-2, pp. 205–226. <https://doi.org/10.1016/j.jsv.2004.06.032>
- [5] McGetrick, P.J., Gonzalez, A. & Obrien, E.J. 2009, 'Theoretical investigation of the use of a moving vehicle to identify bridge dynamic parameters', *Insight - Non-Destructive Testing and Condition Monitoring*, vol. 51, no. 8, pp. 433–438. <https://doi.org/10.1784/insi.2009.51.8.433>
- [6] Zhang, Y., Wang, L. & Xiang, Z. 2012, 'Damage detection by mode shape squares extracted from a passing vehicle', *Journal of Sound and Vibration*, vol. 331, no. 2, pp. 291–307. <https://doi.org/10.1016/j.jsv.2011.09.004>
- [7] Yang, Y., Li, Y. & Chang, K. 2014, 'Constructing the mode shapes of a bridge from a passing vehicle: a theoretical study', *SMART STRUCTURES AND SYSTEMS*, vol. 13, no. 5, pp. 797–819. <https://doi.org/10.12989/sss.2014.13.5.797>
- [8] McGetrick, P.J. & Kim, C.W. 2013, 'A Parametric Study of a Drive by Bridge Inspection System Based on the Morlet Wavelet', *Key Engineering Materials*, pp. 569-570 & pp. 262-269. <https://doi.org/10.4028/www.scientific.net/KEM.569-570.262>
- [9] Yin, S.H. & Tang, C.Y. 2011, 'Identifying Cable Tension Loss and Deck Damage in a Cable-Stayed Bridge Using a Moving Vehicle', *Journal of Vibration and Acoustics*, vol. 133, no.2/021007. <https://doi.org/10.1115/1.4002128>

# Reinforcement Learning for Structural Health Monitoring based on Inspection Data

Simon Pfingstl<sup>1,a,\*</sup>, Yann Niklas Schoebel<sup>1,b</sup> and Markus Zimmermann<sup>1,c</sup>

<sup>1</sup>Technical University of Munich, Laboratory for Product Development and Lightweight Design, Boltzmannstr. 15, 85748 Garching, Germany

<sup>a</sup>simon.pfingstl@tum.de, <sup>b</sup>yann.schoebel@web.de, <sup>c</sup>zimmermann@tum.de

**Keywords:** Reinforcement Learning, Structural Health Monitoring, Crack Growth, Inspection Timing

**Abstract.** Due to uncertainty associated with fatigue, mechanical structures have to be often inspected, especially in aerospace. In order to reduce inspection effort, fatigue behavior can be predicted based on measurement data and supervised learning methods, such as neural networks or particle filters. For good predictions, much data is needed. However, often only a small number of sensors to collect data are available, e.g., on airplanes due to weight limitations. This paper presents a method where data that is collected during an inspection is utilized to compute an update of the optimal inspection interval. For this purpose, we describe structural health monitoring (SHM) as a Markov decision process and use reinforcement learning for deciding when to inspect next and when to decommission the structure before failure. In order to handle the infinite state space of the SHM decision process, we use two different regression models, namely neural networks (NN) and k-nearest neighbors (KNN), and compare them to the deep Q-learning approach, which is state of the art. The models are applied to a set of crack growth data which is considered to be representative of the general damage evolution of a structure. The results show that reinforcement learning can be utilized for such a decision task, where the KNN model leads to the best performance.

## Introduction

The lifetime of cyclically loaded metal structures is limited, due to the propagation of cracks in the material which leads to a failure of the structure after a certain amount of load cycles [1, 2]. Hence, aluminum parts in aircraft structures need to be inspected periodically to find and replace parts with significant crack propagation. Especially assemblies like wing and fuselage have to endure high cyclic stresses during their lifetime. Maintenance and health monitoring are significant factors in aircraft operating costs. For example, the average direct maintenance costs of a Boeing 757-200 had a proportion of about 23% of the total flight operating costs in 2017 [3].

Every opportunity to reduce these costs is beneficial to the aerospace industry and can reduce the overall costs per flight hour. Using machine learning (ML) methods can help to reduce maintenance costs. Therefore, a lot of research is currently done in the field of prognostic health monitoring (PHM). PHM tries to predict the time to failure of a structural system often by using ML methods. Usually, data, which indicates the deterioration of a system, serves as the input of the ML model. The predicted output is the time to failure of the structural system. Often continuous or many data points are needed whereas applied sensors are heavy and increase the weight. Especially in the aerospace industry, this leads to an increase of the fuel burn which might be more costly than operating an aircraft without an SHM system.

Therefore, this paper aims to show the application of reinforcement learning (RL) to an SHM task, which uses only data when an inspection is carried out. The feasibility of the approach is demonstrated using a set of published crack growth data [4], where the crack length serves as the damage index. This data is considered to resemble a degrading system, wherein real-world applications this might be for instance the number of repairs during a maintenance service. Furthermore, we propose another way of how to train the best decision policy and compare it to the state of the art approach in terms of the number of inspections, the wasted remaining life cycles, and the number of fails. By using RL, the planning of inspection dates might be improved and the overall number of inspections decreased.

In the following section, we summarize and discuss different PHM approaches. In sections 3 and 4, we explain the fundamentals of RL and describe how we apply it on an SHM task, respectively. After showing the results in section 5, we discuss and summarize them in the last section.

### Literature Review

In research, a broad amount of possibilities to improve maintenance policies and lower their costs is investigated. One approach to determine the optimal maintenance policy is by Markov decision processes (MDP) or partially observed Markov decision processes (OMDP) [5, 6]. The research shows that MDPs or OMDPs are suitable to determine the optimal maintenance policy and to increase the overall system effectiveness. Moreover, it has been proven that reinforcement Q-learning can find the optimal action-selection strategy for every finite MDP, given sufficient exploration time and random actions [7]. Therefore, we describe structural health monitoring (SHM) as an MDP and use RL for deciding when to inspect next.

Another approach is to predict the damage progress by mathematical surrogate models. E.g. in [8-11], it has been already proven that the propagation of cracks can be predicted with neuronal networks. Even the propagation under overloads and non-linear damage can be predicted with such algorithms [12, 13]. Moreover, it is possible to perform live monitoring with sensor data of an operating system, e.g. in [14]. If the remaining useful life (RUL) can be predicted by a monitoring system, we commonly refer to this as prognostic health monitoring (PHM). Several ways exist to predict the RUL. One method, which has been very successful in the PHM challenge in 2008 [15, 16], was a similarity-based approach [17]. This method uses run to failure data to define a library of degradation paths. The data of the test system is compared to the library, and the most similar is used to determine the RUL. One disadvantage of PHM methods is that they require continuous or rather many sensor data points during the lifetime of a component to predict the damage progress. However, in most structural parts of an aircraft, there are no sensors to monitor the current condition. Additional sensors would lead to heavier aircraft which will inevitably increase the fuel burn and thus the operating costs. Therefore, this work presents an approach that uses only data that is collected during inspections.

### Fundamentals of RL and new Approach

RL is an area of ML, in which a software agent is interacting with a simulated or physical environment. This environment has to be modeled as an MDP. The environment is at a time  $t$  in a state  $S$ , and the agent selects an action  $A$ , which leads the environment in a new state  $S'$ . Array  $A$  consists of all possible actions. The agent gets feedback on the performed action by a reward  $R$ . That allows the agent to learn by itself over time. It does not need a teacher. For finite environments, the agent selects actions, until it reaches a terminal state [18].

Q-learning is a special type of RL, where the agent learns so-called Q-values for an action taken in a state. These values represent the expected reward for performing that action in that

state. First, the Q-values are randomly initialized. Then, in the training step, the values are adopted according to a version of the Bellmann equation (Eq. 1),

$$Q^*(S, A) = (1 - \alpha) Q(S, A) + \alpha [R + \gamma \max(Q'(S', A))] \quad (1)$$

where  $Q^*$ ,  $Q$ , and  $Q'$  are the updated, current, and future Q-values, respectively,  $\alpha$  is the learning rate and  $\gamma$  the discount factor. In Q-learning, the Q-values are trained based on the current and on the future Q-value, i.e. the not yet updated Q-value and the highest achievable reward for doing an action one timestep in the future (temporal difference learning). Q-learning is based on an  $\epsilon$ -greedy strategy. In the learning phase, the agent has the chance  $\epsilon$  to perform a random action, while  $\epsilon$  decreases over time. If  $\epsilon$  is equal to zero, the agent does not execute a random action anymore and will always execute the action with the highest Q-Value (“greedy”). The learning rate  $\alpha$  influences how much the new values replace the old. The discount factor  $\gamma$  is responsible for weighting the future Q-values compared to the current ones. The learning rate, the discount factor, and the  $\epsilon$  parameter thus influence the speed and outcome of the training

The classic Q-learning stores the Q-values of every state in a table. This is a problem for large or infinite state and/or action spaces, where memory usage can overcome the available memory. To solve this problem, usually, a value approximator is introduced to predict the Q-values of every state. This is usually referred to as deep Q-learning which is frequently associated with a NN as the value approximator. An overview and basic description of deep RL and deep Q-learning, in particular, can be found in [19]. The method achieves very good performance in human interaction problems, e.g. playing Atari or board games [20], and is so effective that computers can beat people in extremely complex games with many possible move combinations like Go or Chess [21].

The state of the art approach uses a built-in NN, which’s parameters are trained in the learning phase in order to predict the Q-values. However, this could lead to long training times until the NN predicts the expected Q-values of the Bellmann equation. Furthermore, large steps in the Q-value function might be difficult to approximate and many parameters of the NN would be needed. Another idea, which we want to propose in this paper, is to first train the Q-values by using the default Q-learning approach and store them in a table. Afterward, the learned table can be used to train a mathematical surrogate model. The inputs of the model are the state variables and the outputs are the Q-values for each action. With this approach, a larger variety of mathematical surrogate models can be used, e.g. k-nearest neighbors (KNN), since the data to be trained are already available. A combination of Q-learning and the KNN method was already described in [22, 23], where the authors applied this approach to the Mountain-Car control problem and the Cart-Pole balancing task.

### **Proposed RL Framework for an SHM Decision Process**

First, we describe the maintenance decision task as an MDP. Figure 1 shows the MDP of the SHM problem, where two kinds of states (*in service* and *out of service*) are present.

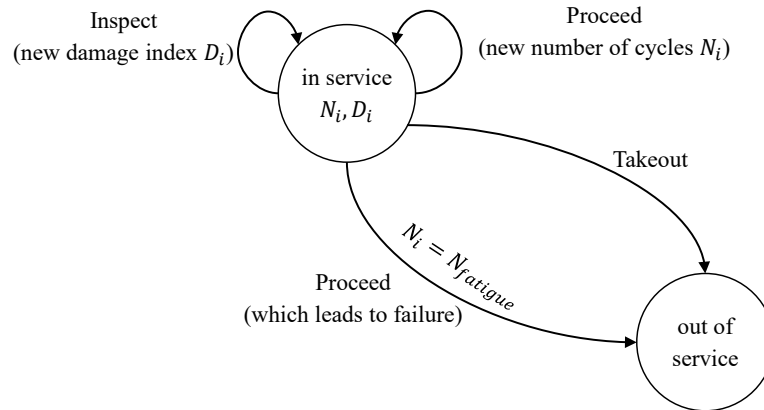


Figure 1: Markov decision problem for the maintenance decision task with crack length as the damage index.

A state  $S$  consists of two variables, the number of cycles  $N$  and the damage index  $D$ . A new state is entered if one or both variables change their values. However, two inspections in a row are not allowed, since this would not change the state and could lead to an infinite loop. In total, three actions are available to change the state:

- *Proceed*. The number of cycles increases by one. The agent does not get any new information about the damage index. Therefore, the last observed damage index stays the same.
- *Inspect*. The number of cycles stays the same, whereas the damage index gets updated by the current one, which corresponds to the current number of cycles.
- *Takeout*. The structure gets decommissioned and the episode ends.

Second, in order to use RL and to train an agent, we defined four different rewards:

- *Move*. The agent receives a positive reward for every proceed-action if the action does not lead to a structural failure. This aims to encourage the agent to use the structure as long as possible.
- *Maintenance*. The agent receives a negative reward for every usually costly inspection since the aim is to achieve a long life with a minimal number of inspections.
- *Fail*. The agent receives a large negative reward if the action leads to a structural failure.
- *Takeout*. The agent receives a mediocre reward, which is lower than the fail reward but larger than the maintenance reward.

Since the damage index is a float number, we have an infinite number of possible states. Moreover, we cannot assure that all states seen by the agent in the learning phase cover all states occurring in the operating phase. This is why we need a value approximator, where the inputs are the state variables (i.e. the number of cycles and the damage index) and the outputs are the Q-values for each action. In this paper, we compare the state of the art approach (built-in NN) with the proposed approach, where we first train the Q-values by using the default Q-learning approach and then train a mathematical surrogate model on it. For the latter, we use two different models, KNN and NN. Therefore, we compare three different models in total.

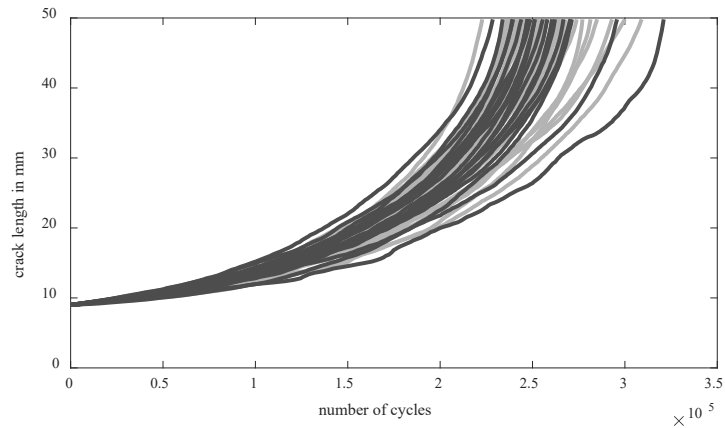


Figure 2: Crack propagation lines split up into a training (light gray) and a test set (dark gray).

The feasibility of using RL for a maintenance decision task is demonstrated by using a set of published crack propagation data [4], where the crack length serves as the damage index. This data is considered to resemble a degrading system. This might be in real-world applications for instance the number of repairs during an inspection. We assume that the overall damage of a structural system is degrading continuously, even if maintenance tasks are executed. Figure 2 shows the 68 crack propagation lines, which are split up into a training set (line 1-47) and a test set (line 48-68). The training set is used to learn the Q-values and to set the parameters of the mathematical surrogate models, whereas the test set is used to evaluate the models.

The number of layers and the number of neurons can be optimized using a hyperparameter optimizer. In this case, we used a fully connected NN with 128 neurons in the first and 64 neurons in the second hidden layer. The output layer has three nodes (one for each action Q-value). A 5-fold cross-validation within the training set led to an optimal KNN parameter at  $k = 250$ . The Q-values are randomly initialized between -5 and 0. For this study, we used the following rewards:  $R_{\text{move}} = 1$ ,  $R_{\text{maint}} = -5$ ,  $R_{\text{fail}} = -500$ ,  $R_{\text{takeout}} = -50$ . These rewards lead to a behavior, where the agent tries to maximize the usage time of the structure. These values could also be optimized, to get a certain behavior of the agent, e.g. most important is safety or a small number of inspections.

## Results

Table 1 shows the evaluation of the test lines 48, 59, and 68, which represent a slow, medium, and fast crack growth, respectively. The blue point indicates an inspection, whereas the red point represents the takeout. It can be seen that the agent with the built-in NN behaves quite statically. The RL model has learned to execute the takeout always at about 225,000 cycles. No inspection is done, neither for fast nor for slow crack growth. In contrast, the agent with the afterward trained NN executes many inspections beginning at about 235,000. This leads to longer usage but also many inspections. For a fast crack growth, the agent misses decommissioning the structure (see figure on the right bottom in Table 1). Also, the agent of the KNN model executes inspections. However, the first inspection is carried out a little earlier than for the NN model leading to no missed takeouts. If the crack length is rather long, the agent executes the takeout action. If the observed crack length is rather short, the agent proceeds some cycles until it inspects next.

Table 1: Comparison of the results.

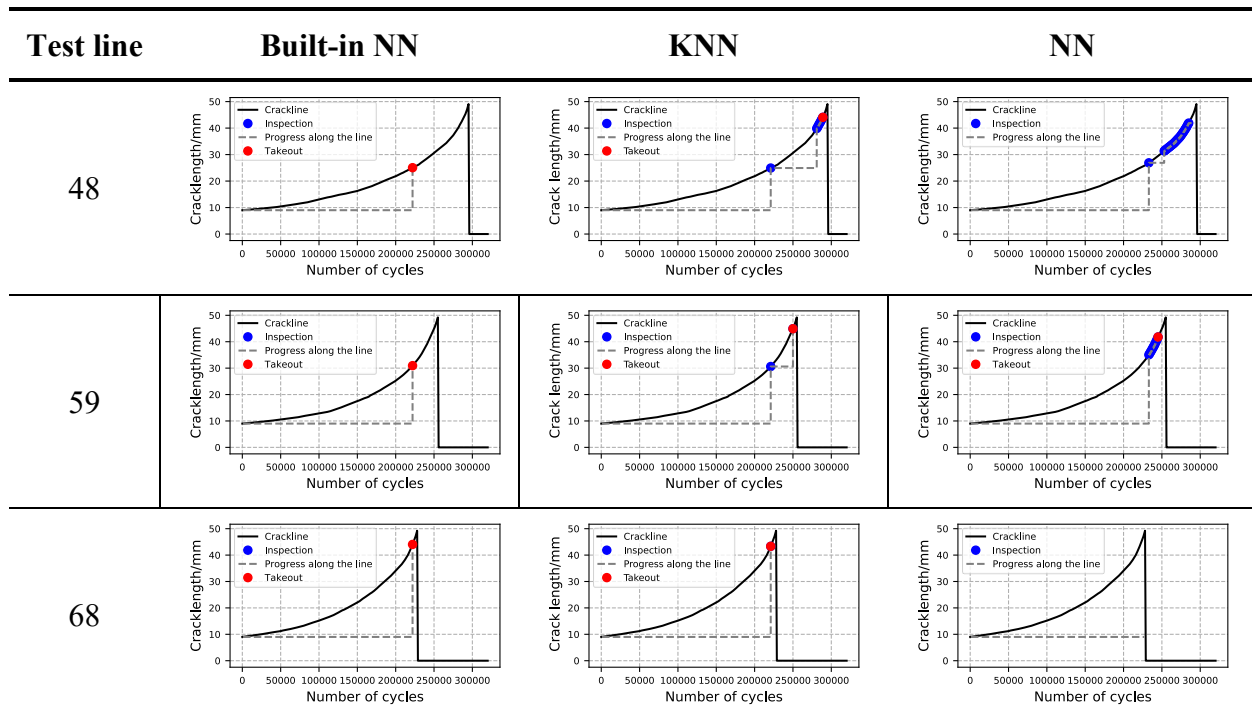


Table 2 compares the three approaches in terms of the number of inspections, the wasted remaining life cycles, and the number of fails evaluated on the test set. The best is if all three measures are zero. The behaviors of the different approaches explained before are consistent with Table 2. The values of the built-in NN show that, due to the lack of inspections, the agent wastes much RUL. The KNN model is better than the NN model since its values are lower in all three measures. This is due to the fact that the Q-values change rapidly at high numbers of cycles. This is a result of the high negative reward when missing the takeout. Apparently, the KNN model can handle this discontinuity better, since it is based on the trained neighbor values. For a regression model like NN, it is difficult to picture this behavior.

Table 2: Comparison of the three approaches evaluated on the test set.

Method	Number of inspections	Wasted RUL	Number of fails
Built-in NN	0	760,000	0
KNN	92	144,000	0
NN	320	153,000	4

### Discussion and Conclusion

The results show that it is possible to use RL to automate the maintenance planning of cyclically loaded parts. One advantage of using RL is that an agent can be trained even though it is not known how to optimally inspect the structure. Even if the trained model will not be applied for

instance due to safety laws, it can be a valuable insight of when to carry out inspections. However, the proposed study is a very simplified example of a real maintenance task. The assumption that a real structure behaves like a continuously degrading system might not be valid, since the structural system is repaired after an inspection. Moreover, a big problem could be data acquisition. Therefore, it would be an interesting task to work together with an aircraft operator to find out if the currently measured data can be used as an input for the proposed method.

Furthermore, the study reveals that using models other than the built-in NN can be beneficial, especially if the Q-values change rapidly. Additionally, the training phase which includes the reinforcement learning phase and the training of a mathematical surrogate model is shorter compared to the start of the art approach. However, the KNN model predicts the Q-values slower than the NN model, since distances to all neighbors have to be computed.

Overall, this work was able to show that Reinforcement Learning has a high potential in tasks like SHM.

## References

- [1] Subra Suresh, *Fatigue of Materials*, Second edition, Cambridge University Press, Cambridge, 1998.
- [2] Stephen J. Burns, *The Theory of Materials Failure*, by Richard M. Christensen, (56), 2015.
- [3] International Civil Aviation Organization (ICAO), *Airlines Operating costs and productivity*, Teheran, 2017.
- [4] D. A. Virkler, B. M. Hillberry, P. K. Goel, *The Statistical Nature of Fatigue Crack Propagation.*, *Journal of Engineering Materials and Technology* 101, 1979, pp. 148–153.
- [5] Mohammad M. AlDurgam, Salih O. Duffuaa, *Optimal joint maintenance and operation policies to maximise overall systems effectiveness*, *International Journal of Production Research* 51 (5), 2013, pp. 1319–1330. <https://doi.org/10.1080/00207543.2012.659351>
- [6] G. K. Chan, S. Asgarpoor, *Optimum maintenance policy with Markov processes*, *Electric Power Systems Research* 76 (6-7), 2006, pp. 452–456. <https://doi.org/10.1016/j.epsr.2005.09.010>
- [7] Francisco S. Melo, *Convergence of Q-learning: a simple proof*, Institute for Systems and Robotics, Lisboa, Portugal.
- [8] K. Zarrabi, W. W. Lu, A. K. Hellier, *An Artificial Neural Network Approach to Fatigue Crack Growth*, *AMR* 275, 2011, pp. 3–6. DOI: <https://doi.org/10.4028/www.scientific.net/AMR.275.3>
- [9] Hassaan Bin Younis, Khurram Kamal, Muhammad Fahad Sheikh, Amir Hamza, Tayyab Zafar, *Prediction of fatigue crack growth rate in aircraft aluminum alloys using radial basis function neural network*, *Archives of Computational Materials Science and Surface Engineering*, pp. 825–830. <https://doi.org/10.1109/ICACI.2018.8377568>
- [10] R. M. V. Pidaparti, M. J. Palakal, *Neural network approach to fatigue-crack-growth predictions under aircraft spectrum loadings*, *Journal of Aircraft* 32 (4), 1995, pp. 825–831. <https://doi.org/10.2514/3.46797>

- [11] J. R. Mohanty, B. B. Verma, D.R.K. Parhi, P. K. Ray, Application of artificial neural network for predicting fatigue crack propagation life of aluminum alloys, *Archives of Computational Materials Science and Surface Engineering* (1/3), 2009, pp. 133–138.
- [12] Wei Zhang, Zhangmin Bao, Shan Jiang, Jingjing He, An Artificial Neural Network-Based Algorithm for Evaluation of Fatigue Crack Propagation Considering Nonlinear Damage Accumulation, *Materials (Basel, Switzerland)* 9 (6), 2016. <https://doi.org/10.3390/ma9060483>
- [13] J. R. Mohanty, B. B. Verma, , P. K. Ray, D.R.K. Parhi, Prediction of mode-I overload-induced fatigue crack growth rates using neuro-fuzzy approach, *Expert Systems with Applications* 37 (4), 2010, pp. 3075–3087. <https://doi.org/10.1016/j.eswa.2009.09.022>
- [14] J.P.M. Smeulers, R. Zeelen, A. Bos, PROMIS - A generic PHM methodology applied to aircraft subsystems, 6-3153-6-3159. <https://doi.org/10.1109/AERO.2002.1036156>
- [15] A. Saxena, K. Goebel, PHM08 Challenge Data Set. NASA Ames Research Center, Moffett Field, CA, 2008, Available online at NASA Ames Prognostics Data Repository <http://ti.arc.nasa.gov/project/prognostic-data-repository>, checked on 7/19/2020.
- [16] Emmanuel Ramasso, Abhinav Saxena, Performance Benchmarking and Analysis of Prognostic Methods for CMAPSS Datasets, *International Journal of Prognostics and Health Management* (5), 2014.
- [17] Tianyi Wang, Jianbo Yu, David Siegel, Jay Lee, A similarity-based prognostics approach for Remaining Useful Life estimation of engineered systems, *International Conference on Prognostics and Health Management*, 2008, pp. 1–6. <https://doi.org/10.1109/PHM.2008.4711421>
- [18] Richard S. Sutton, Andrew G. Barto, Reinforcement learning. An introduction, MIT Press, Cambridge, 1998. <https://doi.org/10.1109/TNN.1998.712192>
- [19] Yuxi Li, Deep Reinforcement Learning: An Overview, 2018, arXiv-ID: 1701.07274v6 [cs.LG]
- [20] Volodymyr Mnih; Koray Kavukcuoglu, David Silver, Andrei A. Rusu, Joel Veness, Marc G. Bellemare et al., Human-level control through deep reinforcement learning (518), *Nature* (7540), 2015, pp. 529–533.
- [21] David Silver, Aja Huang, Chris J. Maddison, Arthur Guez, Laurent Sifre, George van den Driessche et al., Mastering the game of Go with deep neural networks and tree search, *Nature* 529 (7587), 2016, pp. 484–489. <https://doi.org/10.1038/nature16961>
- [22] José Antonio Martín H, Javier de Lope, Darío Maravall, The kNN-TD Reinforcement Learning Algorithm, J. Mira (Ed.): *Methods and models in artificial and natural computation. A homage to Professor Mira's scientific legacy International Work-Conference on the Interplay Between Natural and Artificial Computation, IWINAC 2009*, Santiago de Compostela, Spain, June 22-26, proceedings, part I. 1st ed. Berlin: Springer (Lecture notes in computer science, 5601), 2009, pp. 305–314.
- [23] José Antonio Martín H, Javier de Lope, Darío Maravall, Robust high performance reinforcement learning through weighted k-nearest neighbors, *Neurocomputing* 74 (8), 2011, pp. 1251–1259. <https://doi.org/10.1016/j.neucom.2010.07.027>

# Optimal Waiting Position of a Home Robot for Risk Communication Considering Behavior Patterns of an Occupant

Akira Mita<sup>1,a,\*</sup>, Keita Watanabe<sup>1,b</sup> and Ami Ogawa<sup>1,c</sup>

<sup>1</sup> Department of System Design Engineering, Keio University, 3-14-1 Hiyoshi, Kohoku, Yokohama 223-8522, Japan

<sup>a</sup>amita@keio.jp, <sup>b</sup>w-keita@keio.jp, <sup>c</sup>ami\_ogawa@keio.jp

**Keywords:** Home Robot, Personal Space, Walking Pattern, Risk Communication

**Abstract.** The risk communication in a home between a home robot and an occupant must be smooth in a way that the home robot does not disturb the occupant lives. In this paper, we propose a new method to determine the optimal waiting position considering the personal space and the obstacles such as furniture and the occupant's walking patterns. It is shown that the distance to the wall from the occupant in the direction of the home robot and the standing or sitting posture affect most on the personal space. Furthermore, this personal space is dependent on each individual preference. The performance of the proposed method is much more feasible compared with those obtained in our previous approach.

## Introduction

We observe a significant increase in the number of single person households in all generations. Our research group has proposed a new type of living system, called the “Biofied Building,” in which a home robot is implemented to support the physical and mental health of an occupant. It is one of the important roles for this “Biofied Building” that the danger or the risk of environmental health including the structural health has to be communicated with the occupant in an appropriate manner. The optimal waiting position of the home robot is one of the key factors to be implemented into the system.

The robot's activities including this risk communication must be conducted in a way that the robot does not disturb the occupant lives. In our previous studies ([1], [2]), the following simple two rules have been considered to determine the robot waiting position:

- 1) Keep the appropriate distance from obstacles and the occupant
- 2) Choose areas where the occupant walking frequency is low

However, the optimal waiting positions often cannot be determined because the whole walking history should be reflected in the potential field to determine the waiting positions. Furthermore, the appropriate distance from an occupant is typically determined on a trial and error basis and the effects of individual and environmental differences are not considered.

A method to determine the optimal position and distance is determined in this paper for smooth communication between an occupant and a home robot considering personal space and environmental factors. Furthermore, we propose a new method to use a repulsive potential field based on the probability of choosing the next walking path, which is predicted based on the occupant's current position, instead of using the occupant's whole walking history. We first extracted the factors that affect the personal space for communication based on experiments. As a result, we reveal that the distance to the wall behind the robot and the occupant posture

(standing/sitting) affect the interaction distance. Thus, the personal space descriptions can be generalized using these two factors.

A series of experiments were conducted to show the validity and versatility of the proposed method. The proposed method could reliably estimate appropriate waiting positions of a home robot while avoiding collision.

### Proposed method

The optimal waiting position of a home robot is determined considering the following two areas.

- 1) The area where the occupant can comfortably communicate with the home robot. This area is determined considering a personal space that is defined for each individual and walking paths. This favorable area is modeled by an attractive potential. The potential values are dependent on the probability of the occupant walking patterns.
- 2) The area where the robot is not able to access due to the obstacles such as furniture and the occupant, and the area where the access of the robot is not allowed. The prohibited areas include bathrooms and closets. This inaccessibility is modeled by a repulsive potential. The potential values are dependent on the distance to the obstacles.

We employed the personal space defined by the model proposed in the reference [3]. The size of this area is dependent on the individual preferences, the environments and the other conditions. This space is thus person-dependent. When the personal space is determined, the attractive area is defined by the area close to the boundary of the personal space. This attractive area is assumed to be only available in front of the occupant as described by a blue colored area in Fig. 1. In the figure, the occupant is depicted by a simple symbol described in Fig. 2.

To calculate the repulsive potential, we need to know the position of furniture, the area where robot is not able to approach and the occupant walking patterns. The position of furniture and the area will be pre-assigned. Thus, the important process for us is to predict the occupant walking patterns. We employed a random walk model to represent the walking patterns that allows the occupant move into forward, right, backward and left with a certain probability. In our simulation, we assume that the probability to move to the destination at each step is 60%, 65%, or 70%. A simulation example is shown in Fig. 3.

The flowchart of estimating the optimal waiting position for a home robot is presented in Fig. 4. The lower the potential field, the more suitable the home robot will be. The total potential is represented by the repulsive potential minus the attractive potential.

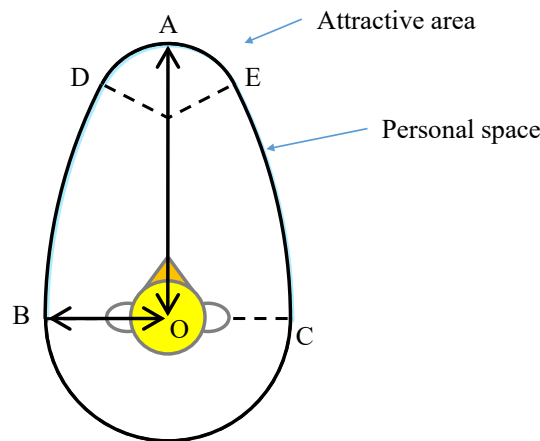


Figure 1 Definition of personal space<sup>[3]</sup> and attractive area

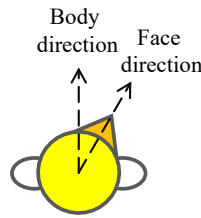


Figure 2 An occupant illustration showing the body and face directions

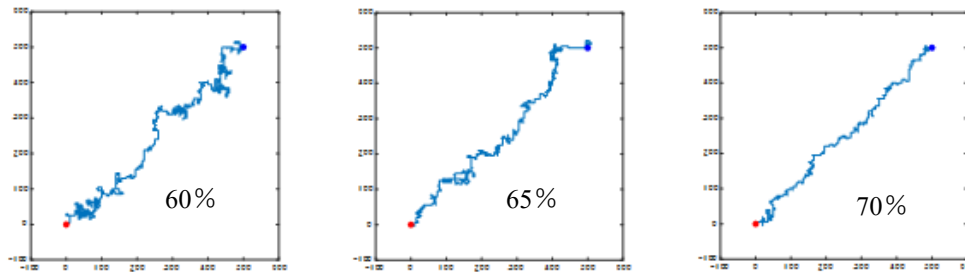


Figure 3 Simulated occupant walk using random walk with higher weights to the destination

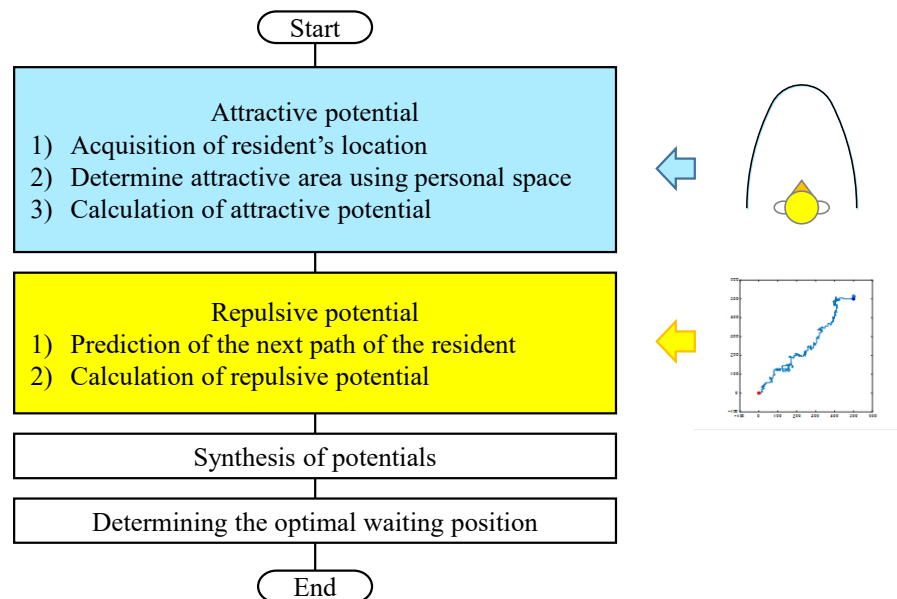


Figure 4 Flowchart of determining optimal waiting position for a home robot

**Experimental evaluation of personal space and attractive area**

The size of the personal space is dependent on several parameters. To identify the key parameters for our home robot, a series of experiments were conducted. The specifications of our prototype home robot are depicted in Table 1. The photo of the robot is shown in Fig. 5. The

experimental setup is presented in Fig. 6. The parameters considered in the experiments are posture, sex, height of the subjects. In addition, among a subject’s life patterns, if he or she was living with a pet or not was also considered. For a home robot, approach direction of front and side was considered. The distance between the occupant and the wall was also considered as shown in Fig. 6.

The total number of the subjects is 19, 13 males and 6 females of low twenties. It turned out that the most dominant parameters are posture (sit or standing) and the distance to the wall. The width of the attractive area around the personal space was set +30 cm and –30 cm determined from the standard deviation as represented by the blue area in Fig. 1.

*Table 1 Specification of the robot used for experiments*

Items	Values
Size (mm)	396(W)×320(D)×540(H)
Wheel diameter (mm)	150
Maximum speed (ms)	5.0
Micro-controller	Mbed LPC1768
Longest running time (hours)	3.5
Motor-wheel connection	Pulleys and belts



*Figure 5 Prototype home robot e-bio Tβ v2*

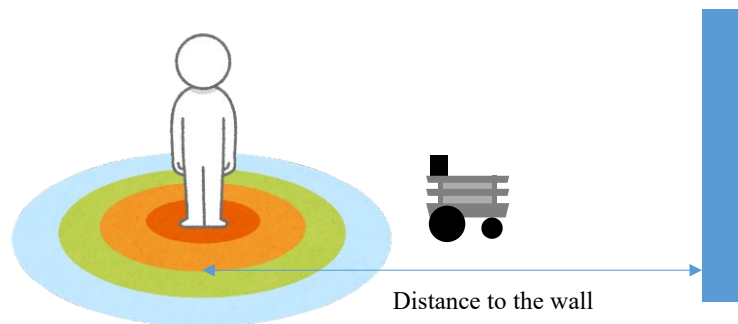


*Figure 6 Experimental setup for evaluating factors affecting personal distance*

### Simulation of optimal waiting positions

A simulation was conducted for the room depicted by Fig. 7. Kitchen, bath rooms and walk-in closet are the areas where the home robot can not approach. This room is chosen from the database CASAS (Center for Advanced Studies in Adaptive Systems)<sup>[4],[5]</sup> in which the life patterns for the duration of two months are recorded. Using the recorded patterns, the probability of the next walking direction was predicted using a Markov model. To consider the variation, the random walk depicted by Fig. 3 were employed.

In Fig. 8, an example is shown. The left result is based on the conventional method<sup>[4]</sup> where all the walking patterns are included to determine the repulsive potential and no attractive potential is considered. The right result is based on the proposed method. Two red areas indicate the optimal waiting positions suggested by the current method. It is clearly shown that the wider and more appropriate waiting area is available using the proposed method.

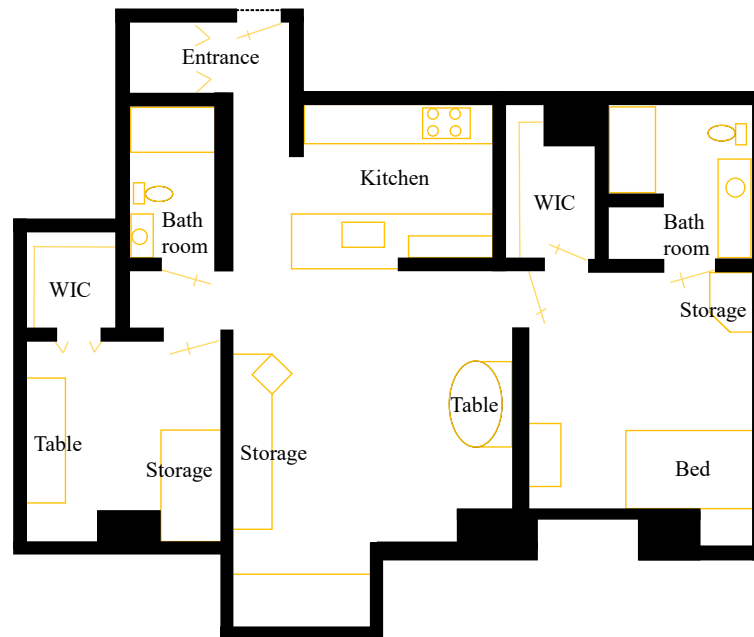


Figure 7 Floor plan of the house used for simulation

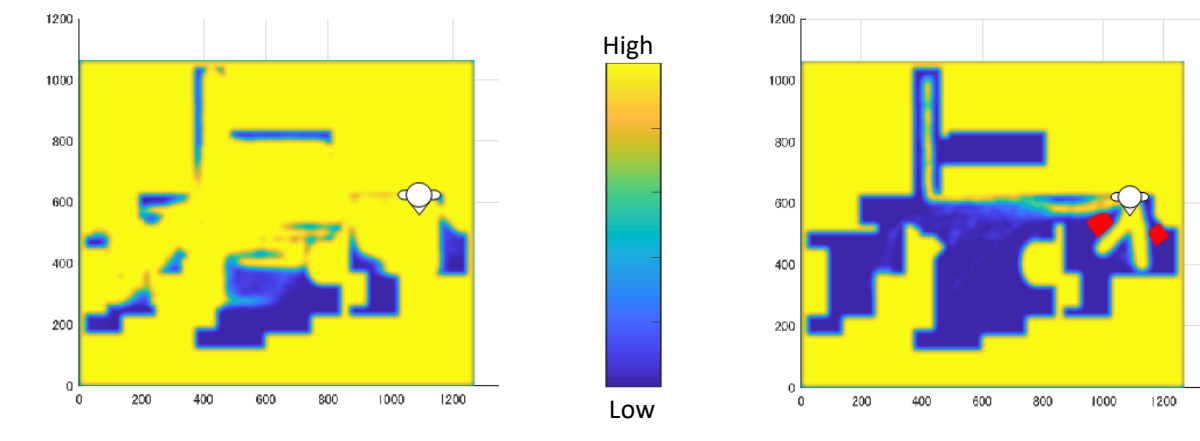


Figure 8 Potential map using a conventional method (left) and the proposed method (right)

### Concluding remarks

A significant increase is observed in the number of single person households in all generations in Japan. We have been working on preventing the danger or the risk of environmental health including the structural health has to be communicated with the occupant in an appropriate manner. This research is aimed at planning the optimal waiting position of the home robot for communicating with the occupant.

The optimal waiting position was determined in such a way that the robot will be in the favorable area with respect to the occupant's personal space and does not interfere with the obstacles. The furniture and the walking paths of the occupant are the most important obstacles to be considered. In our previous studies, we only considered the obstacles and did not include the personal space to decide the optimal position. In addition, the occupant's walking patterns were described by a probability distribution using all walking histories. Thus, it took a lot of time and data to decide the positions. In this study, the prediction of walking path is implemented using a Markov model based on the available walking patterns recorded by the time of prediction. In this paper, simulations were based on the data provided by the CASAS database. It was shown that the performance of the proposed method was much more feasible and flexible than those obtained using our previous approach.

### Acknowledgements

This research was partially supported by a grant from the Japan Society for the Promotion of Science (JSPS KAKENHI 18H00968).

### References

- [1] Iida, M., Mita, A.: A Study on Chasing Algorithm and Walking Parameters Acquisition using Home Robot, *AIJ Journal of Technology and Design*, Vol. 22, No. 50, pp. 253-257, 2016.2 (in Japanese). <https://doi.org/10.3130/aijt.22.253>
- [2] Kimura, T., Ogawa, A., Mita, A.: Path Planning in Residential Space of Home Robot Incorporating Waiting Behavior, *AIJ Journal of Technology and Design*, Vol. 26, No. 62, pp. 407-411, 2020.2 (in Japanese). <https://doi.org/10.3130/aijt.26.407>
- [3] Liu, C.H., Ooeda, Y., Sumi, T.: A Model for Pedestrian Movement with Obstacle Evasion using Personal Space Concept, *Journal of Japan Society of Civil Engineers D*, Vol. 64, No. 4, pp. 513-524, 2008 (in Japanese). <https://doi.org/10.2208/jscejd.64.513>
- [4] Cook, D.J., Crandall, A.S., Thomas, B.L. and Krishnan, N.C.: CASAS: A smart home in a box. *Computer*, Vol. 46, No. 7, pp. 62-69, 2012. <https://doi.org/10.1109/MC.2012.328>
- [5] Washington State University, CASAS: Center of Advanced Studies in Adaptive System. <http://casas.wsu.edu/datasets/> (accessed 07/08/2020).

# Preventing Deterioration of Active Vibration Control Effect Due to Aging Deterioration and Damage based on Deep Learning

Miao Cao<sup>1,a,\*</sup>, Songtao Xue<sup>2,b</sup>

<sup>1</sup> Lect., Department of Architecture, Tohoku Institute of Technology, Japan

<sup>2</sup> Prof., Department of Architecture, Tohoku Institute of Technology, Japan  
Prof., Department of Disaster Mitigation for Structures, Tongji University, China

<sup>a</sup>caomiao@tohotech.ac.jp, <sup>b</sup>xuest@tohotech.ac.jp

**Keywords:** Preventing Deterioration, Active Vibration Control, Deep Learning, Convolutional Neural Network, H<sup>∞</sup> Control

**Abstract.** When designing a building's active vibration control, it is necessary to properly evaluate the effect on the control effect caused by changes in vibration characteristics due to aging deterioration and damage. However, although the previous designs have certain robustness against changes in vibration characteristics, they have insufficient on these control effect. In this paper, we establish a method based on deep learning to identify changes in vibration characteristics. Using this method, we can achieve to prevent reduction of the active control effect.

## Introduction

In Japan, many buildings built after the period of high economic growth have already been shaken by numerous earthquakes, have become damaged and deteriorated, and are now under pressure to be repaired or renewed. Changes in vibration characteristics due to aging deterioration and damage have adverse effects on seismic-resistant buildings and seismic controlled buildings.

In particular, in the case of active control, control is tuned based on the state equation, which includes the vibration characteristics of the structure. Therefore, when aged deterioration or damage occurs, the state equation and the actual situation are inconsistent, which leads to a reduction in control effect.

To prevent such a reduction in control effect, we must identify the vibration characteristics of the structure and reflect them in the equation of state. However, some reports show that the mainstream identification methods have the following problems: The identification accuracy of damping, which has a significant effect on active control, is unstable and varies

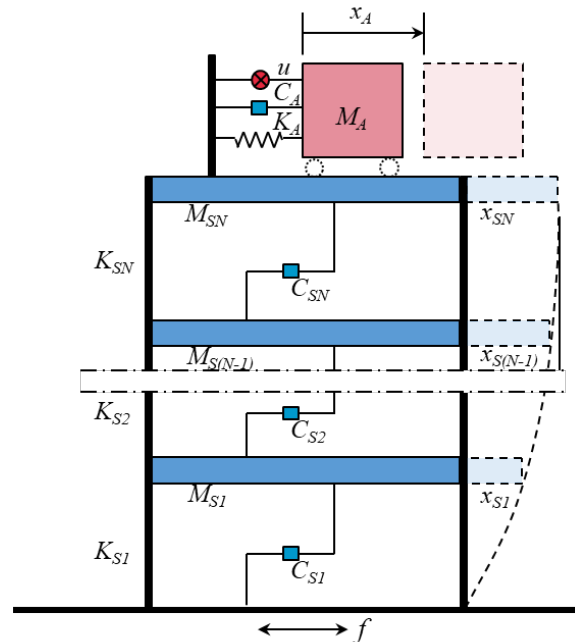


Figure 1 Analytical model of a MDF structure

widely [1], [2]. At present, although we can use a passive control device such as an oil damper jointly [3] to prevent the reduction of the control effect due to such unexpected changes in vibration characteristics, a fundamental solution has not been achieved.

In this paper, we establish a method based on deep learning to identify changes in vibration characteristics due to aging deterioration and damage. Using this method, we can achieve to prevent reduction of the active control effect.

### Mathematical Model

Figure 1 shows an analytical model of a multi-degree-of-freedom structure with active vibration control devices. The equation of motion corresponding to Fig. 1 is expressed by Eq. 1.

$$\begin{bmatrix} M_A & 0 \\ 0 & M_S \end{bmatrix} \begin{Bmatrix} \ddot{x}_A \\ \ddot{x}_S \end{Bmatrix} + \begin{bmatrix} C_A & -C_A \\ -C_A & C_A + C_S \end{bmatrix} \begin{Bmatrix} \dot{x}_A \\ \dot{x}_S \end{Bmatrix} + \begin{bmatrix} K_A & -K_A \\ -K_A & K_A + C_S \end{bmatrix} \begin{Bmatrix} x_A \\ x_S \end{Bmatrix} = \begin{Bmatrix} f_A \\ f_S \end{Bmatrix} + \begin{Bmatrix} -u \\ u \end{Bmatrix} \quad (1)$$

$M_S$ ,  $C_S$ , and  $K_S$  are symmetric matrices of  $N \times N$  used to represent mass, damping coefficient, and stiffness coefficient. We convert the equation of motion into a state-space equation as Eq. 2. Simultaneously, considering the versatility, we choose an electromagnetic force linear actuator as the active vibration control device. Therefore, the control force  $u$  of the device is expressed by Eq. 3, where  $I$  is the control current, and  $\gamma$ ,  $\sigma$  are the actuator coefficient.

$$M\ddot{x} + C\dot{x} + Kx = Ff + Uu \quad (2)$$

$$u = \frac{\sigma}{\gamma} I + \frac{1}{\gamma} \dot{I} \quad (3)$$

The state-space representation of our system is in the following equation.

$$\begin{cases} \dot{X} = AX + B_1 f + B_2 u \\ Y = C_1 X + D_{12} u \end{cases} \quad (4)$$

where

$$X = \{x_{S1}, x_{S2}, \dots, x_{SN}, \dot{x}_A, x_{S1}, x_{S2}, \dots, x_{SN}, x_A, I\}^T \quad (5)$$

$$A = \begin{bmatrix} -M^{-1}C & -M^{-1}K & 0_{N+1,1} \\ I_{N+1,N+1} & 0_{N+1,N+1} & 0_{N+1,1} \\ 0_{1,N+1} & 0_{1,N+1} & -\sigma \end{bmatrix} \quad (6)$$

$$B_1 = \begin{bmatrix} M^{-1}F \\ 0_{N+2,N+1} \end{bmatrix} \quad (7)$$

$$B_2 = \begin{bmatrix} M^{-1}U \\ 0_{N+1,1} \\ \gamma \end{bmatrix} \quad (8)$$

$C_1$  and  $D_{12}$  are observation matrixes with  $2N + 3$  rows and  $n$  columns ( $n$  is the number of observations). We show the above relationship in the block diagram of state feedback control, as Fig. 2.

According to the  $H_\infty$  control theory, we assume that the feedback control law conforms to the following equation [4].

$$u = -\Sigma^{-1}\Theta X \quad (9)$$

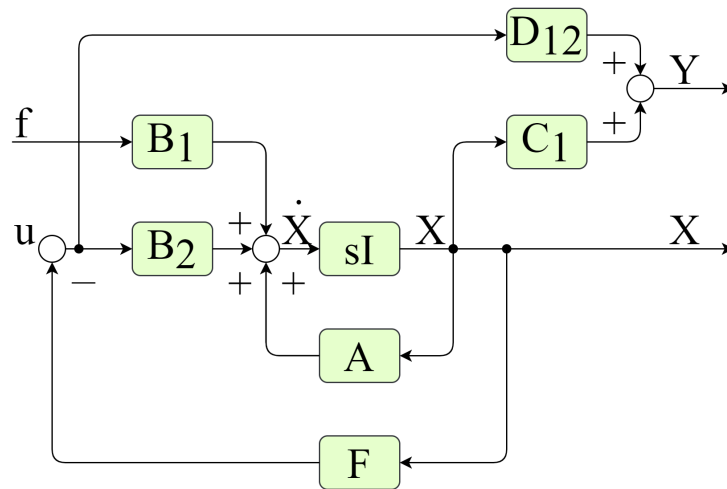


Figure 2 Block diagram of state feedback control

where

$$\left. \begin{aligned} \Sigma &= D_{12}^T D_{12} \\ \Sigma &= D_{12}^T C_1 + B_2^T P \end{aligned} \right\} \quad (10)$$

We can calculate  $P$  by solving the following Riccati equation to obtain the optimal feedback control law.

$$R^T P + PR - PSP + Q = 0 \quad (11)$$

where

$$\left. \begin{aligned} R &= A - B_2 \Sigma^{-1} D_{12}^T C_1 \\ S &= B_1 B_1^T - B_2 \Sigma^{-1} B_2^T \\ Q &= C_1^T C_1 - C_1^T D_{12} \Sigma^{-1} D_{12}^T C_1 \end{aligned} \right\} \quad (12)$$

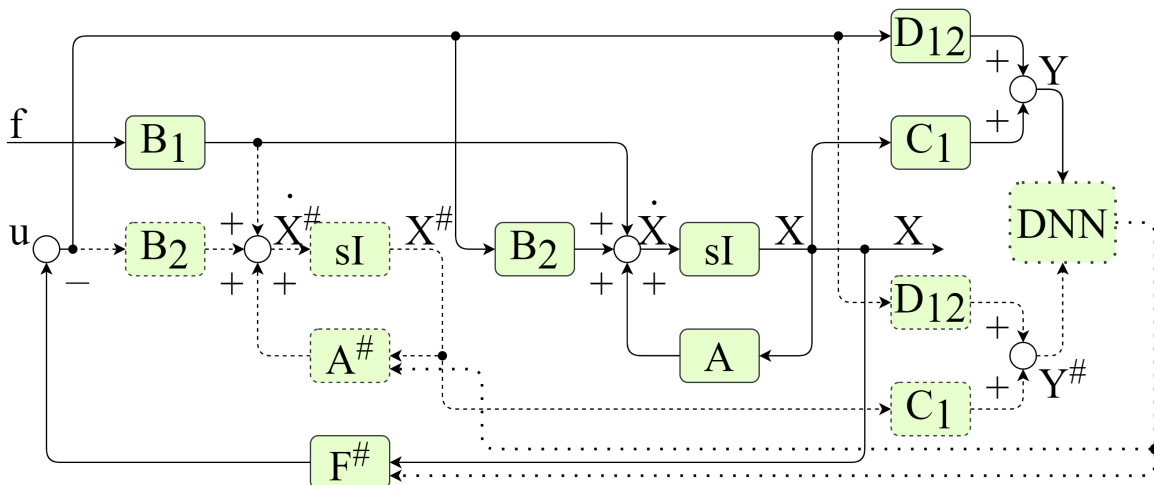


Figure 3 Block diagram of state feedback control based on deep learning when vibration characteristics changed

This optimal feedback control law can play a significant role when the vibration characteristics of the structure we obtain are accurate. However, if the vibration characteristics change due to aging degradation or damage over time, the control status will be shown by the solid line in Fig. 3.

Here, the index # in the symbol means the vibration characteristics before the change. In this status, we calculate the control force  $u$  through an inaccurate feedback control law. Therefore, the control effect we get is not optimal, and may even have the opposite effect.

Although we can use some methods such as the Kalman filter, it requires the assumption that error information is known in advance, the accuracy of identification is not impeccable in this situation. Therefore, we try to use deep learning to identify accurate vibration characteristics. As shown in Figure 3, we compare the output before and after the change and input them into a convolutional neural network(CNN) shown in Fig. 4.

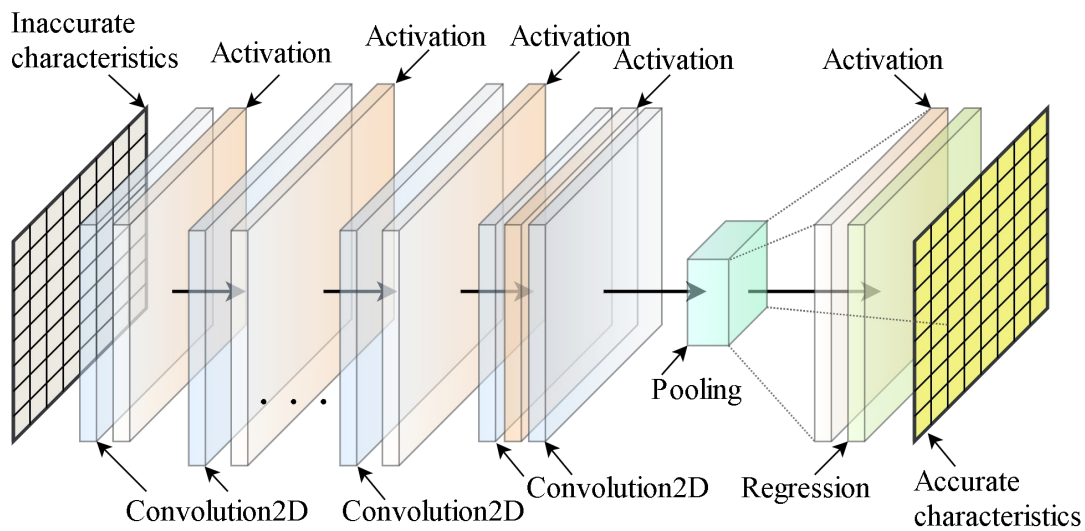


Figure 4 CNN architecture for identifying vibration characteristics

We use unsupervised learning<sup>[5]</sup> to adjust the parameter in the neural network. The regression losses function is shown in Eq. 13.

$$L(x) = \sqrt{\frac{1}{L} \sum_{i=1}^L \{Y[\varphi(x)]^\# - Y\}^2} \tag{13}$$

where  $L$  is the input ground motion duration and  $\varphi$  is the output function of the CNN. We can also use Eq. 14 to calculate the half mean square error between the result of the CNN and the accurate characteristics to evaluate the learning effect after training.

$$E(x) = \frac{1}{2} \sum \sum \{\varphi(x) - \Phi\}^2 \tag{14}$$

where  $\Phi$  are the accurate value of vibration characteristics changed due to degradation and damage.

### Numerical study

We use a multi-degree-of-freedom structure simulation to confirm the effect of the proposed method. The structural characteristics of the model are shown in Table 1.

We use the Rayleigh damping shown in Eq. 15 as the damping coefficient of the structure. The damping coefficient of the AMD is set to the optimum damping, according to Eq 16.

*Table 1 Structural characteristics of model*

Story	Mass[kg]	Stiffness[N/m]	Damping
1	2000	250000	Rayleigh Damping, $h_1=0.02,$ $h_2=0.02$
2	2000	250000	
3	2000	250000	
4	2000	250000	
AMD	320	62500	Optimal tuning

$$\left. \begin{aligned} [C] &= a_0[M] + a_1[K] \\ a_0 &= 2 \cdot \frac{h_1 \omega_2 - h_2 \omega_1}{\omega_2^2 - \omega_1^2} \\ a_1 &= 2(h_2 \omega_2 - h_1 \omega_1) / (\omega_2^2 - \omega_1^2) \end{aligned} \right\} \quad (15)$$

where  $\omega$  is the natural circular frequency of the structure.

$$h_{opt} = \sqrt{\frac{3\mu}{8(1+\mu)}} \quad (16)$$

where  $\mu$  is the mass ratio of the AMD and the structure.

We generate an artificial seismic wave by the non-stationary Kanai-Tajimi model<sup>[6]</sup> shown in Eq. 17 as the input ground motion.

$$G(\omega) = \frac{1+4\eta^2(\frac{\omega}{\omega_g})^2}{(1-\frac{\omega^2}{\omega_g^2})^2+4\eta^2(\frac{\omega}{\omega_g})^2} G_0 \quad (16)$$

where  $\omega_p$  is the unique peak of the spectrum, here is 0.5,  $\eta$  is the sharpness of the peak, and  $G_0$  is the constant power spectral intensity of the excitation. Fig. 5 shows the Fourier spectrum and the acceleration record of the input ground motion.

The dynamic response of the 4<sup>th</sup> story with and without the AMD is shown in Fig. 6. We have confirmed that the effect of the AMD is very significant from Fig. 6. Nevertheless, when the structural characteristics change, the AMD control effect will become shown in Fig. 7. According to the conclusions of references [7] and [8], we can know that the structure's stiffness reduction factor can reach 0.5 or less after a big earthquake. Therefore, we assume the stiffness reduction factor of the whole model to be 0.5. Comparing Fig. 6 and Fig. 7, we find that the dynamic response becomes large. That is because the structure's first natural frequency is closer to the input ground motion's dominant frequency. Although we expect the AMD to provide a vibration reduction effect, the AMD makes the structure's response larger. In other words, the AMD, which can reduce vibration, brings a harmful effect on the structure after vibration characteristics changed. Consequently, when aged deterioration and damage occurs, it leads to a reduction of the control effect.

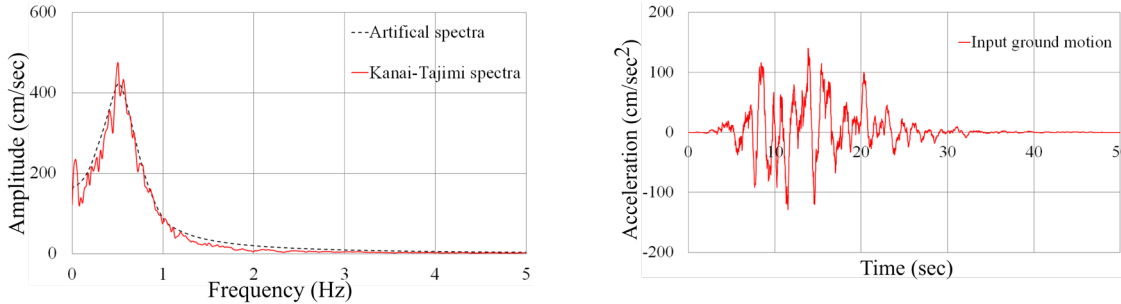


Figure 5 Input ground motion, (left) Fourier spectrum, (right) Acceleration records

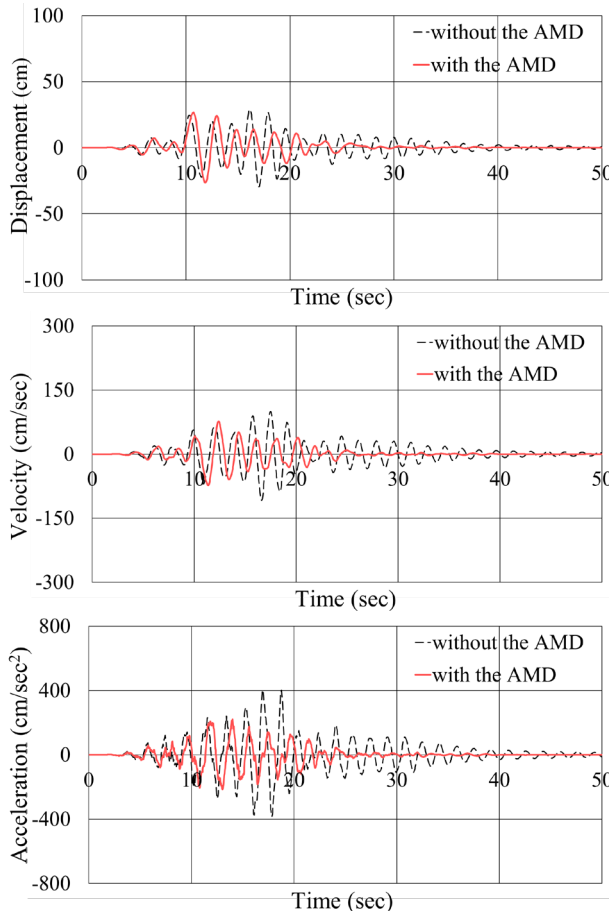


Figure 6 Dynamic response before vibration characteristics changed

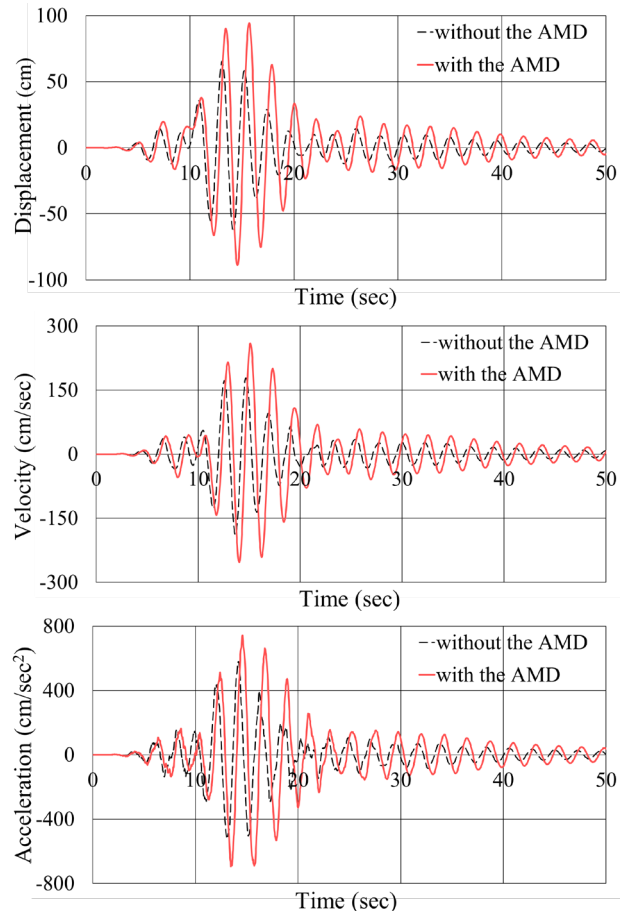


Figure 7 Dynamic response after vibration characteristics changed

We create a convolutional neural network, whose architecture is shown in Table 2, and train it to estimate the accurate value of vibration characteristics. Fig. 8 shows the training regression loss of dynamic response and the heteroscedasticity-adjusted mean squared error (HMSE) of vibration characteristics. We stop the training after 2000 epochs because the results are excellent.

The dynamic response of the 4<sup>th</sup> story with and without the AMD after training is shown in Fig. 9. Comparing with Fig. 7, the control effect of the AMD has increased significantly. Comparing the optimal results of the AMD when using reduced vibration characteristics as the original parameter, we find that the two results are precisely the same. It proves that we can maintain the optimal control effect by using our method even if the structure's vibration characteristics are changed.

*Table 2 Architecture of the CNN*

Layer	Type	Activations	Learnable Parameters	Total Learnable Parameters
1	Input	$5 \times 1 \times 1$	-	0
2	Convolution	$5 \times 1 \times 16$	Weights $3 \times 1 \times 1 \times 16$ Bias $1 \times 1 \times 16$	64
3	Tanh	$5 \times 1 \times 16$	-	0
4	Convolution	$5 \times 1 \times 32$	Weights $3 \times 1 \times 16 \times 32$ Bias $1 \times 1 \times 32$	1568
5	Tanh	$5 \times 1 \times 32$	-	0
6	Convolution	$5 \times 1 \times 64$	Weights $3 \times 1 \times 32 \times 64$ Bias $1 \times 1 \times 64$	6208
7	Tanh	$5 \times 1 \times 64$	-	0
8	Convolution	$5 \times 1 \times 32$	Weights $3 \times 1 \times 64 \times 32$ Bias $1 \times 1 \times 32$	6176
9	Tanh	$5 \times 1 \times 32$	-	0
10	Convolution	$5 \times 1 \times 16$	Weights $3 \times 1 \times 32 \times 16$ Bias $1 \times 1 \times 16$	1552
11	Tanh	$5 \times 1 \times 16$	-	0
12	Convolution	$5 \times 1 \times 4$	Weights $3 \times 1 \times 16 \times 4$ Bias $1 \times 1 \times 4$	196
13	Tanh	$5 \times 1 \times 4$	-	0
14	Convolution	$5 \times 1 \times 1$	Weights $3 \times 1 \times 4$ Bias $1 \times 1$	13
15	Tanh	$5 \times 1 \times 1$	-	0
16	Regression		-	0

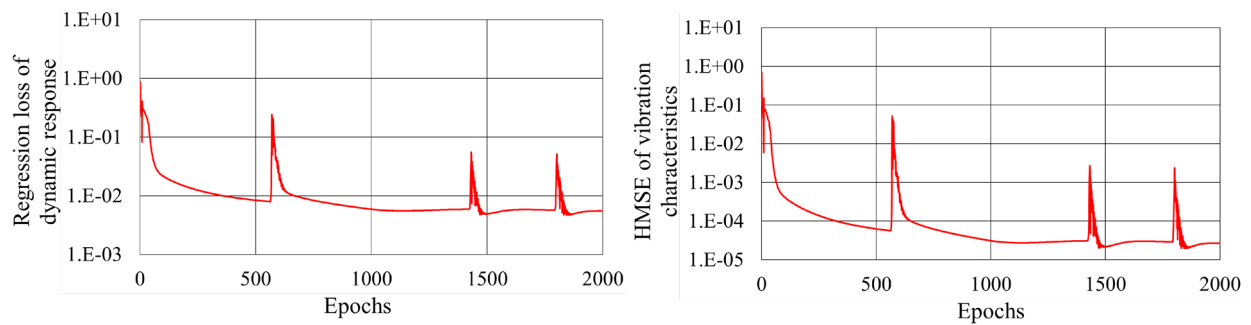


*Figure 8 Training regression loss and the HMSE*

**Summary**

We discussed the changes in the state-space representation of a structure-AMD system before and after the vibration characteristics change due to aging deterioration and damage. After the vibration characteristics change, the AMD, which was tuned to the optimal control by us, will deteriorate the active control effect.

We established a method using the convolutional neural network to identify the accurate characteristics after the change and compared the control effect before and after. Using our method, we successfully achieved the goal of maintaining the control effect.

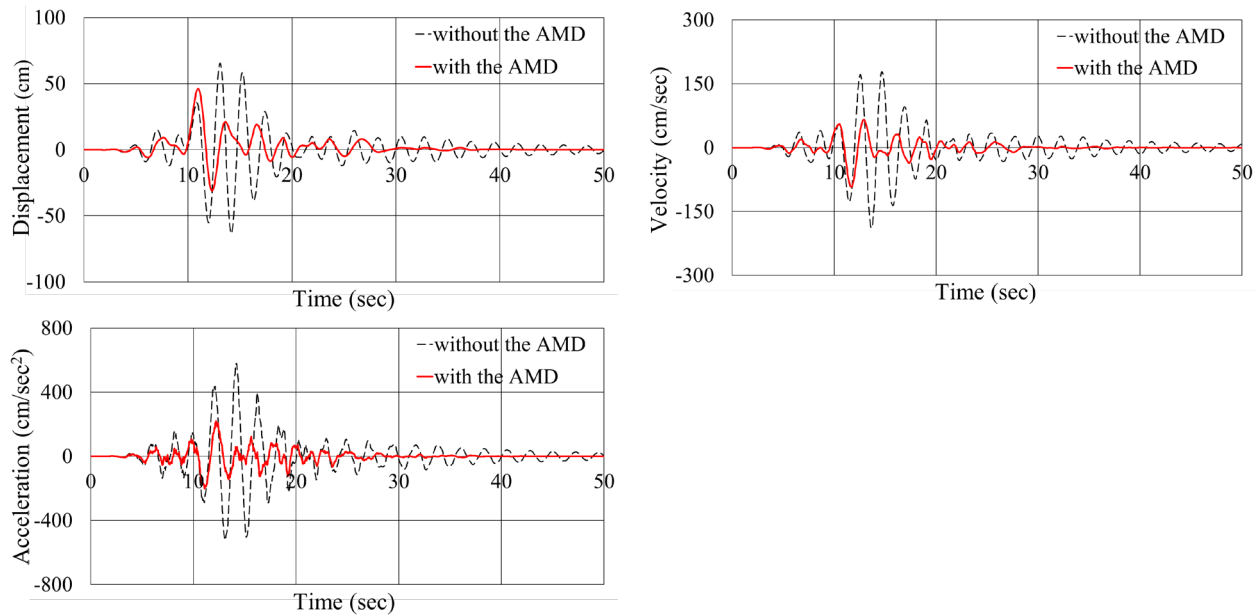


*Figure 9 Dynamic response after training*

## References

- [1] Architectural Institute of Japan, *Intelligible Guide to Structural Control*, first ed., Maruzen, Tokyo, 2014
- [2] Tomohiro MAEDA, Shinta YOSHITOMI and Izuru TAKEWAKI, Stiffness-damping identification of buildings using limited earthquake records and ARX model, *J. Struct. Constr. Eng., AIJ*, Vol. 76, No.666, 2011, pp. 1415-1423. <https://doi.org/10.3130/aijs.76.1415>
- [3] Hayabe Yasuhiro, Inoue Tetsushiro, Maseki Ryota, Nagashima Ichiro, Ochiai Hiroshi and Saito Kenji, The wind-induced response control by oil dampers and active mass damper: (Part 1) Response control systems and evaluation of wind-induced response performance, *Summaries of technical papers of annual meeting, AIJ*, 2004, pp. 71-72
- [4] Peter Dorato, Luigi Fortuna and G. Muscato, *Robust Control for Unstructured Perturbations: An Introduction*, Springer Verlag, 1992. <https://doi.org/10.1007/BFb0039551>
- [5] Diederik P. Kingma and Jimmy Lei Ba, Adam: A method for stochastic optimization, the 3rd International Conference for Learning Representations, San Diego, 2015
- [6] F. R. Rofooei, Aghababaii Mobarake, G. Ahmadi, Generation of artificial earthquake records with a nonstationary Kanai–Tajimi model, *Engineering Structures*, Vol. 23, Issue 7, 2001, pp. 827-837. [https://doi.org/10.1016/S0141-0296\(00\)00093-6](https://doi.org/10.1016/S0141-0296(00)00093-6)
- [7] Miao CAO, Masato MOTOSAKA, Tsoggerl TSAMBA and Kazushi YOSHIDA, Simulation analysis of a damaged 9-story SRC building during the 2011 Great East Japan Earthquake, *Journal of Japan Association for Earthquake Engineering*, Vol.13, No.2,2013, pp. 45-64. [https://doi.org/10.5610/jae.13.2\\_45](https://doi.org/10.5610/jae.13.2_45)
- [8] IYAMA Kahori, KURITA Satoshi, MOTOSAKA Masato, CHIBA Kazuki, HIRAMATSU Hiroki and MITSUJI Kazuya, Modal Identification of a Heavily Damaged 9-story SRC Building by Ambient Vibration Measurements, Vol.13, No.2, 2013, pp. 225-242

# Evaluation of Measurement Accuracy of the MEMS Accelerometer for Long Period and Large Amplitude Vibration

Kenta Hirai<sup>1, a, \*</sup>, Hiroaki Harada<sup>1, b</sup>, Hirotaka Imaeda<sup>1, c</sup>, Akira Mita<sup>2, d</sup>  
Takeshi Suzuki<sup>3, e</sup>, Hironobu Yao<sup>3, f</sup>, Shinji Kitagawa<sup>3, g</sup>  
Minoru Kakinuma<sup>3, h</sup>, Yoshiyuki Komiya<sup>4, i</sup>

<sup>1</sup>Structural Engineering Section, NIKKEN SEKKEI LTD, Tokyo, Japan

<sup>2</sup>Keio University, Kanagawa, Japan

<sup>3</sup>Fuji Electric Co., LTD, Tokyo, Japan

<sup>4</sup>Hakusan Corporation, Tokyo, Japan

<sup>a</sup>hirai.kenta@nikken.jp, <sup>b</sup>haradah@nikken.jp, <sup>c</sup>imaedah@nikken.jp, <sup>d</sup>mita@keio.jp

<sup>e</sup>suzuki-takeshi@fujielectric.com, <sup>f</sup>yao-hironobu@fujielectric.com, <sup>g</sup>kitagawa-shinji@fujielectric.com

<sup>h</sup>kakinuma-minoru@fujielectric.com, <sup>i</sup>yoshiyuki.komiya@hakusan.co.jp

**Keywords:** MEMS Accelerometer, Monitoring System, Measurement Accuracy

**Abstract.** Health monitoring systems are used to assess building damage immediately after an earthquake and have become widely utilized in Japan. For example, the system developed by the authors has been installed in more than 60 buildings since 2014. Such systems mostly rely on accelerometers to estimate the building performance. Recently, Micro electro mechanical system (MEMS) accelerometers have been increasingly applied for such uses due to their economic advantages. However, MEMS accelerometers are known to have relatively low measurement accuracy for certain frequency band excitations compared to servo type accelerometers. Past research has been undertaken to test their measurement accuracy, however, few studies review their performance under long period and large amplitude seismic motions. Evaluation of measurement accuracy in such conditions is essential since the system is also installed in tall buildings and isolated buildings with relatively long natural periods. Therefore, this study evaluates the measurement accuracy of the MEMS accelerometer under long period and large amplitude vibration based on the results of shake table testing.

## Introduction

In recent years large earthquakes have occurred relatively often in Japan, and many more people are interested in building safety. From a Business Continuity Plan (BCP) perspective, the monitoring system have been widely utilized to help assess damage immediately after an earthquake. The authors developed a health monitoring system using accelerometers in 2014. This system has been installed in more than 60 buildings and the validity of the system has been verified (Ishizaki, Imaeda, Harada, Shinohara, 2018).

The monitoring system is also installed in high-rise buildings and isolated buildings with relatively long natural periods. In this condition, the accuracy of accelerometer measurement for long period and large amplitude vibrations is important. Recently, Micro electro mechanical system (MEMS) accelerometers have been increasingly applied for monitoring systems due to their economic advantages. However, MEMS accelerometers are known to have relatively low measurement accuracy for certain frequency band excitations compared to servo type accelerometers. Although past research has been undertaken to test the measurement accuracy of

MEMS accelerometers, few studies review their performance under long period and large amplitude seismic motions. This study evaluates the measurement accuracy of the MEMS accelerometer under long period and large amplitude vibration based on the results of shake table testing.

**Methods**

The experiment equipment comprises a shaking table and eight accelerometers. The shaking table used is a linear motor active mass damper produced by IHI Infrastructure Systems Co., Ltd. These dampers are usually installed in tall buildings to provide supplementary damping, but were chosen for this test setup because they can simulate long period and large amplitude vibration with high accuracy. Table 1 shows the specifications of accelerometers used in this test. Five accelerometers (id101-103 and SU202-2, SU202-3) are MEMS accelerometers and one (SU501-1) is a servo type accelerometer. The servo type sensor (K1, K2) was used as reference accelerometer. The eight accelerometers were installed as shown in figure 2.

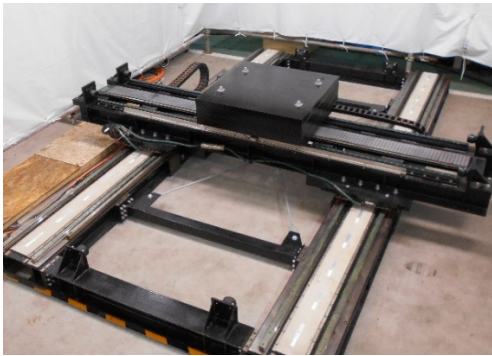


Figure 1: Linear motor active mass damper<sup>[3]</sup>



Figure 2: Installation setup of the sensors

Table 1: Accelerometer specifications

Sensor name	id101,id102,id103	SU501-1	SU202-2, SU202-3	K1, K2 (reference accelerometer)
Type	MEMS	Servo	MEMS	Servo
Frequency range	0.1~50Hz	DC~30Hz	DC~50Hz	DC~500Hz
Number of channels	3 channels	3 channels	3 channels	1 channel
Measuring range	±2G	±4G	±2G	±2G/±4G

Eighteen cases were tested (Table 2). Sine waves and simulated earthquake motion were employed as inputs of the shake table testing. Measurement accuracy was assessed with several frequency cases and amplitude cases to detect frequency dependence and amplitude dependence. Ten waves are provided for one set. In total, 10 sets are implemented to evaluate the measurement accuracy. Simulated earthquake motion were used to evaluate measurement accuracy for actual building response. Tall buildings and isolated buildings were assumed in this test.

Table 2: Shaking table test cases

No	Direction	Freaquency [Hz]	Period [sec]	Amplitude [m]	Number of analyzes
1	X	0.10	10	1.00	10
2	Y	0.10	10		
3	X	0.13	8		
4	Y	0.13	8		
5	X	0.17	6		
6	Y	0.17	6		
7	X	0.17	6	0.60	10
8	Y	0.17	6		
9	X	0.25	4		
10	Y	0.25	4	0.40	10
11	X	0.17	6		
12	Y	0.17	6		
13	X	0.25	4		
14	Y	0.25	4		
15-1	X	Simulated earthquake motion (isolated buildings)		0.20	1
15-2	X	Simulated earthquake motion (isolated buildings)		0.40	1
16-1	X	Simulated earthquake motion (tall buildings)		0.35	1
16-2	X	Simulated earthquake motion (tall buildings)		0.70	1

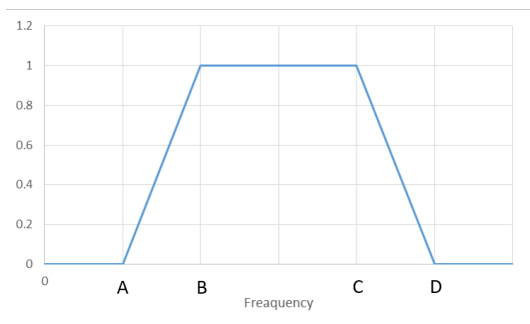
**Shaking table test results**

*Measurement accuracy for accelerometers*

Since the raw data of the shake table tests includes noise in high and low frequency range, data treatment using Band-pass filter (BPF) is usually required to remove the influence of noise. Figure 3 shows specifications of the BPF. Also, Hanning windows were applied to remove the influence of disordered vibration observed at the beginning and end of the waveform because of the shake table characteristics.

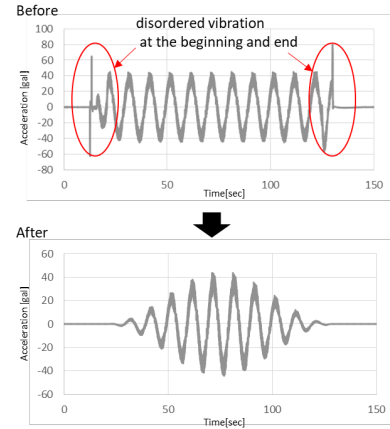
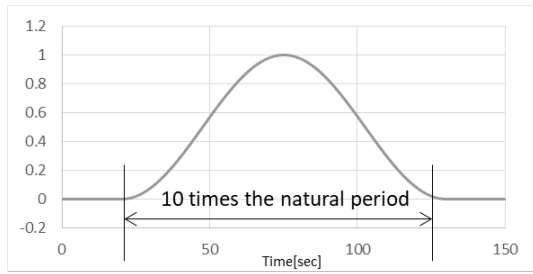
Evaluation of measurement accuracy for acceleration was performed as follows;

1. Apply the Hanning window function to remove the influence of the beginning and end of the waveform
2. Apply Fourier transform
3. Apply BPF to remove the influence of high and low frequencies noise



Natural period of target wave [sec]	Cut off Freaquency [Hz]			
	A	B	C	D
$6 \leq T$	0.1	0.125	25	27
$6 > T$	0.04	0.05	25	27

Figure 3: The specification of BPF



a) The Hanning window function      b) Remove the influence of disorder at start and end  
 Figure 4: The data processed by The Hanning window function

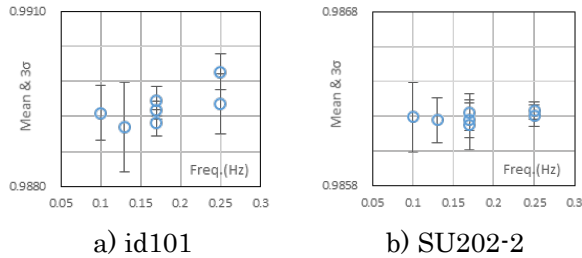
The measurement accuracy of the acceleration is evaluated by using the ratio of the maximum value of the acceleration Fourier spectrum to the reference. The data from the reference accelerometer is used as a reference. First, the ratio for each of the 10 waves in one set of the experiment was calculated. Second, the mean value of the ratio of the 10 waves was determined. Then, the mean and standard deviations of the 10 sets of experiments were calculated. Table 3 shows the mean and standard deviations of the ratios of the maximum acceleration values of the Fourier spectrum in each test case. The average of the maximum values is no less than 0.975 in all cases. Also, the standard deviations show low values, no more than 0.0002537. These results indicate that the MEMS acceleration sensor can have almost the same measurement accuracy as the reference accelerometer. Additionally, no particular difference is observed between the test cases for the X direction and Y direction. This result suggests that there is no sensitivity of the measurement accuracy to direction of excitation.

Figure 5 shows the relationship between the frequency and the mean acceleration maximum value ratios. There appears to be no remarkable relationship although the variation tends to become somewhat larger at low frequencies. Figure 6 shows the relationship between the amplitude and the mean acceleration maximum value ratios.

No remarkable relationship was observed between the amplitude and the measurement accuracy, although the variation tends to slightly increase as the amplitude increases. Given these results, it has been confirmed that the MEMS acceleration sensor can accurately measure the acceleration even for a large amplitude vibrations of 1 m and vibration periods of 10 seconds.

Table 3: Mean and standard deviations of the ratios of the maximum acceleration values

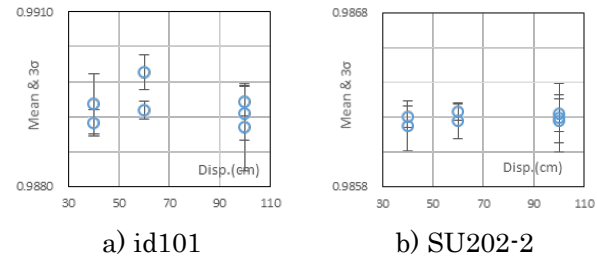
Case No.	Amplitude [cm]	Frequency [Hz]	Direction	id101		id102		id103		SU501-1		SU202-2		SU202-3	
				mean	Deviation	mean	Deviation	mean	Deviation	mean	Deviation	mean	Deviation	mean	Deviation
1	100	0.10	X	0.9893	1.579E-04	0.9874	2.442E-05	0.9892	1.953E-05	0.9963	5.900E-05	0.9862	6.587E-05	1.0102	8.205E-05
2	100	0.10	Y	0.9760	2.021E-04	0.9771	1.563E-05	0.9782	2.224E-05	1.0135	1.469E-05	0.9858	2.535E-05	0.9946	3.324E-05
3	100	0.13	X	0.9890	2.537E-04	0.9873	3.986E-05	0.9892	4.036E-05	0.9962	4.400E-05	0.9862	4.270E-05	1.0102	5.604E-05
4	100	0.13	Y	0.9759	1.386E-04	0.9772	1.967E-05	0.9782	2.233E-05	1.0135	1.837E-05	0.9858	5.192E-05	0.9945	5.602E-05
5	100	0.17	X	0.9895	8.425E-05	0.9877	3.746E-05	0.9895	3.373E-05	0.9962	3.041E-05	0.9862	3.526E-05	1.0102	3.717E-05
6	100	0.17	Y	0.9762	2.285E-04	0.9776	3.980E-05	0.9787	3.873E-05	1.0135	1.351E-05	0.9858	2.969E-05	0.9945	1.589E-05
7	60	0.17	X	0.9893	5.084E-05	0.9875	2.375E-05	0.9894	2.192E-05	0.9962	1.603E-05	0.9862	3.314E-05	1.0102	2.158E-05
8	60	0.17	Y	0.9761	6.675E-05	0.9775	1.925E-05	0.9786	1.934E-05	1.0135	8.924E-06	0.9858	4.518E-05	0.9946	2.071E-05
9	60	0.25	X	0.9900	1.006E-04	0.9882	2.497E-05	0.9901	3.341E-05	0.9962	9.673E-06	0.9862	1.673E-05	1.0102	1.514E-05
10	60	0.25	Y	0.9767	6.861E-05	0.9781	3.099E-05	0.9792	3.243E-05	1.0135	8.963E-06	0.9858	1.793E-05	0.9946	1.523E-05
11	40	0.17	X	0.9891	7.571E-05	0.9872	3.858E-05	0.9891	4.089E-05	0.9963	1.419E-05	0.9861	4.811E-05	1.0102	5.528E-05
12	40	0.17	Y	0.9757	6.462E-05	0.9770	6.052E-06	0.9781	4.528E-06	1.0136	5.079E-05	0.9858	6.177E-05	0.9946	6.198E-05
13	40	0.25	X	0.9894	1.715E-04	0.9876	2.119E-05	0.9894	2.409E-05	0.9962	9.369E-06	0.9862	2.024E-05	1.0102	1.931E-05
14	40	0.25	Y	0.9761	7.376E-05	0.9775	9.610E-06	0.9786	1.450E-05	1.0135	5.446E-06	0.9858	1.488E-05	0.9946	2.801E-05



a) id101

b) SU202-2

*Figure 5: The relationship between the frequency and the measurement accuracy (Direction X)*



a) id101

b) SU202-2

*Figure 6: The relationship between the amplitude and the measurement accuracy (Direction X)*

### *Measurements accuracy for displacement*

BPF was also applied for the evaluation of measurement accuracy for the displacement to remove the influence of high and low frequency noise. The specification of the BPF is the same as the one used for the evaluation of measurement accuracy for acceleration (figure 3). Then, the displacement is calculated by the second integral and the inverse Fourier transform.

Evaluation of measurement accuracy for displacement is performed as follows;

1. Apply Fourier transform
2. Apply BPF to remove the influence of high and low frequency noise
3. Convert to displacement data by second-order integration
4. Apply inverse Fourier transform to calculate displacement time history waveform

Additionally, the displacement data of the linear motor active mass damper was processed as follows.

1. Apply Fourier transform
2. Apply BPF to remove the influence of high and low frequency noise
3. Apply inverse Fourier transform to calculate displacement time history waveform

The measurement accuracy for the displacement is evaluated by using the ratio of the maximum value to the reference. The displacement data of the linear motor active mass damper (D) is used as a reference. First, the positive and negative maximum values of the time history waveform were extracted as shown in Figure 7. Second, the ratio of each maximum values to those of the reference were determined. Third, the mean value of the ratios for 10 waves was calculated. Then, the mean and standard deviations of the 10 sets of experiments were calculated.

The average of the maximum ratio values is no less than 0.9986 and no more than 1.0409 in all cases. Also, the standard deviation show low values, no more than 0.002757. These results indicate that the MEMS acceleration sensor has a high measurement accuracy for displacement. Furthermore, no particular difference is observed between the test cases with X direction and the Y direction. This result again indicates that there is no sensitivity of the measurement accuracy to excitation direction.

Figure 8 shows the relationship between frequency and average displacement maximum value ratio. As is seen in the results of the measurement accuracy of acceleration, the standard deviation tends to increase at low frequencies. This tendency is more significant in the results of the measurement accuracy for the displacement. Figure 9 shows the relationship between amplitude and average displacement maximum value ratio. The accuracy and the variation tend to increase at large amplitudes. This tendency is more remarkable than that of the acceleration results, although

it should be noted that the variation is very small even in the case of large amplitude. Given these results, it has been confirmed that the MEMS acceleration sensor can accurately measure the acceleration even for large amplitude vibrations of 1 m and vibration periods of 10 seconds.

Therefore, it is concluded that the MEMS acceleration sensor has sufficient measurement accuracy as a sensor used for monitoring systems for both accelerations and displacements. The MEMS acceleration sensor can be applied to buildings in which long period and large amplitude vibrations occur.

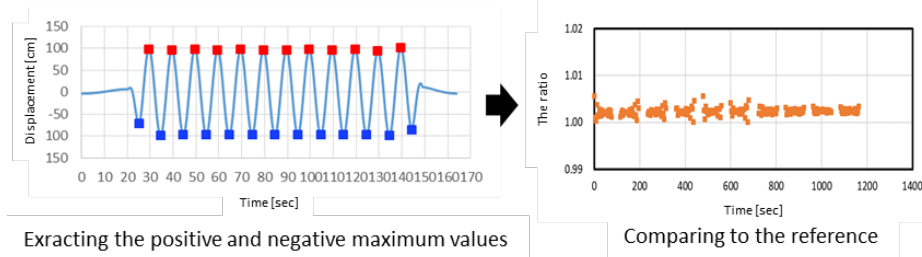
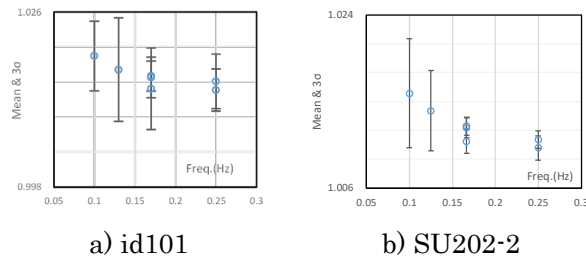


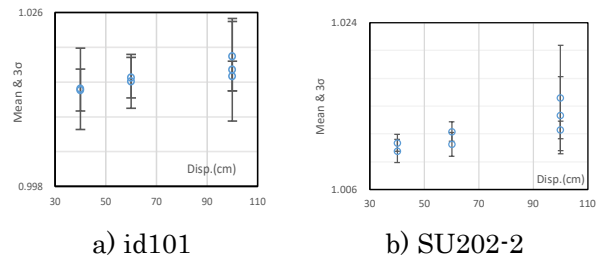
Figure 7: The evaluation method for displacement

Table 4: Averages and standard deviations of the ratios of the maximum displacement values

Case No.	Amplitude [cm]	Frequency [Hz]	Direction	id101		id102		id103		SU501-1		SU202-2		SU202-3		K1,K2	
				mean	Deviation	mean	Deviation	mean	Deviation	mean	Deviation	mean	Deviation	mean	Deviation	mean	Deviation
1	100	0.10	X	1.0190	1.857E-03	1.0170	1.782E-03	1.0189	1.779E-03	1.0263	1.931E-03	1.0158	1.892E-03	1.0406	1.980E-03	1.0300	1.785E-03
2	100	0.10	Y	1.0024	1.679E-03	1.0034	9.165E-04	1.0046	9.311E-04	1.0409	1.285E-03	1.0124	1.199E-03	1.0214	1.285E-03	1.0270	1.005E-03
3	100	0.13	X	1.0168	2.757E-03	1.0151	2.323E-03	1.0170	2.364E-03	1.0244	1.455E-03	1.0140	1.395E-03	1.0387	1.575E-03	1.0281	2.522E-03
4	100	0.13	Y	1.0010	1.685E-03	1.0023	7.810E-04	1.0034	8.360E-04	1.0396	1.221E-03	1.0112	1.163E-03	1.0201	1.143E-03	1.0257	8.389E-04
5	100	0.17	X	1.0158	7.968E-04	1.0139	7.458E-04	1.0158	7.564E-04	1.0227	3.143E-04	1.0124	3.186E-04	1.0370	3.356E-04	1.0265	7.381E-04
6	100	0.17	Y	1.0002	7.836E-04	1.0017	4.691E-04	1.0028	4.740E-04	1.0384	2.026E-04	1.0101	2.317E-04	1.0190	3.566E-04	1.0246	4.833E-04
7	60	0.17	X	1.0155	1.086E-03	1.0137	1.107E-03	1.0156	1.111E-03	1.0226	3.477E-04	1.0123	3.521E-04	1.0369	3.786E-04	1.0265	1.092E-03
8	60	0.17	Y	0.9995	9.682E-04	1.0009	8.506E-04	1.0020	8.630E-04	1.0378	2.095E-04	1.0095	2.319E-04	1.0184	2.501E-04	1.0239	8.879E-04
9	60	0.25	X	1.0149	1.449E-03	1.0131	1.423E-03	1.0150	1.429E-03	1.0213	2.931E-04	1.0110	3.050E-04	1.0356	3.159E-04	1.0251	1.399E-03
10	60	0.25	Y	0.9998	1.353E-03	1.0013	1.202E-03	1.0024	1.202E-03	1.0374	1.719E-04	1.0091	2.003E-04	1.0180	2.219E-04	1.0236	1.226E-03
11	40	0.17	X	1.0137	2.182E-03	1.0118	2.178E-03	1.0137	2.181E-03	1.0212	4.216E-04	1.0109	4.289E-04	1.0355	4.646E-04	1.0249	2.195E-03
12	40	0.17	Y	0.9986	1.605E-03	1.0000	1.598E-03	1.0011	1.603E-03	1.0373	1.751E-04	1.0090	2.084E-04	1.0179	2.330E-04	1.0235	1.636E-03
13	40	0.25	X	1.0135	1.120E-03	1.0116	1.107E-03	1.0135	1.112E-03	1.0204	3.849E-04	1.0102	4.187E-04	1.0347	4.237E-04	1.0243	1.124E-03
14	40	0.25	Y	0.9990	9.684E-04	1.0004	9.493E-04	1.0015	9.379E-04	1.0372	2.359E-04	1.0089	2.599E-04	1.0178	2.608E-04	1.0234	9.546E-04



a) id101  
b) SU202-2  
Figure 8: The relationship between the frequency and the measurement accuracy (Direction X)



a) id101  
b) SU202-2  
Figure 9: The relationship between the amplitude and the measurement accuracy (Direction X)

Measurements accuracy for simulated earthquake motion

Similar to the previous assessments, BPF was applied to remove the influence of high and low frequency noise for the evaluation of measurement accuracy for simulated earthquake motions. The specifications of the bandpass filter are also the same (figure 3) those of the accuracy verification for under 6 seconds. The displacement data was calculated by second-order integration of the acceleration data.

Evaluation of measurement accuracy for displacement was performed as follows;

1. Apply Fourier transform

2. Apply BPF to remove the influence of high and low frequency noise
3. Convert to displacement data by second-order integration
4. Apply inverse Fourier transform to calculate displacement time history waveform

The measurement accuracy is evaluated for simulated earthquake response by using the ratio of the maximum value to the reference. The ratio of the Fourier spectrum maximum value to the reference is calculated to evaluate measurement accuracy for acceleration. The ratio of the displacement maximum value of the time history data to the reference is calculated to evaluate measurement accuracy for displacement. Reference servo accelerometer was used as the reference for acceleration evaluation, and the displacement data of linear motor active mass damper was used as the reference for displacement evaluation.

The displacement maximum values in each test case are shown in Table 5. The maximum ratio of acceleration is no less than 0.986 and no more than 1.012. The maximum ratio of displacement is no more than 1.0379. Therefore, the MEMS acceleration sensor appears to have high measurement accuracy for both acceleration and displacement for simulated earthquake response. Note that the maximum deviation of test case 16-1 is larger than the value mentioned above. However, it should be excluded from consideration because of the lack of measurement in the latter half of the data.

Table 5: The ratios of the maximum values

Case No.	id101		id102		id103		SU501-1		SU202-2		SU202-3	
	Acceleration	Displacement										
15-1	0.989	1.0107	0.987	1.0102	0.989	1.0121	0.997	1.0184	0.987	1.0077	1.012	1.0326
15-2	0.989	1.0139	0.987	1.0129	0.989	1.0148	0.996	1.0213	0.986	1.0112	1.010	1.0356
16-1	0.990	1.0134	0.987	1.0100	0.989	1.0119	0.921	1.0204	0.912	1.0098	0.934	1.0346
16-2	0.989	1.0163	0.987	1.0141	0.989	1.0160	0.997	1.0234	0.987	1.0131	1.011	1.0379

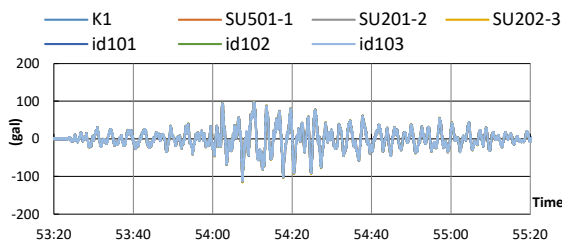


Figure 10: Comparison of acceleration wave (Case No. 15-2)

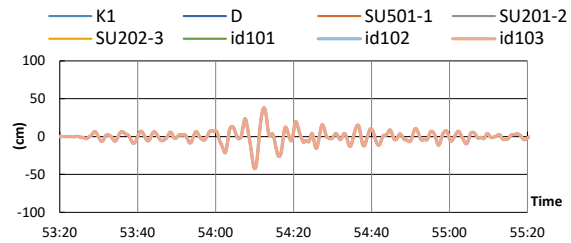


Figure 11: Comparison of displacement wave (Case No. 15-2)

### Conclusions

The evaluation of measurement accuracy of MEMS sensor for long period and large amplitude vibrations is concluded as follows;

- The results of the experiments indicate that MEMS acceleration sensors show great agreement in terms of measurement accuracy compared to reference servo type acceleration sensors for acceleration and displacement.
- While as the period becomes longer and the amplitude becomes larger, the variation in measurement accuracy tends to increase. It is possible to accurately measure vibration amplitudes as large as 1 m and long period vibrations of 10 seconds.

- It is possible to measure vibrations that simulates an earthquake response accurately.
- The MEMS acceleration sensor has sufficient measurement accuracy for use in monitoring systems.

## References

- [1] Nikken Sekkei Structural Monitoring System, Retrieved August 23, 2020, from [https://www.nikken.co.jp/ja/expertise/structural\\_engineering/nikken\\_sekkei\\_structural\\_monitoring\\_system.html](https://www.nikken.co.jp/ja/expertise/structural_engineering/nikken_sekkei_structural_monitoring_system.html)
- [2] T. Ishizaki, H. Imaeda, H. Harada, T. Shinohara, Verification of a Damage Estimation System with a Full Scale Shaking Table Test. Proceedings of The 7th Asia-Pacific Workshop on Structural Health Monitoring, pp.381-388
- [3] IHI Infrastructure Systems Co.,Ltd. website, Retrieved August 23, 2020, from <https://www.ihl.co.jp/iis/news/2018/180618.html>
- [4] T. Yaguchi, Y. Nitta, A. Nishitani “Benchmark Test of MEMS Accelerometer for Structural Monitoring” (in Japanese), Summaries of technical papers of annual meeting of AIJ (2007), pp. 47-48
- [5] M. Takaki, Y. Yamamoto, Y. Uchiyama “The performance test of the MEMS acceleration sensor” (in Japanese), Summaries of technical papers of annual meeting of AIJ (2010), pp. 831-832
- [6] T. Matsushita, K. Yoshida, H. Nishii, K. Goto “Technology Development of Structure Health Monitoring Aiming at Improvement of Resilience Part3 Shaking experiments” (in Japanese), Summaries of technical papers of annual meeting of AIJ (2015), pp. 933-934

# Vibration-Based Detection of Loosened Bolts on Pipes Attached to Bridges

Kobayashi Daiki<sup>1,a,\*</sup>, Ikeguchi Yuta<sup>1,b</sup>, Nakagawa Masafumi<sup>1,c</sup>  
and Aratake Atsushi<sup>1,d</sup>

<sup>1</sup>NTT Corporation, 1-7-1 Hanabatake, Tsukuba, Ibaraki, Japan

<sup>a</sup>daiki.kobayashi.dh@hco.ntt.co.jp, <sup>b</sup>yuuta.ikeguchi.da@hco.ntt.co.jp,  
<sup>c</sup>masafumi.nakagawa.dr@hco.ntt.co.jp, <sup>d</sup>atsushi.aratake.hf@hco.ntt.co.jp

**Keywords:** Civil Engineering, Vibration-Based Detection, Loosened Bolts, Dynamic Analysis, Pipeline

**Abstract.** U-bolts are critical points of maintenance in pipeline facilities supported by girders of bridges. However, it is difficult to detect loosened U-bolts by visual inspection. To avoid this problem, we have developed a vibration-based method to detect loosening of bolts based on measurements of actual equipment. First, the vibration of a communication pipeline attached to a road bridge was measured when vehicles passed over it. During the measurements, the U-bolts were set in tightened and loosened states. We found that the frequency changes between the tightened and loosened states was too small for practical use. On the other hand, a strong spectrum in the high frequency region (above 80 Hz) appeared only in the tightened state. Next, a model facility was built to simulate a communication pipeline attached to bridge. A hammering test and modal and frequency response analyses were performed by using the finite element method (FEM). The results suggested that high frequency peaks appearing only in the tightened U-bolt are due to the higher rate of force transfer of the natural frequency from the platform. In addition, the pipe is strongly fixed when the U-bolt is tightened, which may lead to stronger high order modes that cause complex deformation of the pipe. The conventional method is to detect loosening of bolts from changes in the natural frequency. However, in actual equipment, confirming the absence of a high-frequency spectrum is more suitable for detecting loosened bolts.

## Introduction

The pipelines of communication, electricity and gas infrastructure facilities are essential equipment of society. It is expensive to build underground tunnels, so pipelines are usually attached to girders of road bridges when they cross bodies of water or other roads. Some telecommunications and power pipelines are set on support structures of girders and secured by U-bolts. The U-bolts are critical maintenance points because of the risk of falling parts. Loose bolts are difficult to detect by visual inspection, so the development of an alternative method is desired.

Conventional methods to detecting loose bolts in civil engineering equipment are embedding sensors in bolts, vision-based, and vibration analysis. Sensors embedded in bolts can measure the tightening force [1, 2]. Although this method is very accurate, the replacement cost of such infrastructure equipment in use is high. The vision-based method [3, 4] detects the rotation of the bolt heads from the difference between the initial and observed images. This method is cheaper than embedding sensors in the bolts, but it requires the bridge to be closed in order to take photographs. In this case, scaffolding has to be erected or drones have to be used because there are many blind spots under the girders where the pipes are installed. On the other hand, vibration-based methods [5, 6] may be cheaper than these methods for bolt detection. This is

because dynamic measurements have been possible with optical fibers [7]. In this method, the optical fiber in the communication pipes acts as a dynamic sensor. This method could eliminate the need for on-site inspections and improve inspection quality.

The relationship between vibration and bolt loosening needs to be clarified in order to make fiber optic monitoring practical. He and Zhu [5] reported natural frequency changes in bolts attached to a pipe flange when the bolts were tightened and loosened. Razi et al. [6] devised an energy-based damage index by using empirical mode decomposition of bolts attached to a flange. The target applications of these studies are flanges, not U-bolts. In addition, they tested only models, and their applicability to actual facilities was not examined. Therefore, in this study, we measured U-bolts in actual facilities. On the basis of our results, we propose an optimum looseness detection method for U-bolts of pipelines.

### Actual Equipment Measurements

#### Method

The measurement target was a communication pipeline attached to a road bridge in Japan (Fig. 1). The main girder of the bridge is made of concrete, and the length is 16 m. The main girder has supporting metal to attach the pipeline. The pipes are made of rigid polyvinyl chloride and bonded by U-bolts. An accelerometer was installed at the position shown in Fig. 2. Measuring continued during the daytime to obtain the acceleration when vehicles passed over the bridge. The sampling rate was 1000 Hz. The first half of the measurements were made with the U-bolt tightened, while the second half of the measurements were made with the U-bolt loosened. The acquired data were analyzed with a fast Fourier transform (FFT). The window function of the FFT was the exponential one shown as Eq. 1.

$$w(x) = e^{\frac{x \log \beta}{N-1}}. \quad (1)$$

Here,  $w(x)$  is the weight of the window function,  $x$  is time,  $N$  is the number of data, and  $\beta$  is the window function coefficient ( $\beta = 0.1$ ).



Figure 1. Measured communication pipes attached to the bridge [8]

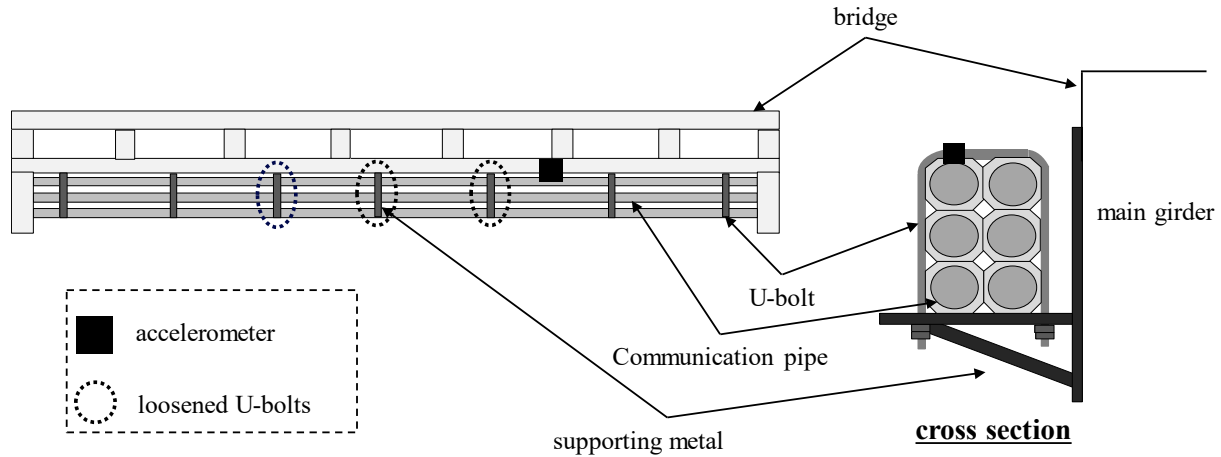


Figure 2. Overview of communication pipes attached to the bridge and setup of measurement

### Results

The FFT data of the acceleration in the tightened and loosened states of the U-bolt are shown in Fig. 3. Nine waveforms for the tightened state and eight waveforms for the loosened state were obtained, which were additively averaged over the frequency domain. The frequency of the spectrum maximum was 15.0 Hz for the loosened state and 15.5 Hz for the tightened state, so the difference was 0.5 Hz. In addition, spectrum peaks at 88 Hz and 144 Hz occurred only in the tightened state.

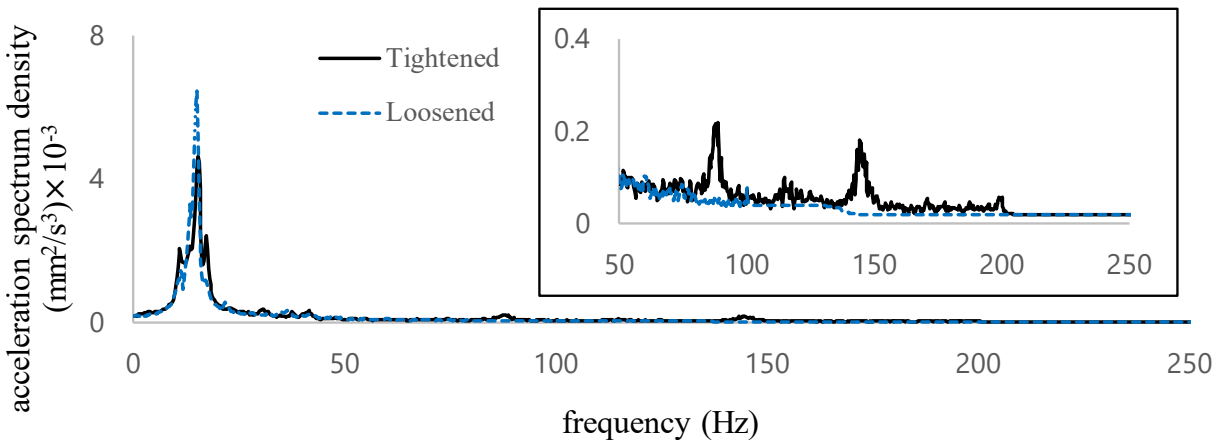


Figure 3. Measured acceleration in tightened and loosened states in actual equipment  
(Expanded view from 50 to 250 Hz is shown in the upper right corner)

### Model Facility Experiment

A model of communication pipes was built for the hammering test and the simulation. The method of detecting loosened U-bolts is discussed by comparing the results of the model facility experiment and the measurements on the actual equipment.

*Method*

A 5.5 m pipe made of rigid polyvinyl chloride was placed on a steel platform and bonded by U-bolts (Fig. 4). An accelerometer and a strain gauge for the plastic material were attached to the surface of the pipe at the center position of the support point. The accelerometer was set in the gravity direction, while the strain gauge was set in the bending direction of the pipe. The position shown in Fig. 4 was hit with a rubber hammer. The number of tests was 10 in both tightened and loosened states, and the results were additively averaged over the frequency domain.

Modal and frequency response analyses were performed on the experimental results. The geometry and conditions of the analyses are shown in Fig. 5, and the contact conditions between the pipe and the platform were set to bond. The platform bottoms of the 12 faces were fixed, and the damping ratio was set to 1%. The analysis software was Ansys Mechanical 2020 R1.

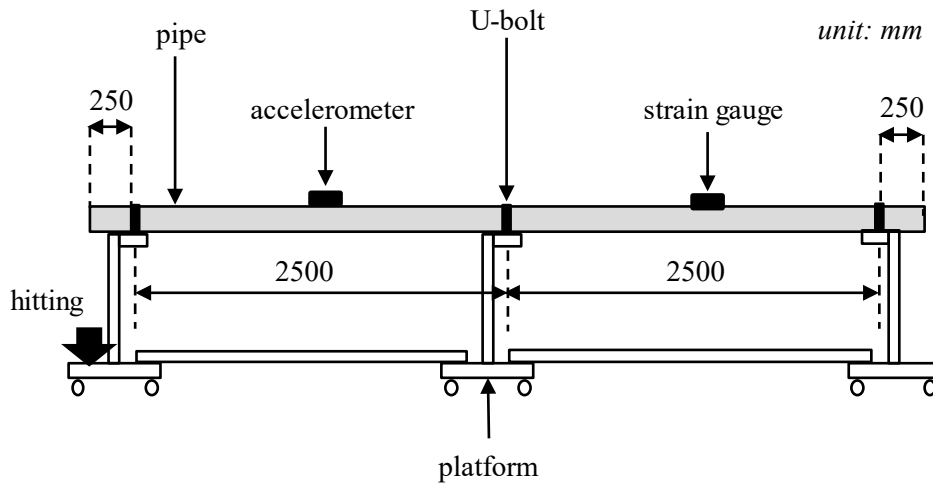


*Figure 4. Overview of a model facility*

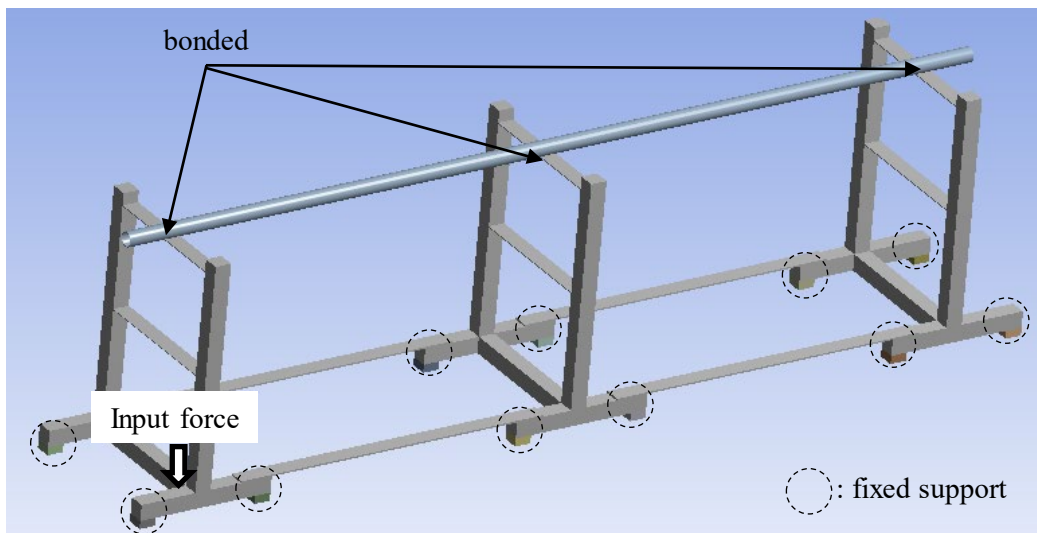


*Figure 5. Overview of FEM model settings*

### Results of Hammering Test

Fig. 6 shows the measured accelerations in the tightened and loosened states. Strong peaks occurred above 100 Hz when the U-bolt was in the tightened state only. The strain data are shown in Fig. 7. Multiple peaks for both tightened and loosened states were observed as in Figure 6. On the other hand, the intensity and frequency of the spectrum peaks above 100 Hz were smaller than those in Fig. 6.

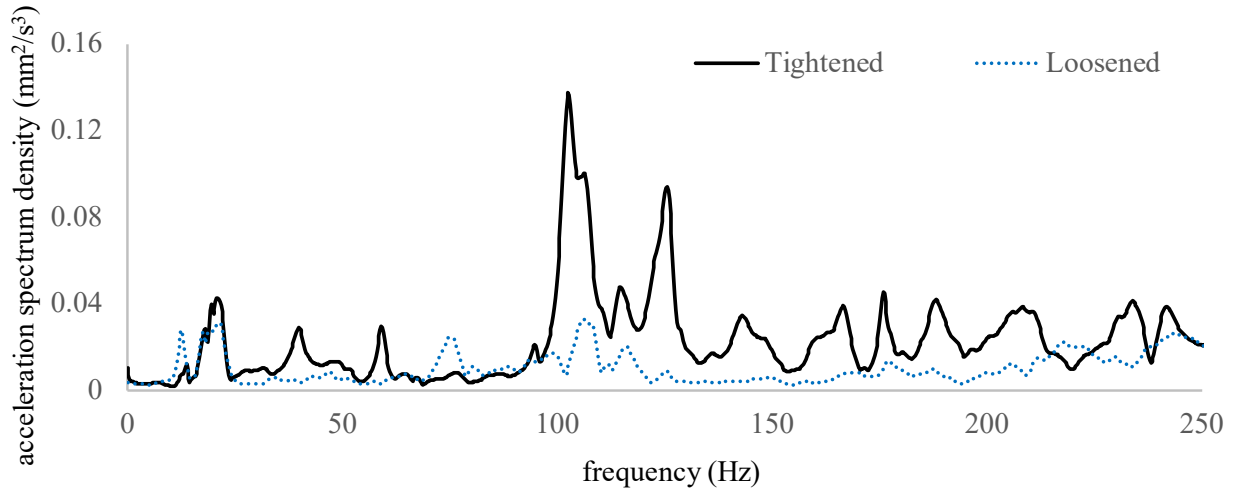


Figure 6. Measured acceleration for tightened and loosened U-bolts

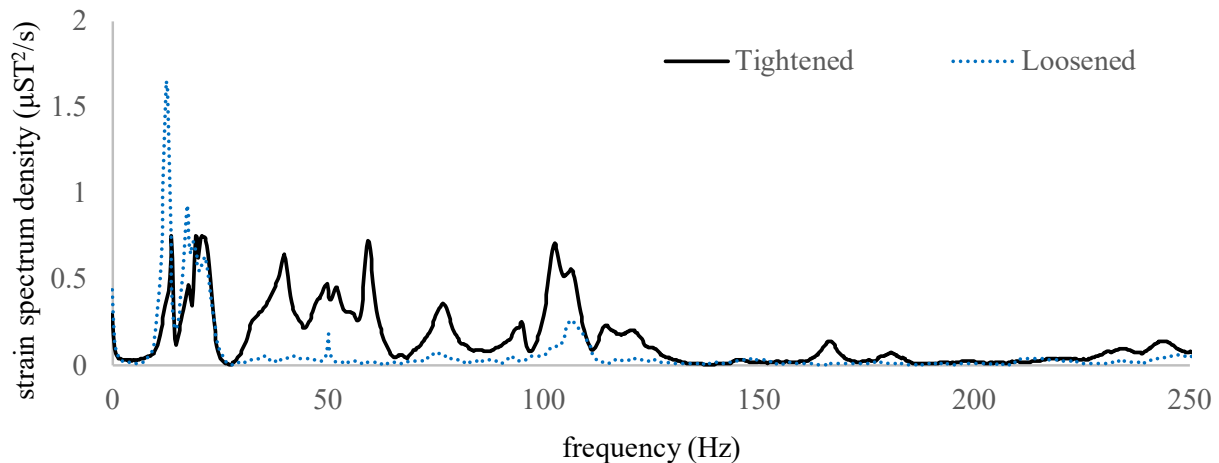


Figure 7. Measured strain in tightened and loosened U-bolts

### Results of FEM Simulation

The results of the frequency response analysis are shown in Fig. 8. The normalized spectrum strength was defined as the relative strength at which the maximum spectrum strength (20.8 Hz) was 1. Strong peaks existed around 21 Hz, 104 Hz and 114 Hz, as in Fig. 6. In addition, there were many peaks above 100 Hz, similar to Fig. 6. Therefore, it is considered that the simulation reproduced the experimental results. The results of the modal analysis are shown in Fig. 9. They

show the relative deformations of the top four peaks above 100 Hz (A to D in Fig. 8). These deformations show complex modes such as multiple waves and cross-sectional deformation.

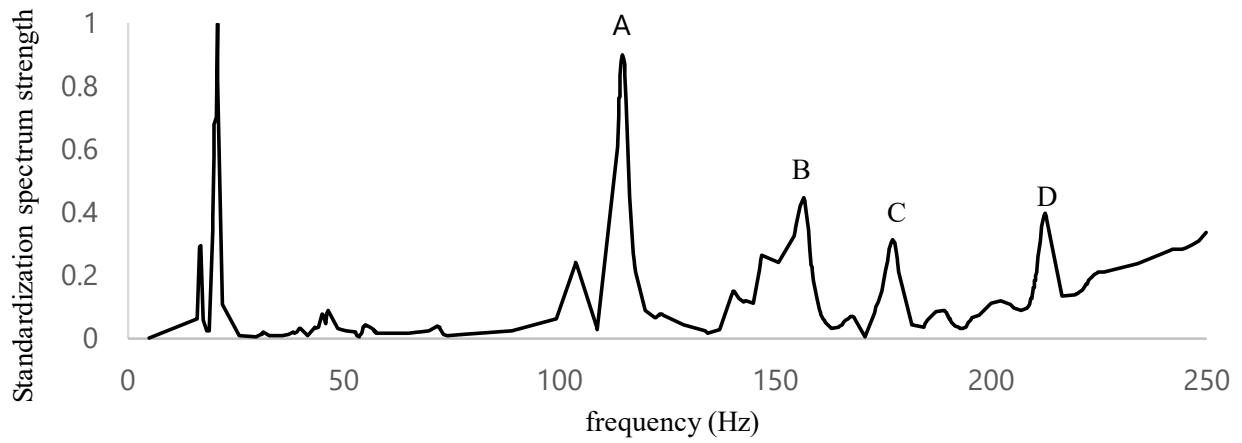


Figure 8. Results of frequency response analysis by FEM

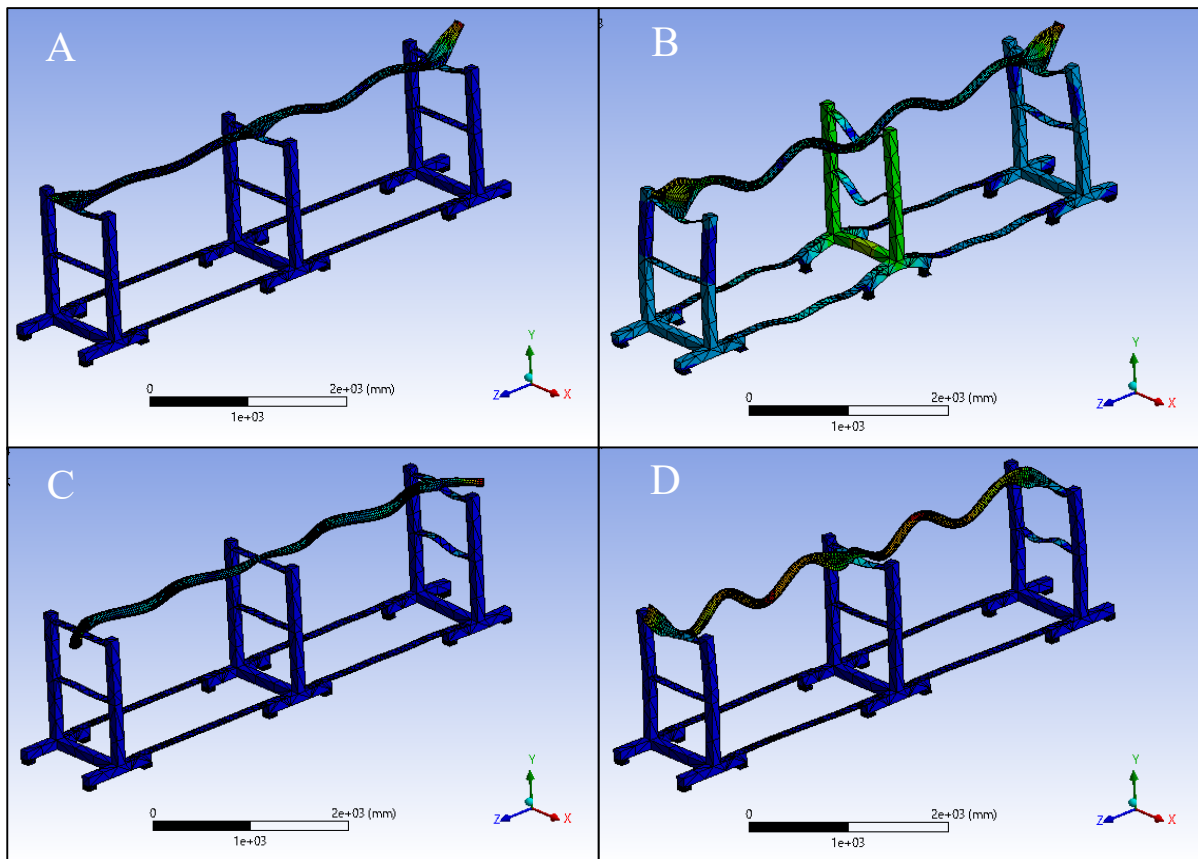


Figure 9. Results of modal analysis by FEM

## Discussion

Measuring the natural frequency shift is the simplest way to detect deteriorations such as loosened bolts. In the measurements of the actual facility shown in Fig. 3, the change in natural frequency was only 3 %. The natural frequency has a measurement error of 5-10% [9], thus, this amount of change is too small for practical use. The change in the natural frequency is proportional to the square root of stiffness, so the natural frequency does not change sufficiently without a large stiffness change [10]. A previous study [5] reported the natural frequency change was over 15% for a bolt attached to the flange of a pipe. The bolts of flanges bear large stresses and contribute significantly to the stiffness of a pipe. However, U-bolts bear low stresses and have little impact on the stiffness of the pipe, so the change in natural frequency is small in this study.

Some peaks in the high-frequency region were observed in both the actual and model facilities only on the tightened state. Acceleration of the pipe was detected above 100 Hz (Fig. 6), but no bending strain was detected (Fig. 7) in that frequency region. These results may indicate that the pipe vibrated with no bending, because the rate of force transfer from the platform to the pipe increased when the U-bolt was tightened. In addition, the modal analysis of the model facility (Fig. 9) showed that the strong acceleration peaks above 100 Hz indicate complex deformation as a high-order mode of the pipe. Since the U-bolt is a node of the pipe, high order modes cannot appear when the fixing force of the node is weak.

From the above, we propose that confirming the absence of an acceleration response in the high frequency region is a more practical method than measuring the change in natural frequency. The remaining issue is a dynamic numerical simulation of the tightened and loosened states; it will improve the reliability of this method.

## Conclusion

We examined a method of detecting loosened U-bolts in pipelines attached to bridges from vibrations. Actual measurements on a facility, a hammering test of model equipment, and a dynamic analysis were carried out. Our findings are as follows:

- Attempting to detect a change in the natural frequency, which is generally used for the detection of deterioration, was not practical, because the change in frequency was too small.
- Acceleration peaks in the high-frequency region (above 80 Hz) occurred only in the case of tightened U-bolts.

It was assumed that the peaks in the high-frequency region reflected the following phenomena:

- The U-bolt is a node of pipe deformation, so when the fixation with the U-bolt is weakened, the deformation is also reduced.
- The vibration from the platform is transmitted to the pipe. The rate of force transfer from the platform to the pipe is higher when the U-bolt is tightened.

We propose that confirming the absence of acceleration peaks in the high-frequency region is a practical method of detecting loosened U-bolts in pipelines. The remaining issue is the dynamic simulation of tightening and loosening. Completing the simulation will improve the reliability of this method.

## References

- [1] H. Yin, T. Wang, D. Yang, S. Liu, J. Shao, and Y. Li, A smart washer for bolt looseness monitoring based on piezoelectric active sensing method, *Applied Sciences*, vol. 6, no. 11, pp. 320-330, 2016. <https://doi.org/10.3390/app6110320>

- [2] N. Shimoi, C. H. Cuadra, H. Madokoro, and M. Saijo, Simple smart piezoelectric bolt sensor for structural monitoring of bridges, *International Journal of Instrumentation Science*, vol. 1, no. 5, pp. 78-83, 2013.
- [3] X. Kong and J. Li, Image registration-based bolt loosening detection of steel joints, *Sensors (Basel)*, vol. 18, no. 4, pp. 1000-1020, 2018.
- [4] J. H. Park, T. C. Huynh, S. H. Choi, and J. T. Kim, Vision-based technique for bolt-loosening detection in wind turbine tower, *Wind and Structures an International Journal*, vol. 21, no. 6, pp. 709-726, 2015. <https://doi.org/10.12989/was.2015.21.6.709>
- [5] K. He and W.D. Zhu, Detecting loosening of bolted connections in a pipeline using changes in natural frequencies, *Proc. ASME 2011 Int. Des. Eng. Tech. Conf. Comput. Inf. Eng. Conf.*, 2011. <https://doi.org/10.1115/DETC2011-47912>
- [6] P. Razi, R. A. Esmael, and F. Taheri, Improvement of a vibration-based damage detection approach for health monitoring of bolted flange joints in pipelines, *Structural Health Monitoring*, vol. 12, no. 3, pp. 207-224, 2013. <https://doi.org/10.1177/1475921713479641>
- [7] Jousset, P., Reinsch, T., Ryberg, T., Blanck, H., Clarke, A., Aghayev, R., Hersir, G.P., Hennings, J., Weber, M., and Krawczyk, C.M. , Dynamic strain determination using fibre-optic cables allows imaging of seismological and structural features, *Nature Communications*, vol. 9, no. 1, pp. 1-11, 2018.
- [8] D. Kobayashi, Y. Ikeguchi, C. Kazato, M. Nakagawa, and A. Aratake, Measurement of actual facilities for detecting loosening bolts attaching to bridge by vibration, *Conference of Japanese Society of Civil Engineering*, 2020. (In Japanese)
- [9] W. Fan, and P. Qiao, Vibration-based damage identification methods: A review and comparative study, *Structural Health Monitoring*, vol. 10, no. 1, pp. 83-111, 2011. <https://doi.org/10.1177/1475921710365419>
- [10] O.S. Salawu, Detection of structural damage through changes in frequency: A review. *Engineering Structures*, vol. 19, no. 9, pp. 718-723, 1997. [https://doi.org/10.1016/S0141-0296\(96\)00149-6](https://doi.org/10.1016/S0141-0296(96)00149-6)

# Extraction of Parameters for 90-degree Turn Prediction Using the IMU-based Motion Capture System

Ami Ogawa<sup>1,a,\*</sup>, Kanako Takeda<sup>1,b</sup> and Akira Mita<sup>1,c</sup>

<sup>1</sup> Department of System Design Engineering, Keio University, 3-14-1 Hiyoshi, Kohoku, Yokohama 223-8522, Japan

<sup>a</sup>ami\_ogawa@keio.jp, <sup>b</sup>kanakota@keio.jp, <sup>c</sup>mita@keio.jp

**Keywords:** Motion Prediction, 90-degree Turn, IMU, Motion Capture System

**Abstract.** Against the increasing number of single households, we have been proposing the “Biofied Building” that provides a safe, secure, and comfortable living space for a resident using a small home robot. The robot can be used for real-time sensing of the resident’s position and behavior. On the other hand, for further use of the robot, such as choosing a path that does not disturb the resident, a phase to predict the resident’s behavior is necessary. Walking, which is one of the most basic activities of daily living, is often targeted in studies of motion prediction. However, most of them deal with steady walking, even though walking in daily life includes unsteady walking such as the turning motion. Therefore, the purpose of this study was to extract the prediction parameters to construct a prediction method for the unsteady 90-degree turn. In this study, we explored the effective prediction parameters for 90-degree turns based on the measured data using the inertial measurement unit (IMU) based motion capture system aiming to introduce the prediction of unsteady walking to the “Biofied Building”.

## Introduction

Because of the increase in the number of elderly single-person households and the diversification of lifestyles, the need for housing which is incorporating monitoring function is rising. Toward this need, we have been proposing the “Biofied Building”, a building system that uses small home robots to provide a safe, secure, and comfortable space for each resident [1, 2]. One of the aims of using robots is sensing the position and movement of the residents in real-time. The prediction of the resident’s movement is effective to achieve more natural robot control, such as choosing paths of movement that does not interfere with the resident.

Recurrent Neural Networks (RNNs), a deep learning method with time-series elements, are widely used for motion prediction [3-5], but it is pointed out that physical constraints of the human body are not taken into account [1]. On the contrary, Kimura et al. proposed a simple method for predicting walking based on the dynamics of the human body [1]. However, the system only targeted steady walking motions even though the daily walking includes unsteady ones. Thus, a system which is adaptable for unsteady motions is needed.

Walking is known as the most basic motion among activities of daily living. It has been reported that more than 40% of the total number of walking is unsteady [6], and among them, the turn motion accounts for about 20% of the walking in daily life [7]. Thus, we targeted the 90-degree turn as one of the unsteady walking motions.

There are three main types of motion measurement systems: an optical motion capture system, which measures the motion of a subject who wears multiple reflective markers by surrounded infrared cameras; an IMU-based motion capture system, which measures the motion by attaches multiple IMU sensors; and a skeletal position tracking function using RGB-D sensors. Although optical motion capture systems are widely used in the medical field due to their high accuracy, they

are not suitable for the measurement of turn motion that requires the long walking path due to their limited measurement range. The skeletal position tracking function of RGB-D sensors is not supposed to measure the turn motion, because the accuracy of the estimation depends on body orientation. On the other hand, the IMU is widely used for motion measurement in living spaces and urban spaces because they are relatively inexpensive and have no measurement environment restrictions. The methods for discriminating walking people and recognizing their motions by analyzing acceleration data has been proposed [8, 9], and it can be applied to motion prediction by focusing on the transition state between motions. Besides, IMU has been widely used in clinical applications, which require relatively high accuracy, and their usefulness has been demonstrated in recent years [10, 11]. Shigeta et al. used IMU sensors to extract gait features in the gait of ASD patients and compared them with those of healthy subjects [11].

The purpose of this study is to reveal the prediction parameters of 90-degree turns aiming to develop with a home robot in the “Biofied Building”. In this paper, we extracted efficient prediction parameters of 90-degree turn based on experimental measurements using an IMU-based motion capture system to obtain acceleration and angular velocity data. This study is positioned as a basic study to introduce a prediction system of unsteady walking to the “Biofied Building”.

### **Proposed method**

The duration of the turn is very short and there is no linearity. Therefore, we tried to detect the transition to the 90-degree turn by comparing it with a highly reproducible steady walking.

A Perception Neuron [12], an IMU-based motion capture system, was used to measure the 90-degree turn (Figure 1). An IMU called a Neuron, which consists of a triaxial acceleration sensor, a triaxial gyroscope, and a triaxial magnetometer is attached to each position to obtain the acceleration and angular velocity data at each sensor position. The 90-degree turn is caused by the change of acceleration and angular velocity of the body’s center of gravity, which is caused by the chain of motion of each body part. Therefore, we focus on the variation of the acceleration and angular velocity of each part of the body. The frame rate was 120 fps, and the data was acquired by wireless communication. The accuracy of the measurements is considered to be within 5 degrees of upper body angular error [13]. MATLAB 2019a (MathWorks Inc., Natick, MA, USA) was used for data analysis. In this study, we use an Axis Neuron, a software for a Perception Neuron, to obtain acceleration and angular velocity data for 19 body parts, including estimates, from 17 sensors. Figure 2 shows the names and locations of each.

Since the accelerometer only detects the gravitational acceleration at resting, the theoretical value of the composite acceleration is 1 G. However, the actual composite acceleration may not be 1 G due to voltage fluctuations. Therefore, we normalized each axis’ acceleration data by dividing the raw data by the mean square of acceleration data of each axis from the second to the 100 frames of resting. Besides, a 5th order Butter-worth low-pass filter [14] was applied to remove the noise caused by the rubbing between the sensor and the clothing, and the phase distortion was corrected by using the `filtfilt` function of MATLAB to deal with the delay. The cutoff frequency of the filter was determined based on the experimental results described in the next section. To remove the bias error in the gyroscope, the average of the angular velocity at resting was calculated and subtracted from the total angular velocity signal. The data from the second to 100 frames were used to calculate the mean value at resting. In this study, the coordinate system of the six axes is defined as shown in Figure 3.



Figure 1 Perception Neuron [12], an IMU-based motion capture system

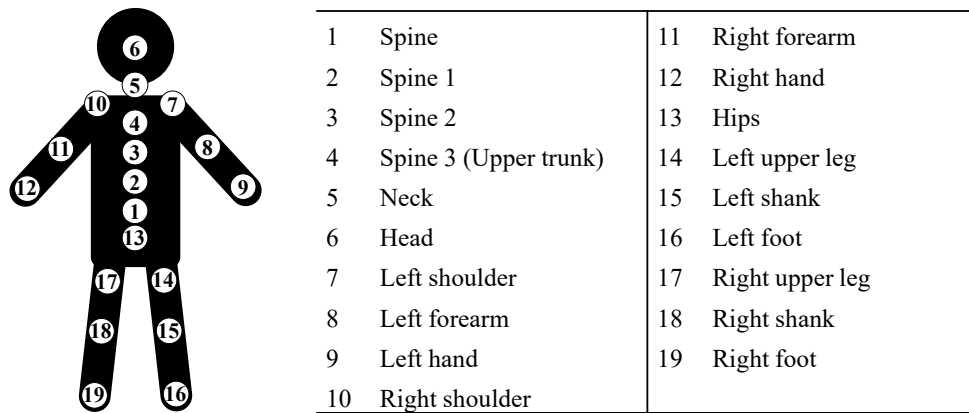


Figure 2 List of positions of acquired data

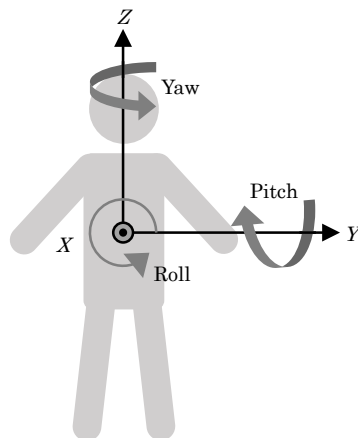


Figure 3 The definition of six axes

### Experiment for extraction of prediction parameters

We measured 90-degree turn and steady walking respectively and compared the acceleration data and angular velocity data. The blue area in Figure 4 is the walking path presented to the subject. Six students in 20s without any gait disorder (M: 3, F: 3) walked three trials in each motion at free walking speed.

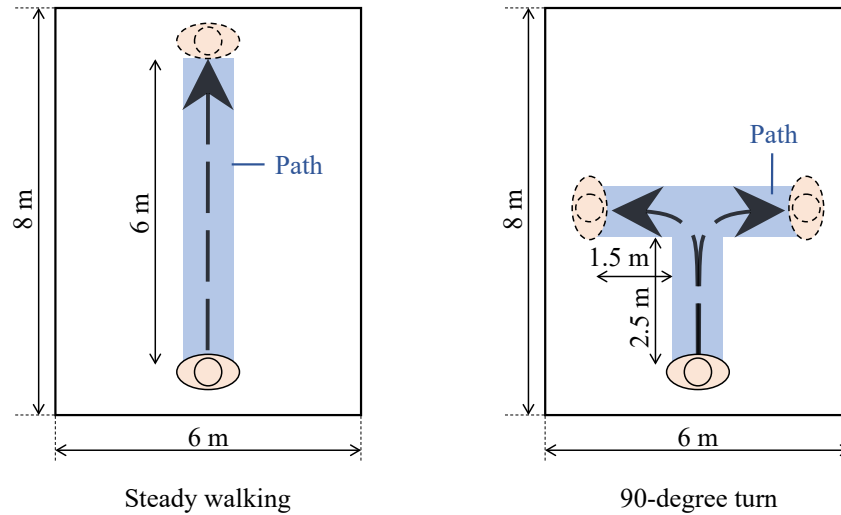


Figure 4 Experimental setup for 90-degree turn and steady walking

### Results & Discussions

Determination of the cutoff frequency. The cutoff frequency was determined based on the experimental results to take into account the peak frequencies of acceleration and angular velocity components caused by the walking motion. In general, it is said that the step frequency ( $f_{step}$ ) appears in the X-axis, Z-axis, and pitch-axis, and the stride frequency ( $f_{stride}$ ) appears in the Y-axis, roll-axis, and yaw-axis in the walking motion. The step is the distance between the heels of both feet, and the stride is the combined length of the left and right steps (Figure 5).

The  $f_{stride}$  was about 0.9 Hz (Mean±SD:  $0.919 \pm 0.096$ ) and the  $f_{step}$  was about 1.8 Hz (Mean±SD:  $1.839 \pm 0.192$ ) according to the results. There was no significant sex difference in this value (p-value = 0.566). This result falls within the range of  $f_{stride}$  and  $f_{step}$  values for a typical walk [15]. Therefore, the cutoff frequency was set to 1.2 Hz for the component with a peak at  $f_{step}$  and 2.5 Hz for the component with a peak at  $f_{step}$ .

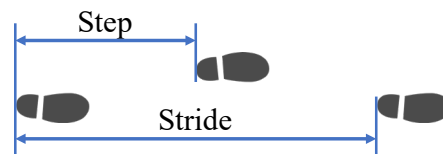


Figure 5 Definition of step and stride

Definition of the section of 90-degree turn. We defined the start and end of 90-degree turns. The right one of Figure 6 shows a graph of the relative angles of the lumbar part to the initial angle in the yaw direction during a 90-degree turn including a steady walking. This can be obtained from

the BVH file output on the Axis Neuron. This data is only used to define the turn section and is not used as a prediction parameter. The minimum and maximum points in the waveform, shown as blue and green points, represent the initial contact (IC) of the right and left feet respectively. IC is defined as the moment when the foot is contacted the floor as shown in the left one of Figure 6.

According to the graph of Figure 6, the subject started walking from the right leg and performed a turn motion after the left IC at the 10th step. The subject performed a steady walking from 2 seconds to 6 seconds, and after 6 seconds, the lumbar rotation decreased almost 90° before entering a steady walking again. The time at which the lumbar rotation decreased as small as left IC which is the one step before was defined as the start of the turn. Similarly, the end time of the turn was defined as the time when the lumbar rotation decreases as small as the next right IC. The range between dashed lines in Figure 6 indicates the section of turn motion.

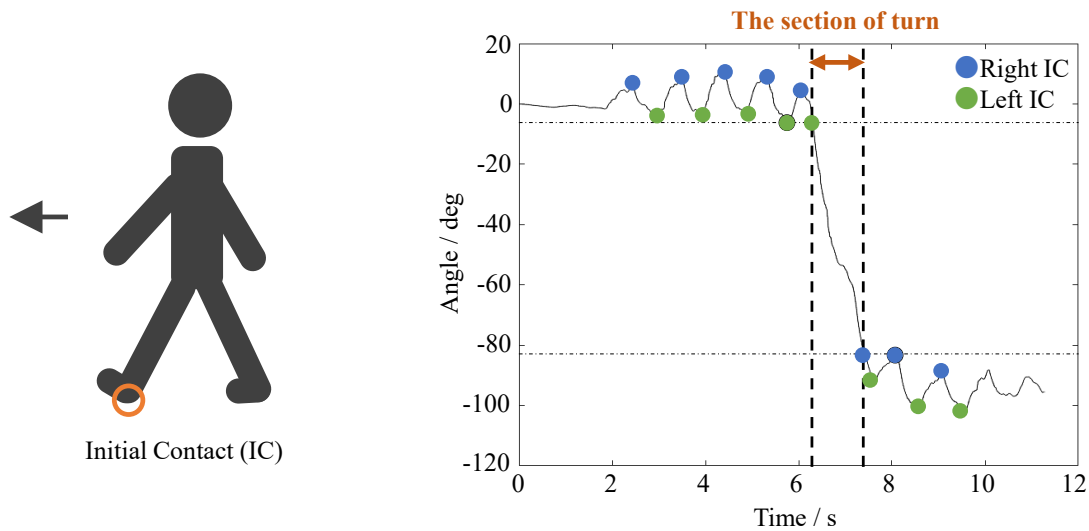


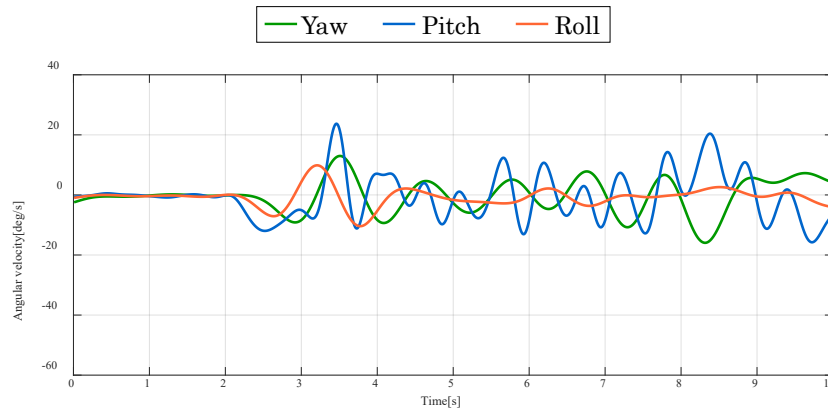
Figure 6 Definition of the section of 90-degree turn

Extraction of prediction parameters. According to the results, we found that the preliminary motion of the 90-degree turn was characterized by the asymmetry of the body’s lateral sway and the kinematic parameters caused by the rotational motion. Figure 7 shows an example of the comparison between a steady walking and a 90-degree turn on the angular velocity data at the head. In this case, the yaw and roll components of the head are extracted as prediction parameters, since their waveform is changing from 6.8 s, while the turn motion is starting at 8.2 s which is shown by the dashed line in Figure 7 (b). In the same way, we extracted the roll and yaw components of angular velocity on the upper body, and Y-axis acceleration of left and right shoulders and shanks as parameters which shows the changes of the waveform before the turn started. The list of extracted predictive parameters is shown in Table 1.

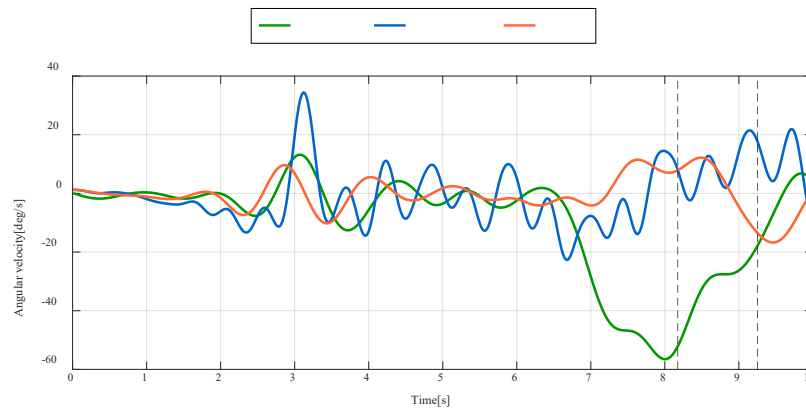
The turn motion is accomplished by slowing down the speed of motion in the straight direction and shifting the center of gravity to the new direction [16]. The significant preliminary movements were observed particularly in the angular velocity yaw and roll components of the head and upper trunk in the results. These suggest that the center of gravity shift of the upper body, including the head, occurs at the earliest stage.

Table 1 Extracted prediction parameters for 90-degree turns.

Observed data types	Positions of sensors
Angular velocity (roll and yaw)	Head, upper trunk
Acceleration (Y-axis)	Left and right shoulders, left and right shanks



(a) Steady walking



(b) 90-degree turn

Figure 7 Comparison of steady walking and 90-degree turn on the angular velocity of the head

Study limitations. The experimental space has no walls or screens, however, it is assumed that many of the turn motions are performed at corners in the actual situations. Thus, additional experiments in the actual environment such as corners are needed.

The age of the subjects in this study was biased and may yield different results in other age groups such as the elderly. Also, the number of participants was small, and reproducibility should be examined.

## Conclusion

In this study, we extracted effective parameters for 90-degree turn prediction, which is a major unsteady motion, using an IMU-based motion capture system to implement the motion prediction phase to the home robot in the “Biofied Building”. The results showed the possibility of the yaw and roll components of the head and upper trunk angular velocity, as well as *Y*-axis acceleration of shoulders and shanks to be used for the 90-degree turn prediction. Our findings can contribute to the further examination of turn motion prediction. The additional consideration for reproducibility confirmation with more participants including the other age groups will be our plan.

## References

- [1] Y. Kimura, A. Ogawa, A. Mita, Research on Motion Prediction in a House using a Markerless and Non-contact Sensor, *AIJ Journal of Technology and Design* 26(63) (2020) 793-797.  
<https://doi.org/10.3130/ajjt.26.793>
- [2] A. Ogawa, A. Mita, Recognition of human activities using depth images of Kinect for biofied building, *Sensors and Smart Structures Technologies for Civil, Mechanical, and Aerospace Systems 2015*, International Society for Optics and Photonics, 2015, p. 94351U.  
<https://doi.org/10.1117/12.2084079>
- [3] Y. Du, W. Wang, L. Wang, Hierarchical recurrent neural network for skeleton based action recognition, *Proceedings of the IEEE conference on computer vision and pattern recognition*, 2015, pp. 1110-1118.
- [4] Y. Horiuchi, Y. Makino, H. Shinoda, Computational foresight: Forecasting human body motion in real-time for reducing delays in interactive system, *Proceedings of the 2017 ACM International Conference on Interactive Surfaces and Spaces*, 2017, pp. 312-317.  
<https://doi.org/10.1145/3132272.3135076>
- [5] J. Martinez, M.J. Black, J. Romero, On human motion prediction using recurrent neural networks, *Proceedings of the IEEE Conference on Computer Vision and Pattern Recognition*, 2017, pp. 2891-2900. <https://doi.org/10.1109/CVPR.2017.497>
- [6] B.C. Glaister, G.C. Bernatz, G.K. Klute, M.S. Orendurff, Video task analysis of turning during activities of daily living, *Gait & posture* 25(2) (2007) 289-294.  
<https://doi.org/10.1016/j.gaitpost.2006.04.003>
- [7] R. Sedgman, P. Goldie, R. Ianssek, Development of a measure of turning during walking, *Advancing rehabilitation: Proceedings of the inaugural conference of the faculty of health sciences*. La Trobe University, 1994.
- [8] Z. He, Activity recognition from accelerometer signals based on wavelet-ar model, 2010 IEEE International Conference on Progress in Informatics and Computing, IEEE, 2010, pp. 499-502.
- [9] T. Iwamoto, D. Sugimoto, M. Matsumoto, A study of identification of pedestrian by using 3-axis accelerometer, *Journal of Information Processing* 55 (2014) 739-749.
- [10] J. Niki, Y. Asai, F. Sugiyama, H. Morimoto, E.B.L. III, E.G. Johnson, N. Kashiwa, I. Wada, The reliability of 6-axial sensor for body segmental movement of head, trunk and pelvis during straight walking and turning (in Japanese), *The journal of health sciences, Nihon Fukushi University* 19 (2016) 19-24.

- [11] M. Shigeta, A. Sawatome, H. Ichikawa, H. Takemura, Correlation between Autistic Traits and Gait Characteristics while Two Persons Walk Toward Each Other, *Advanced Biomedical Engineering* 7 (2018) 55-62. <https://doi.org/10.14326/abe.7.55>
- [12] NoitomLtd., Perception Neuron. <https://neuronmocap.com>. (Accessed 8.1 2020).
- [13] R. Sers, S. Forrester, E. Moss, S. Ward, J. Ma, M. Zecca, Validity of the Perception Neuron inertial motion capture system for upper body motion analysis, *Measurement* 149 (2020) 107024. <https://doi.org/10.1016/j.measurement.2019.107024>
- [14] A. Kondo, Basics of three-dimensional motion extraction Step 1: Measure straight/rotational motion with an accelerometer (in Japanese), *Interface* 42(9) (2016) 47-57.
- [15] D. Han, V. Renaudin, M. Ortiz, Smartphone based gait analysis using STFT and wavelet transform for indoor navigation, 2014 International Conference on Indoor Positioning and Indoor Navigation (IPIN), IEEE, 2014, pp. 157-166. <https://doi.org/10.1109/IPIN.2014.7275480>
- [16] A.E. Patla, S.D. Prentice, C. Robinson, J. Neufeld, Visual control of locomotion: strategies for changing direction and for going over obstacles, *Journal of Experimental Psychology: Human Perception and Performance* 17(3) (1991) 603. <https://doi.org/10.1037/0096-1523.17.3.603>

# Analysis of CFRP Laminates Properties under Different Layup Structure using Finite Element Analysis

Xinye Liu<sup>1,a,\*</sup>, Jinhui Cai<sup>1,b</sup>, Jiusun Zeng<sup>1,c</sup>, Fang Ye<sup>1,d</sup>, Wing Chiu<sup>2,e</sup>

<sup>1</sup>College of Metrology and Measurement Engineering, China Jiliang University, Hangzhou 310018, China

<sup>2</sup>Department of Mechanical and Aerospace Engineering, Monash University, Melbourne, 3800, Australia

<sup>a</sup> p1802085239@cjlu.edu.cn; <sup>b</sup> caijinhui@cjlu.edu.cn; <sup>c</sup> jszeng@cjlu.edu.cn;  
<sup>d</sup> 18a0205108@cjlu.edu.cn; <sup>e</sup> wing.kong.chiu@monash.edu

**Keywords:** Laminate, Finite Element Analysis, Laying Angle, Stacking Sequences

**Abstract.** In order to study the effect of the layup structure on the static strength and low-velocity impact strength of carbon fiber/epoxy composite (CFRP) laminates, theoretical simulation analysis under different laying angles have been carried out. In this study, Finite Element Analysis (FEA) models for different CFRP laminate specimens are created using ANSYS Workbench by changing the relative volume fraction of 0°, 45° and 90° plies in each specimen and their relative location. The FEA results revealed that the increase of relative volume of 90° ply will improve the impact the impact resistance performance, while the increase of relative volume of 45° ply will take the opposite effect. Moreover, when the relative volume fraction of 0°, 45° and 90° plies are the same, the strength performance of the laminate cannot be improved by changing the thickness of the outermost layer. The study illustrated the significant effects of different stacking sequences and laying angles on the tensile and flexural failure mechanisms in composite laminates, leading to some suggestions to improve the design of composite laminates.

## Introduction

Carbon fiber reinforced composite laminate is made of a series of unidirectional carbon fiber reinforced resin-based materials. It has the characteristics of heterogeneity, anisotropy, high intra-layer strength and high comprehensive strength, and has been widely used in military, aerospace and other fields[1,2]. However, this type of laminate has the disadvantages of low interlayer and vertical layer strength, so that the impact of runway gravel, hail and other objects on the composite laminate can easily cause its failure in the service environment[3]. Nowadays, laying angles between layers are mostly standard angles of 0°, ±45° and 90°. The performance of the laminate varies depending on the position of the laying angles. Therefore, the effect of the stacking angles and the stacking sequences on the performance of the laminate is studied[4].

Meng et al.[5] studied the effect of fiber layup on the bending failure of composite laminates by means of 3D finite element analysis. Kannan et al.[6] evaluated the tensile strength of 2D Carbon/Carbon laminates with a center-hole based on the FEA. However, Guo et al.[7] found that the distribution of interlayer stress around the void is related to the layer structure. In addition, the choice of failure criterion has an impact on the FEA of laminates, Naik et al.[8] proposed the minimum weight design of composite laminates using the failure mechanism based, maximum stress and Tsai-Wu failure criteria. And Akbulut et al.[9] proposed an optimization procedure to minimize thickness of laminated composite plates subject to in-plane loading, fiber orientation angles and layer thickness are chosen as design variables. On the other hands, Liu et al.[10]

explore the effects of different failure criterion including Puck, Hashin and Chang-Chang criterion on the dynamic progressive failure properties of carbon fiber composite laminates.

In this paper, the 3D model of CFRP laminates is established through ANSYS Workbench, static structure analysis and explicit dynamics analysis are performed on laminates of different layup structures to study the effect of lay angle and lay sequence on static strength and impact resistance of laminates influences. Then determine the failure criteria of the laminate and analyze its critical failure layer, which provides a theoretical basis for improving the performance of the composite laminate by optimizing the layer structure.

### Experiments

Theoretical Model of Laminates. Establishing 3D FEA models of composite laminates with different stacking sequences in ANSYS Workbench, as shown in Table 1. The size of the specimen is 250mm\*36mm\*2mm, a total of 16 layers and a single layer thickness of 0.125mm. The composite laminates considered in this paper are made of carbon/epoxy prepreg and has a symmetrical structure. The mechanical properties of each lamina are shown in Table 2.

*Table 1 Different lay-ups of the composite laminates*

Specimen Number	Stacking Sequences	Specimen Number	Stacking Sequences
Laminate1	[0 <sub>8</sub> ] <sub>s</sub>	Laminate5	[90/0/90/0/90 <sub>4</sub> ] <sub>s</sub>
Laminate2	[0/90/0/90/0 <sub>4</sub> ] <sub>s</sub>	Laminate6	[+45/0/-45/0/±45 <sub>2</sub> ] <sub>s</sub>
Laminate3	[0/+45/0/-45/0 <sub>4</sub> ] <sub>s</sub>	Laminate7	[90/90/0/0/90 <sub>4</sub> ] <sub>s</sub>
Laminate4	[0/+45/90/-45] <sub>2s</sub>	Laminate8	[+45/-45/0/0/±45 <sub>2</sub> ] <sub>s</sub>

Notes: The numeric subscripts indicate the number of layers stacked in each direction and the subscript [· · ·]<sub>s</sub> indicates that plies are symmetric about the midplane of the laminate.

*Table 2 The mechanical properties of each laminate*

$\rho/\text{kg} \cdot \text{m}^{-3}$	$E_1/\text{GPa}$	$E_2/\text{GPa}$	$E_3/\text{GPa}$	$G_{12}/\text{GPa}$
1490	121	8.6	8.6	4.7
$G_{13}/\text{GPa}$	$G_{23}/\text{GPa}$	$\mu_{12}$	$\mu_{13}$	$\mu_{23}$
4.7	3.1	0.27	0.27	0.4

In the low-velocity impact simulation, a cone bullet with a length to diameter ratio of 3:1 is used to impact the laminate. The bullet is made of structural steel. Its mass, density, elastic modulus and Poisson's ratio are 6.2g, 7850kg·m<sup>-3</sup>, 200GPa and 0.3 respectively.

Meshing and Constrained Boundary Conditions. Since the meshing structure and the degree of density will directly affect the accuracy of the results and the calculation time in ANSYS Workbench, the direct meshing method is selected according to the geometric characteristic of the 3D model of the composite laminate and the force characteristic. After the mesh is divided, referring to its skewness and orthogonal quality parameter, it is found that the optimal mesh sizes for laminates and bullets are 3mm and 2mm, respectively.

In the FEA, the static structural analysis and the explicit dynamic analysis are used. When the static structural module is used for analysis, the two short sides of the composite laminate are constrained and fixed, as shown in Fig. 1, the force is 2500N. While the four sides of the composite laminate are fully constrained when the explicit dynamics module is used for analysis, and the displacement and rotation angle in the three directions are all zero, that is, completely fixed. In

addition, the angular velocity and velocity of the bullet in other directions are constrained to zero in order to better extract the experimental results. Define the initial velocity of the bullet along the coordinate axis Z in the predefined field, and then define the output stress, strain, displacement and velocity in the field. The assembly diagram for the bullet impacting composite laminates is shown in Fig. 2. After the model is built, define the Tsai-Wu failure criterion and the maximum stress failure criterion in the ACP (Post) module to identify the main failure layers of the composite laminate, and view the stress and strain of each layer. The distance between the bullet and the laminate is 5mm, and the total movement time is 0.1ms.

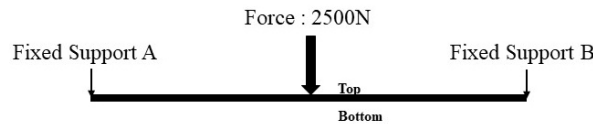


Fig. 1 Schematic graph of the static structural model

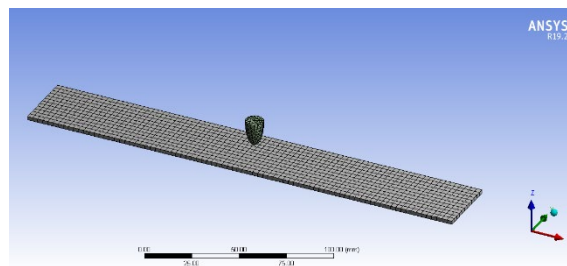


Fig. 2 Assembly diagram for the bullet impacting composite laminated plates

**Analysis**

When the 3D model of the laminate is established, the total deformation value of each laminate can be obtained as shown in Table 3. We use laminate1 as a reference to study the performance of laminates with different layer structure through static structural analysis and explicit dynamic analysis.

Table 3 The total deformation value of each laminate

Specimen Number	Total deformation value (mm)	Specimen Number	Total deformation value (mm)
Laminate1	74.754	Laminate5	84.975
Laminate2	53.225	Laminate6	71.809
Laminate3	50.055	Laminate7	100.94
Laminate4	68.303	Laminate8	80.829

Effect of Stacking Angle on Laminate Performance. Laminate1 only contains 0° plies and its total deformation is 74.754mm. Laminate2 is a part of 0° plies in laminate1 replaced with 90° plies, and its total deformation is reduced to 53.225mm. For laminate3, the 90° plies in laminate2 is replaced with 45° plies, and its total deformation is reduced to 50.055mm. If the laminate contains three ply angles at the same time such as laminate4, its total deformation is better than laminate1, but inferior to laminate2 and laminate3. From this we see that adding 45° plies to the laminate1 with only 0° plies show better bending resistance.

In the explicit dynamic analysis module, set the bullet velocity to 80m/s and the maximum equivalent stresses of laminate1 to laminate4 are 190.71MPa, 391.55MPa, 82.849MPa and 94.776MPa respectively, as shown in Fig. 3. From the laminate3 and laminate4, which can be seen that the equivalent stress of the 45° laminate between adjacent layers is smaller and the impact

resistance is stronger. Moreover, the curve of these two types of laminates are smoother under the continuous impact.

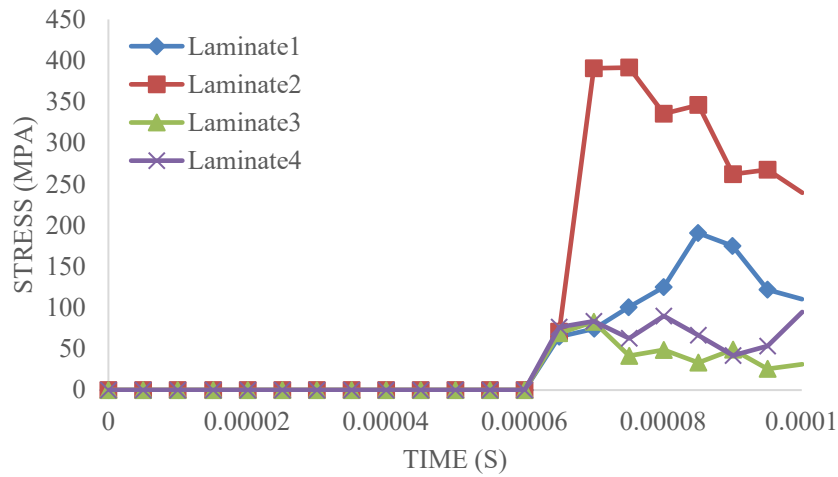


Fig. 3 Equivalent stress curve of laminate1 to laminate4

Effect of Stacking Sequence on Laminate Performance. Laminate2, laminate5 and laminate7 contain the same layer angle, but the stacking sequence has changed. Compared with laminate2, the relative volume fraction of 0° and 90° plies of the laminate5 is changed, and the fiber direction of the outermost layer is also changed. The total deformation of laminate2 is less than the total deformation of laminate5, which has better bending resistance. When changing the thickness of the outermost layer, but the relative volume fraction of 0° and 90° plies remains unchanged, such as laminate5 and laminate7. The total deformation of laminate7 is 100.94mm, which is more than laminate5. However, analyze laminate3, laminate6 and laminate8 in the same way, and they have the same layer angle. Laminate3 has the strongest bending resistance, followed by laminate6, while laminate8 is the worst. The larger the relative volume of 0°, the stronger the performance of the bending strength. And the bending resistance of the laminate cannot be improved by changing the thickness of the outermost layer.

In the explicit dynamic analysis module, set the bullet velocity to 80m/s and the equivalent stresses curve is shown in the Fig. 4 and Fig. 5. The relative volume fraction of 0° and 90° plies are different, such as laminate2 and laminate5. And the relative volume fraction of 0° and 45° plies are different, such as laminate3 and laminate6. Comparing the two types of laminates, it can be found that an increase in the relative volume of 90° ply will improve the impact the impact resistance performance, while an increase in the relative volume of 45° ply will be the opposite. However, when the thickness of the outermost layer of the laminate is increased, the equivalent stress of the laminate is basically not affected.

When the failure mode is set to the Tsai-Wu and the maximum stress failure criterion to observe the main failure modes and layer of each laminate, which can be found that the main failure mode of the laminate1 is the maximum stress failure. While the others are the Tsai-Wu failure mode. Moreover, the 90° ply is more prone to failure, as long as the laminate contains 90° ply, which determines the service life of the laminate. And it can be seen from the Fig.6 that the damage range of the laminate model with 90° ply will be larger and the stress is more dispersed. On the contrary, the stresses of the laminate containing 0° and 45° plies are mainly concentrated in the center of the model.

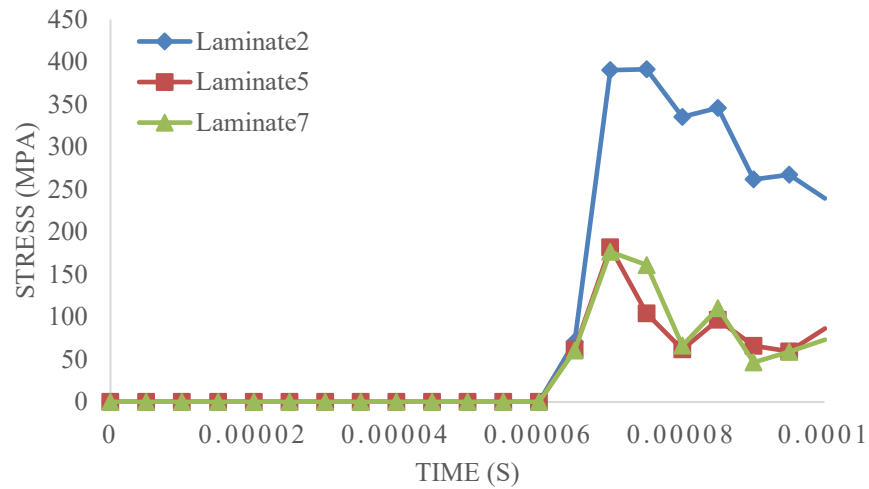


Fig. 4 Equivalent stress curve of laminate2, laminate5 and laminate7

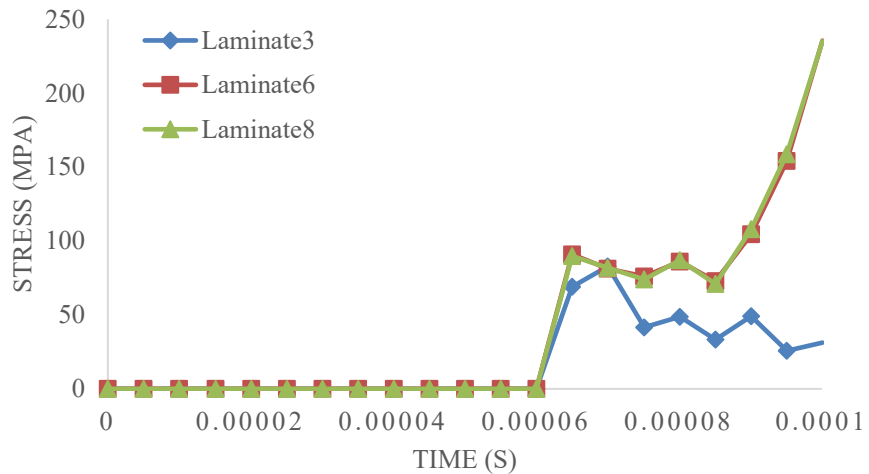


Fig. 5 Equivalent stress curve of laminate3, laminate6 and laminate8

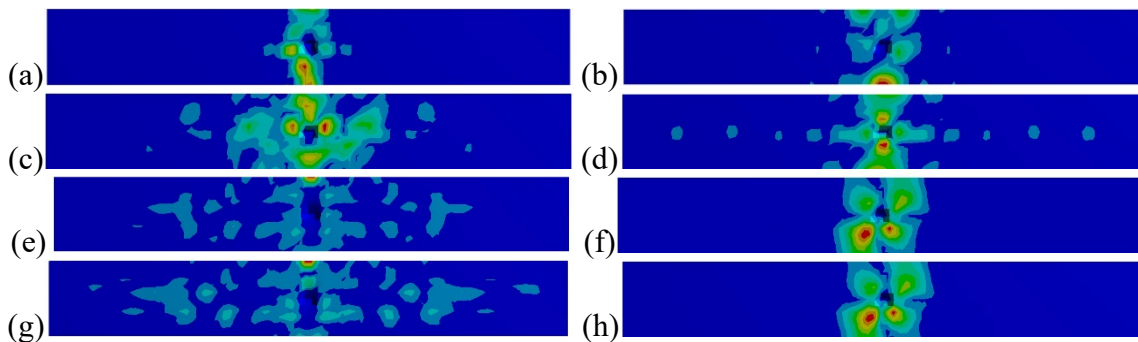


Fig. 6 Equivalent stress diagram of each laminate: (a)laminat1; (b)laminat2; (c)laminat3; (d)laminat4; (e)laminat5; (f)laminat6; (g)laminat7; (h)laminat8

**Conclusion**

According to the FEA results, the following conclusion can be drawn. (1) The laminate with only 0° and 45° plies and has a higher relative volume of 0° ply, which has the stronger bending

resistance performance. (2) It is found that when the relative volume fraction of  $0^\circ$ ,  $45^\circ$  and  $90^\circ$  plies are the same, the strength performance of the laminate cannot be improved by changing the thickness of the outermost layer from the static structure analysis and explicit dynamic analysis. And in all laminate models, the  $90^\circ$  layer is the key layer that is more prone to failure, while the probability of failure at  $0^\circ$  and  $45^\circ$  is basically the same. (3) The laminate with only two types of layer angles, either  $0^\circ$  and  $90^\circ$ , or  $0^\circ$  and  $45^\circ$ . The results show that the increase of relative volume of  $90^\circ$  ply will improve the impact resistance performance, while the increase of relative volume of  $45^\circ$  ply will be the opposite. Layer angle and layer sequence have an impact on the bending resistance and impact resistance of the laminate.

## References

- [1] Liu, DeFu, YongJun Tang, and W. L. Cong. "A review of mechanical drilling for composite laminates." *Composite structures* 94.4 (2012): 1265-1279.  
<https://doi.org/10.1016/j.compstruct.2011.11.024>
- [2] Zhang, Y. X., and C. H. Yang. "Recent developments in finite element analysis for laminated composite plates." *Composite structures* 88.1 (2009): 147-157.  
<https://doi.org/10.1016/j.compstruct.2008.02.014>
- [3] De Baere, Ives, Wim Van Paepegem, and Joris Degrieck. "Comparison of different setups for fatigue testing of thin composite laminates in bending." *International Journal of Fatigue* 31.6 (2009): 1095-1101. <https://doi.org/10.1016/j.ijfatigue.2008.05.011>
- [4] Kashtalyan, Maria, and Costas Soutis. "Analysis of local delaminations in composite laminates with angle-ply matrix cracks." *International Journal of Solids and Structures* 39.6 (2002): 1515-1537. [https://doi.org/10.1016/S0020-7683\(02\)00007-0](https://doi.org/10.1016/S0020-7683(02)00007-0)
- [5] Meng, Maozhou, et al. "3D FEA modelling of laminated composites in bending and their failure mechanisms." *Composite Structures* 119 (2015): 693-708.  
<https://doi.org/10.1016/j.compstruct.2014.09.048>
- [6] Kannan, V. Kamala, et al. "Finite element analysis and notched tensile strength evaluation of center-hole 2D carbon/carbon laminates." *Advanced Composite Materials* 20.3 (2011): 289-300.  
<https://doi.org/10.1163/092430410X550854>
- [7] Guo, Zhangxin, Xiaoping Han, and Xiping Zhu. "Finite element analysis of interlaminar stresses for composite laminates stitched around a circular hole." *Applied Composite Materials* 19.3-4 (2012): 561-571. <https://doi.org/10.1007/s10443-011-9234-7>
- [8] Naik, G. Narayana, S. Gopalakrishnan, and Ranjan Ganguli. "Design optimization of composites using genetic algorithms and failure mechanism based failure criterion." *Composite Structures* 83.4 (2008): 354-367. <https://doi.org/10.1016/j.compstruct.2007.05.005>
- [9] Akbulut, Mustafa, and Fazil O. Sonmez. "Optimum design of composite laminates for minimum thickness." *Computers & Structures* 86.21-22 (2008): 1974-1982.  
<https://doi.org/10.1016/j.compstruc.2008.05.003>
- [10] Liu, P. F., et al. "Finite element analysis of dynamic progressive failure of carbon fiber composite laminates under low velocity impact." *Composite Structures* 149 (2016): 408-422.  
<https://doi.org/10.1016/j.compstruct.2016.04.012>

# Seismic Fragility Analysis of Mid-Story Isolation Buildings

Xiao Song<sup>1,2,a</sup> and Songtao Xue<sup>1,3,b,\*</sup>

<sup>1</sup> Department of Architecture, Tohoku Institute of Technology, Sendai, Japan

<sup>2</sup> Department of Civil Engineering, Henan University, Kaifeng 475001, P.R. China

<sup>3</sup> Department of Disaster Mitigation for Structures, Tongji University, Shanghai, P.R. China

<sup>a</sup> songxiao@henu.edu.cn, <sup>b</sup> xuest@tohtech.ac.jp

**Keywords:** Mid-Story Isolation Buildings, Fragility Curves, Seismic Risk Assessment, Incremental Dynamic Analysis

**Abstract.** Seismic fragility analysis is essential for seismic risk assessment of structures. This study focuses on the damage probability assessment of the mid-story isolation buildings with different locations of the isolation system. To this end, the performance-based fragility analysis method of the mid-story isolation system is proposed, adopting the maximum story drifts of structures above and below the isolation layer and displacement of the isolation layer as performance indicators. Then, the entire process of the mid-story isolation system, from the initial elastic state to the elastic-plastic state, then to the limit state, is simulated on the basis of the incremental dynamic analysis method. Seismic fragility curves are obtained for mid-story isolation buildings with different locations of the isolation layer, each with fragility curves for near-field and far-field ground motions, respectively. The results indicate that the seismic fragility probability subjected to the near-field ground motions is much greater than those subjected to the far-field ground motions. In addition, with the increase of the location of the isolation layer, the dominant components for the failure of mid-story isolated structures change from superstructure and isolation system to substructure and isolation system.

## Introduction

Seismic isolation technology has proven to be one of the most effective strategies for seismic design of structures. The mid-story isolation technology, in which the isolation layer is installed at the inter-story rather than at the base of the building, is gaining popularity recently and can prevent the pounding between the isolation layer and moat walls. It is suitable for the retrofit of existing buildings and other buildings that are not suitable for base isolation. Previous researches demonstrate the effectiveness of the mid-story isolation system for vibration reduction performance under fortification earthquakes [1,2]. However, due to the uncertainty of earthquakes, the intensity of an actual earthquake can be considerably greater than that specified in the seismic code. In addition, near-field earthquakes, characterized by long-period and short-duration, can amplify the seismic responses of buildings and increase the damage probability of mid-story isolation buildings.

Earthquake damage investigations show that casualties are mainly caused by the collapse of building structures. At present, the most widely used approach for seismic performance evaluation is the incremental dynamic analysis [3,4]. Vamvatsikos et al. developed and applied the incremental dynamic analysis to predict collapse under the effect of scaled earthquake records [5]. Mansouri et al. conducted the seismic fragility analysis for 3- and 9-story base-isolated buildings [6]. It was found that the installation of the isolation layer decreased the amount of failure probability. On the other hand, seismic responses subjected to near-field earthquakes are different

from those subjected to far-field earthquakes. Bhandari et al. evaluated the seismic performance of a 10-story base-isolated RC frame under the far- and near-field earthquakes [7]. The results indicated that even for the low PGA value, the near-field earthquakes cause a high probability of damage to the base-isolated structure.

The above literature focused on the performance assessment of base-isolated structures and non-isolated structures. The seismic performance of the mid-isolated system under severe earthquakes is rarely studied, and the failure patterns under severe earthquakes have not been fully understood. To this end, nonlinear dynamic response analysis of a 10-story RC frame, designed according to the seismic design code of buildings in China, is carried out with incremental dynamic analysis (IDA), considering the different locations of the isolation layer for the mid-story isolation buildings. Fragility curves for mid-story isolation structures, corresponding to four performance levels, are generated subjected to near-field and far-field records.

### Fragility analysis method

The seismic fragility of the structures is the exceedance probability of certain damage state under the given intensity of earthquakes. For performance-based seismic design, failure means that the structure cannot meet a certain predetermined performance level. For this study, fragility analysis is performed based on IDA. The main analyzing steps are as follows: 1. Conduct a nonlinear dynamic analysis model for both base-fixed and mid-isolated structures. 2. Select seismic records that representing different site characteristics, select appropriate ground motion intensity measurements, and perform amplitude modulation for each ground motion. 3. Conduct the nonlinear time-history response analysis for under earthquake with a certain intensity, count the records of ground motions that exceed the certain performance level, the probability of exceeding under the intensity of ground motions can be obtained. 4. Scale the ground motions and repeat step 3, then the damage measurements and the exceeding probability under different ground motion intensity can be obtained. 5. Adopt a certain probability model, the fragility curves can be developed corresponding to different earthquake intensity and performance levels of structures.

According to related studies[8,9], it is assumed that the fragility function can be approximated by the log-normal probability distribution function and the fragility function can be defined as follows:

$$P(LS_i | IM = im) = P(DM \geq dm_i | IM = im) \quad (1)$$

Where  $LS$  is the limit state, and  $P(\bullet)$  is the probability of exceeding the given performance level with the earthquake intensity  $IM = im$ , and  $DM$  is the dynamic response of the structure. Consequently, the probability of exceeding the damage measure of the particular intensity can be expressed by Eq. (2)

$$P(DM | IM = im) = 1 - P(DM < dm_i | IM = im) = 1 - \Phi \left[ \frac{\ln dm_i - \mu_{\ln DM | IM=im}}{\sigma_{\ln DM | IM=im}} \right] \quad (2)$$

Where  $\mu$  is the logarithmic median value and  $\sigma$  is the standard deviation of  $DM$ , and  $\Phi(\bullet)$  is the standard normal cumulative distribution function.  $\mu$  and  $\sigma$  can be calculated from IDA. Then, the seismic fragility curves under near- and far-field ground motions corresponding to different performance levels can be obtained.

### Damage measures and damage states

In order to assess the structural performance levels under different intensity ground motions, the inter-story drift of the structures, the deformation, and the stress of the isolation bearings are selected as the damage measures to perform the fragility analysis with different performance

levels. According to the methodology defined in the Federal Emergency Management Agency [10] and the seismic design code of buildings in China, structural performance levels against earthquakes can be clarified into operational, immediate occupancy, life safety, and collapse prevention performance levels. Corresponding to the four performance levels, the damage states are defined as slight (DS1), moderate (DS2), extensive (DS3), and collapse (DS4), respectively. Table 1 shows the damage states thresholds for different damage measures.

Table 1. Damage states thresholds for different damage measures

Damage measures	Damage states			
	Slight (DS1)	Moderate (DS2)	Extensive (DS3)	Collapse (DS4)
Inter-story drift of structures	1/550	1/275	1/150	1/50
Displacement and stress of isolation bearings	--	--	$0.6D_{\max}$ [ $\sigma_{\min}, \sigma_{\max}$ ]	$1.0D_{\max}$ [ $\sigma_{\min}, \sigma_{\max}$ ]

Note:  $D_{\max}$  is the maximum isolator design displacement,  $D_{\max} = \text{Min} \{0.55D, 3T_r\}$ , where  $D$  is the diameter of isolation bearing,  $T_r$  is the total thickness of the rubber layer, and  $\sigma_{\min}, \sigma_{\max}$  are the thresholds of the stress of isolation bearing.

### Selection of earthquake records

The selection of earthquake ground motion records is essential for IDA and fragility analysis. Two types of earthquake ground motions, recommended by FEMA P695[10], are selected, including 13 near-field and 13 far-field records. The elastic acceleration response spectra of selected earthquake records are shown in Fig. 1, and the basic information is tabulated in Tables 2-3.

Table 2. Basic information of selected ground motions (Far-Field records set)

No	Event	Station	Year	$M_w$	PGA(g)	Component
1	San_Fernando	LA-Hollywood_Stor_FF	1971	6.6	0.210	PEL090
2	San_Fernando	LA-Hollywood_Stor_FF	1971	6.6	0.174	PEL180
3	Friuli-Italy-01	Tolmezzo	1976	6.5	0.315	A-TMZ270
4	Imperial_Valley-06	El_Centro_Array_#11	1979	6.5	0.380	H-E11230
5	Superstition_Hills-02	Poe_Road_(temp)	1987	6.5	0.446	B-POE270
6	Cape_Mendocino	Rio_Dell_Overpass-FF	1992	7	0.385	RIO270
7	Cape_Mendocino	Rio_Dell_Overpass-FF	1992	7	0.549	RIO360
8	Northridge-01	Beverly_Hills-14145_Mulhol	1994	6.7	0.416	MUL009
9	Northridge-01	Canyon_Country-W_Lost_Cany	1994	6.7	0.410	LOS000
10	Northridge-01	Canyon_Country-W_Lost_Cany	1994	6.7	0.482	LOS270
11	Kobe-Japan	Nishi-Akashi	1995	6.9	0.503	NIS090
12	Chi-Chi-Taiwan	CHY101	1999	7.6	0.440	CHY101-N
13	Duzce-Turkey	Bolu	1999	7.1	0.728	BOL000

Table 3. Basic information of selected ground motions (Near-Field records set)

No	Event	Station Name	Year	$M_w$	PGA(g)	Component
1	Imperial_Valley-06	El_Centro_Array_#7	1979	6.5	0.3375	H-E07140
2	Superstition_Hills-02	Parachute_Test_Site	1987	6.5	0.3772	B-PTS315
3	Erzican-Turkey	Erzincan	1992	6.7	0.4955	ERZ-EW
4	Erzican-Turkey	Erzincan	1992	6.7	0.5153	ERZ-NS
5	Cape_Mendocino	Petrolia	1992	7	0.5896	PET000
6	Cape_Mendocino	Petrolia	1992	7	0.6624	PET090
7	Northridge-01	Rinaldi_Receiving_Sta	1994	6.7	0.8252	RRS228
8	Northridge-01	Rinaldi_Receiving_Sta	1994	6.7	0.4865	RRS318
9	Northridge-01	Sylmar-Olive_View_Med_FF	1994	6.7	0.8433	SYL360
10	Kocaeli-Turkey	Izmit	1999	7.5	0.2195	IZT090
11	Kocaeli-Turkey	Izmit	1999	7.5	0.1521	IZT180
12	Duzce-Turkey	Duzce	1999	7.1	0.3481	DZC180
13	Duzce-Turkey	Duzce	1999	7.1	0.5353	DZC270

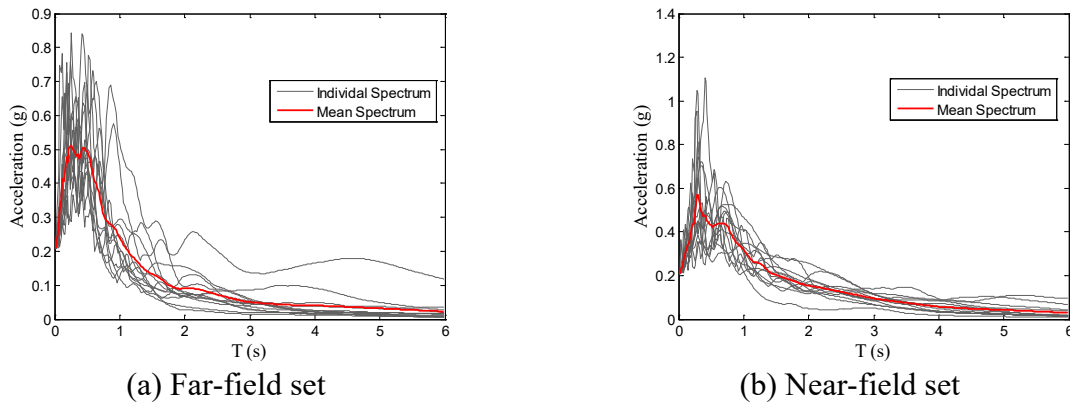


Fig. 1. Acceleration response spectra of selected earthquake ground motion records

### Fragility analysis and risk assessment

#### Structural models for the performance evaluation

In this study, a typical 10-story RC frame building designed according to the seismic design code of buildings in China is selected as the analytical model. The cross-section of columns is 700×700mm, and the cross-section of beams is 250×600mm for all floors. The height is 3.9m for the first floor and 3.6m for other floors. The gravity loads are represented by dead loads 5.0kN/m<sup>2</sup>, live loads 0.5kN/m<sup>2</sup>, for the top floor; dead loads 4.5kN/m<sup>2</sup>, live loads 2.0kN/m<sup>2</sup>, for the typical floors. The frame at the center is chosen for numerical analysis.

To investigate the discrepancies of performance of mid-story isolation structures and non-isolated structure, as well as to reveal the influence of the position of the seismic isolation layer on the structural performance, three numerical models denoted as specimens Non-Iso, Iso-2, and Iso-5, are designed. The isolation layers of Iso-2 and Iso-5 are respectively installed on the top of the 2nd story and 5th story. For mid-isolated structures, stories below and above the isolation layers are denoted as superstructure (Sup) and substructure (Sub). Fig. 2 shows the details of the studied buildings. Bearings adopted for Iso-2 and Iso-5 are LRB 700 and LRB 600 respectively, designed according to the seismic design code in China.

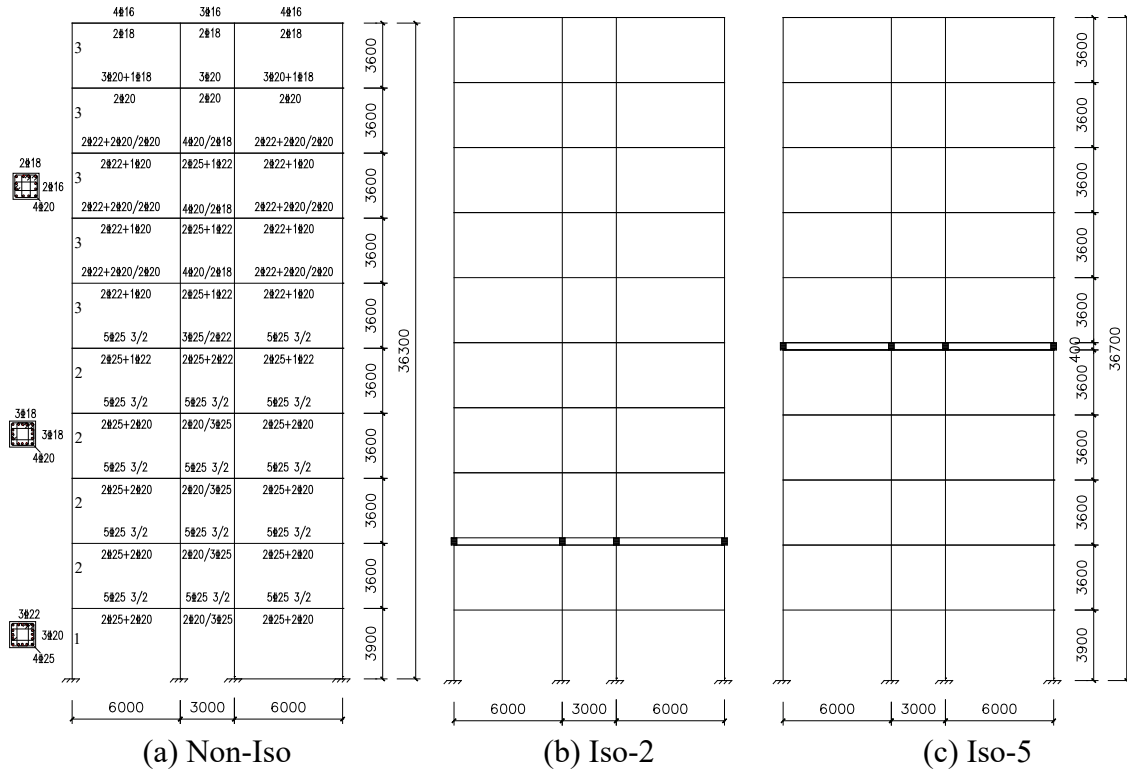


Fig. 2. Structural configuration

Structural dynamic analysis for both non-isolated and mid-story isolation structures is conducted with OpenSees software. Beams, columns, and isolation bearings are modeled as Beam with Hinges, forceBeamColumn, and zeroLength elements. The fundamental periods of the Non-Iso, Iso-2, and Iso-5 are 1.64s, 2.56s, and 2.38s respectively. It should be noted the dynamic characteristics results of mid-story isolation structures are deduced corresponding to the equivalent stiffness (100% shear deformation) of bearings.

*Result and discussion*

Incremental dynamic analyses are performed to evaluate the seismic performance of reinforced concrete frames subjected to far-field and near-field earthquakes. In this study, the PGA level is adopted as the intensity measure for earthquake and the scale factors for PGA vary from 0.05g to 1.0g.

The maximum inter-story drifts obtained for the Iso-2 and Iso-5 under far-field and near-field ground motions are plotted in Figs. 3-4 respectively. Each data point represents the response of nonlinear dynamic time-history analysis. DS1, DS2, DS3, and DS4 respectively represent slight, moderate, extensive, and collapse damage state. Moreover, the maximum inter-story drifts contained that of both superstructure and substructure. It can be observed from Figs. 3-4 that, the seismic responses with different locations of the isolation layer under near-field records are significantly larger than that subjected to the far-field records. It indicates that the impulse effect of the near-field earthquake enlarged the structural responses. Furthermore, with the increase of the location layer, there is a noticeable increase in maximum inter-story drifts.

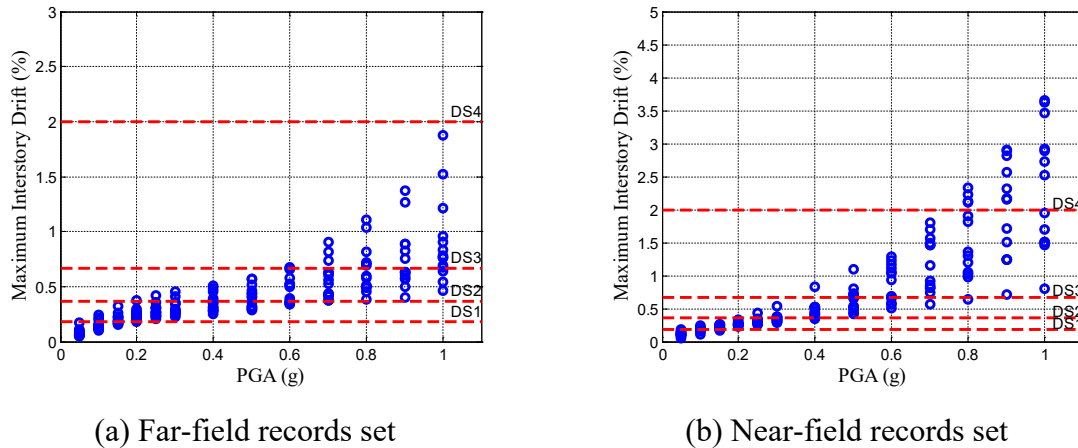


Fig. 3. Distribution of maximum inter-story drift (Iso-2)

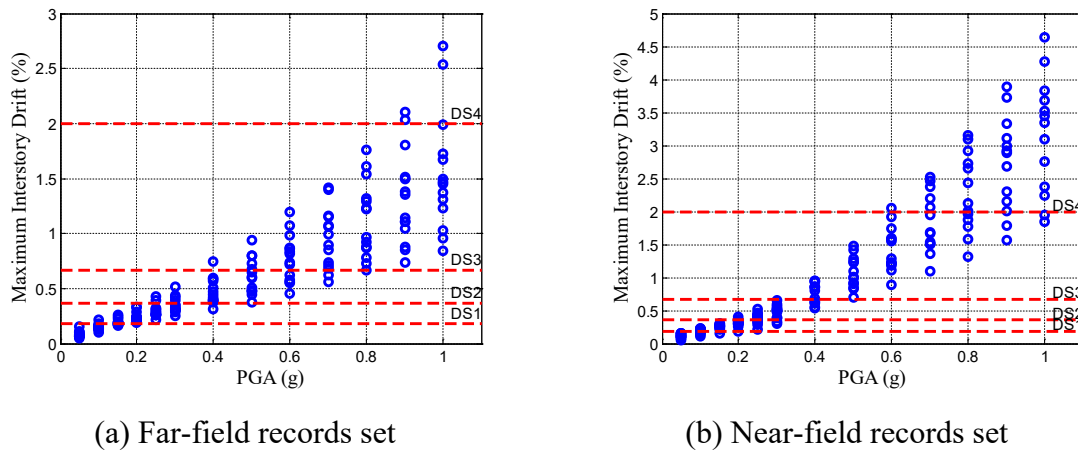


Fig. 4. Distribution of maximum inter-story drift (Iso-5)

The probability density function can be obtained from the statistics of the response data, and then the integration is performed to obtain the damage probability corresponding to each damage state, thereby the seismic fragility curves at four performance levels defined in Table 1 can be depicted. It is found that the stress bearings vary within the allowable range, and hence are not discussed here.

Comparisons of fragility curves between Non-Iso and Iso-2 are shown in Fig. 5, where Non-Iso, Iso-Sub, Iso-Sup, and Iso-LRB represent the non-isolated structure, substructure, superstructure, and isolation layer of the mid-isolated structures, while N and F represent near-field and far-field ground motions respectively. It can be seen that as the structural damage state changes from the slight to the collapsed state, the structural vulnerability curve becomes flat and the probability of damage becomes smaller, which conforms to the structural principle. Regardless of the damage state, the damage probability subjected to the near-field ground motions is much greater than that under the far-field ground motions. The damage probability of Iso-2 decreases significantly compared to Non-Iso, which indicates the efficiency of the mid-story isolation technology. It is important to note that the damage probability of Iso-LRB and Iso-Sup is larger than Iso-Sub in the case of extensive and collapse damage states, as depicted in Figs. 5(c)-(d). Thus, the failure of the structure is mainly caused by the failure of the superstructure and the isolation layer.

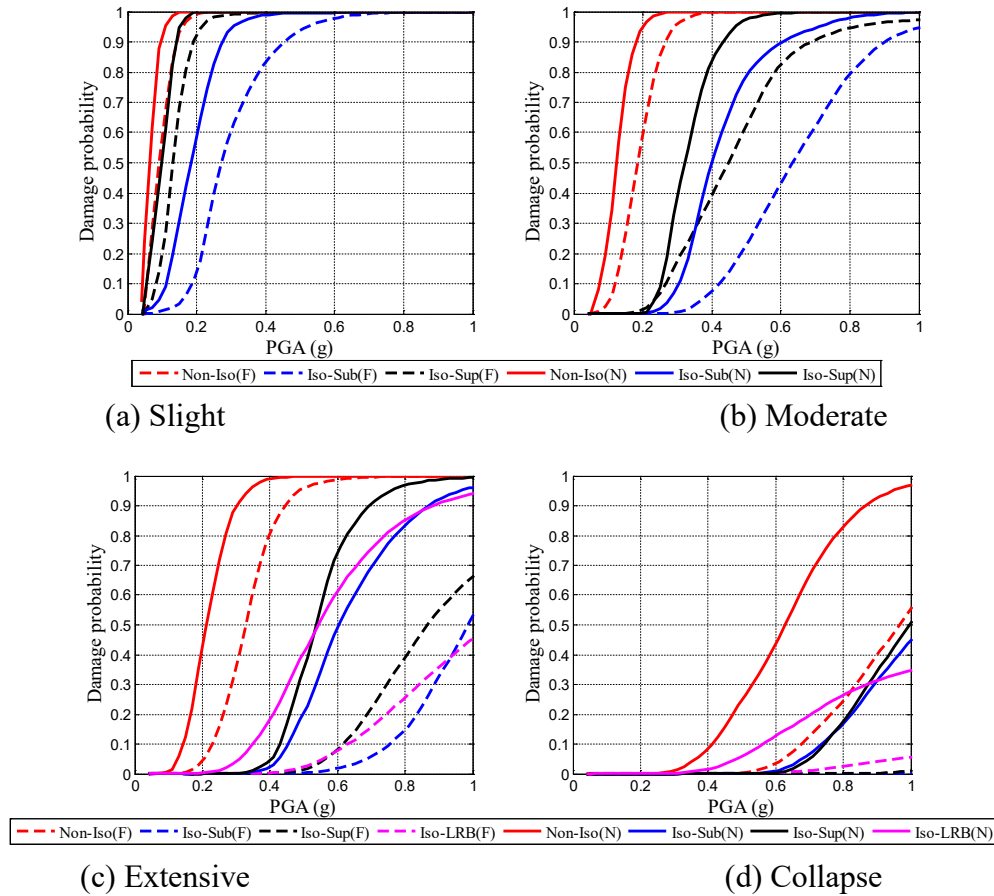


Fig. 5. Comparison of fragility curves between Non-Iso and Iso-2

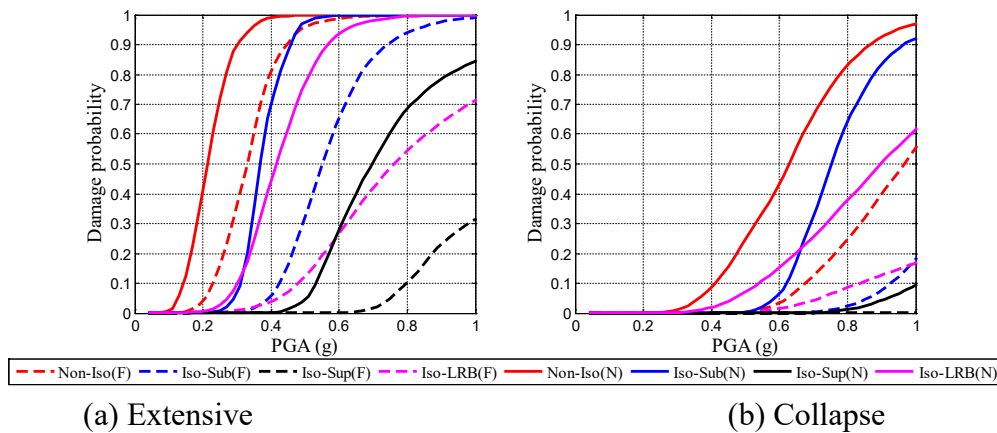


Fig. 6. Comparison of fragility curves between Non-Iso and Iso-5

To investigate the influence of the location of the isolation layer on the performance of mid-story isolation structures, fragility curves for the extensive and collapse damage levels are summarized in Fig. 6. Comparing the results with Fig. 5, it can be seen that the trend of Iso-2 and Iso-5 in the damage probability for different sets of ground motions is almost the same, while the distribution of the damage probability of different parts of the structure are changed when the isolation layer varies from 2nd story to 5th story. In addition, it is obvious that the damage

probability of Iso-LRB and Iso-Sub is larger than Iso-Sup in the case of extensive and collapse states, which indicates that the collapse of Iso-5 is mainly governed by the failure of the isolation layer and substructure.

### Conclusion

In this study, the results obtained from the fragility analysis of two mid-story isolation structures and non-isolated structure, lead to the following conclusion:

1. By installing the isolation layer into the structures, the seismic responses of both superstructure and substructure are effectively reduced, and the damage probabilities of the mid-story isolation structures are significantly reduced comparing to the corresponding non-isolated structure. The same trend can be observed when subjected to different sets of ground motions.

2. The responses and the damage probability of the mid-isolation structures subjected to the near-field earthquakes are much greater than those subjected to the far-field earthquakes.

3. For the structure with a high location of the isolation layer, the mid-story isolated structure still has the desired isolating effect. However, the damage probability of mid-story isolated structures is correlated with the location of the isolation system. With the increase of the location of the isolation layer, the dominant parts for the failure of mid-story isolated structures change from superstructure and isolation system to substructure and isolation system.

### References

- [1] Tsuneki Y, Torii S, Murakami K, et al, Middle-story isolated structural system of high-rise building, The 14th World Conference on Earthquake Engineering, Beijing, China, 2008.
- [2] Nakamizo D, Koitabashi Y, Structural Design of Mid-Story Isolated High-Rise Building-Roppongi Grand Tower, International Journal of High-Rise Buildings, 2018, 7(3): pp.233-242.
- [3] Kircil M S, Polat Z. Fragility analysis of mid-rise R/C frame buildings. Engineering Structures, 2006, 28(9), pp.1335-1345. <https://doi.org/10.1016/j.engstruct.2006.01.004>
- [4] Bakalis K, Vamvatsikos D. Seismic Fragility Functions via Nonlinear Response History Analysis. Journal of structural engineering, 2018, 144(10):04018181.1-04018181.15. [https://doi.org/10.1061/\(ASCE\)ST.1943-541X.0002141](https://doi.org/10.1061/(ASCE)ST.1943-541X.0002141)
- [5] Vamvatsikos D, Cornell C A. Incremental dynamic analysis. 2002, 31(3), pp.491-514. <https://doi.org/10.1002/eqe.141>
- [6] Mansouri I, Ghodrati Amiri G, Hu J W, et al. Seismic fragility estimates of LRB base isolated frames using performance-based design. Shock and Vibration, 2017. <https://doi.org/10.1155/2017/5184790>
- [7] Bhandari M, Bharti S D, Shrimali M K, et al. Seismic fragility analysis of base-isolated building frames excited by near-and far-field earthquakes. Journal of Performance of Constructed Facilities, 2019, 33(3): 04019029. [https://doi.org/10.1061/\(ASCE\)CF.1943-5509.0001298](https://doi.org/10.1061/(ASCE)CF.1943-5509.0001298)
- [8] Shome N. Probabilistic seismic demand analysis of nonlinear structures, 1999.
- [9] Miranda E, Aslani H. Probabilistic response assessment for building-specific loss estimation. Pacific Earthquake Engineering Research Center, 2003.
- [10] Applied Technology Council. Quantification of building seismic performance factors. US Department of Homeland Security, FEMA, 2009.

# Optimal Design of Tuned Mass Damper Inerter for Base-Isolated Buildings

Dawei LI<sup>1,a,\*</sup>, Kohju IKAGO<sup>1,b</sup>, and Songtao XUE<sup>2,c</sup>

<sup>1</sup>International Research Institute of Disaster Science, Tohoku University, Sendai 980-8572, Japan

<sup>2</sup>Department of Architecture, Tohoku Institute of Technology, Sendai 982-8577, Japan

<sup>a</sup>lidaweicc123@163.com, <sup>b</sup>ikago@irides.tohoku.ac.jp, <sup>c</sup>xuest@tohtech.ac.jp

**Keywords:** Tuned Mass Damper Inerter, H2-Norm, Optimal Design, Stationary Analysis

**Abstract.** Tuned mass dampers (TMD) are installed in base-isolated building to suppress the excessive isolator displacement and acceleration responses of primary structure. By incorporating an inerter element into the original configuration, the seismic performance of TMD is significantly enhanced. In this work, optimal solutions of tuned mass damper inerter (TMDI) for improving the seismic resilience of base-isolated building are proposed. The analytical formulations of optimal design of TMDI are respectively developed to minimize the H<sub>2</sub> norm of the displacement of primary structure relative to the base floor and the isolator displacement. The performance of presented optimal methods are validated by using stationary responses under the stochastic excitations. Additionally, the seismic performance of TMDI with parameters obtained from the proposed method are compared with the established methods.

## Introduction

Base isolation (BI) system has been widely employed in public building which is of importance to keep its' functionality [1-2] (e.g. hospital, disaster prevention center) and prevent catastrophic results. The mechanical characteristic of BI is to decouple the resonance of building and ground motions by inserting a very soft base layer between them [3]. Although, BI technique presents attractive benefits in mitigating the earthquake responses of primary structure, some detrimental features, e.g. serious concentration of base isolators deformation, need to be carefully taken into account. In order to reduce the excessive displacement of base floor, the so called "hybrid base isolation system", which consists of traditional base isolators (e.g. lead rubber bearing, friction peculium slide and natural rubber bearing etc.) and additional damping devices, was developed.

It was mentioned that the effectiveness of displacement dependent damper is less than the viscous damper because the adverse contribution of higher modes. Furthermore, it is worthy to note that a high damping ratio of viscous damper may lead to an excessive inter-story drift and acceleration response [4]. Although an active or semi-active damper may overcome above difficulties, it requires stable power supply and active feedback system might be hardly satisfied during a major earthquake. Alternatively, a tuned mass damper, which is able to simultaneously mitigate the displacement of base floor and acceleration response, are recommended to work with base isolators to suppress the isolator displacement [5].

Although, the effectiveness of TMD has been confirmed in previous studies, it should be noted that a large mass ratio is necessary to achieve the designated performance target. An inerter element, which amplifies the mass effect by using the relative motion of two terminals, can be employed to enhance the seismic performance of traditional TMD. A novel configuration consists of a TMD and an inerter element which is called tuned mass damper inerter (TMDI) has been proposed to mitigate the excessive displacement of a single-degree-of-freedom (SDOF) system [6].

With an excellent seismic performance for mitigating the excessive displacement responses and suppressing the acceleration responses, TMDI was gradually popularized in suppressing isolator displacement demand in a BI system [7].

For implementation of TMDI in a BI system, the optimal solutions with numerical optimization algorithm were carried out in [7]. Although, the effectiveness of optimal results has been validated by a lot of benchmark models, it should be noted that the numerical results cannot be readily applied to practical design, because most of practicing engineers are unfamiliar with those methods to derive optimal designs. Thus, an analytical formulation of optimal parameters needs to be developed to fit the request of practical design. Marian and Giaralis [6, 8] presented two analytical formulae to minimize the  $H_2$  and  $H_\infty$  norms of displacement responses of a SDOF system under white-noise excitation and harmonic excitation. An analytical formula which consider the characteristics of a BI system was derived to suppress the excessive isolator displacement by Matteo *et al.* [9].

In this work, two closed-form formulae for suppressing the acceleration of primary structure and excessive isolator displacement were developed. Moreover, an investigation of the influences of external excitation on the optimal solutions were discussed with a series of numerical calculations. To access the effectiveness of proposed method for improving the seismic performance of a BI system under stationary excitation, a performance comparison is carried out in Section 7.

### BI system equipped with a TMDI

On the basis of Kelly’s work [4], a BI system can be simplified as a 2-degree-of-freedom (2-DOF) system as shown in Fig. 1(a).  $m_s$  and  $m_b$  denote the mass of the primary structure and the basement, respectively. The stiffness of primary structure and basement are respectively represented by  $k_s$  and  $k_b$ .  $c_s$  and  $c_b$  are used to denote the inherent damping of primary structure and base isolators. As shown in Fig. 1(b), a TMDI can be simplified to a tuned inerter damper (TID) by removing the physical mass. On the other hand, TMDI is an advanced TMD whose control effect is significantly improved by connecting a ground linked inerter. As mentioned above, we expect to develop a comprehensive closed-form formula of TMDI that can represent TID or TMD by setting the physical mass or inertance as zero. Assume the aforementioned 2-DOF system is subjected to an external excitation  $\ddot{x}_0$ , the governing equations of this hybrid BI system can be expressed as,

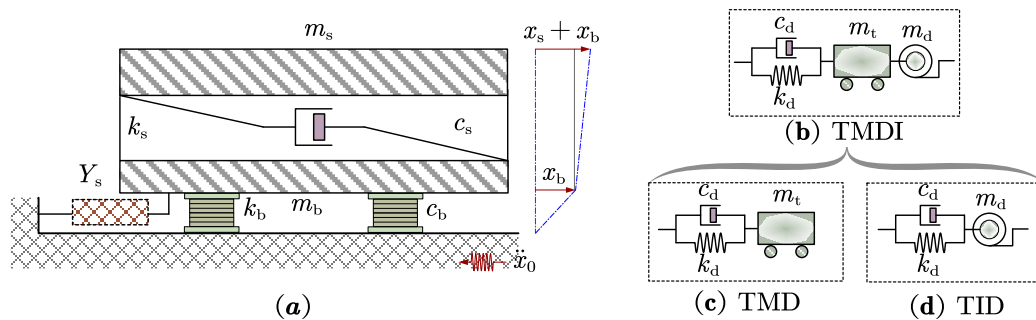


Fig. 1 (a) Schematic of BI system equipped with (b) TMDI, (c) TMD and (d) TID.

$$\begin{aligned}
 m_s \ddot{x}_b + m_s \ddot{x}_s + c_s \dot{x}_s + k_s x_s &= -m_s \ddot{x}_0 \\
 m_{tot} \ddot{x}_b + m_s \ddot{x}_s + c_b \dot{x}_b + k_b x_b + c_d (\dot{x}_b - \dot{x}_d) + k_d (x_b - x_d) &= -m_{tot} \ddot{x}_0 \\
 m_d \ddot{x}_d + m_t \ddot{x}_d + c_d (\dot{x}_d - \dot{x}_b) + k_d (x_d - x_b) &= -m_t \ddot{x}_0
 \end{aligned}
 \tag{1}$$

where,  $m_{tot} = m_s + m_b$  denote the total mass of the BI system,  $m_d$  and  $m_t$  denote the apparent mass of the inerter element and the physical mass of the TMD,  $c_d$  and  $k_d$  denote the damping coefficient and stiffness of the TMDI,  $x_s$ ,  $x_b$  and  $x_d$  denote the relative displacement of the primary structure, isolator and TMDI. The dot over  $x_s$ ,  $x_b$  and  $x_d$  denote the differential operation with regard to the time  $t$ . With introducing the following parameters,

$$\begin{aligned} \mu_s &= \frac{m_s}{m_{tot}}, \mu_d = \frac{m_d}{m_{tot}}, \mu_t = \frac{m_t}{m_{tot}}, \omega_s = \sqrt{\frac{k_s}{m_s}}, \omega_b = \sqrt{\frac{k_b}{m_{tot}}}, \omega_d = \sqrt{\frac{k_d}{m_d + m_t}} \\ \mu_e &= \mu_d + \mu_t, \beta_s = \frac{\omega_s}{\omega_b}, \beta_d = \frac{\omega_d}{\omega_b}, \zeta_s = \frac{c_s}{2\omega_s m_s}, \zeta_b = \frac{c_b}{2\omega_b m_{tot}}, \zeta_d = \frac{c_d}{2\omega_b m_{tot}} \end{aligned} \quad (2)$$

the Laplace transformation of Eq. (1) is rewritten as,

$$\begin{aligned} (\beta_s^2 - \beta_0^2 + 2i\beta_0\beta_s\zeta_s)\mu_s\omega_b^2 X_s - \beta_0^2\mu_s\omega_b^2 X_b + \mu_s X_0 &= 0 \\ -\beta_0^2\mu_s\omega_b^2 X_s + (\beta_d^2\mu_e - \beta_0^2 + 1 + 2i\beta_0\zeta_b + 2i\beta_0\zeta_d)\omega_b^2 X_b - (\beta_d^2\mu_e + 2i\beta_0\zeta_d)\omega_b^2 X_d + X_0 &= 0 \\ -(\beta_d^2\mu_e + 2i\beta_0\zeta_d)\omega_b^2 X_b + [2i\beta_0\zeta_d + (\beta_d^2 - \beta_0^2)\mu_e]\omega_b^2 X_d + \mu_t X_0 &= 0 \end{aligned} \quad (3)$$

where,  $X_s$ ,  $X_b$  and  $X_d$  denote the Laplace transformation of  $x_s$ ,  $x_b$  and  $x_d$ . Frequency ratio of external excitation is defined as  $\beta_0 = \omega_0/\omega_b$ , where  $\omega_0$  is the input frequency of excitation. For simplicity of derivation, inherent damping ratio of primary structure and base isolator are assumed as  $\zeta_s = 0$ ,  $\zeta_b = 0$ . Thus, the displacement amplification ratio  $X_s/X_0$  and  $X_b/X_0$  are expressed as,

$$\begin{aligned} \frac{X_s}{X_0} &= \frac{1}{\omega_b^2} \frac{-2i\beta_0^3\mu_d\zeta_d - \mu_e(\beta_d^2\mu_d + 1)\beta_0^2 + 2i\beta_0\zeta_d + \beta_d^2\mu_e}{a_0\beta_0^6 + a_1\beta_0^5 + a_2\beta_0^4 + a_3\beta_0^3 + a_4\beta_0^2 + a_5\beta_0 + a_6} \\ \frac{X_b}{X_0} &= \frac{1}{\omega_b^2} \frac{-\mu_e(\mu_s - 1)\beta_0^4 + 2i\zeta_d(\mu_s - b_0)\beta_0^3 + \mu_e(\beta_d^2(\mu_s - b_0) - \beta_s^2)\beta_0^2 + 2i\zeta_d\beta_s^2 b_0\beta_0 + \beta_s^2\beta_d^2\mu_e b_0}{a_0\beta_0^6 + a_1\beta_0^5 + a_2\beta_0^4 + a_3\beta_0^3 + a_4\beta_0^2 + a_5\beta_0 + a_6} \end{aligned} \quad (4)$$

In which, all terms of coefficients in Eq. (4) are given as,

$$\begin{cases} a_6 = \beta_s^2\beta_d^2\mu_e & a_5 = 2i\beta_s^2\zeta_d \\ a_4 = -\beta_s^2\beta_d^2\mu_e(\mu_e + 1) - \mu_e(\beta_s^2 + \beta_d^2) & a_3 = -2i\zeta_d(\beta_s^2\mu_e + \beta_s^2 + 1) \\ a_2 = \beta_d^2\mu_e^2 - \beta_d^2\mu_s\mu_e + \beta_s^2\mu_e + \beta_d^2\mu_e + \mu_e & a_1 = 2i\zeta_d(1 + \mu_e - \mu_s) \\ a_0 = \mu_e(\mu_s - 1) & b_0 = \mu_t + 1 \end{cases} \quad (5)$$

Consider the stochastic properties of earthquake ground motions, external excitation can be directly expressed as a sequence of white-noise. According to the basic concepts of stochastic vibration theory, the covariance of system response is obtained from an integrated power spectral density function (PSDF) over entire frequency domain. Therefore, the  $H_2$  norm of above two performance indicators can be expressed as an integral of PSDF of a white-noise  $S_w$  in frequency domain.

$$PI(X_s/X_0) = S_w\omega_b \int_{-\infty}^{\infty} |X_s/X_0|^2 d\beta_0, \quad PI(X_b/X_0) = S_w\omega_b \int_{-\infty}^{\infty} |X_b/X_0|^2 d\beta_0. \quad (6)$$

In  $H_2$  norm-based optimization, the objective function is the covariance of system responses. The optimization procedure of frequency and damping ratios of TMDI with respect to above two performance indicators are illustrated in the following sections.

**Optimal solution for acceleration response of primary structure**

On the basis of Spanos’ pioneering works, the first integral in Eq. (6) can be expressed with following analytical formula,

$$PI\left(\frac{X_s}{X_0}\right) = \frac{S_w}{\omega_b^3} \frac{\beta_s^4 \mu_e^2 \phi_{s,1} + \beta_s^2 \mu_e^2 \phi_{s,2} \beta_d^2 + \mu_e^2 \phi_{s,3} \beta_d^4 + 4 \beta_s^2 \phi_{s,4} \zeta_d^2}{2 \beta_s^{10} \mu_s \mu_e^2 \zeta_d} \tag{7}$$

where, the related coefficients are,

$$\begin{aligned} \phi_{s,1} &= \beta_s^2 \mu_s + 1 \\ \phi_{s,2} &= \beta_s^4 \mu_s (\mu_d - 2 - \mu_t) + 2 \beta_s^2 (\mu_d - 2 \mu_s) - 2 \\ \phi_{s,3} &= \beta_s^6 \mu_s b_0^2 + \beta_s^4 ((\mu_d - \mu_s)^2 + 2 \mu_s b_0) + \beta_s^2 (3 \mu_s - 2 \mu_d) + 1 \\ \phi_{s,4} &= \beta_s^4 \mu_d (\mu_d - \mu_s) + \beta_s^4 \mu_s b_0 + 2 \beta_s^2 (\mu_s - \mu_d) + 1 \end{aligned} \tag{8}$$

To obtain the minimization of above performance indicators, the following equations hold,

$$\partial PI(X_s/X_0)/\partial \beta_d^2 = 0, \quad \partial PI(X_s/X_0)/\partial \zeta_d = 0. \tag{9}$$

Then, the optimal solution is obtained as,

$$\beta_d = \beta_s \sqrt{\frac{-\phi_{s,2}}{2 \phi_{s,3}}}, \quad \zeta_d = \frac{\beta_s \mu_e}{4} \sqrt{\frac{4 \phi_{s,1} \phi_{s,3} - \phi_{s,2}^2}{\phi_{s,3} \phi_{s,4}}}. \tag{10}$$

Additionally, the optimized performance indicator of relative displacement amplitude is given as,

$$PI_{opt}\left(\frac{X_s}{X_0}\right) = \frac{S_w}{\omega_b^3} \frac{\sqrt{4 \phi_{s,1} \phi_{s,3} - \phi_{s,2}^2} \sqrt{\phi_{s,3} \phi_{s,4}}}{\beta_s^7 \mu_s \mu_e \phi_{s,3}}. \tag{11}$$

As indicated in Eq. (11), we have obtained the optimal performance indicator of relative displacement of primary structure. Furthermore, the optimized  $PI(X_s/X_0)$  lead to an optimal formula of absolute acceleration responses of primary structure,

$$\ddot{x}_{s,0} = -2 \zeta_s \omega_s \dot{x}_s - \omega_s^2 x_s. \tag{12}$$

Because the value of damping ratio of primary structure  $\zeta_s$  always locates in the range of [0.02, 0.05], which means that the contribution of  $x_s$  dominate the acceleration responses  $\ddot{x}_{s,0}$ .

**Optimal solution for isolator displacement minimization**

According to the second formulation in Eq. (6), the closed-form formula of performance indicator related to the basement displacement is expressed as,

$$PI\left(\frac{X_b}{X_0}\right) = \frac{S_w}{\omega_b^3} \frac{\beta_s^4 \mu_e^2 \phi_{b,1} + \beta_s^2 \mu_e^2 \phi_{b,2} \beta_d^2 + \mu_e^2 \phi_{b,3} \beta_d^4 + 4 \beta_s^2 \phi_{b,4} \zeta_d^2}{2 \beta_s^6 \mu_e^2 \zeta_d} \quad (13)$$

where, all terms of coefficients of Eq. (13) are,

$$\begin{aligned} \phi_{b,1} &= \beta_s^2 + \mu_s \\ \phi_{b,2} &= \beta_s^4 (\mu_t^2 - 1) \mu_e - 2 \beta_s^2 (\beta_s^2 + \mu_s) b_0 - 2 \mu_s (\beta_s^2 + 1) \\ \phi_{b,3} &= \beta_s^6 b_0^2 (\mu_e + 1)^2 + \beta_s^4 \mu_s (2 \mu_d b_0 + 3 b_0^2) + \beta_s^2 \mu_s (\mu_s + 2 b_0) + \mu_s \\ \phi_{b,4} &= \beta_s^4 (\mu_e + 1) b_0^2 + 2 \beta_s^2 \mu_s b_0 + \mu_s \end{aligned} \quad (14)$$

To obtain the minimization of above performance indicator, following conditions are obtained,

$$\partial PI(X_b/X_0)/\partial \beta_d^2 = 0 \quad \partial PI(X_b/X_0)/\partial \zeta_d = 0 \quad (15)$$

The analytical formulations of optimal parameters are expressed as following,

$$\beta_d = \beta_s \sqrt{\frac{-\phi_{b,2}}{2 \phi_{b,3}}} \quad \zeta_d = \frac{\beta_s \mu_e}{4} \sqrt{\frac{4 \phi_{b,1} \phi_{b,3} - \phi_{b,2}^2}{\phi_{b,3} \phi_{b,4}}} \quad (16)$$

Then, the related optimal performance indicator is estimated as,

$$PI_{opt}\left(\frac{X_b}{X_0}\right) = \frac{S_w}{\omega_b^3} \frac{\sqrt{4 \phi_{b,1} \phi_{b,3} - \phi_{b,2}^2} \sqrt{\phi_{b,3} \phi_{b,4}}}{\beta_s^3 \mu_e \phi_{b,3}} \quad (17)$$

### Validation of the effectiveness of proposed optimal design method

As mentioned in Sections 3 and 4, the optimal solution of frequency ratio  $\beta_d$  and damping ratio  $\zeta_d$  were approximated by minimizing the  $H_2$  norm of two performance indicators of a BI system subjected to a white-noise excitation. Herein, the intensity of the power spectral density (PSD) of the white-noise is assumed as  $5 \times 10^{-4} \text{ m/s}^3$ , and a benchmark model with analytical parameters namely, fundamental frequency  $\omega_b = 2.53$ , frequency ratio, mass ratio and inherent damping ratio of primary structure  $\beta_s = 7.95$ ,  $\mu_s = 0.813$ ,  $\zeta_s = 0.02$ , and a low damping ratio of base isolator  $\zeta_b = 0.02$  was analyzed. The mass ratio is assumed as  $\mu_t = 0.05$ , and  $\mu_d = 0.45$ , the total mass ratio of TMDI  $\mu_e = 0.5$ . The contour plots of two performance indicators with respect to the variations of  $\beta_d \in [0.1, 2]$  and  $\zeta_d \in [0.1, 1]$  are given in Fig. 2.

As shown in Fig. 2 (a) and (b), the proposed optimal solutions lie in the global minimum point in the contour plots of two performance indicators, which validates the effectiveness of proposed method. As shown in above formulations, the optimal parameters and performance indicators are estimated under the assumption that the excitation is a white-noise, it is worth investigating the influences of the variation of filtered excitation models on the related performance.

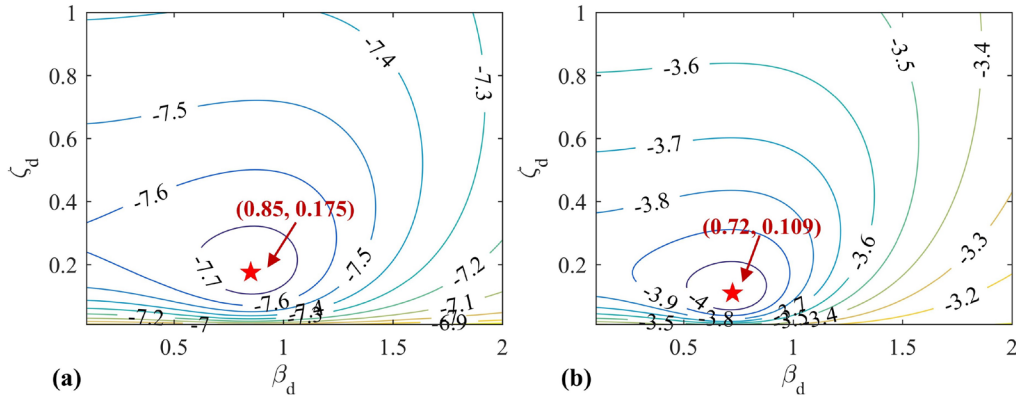


**Fig. 2** Contour plots of (a)  $\lg(PI(X_s/X_0))$  and (b)  $\lg(PI(X_b/X_0))$  of BI system.

**Comparison of optimal design with different power spectral density model.**

In this part, the parameters related to the stochastic excitation model is studied. The one side Clough-Penzien model is used to act the different soil conditions related to the external excitation.

$$S_{\ddot{x}_0\ddot{x}_0} = S_w \frac{\omega_g^4 + 4\zeta_g^2\omega_g^2\omega^2}{(\omega^2 - \omega_g^2)^2 + 4\zeta_g^2\omega_g^2\omega^2} \frac{\omega^4}{(\omega^2 - \omega_f^2)^2 + 4\zeta_f^2\omega_f^2\omega^2} \tag{18}$$

where,  $\zeta_g$ ,  $\omega_g$ ,  $\omega_f$  and  $\zeta_f$  are parameters related to filter model which are given in Table 1.

**Table 1** PSDF filter parameters for model soil conditions

Soil type	$\omega_g$ (rad/s)	$\zeta_g$	$\omega_f$ (rad/s)	$\zeta_f$
Firm	15.0	0.6	1.5	0.6
Medium	10.0	0.4	1.0	0.6
Soft	5.0	0.2	0.5	0.6

Herein, the intensity of one side PSD  $S_w = 1 \times 10^{-3}$  is employed for the excitation. Then, the performance indicators  $PI(X_s/X_0)$  and  $PI(X_b/X_0)$  are estimated by using numerical integration. To investigate the feasibility and effectiveness of proposed method, we also compared the performance indicators obtained from numerical results and analytical results with aforementioned benchmark model. Figs. 3 and 4 depict the optimal design parameters and related performance indicators obtained from analytical formula and numerical optimization procedure.

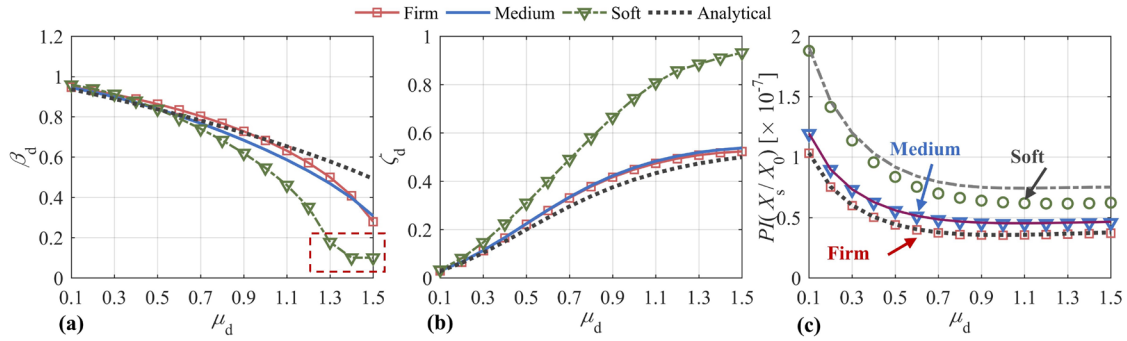


**Fig. 3** Comparison of optimal (a)  $\beta_d$ , (b)  $\zeta_d$  and (c) the related performance indicators  $PI(X_s/X_0)$  with varying mass ratio of inerter and different soil conditions.

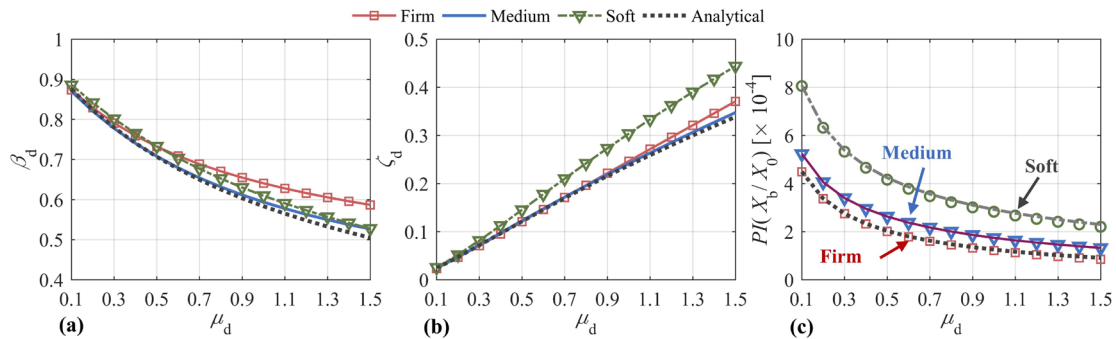


**Fig. 4** Comparison of optimal (a)  $\beta_d$ , (b)  $\zeta_d$  and (c) the related performance indicators  $PI(X_b/X_0)$  with varying mass ratio of inerter and different soil conditions.

As indicated in Fig. 3, the analytical formula coincides with the numerical results for the Firm and Medium soil conditions. However, the numerical results for soft soil condition shows a large difference with analytical formula. Notably, the optimal value of  $\beta_d$  approaches to the lower bound of design parameters for  $\mu_d > 1.4$  with the soft soil condition, that means the mechanical behavior of TMDI is close to the simplified mass damper inerter (MDI). Despite of such a large difference in optimal results, it is worthy to note that the analytical solutions presented a comparable control effect as shown in Fig 3(c). As shown in Fig. 4 (a) and (b), the optimal results obtained from numerical results is slightly larger than those by the analytical formulae. As expected, analytical parameters yield similar performance level with the numerical results as shown in Fig 4 (c).

### Investigation of different optimal formulae developed for TMDI.

In the previous studies, analytical formulae of optimal parameters were developed with various criteria [6,8,9]. Herein, the benchmark model given in Section 5 is employed to investigate the control effect of each model. Given the inertance ratio  $\mu_d = 0.45$ , mass ratio of TMD  $\mu_t = 0.05$ , the transfer function related to basement displacement  $x_b$  and absolute acceleration of primary structure  $\ddot{x}_{s,0}$  are employed to illustrate the seismic response control performance of each method.

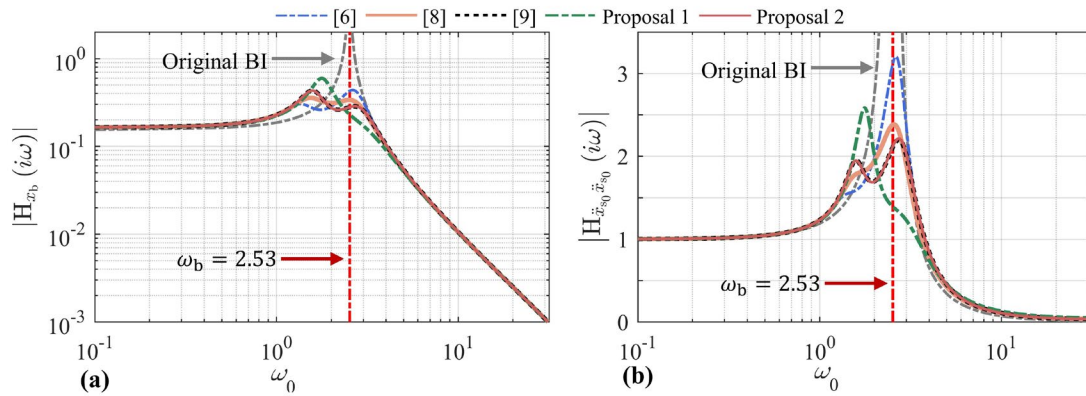


**Fig. 5** Comparison of transfer function of (a)  $x_b$ , (b)  $\ddot{x}_{s,0}$  obtained from different design formulae.

As indicated in Fig. 5, the optimal design formula developed by Matteo [9] presents a result that coincides with Proposal 2. Fig. 5 (a) also shows that two fixed-points were observed in the transfer function curve as developed in [8], which is compatible with its assumption of fixed-point method. For the case of transfer function of  $\ddot{x}_{s,0}$ , it is found that the proposed optimal strategy 1 gives an excellent control effect, when the input frequency is larger than the fundamental frequency  $\omega_b$ . In order to take a further step to illustrate the seismic performance of the designed TMD with optimal parameters presented by the proposed strategies, a stationary analysis of benchmark model excited by the filtered-white-noise with the power spectral density defined in Section 6. The related results are listed in Table 2.

**Table 2** Comparison of stationary responses with different design formulae

Proposals	$\sigma_{x_b}$ [mm]			$\sigma_{\ddot{x}_{s,0}}$ [m/s <sup>2</sup> ]		
	Firm	Medium	Soft	Firm	Medium	Soft
Original BI	52	54	65	0.33	0.34	0.42
Marian 2014[6]	16(-68%)	18(-66%)	23(-65%)	0.12(-65%)	0.13(-64%)	0.16(-61%)
Marian 2017[8]	15(-71%)	17(-68%)	21(-67%)	0.10(-69%)	0.11(-68%)	0.14(-66%)
Matteo 2019[9]	<b>15(-72%)</b>	<b>17(-69%)</b>	<b>21(-68%)</b>	0.10(-68%)	0.11(-68%)	0.14(-66%)
Proposal 1	16(-69%)	18(-66%)	22(-67%)	<b>0.09(-74%)</b>	<b>0.10(-72%)</b>	<b>0.13(-70%)</b>
Proposal 2	<b>15(-72%)</b>	<b>17(-69%)</b>	<b>21(-68%)</b>	0.10(-70%)	0.11(-68%)	0.15(-65%)

As indicated in Table 2, the proposed methods provide excellent performance for suppressing the mean square root of isolator displacement as well as absolute acceleration of primary structure. Specially, the mitigation level provided in [9] almost equals to the proposal 2, which have been validated in above discussions. For the suppression of absolute acceleration response of primary structure, it is observed that the first proposal attains a superior performance than other four strategies.

### Conclusions

In this work, two design formulae related to the minimization of  $H_2$  norm of performance indicator of TMDI were developed. The effectiveness and accuracy of proposed method were validated by

using the numerical simulation results. As illustrated in Section 5, the optimal parameters related to the analytical formula coincides with the numerical results for firm and medium soil conditions. However, the comparison results related to the soft soil condition shows that the numerical results approach to MDI for the mass ratio larger than 1.4, which implies that the MDI is more effect than the TMDI in suppressing the acceleration responses of a BI system when the mass ratio is larger than the total mass of the BI system. However, it is worthy to note that the analytical result presents a comparable performance in suppressing the performance indicator. This implies that the analytical solution is an effective alternative for searching the optimal parameters. The comparison results in Section 6 elucidate that the proposed two design formulae present excellent seismic response control performance in suppressing the absolute acceleration of primary structure as well as the isolator displacement. To this end, the proposed methods are effective for improving the seismic performance of a BI system with a TMDI.

## References

- [1] Y. Nakamura, K. Okada. Review on seismic isolation and response control methods of buildings in Japan. *Geoenvironmental Disasters*. 6 (2019) 1–10. <https://doi.org/10.1186/s40677-019-0123-y>
- [2] Pan Peng, D. Zamfirescu, M. Nakashima, N. Nakayasu, H. Kashiwa. Base-isolation design practice in japan: introduction to the post-kobe approach. *J. Earthqu. Eng.* 9 (2005) 147–171. <https://doi.org/10.1080/13632460509350537>
- [3] F. Naeim, J. M. Kelly. *Design of seismic isolated structures: from theory to practice*. John Wiley & Sons, 1999, pp.1-296. <https://doi.org/10.1002/9780470172742>
- [4] J. M. Kelly. The role of damping in seismic isolation. *Earthq. Eng. Struct. Dyn.* 28 (1999) 3–20. [https://doi.org/10.1002/\(SICI\)1096-9845\(199901\)28:1<3::AID-EQE801>3.0.CO;2-D](https://doi.org/10.1002/(SICI)1096-9845(199901)28:1<3::AID-EQE801>3.0.CO;2-D)
- [5] J. N. Yang, A. Danielians, S. C. Liu. Aseismic hybrid control systems for building structures. *J. Eng. Mech.* 117 (1991) 836–853. [https://doi.org/10.1061/\(ASCE\)0733-9399\(1991\)117:4\(836\)](https://doi.org/10.1061/(ASCE)0733-9399(1991)117:4(836))
- [6] L. Marian, A. Giaralis. Optimal design of a novel tuned mass-damper–inertor (TMDI) passive vibration control configuration for stochastically support-excited structural systems. *Probab. Eng. Eng. Mech.* 38 (2014) 156–164. <https://doi.org/10.1016/j.probenmech.2014.03.007>
- [7] D. De Domenico, G. Ricciardi. An enhanced base isolation system equipped with optimal tuned mass damper inertor (TMDI). *Earthq. Eng. Struct. Dyn.* 47 (2017) 1169–1192. <https://doi.org/10.1002/eqe.3011>
- [8] L. Marian, A. Giaralis. The tuned mass-damper-inertor for harmonic vibrations suppression, attached mass reduction, and energy harvesting. *Smart. Struct. Syst.* 19 (2017) 1-23. <https://doi.org/10.12989/sss.2017.19.1.001>
- [9] A. Di Matteo, C. Masnata, A. Pirrotta. Simplified analytical solution for the optimal design of Tuned Mass Damper Inertor for base isolated structures. *Mech. Syst. Signal Proc.* 134 (2019) 106337. <https://doi.org/10.1016/j.ymsp.2019.106337>

# A 3D Printed, Constriction-Resistive Sensor for the Detection of Ultrasonic Waves

Saeb Mousavi<sup>1,2,a</sup>, Philippe Blanloeuil<sup>1,b</sup>, Thailammai Vinoth<sup>1,c</sup>, David Howard<sup>2,d</sup>,  
Chun H. Wang<sup>1,\*</sup>

<sup>1</sup>School of Mechanical and Manufacturing Engineering, University of New South Wales, Sydney, NSW 2052, Australia

<sup>2</sup>The Robotics and Autonomous Systems Group, Commonwealth Scientific and Industrial Research Organization (CSIRO), Pullenvale, 4069, Australia

<sup>a</sup>s.mousavianchehpoli@unsw.edu.au, <sup>b</sup>p.blanloeuil@unsw.edu.au, <sup>c</sup>t.vinoth@unsw.edu.au, <sup>d</sup>david.howard@csiro.au

\*Corresponding author email: chun.h.wang@unsw.edu.au

**Keywords:** 3D Printing, Constriction-Resistive Sensor, Ultrasound Sensor, Structural Health Monitoring

**Abstract.** Ultrasonic waves, either bulk waves or guided waves, are commonly used for non-destructive evaluation, for example in structural health monitoring. Traditional sensors for detecting ultrasonic waves include metallic strain gauges and piezoelectric ceramics. Recently piezoresistive nanocomposites have emerged as a promising sensor with high sensing range. In this paper, a constriction-resistive based sensor made from a graphene reinforced PLA filament is developed using a fused deposition modelling 3D printing approach as a novel type of ultrasonic sensor for structural health monitoring purposes. The sensor is made of very low-cost and recyclable thermoplastic material, which is lightweight and can be either directly printed onto the surface of various engineering structures, or embedded into the interior of a structure via fused filament fabrication 3D printing. These characteristics make this sensor a promising candidate compared to the traditional sensors in detecting ultrasonic waves for structural health monitoring. The printed sensors can detect ultrasonic signals with frequencies around 200 kHz, with good signal-to-noise ratio and sensitivity. When deployed between two adjacent printed tracks, and exploiting a novel kissing-bond mechanism, the sensor is capable of detecting ultrasonic waves. Several confirmatory experiments were carried out on this printed sensor to validate the capability of the printed sensor for structural health monitoring.

## Introduction

Engineering structures can deteriorate to an unsafe or unrepairable level that can cause dramatic consequences such as endangering human life. Structural Health Monitoring (SHM) has come to prominence can detect defects in their early stage without risking the normal functionality of the structure under inspection. Ultrasonic SHM is an emerging and promising subfield, owing to its ability in monitoring multi-scale structures using both acoustic emission (AE) and guided ultrasonic waves (GUWs) approaches in a broad frequency regime [1–4].

In ultrasonic SHM, it is critical to develop a network of sensors to quantify and locate structural damage [5-7]. A broad range of sensors have been developed for this purpose, including lead zirconate titanate (PZT) wafers [8], carbon nanotube sensors [9,10], optical fibres [11], zinc oxide sensors [12], and graphene/polyvinylpyrrolidone (PVP) sensor [1]. Since a dense grid of sensors is usually required, not only the cost of production is a critical matter, but also sensors' weight and simplicity of fabrication becomes important. In this regard, a number of low-cost piezoresistive

sensors composed of nanocomposite, flexible and low-density materials have been developed [13,14].

In this paper, based on the authors' previous efforts on developing highly sensitive resistive strain sensors [15], a novel approach to strain sensing, called Constriction-Resistive (CR) sensing is applied for the detection of ultrasonic waves. The sensors are fabricated by a simple and low-cost fused deposition modelling (FDM) 3D printing technique and are extremely light weight. The morphology and electrical properties of the CR sensors are characterised. The CR sensor's response to ultrasonic wave is acquired and then validated by comparison with a commercial PZT transducer's response.

### Fabrication and Characterization of CR Sensors

PLA-CNT serves as the sensing material. To fabricate the sensing material, PLA pellets and CNT were dissolved in dichloromethane ( $\text{CHCl}_2$ ) solvent and then dried at room temperature to obtain the PLA-CNT composite with CNT mass fraction of 12%. Then, the composite material was cut into pieces and extruded using a twin-screw extruder (Fig. 1a) to make filaments, which were then used to 3D print the sensor. The fabrication process for the sensors used in this work is fully explained in our previous paper [15, 16] and the step-by-step process is shown in Fig. 1.

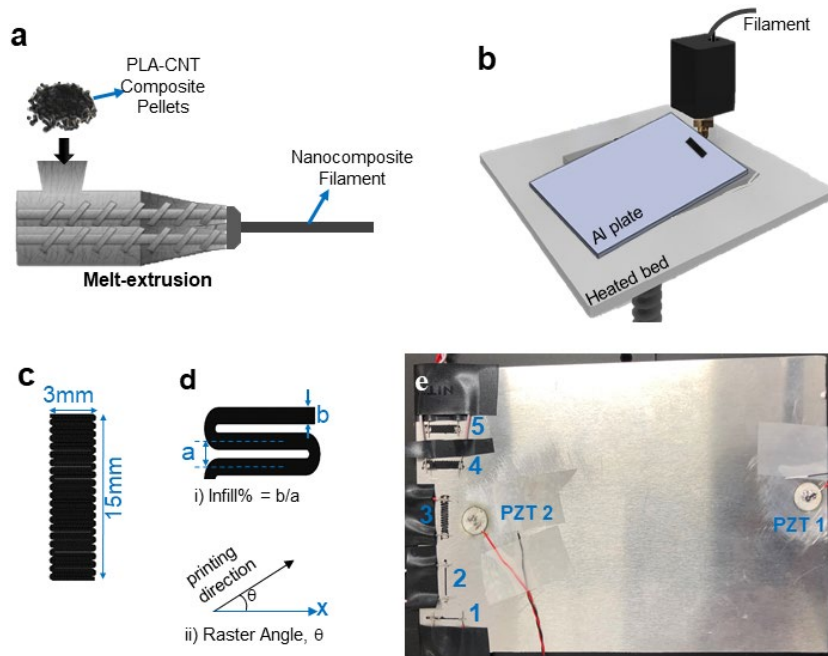


**Fig. 1.** Fabrication process of the CR sensors. (a) PLA pellets and CNT nanofillers are first solution-mixed and then fed into a twin-screw extruder. A filament is extruded through a nozzle at the end of the extruder. (b) The extruded filament is then used to 3D print the sensors on an aluminum plate. (c) dimensions of the printed sensors. (d) Illustrative definition of (i) infill density/ratio of 3D printed sensor layer as ratio between track width,  $b$ , and the track spacing,  $a$ . (ii) raster angle ( $\theta$ ) of 3D printing. (e) An image of the 5 different printed sensors and two PZT transducers on the aluminum plate; 1) a single horizontal line, 2) a single vertical line, 3) a 90% infill density sensor, 4 and 5) two 95% infill density sensors.

When two conducting materials come into contact, the true area of contact at the interface determines the true cross-section through which the electronic flow occurs. The flow of electrons

or current bent together through these contact areas causes an increase in resistance beyond fully conducting surfaces. This contact resistance is also known as constriction resistance [15, 17]. The CR sensors were fabricated using an extremely simple FDM 3D printing technique. Three types of CR sensors and two single-track sensors were fabricated as shown in Fig. 1e. In 3D printing, infill ratio, which is defined as  $b/a$ , where  $b$  is the width of the printed tracks and  $a$  is the spacing between two neighbouring tracks, is an important parameter (Fig. 1d). By changing the infill density one can change the contact level of the printed neighbouring tracks, and therefore the level of constriction resistance existing between them. Changing the infill ratio affects the strength of the kissing bond existing between adjacent tracks. Utilising this parameter, CR sensors can be designed to display significantly higher sensitivity to deformation or vibrations compared to the solid sensors.

Optical images of the sensors with 85%, 90%, 95% and 100% infill densities are shown in Fig. 2. The SEM image of the fractured surface of the 3D printed PLA-CNT sensor (Fig. 2e) confirms the existence of CNT in the polymer matrix.

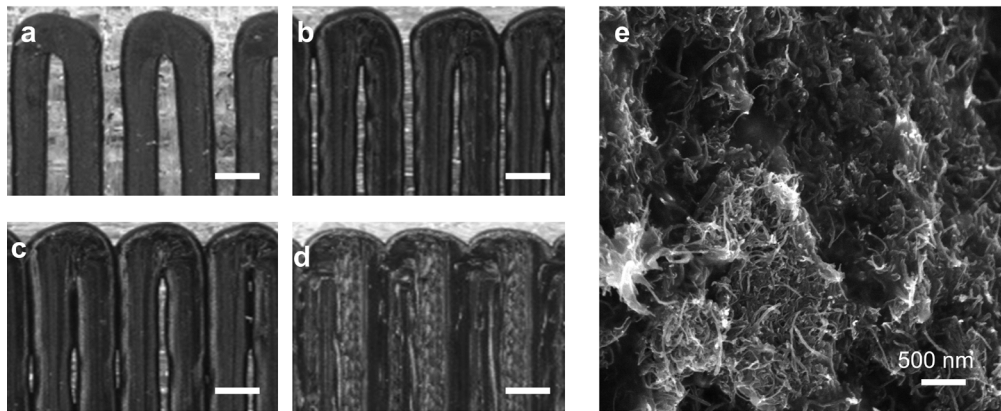


**Fig. 2.** Microstructure characterisation of the sensor materials. Microscopic images of the 3D printed PLA-CNT sensors with different infill densities (a) 85, (b) 90, (c) 95 and (d) 100%. The scale bars are 500  $\mu\text{m}$ . (e) SEM image of fractured cross-sectional view of the 3D printed sensor.

### Sensor Performance in Detection of Ultrasonic Wave

To evaluate the performance of the sensors in the detection of ultrasonic waves, the sensors were 3D printed on an aluminium plate and were tested to see if they can detect the strain induced by a propagating wave in the plate generated by a lead zirconate titanate (PZT) piezoelectric transducer. Strain generated by the wave motion induces a resistance change in the sensors which is then transformed into voltage using a Wheatstone bridge and recorded through an oscilloscope. The schematic of the experimental setup is shown in Fig. 3.

The sensors' signals were recorded for a 3-cycles ultrasonic excitation wave with a frequency of 200 kHz. The results are shown in Fig. 4. Sensors 1 and 2 were unable to detect the source signal, whereas sensors 3, 4 and 5 were able to detect it. Since sensor 1 and 2 are just single tracks, there is no constriction resistance and therefore they do not show any sensitivity to acoustic excitation. On the other hand, sensor 3, 4 and 5 consist of weak contacts between printed tracks which makes them sensitive to the strain induced by the acoustic wave.

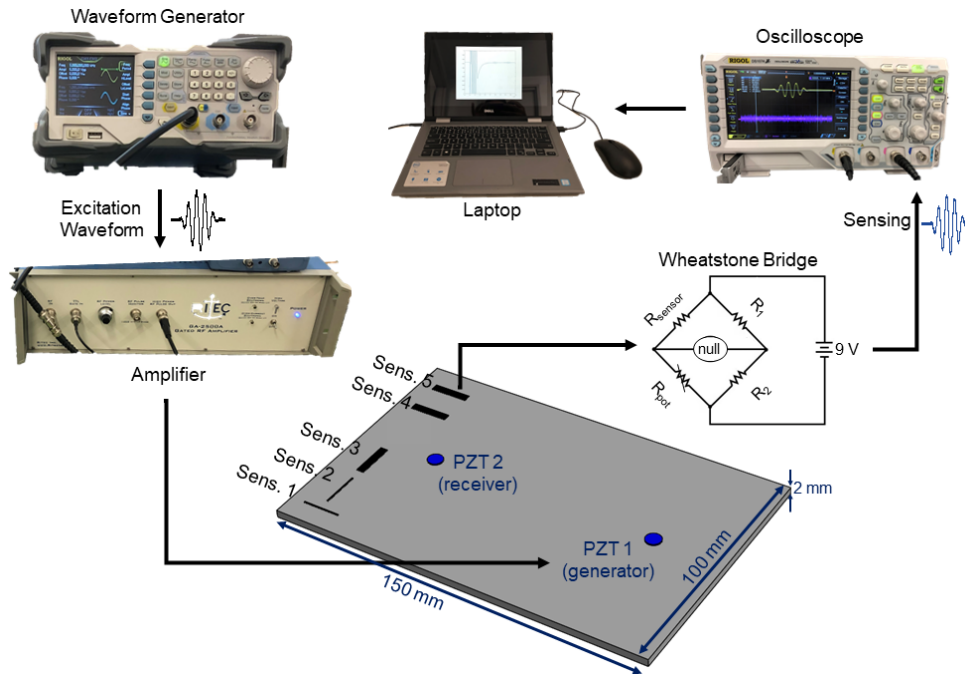


**Fig. 3.** Schematic of the experimental setup. The input signal is first generated in the desired form and then the signal is amplified using the amplifier and then transmitted to PZT 1 to generate the input ultrasonic wave. The sensors' output signal, which is resistance, is transformed into voltage using a Wheatstone bridge and then transmitted to oscilloscope for data acquisition and finally the data is saved on a laptop for further processing.

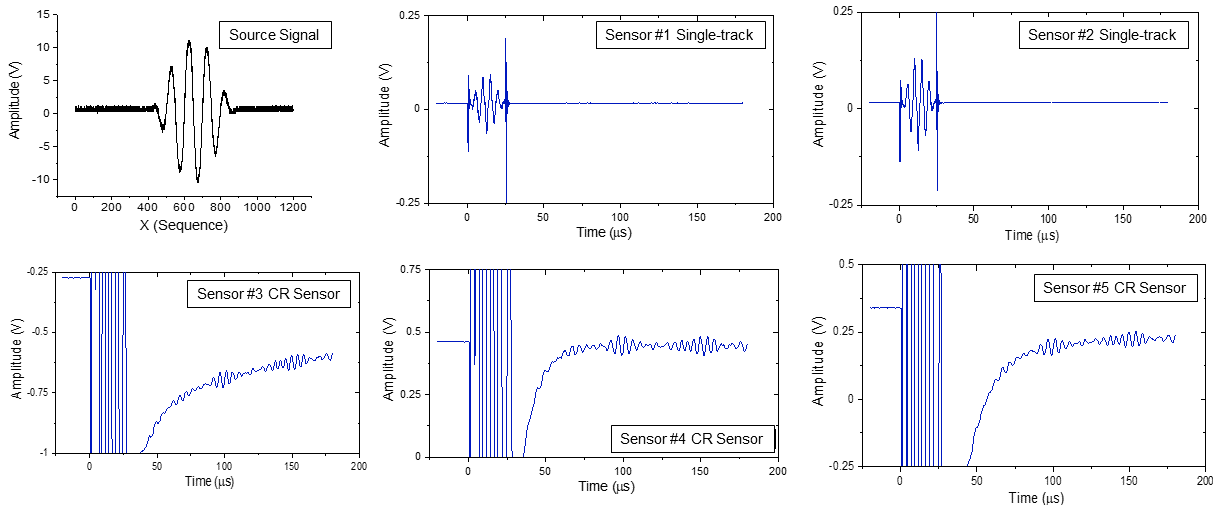


**Fig. 4.** CR Sensors' performance in detection of ultrasonic wave. Sensors 1 and 2 were unable to detect the source signal, whereas sensors 3, 4 and 5 were able to detect it.

In order to verify the sensors' response, a second PZT was attached to the plate near the location of the sensors as a receiver. The strain generated by the wave motion from PZT 1 induces a voltage change in PZT 2. The recorded signal for a 3-cycle 200 kHz tone burst for PZT 2 and CR sensor #4 are plotted in Fig. 5. As shown in this figure, the sensor's response is verified. Although the received signal by the sensor is weaker than the one obtained with PZT 2, the sensor can detect the input signal with a higher resolution and less noise compared to the PZT.

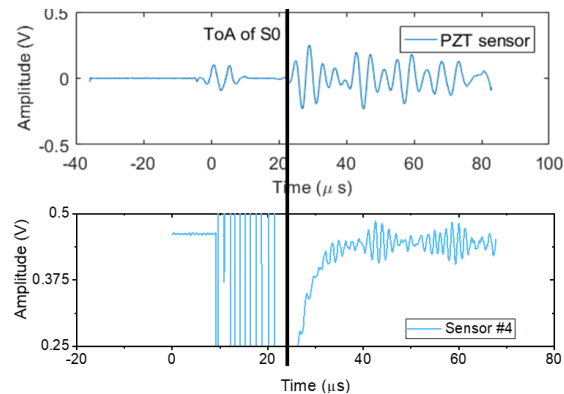


**Fig. 5.** Comparison of the CR sensor's response with PZT 2. This verifies the sensor's response although the received signal by the sensor is weaker than the one obtained by PZT 2.

### Conclusions

We presented a novel design for damage detection and SHM of component. Our 3D printed constriction-resistive strain sensors are responsive to tiny deformations under acoustic vibration. Infill ratio has been found to play a key role in the sensitivity of the sensors. As shown in Fig. 5, the sensors were able to successfully predict the source signals with minimal error. The limitation of the current sensors is their low sensitivity and we are currently conducting more experiments to enhance the sensitivity of the CR sensors. Furthermore, a full study for better understanding of the sensing mechanism is undergoing.

Considering the rapid development of 3D printing techniques, this research paves the way for low cost and accessible techniques to enable in-situ and offline SHM of damaged components.

### Summary

In this paper, a constriction-resistive ultrasonic wave sensor is presented that is fabricated through simple FDM 3D printing and can be employed for structural health monitoring applications.

### References

- [1] W. Cao, P. Zhou, Y. Liao, X. Yang, D. Pan, Y. Li, B. Pang, LM. Zhou, Z. Su, A Spray-on, Nanocomposite-Based Sensor Network for *in-Situ* Active Structural Health Monitoring. *Sensors* 19, 9 (2019) 2077. <https://doi.org/10.3390/s19092077>
- [2] N. Hu, T. Shimomukai, H. Fukunaga, Z. Su, Damage identification of metallic structures using A0 mode of lamb waves. *Struct. Health Monit.* 7 (2008) 271–285. <https://doi.org/10.1177/1475921708090566>
- [3] H. Mei, M.F. Haider, R. Joseph, A. Migot, V. Giurgiutiu, Recent advances in piezoelectric wafer active sensors for structural health monitoring applications. *Sensors* 19 (2019) 383. <https://doi.org/10.3390/s19020383>
- [4] M.F. Haider, V. Giurgiutiu, Analysis of axis symmetric circular crested elastic wave generated during crack propagation in a plate: A Helmholtz potential technique. *Int. J. Solids Struct.* 134 (2018) 130–150. <https://doi.org/10.1016/j.ijsolstr.2017.10.035>
- [5] W. Ostachowicz, R. Soman, P. Malinowski, Optimization of sensor placement for structural health monitoring: A review. *Struct. Health Monit.* 18, 3 (2019), 963-988. <https://doi.org/10.1177/1475921719825601>

- [6] T. Wandowski, P. Malinowski, W. Ostachowicz, Circular sensing networks for guided waves based structural health monitoring. *Mech. Syst. Sig. Process.* 66 (2016) 248–267. <https://doi.org/10.1016/j.ymssp.2015.05.001>
- [7] M. Salmanpour, Z. Sharif Khodaei, M. Aliabadi, Transducer placement optimisation scheme for a delay and sum damage detection algorithm. *Struct. Control Health Monit.* 24 (2017) e1898. <https://doi.org/10.1002/stc.1898>
- [8] R. Takpara, M. Duquennoy, M. Ouafouh, C. Courtois, F. Jenot, M. Rguiti, Optimization of PZT ceramic IDT sensors for health monitoring of structures. *Ultrasonics* 79 (2017) 96–104. <https://doi.org/10.1016/j.ultras.2017.04.007>
- [9] A. D'Alessandro, M. Rallini, F. Ubertaini, A.L. Materazzi, J.M. Kenny, Investigations on scalable fabrication procedures for self-sensing carbon nanotube cement-matrix composites for SHM applications. *Cem. Concr. Compos.* 65 (2016) 200–213. <https://doi.org/10.1016/j.cemconcomp.2015.11.001>
- [10] I. Kang, M.J. Schulz, J.H. Kim, V. Shanov, D. Shi, A carbon nanotube strain sensor for structural health monitoring. *Smart Mater. Struct.* 15 (2006) 737–748. <https://doi.org/10.1088/0964-1726/15/3/009>
- [11] T.H. Loutas, P. Charlaftis, A. Airoidi, P. Bettini, C. Koimtzoglou, V. Kostopoulos, Reliability of strain monitoring of composite structures via the use of optical fiber ribbon tapes for structural health monitoring purposes. *Compos. Struct.* 134 (2015) 762–771. <https://doi.org/10.1016/j.compstruct.2015.08.100>
- [12] H. Gullapalli, V.S.M. Vemuru, A. Kumar, A. Botello-Mendez, R. Vajtai, M. Terrones, S. Nagarajaiah, P.M. Ajayan, Flexible Piezoelectric ZnO-Paper Nanocomposite Strain Sensor. *Small* 6 (2010) 1641–1646. <https://doi.org/10.1002/sml.201000254>
- [13] Z. Zeng, M. Liu, H. Xu, Y. Liao, F. Duan, L. Zhou, H. Jin, Z. Zhang, Z. Su, Ultra-broadband frequency responsive sensor based on lightweight and flexible carbon nanostructured polymeric nanocomposites. *Carbon* 121 (2017) 490–501. <https://doi.org/10.1016/j.carbon.2017.06.011>
- [14] Z. Zeng, M. Liu, H. Xu, Y. Liao, F. Duan, L. Zhou, H. Jin, Z. Zhang, Z. Su, A coatable, light-weight, fast-response nanocomposite sensor for the in situ acquisition of dynamic elastic disturbance: From structural vibration to ultrasonic waves. *Smart Mater. Struct.* 25 (2016) 065005. <https://doi.org/10.1088/0964-1726/25/6/065005>
- [15] S. Mousavi, D. Howard, F. Zhang, J. Leng, CH. Wang, Direct 3D Printing of Highly Anisotropic, Flexible, Constriction-Resistive Sensors for Multidirectional Proprioception in Soft Robots. *ACS Applied Materials & Interfaces* 12, 13 (2020), 15631-15643. <https://doi.org/10.1021/acsami.9b21816>
- [16] S. Mousavi, D. Howard, S. Wu, C.H. Wang, An ultrasensitive 3D printed tactile sensor for soft robotics, arXiv preprint, arXiv:1810.09236.
- [17] Murty, Y. V. Electrical and Electronic Connectors: Materials and Technology. In *Encyclopedia of Materials: Science and Technology*; Buschow, K. H. J., Cahn, R. W., Flemings, M. C., Ilshner, B., Kramer, E. J., Mahajan, S., Veyssi re, P., Ed.; Elsevier, 2001; pp 2483-2494. <https://doi.org/10.1016/B0-08-043152-6/00450-2>

# Damage Identification of High-speed Maglev Guideway Girder Based on Modal Identification

XiangYun Kong<sup>1,a</sup>, JingYu Huang<sup>1,2,b,\*</sup>, XiaoNong Wang<sup>3</sup>,  
ShuoWei Wang<sup>1</sup>, Liang Zhao<sup>1</sup>, ZhiHong Fang<sup>1</sup>

<sup>1</sup> Department of Civiling-Engineering, Tongji University, Shanghai, China

<sup>2</sup> National Maglev Transportation Engineering R&D Center, Tongji University, Shanghai, China

<sup>3</sup> Department of Transportation Engineering, Tongji University, Shanghai, China

<sup>a</sup>kongxiangyun@tongji.edu.cn, <sup>b</sup>huangjingyu@tongji.edu.cn

**Keywords:** High-Speed Maglev, Modal Identification, Guideway Girder, Dynamic Response, Damage Identification

**Abstract.** As a modern high-tech rail vehicle, the maglev train realizes the non-contact suspension and guidance between the train and the guideway, which greatly reduces the resistance of the system. Due to the high-speed operation characteristics of maglev trains, the structural health monitoring of guideway girders is particularly important for the safety and stability of maglev train operation. This paper takes the maglev train guideway girder as the monitoring target, and the finite element model of the maglev vehicle-guideway is established to simulate the running state of the train passing through the guideway girder. The dynamic response data of the guideway girder is obtained in the finite element model, considering healthy states and different damage states of the guideway girder. Then, a modal-based damage identification method is proposed, which obtains the guideway girder damage sensitive characteristics by decomposing the guideway girder acceleration response signal. Finally, based on the measured guideway girder acceleration data, this paper verifies the effectiveness of the damage identification method in guideway girder structure health monitoring, which provides reference and guidance for the future maintenance of the maglev guideway girder.

## Introduction

The 600 km/h high-speed maglev has an irreplaceable role in the transportation of the core city circle. At present, relevant theoretical knowledge and experimental researches are being vigorously carried out. With the continuous improvement of vehicle speed and carrying capacity, the structural health of the high-speed maglev track has become more prominent in operation and maintenance.

Current maglevs are often overhauled based on operating mileage or operating years, however track damage cannot be found in time, and maintenance costs and time costs are high. The structural health monitoring system can provide real-time warning when the track is damaged [1-3], accurately locate the damaged part[4], and ensure driving safety and stability. However, there are few researches on structural health monitoring systems related to maglev rails, especially high-speed maglev rails.

The idea of wavelet theory adopted in this paper was formed at the beginning of last century. The Haar system proposed by Haar is the first orthogonal basis of wavelet specification. In 1980, French mathematician Morlet proposed the wavelet transform. Morlet and French theoretical physicist Grossman jointly proposed several systems of continuous wavelet transform, which are based on invariance under translation and contraction. This immutability allows a signal to be

decomposed according to its independent contributions to space (time) and scale (frequency), It is particularly important that the transform do not lose the original information. Using wavelet transform to identify modal parameters, Firstly, based on the good time-frequency analysis capability of the frequency modulated Gaussian wavelet transform and the band pass filtering property, the system is automatically decoupled. Then the modal parameters are identified from the wavelet transform of the impulse response function. Continuous wavelet transform method for structural modal parameter identification is a new direction in the field of modal analysis, which was first published by Staszewski in 1997[5]. This method takes advantage of the attenuation characteristic of wavelet function, which is similar to the attenuation of structural system's free response signal in form. A clear ridge line can be formed in the time-scale (time-frequency) plane by continuous wavelet transform of free response signal based on stationary phase theory. By extracting the wavelet transform coefficient of the ridge line, the modal parameters of the system can be separated. Ruzzene et al[6] used this method to identify the free response parameters of the multi-degree of freedom system, and pointed out that this method was superior to Hilbert transform in instantaneous frequency identification. Scholars have studied the damping, natural frequency and mode identification of linear systems [7-12]. For the parameter identification of nonlinear system, Staszewski adopts the concept of instantaneous phase to identify the instantaneous frequency and amplitude variation of the system[13]. Yonggang Wang and Jinghua Zhang adopted a different wavelet operation [14] and derivation process from Staszewski to study the extraction of modal parameters and derivation of related theories focusing on linear structural systems. For the selection of wavelet transform parent wavelet, Morlet wavelet was used at the beginning, then Cauchy wavelet [9] and Harmonic wavelet line[7] used in mathematical operations. Simonovski [15] made a comparative study of multiple parent wavelets and obtained the advantages of Morlet wavelet for modal parameter identification.

In summary, the wavelet transform method of modal analysis is a new method of modal parameter identification, which is gradually attracting international attention. The direction of the research problem has been in-depth from the identification of modal parameters such as damping, natural frequency, and mode of linear multi-degree-of-freedom systems to the parameter identification of nonlinear systems.

### Wavelet Transform Theory

Set  $\psi_{a,b}(t) = \frac{1}{\sqrt{|a|}} \psi\left(\frac{t-b}{a}\right)$ ,  $a \neq 0, b \in R$ , in which  $a$  presents the stretch factor (scale

factor), and  $b$  represents the translation parameters.  $\psi_{a,b}(t)$  is a wavelet function which depends on parameter  $a$  and  $b$ . Since  $a$  and  $b$  are continuous value, the corresponding function wavelet basis function family  $\{\psi_{a,b}(t)\}$  is called the continuous wavelet basis function. Let  $\psi(t)$  be a wavelet function, the continuous wavelet transform is defined as formula (1), and the corresponding frequency domain is expressed as formula (2).

$$WT_{\psi} f(a,b) = \frac{1}{\sqrt{|a|}} \int_{-\infty}^{+\infty} f(t) \overline{\psi\left(\frac{t-b}{a}\right)} dt \quad (1)$$

$$\hat{\psi}_{a,b}(w) = \frac{\sqrt{a}}{2\pi} \int_{-\infty}^{+\infty} X(w) \hat{\psi}(aw) e^{jwb} dw \quad (2)$$

Let the window radius of the wavelet function  $\psi(t)$  be  $\Delta t$ , and center be  $t_0$ . Then the window radius of its Fourier transform  $\hat{\psi}(w)$  is  $\Delta w$ , and center is  $w_0$ . The relational expressions of  $t_0$  and  $w_0$  are as formulas (3) and formulas (4), while the relational expressions of  $\Delta t$ ,  $\Delta w$  and  $w_0$  are as formulas (5) and formulas (6).

$$t_0 = \frac{1}{\|\psi\|_2} \int_{-\infty}^{+\infty} t |\psi(t)|^2 dt \tag{3}$$

$$w_0 = \frac{1}{\|\hat{\psi}\|_2} \int_{-\infty}^{+\infty} w |\hat{\psi}(w)|^2 dw \tag{4}$$

$$\Delta t = \frac{1}{\|\psi\|_2} \left[ \int_{-\infty}^{+\infty} (t - t_0)^2 |\psi(t)|^2 dt \right]^{\frac{1}{2}} \tag{5}$$

$$\Delta w = \frac{1}{\|\hat{\psi}\|_2} \left[ \int_{-\infty}^{+\infty} (w - w_0)^2 |\hat{\psi}(w)|^2 dw \right]^{\frac{1}{2}} \tag{6}$$

The center of the window of  $\psi_{a,b}(t)$  is  $t_{a,b} = at_0 + b$  and the width is  $\Delta t_{a,b} = a\Delta t$ . The center of the window of  $\hat{\psi}_{a,b}(w)$  is  $w_{a,b} = \frac{1}{a}w_0$ , and the width is  $\Delta w_{a,b} = \frac{1}{a}\Delta w_0$ . The wavelet coefficient where the function  $f(t)$  at a certain scale factor  $a$  and translation parameter  $b$  represents the size of the frequency components in the frequency window with the center frequency of  $\frac{w_0}{a}$  and the width of  $\frac{2w_0}{a}$  in the time period  $2a\Delta t$  at the position  $b$ . When the function  $\psi(t)$  satisfies the allowable condition of formula (7), the inverse transformation of continuous wavelet transform is as formula (8).

$$C_\psi = \int_{-\infty}^{+\infty} \frac{|\hat{\psi}(w)|^2}{|w|} dw < \infty \tag{7}$$

$$f(t) = \frac{1}{C_\psi} \int_{-\infty}^{+\infty} \frac{1}{a^2} da \int_{-\infty}^{+\infty} WT_\psi f(a,b) \psi_{(a,b)}(t) db \tag{8}$$

As the wavelet generated by the base wavelet  $\psi_{a,b}(t)$  acts as an observation window for the signal being analyzed in the wavelet transform,  $\psi(t)$  satisfies the constraint condition of the general function, as shown in formula (9).

$$\int_{-\infty}^{+\infty} |\psi(t)| dt < \infty. \tag{9}$$

**Modal Parameter Identification And Selection of Wavelet Function**

*Basic principle of modal parameter identification based on Wavelet Transform*

Suppose the signal to be identified is  $x(t) = A(t) \cos(\omega t)$ . The analytic signal obtained by Hilbert transform is formula (10), where  $H[x(t)]$  is the Hilbert transform of  $x(t)$ , as in formula (11).

$$x_a(t) = x(t) + jH[x(t)] = A(t)e^{j\omega t} \tag{10}$$

$$H[x(t)] = x(t) * \frac{1}{\pi t} = \frac{1}{\pi} \int_{-\infty}^{+\infty} x(\tau) \frac{1}{t-\tau} d\tau. \tag{11}$$

The analytic signal after Hilbert transform has the same amplitude and frequency range as the original signal, which contains the phase information of the original data. The wavelet transform relationship between signal  $x(t)$  and its analytical signal  $x_a(t)$  is shown in formula (12), and the specific analytical formula is shown in formula (13).

$$\mathcal{W}_x(a, b) = \frac{1}{2} \mathcal{W}_{x_a}(a, b) \tag{12}$$

$$\mathcal{W}_\psi(a, b) = \langle x(t), \psi_{a,b}(t) \rangle = \frac{1}{2} \langle x_a(t), \psi_{a,b}(t) \rangle = \frac{1}{2\sqrt{a}} \int_{-\infty}^{+\infty} A(t) e^{j\omega t} \psi^*\left(\frac{t-b}{a}\right) dt \tag{13}$$

Since the wavelet function  $\psi_{a,b}(t)$  has compact support, the Taylor series of  $A(t)$  near  $t = b$  can be expanded as formula (14).

$$\mathcal{W}_\psi(a, b) = \langle x(t), \psi_{a,b}(t) \rangle = \frac{1}{2} \langle x_a(t), \psi_{a,b}(t) \rangle = \frac{1}{2\sqrt{a}} \int_{-\infty}^{+\infty} [A(b) + o(A(b))] e^{j\omega t} \psi^*\left(\frac{t-b}{a}\right) dt \tag{14}$$

Omitting the higher order terms, we get the following results:

$$\mathcal{W}_\psi(a, b) = \langle x(t), \psi_{a,b}(t) \rangle = \frac{1}{2} \langle x_a(t), \psi_{a,b}(t) \rangle = \frac{\sqrt{a}}{2} A(b) e^{j\omega b} \psi^*(a\omega) \tag{15}$$

*System modal parameter identification*

The expression of the impulse response function of single-degree-of-freedom viscous damping system is shown in formula (16), where  $A_0$  is the vibration amplitude.  $\omega_d$  and  $\omega_n$  are respectively the pi ratio of the system without damping and with damping, and  $\omega_d = \sqrt{1 - \xi^2} \omega_n$ ;  $\xi$  is the damping ratio.  $\varphi_0$  represents the initial phase.

$$x(t) = A_0 e^{-\xi \omega_n t} \cos(\omega_d t + \varphi_0) \tag{16}$$

The wavelet transform of impulse response function of single-degree-of-freedom viscous damping system is shown in formula (17), then the modulus and phase of wavelet transform coefficients are shown in formula (18). The relationship between damping and frequency of transformed system is shown in formula (19).

$$w_x(a, b) = \frac{\sqrt{a}}{2} A_0 e^{j(w_d b + \varphi_0)} \psi^*(a w_d) e^{-\xi w_n b} \quad (17)$$

$$\begin{cases} |w_x(a, b)| = \frac{\sqrt{a}}{2} A_0 e^{-\xi w_n b} |\psi^*(a w_d)| \\ \arg(w_x(a, b)) = w_d b + \varphi_0 \end{cases} \quad (18)$$

$$\begin{cases} \xi w_n = -\frac{d}{db} (\ln |w_x(a, b)|) \\ w_d = \frac{d}{db} (\arg(w_x(a, b))) \end{cases} \quad (19)$$

The expression of impulse response function of multi-degree-of-freedom viscous damping vibration system is shown in formula (20), where  $A_i(t) = A_{0i} e^{-\xi_i w_{ni} t}$ ; N represents the modal order.  $A_{0i}$ 、 $w_{ni}$ 、 $w_{di}$  and  $\xi_i$  are respectively the  $i$ -th order amplitude, natural frequency of undamped vibration, natural frequency of damped vibration and damping ratio, and  $w_{di} = \sqrt{1 - \xi_i^2} w_{ni}$ .

$$x(t) = \sum_{i=1}^N A_i(t) \cos(w_{di} t + \varphi_i) \quad (20)$$

The impulse response function of multi-degree-of-freedom viscous damping vibration system is subjected to wavelet transformation as formula (21).

$$w_x(a, b) = \int_{-\infty}^{+\infty} \sum_{i=1}^N A_i(t) \cos(w_{di} t + \varphi_i) \varphi_{a,b}^*(t) dt \quad (21)$$

Considering the linear nature of the wavelet transform, expanding the Taylor series  $A(t)$  near  $t = b$ , and omitting the higher-order terms, it turns to formula (22). Decoupling the modes of each order, the wavelet transform expression of each independent mode after decoupling is shown in formula (23).

$$W_x(a, b) = \sum_{i=1}^{i=N} \frac{\sqrt{a}}{2} A_{0i} e^{j(w_{id}b + \varphi_i)} \psi^*(aw_{id}) e^{-\xi_i w_{in} b} \quad (22)$$

$$W_x(a_i, b) = \frac{\sqrt{a_i}}{2} A_{0i} e^{j(w_{id}b + \varphi_i)} \psi^*(aw_{id}) e^{-\xi_i w_{in} b} \quad (23)$$

$$\begin{cases} \xi_i w_{in} = -\frac{d}{db} (\ln |W_x(a_i, b)|) \\ w_{id} = \frac{d}{db} (\arg(W_x(a_i, b))) \end{cases} \quad (24)$$

To sum up, for a system with degrees of freedom, calculate the wavelet transform coefficient of the response function of each degree of freedom for the K-th degree of freedom at a certain time ( $b = b_t$ ) according to formula (23). Thus the  $i$ -th vibration mode of multi-degree-of-freedom system is obtained as formula (25). Different modes can be obtained by taking different values of  $i$ .

$$\phi^{(i)} = [w_{h_i,1}(a_i, b_t), \dots, w_{h_i,k}(a_i, b_t), \dots, w_{h_i,N}(a_i, b_t)] \quad (25)$$

### High-speed Maglev Experiment Analysis

The long-span beam is a typical representative of traditional structural system, and has many similarities with bridges. It is generally composed of beam body, bearing, buttress and foundation. The track beam used in high-speed maglev is called guideway. Due to the levitation characteristics of maglev transportation, such a guideway has high requirements for deformation and low tolerance for damage. Therefore, health monitoring and damage identification are of great significance. In this paper, an online real-vehicle vibration experiment study was conducted on the Shanghai high-speed maglev test line. In this study, 21 measuring points were arranged for a single-span track beam with a span of 12 meters for testing, including 14 vertical measuring points and 7 lateral measuring points. The acceleration time-domain curves of measuring points No.7(vertical), No.8(vertical), and No.18(lateral) are shown in Fig.1.

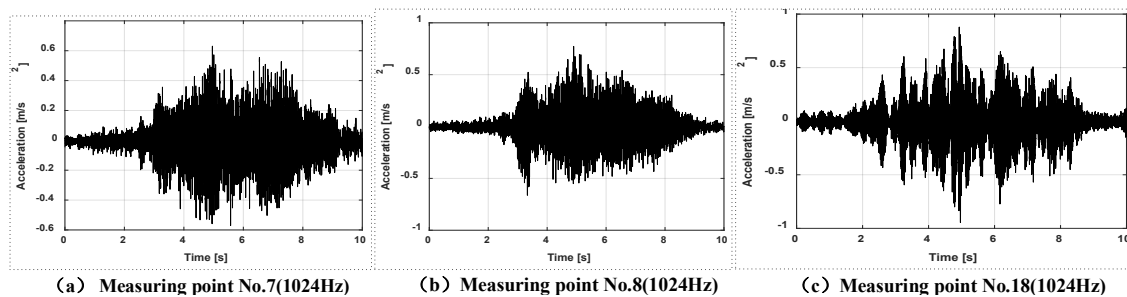


Fig. 1 Time domain diagrams of vibration acceleration

The three measuring points are all located near the middle span of the bottom of the guide rail. The response of the guideway excited by the maglev vehicle is obvious. The peak value of vertical acceleration is between  $0.6-0.8\text{m/s}^2$ , and the peak value of lateral acceleration is between  $0.8-1.0\text{m/s}^2$ . The mass of the vehicle is about  $60\text{t}$ , and the preliminary estimation of the acceleration time-domain curve is reasonable and effective.

In order to further verify the accuracy of the test data, this paper introduces the correlation function for comparative analysis to determine whether the measuring points or test equipment have the relevant coupling. The acceleration time-domain curves of measuring points No.7, No.8 and No.18 are real functions, and their correlation functions are shown in Fig.2.

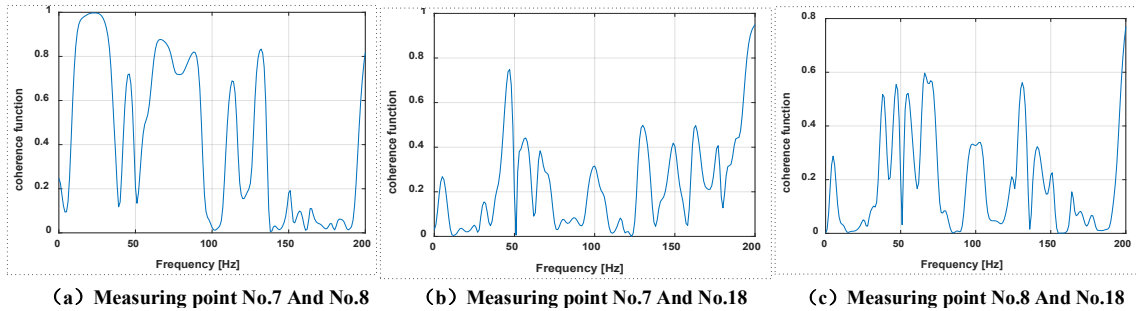


Fig. 2 Correlation functions of measuring points

Comparing these functions, the correlation between measuring points No.7 and No.8 is relatively large. The two measuring points are located on both lateral sides of the same cross-section of the beam, and they are both vertical accelerations. Therefore, the correlation is quite high in the low frequency range. The guideway vibration is dominated by low-frequency vibration, which is concentrated below  $100\text{Hz}$ . This is consistent with the measured data. The correlation between measuring points No.7 and No.8 clearly decreased, especially in the low frequency range. In the low frequency range, the correlation function is lower than  $0.8$ , which can be considered uncorrelated. It fully shows that the coupling degree of lateral vibration and vertical vibration of the guideway is relatively low, which is consistent with the theoretical analysis. Similarly, the correlation between measuring point No.8 and No.18 is also low.

The power spectrum represents the change of signal power with frequency in the unit frequency band, and reflects the distribution of signal power in the frequency domain. The shape of the power spectrum is without obvious burrs, and is relatively smooth, as shown in Fig. 3, which indirectly proves the accuracy of the experiment.

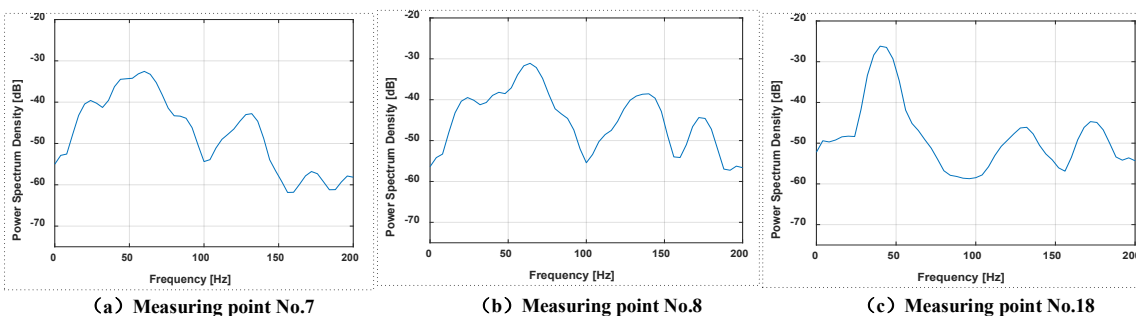
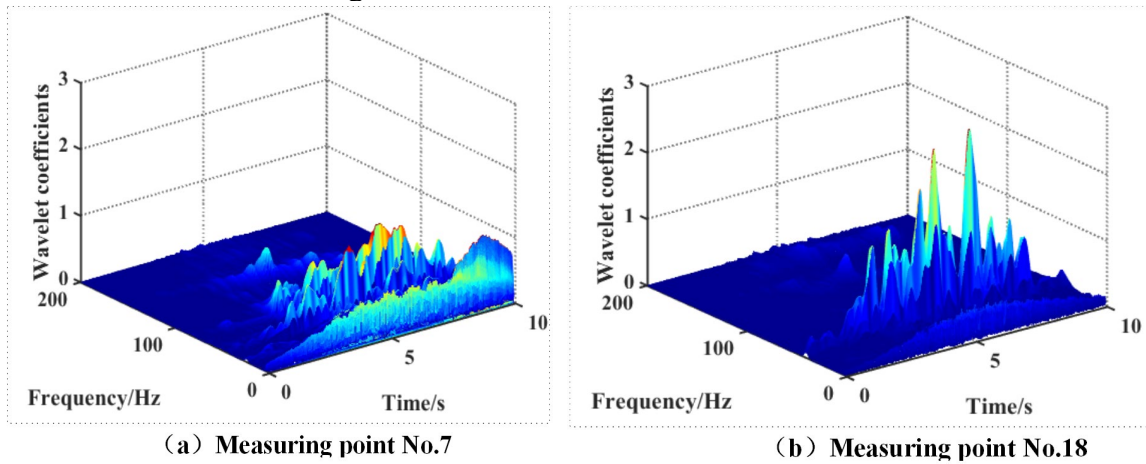


Fig. 3 Power spectrum density

The modal identification can be performed after Wavelet transform of the measuring point data. Take the measuring point No.7 and No.18 as an example, and the results of Wavelet transformation are shown in Fig.4.



*Fig. 4 Time domain and frequency domain comparison of Wavelet transform*

According to the three-dimensional graph of the time, frequency, and Wavelet coefficients of the acceleration data of the measuring points, the vibration frequency of the measuring points is mainly concentrated in the low frequency below 100Hz. In other words, low frequency vibration is dominant.

### Conclusion

The vibration test of Shanghai high-speed maglev test line fully reflects the vibration characteristics of the high-speed maglev guideway system after long-term use, for instance, the vibration frequency can be filtered by wavelet transform, and some vibration characteristics of guideways can be obtained. It is of particular significance for the following experiments and simulation model iterative updating, modal identification flaw detection and maglev guideways health monitoring experiment. According to the experimental analysis, it can be concluded that:

- 1) It is low that the coupling degree of vertical and lateral vibration of long-span high-speed maglev guideway. In the health monitoring experiment, it should be considered and compared respectively, and the specific quantitative correlation function is used to assist data processing and analysis;
- 2) By comparing the modal simulation and measured data of the high-speed maglev guideway, the vibration of the high-speed maglev guideway is mainly concentrated in the low-frequency band below 100Hz, and it is difficult for the operation of maglev vehicle to stimulate high-frequency vibration;
- 3) The lateral vibration of the high-speed maglev guideway is obvious, which will affect the lateral guide gap of high-speed maglev. Therefore, it can not be ignored in health monitoring, and vertical suspend gap and lateral guide gap should be considered comprehensively.

### References

- [1] Entezami A, Sarmadi H, Behkamal B, et al. Big Data Analytics and Structural Health Monitoring: A Statistical Pattern Recognition-Based Approach[J]. Sensors, 2020, 20(8):2328. <https://doi.org/10.3390/s20082328>

- [2] Yang J, Sha G, Zhou Y, et al. Statistical pattern recognition for structural health monitoring using ESN feature extraction method[J]. 2018.  
<https://doi.org/10.2316/Journal.206.2018.6.206-4686>
- [3] Wang Q A, Ni Y Q. Measurement and Forecasting of High-Speed Rail Track Slab Deformation under Uncertain SHM Data Using Variational Heteroscedastic Gaussian Process[J]. Sensors, 2019, 19(15):3311. <https://doi.org/10.3390/s19153311>
- [4] Liu X Z , Xu C, Ni Y Q. Wayside Detection of Wheel Minor Defects in High-Speed Trains by a Bayesian Blind Source Separation Method[J]. Sensors, 2019, 19(18):3981-.  
<https://doi.org/10.3390/s19183981>
- [5] W.J. Staszewski, Identification of damping in m.d.o.f systems using time-scale decomposition, Journal of Sound and Vibration. 1997(203). 283–305. <https://doi.org/10.1006/jsvi.1996.0864>
- [6] M. Ruzzene, A. Fasana, L. Garibaldi, B. Piombo, Natural frequencies and dampings identification using wavelet transform: application to real data. Mechanical Systems and Signal Processing. 1997(2). 207-218. <https://doi.org/10.1006/mssp.1996.0078>
- [7] P. Argoul, T. P. Le, Wavelet analysis of transient signals in civil engineering, Novel Approaches in Civil Engineering, Lecture Notes in Applied and Computational Mechanics, 2003(14), 200-213
- [8] B. Boashash, P. O. Shea, Polynomial Wigner-Ville distributions and their relationship to time-varying higher order spectra. IEEE trans. Signal Process. 1995(43): 216-220.  
<https://doi.org/10.1109/78.258143>
- [9] B. Eschdi'e, B. Tor'esanni, Wavelet representation and time-scaled matched receiver for asymptotic signals. Proc. EUSIPCOV, Barcelona, 1990,305-308
- [10] B.A.D. Piombo, A. Fasana, S. Marchesiello, et al. Modeling and identification of the dynamic response of a supported bridge. Mechanical Systems and Signal Processing, 2000,14(1): 75-89.  
<https://doi.org/10.1006/mssp.1999.1266>
- [11] R.W.Baker, M.J.Hinich, Statistical monitoring of rotating machinery by cumulant spectral analysis. IEEE signal Processing workshop on Hinger-Order Statistic. 1993:187-191
- [12] B.Boashash , Estimating the Instantaneous Frequency of a signal Part 1: Fundamentals. Proceedings of the IEEE, 1992,80(4), 520-538. <https://doi.org/10.1109/5.135376>
- [13] W.J.Staszewski, Copper J.E. Flutter data analysis using the wavelet transform. Proceedings of the International Seminar on New Advances in Modal Synthesis of Large Structures: Nonlinear, Damped and Non-deterministic Cases, Lyon, France, 1995, 203-214
- [14] Y.G.Wang,J.H.Zhang, The application of wavelet transform in dynamic system identification, Structure & Environment Engineering 1997(4) :22-29.
- [15] I.Simonovski, M.Boltezar, The norms and variances of the Gabor, Morlet and General harmonic wavelet functions. Journal of Sound and Vibration. 2003(264): 545-557.  
[https://doi.org/10.1016/S0022-460X\(02\)01206-3](https://doi.org/10.1016/S0022-460X(02)01206-3)

# Changes in Center of Mass during Preliminary Motion for Prediction of Direction Change

Nene Sugimoto<sup>1,a,\*</sup>, Ami Ogawa<sup>2,b</sup> and Akira Mita<sup>2,c</sup>

<sup>1</sup> School of Science for Open and Environmental Systems, Keio University, 3-14-1 Hiyoshi, Kohoku, Yokohama 223-8522, Japan

<sup>2</sup> Department of System Design Engineering, Keio University, 3-14-1 Hiyoshi, Kohoku, Yokohama 223-8522, Japan

<sup>a</sup>nex2\_0319@keio.jp, <sup>b</sup>ami\_ogawa@keio.jp, <sup>c</sup>mita@keio.jp

**Keywords:** Motion Prediction, Direction Change Motion, Motion Capture System

**Abstract.** In recent years, the number of single elderly people has been increasing, and the needs of residents have been diversifying. Towards these backgrounds, we propose the concept of "Biofied bulding". The aim of Biofied Building is to create living spaces where residents can live safely, securely and comfortably. Small robots are used as an interface between residents and living space in Biofied Building. The aim of using robots is to sense the position and movement of residents in real time and providing feedback to them. However, the present control systems of the robot do not have enough functions to estimate the risk of accidents such as falls and choose the pathways which do not disturb residents. Therefore, the purpose of this research is to recognize and predict human behavior in a living space by using a robot to realize Biofied Building. In particular, we focus on the direction change motion, which is an important behavior in a living space, and extract the prediction parameters. In particular, it is reported that the direction change motion account for about 20% of gait during the daily life. Therefore, our research group decided to focus on direction change motion. In this study, we focused on the center of the head to extract parameters for prediction of the direction change motion. There are features in the velocity change of the center of the head compared with straight-line gait. There was a velocity amplification of the opposite direction of the direction change before the start of the motion. It is assumed that the shift of the center of mass make it to easier to step out to the direction of the turn.

## Introduction

In recent years, the number of single households has been increasing and lifestyle has been diversified. Towards these backgrounds, we suggest the concept of "Biofied Building" in which a small sensor agent robot provides a safe, secure, and comfortable living space. The purpose of using the robot is sensing the positions and motions of residents in real-time. However, the present control systems of the robot do not have enough functions to estimate the risk of accidents such as falls and choose the pathways which do not disturb residents. A motion prediction will be a key function of the robot control system to realize more safe, secure, and comfortable living spaces.

Many conventional motion prediction methods use RNN (Recurrent Neural Networks). These methods mainly have two problems. The one is that it is difficult to implement due to the necessity of the big data and the large calculation cost. The other is that the physical constraint of the body is not considered. Hence, our previous study proposed a simple motion prediction method of gait based on human dynamics. However, the method needs to expand to be applied to non-steady motion since its target assumed only steady motion.



Among the gait which is the most basic one of activities of daily living, the gait in which the paths are not straight account for over 40%, and direction change motion account for about 20%<sup>[1][2]</sup>. Therefore, our research group decided to focus on direction change motion.

The motion prediction systems can be distinguished into three types: the optical motion capture system, the inertial motion capture system, and the skeleton tracking function by RGB-D sensors. Our research group has conducted an exhaustive extraction of predictive parameters for the direction change motion using an inertial motion capture system. However, this method has a problem that an inertial motion capture system is a contact sensor. Therefore, we aimed to establish a more practical system by using RGB-D sensors. As a first step, we investigated parameters of motion predictions by using the optical motion capture system and aimed to establish a motion prediction method.

### Device and Experiment

*Device: VICON (The optical motion capture system)<sup>[3]</sup>*

A motion capture system measures the body and joint position of time series. In recent years, motion capture systems have been used in a wide range of applications such as human motion analysis, rehabilitation, humanoid robotics, and residential and urban space evaluation. The optical motion capture system captures marker position which are attached body parts using multiple cameras to estimate the three-dimensional position. We have been developing a system to estimate the human body's position and joint angles by mapping the markers to a predefined articulated human body model. This is called inverse kinematics. There are two advantages of this system. First of all, it is small, lightweight and wireless. Therefore, subjects can move relatively freely. Secondary, the accuracy of absolute position is high. On the other hand, it needs a lot of technology and space to install and calibrate multiple cameras.

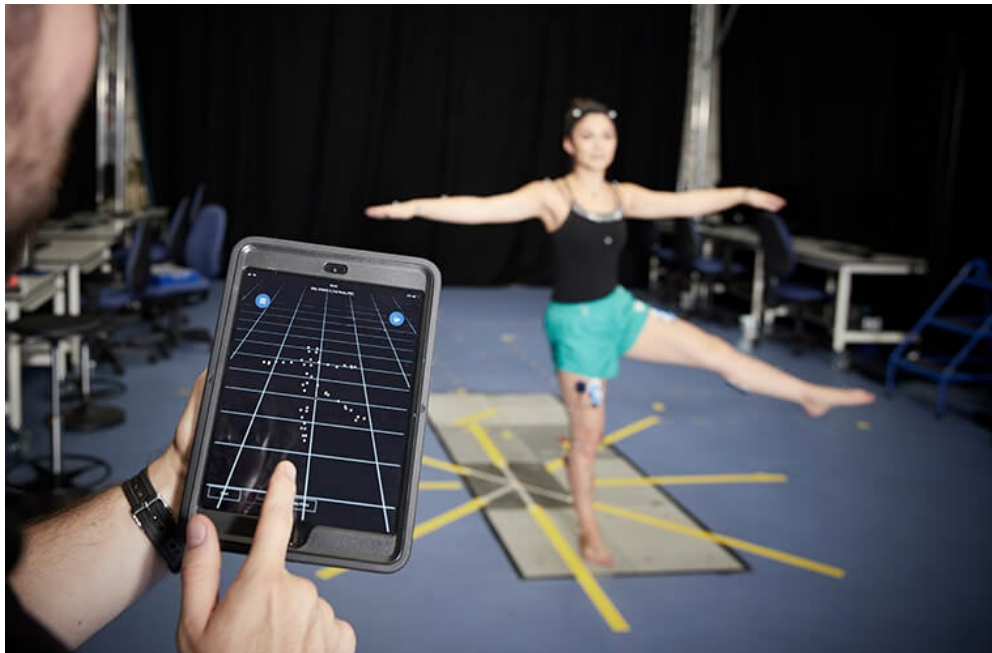


*Fig.1 VICON (The optical motion capture system)<sup>[3]</sup>*

### *Experiment*

The experiment was conducted on the campus of Keio University. Subjects were 6 students in their twenties (males: 2, females: 4). They were required to make a direction change motion voluntary within a specified range. They were not specified their own walking speed, they walked with their own comfortable walking speed. This experiment image is shown in Fig. 2. The number of trials was one each for straight-line and direction change, and the data of 12 trials were used.



*Fig.2 The condition of the experiment*

### *Definition of direction change period*

We define the initiation and termination of direction change motion. The definition was based on a previous study.<sup>[4]</sup> The angle of the lumbar region in steady gait before the direction change was a standard, and the relative angle in the direction of rotation was used for the definition. The relative angles are shown in Fig. 3. These values were calculated from the placement of lumbar taken by VICON. Fig. 3 shows that the subject walked in the straight-line from 0 to 2 seconds, and after 2 seconds, the subject's lumbar rotation increased and changed by almost 90° and subject walked in a steady gait again. The start time of the direction change was defined as the time when the rotation angle of the lumbar region exceeds a minimum value of one step before the end of the steady gait and the swing leg's heel contacts the ground. Likewise, the end time of the direction change was defined as the time when the rotation angle of the lumbar region exceeds the maximum value of rotation angle and the swing leg's heel contacts the ground.

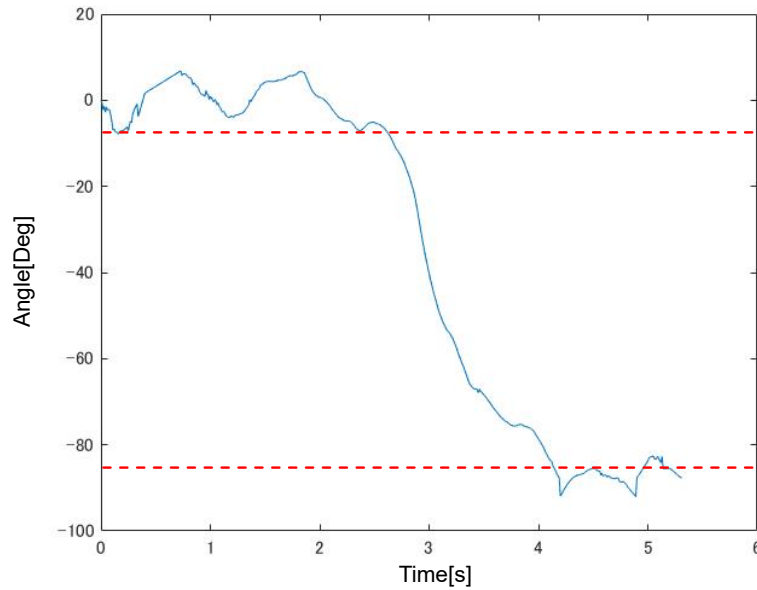


Fig. 3 Definition of direction change period

*Parameter for prediction*

We consider the difference between the straight-line gait and direction change. As the direction change is a circular motion performed on the walking surface, it is assumed that the centrifugal force is added as an inertial force apart from the ground reaction force and gravity during the direction change. In order to resist the inertial force, it is considered to be efficient to change direction by shifting the center of gravity of the body by tilting the trunk in advance. In addition, the previous study [5] shows that the head movement is the most preceding movement in the direction change motion. Therefore, we focused on the movement of the head's center of mass to capture the cues for prediction of direction change motion.

In Fig.4 shows that the 4 retro-reflective marker were placed at the following anatomical locations of head; the right forehead (RFHD), left forehead (LFHD), right back of head (RBHD), left back of head (LBHD). As the center of mass of the head, the values of the midpoint of these four points were used. In this study, we focused on the changes of the left and right sides of the head (x-y direction) during direction change. Therefore, we did not consider the height (z direction) of the head.

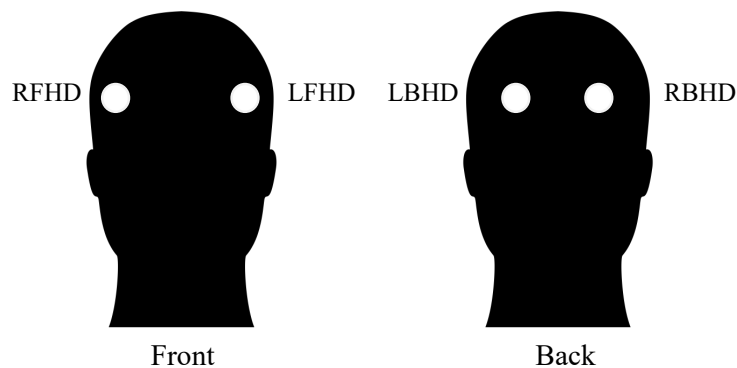
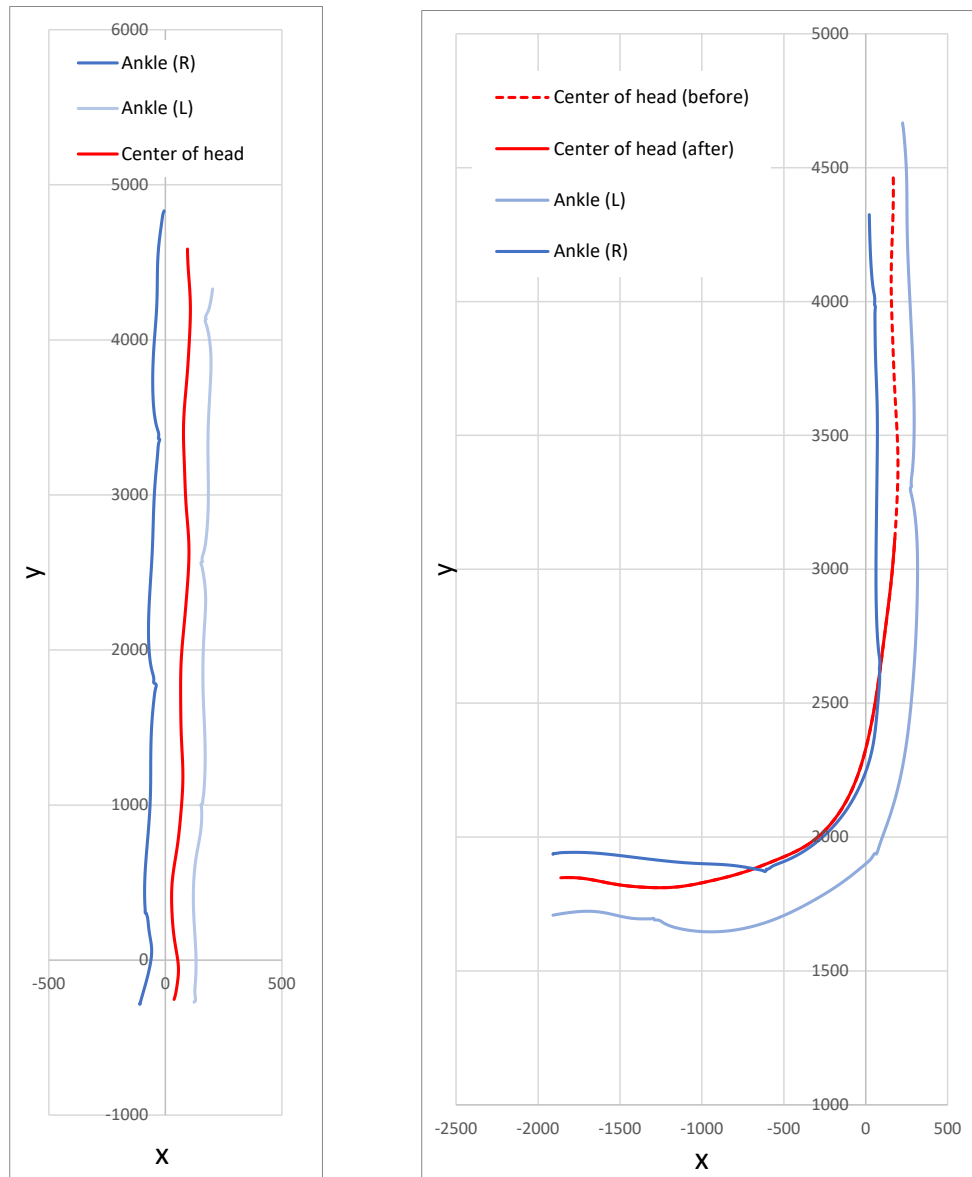


Fig. 4 Marker placement of head

## Result

### Position change of center of mass

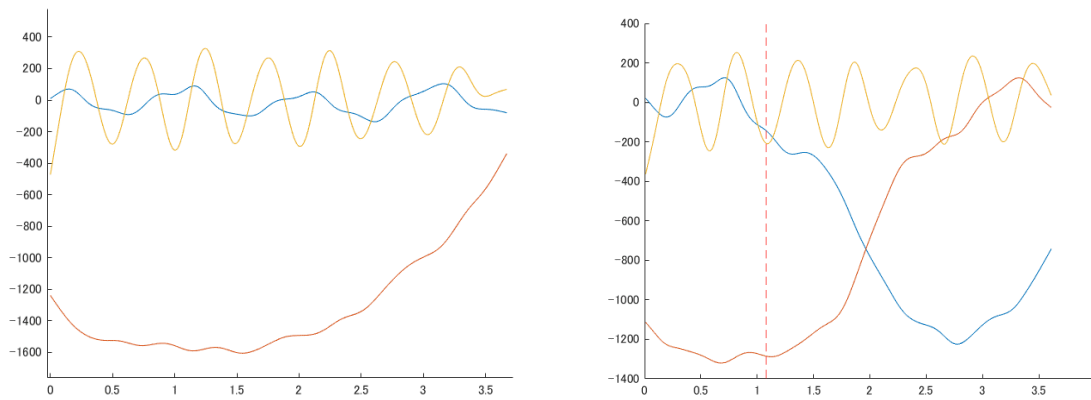
Figs. 5 and 6 show the trajectory of the center of gravity of the head and both ankles, in straight-line gait and direction change. In Fig. 5 (b), the trajectory of the center of the head before the change of direction is shown as a dashed line and the trajectory after the start of the direction change is shown as a solid line. In the straight-line gait in Fig. 5 (a), the center of the head is located between the left and right ankles and draws a straight trajectory, whereas in Fig. 5 (b), the center of head shifts to the right side immediately after the start of the direction change. However, there were no signs that were useful in predicting, therefore we focused on the changes of the velocity of the center of head and plotted it in Figure 6.



(a) the straight-line gait (b) the direction change  
Fig. 5 Trajectory of center of head and ankle positions

*Velocity change of center of mass*

The dashed red line in Fig. 6 is the start time of the direction change motion. Fig. 6 shows that the value of the x-velocity before the direction change motion is larger than the those in the straight-line gait. This result was shown in 5 of the 6 subjects and Table.1 shows the amplification of the velocity in the x-axis. The average value of the velocity in the straight-line gait were used. It shows that it is amplified by 20-80% compared to the straight-line gait. This amplification occurred around the time when the opposite foot of the initiation foot of the direction change contacted the ground. Therefore, the center of head shifted to the left side once before the direction change. That made it easier to step out to the right side. However, there are individual differences in this behavior and there is a bias in the amplification rate.



(a) the straight-line gait                      (b) the direction change  
 Fig. 6 Velocity changes of center of mass of head  
 (blue line: X, red line: Y, yellow line: Z)

Table. 1 Amplification factor of velocity changes of center of head

Subject	Direction change (x) peak [mm/s]	Straight-line gait (x) average [mm/s]	Amplification factor [%]
1	157.2	126.6	24.17
2	124.3	79.00	57.34
3	295.0	284.0	3.89
4	306.4	207.5	47.70
5	191.6	141.0	35.89
6	124.1	71.27	74.18

**Conclusion and Future plan**

In this study, we focused on the center of the head to extract parameters for prediction of the direction change motion. In the velocity change of the center of the head, compared with straight-line gait, there was an amplification of the velocity opposite direction of the direction change before the start of the motion. It is assumed that the shift of the center of mass make it easier to step out to the direction of the turn.

In the future, it is necessary to compare the conditions of the direction change motion to make it more versatile. The conditions of the direction change motion mean "step turn" and "spin turn", change of direction angles [6]-[9]. In addition, there is a task to increase the number of subjects. Furthermore, we need to investigate the center of gravity of each segment and the relationship between segments during preliminary action of the direction change.

## References

- [1] Glaister, B.C., Bernatz, G.C., Klute, G.K., Orendurff, M.S.: Video task analysis of turning during activities of daily living, *Gait & posture*, Vol. 25, No. 2, pp.289-294, 2017.  
<https://doi.org/10.1016/j.gaitpost.2006.04.003>
- [2] Sedgman, R., Goldie, P.: Development of a measure of turning during walking, In *Advancing rehabilitation: Proceedings inaugural conference of Faculty of Health Sciences, La Trobe University, Melbourne, Australia, 1994*
- [3] VICON <https://www.vicon.com/> (2020/08/26 access)
- [4] Takeda, Ogawa, Mita, Prediction of direction change motion using kinematic parameters for implementation of home robot, University of Keio, thesis
- [5] Ashburn A., Kampshoff C., Burnett M., Stack E., Pickering R.M., Verheyden G. Sequence and onset of whole-body coordination when turning in response to a visual trigger: Comparing people with Parkinson's disease and healthy adults, (2014) *Gait and Posture*, 39 (1), pp. 278-283.  
<https://doi.org/10.1016/j.gaitpost.2013.07.128>
- [6] He C, Xu R, Zhao M, et al. Dynamic stability and spatiotemporal parameters during turning in healthy young adults. *Biomed Eng Online*. 2018;17(1):127. Published 2018 Sep 21.  
<https://doi.org/10.1186/s12938-018-0558-5>
- [7] Hase K, Stein RB. Turning strategies during human walking. *J Neurophysiol*. 1999;81(6):2914-2922. <https://doi.org/10.1152/jn.1999.81.6.2914>
- [8] A. Ashburn, Sequence and onset of whole-body coordination when turning in response to a visual trigger: Comparing people with Parkinson's disease and healthy adults, *Gait & Posture* 39 (2014) 278-283. <https://doi.org/10.1016/j.gaitpost.2013.07.128>
- [9] Orendurff, Michael S., et al. "The kinematics and kinetics of turning: limb asymmetries associated with walking a circular path." *Gait & posture* 23.1 (2006): 106-111.  
<https://doi.org/10.1016/j.gaitpost.2004.12.008>

# Innovation and Practice of Cable-Pylon Anchorage Zone Using Group Aggregated Anchor System

Yonggao Yin<sup>1,a</sup>, Qian Li<sup>2,a,\*</sup>, Jiangguo Lv<sup>1,b</sup>, Zhu Yu<sup>1,c</sup>

<sup>1</sup>Anhui Transportation Holding Group Co., Ltd, Hefei, China

<sup>2</sup>Research Institute of Highway Ministry of Transport, Beijing, China

<sup>a</sup>601060901@qq.com, <sup>b</sup>12771320@qq.com, <sup>c</sup>348361184@qq.com

**Keywords:** Cable-Stayed Bridge, Cable-Pylon Anchorage Zone, Group Aggregated Anchor System, Structure, Construction

**Abstract:** With the development of the cable-stayed bridge, the anchorage form on pylon of cable-stayed has been improved and innovated continuously, and the anchorage methods such as circumferential prestressed anchorage, steel anchor beam and steel anchor box have been gradually formed and developed, which further increases the span of cable-stayed bridge and meets the social needs of economic development and environmental integration. The group aggregated anchorage system between cable and pylon is a kind of anchorage form outside the pylon, which has the characteristics of clear force transmission, simple structure and high construction efficiency. It has been successfully applied in Chizhou Yangtze River Bridge for the first time. The main span of Chizhou Yangtze River Bridge is 828m, and the cable-stayed bridge with spatial cable plane of two towers is constructed. Six steel beams are deployed between tower legs to anchor 54 pairs of cables respectively. The steel beams and the concrete tower columns are effectively connected by prestressed anchors, shear nails and short steel bars, which could transfer the cable force to the tower column reliably. This kind of anchoring system has clear force transmission, which could reduce the tensile stress of concrete tower column and the risk of concrete cracking. Meanwhile, the steel beam could be constructed by the engineering manufacture and the field installation, which could reduce the working time at height, further the construction quality and safety could be controlled. Based on the construction of Chizhou Yangtze River Bridge, this paper mainly introduces the proposal, construction, key construction technology and engineering application effect of group aggregated anchorage system. The engineering practice proves that this new type of anchorage could not only meet the basic requirements of the intrinsic safety of the bridge, but integrate with the regional culture to create the beauty of natural harmony as well.

## Introduction

The construction of cable-stayed bridge in China is relatively late. The first cable-stayed bridge is Yunyang Bridge in Sichuan Province, which was built in 1975. The span of this double tower cable-stayed bridge is 75.84m. The construction of this bridge has promoted the development of cable-stayed bridge in China. In the following ten years, the dense cable system was developed and applied. The completion of Shanghai Maogang Bridge and Jinan Yellow River Bridge brought the construction of cable-stayed bridge into the 200-meter era. Since the 1990s, due to the needs for crossing wider river, cable-stayed bridge has been developed rapidly, and the main girder has been lighter <sup>[1]</sup>. At this stage, the span of cable-stayed bridge has exceeded 600m, even reached the kilometer level. A series of landmark bridges have been built in succession, including Shanghai Yangpu Bridge, Wuhan Baishazhou Bridge, Sutong Yangtze River Bridge, Hong Kong



Stonecutters Bridge. The breakthrough and innovation of cable-stayed bridge construction technology has made the development and construction of cable-stayed bridges in China into the world's advanced ranks.

The span capacity of cable-stayed bridge is improved continuously, which means that the load level would increase, and the structural safety problem would become more prominent. The anchorage structure of stay cable and bridge tower is an important structure to transfer the local concentrated force of a cable to the tower column safely and uniformly [2]. The structure of Cable Tower Anchorage Zone is closely related to many factors, such as the layout and quantity of cables, the form and structure of cable tower. Besides, the stress state is complex, which is one of the focuses and difficulties in the design and construction of cable-stayed bridge [3-4]. The common forms of cable anchorage include side wall anchorage, steel beam anchorage, cross anchorage, steel anchor box, etc.[5]. With the development of cable-stayed bridge, the cable tower anchorage structure is also constantly improved and innovated.

### **Anchorage of Cable and Concrete Tower**

In the early stage, the tower column in the anchorage section of medium and small span cable-stayed bridge was solid section, and the cross anchorage structure was mostly used, while it is rarely used at present. In recent years, non-staggered anchorage structure has been widely used in long-span cable-stayed bridges, such as circumferential prestressed anchorage, steel anchor beam and steel anchor box anchorage.

The circumferential prestressed anchorage method uses the external force generated by the prestressed steel bundle to balance the internal force generated by the cable force in the tower column. It has the characteristics of simple structure, low engineering cost and small maintenance workload in the later stage. It is widely used in Yangpu Bridge, Jingzhou Yangtze River Highway bridge, South Branch of the Second Nanjing Yangtze River Bridge, etc. However, due to the extrusion of prestressed tendons in the bending zone, the stress distribution is complex, and the values of elongation and friction coefficient are not clear, and the data measured by the test are quite discrete<sup>[6-7]</sup>. In addition, according to the related research results<sup>[8-9]</sup>, when the span exceeds 800m, the prestressed tendon tonnage is very large, and the thickness of tower column wall and the number of prestressed steel strands will increase, resulting in prestressed tension. Therefore, the circumferential prestressed anchorage is not suitable for the super long-span inclined bridge. Instead, the steel anchor beam steel (or concrete) corbel combination anchorage form and steel anchor box anchorage form are used.

The steel beam in the anchoring form of steel beam is installed inside the hollow tower column and supported on the concrete or steel corbel of the inner wall of the concrete tower column, which is an independent and stable component, and mainly bears the horizontal tension, vertical component force and eccentric bending moment of the cable. The steel beam sustains the horizontal component of the stay cable, which could effectively reduce the tension stress produced by the horizontal component of the cable in the concrete tower column. This kind of anchorage structure is simple and clear, and has been widely used in cable-stayed bridges at home and abroad, such as Jintang Bridge, Jingyue Yangtze River Highway Bridge, North Branch of Xiazhang Bridge, etc. After continuous improvement, the steel beam-steel corbel anchorage form could adapt to the space cable surface, easy to achieve the industrial production of integral assembly, and the construction could be faster.

Compared with prestressed anchorage and steel anchor beam anchorage, the steel anchor box anchorage is widely used in cable-stayed bridges with span greater than 600m, such as Sutong Yangtze River Highway Bridge, Stonecutters Bridge, Normandy Bridge in France, Hangzhou Bay

Sea Crossing Bridge, etc. The main components of steel anchor box are composed of pulling plate along bridge direction, end bearing plate, web, bearing plate under anchor, anchor plate, stiffening rib, working platform and others<sup>[10]</sup>. The horizontal component of the stay cable is borne by the steel anchor box pulling plate, and the vertical component of the stay cable is transmitted to the concrete tower through the stud. The advantages of steel anchor box anchorage are similar to that of steel anchor beam, which could be made in factory, installed on site, and easy to detect and maintain. Moreover, the steel structure has reliable stress and easy to control the position and angle of anchor point. However, due to the large amount of steel used, the internal space of the tower column is required to be large, and the hoisting equipment and installation demand high accuracy. What's more, under the condition of the cable balanced horizontal force, the concrete of the tower column would also produce tension stress, which is unfavorable to the durability of the structure.

According to statistics, the steel-concrete composite anchorage system is used for built cable-stayed bridges where the span is more than 600m. This anchorage system could full perform the tensile strength of steel and the compressive properties of concrete materials, and could realize factory prefabrication, controllable construction quality, high safety and easy maintenance, which has been widely used in super long-span cable-stayed bridges.

### **The Group Aggregated Anchorage System and Construction Technology**

#### *The Group Aggregated Anchorage System*

The group aggregated anchorage system is a relatively new type of stay cable tower anchorage system. The cable is grouped and separately anchored on multi-channel steel beams between towers. The steel beam and concrete tower column are reliably connected by prestressed anchor rod, shear nail and short steel bar, so as to achieve the external anchorage of stay cable tower end<sup>[11,12]</sup>. The cable plane layout of the structure of the grouped aggregated cable tower is more novel and unique, which enhances the visual appreciation and impact force. It has been proposed and applied in Chizhou Yangtze River Bridge for the first time.

Chizhou Yangtze River Highway Bridge (see Figure 1) is a cable-stayed bridge with two pylons and spatial cable plane with main span of 828m. As is known to all, every bridge across the river is a landmark structure of a city, which needs functional, cultural and aesthetic value. In the design process of the main tower of the bridge, since Chizhou Yangtze River Highway Bridge is located in Chizhou Jiuhua Mountain Buddhist holy land, the construction team creatively integrates Buddhist cultural elements into the main tower design of the bridge. The main tower adopts the vase type concrete cable tower scheme. In the upper tower section, 54 pairs of stay cables divided into 6 groups and anchored on the steel cross beams between towers, so as to create the radiation effect of Buddha beads beam, and closely echo the bridge aesthetics and regional culture.



*Fig. 1 Effect Drawing of Chizhou Yangtze River Highway Bridge*

The steel cross beam between towers of the bridge adopts box structure. There are three diaphragms set in the middle along the transverse direction of the bridge, and the anchor box of the cable is set between the diaphragms (see Figure 2). The end of the steel beam is welded with the embedded steel plate on the concrete tower wall, and the high-strength anchor rod is used to connect the steel beam and the tower column. One end of the anchor bolt is anchored on the anchorage bracket of the steel beam side, and the other side is anchored on the steel anchor plate in the concrete tower column. The tension is carried out by the step-by-step tensioning and anchoring technology. What's more, the embedded steel plate is welded with the vertical reinforcement of the outermost layer of the tower column through short steel bars. The bridge load is transmitted to the tower column through the cable, and the horizontal component of the cable is borne by the vertical and horizontal steel plate of the steel beam, meanwhile the vertical component is transferred to the steel beam, which produces bending moment and shear force at the beam end of the steel beam. The bending moment is mainly borne by the prestressed anchor rod, and the steel-concrete joint surface produces large static friction force by using the split anchor rod, which could resist the shear effect. Such structure could significantly improve the force of concrete tower columns.

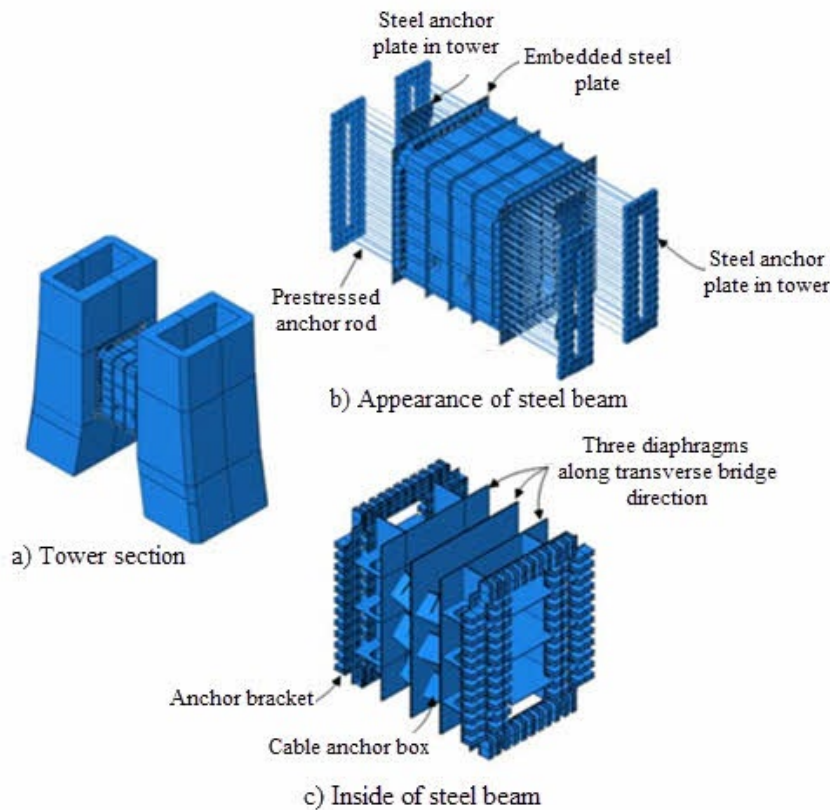


Fig. 2 Structural Diagram of Steel Beam between Towers

#### Key Construction Technology of the Group Aggregated Anchorage System

The construction of the group aggregated anchorage system mainly involves the fabrication and processing of the steel beam between the towers, the installation of the steel beam between the towers, and the installation and tension of the stay cables. The first three items are closely related to the anchoring structure and are the important factors affecting the construction quality and safety of the tower columns.

The steel beam between the towers of Chizhou Yangtze River Highway Bridge is 7.0m high, 5.5m wide along the bridge direction and 7.0m wide in the transverse direction. The steel beam is divided into three sections along the transverse direction of the bridge, and the middle block is divided into two blocks along the longitudinal direction of the bridge. The four blocks are connected by high-strength bolts. The maximum weight of a single block is 68t (see Figure 3). Since there are many groups of cable anchor boxes and diaphragms inside the steel beam, many small boxes and lattice space are formed inside the steel beam. The welding seam is dense, and the plate is thick; furthermore, there are many penetration welds and deep groove welds. The welding deformation control and weld quality would directly affect the site construction accuracy and structural bearing performance.

Welding deformation could be ensured by assembly process, welding method and welding sequence. The middle block could be assembled according to the sequence of separately assembling anchor box unit, middle web, side web, top and bottom plate, joint plate, reinforcement plate and stiffening rib, in which the key point is the angle accuracy of anchor head. Besides, the assembly sequence of side block could be organized as follows: embedded steel plate positioning, web, wall plate, top and bottom plate, stiffening plate, anchor plate, stiffening rib and drilling connection hole, in which the key point is to control the perpendicularity of main frame structure and embedded plate.

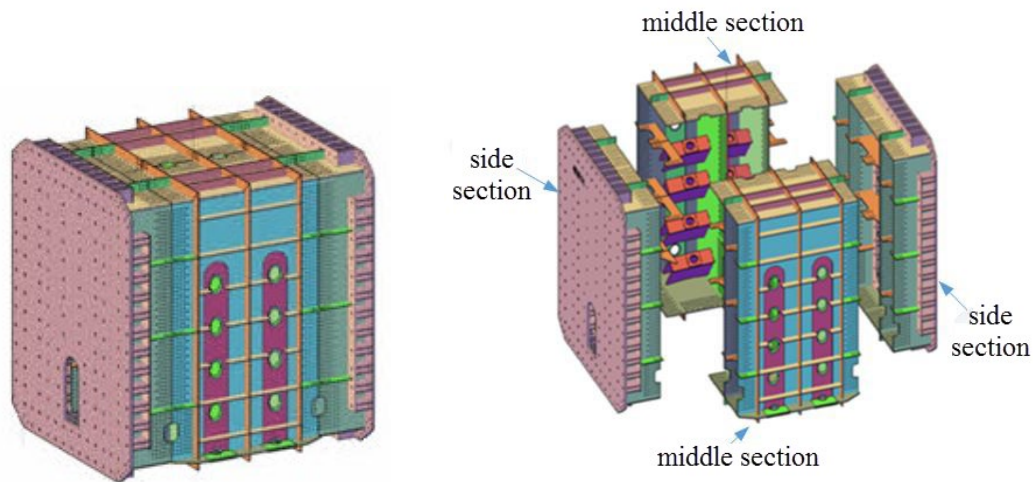


*Fig. 3 Diagram of Blocks of Steel Beam between Towers*

According to the characteristics of the steel beam, combined with the mature construction method of the hoisting operation of high tower and large components, the steel beam installation scheme of "large tonnage tower crane + section steel bracket + three-way Jack positioning system + shape steel and steel wire rope soft hard combination anti overturning system" is proposed (see Figure 4). The installation process is designed as follows: embedding steel beam installation bracket, installing steel beam mounting bracket, large tonnage tower crane hoisting steel beam according to the sequence of side section, middle section and side section, using three-way positioning jack to adjust position, tightening splicing plate and high bolt between steel beam segments, installing steel beam high-strength anchor rod, casting tower column concrete for twice, and tensioning high-strength anchor rod.



*Fig. 4 Wind Rope Pulling and Section Steel Support Locking*



*Fig. 5 Installation of Middle Section of Steel Beam*

### **Effect of Engineering Application**

Taking the Chizhou Yangtze River Highway Bridge project as the research object, and focusing on the design and construction of the group aggregated anchorage system, a series of theoretical analyses, numerical simulations, model tests and process tests are performed. From theoretical analysis to experimental research and real bridge detection, and then to engineering practice, the technological achievements, including the design and construction key technology of the grouped aggregated anchorage system, have been continuously supplemented and improved. According to the scientific research and engineering practice, the grouped aggregated anchorage system has the characteristics:

(1) The external anchorage of the stay cable tower would not occupy the internal space of the tower column, and the structural size of the main tower is optimized.

(2) The vertical component of the cable force is transformed into the bending moment at the end of the beam, which is borne by the high-strength anchor rod, and would not act on the tower wall directly, so as to reduce the concrete tensile stress and avoid the concrete tower column cracking.

(3) The construction of steel beam outside the tower could greatly improve the installation efficiency. According to calculations, compared with the independent anchorage system, the installation efficiency of single group of aggregated anchorage system could be increased by about 50%.

(4) Using small steel beam instead of concrete beam, there is no need to set up large support platform on site. Steel beams could be prefabricated in factory and assembled on site, which could improve accuracy, save materials, shorten construction period and reduce safety risk.

(5) After the installation of the first steel beam of the cable tower is completed, the cable tower has a stable structure, and the upper structure of the cable-stayed bridge could be normally promoted according to the construction steps of the tower and beam, and the synchronous construction of the tower and beam could be reached. Moreover, one steel beam could meet the hanging of multiple pairs of stay cables, which is easy to install and would greatly save the construction period.



*Fig. 6 Synchronous Construction Site of Tower and Beam*

### Summary

Based on the development trend of cable-stayed bridge construction and the demand of long-span construction, the group aggregated anchorage system could make full use of the material characteristics. Based on that, the structure is simple, the force transmission being clear, and the efficiency is high. This system could further improve the durability of the structure, as well as the span capacity and bearing capacity of the cable-stayed bridge. Stresses of three diaphragms and cable anchor box inside steel beam should be monitored in construction and operated stage. And the prestressed force of anchor rod need to be tested at regular intervals to ensure that steel beam can be connect tightly with concrete tower.

### References

- [1] Zhuanghong Lou. Collection of papers on bridges by Zhuanghong Lou [M]. Beijing: *China Communications Press*, 2004.
- [2] Shilin Liu, Zhitao Liang, Jinlong Hou, Fanchao Meng. Cable-stayed Bridge [M]. Beijing: *China Communications Press*, 2002.
- [3] Changpeng Liu, Xigang Zhang, Rengui Wang, Feng Wen. Study on Stress and Structural Characteristics of Cable Tower Anchorage Zone of Composite Structure [J]. *Highway*, 2012 (1): 117-121.
- [4] Qifen Wei, Ying Chang, Wenhai Ye, Kai Bai. Structural Design and Calculation of Cable Tower Anchorage Zone of Edong Yangtze River Highway Bridge [C]. *The 20th National bridge Academic Conference*, Wu Han, Hu Bei Province, May 15<sup>th</sup>, 2012.
- [5] Industry recommended standards of the People's Republic of China. Guidelines for Design of Highway Cable—stayed Bridge [S]. Beijing: *China Communications Press*, 2007.
- [6] Lu Shen, Wenliang Qiu. Analysis and Experimental Study on Prestress Loss of Circumferential Steel Tendons in Anchorage Zone of Pylon of Long Span Cable-stayed Bridge [J]. *Journal of Water Resources and Architectural Engineering*, 2016, 14(2): 97-99.

- [7] Yiqiang Xiang, Shaoping Yi, Xiaoqing Du, Xing Xu. Study on Full Scale Model of Cable-stayed Pylon Segment of Nancha Bridge of The Second Nanjing Yangtze River Bridge [J]. *China Civil Engineering Journal*, 2000, 33(1): 16-22.
- [8] Byung-Wan Jo, Yunn-Ju Byun, Ghi-Ho Tae. Structural Behavior of Cable Anchorage Zones in Prestressed Concrete Cable-stayed Bridge[J]. *Canadian Journal of Civil Engineering*, 2002, 29(1): 171-180. <https://doi.org/10.1139/101-087>
- [9] Burdet O. Analysis and Design of Anchorage Zones in Post-Tensioned Concrete Bridges[D]. Austin: University of Texas at Austin, 1990.
- [10] Xigang Zhang, Yuqing Liu. Anchorage structure of composite cable tower [M]. Beijing: *China Communications Press*, 2010.
- [11] Canwen Yang, Qiang Zhang, Jianhua Shi. Design of Main Navigable Span Bridge of Chizhou Yangtze River Highway Bridge [J]. *Bridge Construction*, 2016, 46(4): 92-96.
- [12] Po Wen, Qiang Zhang, Jianhua Shi. Design of Anchorage Structure for Upper Beam of Main Bridge Tower of Chizhou Yangtze River Highway Bridge [J]. *Bridge Construction*, 2017, 47(2): 83-88.

# Experimental Research on the Bearing Capacity of the Widening Segment of Precast Small Box Girder

Liqiao Xia<sup>1,a</sup>, Qian Li<sup>2,a,\*</sup>, Han Ding<sup>2,b</sup> and Zengshun Tian<sup>3,c</sup>

<sup>1</sup> Wenzhou Highway Investment Co., Ltd, Wenzhou, China

<sup>2</sup> Research Institute of Highway Ministry of Transport, Beijing, China

<sup>3</sup> Shandong Provincial Communications Planning and Design Institute, Jinan, China

<sup>a</sup> 601060901@qq.com, <sup>b</sup> 1143094892@qq.com, <sup>c</sup> 1262820484@qq.com

**Keywords:** Precast Small Box Girder, Splicing Technology, Segment Experiment, Shear Value, Deflection Difference

**Abstract:** Widening the existing expressway is an important way to solve the problems like road traffic congestion and level of service declining in the existing highway network. Besides, for the highway with large traffic volume and lack of detour roads, it is inevitable to open to traffic at the same time of construction. Taking a 20 m precast small box girder bridge widening project as the research object, the ABAQUS finite element entity model of the whole bridge and full-scale segment experiment is established, and the boundary conditions and loading force values of the segment model are determined by the similarity analysis. The numerical simulation calculation of the deflection difference between both sides of the joint and the joint reinforcement strain of the full-scale segment test model is performed, and results are compared with the experimental measured values, so as to verify the rationality of the finite element model. Moreover, this research further studies the shear transfer mechanism and bearing capacity of concrete joints with the finite element calculation, and the force-displacement curve of concrete joint loading in whole process is calculated. According to results, the early strength of concrete develops rapidly, while the deflection difference on both sides of the joint drops rapidly, and the deflection difference basically remains unchanged after 8 hours of casting. The shear transfer of joint concrete in the overall analysis model and section test model develops rapidly in the early stage, since then tends to be stable gradually. Results of the bearing capacity test describe that when the bottom reinforcement of the joint reaches the tensile strength and the deflection of the joint increases rapidly, the ultimate bearing capacity could be reached, and the most unfavorable part of the test joint could bear 17 times of 55t wheel load. It is demonstrated that the traffic control scheme of closing and widening the joint adjacent to the lane in the first three days could ensure the reliable casting performance of the concrete joint when the traffic is not interrupted. The research results would provide technical guidance for the design and construction of the same type of bridge.

## Introduction

With the rapid development of economy, the existing road network could hardly support the rapid growth of traffic volume. In order to relieve such huge transportation pressure, the government not only constructs new freeways, but widens and reconstructs the existed freeways with large traffic volumes to increase the traffic capacity as well, such as Shanghai-Nanjing Freeway, Shanghai-Hangzhou-Ningbo Freeway and Shenyang-Dalian freeway<sup>[1]</sup>. As is known to all, the reconstruction project would inevitably have negative effects on normal operation of road sections to be widened. Therefore, it is of great social and economic benefits to explore the construction quality of bridge widening project under the condition of uninterrupted traffic, establish

reasonable traffic control schemes and verify the reliability of concrete joint casting under traffic load.

For the construction technology of bridge widening, domestic and foreign scholars have carried out a lot of experimental and theoretical researches<sup>[2-6]</sup>. Under the traffic load, the deflection difference changes with time at the joint between new and old bridges, which is bound to affect the quality and strength of joint concrete casting in construction. According to the investigation of the completed bridge widening project, the interface between old and new concrete is likely to appear early cracks, leading to the weakening of lateral connection and the reduction of overall structural stiffness, which could affect the traffic safety and the beauty of the bridge deck seriously, and increase the maintenance and repair costs in the later stage.

In this paper, the 1-meter segment of the precast small box girder is selected as the experimental object. The 5-axis 55t vehicle is applied and the most unfavorable loading is determined. Based on that, the whole process of construction maintenance loading is simulated. The deflection difference between the two sides of the joint and the strain of the reinforcement in the joint of the full-scale segment test model are simulated and compared with the experimental data, so as to verify the rationality of the finite element model. Moreover, through the finite element calculation, the shear transfer mechanism and bearing performance of concrete joint are studied in further, and the force-displacement curve of the whole process of concrete joint loading is calculated.

**Traffic Organization Scheme During Construction**

During the widening construction under traffic serving conditions, in order to ensure the quality of joint concrete casting and reduce the maximum deflection difference on both sides of wet joint, the most simple and effective way is to implement traffic control. The proposed traffic control in the reconstruction project in this paper is shown in Table 1, which is performed by closing the lane adjacent to the widening joint.

*Table 1 Traffic organization scheme*

No.	With traffic control	Without traffic control
Description	The lane adjacent to the closed and widened joint is used as the construction working surface together with the emergency lane, and the rest lanes are open to traffic and bear the standard lane load	All two lanes of the old bridge are open to traffic and bear the standard lane load. The emergency lane of the old bridge is used as the construction working surface
Diagram		

Traffic control is implemented in the first three days of the reconstruction project. The lane adjacent to the joint and the emergency lane are used as the construction working surface, and the rest lanes are open to traffic and bear the standard lane load.

**Mechanical Performance Analysis**

*Project Overview*

The total length of an overpass is 8.7km, and most of the superstructure adopts prestressed concrete simply supported small box girder with standard span of 16m and 20m, with continuous

deck. Bridge widening design complies with the principle of "old bridge old standard, new bridge new standard", and the standard cross section of the new and old small box girder bridge is shown in Figure 1.

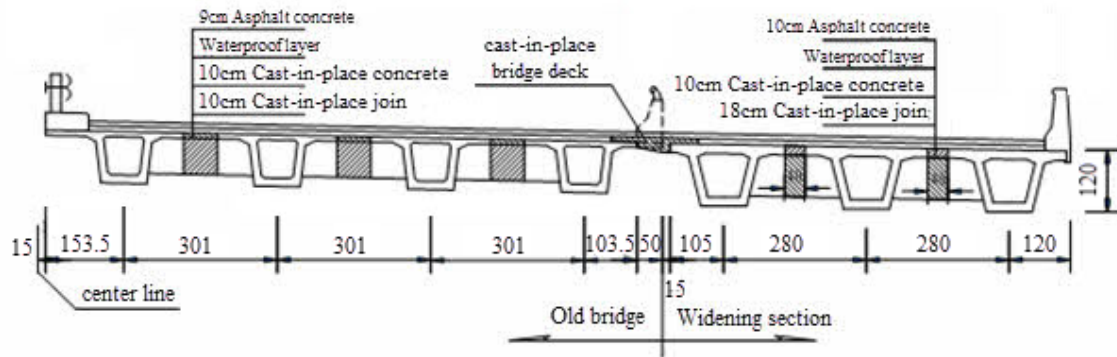


Fig. 1 Standard cross section of small box girder bridges widening (unit: cm)

The widening design scheme of precast small box girder bridge is described as below:

(1) The Superstructures are connected, while the substructures are separated. The wing plate at the joint of new and old box girder adopts rigidity connection, and the lower structure cap beam is not connected.

(2) The side of the new bridge is assembled by three 20m small box girders. The height of single small box girder is 1.2m, and the transverse center distance of adjacent small box girders is 2.8m.

(3) The new and old box girders are only connected by flange plates without end diaphragms.

(4) Cut off 50cm wing slab concrete of guardrail and side beam of old bridge, retain internal reinforcement, and reserve reinforcement for wing plate of new bridge edge beam.

(5) The transverse center distance of the box girder on both sides of the joint is 2.735m, the width of wet joint being 75cm, and the thickness changes from 28cm on the new bridge side to 20cm on the old bridge side.

#### Establishment of Finite Element Model

The overall model of the widening bridges is shown in Figure 2. The precast small box girder bridge is mainly composed of four parts: asphalt pavement, concrete pavement, prefabricated small box girder and rubber bearing. Binding constraints are applied between asphalt pavement and concrete pavement, concrete pavement and main beam, and between main beam and support, that is, the main and secondary surfaces are not separated in the analysis process. The diagram of full-scale segmental test model is shown in Figure 3.

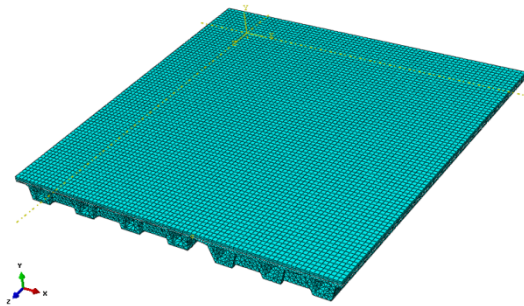


Fig. 2 Finite element model

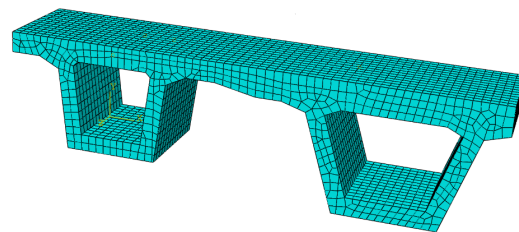
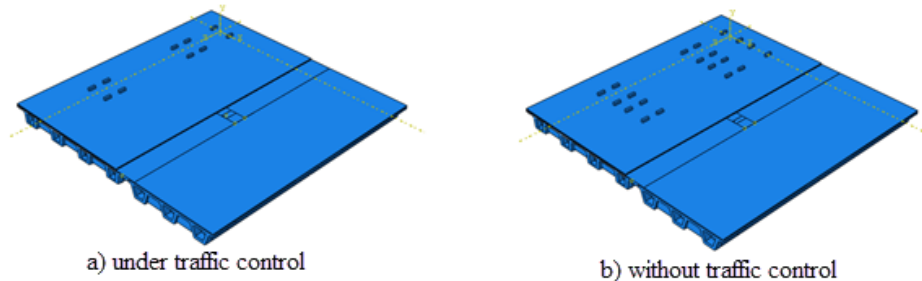


Fig. 3 Diagram of full-scale segmental test model

#### Determination of Boundary Conditions for Full Scale Segmental Test Model

Midas Civil software is used to build old bridge model. The regulations of axle load of 5-axle total with 55-ton weight should be referred to the general design specification for highway bridges and culverts in 1989<sup>[7]</sup>, together with the longitudinal and horizontal arrangement of vehicle fleet. Based on that, the most disadvantageous loading position of vehicle load with or without traffic control scheme could be determined by the unique moving load tracker function. The load distributions under and without traffic control are shown in Figure 4 and Figure 5.



*Fig. 4 Load distribution under two traffic control schemes*

Considering the most unfavorable loading case, the deflections of the mid-span on the widened side of the old bridge under traffic control schemes and without control are 1.822mm, 4.893mm respectively.

In the full-scale segment model test, the loading force of the old bridge box girder is used as the control indicator to carry out cyclic loading. The joint concrete is loaded in two working conditions for five days. For the first working condition, the joint concrete is loaded for three days under traffic control, and for the second condition, the joint concrete is loaded for two days without traffic control.

According to the results of finite element calculation, the peak value of load force in the first working condition is 10kN, and the corresponding deflection value of the old bridge box girder under independent state is 2mm. Then the rain flow method is used to collect the loading period and time of the real bridge. The loading period is defined as 12s, and the loading time of each cycle is 2s. The loading mode is shown in Figure 5.

After the traffic control is terminated, the bridge is loaded in different levels. The level and frequency of loading force in the second working condition are: loading 26kN for 6 times/h, 20kN for 24 times/h, 15kN for 46 times/h, 10kN for 78 times/h, and 5kN for 146 times/h. According to the sampling frequency of the real bridge in field, the loading period is 12s, and the loading time of each cycle is 2s. The diagram of loading mode is shown in Figure 6.

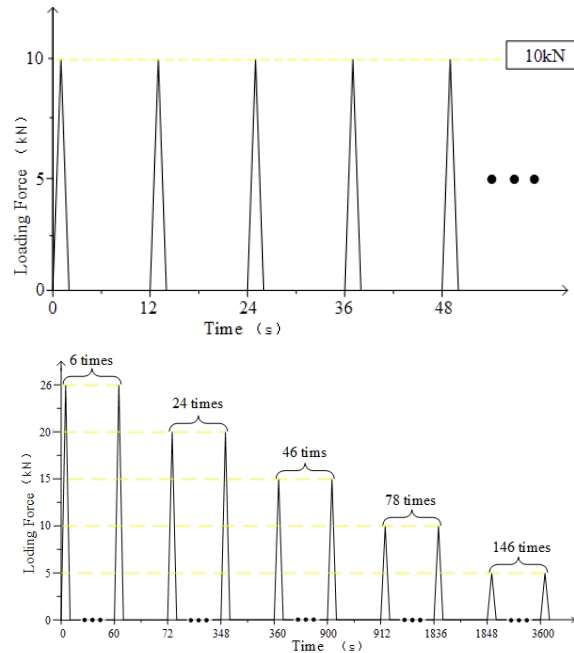


Fig. 5 Loading mode under traffic control Fig. 6 Loading mode after releasing traffic control

The new bridge part of the test component is pre-pressed with I-beam, and then connected with the pedestal by screw. Spring supports are installed at the bottom of some beams on old bridges. The electro-hydraulic servo loading system generates the loading force and allows the vertical displacement of the box girder, so as to simulate the dynamic deflection of real bridge. The layout of the overall model is depicted in Figure 7.

After repeated calculation, the results show that the shear force and bending moment of the whole and segment models are equivalent well with the development age of joint concrete, when the spring stiffness of bearing  $K = 1.373 \times 10^6 (N/m)$ . Based on the spring stiffness, the loading forces before and after traffic control is 10kN and 26kN respectively.

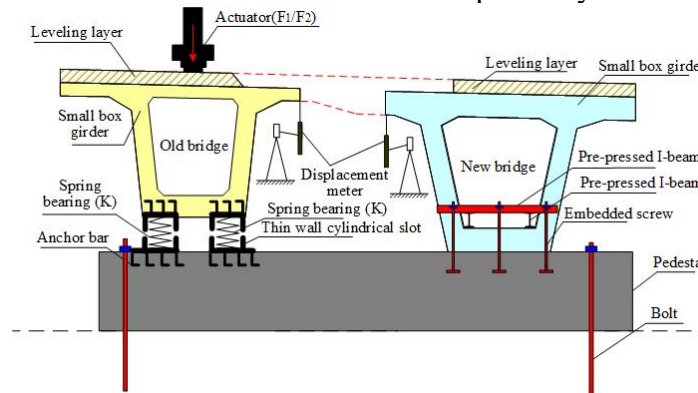


Fig. 7 Overall layout of full scale segmental model

Numerical simulation and experimental curve of displacement on both sides of joint are depicted in Figure 8. According to the development model of concrete elastic modulus, the displacement of joint on old bridge side decreases rapidly, reaches 0.53mm after 8 hours and gradually tends to be stable. On the contrary, the displacement of joint on new bridge side increases rapidly in the first 4 hours, then slowly increases to 0.27mm and remains unchanged. The

displacement of the new bridge side changes abruptly from 0.33mm to 0.25mm while the construction framework is removed after 40 hours, and then the displacement increases slightly, and finally tends to be stable. In the first 22 hours, the obvious change of the displacement is attributed to the slow development of the actual elastic modulus of concrete and the influence of dynamic deflection.

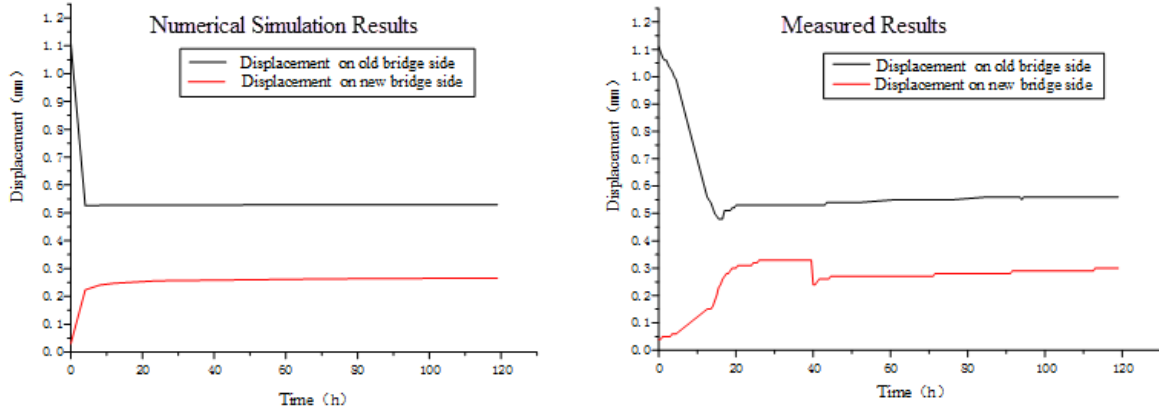


Fig. 8 Displacement curve on both sides of joint

The comparison between measured and calculated deflection difference curves on both sides of joint is displayed in Figure 9.

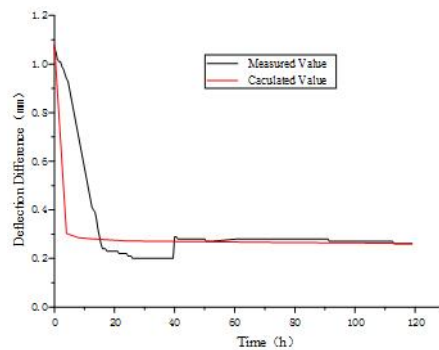


Fig. 9 Comparison of deflection on both sides of joint

The top reinforcement of the joint is in tension and the bottom reinforcement is under compression. It could be observed from Figure 10 that the calculated strain of reinforcement at the top and bottom of the joint is quite consistent with the measured value in the early stage. After the concrete age for 1-day, the measured value is smaller than the calculated value.

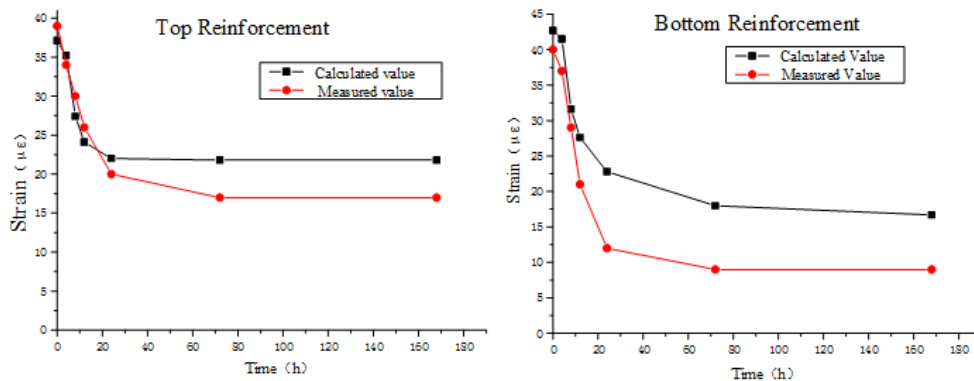


Fig. 10 Strain of reinforcement of the joint

## Research on Shear Transfer Mechanism and Ultimate Bearing Capacity of Concrete Joint in Segmental Model

### Research on Shear Transfer Mechanism

Elastic modulus of concrete (Eq.1) was determined according to the regulation CEB-FIP MC90 as below:

$$E_c(t) = E_c \cdot \exp(0.5s[1 - (28/t)^{0.5}]) \quad (1)$$

Where:  $E_c$ —Elastic modulus of concrete at 28 days of age

$s$ —Coefficient of cement type. This value is 0.2 for fast setting high strength cement, 0.25 for wing plate cement, and 0.38 for retarded cement.

$t$ —Days after concrete casting.

In ABAQUS finite element model, the elastic modulus value of joint concrete is given with the development of age, and the growth trend of shear force of joint concrete of whole and segment test models with curing age is calculated and analyzed. The shear transfer value of concrete joint at 1m section at the mid-span is taken for the overall model, which could accurately reflect the stress state of the whole structure. It can be seen from Figure 11 that the shear transfer rate of the whole and segment model joints is very fast in the early stage, and then gradually tends to be stable.

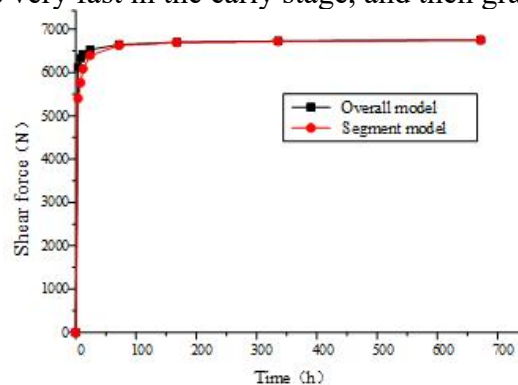


Fig. 11 Shear transfer curve of overall and segment models

### Research on Ultimate Bearing Capacity

The plastic damage model of concrete is used to calculate the ultimate bearing capacity level of the full-scale segment test model. The peak point of the force-displacement curve is taken as the failure point of the component, and all the joint reinforcement reaches the yield strength. The loading actuator is deployed at the chamfering of the box girder side of the old bridge on the top of the joint, which is the weakest position of the structure.

As illustrated in Figure 12, the yield stress and inelastic strain curve of C50 concrete in compression stage, as well as the yield stress and cracking strain curve in tension stage, are derived respectively, which is the failure criteria of concrete constitutive relation.

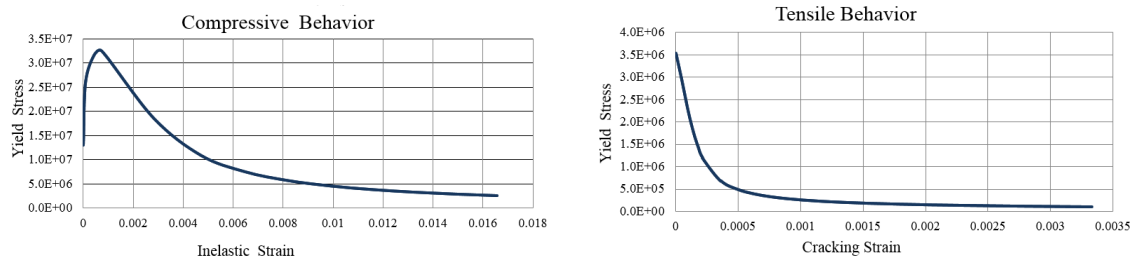


Fig. 12 Failure criterion of concrete

Failure model adopts the displacement convergence standard, and the increment step size is set to 0.001. Then the damage factors of compression and tension are calculated, which are denoted as  $d_c$  (Eq.2) and  $d_t$  (Eq.3) respectively:

$$d_c = 1 - \frac{\sigma_c E_0^{-1}}{\varepsilon_c^{pl}(1/b_c - 1) + \sigma_c E_0^{-1}} \quad (2)$$

Where:  $b_c = \varepsilon_c^{pl} / \varepsilon_c^{in}$ .

$$d_t = 1 - \frac{\sigma_t E_0^{-1}}{\varepsilon_t^{pl}(1/b_t - 1) + \sigma_t E_0^{-1}} \quad (3)$$

Where:  $b_t = \varepsilon_t^{pl} / \varepsilon_t^{ck}$ .

The monotonic load displacement curve of solid model simulation test component is shown in Figure 13. When the loading force increases from zero to 790kN, the slope of the curve remains unchanged, and the stress of concrete is basically in the elastic stage. Meanwhile, the tensile strain at the bottom of the joint concrete could reach the cracking value, a small number of microcracks appearing, and the tensile stress at the bottom of the joint is mainly borne by the reinforcement. When approaching the yield point, a small amount of plastic deformation could occur. Besides, the deflection curve is slightly concave, in the meantime, the cracks would continue to extend and develop. When the loading capacity increases to 1190kN, the reinforcement at the bottom of the joint would reach the maximum strength, the concrete cracks would develop rapidly, and the bearing capacity of the structure would decrease rapidly.

Referring to the standard load of 55T heavy vehicle, the load of rear axle is 140kN, and the weight of one side wheel is 70kN. Therefore, the most unfavorable position of joint is fully able to bear 17 times of 55T heavy vehicle wheel load, i.e., the widening measures are reliable.

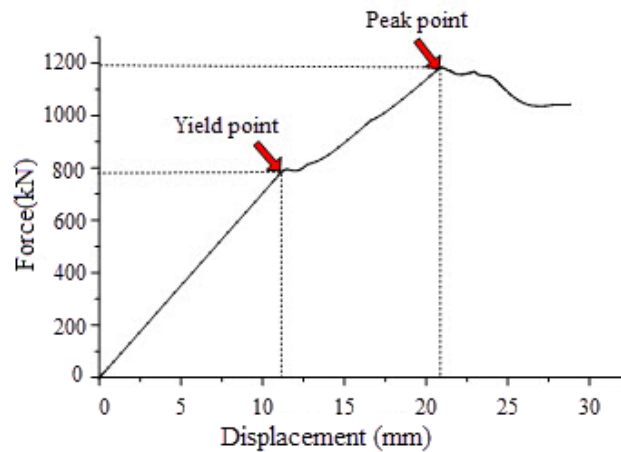


Fig. 13 Load-displacement curve of full scale segment model

### Summary

In this paper, through the full-scale segment test model, the deflection difference on both sides of the joint and the strain of the joint reinforcement are simulated and compared with the experimental data, which verifies the reliability of the three-dimensional solid finite element model, and could accurately calculate the joint shear transfer value and monotone loading curve. Through the above research and analysis, it could be summarized that:

(1) The early strength of concrete develops rapidly, and the deflection difference decreases rapidly. The maximum decrease of deflection difference is 27% one day before casting, and remains unchanged after casting.

(2) Based on the calculation and analysis of the development of the shear force of the joint concrete of the whole and section test models with the curing time, it is concluded that the shear transfer of the joint concrete develops rapidly in the early stage, and then gradually tends to be stable, and the segment model could accurately reflect the stress state of the whole structure.

(3) The load-displacement curve of the full-scale segment test model is obtained. The most unfavorable position of the joint is fully able to bear 17 times of 55T heavy vehicle wheel load, and the measures are reliable.

(4) The deflection difference is an important index to reflect the performance of widening bridge. The mid-span deflection difference should be monitored during the construction and operation stage. The maximum stress of the joint concrete appears near the beam end support, so monitoring points should be considered.

## References

- [1] Xuejun Wang, Jinsheng Du, et al. Discussion on Several Problems in Bridge Widening of Freeway [J]. *Highway*, 2008 (7): 169-174.
- [2] Wei Li. Key Technology of Shenyang to Dalian Freeway Extension Project [C]. On *2006 National Freeway Reconstruction and Expansion Technology Seminar*, 2006.
- [3] MA Chun-sheng, SONG Shen-you. Design of Connection Between New Beam and Old One of Huzhou Bridge on Guangfo Freeway [J]. *Highway*, 2003 (8): 63-66.
- [4] Yande Gui. Discussion on Design Method of Freeway Widening [J]. *Highway*, 2004 (7): 59-64.
- [5] Hua Bin, Li Jie, et al. Research on the Key Widening Technology for PC Bridge [J]. *Modern Transportation Technology*, 2006 (5): 72-77.
- [6] Qingjie Wen, Jianshu Ye. Analysis of Shrinkage and Creep Effect in Widening Reinforced Concrete Girder [J]. *Journal of Southeast University*, 2006, 36 (4): 596-600.
- [7] Industry Standard of Ministry of Transport. General Specifications for Design of Highway Bridges and Culverts [S]. Beijing: *China Communications Press*, 1989.

# Experimental Research on the Effectiveness of Speed Reduction Markings based on Drivers' Operating Performance: A Driving Simulation Study

Han Ding<sup>1,a</sup>, Li Cui<sup>2,b</sup>, Xiaohua Zhao<sup>3,c,\*</sup>, and Wanheng Li<sup>1,d</sup>

<sup>1</sup>Bridge & Tunnel Research Center, Research Institute of Highway Ministry of Transport, No. 8 Xitucheng Road, Haidian District, Beijing 100088, P. R. China

<sup>2</sup>Research and Development Center of Transport Industry of Spatial Information Application and Disaster Prevention and Mitigation Technology, CHECC Data Co., Ltd., China Highway Engineering Consultants Corporation, Jiahao Center, No.116, Zizhuyuan Road, Haidian District, Beijing 100097, P. R. China

<sup>3</sup>College of Metropolitan Transportation, Beijing University of Technology, Chaoyang District, Beijing 100124, P.R. China

<sup>a</sup>1143094892@qq.com, <sup>b</sup>cuili90319@sohu.com, <sup>c</sup>zhaoxiaohua@bjut.edu.cn, <sup>d</sup>wh.li@rioh.cn

**Keywords:** Traffic Safety, Speed Reduction Markings, Driving Simulation, Decelerating Decision, Operating Performance

**Abstract.** Speed reduction markings (SRMs), which are widely used on highways and urban roads in China, are designed to inform drivers of the upcoming road conditions and thus encourage them to reduce travel speed. The objective of this paper is to test the effectiveness of SRMs on drivers' operating performance and decision to decelerate in downhill segments on urban roads. Data of gas and brake pedal use was collected in a driving simulator experiment, and a subjective questionnaire survey was conducted. Two indicators—the operating frequency and operating power—were proposed to evaluate drivers' operating performance due to SRMs. Results of the subjective questionnaire study showed that the majority of subjects were affected by SRMs while driving through downhill segments with distinct roadway grades (3%, 2%, 1.5% and 1% in experimental scenarios). In terms of the operating frequency, the results of the analysis of variance with repeated measures (rANOVA) and the contrast analysis (S-N-K method) showed that transverse speed reduction markings (TSRMs) were significantly effective in influencing drivers' frequency of letting off the gas pedal when roadway grades of downhill segments were 3%, 2%, and 1.5% ( $p < 0.05$ ), while longitudinal speed reduction markings (LSRMs) had little effects; both types of SRMs are effective in increasing the frequency of pressing the brake pedal in all four downhill segments. For the operating power, the gas pedal power was significantly affected by TSRMs in all four roadway scenarios; TSRMs also tended to increase the brake pedal power when the roadway grades were 2% and 1.5%, while both types of SRMs had similar effects in road sections with roadway grades of 3%.

## Background

According to (1), as one of the main contributing factors of traffic crashes, speeding alone accounted for 11.7 percent of all traffic fatalities in 2012 in China. To better deal with this issue, speed control devices are usually deployed at sites where speeding-related traffic crashes are more likely to happen. Particularly, speed reduction markings (SRMs) are widely used on highways and urban roads in China, because they are not only capable of alerting drivers to decelerate, but bringing fewer negative effects on drivers and vehicles as well. SRMs are classified into



longitudinal speed reduction markings (LSRMs) and transverse speed reduction markings (TSRMs), and normally placed within or prior to curves, downhill segments, or other road features where drivers need to control their speed (2,6). Meanwhile, the 2009 U.S. *Manual on Uniform Traffic Control Devices* (the 2009 MUTCD) also offers detailed illustrations for installation and design principles of SRMs (3,6). Since the design and application of SRMs are unique in China, it is necessary to evaluate the effectiveness of these SRMs in the China National Standard of Traffic Control Devices.

In contrast to the extensive use, it is still unclear whether SRMs could reduce or affect vehicle speeds and to what extent SRMs reduce vehicle speeds. Numerous research studies have been conducted to evaluate the effectiveness of SRMs or the similar pavement lines. For example, Gates et al. (4) researched the effectiveness of transverse bar pavement markings on freeway curves; Katz (5) and Ding et al. (6) evaluated the effects of SRMs by driving simulator experiments. In those research studies, the speed index was selected to observe the effectiveness of SRMs. In actual, the vehicle speed was the most common indicator, which was used to measure the deceleration capability of SRMs in other relevant research (7, 8).

However, SRMs belong to nonintrusive speed control devices and are not enforceable in China, which sometimes leads no change in vehicle speeds when drivers are travelling through SRMs. In fact, according to the national standard (2), the main purpose of SRMs is to alert drivers to decelerate. If a driver perceives the existence of SRMs and decides to slow down, one could say that SRMs are effective, regardless of the magnitude of speed change. From this perspective, some researchers turned to probe into the operating principle, and discovered that SRMs would generate some warning or perceptual effects together with speed changes. For example, Kaber et al. (9) pointed out that a driver's conscious control is associated with the driver's reactions to roadway conditions. Zheng (10) stated that SRMs could cause some effects on drivers' perception, as if they were driving faster or the lane became narrower. Those influences on drivers' perception would make them decelerate.

Furthermore, based on the perception-judgment-manipulation mechanism (11), drivers' operating performance is highly associated with perception and judgment. If SRMs make drivers decide to decelerate, drivers will execute related maneuvers. Among all kinds of operating performances, letting off the gas pedal and/or pressing the brake pedal can directly reduce vehicle speed. Consequently, researchers can validate the effectiveness of SRMs on drivers' consciousness and judgment of decelerating by measuring drivers' gas and brake pedal performances. For instance, Ding et al. (12) chose the decelerating operating frequency as one of the indicators to evaluate the effectiveness of SRMs. Other researchers have also discussed the indicators of driving operating. For example, Mulder et al. (13) illustrated drivers' neuromuscular measurements of gas pedal positions and manner by how much force drivers applied to the pedal when driving in the simulator. Rakauskas et al. (14) also used the gas pedal position to measure the effects of cell phone conversations on driving performance.

Existing research has usually been performed through field studies, so that data which reflect vehicle operation status (including speed, acceleration, etc.) could be acquired. Besides, considering the characteristics of nonintrusive speed control devices, the objective of this paper is to test the effectiveness of SRMs on drivers' operating performance and decision to decelerate. Compared to field tests, a simulation study can additionally record drivers' operating performance data, such as accelerating, decelerating, steering, and gear shifting. Field tests could make sure the reliability of speed and operating performance data, however, it is difficult to evaluate the changes in speed or performance due to presence of SRMs because vehicle's

operating and driver's performance are actually affected by numerous factors, such as presence of SRMs, road alignments, traffic volume and density. The driving simulator study could help us isolate other confounding factors, and observe the effect of SRMs alone on vehicle status or driver's performance. Therefore, a driving simulator experiment was conducted. Particularly, it has to be pointed out that this paper shared the same experiment with (6); nevertheless, this paper used driver's operating data, i.e., accelerator and brake pedals, while the data set of speed and acceleration was analyzed in (6), corresponding to the different research objectives.

## Method

### *Subjects*

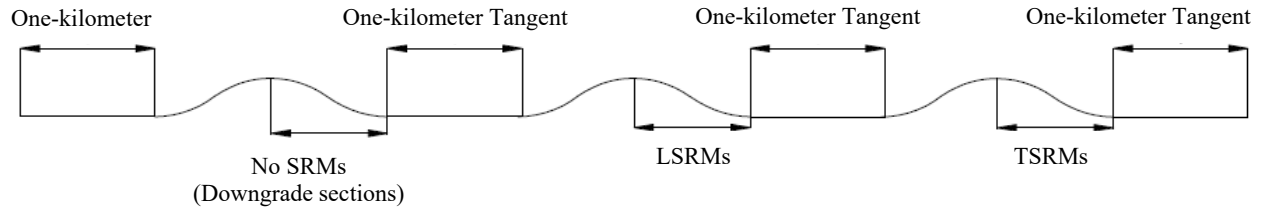
In this study, female subjects account for a small number of the total participants, based on the demographic characteristics of licensed drivers in China (15). Twenty-seven male and three female subjects, ages 18 to 42, with an average age of 24.8 years and an average driving experience of 3.3 years, were recruited by advertisement. Specifically speaking, percentages of participants in different age groups (18-25, 25-30 and >30) were 45%, 45% and 10%, respectively. To capture subjects' actual reactions to the presence of SRMs, participants were not informed of the purpose of the study.

### *Apparatus*

Technical parameters of a fixed-base driving simulator used in this experiment have been introduced (6,12); the real-time data were collected, including operating performance data (e.g., accelerating, decelerating and steering). The values of gas and brake pedal range from 0 to 1, denoting the press intensity of these two pedals. For instance, "0" denotes that drivers are not pressing, while "1" represents that drivers are fully pressing. The data acquisition frequency is 30Hz, and the virtual scenario was projected onto three large screens, providing a 130° field of view. Moreover, the driving simulator can also generate various sensory effects to participants, such as visual, auditoria and tactile effects.

### *Scenarios*

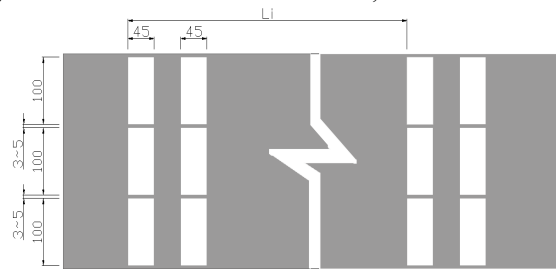
As mentioned in the national standard, SRMs should be placed on or prior to downhill segments. According to the Chinese industrial standard *Code for Design of Urban Road Engineering* (CJJ37-2012) (16), roadway grades of downhill segments in urban Beijing range from 1% to 3%, due to geographic and climatic conditions, and road designers typically choose roadway grades from 1.5% to 2%. Therefore, this study designed a total of 12 experimental segments [i.e., 3 (No SRMs vs. LSRMs vs. TSRMs)  $\times$  4 (roadway grades of 3% vs. 2% vs. 1.5% vs. 1%)], and four virtual scenarios were created, as mentioned in (6). Each scenario featured an eight-lane, divided urban expressway, with four one-kilometer tangents and three downhill segments; in all scenarios, the downhill segments were equipped with no SRMs, LSRMs or TSRMs, respectively (see Fig. 1 (a) and (b)). Additionally, roadway grades of three downhill segments in one scenario were the same. Scenarios 1 to 4 were named as 3-PCT (abbreviation for percentage) scenario, 2-PCT scenario, 1.5-PCT scenario and 1-PCT scenario, representing different roadway grades. Detailed designs of two types of SRMs are shown in Fig. 1 (c)-(e), and alignment parameters of virtual scenarios are listed in Table 1. Besides, the vibratory feeling produced by TSRMs could be simulated by the dynamic module in this driving simulator, and subjects would experience such vibratory feelings while traveling through TSRMs.



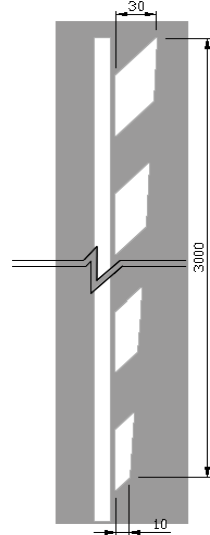
(a) Profile graph of scenarios



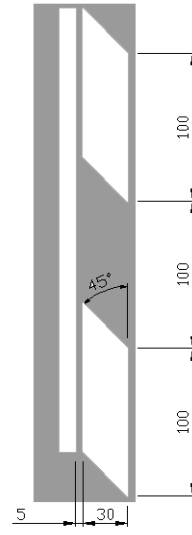
(b) Downhill sections with No SRMs, LSRMs and TSRMs



(c) Detailed designs of TSRMs (in cm.)



(d) Transition taper of LSRMs (in cm.)



(e) Detailed designs of LSRMs (in cm.)

*Fig.1 Scenario design*

*Table 1 Alignment parameters of virtual scenarios*

Scenario No.	Roadway grades (%)	Length of downhill sections (m)	Elevation of downhill sections (m)	Length of entire scenario (m)	Lane widths (m)
1	3	942.15	15	9652.90	3.75
2	2	704.68	7	8228.08	
3	1.5	659.42	5.3	7956.52	
4	1	554.74	4.8	7328.44	

*Procedures*

Since this paper shared the same experiment method with (6), the procedures have been fully introduced. Subjects were first required to fill out a questionnaire, which recorded their basic information, as well as their physiological and psychological conditions. Then they were required to perform a practice drive for 5-10 minutes on a specific alignment to become familiar with the driving simulator.

After the practice drive, subjects participated in the first driving experiment, in which the operating performance data were collected. During the first experiment, each subject drove from scenario 1 (3-PCT scenario) to scenario 4 (1-PCT scenario) in sequence. Each scenario was driven once, and the entire driving experiment lasted approximately 30 to 40 minutes.

The second driving experiment took place 10 minutes after the first one, so as to avoid fatigue. The main objective of the second experiment was to obtain subjective evaluations of SRMs in downhill segments. Therefore, a subjective questionnaire was designed to ask subjects whether SRMs prompted them to reduce speeds. During the second driving, one operator would sit in the driving simulator. The operator would read questions to subjects and complete the questionnaire when each subject left the road sections equipped with SRMs and entered into following tangents in one scenario, so as to acquire the fresh feeling of subjects about SRMs. It was pre-validated that the tangent was long enough for subjects to recall and answer questions, and subjects could continue their normal driving in following downhill segments. Each scenario would also be driven for once, and the whole driving also lasted for 30 to 40 minute. When the second experiment was finished, subjects left the driving simulator and filled out a questionnaire to report their subjective evaluations of the driving simulator, together with the physiological and psychological status at post-test.

**Analysis and Results**

*Subjective questionnaires*

In this experiment, one questionnaire required subjects to evaluate the performance of the driving simulator subjectively. The evaluation items included the brake, accelerator, scenarios, and SRMs, among other items. The ratings ranged from 0 (“not at all similar to the real world”) to 10 (“extremely similar to the real world”). The results are shown in Table 2.

*Table 2 Ratings of subjective evaluation of driving simulator*

	Overall	Steering	Accelerator	Brake	Clutch	Gear	Scenario	SRMs
<b>Mean</b>	<b>7.8</b>	<b>8.0</b>	<b>7.7</b>	<b>7.2</b>	<b>8.3</b>	<b>8.3</b>	<b>8.0</b>	<b>8.7</b>

The other questionnaire (which was also stated in (6)) was administered to get participants’ subjective views of the effectiveness of SRMs, and results are shown in Fig. 2. For example, in the downhill segment with a roadway grade of 3%, 83.3% of subjects were reported to reduce speeds

due to the presence of LSRMs, and 86.7% of subjects were influenced by TSRMs. The following was observed:

- 1) The majority of subjects decelerated for both types of SRMs in all four scenarios.
- 2) TSRMs in segments with a grade of 3% were associated with the highest percentage of subjects slowing down, and the percentages of subjects slowing down on a downhill segment with other grades (i.e., 1%, 1.5% and 2%) were similar but slightly lower.
- 3) The effects of LSRMs in all four scenarios were lower than the effects of TSRMs.
- 4) The percentage of subjects slowing down on a downhill segment with LSRMs apparently decreased as the roadway grades decreased.

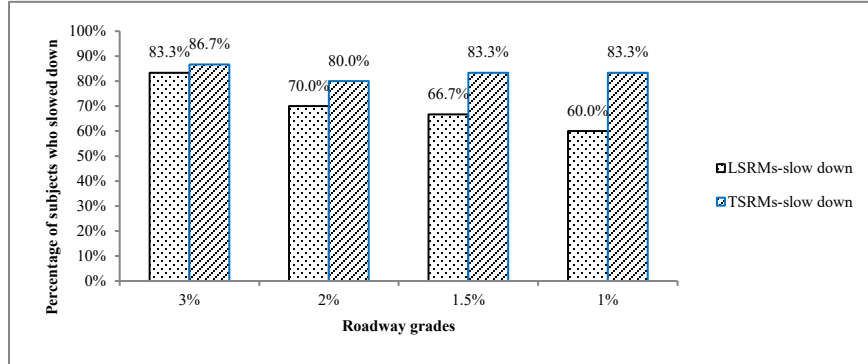


Fig. 2 Percentage of subjects slowing down due to the presence of SRMs

### Operating frequency

In this paper, effects of SRMs on drivers’ operating performance and driving decisions will be discussed. Among all operating performances, letting off the gas pedal and pressing the brake pedal are two separate actions that can directly control vehicle speeds. Therefore, the operating frequency, measuring how frequently a driver lets off the gas pedal or presses the brake pedal, is analyzed to reflect the change in drivers’ decisions.

### Frequency of letting off the gas pedal

The results of average frequencies of letting off the gas pedal with respect to different types of SRMs and roadway grades are presented in Fig. 3. It indicates that in the 3-PCT, 2-PCT and 1.5-PCT scenarios, drivers release the gas pedal noticeably less often in road sections paved with TSRMs than sections with No SRMs and LSRMs. In 1-PCT scenario, drivers let off the gas pedal less in road sections with SRMs than those with No SRMs; however, there is no difference between these two types of SRMs. In terms of roadway grades, the average frequency of releasing the gas pedal in the 3-PCT scenario is apparently higher than the ones in the other three scenarios.

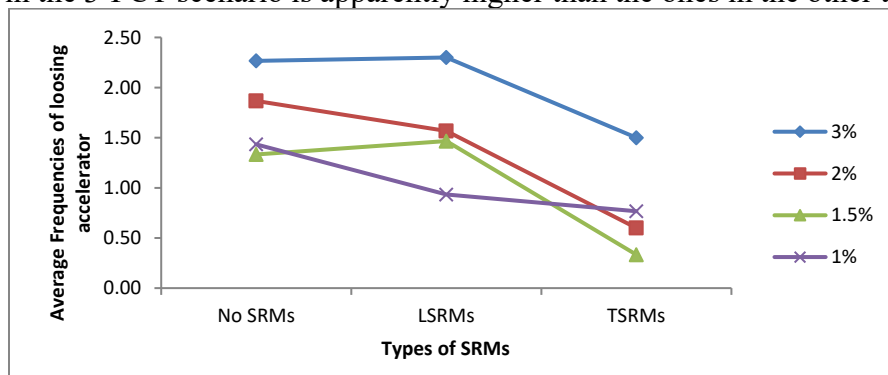


Fig. 3 Average frequencies of letting off the gas pedal

The analysis of variance with repeated measures (rANOVA) was conducted to compare the impacts of SRMs and roadway grades on average frequencies of letting of the gas pedal. The results revealed significant differences in the indicators among three types of SRMs (No SRMs, LSRMs and TSRMs) ( $F_{(2,58)}=26.508$ ;  $P<0.001$ ) and four roadway grades (3%, 2%, 1.5% and 1%) ( $F_{(3,87)}=11.160$ ;  $P<0.001$ ).

The ANOVA was further used to identify the differences in the indicators between distinct types of SRMs and roadway grades. In the 3-PCT ( $F_{(2,58)}=4.032$ ,  $P=0.023$ ), 2-PCT ( $F_{(2,58)}=7.212$ ,  $P=0.002$ ) and 1.5-PCT ( $F_{(2,58)}=12.293$ ,  $P<0.001$ ) scenarios, results of the ANOVA showed significant main effects of the type of SRMs on the average frequencies. For all three scenarios, a contrast analysis (S-N-K method) revealed that the average frequencies in the vertical curve with TSRMs were significantly lower than that without SRMs and LSRMs ( $P<0.05$  in all contrasts). The test results suggested that TSRMs had statistically significant effects on the frequency of letting off the gas pedal in downhill segments whose roadway grades were 3%, 2% and 1.5%.

In the 1-PCT scenario, however, results of ANOVA reflected that there was no significant main effect of the type of SRMs on the average frequencies ( $F_{(2,58)}=2.932$ ;  $P=0.061$ ). The test results implied that neither LSRMs nor TSRMs had statistically significant effects on letting off the gas pedal in downhill segments whose roadway grades were 1%.

For LSRMs ( $F_{(3,87)}=5.752$ ,  $P=0.001$ ) and TSRMs ( $F_{(3,87)}=5.868$ ,  $P=0.001$ ), analytical results showed significant main effects of roadway grades on the average frequencies. The contrast analysis determined that the average frequencies in the 3-PCT scenario with SRMs are significantly higher than the indicators in the other three scenarios, which inferred that SRMs could induce subjects to let off the gas pedal more in downhill segments with roadway grades of 3%, when compared with the other three roadway grades.

#### *Frequency of pressing the brake pedal*

For all drivers, the average frequencies of pressing the brake pedal with respect to different types of SRMs and roadway grades are presented in Fig. 4. There is a clear increasing tendency for this indicator in 3-PCT, 2-PCT and 1.5-PCT scenarios, and drivers press the brake pedal the most in road segments with TSRMs. In the 1-PCT scenario, drivers will press the brake pedal more in road sections with SRMs than without SRMs; however, there is no considerable difference between these two kinds of SRMs.

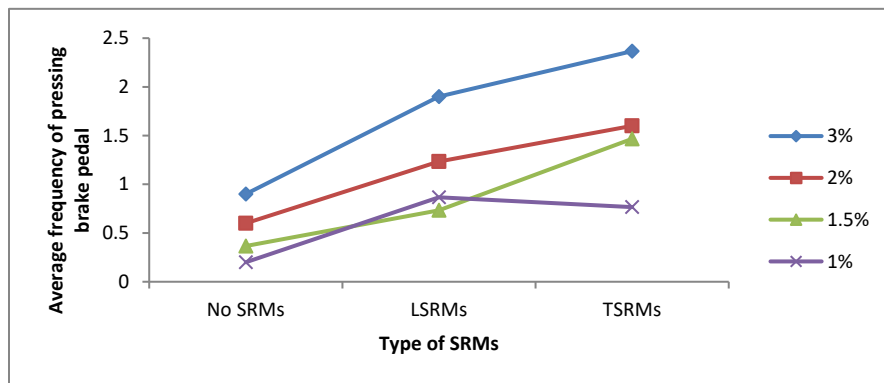


*Fig. 4 Average frequencies of pressing the brake pedal*

In terms of roadway grades, average frequencies of pressing the brake pedal in the 3-PCT scenario are apparently greater than that in the other three scenarios for both kinds of SRMs;

particularly, the indicators for TSRMs in the 1.5-PCT and 2-PCT scenarios are higher than the one in the 1-PCT scenario, yet these frequencies are still lower than the frequency related to the 3-PCT scenario.

The rANOVA was used to compare the impacts of SRMs and roadway grades on the average frequency of pressing the brake pedal. The results showed significant differences in the indicator associated with types of SRMs ( $F_{(2,58)}=17.265$ ;  $P<0.001$ ) and roadway grades ( $F_{(3,27)}=7.058$ ;  $P=0.001$ ).

The ANOVA was used to evaluate the effectiveness of SRMs with different roadway grades, in terms of average frequencies of pressing the brake pedal. In the 3-PCT ( $F_{(2,58)}=7.817$ ,  $P=0.001$ ), 2-PCT ( $F_{(2,58)}=9.412$ ,  $P<0.001$ ), 1.5-PCT ( $F_{(2,58)}=13.699$ ,  $P<0.001$ ) and 1-PCT ( $F_{(2,58)}=4.537$ ,  $P=0.015$ ) scenarios, results indicated significant main effects of the type of SRMs on the average frequencies. The contrast analysis revealed that the average frequency associated with SRMs was significantly more than the one in the road section without SRMs in 3-PCT, 2-PCT and 1-PCT scenarios, while the average frequency associated with TSRMs was significantly more than the ones in the road segment without SRMs and LSRMs in 1.5-PCT scenario ( $P<0.05$  in all contrasts). The test results suggested that SRMs had statistically significant effects on pressing the brake pedal in downhill segments whose roadway grades were 3%, 2% and 1%, and only TSRMs had statistically significant effects on pressing the brake pedal in downhill segments whose roadway grades were 1.5%.

In terms of roadway grades, results of the ANOVA showed significant main effects of roadway grades on the average frequencies of braking in road segments equipped with LSRMs ( $F_{(3,87)}=7.094$ ,  $P<0.001$ ). The contrast analysis determined that the average frequencies of pressing the brake pedal in the 3-PCT scenario with LSRMs are significantly higher than that in the other three scenarios ( $P<0.05$  in all contrasts). The test results inferred that LSRMs could make subjects press the brake pedal more in downhill segments with roadway grades of 3% than in the three other roadway grades.

For road segments equipped with TSRMs, results of the ANOVA were similar to the results for LSRMs ( $F_{(3,87)}=9.291$ ,  $P<0.001$ ). The four kinds of roadway grades were divided into three levels: 3%, 2% and 1.5%, and 1%, according to the contrast analysis ( $P<0.05$  in all contrasts). Specifically, the average frequencies of pressing the brake pedal in the 3-PCT scenario were the highest, while the indicator in the 1-PCT scenario was the lowest. The test results indicate that TSRMs would affect drivers' frequency of pressing the brake pedal in downhill segments with roadway grades of 3%, and such effects would become weaker for roadway grades of 2% and 1.5%.

### *Operating power*

As mentioned above, the conclusion was reached that two types of SRMs, either combined or used singly, could affect drivers' operating frequencies in road segments with different roadway grades. Nevertheless, the operating frequency could only describe how many times drivers press gas pedal or brake pedal, and the intensity of pedal pressure and duration of pedal use can also reflect drivers' operating performance, as shown in Fig. 5 (a) and (b). To evaluate the effects of SRMs on drivers' operating performance more comprehensively, the *operating power* is introduced in this research, which includes the *gas pedal power* and *brake pedal power*.

For each subject, the driving simulator records his/her intensity of pressing the gas and brake pedal, and the profile of press intensity can be plotted. For example, Fig. 5 shows press intensity profiles of the brake pedal of one subject in two scenarios. The operating power represents the area

surrounded by the x-axis, y-axis, and press intensity profile, which is defined simultaneously by press intensity and duration. As the area increases, a driver presses on the gas or brake pedal with more power. Through calculating the area, researchers could compare the effects of SRMs on drivers' operating power.

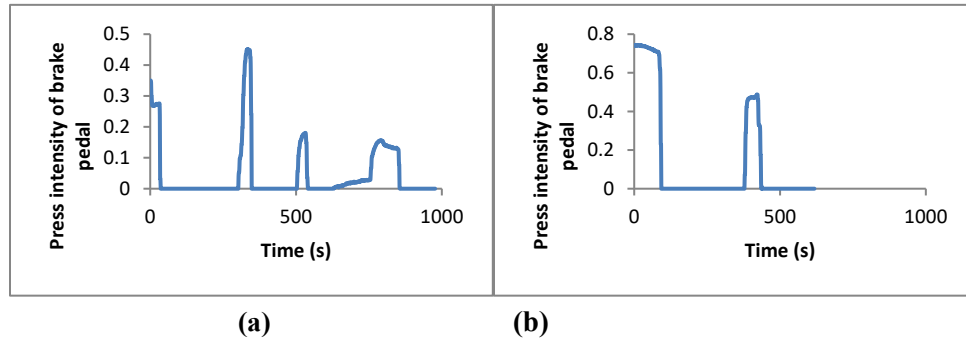


Fig. 5 Press intensity of the brake pedal of one subject in two scenarios

*Gas pedal power*

The results of the average power of pressing the gas pedal with respect to different types of SRMs and roadway grades are presented in Fig. 6. For all scenarios, SRMs lowered the gas pedal power, which implies that TSRMs have better effects on lowering gas pedal power than LSRMs. Besides, it seems that gas pedal power tends to decline when the roadway grade decreases.

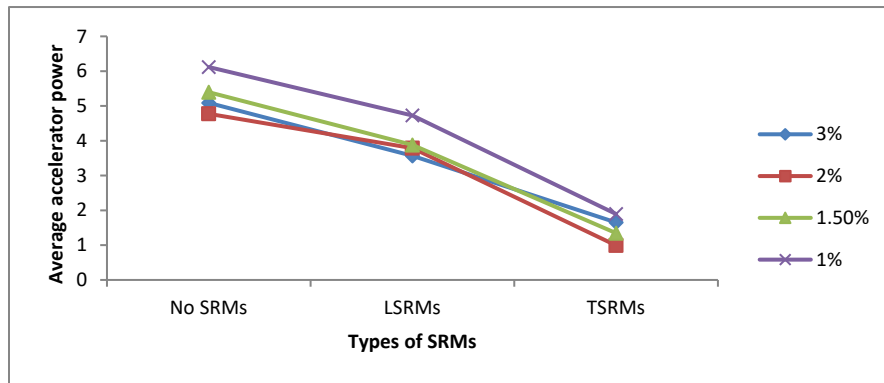


Fig. 6 Average gas pedal powers

The rANOVA was used to compare the impacts of SRMs and roadway grades on gas pedal power. The analytical results showed significant differences in gas pedal power among types of SRMs ( $F_{(2,28)}=18.409$ ;  $P<0.001$ ), while no effects for roadway grades ( $F_{(3,27)}=2.613$ ;  $P=0.072$ ).

For all scenarios, results of ANOVA showed significant main effects of the type of SRMs on gas pedal power ( $F_{(2,58)}=10.095$ ,  $P<0.001$  for the 3-PCT scenario;  $F_{(2,58)}=11.387$ ,  $P<0.001$  for the 2-PCT scenario;  $F_{(2,58)}=14.454$ ,  $P<0.001$  for the 1.5-PCT scenario;  $F_{(2,58)}=11.041$ ,  $P<0.001$  for the 1-PCT scenario). The contrast analysis indicated that the gas pedal power in the downhill segments with TSRMs was significantly lower than that in the other two segments without SRMs and LSRMs ( $P<0.05$  in all contrasts). The test results suggested that TSRMs had statistically significant effects on the drivers' gas pedal operating in downhill segments whose roadway grades were 3%, 2%, 1.5% and 1%, while LSRMs did not have such significant effects.

### Brake pedal power

For all drivers, the results of the average power of pressing the brake pedal with respect to different types of SRMs in each scenario are presented in Fig. 7. For 3-PCT, 2-PCT and 1.5-PCT scenarios, SRMs could increase the brake pedal power; specifically, TSRMs might have better effects than LSRMs. Meanwhile, like the results of frequencies of pressing the brake pedal, drivers tend to apply more power in road segments with SRMs than without SRMs in the 1-PCT scenario.

In terms of roadway grades, average brake pedal powers in the 3-PCT scenario are apparently more than that in the other three scenarios for both kinds of SRMs; furthermore, the indicators for TSRMs in the 1.5-PCT and 2-PCT scenarios are higher than the one in the 1-PCT scenario, yet these powers are still lower than the power related to the 3-PCT scenario.

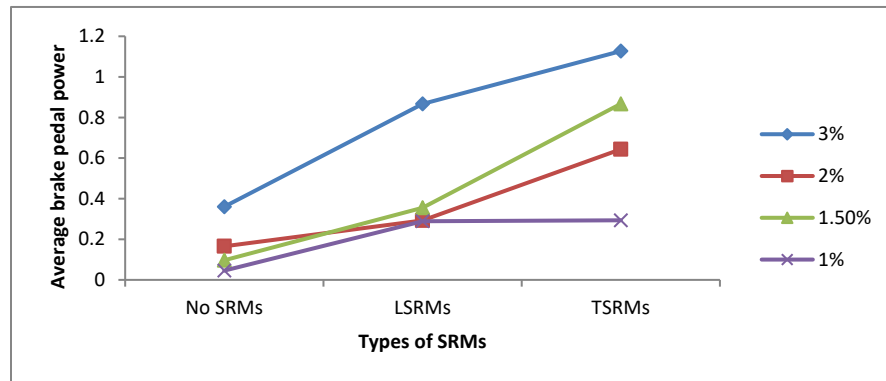


Fig. 7 Average brake pedal power

The rANOVA was used to compare the impacts of SRMs and roadway grades on brake pedal power. The results showed significant differences in brake pedal power among types of downhill segments ( $F_{(2,28)}=10.659$ ;  $P<0.001$ ) and roadway grades ( $F_{(3,87)}=15.582$ ;  $P<0.001$ ).

The ANOVA was used to evaluate the effectiveness of SRMs on brake pedal power in downhill segments with different roadway grades. In the 3-PCT scenario ( $F_{(2,58)}=7.140$ ,  $P=0.002$ ), results showed significant main effects of the type of SRMs on brake pedal power. The contrast analysis revealed that the brake pedal power in the vertical curve with SRMs was significantly higher than brake pedal power in the other road segments without SRMs ( $P<0.05$  in all contrasts). The test results suggested that SRMs had statistically significant effects on the brake pedal power in downhill segments whose roadway grades were 3%.

In the 2-PCT ( $F_{(2,58)}=11.685$ ,  $P<0.001$ ) and 1.5-PCT ( $F_{(2,58)}=4.230$ ,  $P=0.019$ ) scenarios, the contrast analysis stated that the brake pedal power in the vertical curve with TSRMs was significantly higher than the ones in the other two road segments without SRMs and LSRMs ( $P<0.05$  in all contrasts). The test results stated that TSRMs had statistically significant effects on the brake pedal power in downhill segments whose roadway grades were 2% and 1.5%.

In the 1-PCT scenario, however, results of the ANOVA reflected that there was no significant main effect of the type of SRMs on the brake pedal power ( $F_{(2,58)}=2.785$ ;  $P=0.070$ ). The test results implied that neither LSRMs nor TSRMs had statistically significant effects on the brake pedal power in downhill segments whose roadway grades were 1%.

In terms of different roadway grades, ANOVA and contrast analysis revealed the same results as average frequencies of pressing the brake pedal. On one hand, LSRMs ( $F_{(3,87)}=7.094$ ,  $P<0.001$ ) could make subjects apply more power to the brake pedal in downhill segments with roadway grades of 3% than in the other three roadway grades ( $P<0.05$  in all contrasts). On the other hand, TSRMs ( $F_{(3,87)}=9.291$ ,  $P<0.001$ ) would affect drivers' brake pedal power in

downhill segments with roadway grades of 3%, and such effects would become weaker related to roadway grades of 2% and 1.5% as well.

## Discussion

This paper was to evaluate the effectiveness of SRMs on drivers' operating performance and their decisions to decelerate in downhill segments with different roadway grades. The experiment was performed in a driving simulator. In previous works, Xu (17) validated the effectiveness of the Beijing University of Technology driving simulator, and testified that the driving simulator had relative effectiveness on physiological and psychological parameters. Ding et al. (6) had also validated the effectiveness of driving simulator on travel speed in downhill segments equipped with SRMs, compared to the speeds collected in the field. According to Ding et al. (6), the driving simulator had the relative effectiveness in terms of simulating travel speeds, and the speed variation trend in the downhill segments equipped with SRMs was highly similar to the trend in the real road environment.

Two indicators—the operating frequency and operating power—are introduced to measure the effects of SRMs on drivers' operating performance and decision to decelerate. In detail, there is a subtle difference between these two indicators. On one hand, the operating frequency is a more intuitive indicator, which can reflect a driver's consciousness and the decision to decelerate. On the other hand, the operating power is an indirect indicator, which takes intensity and duration into consideration, as well as frequency. Compared with the operating frequency, the operating power on the gas and brake pedals will influence vehicle operations, especially travel speeds.

Considering driver's actions, it is assumed that letting off the gas pedal implies that the driver is conscious of decelerating, while pressing the brake pedal infers that the driver decides to slow down. Referring to results of the operating power, it has been concluded that: 1) TSRMs could significantly decrease the gas pedal power in all kinds of downhill segments; 2) TSRMs could also significantly increase the brake pedal power in 1.5-PCT, 2-PCT and 3-PCT scenarios; and 3) LSRMs could only influence the brake pedal power in 3-PCT scenario. Therefore, it is probable that: 1) TSRMs will influence driver's consciousness of decelerating in all scenarios; 2) TSRMs will also enhance driver's decision to decelerate in all 1.5-PCT, 2-PCT and 3-PCT scenarios; and 3) LSRMs could only strengthen driver's decision to slow down in 3-PCT scenario. In terms of roadway grades, it appeared that driver's consciousness of controlling speed would not be influenced by the roadway grade; however, driver's decision to decelerate will become stronger when the roadway becomes steeper.

It has been mentioned that SRMs have significant effects on the frequency of pressing the brake pedal in the 3-PCT, 2-PCT and 1-PCT scenarios, but only TSRMs have such effects in the 1.5-PCT scenario. However, researchers have hypothesized that both types of SRMs will have effects in the 3-PCT, 2-PCT and 1.5-PCT scenarios, while they are ineffective in the 1-PCT scenario. This inconsistent phenomenon is the original motivation to determine the limitations of the operating frequency and to develop a more comprehensive indicator, representing the operating performances of the gas and brake pedals more precisely. Recognizing that the press intensity and duration can also be affected by SRMs, the concept *operating power* is finally introduced in this study.

As illustrated above, it has been stated that only TSRMs could reduce the gas pedal power in all road scenarios. Besides, TSRMs can also make drivers apply more power on the brake pedal in downhill segments with roadway grades of 3%, 2% and 1.5%, while LSRMs can have such effects when the roadway grade is 3%. Therefore, like the results of the previous indicator, LSRMs will have no impacts on drivers' gas pedal operating in all four scenarios, together with brake pedal

operating in road segments with roadway grades of 2%, 1.5% and 1%. Moreover, LSRMs can influence brake pedal operating only in the 3-PCT scenario. On the contrary, TSRMs could not only lower drivers' gas pedal power in all four scenarios, but increase the brake pedal power when roadway grades are 3%, 2% and 1.5% as well. It is implied that TSRMs can make drivers execute fewer gas pedal operations and more brake pedal operations in reverse when roadway grades are 3%, 2% and 1.5%; for roadway grades of 1%, TSRMs will simply encourage the driver to perform fewer gas pedal operations, and drivers' attention will not be directed to the brake pedal operating. These assumptions could be tested in future research.

Since the order of the SRMs conditions was the same (no SRM, LSRMs, and TSRMs) in all scenarios, this could lead to a learning effect. Therefore, especially in Fig. 2 (a), one-kilometer tangents, which connected downgrade sections related to different SRMs conditions, were designed to fade subjects' memory or impression of the previous downgrade section, so as to eliminate or reduce the learning effect. In fact, the average and standard deviation of speeds at the beginning of downgrade sections of all subjects were listed in Table 3. It is apparent that scenario, the average and standard deviation of speeds at the beginning of downgrade sections with No SRMs, LSRMs and TSRMs are approximately the same in the same scenario, and it implies that the learning effect is controlled, and it would not substantially influence the results and conclusions. What's more, the analysis of variance with repeated measures (rANOVA) is commonly used to validate the significant effects of treatments in repeated measures. Since the repeated measures were usually organized in the same time sequential order for all subjects, rANOVA was conducted to evaluate the effectiveness of SRMs on drivers' performance.

*Table 3 The average and standard deviation of speeds at the beginning of downgrade sections with different SRMs conditions in all scenarios (in km/h)*

Roadway grades	No SRMs		LSRMs		TSRMs	
	Mean	Std.	Mean	Std.	Mean	Std.
3%	104.9	12.2	104.7	14.6	108.5	13.3
2%	106.5	10.6	107.9	13.5	110.7	15.4
1.50%	110.2	13.7	109.1	12.6	110.1	16.8
1%	115.5	15.7	114.1	13.0	113.7	11.7

The previous research (6) was repeatedly referenced in this paper, since the methodology was the same. However, the objectives and interest areas were totally different between these two studies. In (6), the impacts of SRMs on vehicle moving status were mainly considered, thus speed and acceleration data were used. Nevertheless, the variation of speed and acceleration was led by driver's consciousness and decision to decelerate, presented as the gas pedal and brake pedal use, and the data and analysis in (6) was insufficient in mining the relationships between SRMs and driver's operating characteristics. Therefore, the objective of this paper, which was to observe the effects of SRMs on driver's consciousness and decision to decelerate, was confirmed immediately. Additionally, this paper could be viewed as a stretch or inheritance of (6).

Although different data sets were used due to distinct objectives, there were still some similarities in the results of these two studies, and some relationships might be found in the indexes. For example, SRMs were effective when roadway grades were 3%, 2% and 1.5%, and TSRMs had better effects in 2-PCT and 1.5-PCT scenarios, according to (6). Similarly, TSRMs would affect driver's brake pedal use when roadway grades were 3%, 2%, and 1.5%, while LSRMs would only have effects on brake pedal use in 3-PCT scenario. However, the

similarities between the speed index and driver's gas pedal were not so obvious, compared to the brake pedal power. It was assumed that in this experiment condition, driver's speed behavior was more identical with the brake pedal use, which was also in accordance with the assumptions stated before, that is, pressing the brake pedal infers that the driver decided to slow down; in addition, driver's speed behavior was less uniform with the gas pedal use, since letting off the gas pedal implied that the driver was conscious of decelerating, which might have weaker effects on speed reduction.

### Conclusions and Recommendations

This paper evaluated the effectiveness of SRMs on drivers' operating performance and decisions to decelerate in downhill segments with different roadway grades. By analyzing the data collected in a driving simulator, this research has reached the following conclusions:

- According to the questionnaires, the majority of subjects were encouraged to reduce speeds while driving through downhill segments with LSRMs and TSRMs in all four scenarios. Moreover, TSRMs were more effective than LSRMs in leading subjects to decelerate in all scenarios.
- It is seemed that operating power is an appropriate and comprehensive indicator, which could measure drivers' control performances, since it reflects press frequency, intensity and duration at the same time.
- TSRMs are significantly effective in influencing drivers to let off the gas pedal when roadway grades of downhill segments were 3%, 2%, 1.5% and 1%, while LSRMs have no effects. The frequency of pressing the brake pedal was significantly affected by both types of SRMs when the roadway grades of downhill segments were 3%, 2% and 1%, and by TSRMs in road sections with a roadway grade of 1.5%.
- TSRMs can significantly influence drivers' gas pedal operations in all road scenarios, and the brake pedal power when roadway grades are 3%, 2% and 1.5%. LSRMs do not affect drivers' gas pedal operations, and are effective on brake pedal operating only in downhill segments with a roadway grade of 3%.

In summary, this paper discussed the effectiveness of LSRMs and TSRMs on driver's operating performance in downhill segments of urban roads with different roadway grades, based on a driving simulator experiment. In future research, in order to develop guidelines about optimal placement of SRMs the relationship between SRMs and driver's operating performance needs to be evaluated in other road conditions.

### Acknowledgements

This study was funded by the National Key R&D Program of China (2018YFC0809606).

### References

- [1] Statistics of Traffic Crashes in China in 2012. Retrieved Mar 18, 2013, from [http://www.tranbbs.com/MResearch/Daten/MResearch\\_111913.shtml](http://www.tranbbs.com/MResearch/Daten/MResearch_111913.shtml).
- [2] Standardization Administration of the People's Republic of China. *Road Traffic Signs and Markings* (GB5768-2009). Beijing, 2009.
- [3] Federal Highway Administration. *Manual on Uniform Traffic Control Devices for Streets and Highways* (2009 Edition). U.S. Department of Transportation, 2009
- [4] Gates, T. J,X. Qin, and D. A. Noyce. Effectiveness of Experimental Transverse-Bar Pavement

- Marking as Speed-Reduction Treatment on Freeway Curves. In *Transportation Research Record: Journal of the Transportation Research Board*, No.2056, Transportation Research Board of the National Academies, Washington, D.C., 2008, pp. 95-103. <https://doi.org/10.3141/2056-12>
- [5] Katz, B. J. Peripheral Transverse Pavement Markings for Speed Control. *Dissertation submitted to the faculty of the Virginia Polytechnic Institute and State University in partial fulfillment of the requirements for the degree of Doctor of Philosophy in Civil Engineering*. Blacksburg, Virginia, 2007.
- [6] Ding, H., X. H. Zhao, J. Rong, and J. M. Ma. *Experimental Research on the Effectiveness and Adaptability of Speed Reduction Markings in downgrade Sections on Urban Roads: A Driving Simulation Study*. Research Report in Transportation Research Center in Beijing University of Technology, 2014. <https://doi.org/10.1016/j.aap.2014.11.018>
- [7] Meyer, E. Application of Optical Speed Bars to Highway Work Zones. In *Transportation Research Record: Journal of the Transportation Research Board*, No. 1657, Transportation Research Board of the National Academies, Washington, D.C., 1999, pp. 48-54. <https://doi.org/10.3141/1657-07>
- [8] Jiang, J., Z. J. Wang, J. Wu, and J. Lu. Effectiveness and Adaptability Analysis of Typical Speed Control Measures. *Journal of Transport Information and Safety*, Vol.28, No.155, 2010, pp.96-99.
- [9] Kaber, D. B., Y. L. Liang, Y. Zhang, M. L. Rogers, and S. Gangakhedkar. *Experimental Driver performance effects of simultaneous visual and cognitive distraction and adaptation behavior*. *Transportation Research Part F: Traffic Psychology and Behavior*, 15 (2012), pp.491-501. <https://doi.org/10.1016/j.trf.2012.05.004>
- [10] Zheng, F. *Research on Design and Application of Road Speed Control Facilities*. In *Master Thesis of Jilin University*, Jilin University, Changchun, 2007
- [11] Ren, F. T., X. M. Liu, and J. Rong. *Traffic Engineering (Second Edition)*. China Communications Press, Beijing, 2008.
- [12] Ding, H. X. H. Zhao, J. Rong, and J. M. Ma. *Experimental Research on the Effectiveness of Speed Reduction Markings Based on Driving Simulation: A Case Study*. *Accident Analysis & Prevention* 60 (2013): 211-218. <https://doi.org/10.1016/j.aap.2013.08.007>
- [13] Mulder, M., M. Mulder, M.M. van Paassen, and D.A. Abbink. *Haptic Gas Pedal Feedback*. *Ergonomics*, Vol. 51, No. 11, 2008, pp. 1710-1720. <https://doi.org/10.1080/00140130802331583>
- [14] Rakauskas, M. E., L. J. Gugerty, N. J. Ward. *Effects of Naturalistic cell phone conversations on driving performance*. *Journal of Safety Research* 35 (2004): 453-464. <https://doi.org/10.1016/j.jsr.2004.06.003>
- [15] China Has More Than 0.236 Billion Licensed Drivers and 0.225 Billion Registered Vehicles. Retrieved May 30, 2012, from <http://news.mycar168.com/2012/02/263721.html>.
- [16] The Ministry of Housing and Urban-Rural Development of the People's Republic of China. *Code for Design of Urban Road Engineering (CJJ37-2012)*. Beijing, 2012.
- [17] Xu, S. L. The Study on the Discriminating Method of Driving Fatigue Based on Physiological Signal. In *Master Thesis of Beijing University of Technology*, Beijing University of Technology, Beijing, 2012.
- [18] China Has More Than 0.3 Billion Licensed Drivers. Retrieved Nov 27, 2014, from <http://www.mps.gov.cn/n16/n1237/n1342/n803715/4287614.html>

# Numerical Simulation on Micro-damage Detection In CFRP Composites Based on Nonlinear Ultrasonic Guided Waves

Chang Jiang<sup>1,a</sup>, Weibin Li<sup>1,b,\*</sup>, Mingxi Deng<sup>2,c</sup> and Ching-Tai Ng<sup>3,d</sup>

<sup>1</sup>School of Aerospace Engineering, Xiamen University, China

<sup>2</sup>College of Aerospace Engineering, Chongqing University, China

<sup>3</sup>School of Civil, Environmental & Mining Engineering, University of Adelaide, Australia

<sup>a</sup>jiangc632@gmail.com, <sup>b</sup>liweibin@xmu.edu.cn, <sup>c</sup>dengmx65@yahoo.com,  
<sup>d</sup>alex.ng@adelaide.edu.au

**Keywords:** Nonlinear Guided Waves, Composites, Micro-Damage, Random Defects

**Abstract.** Micro-damages such as pores, closed delamination/debonding and fiber/matrix cracks in carbon fiber reinforced plastics (CFRP) are vital factors towards the performance of composite structures, which could collapse if defects are not detected in advance. Nonlinear ultrasonic technologies, especially ones involving guided waves, have drawn increasing attention for their better sensitivity to early damages than linear acoustic ones. The combination of nonlinear acoustics and guided waves technique can promisingly provide considerable accuracy and efficiency for damage assessment and materials characterization. Herein, numerical simulations in terms of finite element method are conducted to investigate the feasibility of micro-damage detection in multi-layered CFRP plates using the second harmonic generation (SHG) of asymmetric Lamb guided wave mode. Contact acoustic nonlinearity (CAN) is introduced into the constitutive model of micro-damages in composites, which leads to the distinct SHG compared with material nonlinearity. The results suggest that the generated second order harmonics due to CAN could be received and adopted for early damage evaluation without matching the phase of the primary waves.

## Introduction

Composite materials are gaining increasing interest from researchers for their excellent performances which are superior to metals in aerospace engineering and many other fields. Carbon fiber reinforced plastics (CFRP), as an important type of composites, can provide high-strength, high-durability against corrosion and many other great mechanical properties [1-3]. However, due to its distinct material composition, microstructures and manufacturing process, micro-damages such as micropores, closed delamination/debonding and fiber/matrix crack could occur when subjected to thermal, chemical and mechanical loads [4]. As invisible as those defects could be, long term accumulation of micro damages can lead to sudden structural disaster. Therefore, it is of vital importance to develop advanced non-destructive technologies to detect and evaluate the early damage state of CFRP materials.

Among conventional non-destructive testing techniques, ultrasonic testing methods have been favored over thermal infrared and radiographic ones due to their cost-effective features [5]. Nevertheless, linear acoustic characteristics, such as the appearance of pulse echoes, attenuation and variation of wave velocity, could be too subtle to be applied for early damage assessment. The micro-damages in CFRP plates usually have little influence on the propagation of ultrasonic primary waves. For this problem, promising solutions have been proposed including nonlinear

ultrasonic techniques, which often involves the second harmonic generation (SHG) resulted from the interaction of material nonlinearity with primary waves [6].

On the other hand, nonlinear guided wave techniques have recently been widely investigated, since point-wise detection with bulk wave transducers can be inefficient, and could not cope with relatively thin plate in which pulse cycles are not sufficient for nonlinearity analysis [7-8]. The combination of ultrasonic nonlinear response with guided waves in micro-damaged material, can potentially enhance the sensitivity and efficiency of the evaluation process. However, one of the main concerns whilst dealing with such applications is the dispersion nature of guided waves. It has been reported that synchronism and non-zero power flux conditions are required for SHG with cumulative effect using a single excitation of primary guided waves [9].

In recent years, the contact acoustic nonlinearity (CAN) caused by local closed defects such as delamination and crack are drawing attentions from researchers [10-11]. This paper mainly aims at exploring the application potential of nonlinear ultrasonic guided waves to assess early damages in CFRP laminated plates. Numerical studies on the CAN caused by randomly distributed micro-defects are conducted. The received ultrasonic response are analyzed in terms of time and frequency domains adopting the primary guided waves of asymmetric Lamb mode. Discussions upon the received nonlinear ultrasonic responses caused by single and multiple micro-damage interfaces are as well provided.

### Numerical investigations

Material, geometry and physics. The composite material adopted in this study are composed of T300/M914 carbon fiber reinforced plastics, of which the thickness is 2 mm. The laminated plates are layered as [0/90/0/90]<sub>s</sub> order. To assure sufficient calculation efficiency and accuracy, the geometry size of the finite element model is 140 mm × 10 mm × 2 mm, as shown in Fig. 1. The left end face of the model is prescribed with Hanning-windowed displacement excitation up to 100 nm. The front, back and right face are set with low reflection boundary condition, which can significantly absorb waves approaching there, and in the meantime enhance the signal-to-noise ratio of primary and harmonic waves.

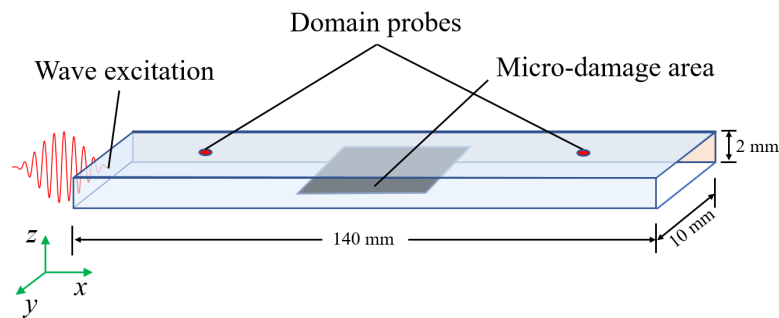


Fig. 1. Illustration of the model geometry and physical setups.

Micro-damage area settings. A number of circular nonlinear interfaces are randomly distributed in the designed damage area, of which the size is 10 mm × 10 mm and the location is the center of the model in both x and z direction. It should be noted that the damage area is a 3D space in the extended simulation as presented in Fig. 2(b). Those interfaces (shown in Fig. 2(a)), of which radii range from 2 mm to 10 mm, are built and set to be able to decouple the displacements of their two sides with a bilinear stress-strain relation [12]. As a result, they act as local sources of acoustic nonlinearity corresponding to damages such as closed delamination, and can result in

ultrasonic nonlinear response, which are to be picked up by domain probes deployed in the upper surface of the model.

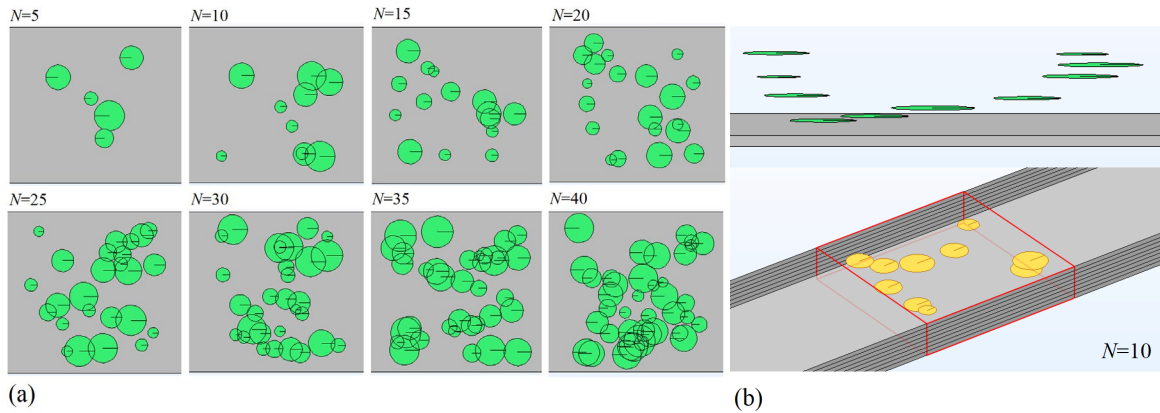


Fig. 2. Demonstration of the nonlinear mechanical interfaces randomly distributed in the damage area, (a) top view, (b) 3D view.

Guided wave modes. To obtain suitable guided wave modes for signal excitation and receiving, the dispersion curves of such material are plotted as Fig. 3. The frequency of the primary  $A0$  mode guided waves to be excited is chosen as 0.2 MHz. Consequently, possible generated second order harmonics through interaction of micro-damages with the primary waves are supposed to be at the frequency of 0.4 MHz. As one can see from Fig. 1(a), the phase velocity of primary waves differ from the potential second harmonics. Therefore, the received ultrasonic nonlinear response can include mainly contact acoustic nonlinearity rather than material nonlinearity, referencing [13]. However, according to Fig. 1(b), the potential  $A0$  mode second harmonics share the same group velocity of the primary waves, suggesting that the generated harmonics can be predicted and received by corresponding calculation.

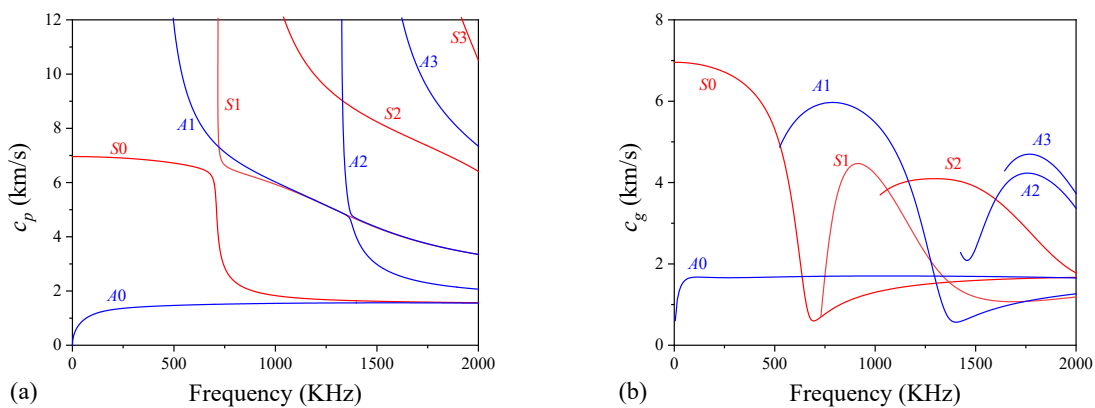


Fig. 3. Dispersion curves of Lamb guided waves in T300/M94 laminated plates, (a) phase velocity, (b) group velocity.

Mesh and solver configurations. The whole model as the wave guide is meshed with free triangle elements, of which the maximum size is defined as  $\lambda/20$ . The time step of the transient

solver is set as  $1/20f$  ( $\lambda$  and  $f$  is the wavelength and frequency of the primary waves, respectively). The above setups can ensure moderate accuracy of the numerical results.

### Results & Discussions

Verification of contact acoustic nonlinearity. Firstly, a single nonlinear mechanical interface of varying depth and size is introduced into the model for investigation of CAN. As shown in Fig. 4(a), the group velocity of the primary waves is calculated as about 1600 m/s, which is in accordance with that of A0 mode waves at the frequency of 0.2 MHz. With FFT applied to the 10-cycle transmission waves received at  $x=0.105\text{m}$ , the frequency spectrum is obtained as shown in Fig. 4(b). It is noted that there is no second harmonics generated in a model without nonlinear interfaces set in ( $R=0$  mm), and the magnitude of the second harmonics increase with the radius of the damage interface (the depth is fixed as 0.2 mm) as presented in Fig 4(b) and Fig. 5(a). Besides, the Fig. 5(b) shows a trend that the closer the nonlinear interface is to the center of the model along thickness direction, the greater the magnitude of the generated second harmonic waves is. Such result could be related to the wave structure of the primary wave mode.

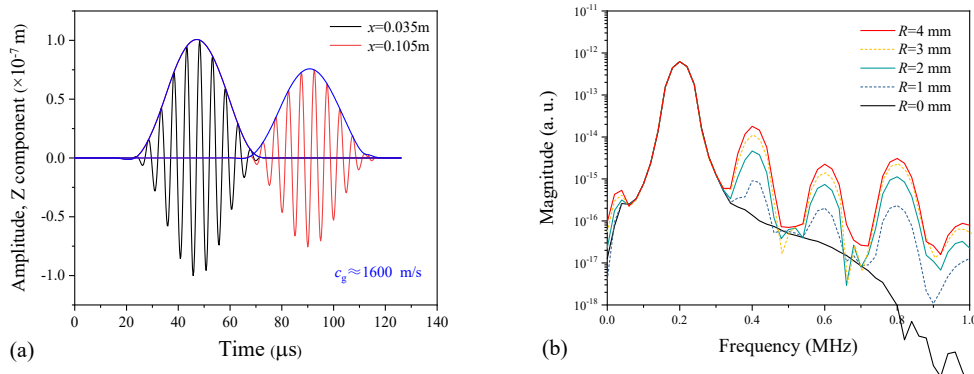


Fig. 4. Time domain (a) and frequency domain (b) of the received guided wave signals from two probes.

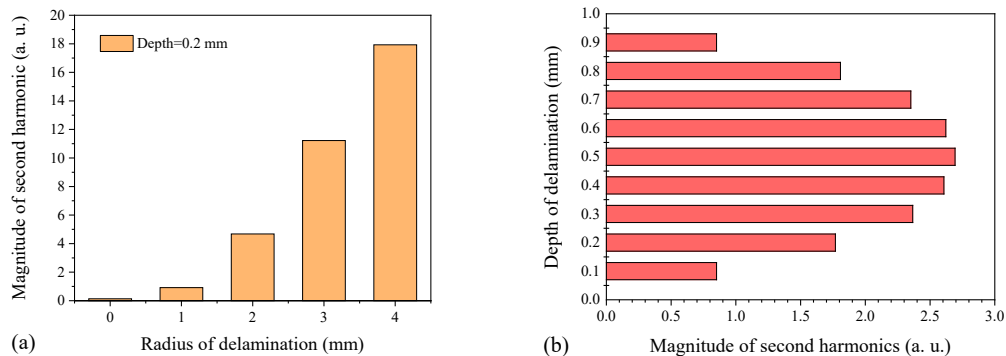


Fig. 5. Parametric studies of the relation between the magnitude of second harmonics and a single closed delamination modeled by a nonlinear mechanical interface through change of the (a) radius, (b) burial depth.

Furthermore, two other investigations are implemented while a number of the nonlinear interfaces are randomly distributed in the designed micro-damage plane field and the three dimensional space, respectively. Fig. 6 and Fig. 7 show the numerical simulation results. As seen from Fig. 6, the magnitude of the newly generated harmonics at the frequency of 0.4 MHz increase with the number ( $N$ ) of the artificial damage interfaces which are distributed in the designed plane field located in the middle depth of the laminate. On the other hand, the almost same result applies to the case in which the interfaces are randomly distributed in the 3D damage area (see Fig. 2(b)), as seen in Fig. 7. It is noted that when  $N=5$  the magnitude of the quadratic nonlinearity in the received transmission waves is a bit greater than that when  $N=10$ , as shown in Fig. 7(b). This could mainly be due to that the different depths of the interfaces influence more on the second harmonic generation than the number of defects when there is obviously less of them buried in the model. However, if a large number of micro-defects such as pores and micro-delaminations occur in a relatively concentrated area, the total nonlinear ultrasonic response measured by SHG will be satisfactory index of the number of the damages regardless of their burial depth.

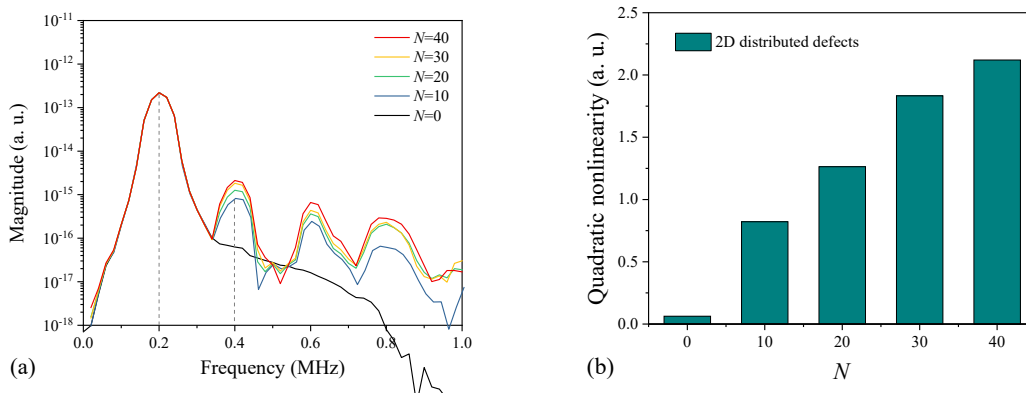


Fig. 6. Frequency domain (a) and the magnitude comparison of the quadratic nonlinearity (b) of the received transmission waves while defects are laid out in the plane damage area.

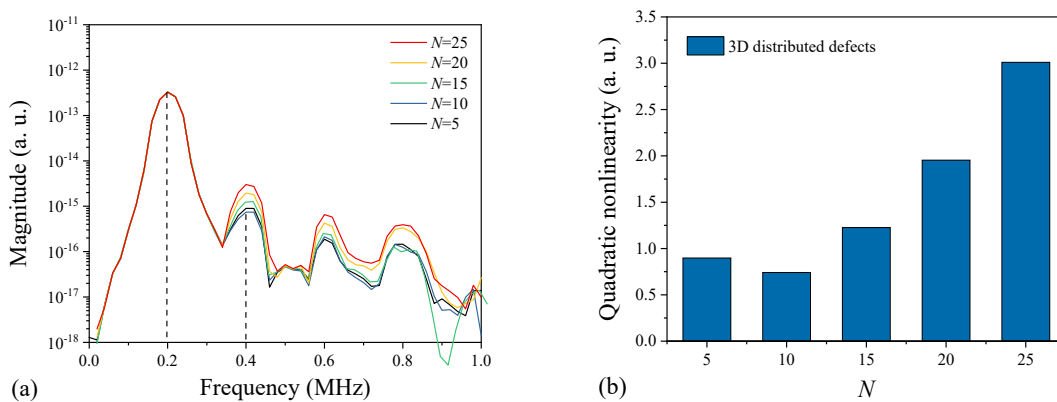


Fig. 7. Frequency domain (a) and the magnitude comparison of the quadratic nonlinearity (b) of the received transmission waves while defects are laid out in the 3D damage area.

### Conclusion

This paper mainly focuses on the feasibility study of micro-damage detection in carbon fiber reinforced plastics using second harmonics generation induced by contact acoustic nonlinearity.

Nonlinear stress-strain relationship is introduced in the model of damage interface, and ultrasonic nonlinear responses involving Lamb guided waves are analyzed in terms of time domain and frequency domain. Results show that the contact acoustic nonlinearity in CFRP composites can be strong sources of nonlinear acoustic response, which can be detected through the measure of higher harmonics without being limited by the phase matching condition.

## References

- [1] Zhao JL, Chillara VK, Ren BY, et al. Second harmonic generation in composites: Theoretical and numerical analyses. *Journal of Applied Physics*. 2016. <https://doi.org/10.1063/1.4941390>
- [2] Kim EH, Rim MS, Lee I, et al. Composite damage model based on continuum damage mechanics and low velocity impact analysis of composite plates. *Composite Structures*. 2013. <https://doi.org/10.1016/j.compstruct.2012.07.002>
- [3] Zhao GQ, Wang B, Wang T, et al. Detection and monitoring of delamination in composite laminates using ultrasonic guided wave. *Composite Structures*. 2019. <https://doi.org/10.1016/j.compstruct.2019.111161>
- [4] Wang B, Zhong SC, Lee, TL, et al. Non-destructive testing and evaluation of composite material/structures: A state-of-the-art review. *Advances in Mechanical Engineering*. 2017. <https://doi.org/10.1177/1687814020913761>
- [5] Marcantonio V, Monarca D, Colantoni A, et al. Ultrasonic waves for materials evaluation in fatigue, thermal and corrosion damage: A review. *Mechanical Systems and Signal Processing*. 2019. <https://doi.org/10.1016/j.ymsp.2018.10.012>
- [6] Scott K, Kim JY, Jacobs L. Signal processing methods for second harmonic generation in thin specimens. *NDT and E International*. 2018. <https://doi.org/10.1016/j.ndteint.2018.02.001>
- [7] Zhu WJ, Xiang YX, Liu CJ, et al. A feasibility study on fatigue damage evaluation using nonlinear Lamb waves with group-velocity mismatching. *Ultrasonics*. 2017. <https://doi.org/10.1016/j.ultras.2018.06.002>
- [8] Li WB, Cho Y. Combination of nonlinear ultrasonic and guided wave tomography for imaging the micro-defects. *Ultrasonics*. 2016. <https://doi.org/10.1016/j.ultras.2015.10.016>
- [9] Hasanian M, Lissenden CJ. Second order harmonic guided wave mutual interactions in plate: Vector analysis, numerical simulation, and experimental results. *Journal of Applied Physics*. 2017. <https://doi.org/10.1063/1.4993924>
- [10] Solodov IY, Krohn N, Busse G. CAN: an example of nonclassical acoustic nonlinearity in solids. *Ultrasonics*. 2002, 40:621–625. [https://doi.org/10.1016/S0041-624X\(02\)00186-5](https://doi.org/10.1016/S0041-624X(02)00186-5)
- [11] Aleshin V, Delrue S, Trifonov A, et al. Two dimensional modeling of elastic wave propagation in solids containing cracks with rough surfaces and friction - Part I: Theoretical background. *Ultrasonics*. 2018, 82:11-18. <https://doi.org/10.1016/j.ultras.2017.07.002>
- [12] Broda D, Staszewski WJ, Martowicz A, et al. Modeling of nonlinear crack-wave interactions for damage detection based on ultrasound – A review. *Journal of Sound and Vibration*. 2014, 333:1097-1118. <https://doi.org/10.1016/j.jsv.2013.09.033>
- [13] Li WB, Deng MX, Hu N, et al. Theoretical analysis and experimental observation of frequency mixing response of ultrasonic Lamb waves. *Journal of Applied Physics*. 2018, 124:044901. <https://doi.org/10.1063/1.5028536>

# Novel Outside-Facility Renovation Technology to Improve Cost-Effectiveness by Long-Term Safe Use

Masaki Waki<sup>1,a,\*</sup>, Soichi Ishikawa<sup>1,b</sup>, Gen Kobayashi<sup>1,c</sup>, Ryouichi Kaneko<sup>1,d</sup>, and Hiroaki Tanioka<sup>1,e</sup>

<sup>1</sup> NTT Access Network Service Systems Laboratories, 1-7-1 Hanabatake Tsukuba-shi Ibaraki pref., Japan

<sup>a</sup>masaki.waki.me@hco.ntt.co.jp, <sup>b</sup>souichi.ishikawa.ck@hco.ntt.co.jp mail,  
<sup>c</sup>gen.kobayashi.wn@hco.ntt.co.jp, <sup>d</sup>ryouichi.kaneko.kv@hco.ntt.co.jp,  
<sup>e</sup>hiroaki.tanioka.nh@hco.ntt.co.jp

**Keywords:** Utility Pole, Telecommunication, FTTH, Outside-Facility

**Abstract.** In order to provide telecommunication and FTTH services, we, NTT, have installed a large number of facilities such as utility poles and optical cables. The number of poles is about 11.9 million and the total length of all installed cables is now about 2.3 million km. These facilities are inspected and maintained by visual inspection by workers every 5 to 10 years, which imposes great costs on the operator. Therefore, we are researching a novel outside-facility renovation technology that can improve cost-effectiveness by long-term safe use. This technology consists of two techniques: a visualization technique of unbalanced tension and a quantitative analysis technique to determine the relationship between unbalanced tension and structural deterioration. In this paper, we describe the concept of the proposed technology. When a utility pole is newly installed, its design assumes that the maximum load consists of wind pressure on the cables. However, when it is impossible to construct a guy wire for bearing the load applied to the utility pole, an unbalanced load occurs because the load cannot be balanced. In addition, when the number of users of various services increases and cables are newly laid, unbalanced loads are generated. Utility poles carrying these unbalanced loads are at significant risk of collapse due to the presence of deflection, inclination, and cracks. Our proposal focuses on the unbalanced load itself, and by detecting and countering it, we aim to enable the use of outside-facilities for a longer period than at present and to reduce replacement costs without sacrificing safety and security. In addition, we also describe how ensuring the long-term safe use of outside-facilities can improve cost-effectiveness. The proposed technique first acquires 3D point cloud data by using 3D laser scanner. It then creates a 3D facility model and calculates the tension in utility poles and cables. In addition, we introduce a novel method to estimate the loads and tension of a whole span from part of the span. Experiments are conducted to compare the estimated and measured values. The results confirm the good agreement of the values (within 10%) which validates the proposal. We aim to realize a tension visualization scheme with improved accuracy.

## Introduction

To provide telecommunication and FTTH services, NTT has installed a large number of facilities such as utility poles and optical cables. Fig. 1 shows an example of the configuration of optical communication equipment in NTT's access network. In addition to optical cables serving as communication paths, NTT is responsible for various outdoor facilities such as utility poles for laying optical cables on the ground, cable tunnels for laying cable underground, and closures for connecting optical cables. There are about 11.8 million poles and a total length of about two

million km of cable has been installed [1]. These facilities are mainly maintained and inspected visually at great expense by on-site maintenance staff every 5 to 10 years.

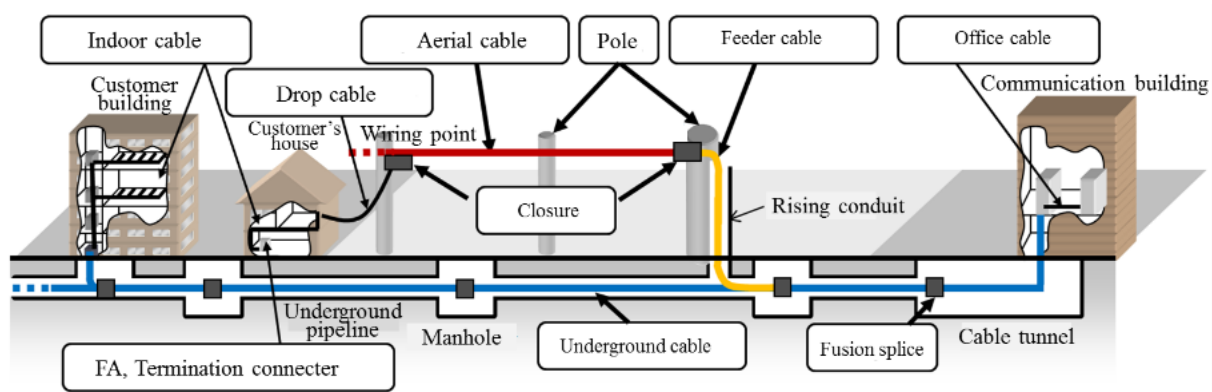


*Fig. 1 Outside facilities for FTTH*

To date, NTT has been using MMS (Mobile Mapping System) equipped with a laser scanner; 3D models of utility poles were obtained from 3D point groups gathered while driving on the road. Metrics of structural deterioration such as inclination and deflection on a desk were examined and put into practical use to enhance inspection operations [2-4].

In order to achieve long-term safe use of the facilities, this study focuses on the mechanisms of structural deterioration, preventing new deterioration factors from occurring in the future, and alleviating the partial degradation that has already occurred to maintain a "healthy condition" without any structural risk. In addition, the system will replace inspection workers, which is an issue in the current inspection process, and enable easy and accurate health monitoring at the same time.

Fig. 2 shows the process of structural deterioration. This figure shows that the utility poles were structurally sound as designed and constructed, but structural deterioration occurred due to various factors when installed. The various factors are "Influence of attaching materials", which is the increase in load caused by the addition of attachments due to the increase in customers, and "Influence of complex and diverse loads and tension", which is the increase in load imposed by other poles, "The gap between design and actual facilities", the difference between design and actual equipment, and "Natural environment", due to increased wind speeds and disasters. In the current inspection system, inspection workers visually check the utility poles one by one and decide whether to renew or tag for continuous observation according to the degree of structural deterioration such as deflection and inclination. However, manually inspecting the numerous poles every 5 to 10 years is extremely cost-ineffective, as a lot of manpower and labor is required.

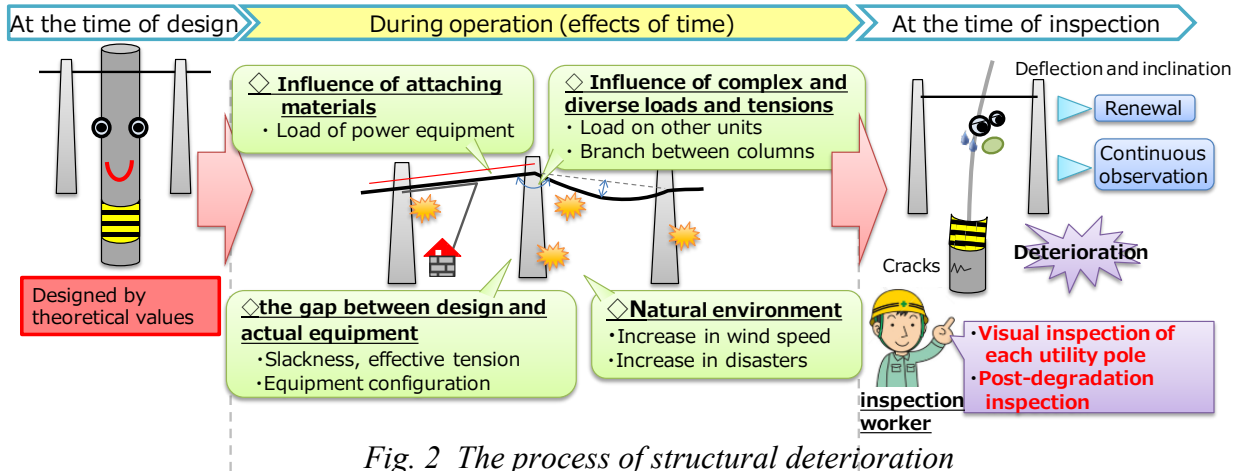


Fig. 2 The process of structural deterioration

In order to achieve these goals, we started two research projects: (i) Load visualization technique, (ii) Relationship between unbalanced loads and structural deterioration. In this paper, we describe the former.

**(i) Load visualization technique**

In order to visualize the structural loads carried by outside facilities, we need to calculate the force transmitted from the cable attached to the utility pole (horizontal tension) and the load of other attached materials, and to calculate the moments carried by the utility pole. To achieve this, a 3D point cloud data are acquired by a mobile or fixed laser scanner as shown in Fig. 3. These are used in order to accurately determine the positions at which the horizontal loads are generated. Since the 3D point cloud can use the data acquired by the above technique [2-4] as it is, no new acquisition work is required.

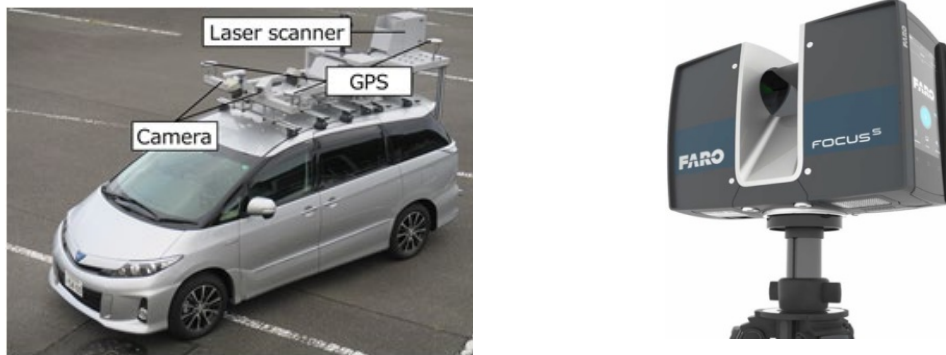


Fig. 3 Mobile and Fixed Laser Scanners

A typical 3D point cloud acquired by these laser scanners is shown in fig. 4. From the figure, it can be seen that there are several cables between the two utility poles and that trees, buildings, etc. have also been acquired as point clouds (Top of Fig. 4). We extract only the necessary information, that is, a point cloud of utility poles and cables (middle section). Next, in order to obtain the horizontal tension from the positional relation between utility poles and the slack of the cable, the catenary function representing the shape of the cable is calculated by the following approximate formula (Lower section).

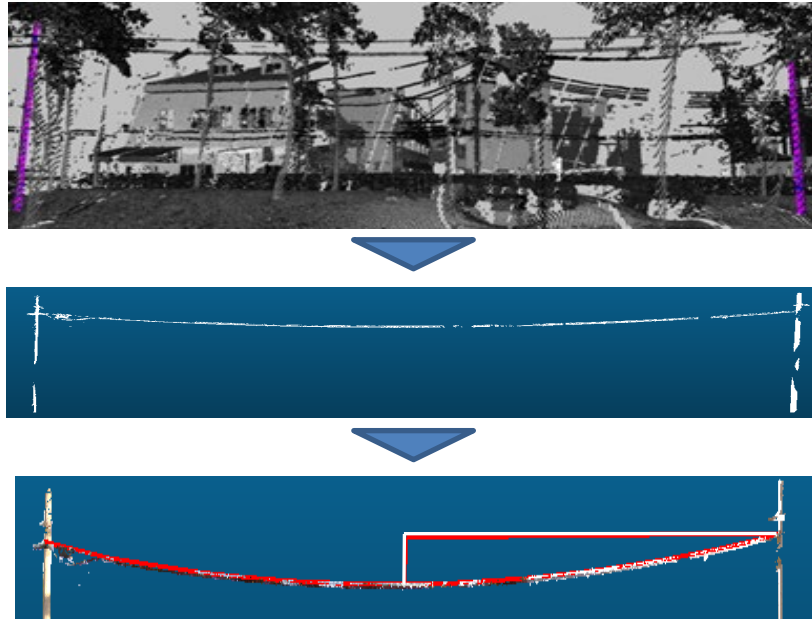


Fig. 4 Method for calculating horizontal tension of cable using 3D point cloud

$$T = \frac{WS^2}{8d} \tag{1}$$

Here,  $T$ : horizontal tension of the cable,  $W$ : cable weight per unit length,  $S$ : distance between utility poles, and  $d$ : cable slack.

The accuracy of the horizontal tension estimations was examined using the experimental setup shown in Fig. 5.

As shown in the figure, a load cell for measuring tension in wire direction was installed at the end of a cable laid between utility poles separated by  $S$ , and the horizontal tension was changed by changing slack value  $d$ . A fixed laser scanner was used to measure the slackness.

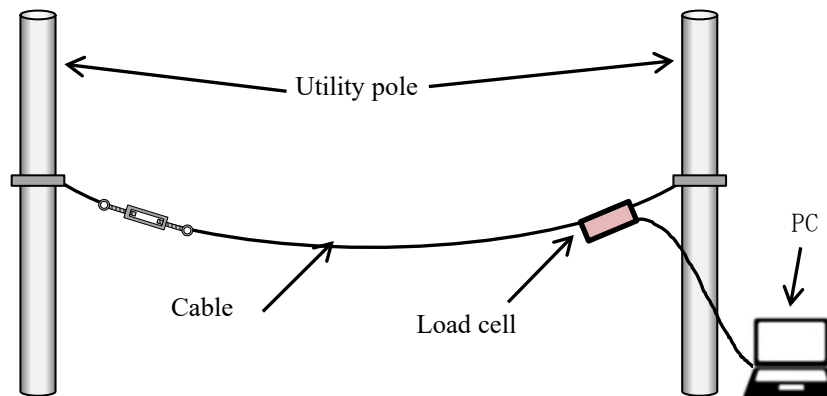
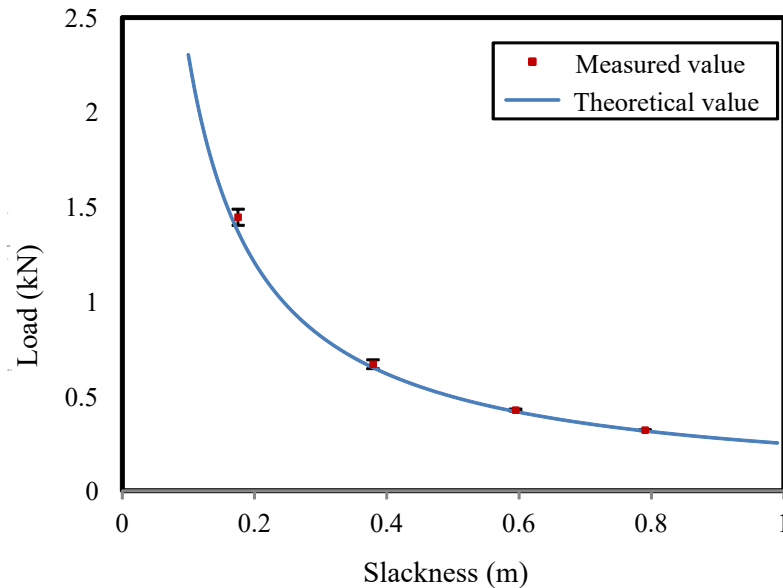


Fig. 5 Experimental setup

Figure 6 compares measured and estimated loads (determined using equation (1)). In the experiment, the slack value was varied from 0.2 ~ 0.8 m, and the calculated value calculated by equation (1) was compared with the measured value yielded by the technique of Fig. 3. The measurement by the laser scanner was carried out 30 times, and there were respectively shown average values with maximum and minimum value.

The figure confirms good agreement between the measured and calculated values. The very low error of just 3.6% conforms the usefulness of this visualization technique.



*Fig. 6 Comparison of measured and calculated values*

When this technology is put into practical use, the utility poles on both sides of the road will be captured by mobile laser scanners. Utility poles that cannot be observed from a road can be covered by fixed laser scanners. This will greatly improve inspection efficiency, and significant cost reductions by the elimination of most manual inspection be expected.

As shown in Fig. 7, a program was developed to obtain the information necessary for load estimation from the point groups, display the positions of the utility poles and cables on a 2D map, and visualize the load applied to the utility poles in 3D.

As a result, the inspection worker can quantitatively and accurately understand the loads applied to the utility pole. By countering excessive loads, the structural deterioration can be suppressed, and so realize the long-term safe use of outside facilities.

### **Conclusion**

This paper described an efficient inspection method for realizing the long-term safe utilization of facilities. It automates the determination of loads placed on utility poles and so allows outside facilities to be maintained in "healthy condition" without structural risk.

The proposal gathers point cloud data of cables and poles, processes the data to determine sides loads, and offers an effective map-based visual interface to assist in corrective work.

In the future, we plan to examine the applicability of this method to actual equipment using laser scanners and software.

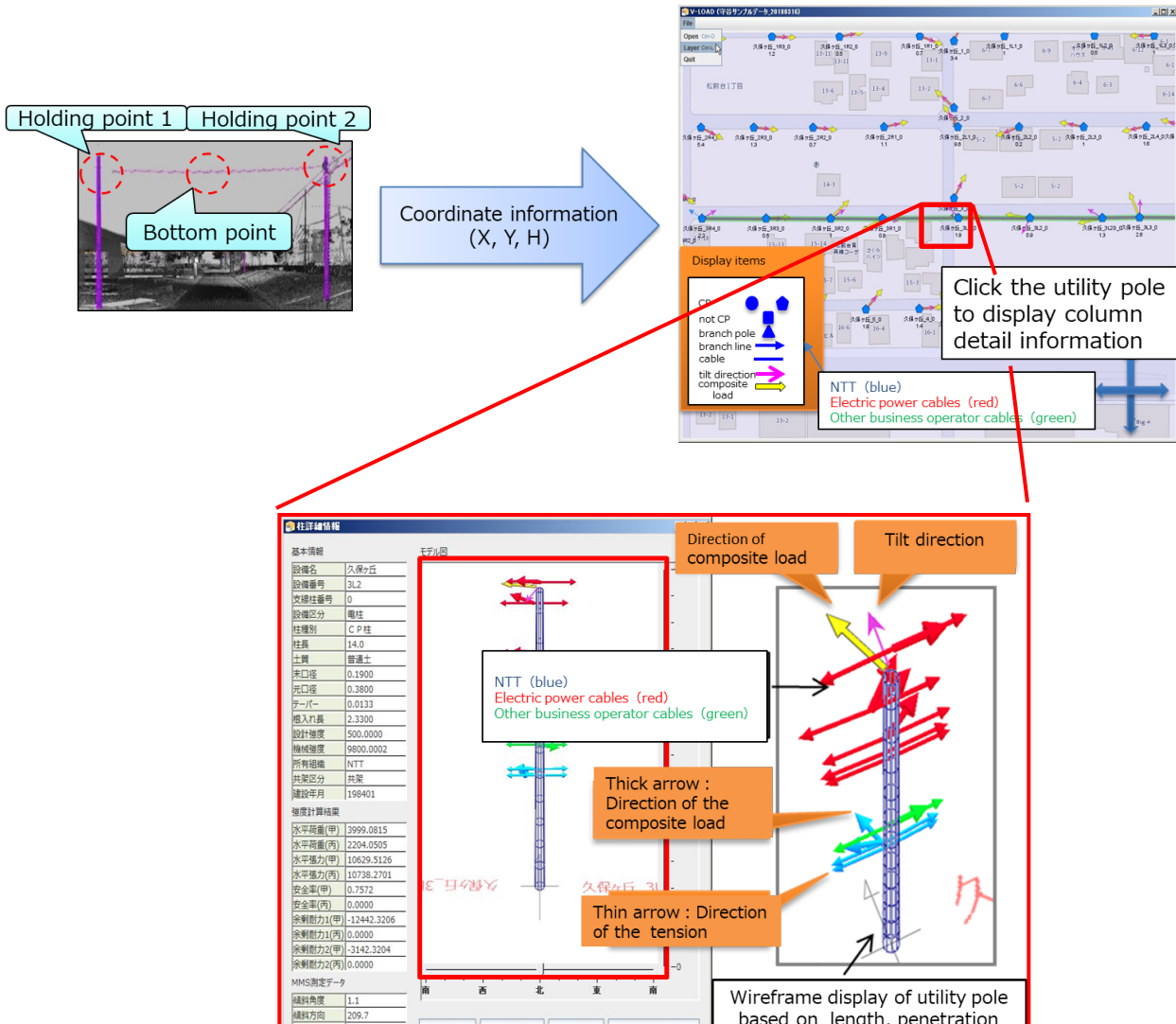


Fig. 7 Software to visualize loads based on this technology

**References**

[1] Information NTT East: Telecommunication Facilities, Information NTT East < [https://www.ntt-east.co.jp/databook/pdf/2019\\_allpage.pdf](https://www.ntt-east.co.jp/databook/pdf/2019_allpage.pdf) >, (Retrieved 27.7.2020)

[2] T. Kurashima, H. Ieda, and M. Waki: Three-dimensional off-site access facility management technology using a mobile mapping system, 3rd Report, Shin-Gaku Gijutsuho, OFT2015-6, pp. 25-30, 2015.

[3] M. Waki, T. Goto, K. Katayama, and T. Kurashima: A study for the application of three-dimensional facility management technology to maintenance and inspection work - Three-dimensional off-site access facility management technology using mobile mapping system, 7th Report, Shin-Gaku Gijutsuho, OFT2016-22, pp. 25-28, 2016.

[4] M. Waki, T. Goto, and K. Katayama: 3D facility management technology using a mobile mapping system (MMS), Communications Society Magazine of the Institute of Electronics, Information and Communication Engineers, vol. 12, no. 1, pp. 39-45, 2018. <https://doi.org/10.1587/bplus.12.39>

# Technique for Analyzing Relationship Between Unbalanced Load and Structural Deterioration in Outside Facilities

Soichi Ishikawa<sup>1,a,\*</sup>, Gen Kobayashi<sup>1,b</sup>, Masaki Waki<sup>1,c</sup>,  
Ryouichi Kaneko<sup>1,d</sup>, and Hiroaki Tanioka<sup>1,e</sup>

<sup>1</sup>NTT Access Network Service Systems Laboratories, 1-7-1 Hanabatake Tsukuba, Ibaraki, Japan

<sup>a</sup>souichi.ishikawa.ck@hco.ntt.co.jp, <sup>b</sup>gen.kobayashi.wn@hco.ntt.co.jp,

<sup>c</sup>masaki.waki.me@hco.ntt.co.jp, <sup>d</sup>ryouichi.kaneko.kv@hco.ntt.co.jp,

<sup>e</sup>hiroaki.tanioka.nh@hco.ntt.co.jp

**Keywords:** Civil Structure, FEM, Utility Pole

**Abstract.** In order to provide telecommunication and FTTH services, NTT have installed so many facilities such as utility poles and optical cables. The number of poles is about 11.8 million and the total length of all installed cables is about 2.3 million km. These facilities are now maintained and inspected visually by on-site maintenance staff at great expense. Therefore, we are researching a novel outside-facility renovation technology that increases cost-effectiveness by ensuring the long-term safe use of facilities. When a utility pole is newly constructed, it is designed under the assumption of a maximum load such as wind pressure being applied to the pole via cables and auxiliary attachments. However, the loads can become imbalanced when the guy wire cannot be tensioned as they cross private land or when there are obstacles, etc. We call this condition that unbalanced loads occur. Unbalanced loads are one of the key reasons for the structural deterioration of utility poles. After the deterioration occurs, the risk of pole collapse increases, because deflection and inclination are generated and finally the cracks propagate until collapse. The conventional solution is to replace the damaged pole. However, in many cases, the loads are created by other contiguous poles, so unbalanced loads occur again. Therefore, we are developing a method that can identify the reason by regarding sets of utility poles as "facility systems" and analyzing unbalanced loads quantitatively by FEM. In our research, simulation accuracy is improved by determining the quantitative differences obtained by comparing the calculated results obtained by FEM with measured values obtained by using a reaction wall. The simulations of structural degradation due to unbalanced loads taking into account the deformation of cables due to wind velocity and air temperature in addition to various material properties such as hysteresis and the sectional model of the utility poles. In addition to the above, the effect of soil is considered as a spring element, and the analysis involves the elements of horizontal spring (K<sub>xi</sub>, K<sub>zi</sub>) and vertical spring (K<sub>v</sub>). While the calculated and the measured values show good agreement, there is some small error. This error is considered to be due to the influence of parameters such as tensile and compressive strength, and we aim to improve the simulation accuracy by considering these effects in the future.

## Introduction

We, NTT, have installed more than 11.8 million telephone poles (Here in after referred to as utility poles) and 2.28 million km of cable etc. in order to provide metallic and FTTH services such as telephone and Internet [1]. New construction, renewal and inspection work on these outside facilities are carried out at legally specified intervals, and their maintenance needs enormous time and labor costs.

We have started using MMS (Mobile Mapping System) equipped with a laser scanner that can be driven on public roads, and 3D models of utility poles have been obtained from 3D point clouds. We estimate metrics of structural deterioration such as inclination and deflection, and put the data into practical use for inspection operations [2]- [4].

This study uses the mechanisms leading to structural deterioration to realize the long-term safe utilization of facilities.

In order to achieve this goal, we need two technologies. The one is “load visualization” which makes it possible to visualize where the unbalanced loads exist and their magnitude, which is a major factor triggering structural deterioration. Another is “the relationship between the unbalanced loads and the structural deterioration”, which explains how to eliminate the unbalanced loads revealed by the visualization. This paper shows “the relationship between the unbalanced loads and the structural degradation”.

### **Load visualization technology and the relationship between the unbalanced load and structural deterioration**

When utility poles are newly constructed, the design assumes the maximum design load such as wind pressure and cable loading. However, unbalanced loads are likely to occur because guy wire cannot be constructed by the case of stringing on the private land and the existence of obstacles, etc. So, unbalanced loads are also generated even when cables are laid as designed.

A utility pole experiencing these unbalanced loads suffers deflection and inclination, after which cracking can occur that may trigger pole collapse. The 3D point clouds being gathered can measure the deflection and inclination with high-precision, and identify what needs to be inspected.

The purpose in this study is ensure that outside facilities can be used safely for longer periods than is now possible. The key is identifying unbalanced loads and their causes. This allows corrective measures to be undertaken which reduce renewal costs without sacrificing safety or security.

### **Technology for understanding the relationship between unbalanced loads and structural deterioration**

Until now, structural deterioration has been judged by the visual inspection of every single utility pole. However, in the example shown in Fig.1, since the guy wire exists only at one end of a string of utility poles, the utility poles hosting the guy wire gradually incline due to the unbalanced loads. In this case, the defective utility pole identified by the conventional inspection regime (the second on the left) is renewed, but the fundamental problem causing the unbalanced loads remain. For that reason, the structural deterioration occurs again in a few years.

In order to solve the above problem, we introduce the concept that a set of utility poles is regarded as one “facility systems”. As shown in Fig.2, when a defective utility pole is found, the entire system is inspected to clarify the cause of the unbalanced loads. Determining and rectifying the problem allows the outside facility to be safely utilized for longer periods than is currently available. Solutions to persistent unbalanced loads include the use poles of higher strength.

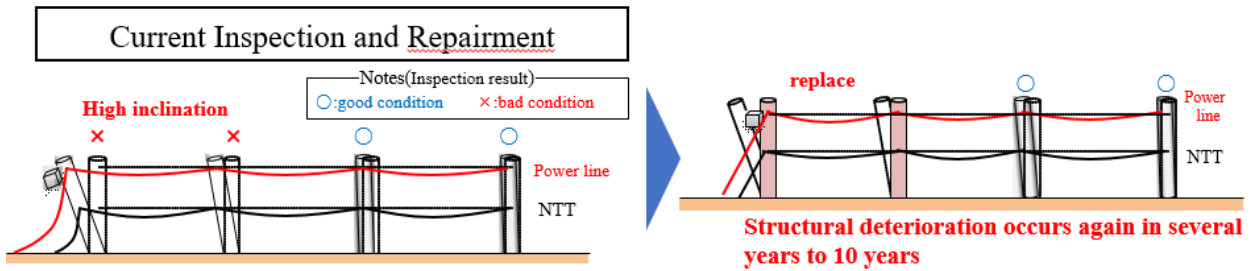


Fig.1: Examples of facility failures that cannot identified by the current inspection regime

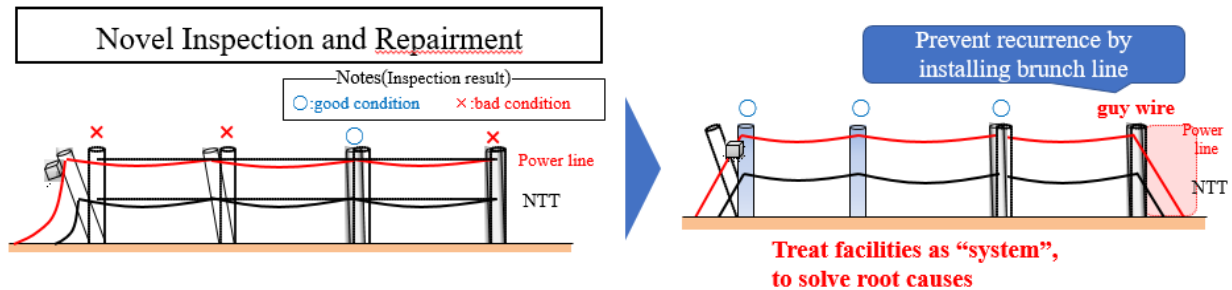


Fig.2: Examples of Renewal in "System" Repair guy wire

For this examination, simulation accuracy is improved by comparing the calculated value using FEM (finite element method) with the measured value obtained from a load propagation experiment.

The simulation of the structural degradation due to unbalanced loads consider the deformation of cables due to wind pressure and air temperature, in addition to various material characteristics such as the cross-sectional model of utility poles and hysteresis as shown in Fig.3.

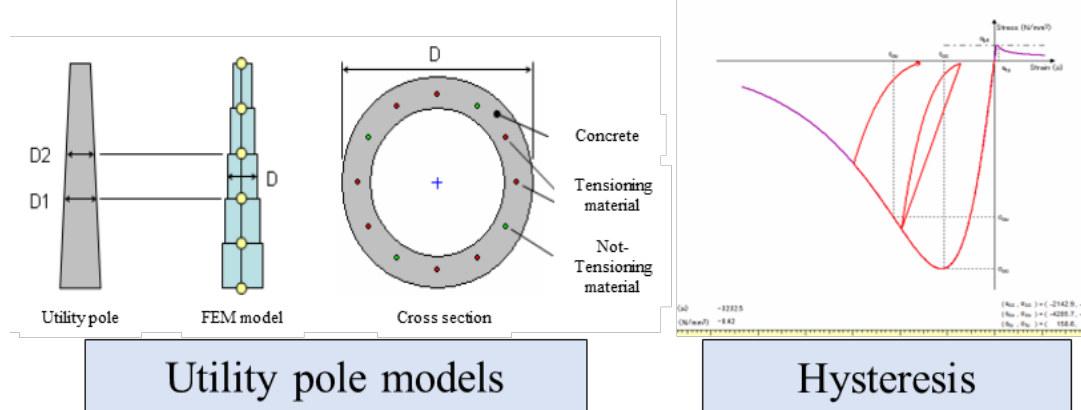


Fig.3: pole elements used in the simulation

When wind blows across the cable, the tension on the supporting utility poles increases, and the magnitude is given as follows.

$$P_c = K \cdot \sum d \cdot S \tag{1}$$

Here,  $P_c$  represents the load in the cable,  $K$  is coefficient that depends on the type of wind pressure load,  $\sum d$  represents the sum of the outer diameters of the cable, and  $S$  represents the average pole separation distance.

However, it is necessary to carry out the analysis three-dimensionally, because the wind direction is highly variable. In addition, if the ambient temperature is lower than when the cable was laid, the tension increases because the cable shrinks, while the opposite is true if the ambient temperature is higher. A unified expression is given below.

$$d_1^3 + \left\{ \frac{3}{8} S^2 \left( \frac{T_0}{EA} - \alpha(\theta_1 - \theta_0) \right) - d_0^2 \right\} d_1 = \frac{3W_1 S^4}{64EA} \quad (2)$$

Variables are defined as  $d_0$ : slack in no wind condition,  $d_1$ : slack with wind,  $S$ : distance between utility poles,  $T_0$ : tension in no wind condition,  $E$ : Young's modulus of cable,  $A$ : cross-sectional area of cable,  $\alpha$ : thermal expansion rate of cable,  $\theta_0$ : temperature in installation condition,  $\theta_1$ : current temperature,  $W_1$ : cable weight per unit length are respectively expressed.

In addition to the above, the effect of soil reaction force is considered by assuming spring elements; the analysis considers the horizontal spring elements ( $K_{xi}$ ,  $K_{zi}$ ) and vertical spring element ( $K_v$ ) as given by the following equation.

$$K_{xi} = K_{zi} = K \cdot A_h \quad (3)$$

$$K_v = K \cdot A_v \quad (4)$$

$$A_h = D_i \cdot L_i \quad (5)$$

Here,  $K_{xi}$ ,  $K_{zi}$ : horizontal ground spring elements,  $K_v$ : vertical ground spring element,  $K$ : ground reaction coefficient,  $A_h$ : horizontal projected area of the pole member, and  $A_v$ : area of the pole bottom face, respectively.

Fig.4 shows the analytical results of the loads in a "facility systems" and the pole model before and after the analysis for a single utility pole. The figure shows that structural deterioration characteristics such as inclination and deflection occurred and unbalanced loads were generated in the left pole without guy wire as indicated by the FEM using equations (2) to (5) for pole models created using various material properties. This simulation of the system and a single body made it possible to elucidate the relationship between unbalanced loads and structural deterioration.

Next, we constructed an experimental setup capable of imposing loads on an actual utility pole. In order to accurately apply the load to the utility pole, a reaction wall, shown in Fig.5, was used.

Fig.5 shows a birds-eye view of the reaction wall. The reaction wall can apply loads in excess of the largest design loads for the utility poles used by NTT. This system allows us to control the utility pole's deterioration, since the additional load could be accurately determined. In the future, the equipment which fixes the utility pole will be mounted so that the experiment except for the effect of the soil in "system" composed of multiple utility poles and cables may be possible.

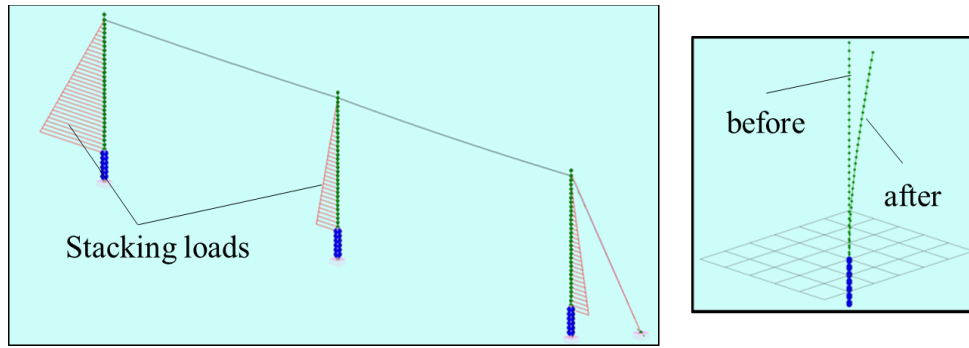


Fig4: Analysis of structural deterioration in utility poles using finite element method (FEM)

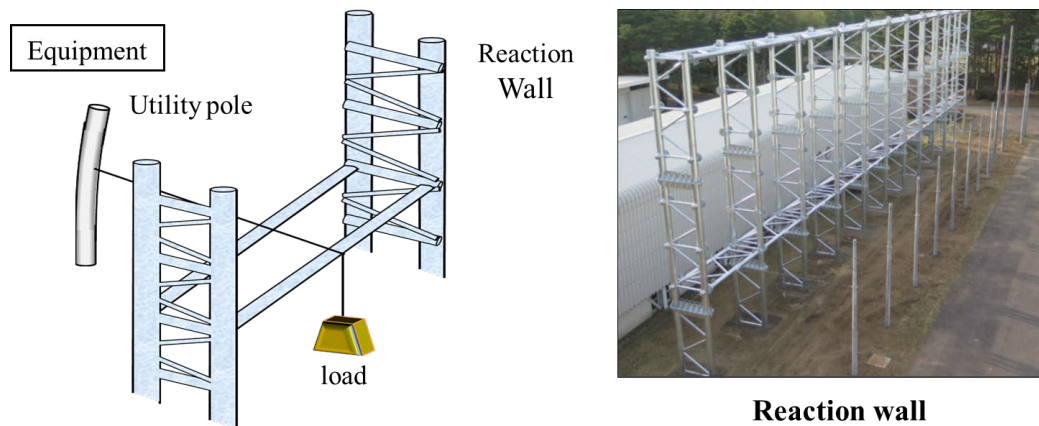


Fig5: Loading via Reaction Wall

Using the experimental setup shown in Fig.5, loading to  $2/3^{\text{rd}}$  of the design load of the utility pole (1.3kN) was applied for up to 40 days and we measured deflection values. The results are compared with the simulation results in Fig.6. The measured deflection was captured by a fixed laser scanner. In this figure, the error between the calculated value and the measured value shows good agreement in the range of  $2\sigma$ . However, since we are aiming to use this simulation for practical use, further improvement of the error to be within  $1\sigma$  is necessary.

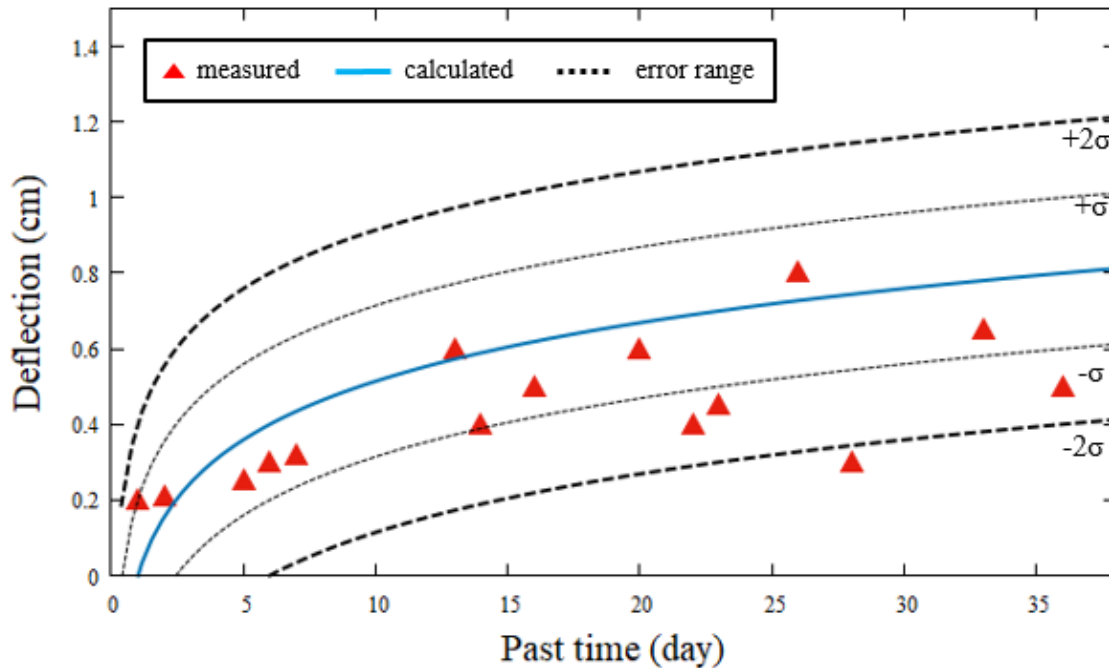


Fig6: Comparison of pole deflection due to loading over time

### Summary

The paper detailed our proposal to identify the relationship between unbalanced loads and structural deterioration of utility poles. FEM-based simulations elucidated the structural deterioration with high precision. Research and development activities will continue to realize further enhancement of the proposal, and enable its application to outside facilities for practical use; the goal is to reduce the cost of maintenance activities without sacrificing safety or security.

### References

- [1] Information NTT East: Telecommunication Facilities, Information NTT East [https://www.ntt-east.co.jp/databook/pdf/2019\\_allpage.pdf](https://www.ntt-east.co.jp/databook/pdf/2019_allpage.pdf), (Retrieved 27.7.2020)
- [2] T. Kurashima, H. Ieda, and M. Waki: “Three-dimensional off-site access facility management technology using a mobile mapping system”, 3rd Report, Shin-Gaku Gijutsuho, OFT2015-6, pp. 25-30, 2015.
- [3] M. Waki, T. Goto, K. Katayama, and T. Kurashima: “A study for the application of three-dimensional facility management technology to maintenance and inspection work - Three-dimensional off-site access facility management technology using mobile mapping system”, 7th Report, Shin-Gaku Gijutsuho, OFT2016-22, pp. 25-28, 2016.
- [4] M. Waki, T. Goto, and K. Katayama: “3D facility management technology using a mobile mapping system (MMS)”, Communications Society Magazine of the Institute of Electronics, Information and Communication Engineers, vol. 12, no. 1, pp. 39-45, 2018. <https://doi.org/10.1587/bplus.12.39>

# Structural Health Monitoring (SHM) of Space Structures

Aswin Haridas<sup>1,a,\*</sup> and Holger Speckmann<sup>1,b</sup>

<sup>1</sup> Testia GmbH, Cornelius-Edzard-Str. 15 - 28199 Bremen, Germany

<sup>a</sup>aswin.haridas@airbus.com, <sup>b</sup>holger.speckmann@airbus.com

**Keywords:** Structural Health Monitoring, Space Structures, Asset Monitoring, Optical Fiber Sensors, Future Technologies

**Abstract.** Recent years have seen an increased interest in exploring outer space for space tourism or for unmanned or manned planetary explorations. The captivated interests among various stakeholders to employ advanced technologies to meet the requirements of these missions have necessitated the use of newly developed asset monitoring systems to ensure robustness and mission reliability. Although, Non-Destructive Testing (NDT) methods provide sufficient information about the state of the structure at the time of inspection, the need for continuously monitoring the health of the structure throughout the mission has asserted the use of Structure Health Monitoring (SHM) technologies to increase the levels of safety and thereby, reducing the overall mission costs. However, since the implementation of SHM technologies for space missions can be affected by several factors including, environmental conditions, measurement reliability and unavailability of adequate standards, additional considerations on its employability must be reconsidered. This article demonstrates a structured approach to compare the capabilities of some of the most promising SHM technologies in consideration of these influential factors. Additionally, remarks on the feasibility of employing these SHM technologies and the role they could play in such critical missions would be elaborated.

## Introduction

Over the past few decades, several stakeholders in the space exploration sector have thoroughly understood and implemented strategies for monitoring mission critical structures to ensure improved levels of mission safety, reliability & affordability [1, 2]. Prominent stakeholders including ESA and NASA have therefore incorporated Structural Health Monitoring (SHM) sensors and systems for on-board condition monitoring, fault detection and to generate prescriptive recovery actions. In addition, in order to pave the way towards having reusable space assets, reducing the vehicle downtime, operating costs and the maintenance costs, these stakeholders are also investigating approaches to understand and predict the lifetime of a mission critical structure.

SHM was born from the conjunction of several techniques that share a common basis with Non-Destructive Testing (NDT). In fact, by permanently installing and integrating some of the NDT sensor technologies onto the structure of interest, they could be converted into SHM techniques. Some of the most commonly used SHM technologies include, conventional strain gauges, fiber optic sensors and acoustic sensing techniques, among many others [3]. Since the fundamental basis of each of these technologies are different, their performance is highly dependent on the use-case under consideration. For monitoring the health of space structures, one such performance hindering parameter is the ambient space condition itself (ambient temperatures vacuum, cosmic radiation and electromagnetic emissions) [4]. Therefore, when selecting appropriate SHM techniques for such application, the capability of the sensors must be fully

understood and their performance must be optimized to compensate for the influences of the space environment.

Even though, several studies investigate the performance of SHM technologies for monitoring the assets in a space environment, the majority of the research have looked into the performance of an individual SHM technology [1, 2, 5, 6]. Furthermore, since the application of SHM for space assets is a relatively new innovation, additional developments, especially for standardizing the behavior of such sensors and systems are quintessential. This would require the creation of standards to define the minimum requirements for a SHM system, which is nonexistent.

In this context, this paper investigates into the most commonly used SHM technologies and compares their performance based on a set of requirements. These requirements have been derived from several factors including, environmental conditions, measurement reliability and the technology maturity. In addition, since the system requirements for space applications can be comparable with (to an extent) the ones defined for fixed wing aircrafts, we have used the SAE ARP 6461 standards for our study [7]. This standard provides, “*Guidelines for implementation of structural health monitoring on fixed wing aircrafts*”, which could be relevant for applications including (not limited by), helicopters, space crafts and launchers. Since it is impossible to compare the performance of all of the available SHM systems for space asset monitoring, we have limited our scope to identify and compare some of the most commonly used and promising sensor technologies. The work done in this article is a follow-up to our previous work, wherein we had evaluated the performance of fiber optic sensors, Piezoelectric Wafer Active Sensors (PWAS), Acoustic Emission (AE) sensors and conventional strain gauges in meeting the requirements posed by the space sector [8]. Upon studying the capabilities of each of these sensor technologies and its alignment with the requirement list for monitoring operation parameters & damage parameters, fiber optic sensors were determined to be the most promising. Although, PWAS (e.g. SMART sensors from Acellent™) were observed to be not so capable in monitoring the operational parameters, their ability in monitoring damage parameters, especially in the case of composite structures, provide a promising solution for the future of monitoring futuristic space structures. Therefore, the analysis and evaluation presented in this paper compares the capability of the fiber optic sensors with two additional promising sensor technologies for monitoring the health of aerospace structures, namely, Comparative Vacuum Monitoring (CVM) and Surface Acoustic Waves (SAW). The next few sections would detail the capabilities of each of these sensor technologies which would be followed by the definition of the set of requirements. The aim of the analysis is to determine one (or more) promising technology (or technologies), which can be envisaged to revolutionize the space industry in the near future by setting very high standards for safety, reliability and robustness.

### **Optical Fiber Sensors**

The use of sensors based on fiber optic technology for strain sensing, vibration monitoring, temperature measurements etc., have gained momentum due to its higher sensitivity & form factor. In essence, a fiber optic sensor fundamentally consists of an optical source that is optically aligned with a single mode fiber optic cable. The relationship between the optical properties of the signal (light) transmitted through the optical fiber and the measurement parameter is used to measure the structural condition & performance in real-time. Depending on the sensing mechanism, fiber optic sensors can be classified into three broad categories, namely, single point sensors, multiplexed sensors and distributed sensors [9, 10].

Single point sensing technology consists of one small, durable and highly accurate measurement device connected to a high-bandwidth fiber optic cable. Fiber Bragg Grating (FBG),

which is one of the most commonly used fiber optic sensing system, is an example of this category. In essence, a FBG sensing unit is manufactured by modifying a single-mode optical fiber using a UV laser. The resultant germanium-doped microstructures creates a periodic variation in the refractive index altering the optical properties of the coherent light source passing through the optical fiber. The periodic variations in refractive index, also called Bragg gratings inherently reflect a very narrow wavelength, while transmitting all the other wavelengths through the optical fiber. The wavelength band reflected by the Bragg gratings are strongly dependent on the grating period and thus any external perturbations that affect the same can be correlated with the shift in the reflected wavelength band. Using an instrument, which is known as an interrogator (i.e. the data acquisition device), the shift in the wavelength is recorded. From an application standpoint, these sensors are multiplexed and located at strategic locations along the fiber to create a series of connected units for a quasi-distributed measurement [9].

A distributed fiber optic sensor on the other hand relates the changes in scattered light along the entire length of the optical fiber. The change in scattered light is used to determine the local variation of physical quantities (strains or temperature) [10]. In this case, the entire fiber acts as the sensor element. Depending on whether the mechanism of scattering the light within an optical fiber is elastic or inelastic, the sensing technique can be classified, Rayleigh, Brillouin and Raman scattering techniques. Whilst Rayleigh scattering is a physical phenomenon caused due to non-propagating density fluctuations (scattered power is proportional to the input power), Brillouin and Raman scattering result from inelastic physical phenomenon causing large degrees of frequency shifts. Considering the advantages of each of the techniques in the measurement of physical quantities, Rayleigh and Brillouin scattering are being widely investigated for strain measurement applications and Raman scattering is being studied for temperature measurements. Fiber optic sensing technologies have seen widespread applications for monitoring the operational parameters (strains & temperatures) in several industries, including, infrastructure, aeronautical, automotive and for mainstream industrial processes (not limited to) [9, 10].

To ensure the accuracy, repeatability and stability of the measurements made by the fiber optic sensor, multiple parameters play an important role. In the case of applications that require the sensor to be mounted on the surface of the structure of interest, the choice of adhesive is of prime importance. This coating must be able to protect the sensor from mechanical and environmental influences, maximizing its performance. Generally, the sensors are coated using a polymer, acrylate or polyamide base. Parameters including, the choice of adhesive for mounting the fiber, the implementation strategy (externally mounted or embedded) and sensor orientation (important for composite structures) must be optimized [4, 11].

These sensors, which are also minimally influenced by EMI induced noise, are comparatively inexpensive and lightweight. Combined with the possibility of performing measurements over long distances, the applicability of the same for a space environment is promising. However, the lack of suitable standards and the need for discriminating the wavelength shift due to strains and temperature necessitate trials and field tests prior to implementing the same for space applications in the near future [9-11].

### **Surface Acoustic Wave (SAW)**

Typically, a SAW sensor constitutes a piezoelectric substrate on which a periodic comb-shaped inter digital transducer (IDT) pattern is developed using a photolithographic process. The electrodes are generally manufactured using inert alloys, for example, Au, Cr/Au/Cr, etc. When an AC voltage is applied across the IDTs, an acoustic wave is generated which travels across the surface of the crystal (perpendicular to the IDT). The generated acoustic waves are confined to the

surface of the substrates and they have a penetration depth of a few wavelengths. A basic SAW sensor that contains two IDTs on a piezoelectric surface is shown in Figure 1. The input IDT generates the acoustic wave which is collected/reflected by the output IDT [12].

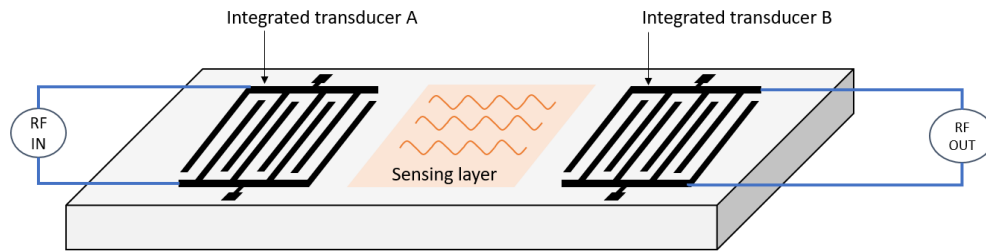


**Fig. 1.** A basic SAW sensor (Adapted from [12])

Based on the sensing mechanism, a SAW sensor can be classified into two broad categories, namely, direct or indirect. While the former directly measures the variation of the physical quantities such as temperature, pressure, torque, etc., the second type the SAW device transforms the output of another direct sensor to the electrical signal convenient for further processing. Both types can be accessed wirelessly. Furthermore, the operational modality of the SAW sensors have been demonstrated both in an active and passive mode. In case of the former, the SAW sensors would require batteries to be placed preferably in close proximity. However, for applications which require the sensor to operate in a high temperature environment ( $\sim 1500^{\circ}\text{C}$ ), for example, within a propulsion system or inside gas pipes, the passive (wireless without batteries) modality would be preferred. In case of the other temperature extreme, i.e. for cryogenic environments, the successful operation of the SAW sensors have been studied and demonstrated [13]

Since these sensors can withstand high temperatures up to about  $1500^{\circ}\text{C}$  and have a high resistance to ionizing radiation (demonstrated tolerance- upto 10 Mrad) without power loss, they are a promising contender for space applications [13]. Although SAW sensors provide several benefits for such critical applications, one of the main challenges for the continuous wireless operation of these sensors is power generation. Often, batteries are not recommended to be used due to the inaccessibility of the inspection area or due to the exposure to large temperature extremes. Which is why, these sensors are mostly implemented in the passive mode. Additional factors that affect the measurements made by the SAW sensors include, a) dependence on vibration and mechanical shocks, b) dependence on the temperature variation (causing the output frequencies to shift; can be compensated) and c) the bandwidth of the Radio Frequency (RF) communication channel (limiting the number of sensors that can be wirelessly connected). In addition to these factors, the importance of defining a certification regime for wireless sensor networks is an additional challenge (considering the interference of wireless devices with other electronics) [12-13].

### **Comparative Vacuum Monitoring (CVM)**

A CVM sensor is a simple pneumatic sensor technology that has been used to continuously and autonomously monitor the onset of cracks. These sensors are permanently adhered onto the structure of interest to monitor their critical regions. The basic principle of a CVM sensor is to maintain a small volume in low vacuum that is extremely sensitive to ingress of air and thus highly sensitive to leakage. The working principle of a typical CVM sensor is shown in Figures 2 (a) and 2 (b). In both these figures, the actual sensing part, which is a sensor pad can be visible onto which several fine galleries containing a low vacuum are incorporated, alternative with galleries at the

nominal atmospheric pressure. To maintain the vacuum in the respective galleries, a vacuum source is used, which can be seen in Figures 2 (a) and 2 (b). In addition, to measure the differential pressure between these galleries, a differential pressure flow meter is incorporated. In the absence of a crack, the differential flow pressure values are show the baseline values (see Figure 2 (a)). However, if a crack develops within the structure (see Figure 2 (b)), the vacuum galleries are disturbed by the ingress of air from the galleries at nominal atmospheric pressure. This in turn would be measured as a drop in pressure differential by the flow meter. Subsequently, using the data from the flow meter, control systems and software management tools are engaged to process the data. Further, the final information about the position and size of the crack is visually presented to the user. Typically, with gallery spacing of 250  $\mu\text{m}$  a crack as small as 100  $\mu\text{m}$  can be identified [14-16].

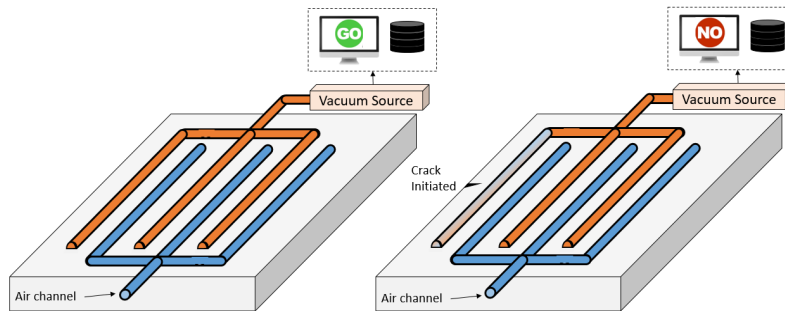


**Fig. 2.** The working principle of CVM sensors, (a) normal state, (b) during the onset of a crack (adapted from [14]).

Being a relatively simple technique that require no electrical excitation, the CVM sensors have been widely employed for the inspection of aircraft structures and to address the critical infrastructure surety needs [14]. This said, the application range of these sensors are not limited and they span several industries, including, mining structures, trains & subway vehicles, cars, trucks and heavy machinery, to name a few [15-16]. Some of the benefits offered by CVM include, a) its high maturity levels for immediate implementation (successfully tested and validated in actual test environments), b) the possibility of incorporating self-diagnostics, c) the possibility of improving the system portability for in-service inspections and d) its use-case flexibility, which allows these sensors to be also used for applications that necessitates embedded sensing (for e.g. monitoring of aircraft riveted lap and butt joints or those that require a through the thickness assessment). However, since the CVM sensor detects the initiation of defects based on measurement deviation from a base-line reading from the pressure flow meter, the same must be thoroughly calibrated before the test to avoid any false positives. Therefore, if there is a known defect on the location of sensor application, the detector would measure a non-zero base value. This remains one of the disadvantages of the sensor apart from the installation effort. Also, it must be noted that the sensitivity of the sensor is dependent on the gallery wall thickness [15].

### Feasibility Analysis Using a Decision Matrix

To compare the capabilities of the SHM technologies, a decision matrix stating the list of requirements were compiled based on prior experience along with the inputs from the ArianeGroup. This decision matrix is similar to the one prepared in our previous work [8]. In general, the aim is to assess the capabilities of the SHM technologies based on the requirements in system parameters, condition monitoring parameters, damage monitoring parameters and environmental parameters. In order to achieve a fair comparison between the techniques, a weighted decision matrix would be prepared. In order to do so, a ranking score would be assigned

and each of the technologies would be ranked depending on its performance in comparison with the desired state.

Table 1. Decision matrix definition

Parameters	Desired State	Decision Matrix Score		
		1	0.5	0
<b><u>System Parameters</u></b>				
Total weight	Low	Low	Medium	High
Installation effort (cost)	Low	Low	Medium	High
Power consumption	Low	Low	Medium	High
Transmitting data to a remote location	Yes	Yes		No
Self-diagnostic ability	Yes	Yes		No
Possibility of repair for accessible areas	Yes	Yes	Partially**	No
Measurement accuracy, repeatability, resolution & robustness	High	High	Medium	Low
Monitoring area	Large	Large		Small
Sensor cost/ unit area	Low	Low	Medium	High
Data acquisition time	Low	Low	Medium	High
Sensor application location*	Ext. & emb	Ext. & emb.	Ext. & semi emb.	Only ext.
TRL level	High	TRL 8-9	TRL 6-7	TRL <6
<b><u>Condition Monitoring Parameters</u></b>				
Strain measurement range	High	Large		Small
Temperature measurement range	High	Large		Small
Distributed sensing capability	Yes	Yes		No
<b><u>Damage Monitoring Parameters</u></b>				
Defect measurement sensitivity	High	Yes	Yes w/o location	No
Identifying the defect type	Yes	Yes		No
<b><u>Environmental Parameters</u></b>				
Resistance to cosmic radiation with high energy	High	Yes		No
Resistance to electromagnetic radiation	High	Yes		No
Usable in vacuum ( $10^{-10}$ and $10^{-11}$ Atm)	Yes	Yes		No
Usable in low gravity	Yes	Yes		High

\* Ext. and emb. – External and embedded \*\*Depends on whether the sensor is embedded and the use case

To determine the capability of the SHM techniques, a ranking score (based on how the technique satisfies a requirements) is assigned, which is combined with a weighting factor. The results of this analysis is shown in Table 2.

From an initial analysis of the weighted sum, the capabilities offered by the fiber optic sensors dominate the other two SHM technologies. Apart from being immune (partially; requires further tests) to ambient conditions, the main advantage of fiber optics sensors arise due to its multiplexing capability. Having several sensor points distributed over the length of an optical fiber, one can minimize the overall weight per sensor (relative to other sensors). Furthermore, the overall costs for procuring and implementing fiber optic sensors are also minimal compared with the CVM and SAW sensors. In comparison, the capabilities of SAW sensors are observed to be comparable to the fiber optic sensors. However, essentially being a point sensor, the advantages

they offer are diluted (increased weight & installation effort and cost) in comparison to the fiber optic sensors when considering larger scales of implementation. CVM sensors on the other had offer minimal advantages in meeting the requirements posed by the space sector. Although CVM sensors are easy to use and offer self-diagnostic capabilities, they are seen to minimally add value due to the implementation effort (higher installation cost) and due to their non-immunity for applications in the space environment (requires further tests to confirm).

Table 2. Evaluation table

<u>Key</u>	a) Fiber optic sensors b) CVM	c) SAW		
		Parameters	Weighing factor	a)
Total weight	5	1	0	0
Installation effort (cost)	3	0.5	0	0.5
Power consumption	3	0.5	0.5	0.5
Transmitting data to a remote location	4	1	1	1
Self-diagnostic ability	3	0	1	0
Possibility of repair for accessible areas**	4	0.5	1	1
Measurement accuracy, repeatability, resolution & robustness *	5	1	1	1
Monitoring area	2	0	0	0
Sensor cost/ unit area	2	1	0	0
Data acquisition time	2	1	0	1
Sensor application location*	3	1	0.5	0
TRL level	4	0.5	1	0
Strain measurement range	5	1	0	1
Temperature measurement range	5	1	0	1
Distributed sensing capability	3	1	0	0
Defect measurement sensitivity	5	0.5	1	1
Identifying the defect type	5	0	0	1
Resistance to cosmic radiation with high energy	5	1	0*	1
Resistance to electromagnetic radiation	5	1	0	1*
Usable in vacuum (10 <sup>-10</sup> and 10 <sup>-11</sup> Atm)	5	0*	0*	0*
Usable in low gravity	5	0*	0*	0*
<b>Total</b>		53.5	28	48

\* Requires further tests to confirm      \*\* considering the popularity of embedding the sensors

**Summary**

This work was inspired by the rapid growth of the space exploration sector and due to the rising criticality in monitoring the health of mission critical structures. In this article, three of the most commonly used/ promising SHM techniques are introduced and compared with each other on the basis of a set of requirements prepared from our prior experience and inputs from the ArianeGroup. Three sensors, namely, fiber optic sensors, CVM sensors and SAW sensors are compared considering system parameter, operational parameters (condition and damage monitoring) and environmental parameters. Using a weighted evaluation, fiber optic sensors were observed to be the most promising due to their multiplexing capabilities. Even though SAW

sensors are observed to be comparable to the performance of fiber optic sensors, the complexities added during the large scale implementation of the same is observed to hinder its overall performance. CVM sensors on the other hand fail to be comparable with the capability of fiber optic sensors & the SAW sensors. Although CVM sensors offer several advantages for aeronautical applications, there is a sufficient gap in understanding its capability for space applications, which could be a potential interest domain for further research. In conclusion, the research presented in the article covers a small scope of available sensors. The intention of the same is to spark interests and provide a strategy in technology comparison that could facilitate future space missions, making them safer, reliable and dependable.

## References

- [1] W. L Richards, E. Madaras, W.H. Prosser, G. Studor, NASA Applications of Structural Health Monitoring Technology, 9th International Workshop on Structural Health Monitoring, September 10–12, (2013).
- [2] M. Iain, N. Karafolas, Fiber optic sensing in space structures: the experience of the European Space Agency, In 17th International Conference on Optical Fibre Sensors, 5855 (2005), 262-269. International Society for Optics and Photonics. <https://doi.org/10.1117/12.623988>
- [3] H. Speckmann, R. Henrich, Structural health monitoring (SHM)–overview on technologies under development, In Proc. of the World Conference on NDT, Montreal-Canada, (2004).
- [4] B. Daniel, C.P Fritzen, A. Güemes, Structural health monitoring. Vol. 90. John Wiley & Sons, 2010.
- [5] M. Simone, G. Tumino, P. Gaudenzi. "Structural health monitoring for future space vehicles." Journal of intelligent material systems and structures 17, no. 7 (2006): 577-585. <https://doi.org/10.1177/1045389X06059077>
- [6] I. Tansel, P. Chen, X. Wang, A. Yenilmez, B. Ozelik, Structural health monitoring applications for space structures, In Proceedings of 2nd International Conference on Recent Advances in Space Technologies, 288-292 (2005), IEEE.
- [7] F. Peter. "New guidelines for implementation of structural health monitoring in aerospace applications." SAE International Journal of Aerospace 6, no. 2013-01-2219: 525-533 (2013). <https://doi.org/10.4271/2013-01-2219>
- [8] A. Haridas, C.M Giraldo, H. Speckmann, Structural Health Monitoring (SHM) goes to space: submitted to 10th European Workshop on Structural Health Monitoring, EWSHM 2020. [https://doi.org/10.1007/978-3-030-64594-6\\_39](https://doi.org/10.1007/978-3-030-64594-6_39)
- [9] C.E. Campanella, A. Cuccovillo, C. Campanella, A. Yurt, V. Passaro, Fibre Bragg grating based strain sensors: review of technology and applications, Sensors 18, no. 9 (2018), 3115. <https://doi.org/10.3390/s18093115>
- [10] B. Glisic, Distributed fiber optic sensing technologies and applications—an overview, ACI Spec. Publ 292 (2013): 1-18.
- [11] C.M. Giraldo, J.Z. Sagredo, J.M Gómez, P. Corredera, Demonstration and methodology of structural monitoring of stringer runs out composite areas by embedded optical fiber sensors and connectors integrated during production in a composite plant. Sensors, 17(7), 1683 (2017). <https://doi.org/10.3390/s17071683>

[12] M.F. Hribšek, D.V. Tošić, M.R. Radosavljević, Surface acoustic wave sensors in mechanical engineering. *FME transactions*, 38(1) (2010), 11-18.

[13] W.C. Wilson, D.F. Perey, G.M. Atkinson, R.O. Barclay, Passive wireless SAW sensors for IVHM. In 2008 IEEE International Frequency Control Symposium, 273-277, IEEE.  
<https://doi.org/10.1109/FREQ.2008.4623003>

[14] H. Stehmeier, H. Speckmann, Comparative vacuum monitoring (CVM). In Proceedings of the 2nd European Workshop on Structural Health Monitoring, Munich, Germany, (2004) 7-9.

[15] D. Roach, Real time crack detection using mountable comparative vacuum monitoring sensors, *Smart structures and systems* 5, no. 4 (2009): 317-328.  
<https://doi.org/10.12989/sss.2009.5.4.317>

[16] D. Roach, Use of Comparative Vacuum Monitoring Sensors for Automated Wireless Health Monitoring of Bridges and Infrastructure, United States: N. p., 2018. Web.  
<https://doi.org/10.1201/9781315189390-372>

# Research on Fatigue Life of Lifting Equipment Based on Nonlinear Cumulative Damage Theory

Li Chen <sup>1,a,\*</sup>, Keqin Ding <sup>1,b,\*</sup>

<sup>1</sup> China Special Equipment Inspection and Research Institute, Beijing 100029, China

<sup>a</sup>ChenLi111528@163.com, <sup>b</sup>503718617@qq.com

**Keywords:** Fatigue Life, Nonlinear Cumulative Damage, Lifting Equipment

**Abstract.** The lifting equipment is applied more and more extensively with the fast development of economy. The fatigue and safety problems of lifting equipment in service are more and more prominent. This paper presents a nonlinear fatigue damage and life assessment approach for existing lifting equipment and the nonlinear effects of the fatigue damage accumulation due to random dynamic stress spectrum. The stress spectrum monitoring data was analyzed by the modified four peak-valley values fast rain-flow counting method for fatigue analysis. By considering nonlinear effects, the calculation for cumulative damage and prediction for fatigue life of the lifting equipment's hot region were calculated based on the nonlinear damage theory and the nominal stress method. The predicted fatigue damages are different when using the linear and nonlinear fatigue damage rules. According to the engineering application results, the real crack generation time is consistent with that of our estimation method, which demonstrates that our nonlinear prediction model and method for fatigue life are effective. The nonlinear damage theory is recommended for use in fatigue and damage prediction of lifting equipment in service.

## Introduction

For many years, life prediction involving fatigue and damage assessment of key structure parts has been the research hot spot for experts and scholars, in many fields concerning national welfare and the people's daily life such as lifting equipment in service, engineering machinery, special equipment, etc. The safe problem of lifting equipment in service induced by fatigue and damage is becoming increasingly important.

A comprehensive review of many fatigue damage theories can be found elsewhere. Generally speaking, it can be divided into three categories, linear cumulative damage theory, double linear cumulative damage theory and nonlinear cumulative damage theory. Different fatigue damage theories have different accuracy and computational complexity. At present, Miner's linear cumulative damage theory is mainly used in engineering [1-2]. Although Miner's linear cumulative damage theory is simple and easy to use, the linear damage theory has been demonstrated to be unreliable. Studies [3] show that the median damage values to test specimens under certain loading conditions range from 0.15 to 1.06. This is attributable to the fact that the relationship between physical damage and cycle ratio is not unique and varies from one stress level to another. Due to the complexity of fatigue damage evolution process and its mechanism, the nonlinear cumulative damage theory is needed [4-5].

In this paper, the fatigue life of large lifting equipment is studied based on the two-parameter rain flow fast counting program and the nonlinear cumulative damage theory.

## Fatigue life prediction method of lifting equipment

Nominal stress method is a mature method for fatigue life estimation, and its prediction range is generally high cycle fatigue. The fatigue life of lifting equipment generally belongs to high cycle

fatigue, so the nominal stress method will be used in this paper. The prediction steps are shown in figure 1.

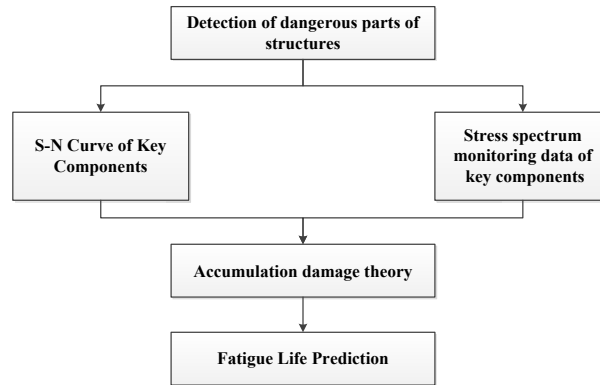


Figure 1 Fatigue Life Prediction Procedures

As shown in figure 1, obtaining S-N curves of key components is the basis for estimating fatigue life of components by nominal stress method. If the S-N curve of key components can be obtained directly through fatigue test of full-scale key components, the fatigue life of components can be accurately estimated. Generally speaking, the geometric shapes of key components are complex and diverse, so it is difficult to obtain the S-N curve directly from the fatigue test of full-scale key components.

The commonly used method is to estimate the S-N curve of key components according to the S-N curve of standard sample materials.

The S-N curves of typical sample materials can be expressed as follows:

$$N\sigma^m = C \tag{1}$$

Or in logarithmic form:

$$\lg(N) = \lg(C) - m \lg(\sigma) \tag{2}$$

In order to estimate S-N curves of key components from S-N curves of standard sample materials, the influence of other factors should be taken into account. The expression of S-N curves of key components is as follows:

$$N(K_{\sigma D}\sigma)^m = C \tag{3}$$

Where  $K_{\sigma D}$  is the correction coefficient of S-N curve of key components, which characterizes the influence of other factors (Including Fatigue notch coefficient  $K_f$ , Specimen Size coefficient  $\varepsilon$ , Surface Finishing coefficient  $\beta$ , Type of loading  $C_L$  etc.) on fatigue properties of materials. C and m are material constants related to materials. Taking logarithm of formula (3) :

$$\lg(N) = \lg(C) - m \lg(K_{\sigma D}\sigma) \tag{4}$$

**Nonlinear fatigue cumulative damage theory**

The damage curve for another life level ( $N_{i,f}$ ) is then given by the power law damage equation defined as:

$$D_i = \left( \frac{n_i}{N_{i,f}} \right)^{0.4} \left( \frac{N_{i,f}}{N_{1,f}} \right)^{0.4} \tag{5}$$

For multiple life levels (e.g.,  $N_{1,f} < N_{2,f} < \dots < N_{n,f}$ ), the damage curves (as shown in Figure 1) can be constructed expeditiously by letting the damage curve for the lowest life level be the reference life.

Nonlinear damage curves are shown in figure 2.

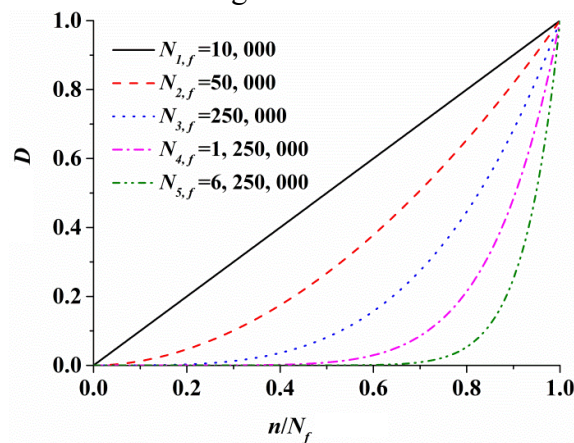


Figure 2 Nonlinear fatigue cumulative damage theory

**Data analysis based on rain-flow cycle counting method**

Based on the four peak valley value rain flow counting method [6-7], as shown in figure 3, the docking is processed from the peak or valley value in advance, and the final cycle count can be completed with only one rain flow count.

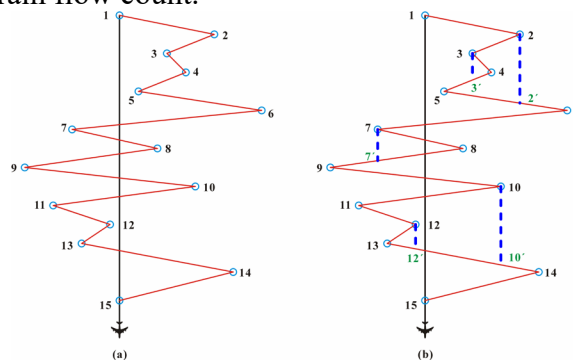
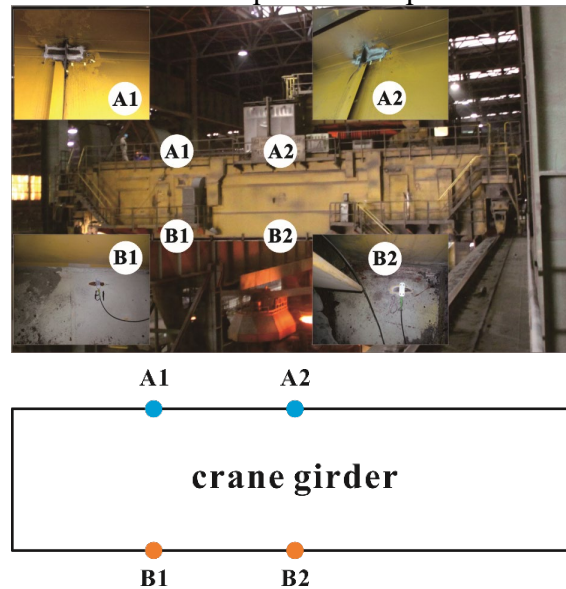


Figure 3 Rain-flow cycle counting method

The separation of the data to be processed and the data that needs to be kept can avoid repeated displacement of the data and greatly improve the processing efficiency.

**Engineering application**

*The monitoring position of metallurgy crane.* The position of metallurgy crane plane stress state monitoring based on fiber Bragg grating sensor is shown in figure 4. The risk of crack initiation on position A2 is highest. So the random stress spectrum on position A2 is studied.



*Figure 4 Fiber gratings position of monitoring point*

*Stress monitoring based on fiber Bragg grating sensor.* As shown in figure 5, the main technical advantages of stress monitoring based on fiber Bragg grating sensor are as follow:

- (1) Fiber Bragg grating sensor can be multiplexed so that many sensors lie along a single fiber line. They are compatible with fiber optic data lines, which support huge necessary band width, which in turn support large number of sensors.
- (2) Very micro thin. Therefore it can be made compatible with different composite material without changing mechanical properties.
- (3) They can withstand high temperatures and pressure and are highly immune to electromagnetic interference.

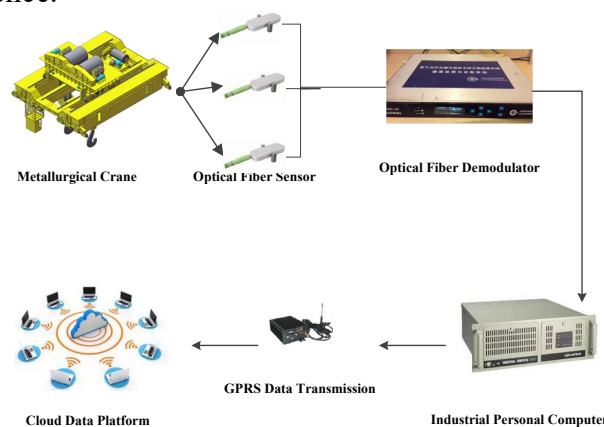


*Figure 5 Structural Health Monitoring System for Lifting Equipment*

Stress monitoring data based on structural health monitoring system are shown in figure 6.

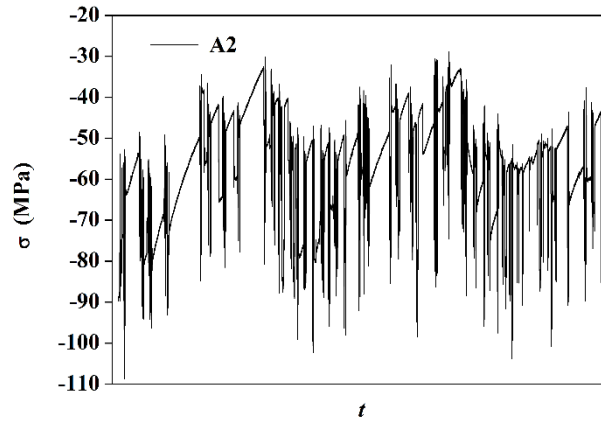


Figure 6 Structural Health Monitoring System for Lifting Equipment

The result based on nonlinear damage theory.

Table 1 Procedures for Fatigue Life Estimations Based on nonlinear damage theory

Blocks	D <sub>1</sub>	D <sub>12</sub>	D <sub>123</sub>	D <sub>1234</sub>	D <sub>1-5</sub>	D <sub>1-6</sub>	D <sub>1-7</sub>	D <sub>1-8</sub>
1	0.0111	0.0111	0.0118	0.0127	0.0138	0.0145	0.0151	0.0153
2	0.0264	0.0264	0.0275	0.0289	0.0309	0.0322	0.0334	0.0339
3	0.0450	0.0450	0.0463	0.0483	0.0510	0.0531	0.0549	0.0557
4	0.0668	0.0668	0.0683	0.0708	0.0745	0.0773	0.0798	0.0809
5	0.0920	0.0920	0.0938	0.0968	0.1013	0.1049	0.1083	0.1097
6	0.1208	0.1208	0.1228	0.1263	0.1318	0.1363	0.1405	0.1424
7	0.1535	0.1535	0.1557	0.1597	0.1662	0.1716	0.1768	0.1791
8	0.1902	0.1902	0.1926	0.1972	0.2047	0.2111	0.2174	0.2202
9	0.2313	0.2313	0.2339	0.2390	0.2476	0.2551	0.2626	0.2659
10	0.2770	0.2770	0.2798	0.2855	0.2952	0.3039	0.3126	0.3166
11	0.3277	0.3277	0.3307	0.3370	0.3479	0.3578	0.3679	0.3725
12	0.3836	0.3836	0.3869	0.3937	0.4060	0.4172	0.4288	0.4341
13	0.4452	0.4452	0.4486	0.4561	0.4697	0.4823	0.4956	0.5017
14	0.5127	0.5127	0.5164	0.5246	0.5396	0.5537	0.5686	0.5756
15	0.5867	0.5867	0.5906	0.5994	0.6159	0.6316	0.6484	0.6563
16	0.6674	0.6674	0.6715	0.6810	0.6990	0.7165	0.7353	0.7442
17	0.7553	0.7553	0.7596	0.7698	0.7895	0.8088	0.8298	0.8398
18	0.8508	0.8508	0.8554	0.8663	0.8878	0.9090	0.9323	0.9434
<b>19</b>	<b>0.9545</b>	<b>0.9545</b>	<b>0.9593</b>	<b>0.9709</b>	<b>0.9942</b>	<b>1.0174</b>	<b>1.0432</b>	<b>1.0556</b>

According to table 1, the fatigue life of the hot spot area are as follows:

$$\text{Fatigue Life} = 19(\text{Years}) \tag{6}$$

The metallurgical crane was put into operation in 1997. 20 years later, cracks were detected in hot spot area A2 in 2017. The real crack generation time (20 years) is consistent with that of our estimation (19 years), which demonstrates that our prediction model and method for fatigue life are effective and give a method for the evaluation of the lifting equipment's fatigue life.

## Conclusion

In this paper, the nominal stress method is used as the basic method of fatigue life prediction. First, the monitoring stress spectrum is processed by two-parameter rain-flow counting method. Then, the fatigue cumulative damage caused by monitoring stress spectrum is calculated based on the nonlinear fatigue cumulative damage theory. Finally, the fatigue life is analyzed and predicted.

According to the engineering application results, the real crack generation time is consistent with that of our estimation, which demonstrates that our prediction model and method for fatigue life are effective and give a method for the evaluation of the lifting equipment's fatigue life.

## Acknowledgments

This research was supported by National key technologies Research & Development program through 2017YFC0805100.

## References

- [1] Nykänen T, H Mettänen, T Björk, A Ahola. (2016) Fatigue assessment of welded joints under variable amplitude loading using a novel notch stress approach. *International Journal of Fatigue*, 101: S0142112316304315. <https://doi.org/10.1016/j.ijfatigue.2016.12.031>
- [2] Durodola J F, N Li, S Ramachandra, A N Thite. (2017) A pattern recognition artificial neural network method for random fatigue loading life prediction. *International Journal of Fatigue*, 99: 55-67. <https://doi.org/10.1016/j.ijfatigue.2017.02.003>
- [3] Lee Y L, M W Lu, R C Segar, C D Welch, R J Rudy. (1999) Reliability-based cumulative fatigue damage assessment in crack initiation. *International Journal of Materials & Product Technology*, 14: 1-16. <https://doi.org/10.1504/IJMPT.1999.036257>
- [4] Shang D G, W X Yao. (1999) A nonlinear damage cumulative model for uniaxial fatigue. *International Journal of Fatigue*, 21: 187-194. [https://doi.org/10.1016/S0142-1123\(98\)00069-3](https://doi.org/10.1016/S0142-1123(98)00069-3)
- [5] Wu W F, T H Huang. (1991) A statistical nonlinear cumulative damage rule and fatigue life prediction under random loading. *International Journal of Pressure Vessels & Piping*, 47: 1-16. [https://doi.org/10.1016/0308-0161\(91\)90083-E](https://doi.org/10.1016/0308-0161(91)90083-E)
- [6] Gupta S, I Rychlik. (2007) Rain-flow fatigue damage due to nonlinear combination of vector Gaussian loads. *Probabilistic Engineering Mechanics*, 22: 231-249. <https://doi.org/10.1016/j.probengmech.2007.04.003>
- [7] Rychlik I, S Gupta. (2007) Rain-flow fatigue damage for transformed gaussian loads. *International Journal of Fatigue*, 29: 406-420. <https://doi.org/10.1016/j.ijfatigue.2006.05.006>

## Keyword Index

- 3D Printing 272  
 90-degree Turn 241
- Acoustic Emission 95, 186  
 Acoustic Projector 1  
 Active Vibration Control 217  
 Aircraft Fatigue Test 154  
 Anaerobic Reactor 61  
 Artificial Neural Network 61  
 Asset Monitoring 343
- Barely Visible Impact Damage 29  
 Bending-Shear Model 170  
 Bulk Waves 105
- Cable-Pylon Anchorage Zone 294  
 Cable-Stayed Bridge 294  
 Civil Engineering 233  
 Civil Structure 337  
 Classification 186  
 Composite Materials 186  
 Composites 29, 325  
 Constriction-Resistive Sensor 272  
 Construction 294  
 Continuous Fibre Gratings 21, 37  
 Convolutional Neural Network 186, 217  
 Crack Growth 203  
 Cylindrical Defect 105
- Damage Detection 131  
 Damage Identification 121, 278  
 Data Analysis 61  
 Data Preparation 61  
 Decelerating Decision 311  
 Deep Learning 217  
 Deflection Difference 302  
 Deltoid 161  
 Diagnosis 186  
 Digital Image Correlation 21  
 Direction Change Motion 294  
 Distributed Strain Measurement 21  
 Distributed Strain Sensing 37  
 Drive-by Bridge Inspection 195  
 Driving Simulation 311  
 Dynamic Analysis 233  
 Dynamic Pulse Phase Thermography 29  
 Dynamic Response 278
- Embedded Length Assessment 131
- Fatigue Crack 95  
 FEM 337  
 Fiber Optic Sensing 146
- Fibre Bragg Gratings 45  
 Fibre Optics 21  
 Fibre Optics 37  
 Finite Element Analysis 21, 105, 249  
 Finite Element Modelling 87  
 Floating Cover 71, 79  
 Fragility Curves 255  
 FTTH 331  
 Future Technologies 343
- Geomembrane 79  
 Grating Inscription 45  
 Group Aggregated Anchor System 294  
 Group Velocity 105  
 Guided Wave Features 154  
 Guided Waves 131  
 Guideway Girder 278
- H2-Norm 263  
 H $\infty$  Control 217  
 HDPE Membrane 71  
 Helicopter Gearbox 10  
 High-Speed Maglev 278  
 Home Robot 211
- IMU 241  
 Incremental Dynamic Analysis 255  
 Inerter System 170  
 Inspection Timing 203
- Kalman Filter 113  
 Kissing Bonds 53
- Lamb Wave 95  
 Laminate 249  
 Laser Metal Deposition 37  
 Laying Angle 249  
 Line Scan Thermography 29  
 Long Short-Term Memory 61  
 Loosened Bolts 233  
 Low Energy 53
- Machine Learning 61  
 Macro Fiber Composites 131  
 Magnetic Force 1  
 Maximum Inter-Story Drift Angle 179  
 Maximum Inter-Story Drift 113  
 Measurement Accuracy 225  
 MEMS Accelerometer 225  
 Micro-Damage 325  
 Mid-Story Isolation Buildings 255  
 Migration Index 154  
 Modal Identification 278  
 Monitoring System 225  
 Motion Capture System 241, 287  
 Motion Prediction 241, 294

Multi-Dimensional Gaussian Mixture Model	154	Structure	294
Non-Contact Inspection	71	Telecommunication	331
Non-Destructive Testing	29, 53	Timber Utility Poles	131
Nonlinear Cable Bracing	170	T-joint	161
Nonlinear Guided Waves	325	Tonpilz	1
Operating Performance	311	Topology Optimisation	10
Optical Fiber Sensors	343	Traffic Safety	311
Optical Fiber	161	Trans-Jacket Gratings	45
Optical Fibre Sensors	45	Tuned Mass Damper Inerter	263
Optimal Design	263	UAV Photogrammetry	71
Optimization Design	170	Ultrasound Sensor	272
Osseointegrated Implant	87	Utility Pole	331, 337
Outside-Facility	331	Vehicle Bridge Interaction	195
Parameter Optimization	195	Vehicle Configuration	195
Personal Space	211	Vertical Vehicle Displacement	195
Piezoelectric Sensor Network	121	Vibration Analysis	87
Pipeline	233	Vibration Energy Harvesting	10
Pipes Condition Monitoring	146	Vibration Mitigation	170
Precast Small Box Girder	302	Vibrational Response	87
Preventing Deterioration	217	Vibration-Based Detection	233
Process Monitoring	161	Walking Pattern	211
Quasi-Active Thermography	79	Wave Propagation	95
Random Defects	325	Wood-Frame Construction	179
Reinforcement Learning	203		
Relaxor Ferroelectric Single Crystal	1		
Reliability	186		
Remote Sensing	71		
Residual Stress	37		
Resin Infusion	121		
Risk Communication	211		
Robotic Inspection	29		
Scattered Field	105		
Scums	71		
Segment Experiment	302		
Seismic Risk Assessment	255		
Sensor Fatigue	45		
Sewage Treatment Plant	79		
Sewage Treatment	71		
Shear Structure Modal Coordinates	113		
Shear Value	302		
Sonic Thermography	53		
Space Structures	343		
Speed Reduction Markings	311		
Splicing Technology	302		
Stacking Sequences	249		
State-Space Equation	113		
Stationary Analysis	263		
Structural Health Monitoring	71, 79, 121, 131, 146, 154, 179, 203, 272, 343		

## About the Editors

---

### **Dr Nik Rajic**

Nik Rajic leads the Material State Awareness Group in the Aerospace Division of the Australian Defence Science and Technology Group. His research interests include structural health monitoring, wide-area non-destructive inspection and experimental mechanics. He engages extensively with academia and industry on development and transition of new technologies to improve capability in material state awareness.



### **Professor Martin Veidt**

Martin Veidt is Professor in Applied Mechanics at the University of Queensland in Brisbane, Australia. He has worked in the area of ultrasonic non-destructive evaluation and structural health management for more than 30 years. He has made important contributions in guided wave ultrasonics, nonlinear ultrasonics and numerical modelling of damage initiation and progression in fibre-reinforced composites.



### **Professor Akira Mita**

Akira Mita is the Professor of the Department of System Design Engineering at Keio University. He obtained B.S. from Tohoku University, M.S. from Kyoto University and Ph.D. from the University of California at San Diego. His research interests include sensor network, system identification, and structural health monitoring. He is the recipient Prize of Architectural Institute of Japan, May 29, 2009 on his contribution on structural health monitoring for buildings. He recently proposed a new concept called “Biofied Building.”



### **Professor Nobuo Takeda**

Professor Nobuo Takeda, is currently Chairman, Japan Transport Safety Board (JTSB) and Professor Emeritus, the University of Tokyo. His research includes experimental micromechanics of composites and smart composite structural health monitoring (SHM) and life cycle monitoring (LCM). He has led several Japanese national projects on structural health and process monitoring of aerospace composite structures mainly based on optical fiber sensors. He was President of International Committee of Composite Materials (ICCM, 2015-2016) and Japanese Representative of International Committee on Aeronautical Fatigue (ICAF, 2009-2017).



## **Professor Wingkong Chiu**

W.K. Chiu is a member of academic staff at the Department of Mechanical and Aerospace Engineering, Monash University, Australia. His research interests include structural health monitoring and fatigue analyses of advanced composite structures. Chiu has a strong record in national and international research collaborations with academic institutions and industries. He has a passion for promoting structural health monitoring research in Australia and overseas.

